

Space-borne Application of GNSS Reflectometry For Global Sea State Monitoring

Ka Bian

Submitted for the Degree of
Doctor of Philosophy
from the
University of Surrey



Surrey Space Centre
School of Electronics and Physical Sciences
University of Surrey
Guildford, Surrey GU2 7XH, UK

November 2007

© Ka Bian 2007

Abstract

This research focuses on modelling the relationship between wind conditions, sea roughness and GNSS reflections received from Low Earth Orbit (LEO). The motivation for this study lies in the recent development of a GNSS reflections receiver platform for the UK-DMC satellite and the numerous advantages proposed GNSS Reflectometry can provide in Earth Observation and global disaster monitoring.

The first part of the thesis focuses on the simulation procedure of received GPS-R Delay-Doppler Map (DDM). Airborne GPS-R scatterometric model has been adapted into this space-borne application research. After deriving DDM simulations according to reflection scenario, the results of two-dimensional data-model fitting are presented and analysed. The sensitivity discussion of current GPS-R model suggests some limitations of the modelling method, especially under medium and high wind speed ranges.

In the second part, we investigate the inversion scheme of DDMs for the purpose of extracting a statistical wave model empirically. The similar model structure of DDM simulation is used but the processing order is turned over. After deconvolution, DDMs are inversed back to spatial energy maps and spatial slope probability maps. Three inversion algorithms are developed and compared. Preliminary synthetic and real data experiments give evidence of the feasibility of the inversion methodology.

Finally, in the third part of this research, a new geometric wave slope statistical model is discussed in the context of wave field simulations. The sensitivity of obtained statistical model is discussed in terms of wind speed, wave direction and observing incident angle. This provides an alternative view point to look into the wave slope probability properties and compensate the traditional theoretic and empirical wave modelling methods.

Key words: GNSS-Reflectometry, Delay-Doppler Map inversion, wind conditions, sea surface roughness, slope probability density function, statistical wave slope model.

Email: K.Bian@sstl.co.uk; WWW: <http://www.ee.surrey.ac.uk/SSC/>

Acknowledgements

Firstly I would like to express my gratitude to the Surrey Space Centre (SSC) at the University of Surrey, who sponsors me through these three years of learning and research, enlarging my scope and giving me a priceless experience of all the ups and downs during this PhD time.

I wish to acknowledge my supervisors Dr. Stephen Mackin, Dr. Alexandre Pechev, and the Director of SSC, Professor Sir Martin Sweeting, for their considerable guidance, encouragement and tolerance through my research program. Many thanks to Mounir Adjrad for his significantly helpful advice on my research work. I also appreciate the help from Dr. Scott Gleason and Dr. Martin Unwin, for providing the data, and their constructive remarks on my transfer report and presentations.

I would like to say thanks to all the colleagues and friends in SSC, those who have graduated and those who are still in. They help me overcome the language problems and the cultural differences, sharing good times with me. Special thanks go to David Bamber, and all my family members in China for their never ending support and encouragement.

Last but not least, I wish to dedicate this thesis as a tribute to Dr. Tanos Elfouhaily, who passed away suddenly in July 2006. His scientific achievements will stay in this world and keep inspiring many other people like me.

Table of Contents

1. Introduction

1.1	Overview	1-1
1.2	Motivation of this research	1-3
1.3	Research contributions	1-7
1.4	Thesis structure	1-9
	<i>References</i>	1-10

2. Background and Literature Review

2.1	Wind and waves	2-1
2.2	GNSS and GPS	2-5
2.3	GPS-R research status	2-8
2.4	UK-DMC GPS-R experiment	2-10
2.5	Summary	2-12
	<i>References</i>	2-13

3. PDF-based GPS-R Scatterometric Model

3.1	Introduction	3-1
3.2	Wave spectrum model	3-2
	3.2.1 Theory	3-2
	3.2.2 Experimental wave spectrum models	3-6
3.3	Wave slope probability concept	3-10
	3.3.1 Overview	3-10
	3.3.2 Cox-Munk modelled slope PDF	3-12
	3.3.3 Elfouhaily modelled slope PDF	3-15
3.4	Electromagnetic (EM) model	3-17
	3.4.1 Z-V model	3-17
	3.4.2 NRCS calculation	3-18

3.5	Delay-Doppler Map generation	3-20
3.5.1	GPS signal acquisition procedure	3-20
3.5.2	Creation of DDM from spatial energy distribution	3-21
3.5.3	GPS Ambiguity Function	3-22
3.6	Conclusions	3-24
	<i>References</i>	3-25

4. GPS-R Delay Doppler Map Simulation

4.1	Introduction	4-1
4.2	Simulation procedure	4-1
4.2.1	Searching for specular point	4-2
4.2.2	Choosing valid datasets	4-5
4.2.3	Coordinate system rotation	4-7
4.2.4	Antenna pattern	4-7
4.2.5	Delay and Doppler calculation	4-9
4.2.6	UK-DMC DDM processing	4-10
4.2.7	Image correlation and geometrical compensation	4-11
4.3	Case studies	4-12
4.3.1	R13 data	4-13
4.3.2	R12 data	4-19
4.3.3	Summary	4-22
4.4	Sensitivity analysis of current GPS-R model	4-22
4.5	Conclusions	4-25
	<i>References</i>	4-26

5. Delay-Doppler Map Inversion Model

5.1	Introduction	5-1
5.2	DDM Inversion scheme	5-1
5.3	DDM deconvolution	5-4
5.3.1	Review	5-4
5.3.2	Fourier-Wavelet algorithm	5-7
5.3.3	Wiener vs. ForWaRD	5-8
5.3.4	Least-Square and Richardson-Lucy vs. ForWaRD	5-13

5.4	Spatial patch searching method	5-17
5.4.1	Cartesian vs. Polar	5-17
5.4.2	Delay Contour Grid (DCG) method	5-18
5.5	Conclusions	5-21
	<i>References</i>	5-22

6. DDM Inversion : from Bin to Patches

6.1	Overview	6-1
6.2	The Average Method	6-3
6.2.1	Methodology	6-3
6.2.2	Synthetic DDM inversion	6-4
6.3	The Differential Method	6-10
6.3.1	Two-bin Differential Method	6-10
6.3.2	Three-bin Differential Method	6-13
6.3.3	Synthetic DDM inversion	6-15
6.3.4	UK-DMC DDM inversion	6-19
6.4	1-D Probability Inversion	6-21
6.4.1	Methodology	6-21
6.4.2	Synthetic DDM 1-D inversion	6-21
6.4.3	UK-DMC DDM 1-D inversion	6-23
6.5	Conclusions	6-30
	<i>References</i>	6-31

7. Geometrical Modelling of Wave Slope PDF

7.1	Introduction	7-1
7.2	Geometric modelling methodology	7-3
7.2.1	Wave height field modelling	7-3
7.2.2	Slope angle estimation	7-3
7.3	Sensitivity analysis of geometrical slope PDF model	7-6
7.3.1	Wind speed effect	7-6
7.3.2	Directional wave effect	7-8
7.4	Observing incident angle effect in reflection geometry	7-11
7.4.1	Case 1 – Patch on receiver’s side	7-11

7.4.2	Case 2 – Patch on GPS emitter’s side	7-16
7.4.3	Summary	7-18
7.5	Conclusions	7-19
	<i>References</i>	7-20

8. Conclusions and Future Work

8.1	Conclusions	8-1
8.2	Future work	8-3
8.2.1	Empirical wave slope PDF model derivation	8-3
8.2.2	Ocean reflection rendering based on geometrical wave model ..	8-4
	<i>References</i>	8-4

Appendix I: Delay-Doppler Map Simulation Experiments

1.	R10 Dataset	AI-1
2.	R12 Dataset	AI-5
3.	R13 Dataset	AI-9
4.	R14 Dataset	AI-13
5.	R15 Dataset	AI-17
6.	R18 Dataset	AI-21

Appendix II: Sensitivity Analysis of Elfouhaily Modelled Slope PDF

1.	Wind speed effect	AII-1
2.	Wind direction effect	AII-2
3.	Observing incident angle effect	AII-5

Appendix III: The Differential Method Inversion of R12 and R13

1.	R12 Case	AIII-1
2.	R13 Case	AIII-3

List of Symbols

a	Wave amplitude
b_{xy}	Co-variance of Gaussian slope PDF
B_l, B_h	Low/high frequency correction term of Elfouhaily Elevation Spectrum
c	Phase velocity
c_g	Group velocity
d	Local water depth
ds	Patch area on reflection surface
d_x, d_y	Displacements between two images
D	Film density
E	Wave energy Exposure value
f	Wave frequency
f_d	Doppler shift of reflection signal
g	Gravitational constant
g_1, g_2	Two images
G_1, G_2	Spectrum contents of two images
G_R	Receiving antenna power gain
G_T	Transmitting antenna power gain
h	Point Spread Function in convolution
H	Sea surface irradiance
$H_{1/3}$	Significant Wave Height (SWH)
H_i, H_j	Hermite polynomials
I_C	Pixel values of noise-free un-blurred DDM
I_B	Pixel values of noisy AF-blurred DDM
I_D	Pixel values of deconvolved DDM
k	Wave number
K_*	Wave-number boundary,
L	Reflection path length from GPS to patch and then to UK-DMC Wave length

\bar{n}	Normal vector of local sea surface patch
N	Radiance of sea surface in the line of sight
	Number of signal samples
p	Wave slope probability
P_r	Reflected signal power from sea surface patches
P_T	Transmitter power output
\vec{q}	Normal vector of sloped patch, which bisects emitter-patch-receiver angle
q_z	Projection of \vec{q} along z direction
\vec{q}_\perp	Projection of \vec{q} in xy plane
Q	Geometry-related factor in reflection power calculation
R_R	Range between patch and GPS-R receiver
R_T	Range between GPS satellite and patch
s_x, s_y	Slope components of x, y directions
S	Slope probability of reflection patch
\cdot	Omni-directional Elevation Spectrum
S_M	Averaged wave spectrum
S_n	Wave spectrum
T	Coherent integration time
	Constant factor in reflection power calculation
$U_{19.5}$	Wind speed measured at a height of 19.5 m above the sea surface
$x_1 y_1 z_1$	Local specular-point-centred coordinate system
$x_D y_D z_D$	Coordinate frame for specular point search
z_x, z_y	Slope components of x, y directions
α	Observing incident angle
β	Elevation angle of patch
ζ	Ocean surface displacement
λ	Angle between the principle axis of camera and the reflected ray
	GPS L1 carrier wavelength
λ^f	Fourier shrinkage term
λ^w	Wavelet shrinkage term
μ, ν	Coordinate position on the film plane
ν	Observing Incident angle
\vec{v}	UK-DMC satellite velocity vector
ρ	Reflection coefficient
$\vec{\rho}$	Location vector from specular point towards patch

ρ_w	Water density
σ_0	Normalised Radar Cross Section (NRCS).
σ_1, σ_2	Variances of Gaussian slope PDF
φ	Azimuth direction of waves
φ_0	Wind direction in the observing baseline coordinate system
τ	Transmission coefficient of sea water Time delay of reflected signal
τ_c	C/A code chip length
ϕ	Scalar function in wavelet analysis
ψ	Wavelet function in wavelet analysis
ω	Angular frequency
\mathfrak{R}	Geometric Fresnel coefficient

Chapter 1. Introduction

1.1 Overview

We human beings are such fragile creatures when faced with the devastating wrath and upheaval of ocean borne disasters. Thousands of people lost their lives during the 2004 Indonesia tsunami [BBC 2005], and 80% of New Orleans city was left under a flood caused by Hurrican Katrina [BBC 2006]. Sea conditions have also played an important role in several severe ferry accidents in recent years [Gleason 2005]. Shipwrecks and leaking oil tankers, such as the Prestige sunk in 2002, cause great environmental damage which is almost irreversible [NS 2003]. A global ocean disaster monitoring system is therefore urgently required. This system should have thorough coverage of sea states monitoring and rapid response to potential ocean disasters.

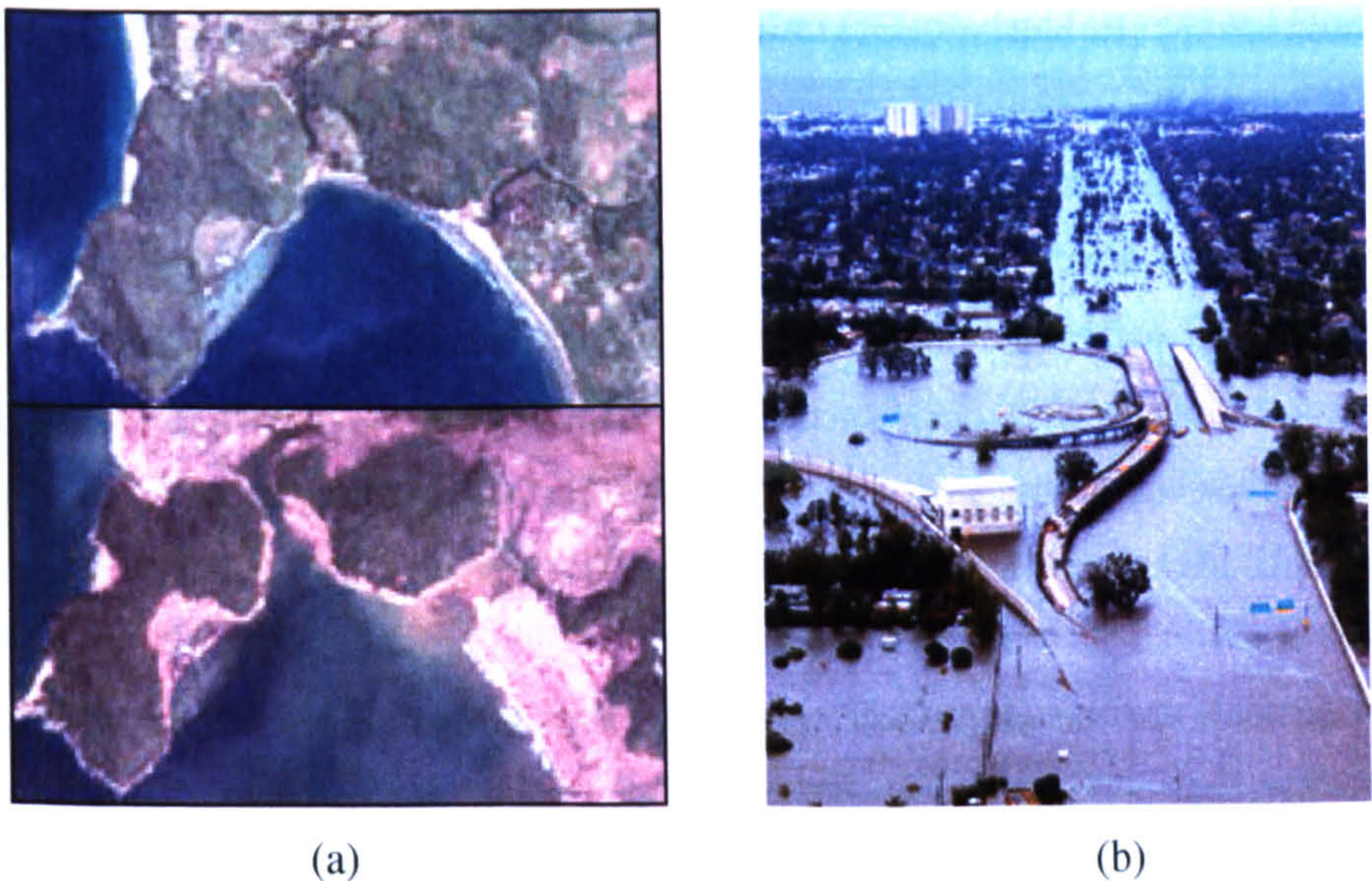


Figure 1-1: Ocean disasters in recent years. (a) Satellite images of 2004 tsunami impact - Banda Aceh (Indonesia) before and after the destructive waves hit [NG 2005].
(b) Flooded area of northwest New Orleans [BBS 2006].

In addition to such an ocean disaster warning system, long-term reliable global ocean status data is also needed for purposes such as climate modelling and meteorological research. Approximately 70% of the Earth is covered by the ocean. This gigantic water body plays a

very significant role in water-air energy exchange and directly affects atmospheric activities. Any small variation in sea conditions may cause potential great disturbance somewhere else. The fluctuations our climate system is now undergoing increase the difficulties for precise climate modelling and prediction [NAS 2003] [RS 2005]. Accurate, stable and long term observation of ocean and atmosphere is required in order to monitor and understand global climate change.

In recent decades, satellite-based remote sensing has become an increasingly important tool in the field of oceanography. Compared to traditional *in-situ* data collection, mainly performed by ships and buoys, remote sensing techniques can provide more comprehensive knowledge of ocean activities. Ocean-based observations from such satellite oceanography platforms are performed by either passive or active sensors. Passive sensors can measure visible, infrared and microwave wavelength reflection and emission from oceans. These data can be processed to obtain information of ocean colour, water quality, sea-surface thermal transfer conditions, surface roughness, films and slicks. Active radar measures the return time and shape of the emitted pulse allowing for study of ocean altimetry and sea states. The highly frequent and detailed knowledge obtained through satellite ocean observations has already significantly improved our understanding of oceanography in biological, chemical and physical research fields [Stewart 1985] [Robinson 2003]. Satellite oceanography has also benefited from the advancements in space technologies over recent years. Modern radar equipment, such as high-resolution imagers and Synthetic Aperture Radar (SAR), has enhanced the accuracy of ocean-based measurements. Small satellite constellation concepts have shown great potential for enlarging the scope of oceanic remote sensing by reducing the mass and consequent launch cost of satellite missions. Recent developments in satellite oceanography have investigated the use of Global Positioning System (GPS) signals, reflected from the ocean surface, to detect sea states, which has generated much interest.

GPS was first built for the purpose of positioning and navigation. However, its usage has extended far beyond the designer's original intentions, providing a rich source of signals in the remote sensing field. GPS reflectometry (GPS-R), literally, is to study the properties of the Earth's surface using reflected GPS L-band signals, with Time of Arrival (TOA) and frequency content being the main object for research. GPS-R signals have been proven to be sensitive to sea states and near-surface wind conditions [Zavorotny 2000][Soulat 2004a], soil moisture [Masters 2000][Torres 2004], ice states [Komjathy 2000][Wiehl 2003], atmospheric electronic contents (ionosphere and troposphere) [Katzberg 2001][Pallares 2005] and current motions [Cardellach 2001]. In the next few years, GPS satellites will be upgraded to more powerful signals and more civilian carrier frequencies [Fontana 2001][Lazar 2002]. The

European navigation system Galileo [Benedicto 2000][ESA 2006] and the Geostationary Navigation Overlay Service (EGNOS) [Toran-Marti 2004][Ventura-Traveset 2005] are expected to significantly enrich this research area .

Realising the potential values of the GPS-R technology, Surrey Satellite Technology Limited (SSTL) launched the UK-DMC (Disaster Monitoring Constellation) satellite in September 2003, which accommodated a special antenna capable of receiving GPS-R data. The ground station in SSTL can schedule, receive and process GPS-R data routinely from different oceans across the Earth. The UK-DMC is the only GPS-R experimental platform currently in operation and represents a milestone in GPS-R research, providing an essential data source for future analysis and modelling. Previous GPS-R research using SSTL's UK-DMC has demonstrated that GPS signals scattered from the ocean surface can be detected from a Low Earth Orbit (LEO) satellite altitude. Although the signals have been proven to have a definite correlation with wind conditions (near the sea surface), sea ice age and soil humidity [Gleason 2006], a detailed model of such interactions has yet to be realised.

In continuation of the above, the primary aim of this research is to model the interaction of GPS scattered signals with the ocean surface, under variable sea roughness conditions, and establish practical methods to estimate sea states from GPS-R data, as received from a LEO space-borne platform. To achieve this goal, an existing air-borne GPS-R model is first adapted to analyse the UK-DMC GPS-R data for the purposes of deriving sea roughness and sea surface wind information. Through systematic analysis, however, the limitations of such a theoretic model are identified. A new methodology that uses the reflected GPS signal pattern to predict statistical parameters of the local sea surface is therefore developed and proposed as a candidate for deriving future GPS-R models. Several key algorithms in this method have been tested using simulations and real GPS-R datasets from the UK-DMC receiver. Alongside preliminary research of GPS-R empirical model, we also explore a sea-surface simulation-based statistical modelling method. This provides comparative reference for future extensive GPS-R data analysis given incomplete and inaccurate in-situ ground truth.

1.2 Motivation of this research

Although GPS-R technology has raised broad interests across the oceanographic field, owing to its advantages in ocean observation, it is still in a relatively immature state with many potential issues. A GPS-R receiver is a multi-static passive radiometer, i.e., the emitter and

the receiver are not on the same platform. In comparison to conventional mono-static radar altimeters and scatterometers, such as TOPEX / Poseidon, ERS-RA and QuikSCAT, the main advantages of this multi-static receiver are:

1. Coverage

Currently, there are more than 25 actively broadcasting satellites in the GPS constellation providing intensive signal coverage globally. If such array of signals can be utilised, the spatial-temporal coverage of an ocean-observation-based GPS-R system would be significantly increased. Due to the Code Division Multiple Access (CDMA) signal property, each LEO GPS receiver is able to observe more than 8 GPS reflection signals simultaneously, whilst within the line of sight. An active radar instrument, however, can only observe one patch of sea surface at around nadir pointing position.

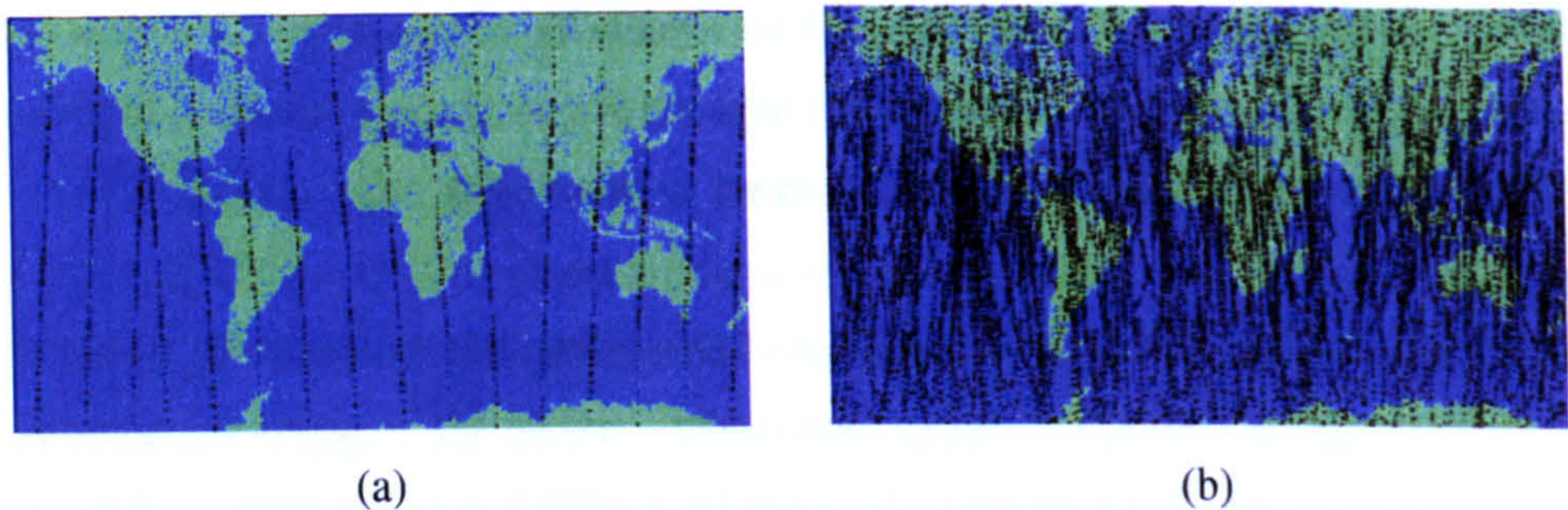


Figure 1-2: Global visions for 24 hours [Martin-Neira 1998].

(a) altimeter sub-satellite track. (b) simulated LEO GPS-R receiver satellite scenario.

2. Cost

Passive multi-static radar satellites consume less power and require less complex payloads and platform support (such as solar panel and emitter antenna) than their active radar equivalents. GPS-R receivers are very similar to GPS direct signal receivers. By using the state-of-art technology and off-the-shelf components, onboard GPS-R receiver can be compact, economical and easy to design. Such features simplify GPS-R platform integration and maintenance, and significantly reduce the cost of GPS-R receiver satellite. Therefore it is affordable and practical to form a constellation of satellites with GPS-R platforms such that ocean observation coverage may be increased.

A future constellation of LEO satellite with GPS-R capabilities would represent a momentous step forward in oceanographic observation. Although it may not replace the well-established mono-static radars, GPS-R would easily constitute a viable and complementary system. However, there exist many difficulties in achieving this target, among which some major barricades for GPS-R system include:

1. Data shortage

There is a lack of experimental data for GPS-R research, especially from space-borne altitudes. The insufficiency of data and corresponding in-situ ground truth is a principle problem in the modelling procedure, which hampers complete validation of theory models and development of empirical models.

2. Weak signal

The reflected GPS signal is much weaker than active radar signals, which makes it difficult to track and process. Initial link budget calculations have roughly estimated that the received GPS-R signal power is about -170 dBW [Martin-Neira 1993], which is 10 dBW lower than direct L1 C/A signals (-160dB) [Wong 2005]. There will be a trade-off between incoherent integration time for noise reduction and dynamic capability of the measurement.

3. Insufficient model

For theoretical analysis the microwave scattering phenomenon from ocean surface is very complicated to quantify. The model currently used in air-borne GPS-R sea state detection is based on simple assumptions and has not been verified systematically. This model may not be accurate enough for practical usage, especially in space-borne applications.

4. Accuracy limitation

GPS C/A code ranging limits the GPS-R measurement accuracy, such that it falls short of C-band or Ku-band frequency microwave used by mono-static radars. GPS carrier phase measurements have been considered to overcome this impediment, but such techniques are still in an early research stage [Rivas 2003] [Cardellach 2004].

In the near future, the above data shortage problem will most likely be solved, initially by the increased use of the UK-DMC GPS-R platform, and subsequently the launch of further small/micro satellite with GPS-R receivers. In terms of the weak signal problem, Gleason's previous work has proven that following post-data processing, GPS-R data reflected from Earth surface can be detected and that the signal pattern correlates with surface reflection properties [Gleason 2006]. Signal strength makes quantification difficult however. This research focuses on the insufficient modelling problem in GPS-R technology. Through simulations and real space-borne data analysis, a novel method is proposed to statistically model the relationship between the GPS reflection pattern and ocean surface roughness. More GPS-R data processing following this method, combined with filter approach, will give an

empirical model for practical GPS-R sea states and surface wind measurements. Theoretic modelling research can also benefit from this data processing procedure. For the accuracy problem, new signal structure has been designed for Galileo Navigation system [Blunt 2007] apart from signal carrier phase interferometric research. This problem is beyond the scope of this thesis.

In conclusion, the potential applications of GPS-R have grown widely since its initial proposal in later 80s [Hall 1988], with particular advantages being found in the field of oceanic remote sensing. Research of GPS-R applications from satellite altitude has been held back however, due to the lack of experimental space-borne platforms. The UK-DMC satellite provides a unique long-term opportunity to collect and study GPS-R signals from Low Earth Orbit (LEO) altitude. Previous studies using UK-DMC GPS-R data have demonstrated that GPS signals scattered from the ocean surface can be detected following offline processing. These signals have been proven to have a definite correlation with wind conditions (near sea surface), sea ice age and soil humidity. These significant findings have confirmed the feasibility of using UK-DMC data for GPS-R research and opened the gate for a wide range of potential investigation directions in this field.

This PhD study chooses to focus on sea states detection using space-borne GPS-R, with topics such as ice age and terrain surface detection being deemed beyond the scope of this research. Though received UK-DMC GPS-R data have been qualitatively connected to sea states parameters in previous research, such preliminary exploration still needs to be carried into a more quantitative application level. The motivation for this research is to evaluate and improve the existing GPS-R sea states modelling technique, and utilise UK-DMC GPS-R data to validate such methods.

1.3 Research contributions

The contributions of this research relate to GPS-R signal modelling and statistical wave property study, and can be separated into four categories:

1.3.1 Analysis of UK-DMC GPS-R data in Delay and Doppler dimensions

Although, earlier space-borne GPS-R research has demonstrated the correlations between sea states, reflection geometry and received data patterns, this has mainly been simulated in the

Delay, or time, dimension. This research is the first to systematically process and analyse the UK-DMC GPS-R data in both Delay and Doppler dimensions in the form of Delay-Doppler Map (DDM). The procedure of proposed data processing method includes geometric specular point calculation, Doppler bias reduction, simulated Delay-Doppler Map generation and data-model matching.

1.3.2 Evaluation of air-borne GPS-R model for space-borne applications

To measure the capacity of GPS-R for sea states detection from satellite altitude, we investigate several test experiments using UK-DMC datasets and analyse the data-model fitting results quantitatively. From the case studies, we have discovered that the current air-borne GPS-R scatterometric model is particularly insensitive to medium and high range wind speeds. From such analysis we are able to conclude that the extraction of such wind information from received space-borne GPS-R data is difficult without a-priori knowledge.

1.3.3 Development of Delay-Doppler Map inversion scheme

Traditionally GPS-R data is analysed in either Delay or Doppler dimension. As detailed in section 1.3.1 this research considers analysis of space-borne GPS-R data in both Delay and Doppler dimensions in the form of DDM. Despite this, and as identified in section 1.3.2, extraction of wind information from space-borne GPS-R data remains difficult. As such, we propose a DDM inversion method, which is able to calculate the spatial distribution of scattered GPS signal energy leaving the ocean surface. This allows us to form a better understanding of the statistical characteristics of ocean waves which, with further study, should allow an empirical statistical wave model to be derived from received GPS-R datasets. The DDM inversion scheme was first tested using simulated data and then later verified with real UK-DMC GPS-R datasets. With both simulated and real data the inversion procedure was able to build a probability map of spatial wave slopes. The three main steps of the DDM inversion are described below.

1. Deconvolution

The GPS Ambiguity Function (AF) causes blurring within DDMs. The first step is therefore deconvolution, such that the effect of GPS AF can be removed. In addition to traditional Fourier-based and Bayes-based methods a newly developed Fourier-Wavelet hybrid approach is tested on simulated DDMs. The Fourier-Wavelet method shows most promise in DDM deblurring and is therefore adopted in our inversion scheme as the prime candidate for the deconvolution.

2. Spatial patch searching

In order to accurately map the distribution of GPS-R energy leaving the ocean surface the spatial reflection patches that correspond to each Delay-Doppler bin must first be found, prior to the determination of spatial energy distribution. Although this is normally achieved with a Cartesian based searching method, a new approach, that simplifies the procedure from 2-D to 1-D, is also developed. This new approach is mapped according to Delay contours on reflection surface and approximately equivalent to a near-polar coordinate system. As such this technique solves a resolution mismatching problem introduced by traditional Cartesian-based searching method.

3. Bin-to-Patch conversion

Bin-to-Patch conversion is the key step in our DDM inversion scheme. Three algorithms have been established for re-distributing the power from each Delay-Doppler bin to its corresponding spatial patches upon the ocean surface. Each Delay-Doppler bin may correspond to multiple ground surface patches. Each algorithm therefore attempts to re-distribute a bin's energy according to a different pattern. The Average Method and the Differential Method both consider Delay and Doppler information such that the probability distribution of wave slopes can be mapped into two dimensions. The 1-D Inversion Method, however, only considers dissemination of energy into the Delay domain. While the first two methods have good spatial accuracy, the final method has stronger robustness to noise. The 1-D Inversion Method has been tested with real UK-DMC data to obtain actual measurement of wave slope probability. This has been compared with Gaussian approximations of wave slope probability that are conventionally applied in GPS-R modelling.

1.3.4 Geometric modelling study on wave statistical property estimation

If we consider the probability of different wave slope angles for a given ocean patch, over a certain time period, then this will result in a probability density function (PDF), which we assume valid to all patches nearby, and vice versa. Based on this assumption, we propose a new viewpoint that models the wave slope PDF geometrically. This method is inspired by sea surface simulation for visual effect demonstrations. The simulation of wave surfaces from Pierson-Moskowitz model has been adopted into the modelling procedure. An estimation algorithm has been developed to calculate the normal vector for each curved slope surface. Geometrically modelled slope PDFs have been analysed as a function of wind speeds and wave directions.

Since observing incident angle is an important factor in GPS-R reflection geometry, its effects on received GPS-R signal properties, when using the geometric modelling method, are also discussed. The analysis of such effects may be useful in further understanding of GPS-R signal patterns and improving the GPS-R sea states modelling accuracy.

1.4 Thesis Structure

This thesis consists of 8 chapters. Chapter 1 is the overview of the whole research.

Chapter 2 describes the background of this research. Relevant concepts of wind-wave detection and global navigation systems are first summarised. A literature review of previous theoretical and experimental GPS-R research is reported. Then the following section outlines the UK-DMC GPS-R platform, which is used to provide solid verification data to support this research.

Chapter 3 details the structure of the existing air-borne GPS-R scatterometric model. In this structure, wave spectrum models and slope PDFs are used to describe the sea surface characteristics, and an electro-magnetic (EM) model is employed to re-construct the reflection geometry. The spatial energy distribution of the reflected signals from the ocean surface is modelled and then converted into Delay-Doppler dimensions as viewed by the onboard GPS-R sensor.

Chapter 4 describes the simulation procedure step by step and compares the simulated results to real data. GPS-R data from two UK-DMC case studies are analysed quantitatively. The sensitivity of the traditional wave slope PDF model to wind information is analysed, with problems, which limits the sea states monitoring ability of GPS-R platforms, being revealed.

To overcome the difficulties identified in Chapter 4, Chapter 5 proposes a methodology to inverse the above model, such that received GPS-R data in the form of Delay-Doppler Map (DDM) is converted into a spatial energy distribution map. Furthermore, we highlight the possibility of empirically constructing a new statistical wave model from this spatial energy map. Apart from describing the scheme used for DDM inversion, we also explore the DDM deconvolution algorithms and a new approach for matching spatial patches to Delay-Doppler bins.

Chapter 6 continues the discussion in DDM inversion, focusing on the spreading of Delay-Doppler bin power into corresponding spatial patches, which is the key step of the inversion procedure. Three methods of distributing bin power are proposed, each with a different dispersal pattern. Alongside the algorithm explanation, simulated inversion results are presented, allowing the three methods to be compared in term of robustness. The results of DDM inversion using real UK-DMC data are also examined.

Chapter 7 studies the statistical properties of waves from a geometric modelling viewpoint. We describe the procedure of estimating the wave slope PDF, following simulation of wave height fields, and analyse the sensitivity of the output PDF to wind speed and directional waves. The final section in this chapter discusses the effect of observing incident angle on reflection geometry.

Chapter 8 concludes the above research and proposes some future work in this area.

References

- [BBC 2004] BBC indepth Tsunami disaster,
http://news.bbc.co.uk/1/hi/in_depth/world/2004/asia_quake_disaster/default.stm
- [BBC 2005] BBC indepth Hurricane Katrina,
http://news.bbc.co.uk/1/hi/in_depth/americas/2005/hurricane_katrina/default.stm
- [Benedicto 2000] J. Benedicto, S.E. Dinwiddy, G. Gatti et al., GALILEO: Satellite System Design and Technology Developments, ESA document, November 2000
http://esamultimedia.esa.int/docs/galileo_world_paper_Dec_2000.pdf
- [Blunt 2007] P. Blunt, Advanced global navigation satellite system design, PhD Thesis, Surrey Space Center, Surrey Satellite Technology Ltd., Surrey, UK, February 2007
- [BBS 2006] Human Rights Day and Hurricane Katrina, BBS News website,
<http://bbsnews.net/article.php/20061209232342607>, December 2006

- [Cardellach 2001] E. Cardellach, M. Belmonte, A. Rius et al., Ocean Tide Measurement by Scattered Signal from the Global Positioning System, AGU Fall Meeting proceedings, December 2001
- [Cardellach 2004] E. Cardellach, C.O. Ao, M. de la Torre-Juarez et al., Carrier phase delay altimetry with GPS-reflection/occultation interferometry from low Earth orbiters, Geophysical Research Letters, Vol.31, Issue 10, May 2004
- [ESA 2006] The First Galileo Satellites: Galileo In-Orbit Validation Element (GIOVE), ESA publication 2006, <http://www.esa.int/esapub/br/br251/br251.pdf>
- [Gleason 2005] S. Gleason, Sea Monitoring for Detecting Dangerous Seas and Tsunamis Using Space Based GNSS Bi-static Radar Technology, Geoscience and Remote Sensing Symposium, IGARSS 2005 Proceedings, Vol.7, page 4773-4776, July 2005
- [Gleason 2006] S. Gleason, PhD Thesis, Surrey Space Centre, Surrey Satellite Technology Ltd., Surrey, UK, December 2006
- [Fontana 2001] R.D. Fontana, T. Stansell, W. Cheung, The Modernized L2 Civil Signal, GPS World, September 2001
- [Hall 1988] C. Hall and R. Cordey, Multistatic Scatterometry, IEEE IGARSS '88 Proceedings, Edinburgh, Scotland 1988
- [Katzberg 2001] S.J. Katzberg, J.L. Garrison, Surface Reflected Signals from the Global Positioning System for Ionospheric Measurements: Experimental Results at Aircraft Altitudes, International Journal of Remote Sensing, Vol.22, No. 4, March 2001
- [Komjathy 2000] A. Komjathy, J. Maslanik, V.U. Zavorotny et al., Sea Ice Remote Sensing Using Surface Reflected GPS Signals, Geoscience and Remote Sensing Symposium, IGARSS 2000, Vol. 7, page 2855-2857, July 2000
- [Lazar 2002] S. Lazar, Modernization and the Move to GPS III, Crosslink, Satellite Navigation, Vol.3, No.2, 2002
<http://www.aero.org/publications/crosslink/summer2002/07.html>
- [Masters 2000] D. Master, V. Zavorotny, S. Katzberg et al., GPS Signals Scattering from Land for Moisture Content Determination, Geoscience and Remote Sensing Symposium, IGARSS 2000, Vol. 7, page 3090-3092, July 2000
- [Masters 2004] D. Masters, Surface Remote Sensing Applications of GNSS Bistatic Radar: Soil Moisture and Aircraft Altimetry, PhD Thesis, University of Colorado at Boulder, 2004

- [Martin-Neira 1993] M. Martin-Neira, A Passive Reflectometry and Interferometry System (PARIS) – Application to Ocean Altimetry, ESA Journal, Vol.17, No. 4, 1993
- [Martin-Neira 1998] M. Martin-Neira, C. Mavrocordatos and E. Colzi, Study of a Constellation of Bistatic Radar Altimeters for Meso-scale Ocean Applications, IEEE Trans. On Geoscience and Remote Sensing, Vol.36, No.6, November 1998.
- [NAS 2003] Climate Change Science: An Analysis of Some Key Questions. National Academy of Science, Washington USA, 2003, <http://www.nap.edu/html/climatechange>
- [NG 2005] Photo Gallery: Tsunami Aerial Views, National Geographic website, <http://green.nationalgeographic.com/environment/photos/tsunami-aerial/bandaacehaftertsunami.html>, January 2005 (photograph from Digital Globe)
- [NS 2003] Prestige oil spill far worse than thought , New Scientist website, August 2003 <http://www.newscientist.com/article.ns?id=dn4100>
- [Pallares 2005] J.M. Pallares, G. Ruffini, L. Ruffini, Ionospheric Tomography Using GNSS Reflections, IEEE Transactions on Geoscience and Remote Sensing, Vol. 43, No. 2, February 2005
- [Rivas 2003] M. Belmonte-Rivas, M. Martin-Neira, Tracking the GPS Carrier after Reflection on a smooth sea surface, EGS-AGU-EUG Joint Assembly meeting, April 2003
- [Robinson 2003] Ian Stuart Robinson, Measuring the Oceans from Space: the Principles and Methods of Satellite Oceanography, Springer-Verlag Berlin and Heidelberg GmbH & Co. K, January 2003, ISBN-10: 3540426477
- [RS 2005] Facts and Fictions about Climate Change, the Royal Society, UK, March 2005 <http://www.royalsoc.ac.uk/downloaddoc.asp?id=1630>,
- [SOS 2005] Satellite Observing Systems Ltd., GANDER storm damage, <http://www.satobsys.co.uk/GANDER/webpages/ganstorm.html>
- [Soulat 2004a] F. Soulat, M. Caparrini, O. Germain et al., Sea State Monitoring Using Coastal GNSS-R, Geophysical Research Letters, June 2004
- [Soulat 2004b] F. Soulat, Sea Surface Remote-sensing with GNSS and sunlight reflections, PhD thesis, University Politecnica de Catalunya / Starlab, 2004
- [Stewart 1985] Robert H. Stewart, Methods of Satellite Oceanography, University of California Press, April 1985, ISBN-10: 0520042263.

[Torres 2004] O. Torres, M.S. Grant and D. Bosch, Soil Moisture and Vegetation Effects on GPS Reflectivity From Land, American Geophysical Union meeting, December 2004

[Toran-Marti 2004] F. Toran-Marti, J. Ventura-Traveset, The ESA EGNOS Project: the first step of the European Contribution to the Global Navigation Satellite System (GNSS), http://www.egnospro.esa.int/Publications/EGNOS%20iono%20perfo%20ENC%202005_final.pdf , NAVIGARE, 2004

[Ventura-Traveset 2005] J. Ventura-Traveset, L. Gauthier, F. Toran et al., EGNOS Status, Performances and Planned Evolutions (2006-2010), European Navigation Conference 2005 <http://www.egnospro.esa.int/Publications/EGNOS%20Status%20and%20Evolution%20ENC%202005.pdf>

[Wiehl 2003] M. Wiehl, B. Legresy, R. Dietrich, GNSS Signal Reflections from Ice Sheets and Their Remote Sensing Potential for Upper 100m Firm, EGS-AGU-EUG Joint Assembly meeting, France, April 2003

[Wong 2005] Ronald Wong, GPS Carrier Phase Multipath Mitigation by Spectral Analysis for LEO Satellite, PhD Thesis, Surrey Space Centre, University of Surrey, UK, 2005

[Zavorotny 2000] Z.U. Zavorotny, A.G. Voronovich, S.J. Katzberg et al., Extraction of Sea State and Wind Speed from Reflected GPS Signals : Modelling and Aircraft Measurements, GeoScience and Remote Sensing Symposium Proceedings, IGARSS 2000, Vol. 4, Page 1507-1509, July 2000

Chapter 2. Background and Literature Review

2.1 Wind and waves

Ocean waves are sea surface oscillations, which can be classified into two categories according to their sources. Small scale impacts, like a rock thrown into the sea, or large impacts, as with earthquakes, generate *Impact waves*. *Wind waves* however, are generated by momentum transferring from wind to water, which is the principle mechanism of heat flux transfer between the atmosphere and the ocean surface. Individual water particles on the sea surface rarely move with the waves, but rather they transfer energy and momentum by moving in an orbital path around their original positions [Kinsman 1965] [Knowles 2004]. This research focuses on wind waves.

Wind speed, length of time (duration) and distance (fetch) of open water that the wind has blown over, are the three main factors that influence the formation of wind waves. Although water depth also affects wave properties, this research only consider deep water cases. Shallow water waves are beyond the scope of this discussion. The three different types of wind waves are ripples (capillary waves), seas and swells. Ripples are the smallest waves and have periods less than 0.1 sec. They are generated by a small puff of wind and restored by surface tension. Seas have comparatively longer periods, are generated under sustained wind or storms and are restored by gravity. This means the waves can last longer following the decay of the initial wind force. Seas are normally composed of waves of different directions and wavelengths. When travelling away from the wind origin, these waves will spread and form swells, which are generally more stable and well-defined than seas [Holben 2000] [Nave 2005]. An important fact in wind-wave relations is that the energy of waves increases rapidly with wind speed. In fact, the energy and the amplitude of waves are proportional to the 4th and the 3rd power of the wind speed, respectively. High waves generated by strong winds are therefore rather destructive [Anthoni 2000]. The relationship between wind and waves represents an area of great study in oceanographic research. Below is the beaufort table, which categorises wind speed into 12 levels and describes the associated sea conditions.

Table 1 Beaufort table of sea surface winds and sea conditions [Huler 2004]

Beau -fort	Description	Wind speed m/s	Sea conditions
0	Calm	0	Sea like a mirror
1	Light air	0.5~1	Ripples but without foam crests
2	Light breeze	2~3	Small wavelets. Crests do not break
3	Gentle breeze	4~5	Large wavelets. Perhaps scattered white horses
4	Moderate breeze	6~8	Small waves. Fairly frequent white horses
5	Fresh breeze	9~11	Moderate waves, many white horses
6	Strong breeze	12~13	Large waves begin to form; white foam crests, probably spray
7	Near gale	14~16	Sea heaps up and white foam blown in streaks along the direction of the wind
8	Gale	17~20	Moderately high waves, crests begin to break into spindrift
9	Strong gale	21~23	High waves, dense foam along the direction of the wind. crests of waves begin to roll over, spray may effect visibility
10	Storm	24~27	Very high waves with long overhanging crests, the surface of the sea takes a white appearance, the tumbling of the sea becomes heavy and shock like, visibility affected
11	Strong storm	28~31	Exceptionally high waves, the sea is completely covered with long white patches of foam lying in the direction of the wind, visibility affected
12	Hurricane	32 +	The air is filled with foam and spray, sea completely white with driving spray. visibility very seriously affected

Given a constant wind speed and a sufficient fetch and duration, the height and wavelength of the waves will reach their full potential and stabilise. This situation, termed as a “fully developed sea”, is the equilibrium status of wind-wave energy transfer. As a result of previous wave modelling and experimental data studies we are able to estimate the fetch and duration necessary to attain a fully developed sea, from a certain wind speed. When wind speed increases, so will the required duration and fetch. For example, 5.5 m/s winds will need to blow for 2.75 hours and 24 km to enter the fully-developed stage. 11 m/s wind, however, will need more than 11 hours duration time, which is difficult to achieve realistically,

considering an unstable meteorological environment. As such a fully developed sea is hard to attain with high wind speeds [Knowles 2004].

Ocean wave properties are hard to measure owing to the complex nature of waves and the massive scale of the ocean itself. Here we review several current methods for measuring waves.

Traditionally, sea states are estimated by observers at sea, such as wave gauges and buoys. Wave gauges are platforms that are fixed to the sea floor and equipped with pressure, sound, infrared beams and radio wave sensors, for the purpose of determining the distance from the ocean floor to the sea surface. Wave direction can also be obtained with arrays of bottom-mounted wave gauges, which are commonly used for long wave monitoring in coastal areas. Buoys are floating platforms, anchored to the sea bed, which have many different applications. Typical weather buoys are equipped with sensors to measure air temperature, barometric pressure, wind condition and wave spectrum. These data can be reported via satellite radio links to ground stations for oceanographic and meteorological research [NDBC 2006].

GPS buoys have been developed in recent years for the purpose of calibrating radar altimeters [Born 1994] [SEAL 2001] [Martinez-Benjamin 2003] [Bisnath 2003] [Yoo 2004]. Along with GPS-Reflectometry, this technique forms another example of GNSS applications in oceanographic observation.

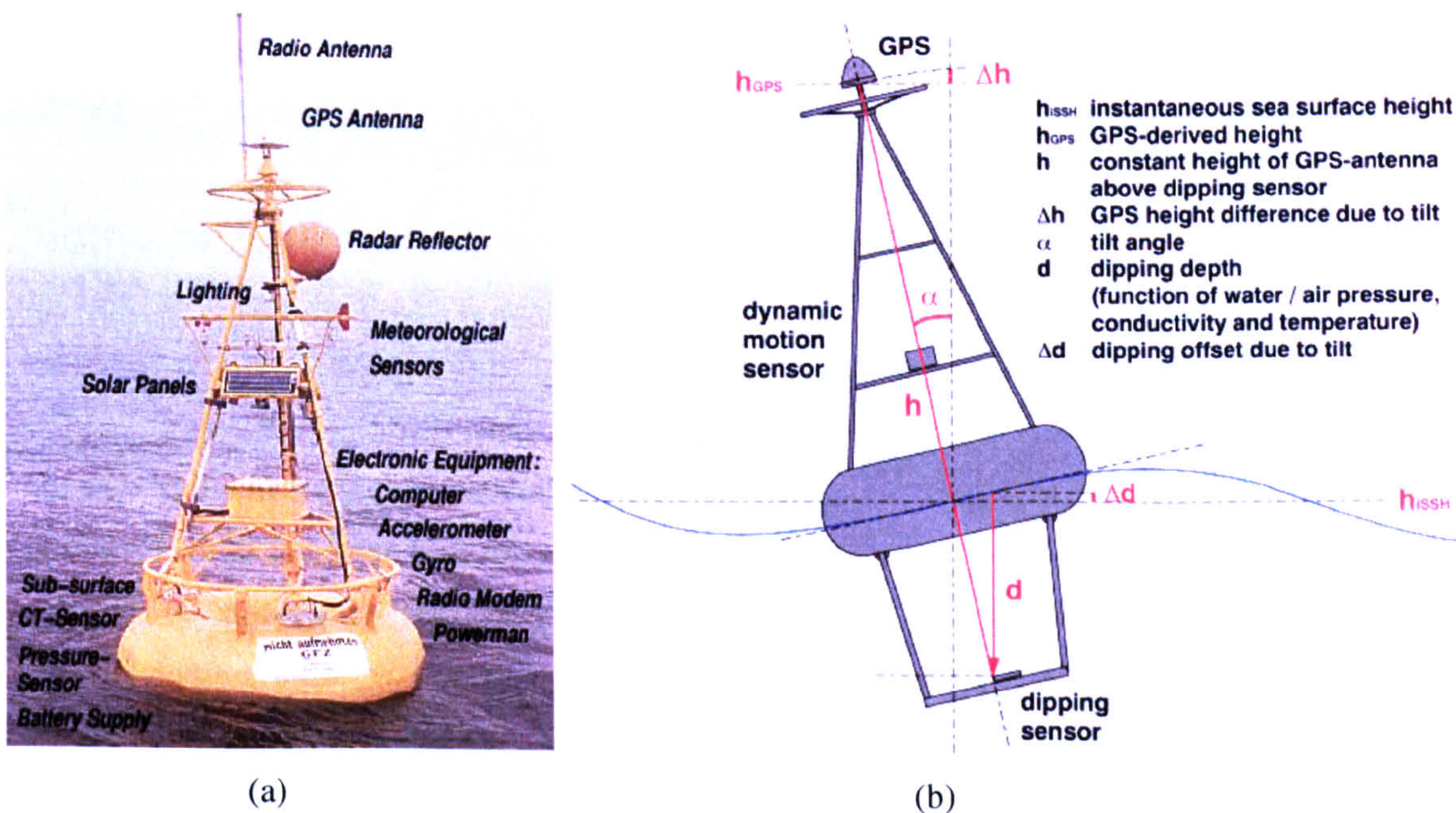


Figure 2-1: GPS-buoy in the North Sea [SEAL 2003]. (a) buoy outlook. (b) measuring principle.

As shown in Figure 2.1(a) the GPS antenna, which is mounted on top of the buoy, is able to receive signals from several GPS satellites simultaneously and calculate the local sea level. To achieve altimetric measurements with high accuracy, the height that the GPS antenna is mounted, relative to the ocean surface, must be carefully modelled. This GPS antenna height is dependent upon the instantaneous orientation of the buoy, normally measured through tilt angle and dipping depth (Figure 2-1(b)), and therefore should be considered with each single GPS measurement.

Satellite remote sensing compliments in-situ sea states monitoring and broadens the horizon of ocean observations. Three main satellite sensors which are commonly used for ocean wave detection are altimeters, Synthetic Aperture Radars (SAR) and scatterometers. Satellite altimeters first attracted scientific attention when the satellites GEOS-3 and SEASAT were launched in 1975 and 1978 respectively. Subsequent altimetric platforms, such as satellites ERS (1&2), Topex/Poseidon and Jason, have been widely used for monitoring wave height and wave energy density for nearly 20 years. Altimeter radars transmit short pulses towards nadir, with the return time of the pulse yielding the height of the satellite relative to the sea surface. To then derive the sea surface height relative to the Earth surface, the shape of the geoid needs to be known to at least the same accuracy as the altimetric measurement [Robinson 1994]. By recording and analysing the received altimetric signals, wave height can be determined from the scattering pattern of the received data [Stewart 2005].

SAR is able to provide high-resolution wave images from space-borne platforms, such as the satellites Seasat and ERS-1&2. Not only surface waves and swells can be observed by SAR, but also other oceanographic processes, such as inner waves which appear as wave-like features on SAR images. By analysing these images additional information can be obtained, such as directional spatial distribution of swell-wave fields [Robinson 1994] [Stewart 2005].

Scatterometry concerns the study of scattered radar signals from the Earth surface. Normally backscattered signals are obtained by the receiver on the same platform of the radar emitter. Forward-scattered signals can be collected however, by bi-static receivers. In either case the radar cross section (RCS) parameter, which represents the physical attributes of the reflection surface, can be extracted from the measurements. For ocean remote sensing, the primary application of satellite scatterometry is for observing near-surface winds, especially for hurricanes. NASA's Quick Scatterometer satellite (QuikSCAT) was launched in 1999, for the purpose of measuring near-surface wind vectors under all weather and cloud conditions across the ocean. The received data are vital in the research of air-sea interactions and their

effects on the weather and climate. Scatterometer data can also be applied in polar ice observation and unusual climate change monitoring such as with El Niño [SeaWinds 2005]. Our research is within the area of scatterometry, with more technical details related to this field being given in the following chapters.

2.2 GNSS and GPS

Presently there are two main **Global Navigation Satellite Systems** (GNSS) operational in orbit. One of these is the **Global Positioning System** (GPS), launched by the United States in the 1970s, while the other is Russia's **GLObal NAvigation Satellite System** (GLONASS). The Beidou constellation (also know as Compass Navigation System) represents an alternative system that is being independently developed by China. The first 4 geo-stationary satellites in the Beidou constellation are currently in orbit and capable of providing limited coverage and applications [BDStar 2007][Sino 2007a]. Following launch, the second group of satellites (Beidou-2) will make the Beidou system a fully functional global navigation system [Sheridan 2007] [Sino 2007b] [CAST 2007]. The European navigation constellation Galileo has also been proposed as an alternative system to GPS and GLONASS. Galileo will include 30 Medium Earth Orbit (MEO) satellites flying in three orbital planes. The system is designed to offer two signal bands of Open Service (OS) and high accuracy encrypted signals [Issler 2003] [Galileo 2005] [Blunt 2005]. The first Galileo In-Orbit Validation Element (GIOVE-A) test platform, built by SSTL, has been successfully launched in late 2005 [SSTL 2005] [BBC 2006]. The current plan of a fully operational Galileo system is scheduled around 2012.

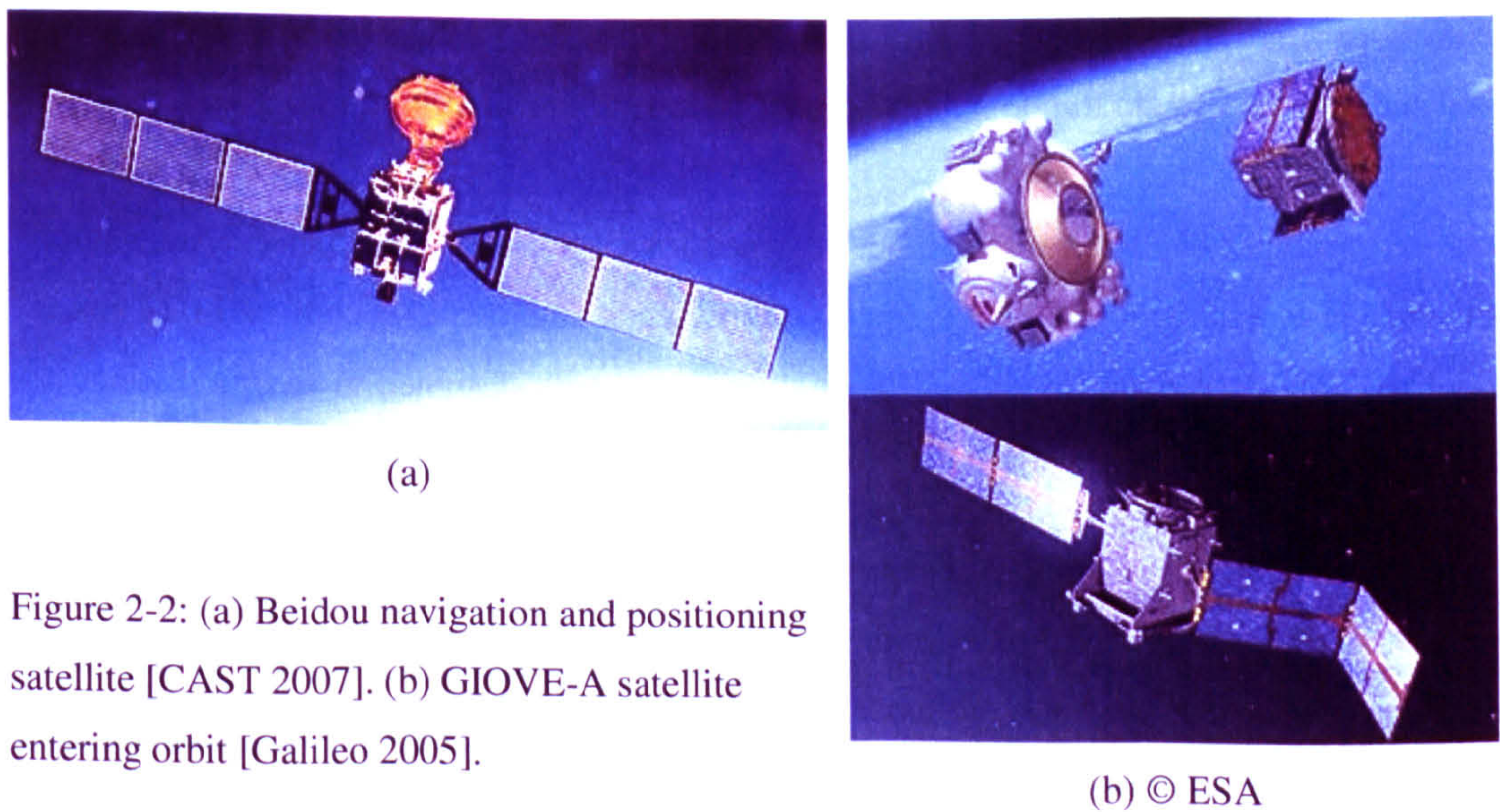


Figure 2-2: (a) Beidou navigation and positioning satellite [CAST 2007]. (b) GIOVE-A satellite entering orbit [Galileo 2005].

(b) © ESA

The Beidou and Galileo systems are both in an immature status, and so are not considered in this thesis. GLONASS broadcasts navigation signals in Frequency Division Multiple Access (FDMA) format, which requires a different signal processing method to the one applied in this research, and is therefore also beyond the scope of this thesis. Our study will focus on the reflectometry applications of GPS (GPS-R) with navigation signals being in Code Division Multiple Access (CDMA) format, which has been commonly used in communication and navigation systems owing to its efficiency and uniqueness. As such, and unless otherwise stated, any reference to GNSS-R within this thesis can be assumed to relate to GPS-R research. The following sections will overview the GPS constellation and its signal characteristics.

The GPS constellation system currently has 30 operational MEO satellites in orbit, with a 12 hours period and an altitude of approximately 20,200 km above the Earth surface. 24 of these satellites are distributed equally among six near-circular orbital planes, such that, for most regions across the Earth, at least 6 satellites will be within line of sight. The additional 6 satellites provide redundant information, which improves the reliability and availability of the system [Kaplan 1996].

The principle data that GPS satellites broadcast are called the Navigation Message, which contains three parts. The first section of the Navigation Message indicates GPS date and time, plus the health status of the satellite. The second section contains ephemeris data, which is used to calculate accurate satellite position. Up-to-date ephemeris data is needed to minimize error when calculating the receiver's location. The third section is the almanac, which describes the locations and status of all GPS satellites, helping GPS receivers to decide which satellites are nearby and can be used for determining position. Navigation Message data are modulated into the Pseudo Random Noise (PRN) code [Parkinson 1996] [Tsui 2002].

There are two types of PRN codes that are designed for GPS usage. The Coarse / Acquisition (C/A) code is accessible to the public. Each satellite sends a unique C/A code of 1,023 bits at 1.023 MHz. The C/A code for each GPS satellite is specially designed to have a distinctive signature and will output a white-noise-like pattern when correlating with other PRN codes. This exceptional orthogonal property allows the GPS receivers to easily identify multiple satellite signals within the same carrier frequency. The second type of PRN code in the GPS system is Precise code, or P-code, which is encrypted into the Y-code. This code is only used by valid decryption authorities.

Following PRN modulation, the navigation data are then transmitted mainly by two low power radio signals, designated L1 and L2, and to a lesser extend, L3, L4 and L5. Civilian GPS signals are carried by the L1 frequency at 1575.43 MHz. This UHF band signal can travel through clouds, glass and plastic but can not penetrate buildings, soil or water bodies. Encrypted P(Y)-code data, which are only for authorized users, are transmitted by both L1 and L2 bands. Although navigation data are also transmitted on bands L3, L4 and L5, these signals are restricted to military and future GPS applications, such as safety-of-life (SoL) service [El-Rabbany 2006]. The main modulation structure of GPS signals in L1 and L2 bands is seen in Figure 2-3.

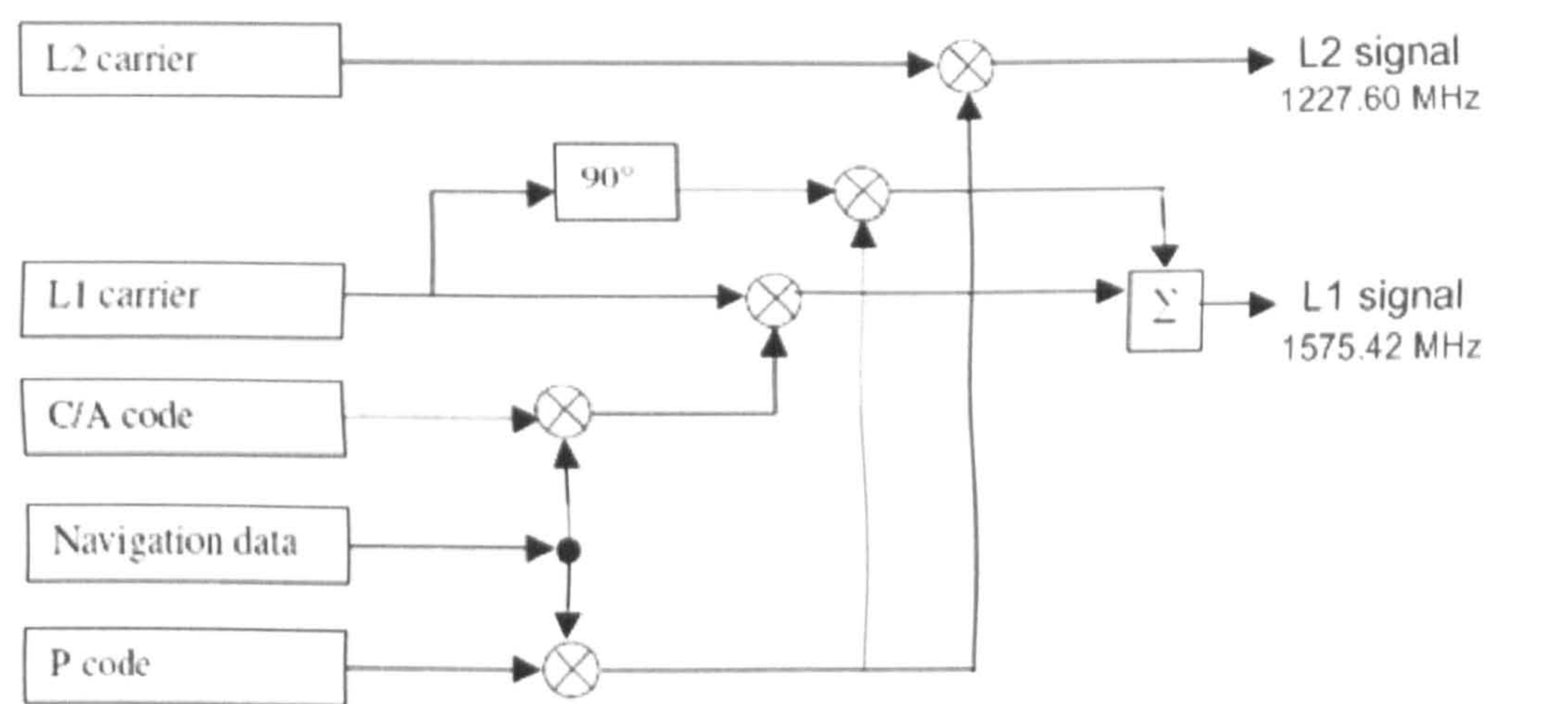


Figure 2-3: GPS L1/L2 signal modulation structure [Kaplan 1996].

In this research we consider only the C/A code signal in the L1 band. Future GPS-R research may take advantage of the phase difference in dual-frequency signals (L1&L2) to derive highly accurate sea surface wave information. This is still in the validation stage however and therefore not within the scope of this thesis.

Once a GPS signal (direct or reflected) is received, it is first down-converted from L-band to Intermediate Frequency (IF). Following analog to digital conversion (ADC), the PRN code offset and Doppler shift of the carrier frequency are estimated using a signal acquisition procedure. This procedure is a two-dimensional searching process in which a replica carrier, with a certain PRN code, is aligned and cross-correlated with the received signal. For direct GPS receivers, when the code offset and carrier Doppler shift of the replica signal both match the received signal, the output power from the correlator reaches a threshold. The code offset and Doppler shift will then be fed into a tracking loop, as a reference, to decode the PRN series and extract useful navigation data [Krumvieda 2001] [Tsui 2002] [Wong 2005]. The

above searching and correlation procedure is applied to reflected, in addition to direct, GPS signals.

The C/A code offset, which represents the time delay of a given signal, will be referred to as the Delay for the duration of this thesis. Similarly, the Doppler shift of a carrier signal, which represents the comparative motion between the GPS emitter and receiver, will be referred to as the Doppler. Delay and Doppler are the two significant areas of study within GPS-R signal analysis. The correlation output of GPS-R signals has a more complex pattern than that of direct GPS signal. By analysing the shape and magnitude of these patterns we aim to extract useful information about waves and sea surface wind.

2.3 GPS-R research status

Even before GPS satellites achieved initial operational capability, [Hall 1988] had proposed and analysed the feasibility of using GPS reflection signal as a potential scatterometric measuring tool. In the 90s, once GPS navigation functions had become fully recognised, conceptual study of GPS-R received increased attention, such as with [Martin-Neira 1993] and [Garrison 1998].

Two main GPS-R applications in oceanographic research are the altimetry, for sea level height determination, and the scatterometry for sea surface roughness measurement. Both study the pattern of received power after the Delay-Doppler correlation procedure, as described in section 2.2. As shown in Figure 2-4, when viewed in the Delay dimension, there is a time delay between the leading edges of the direct signal and reflected signal waveforms, which contains topography information of the sea surface. Alternatively by studying the shape of the trailing edge of the reflected waveform, the sea states and wind conditions can be determined [Masters 2004][Emery 2001].

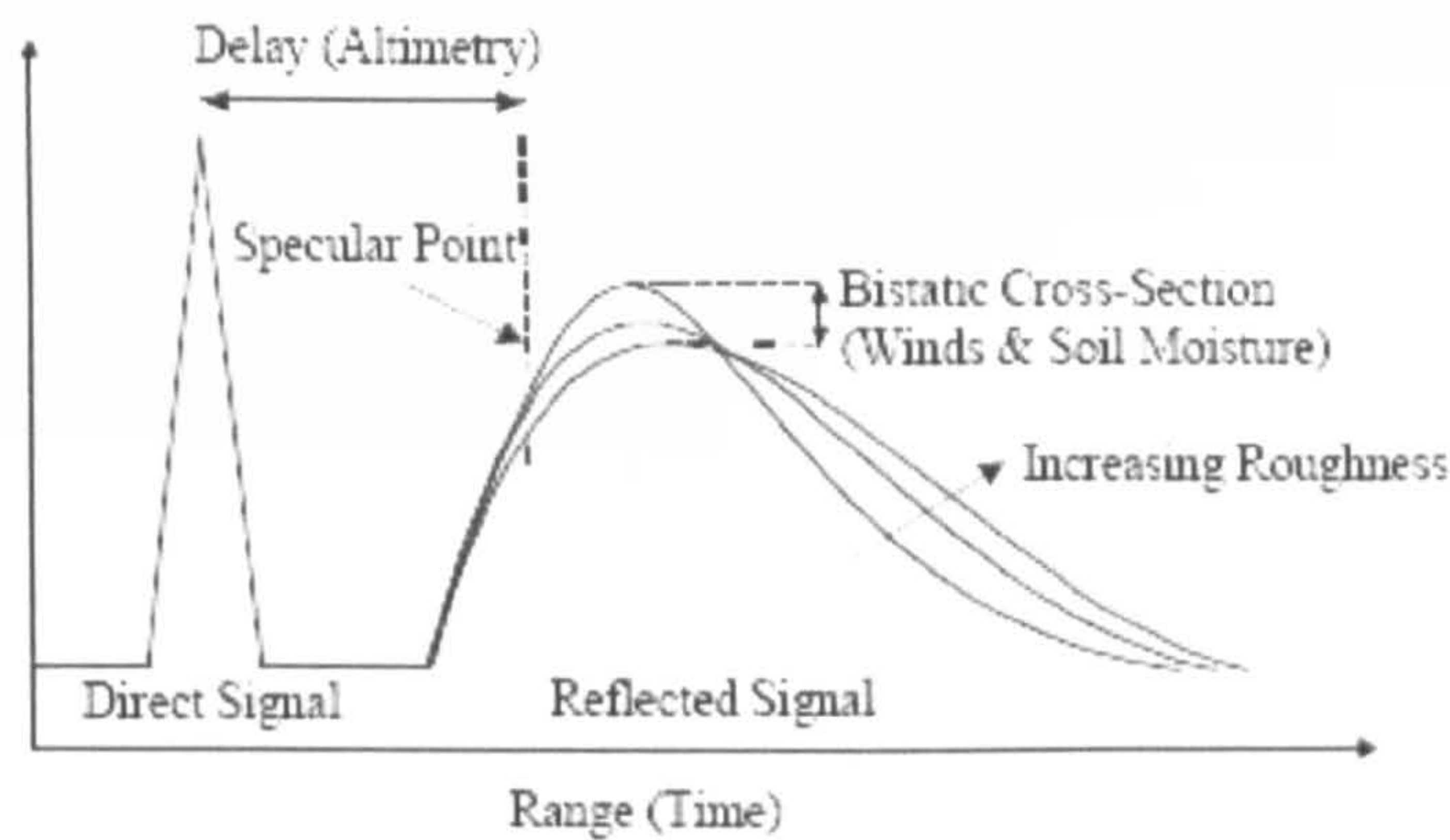


Figure 2-4: GPS 1-D direct and reflected waveforms [Emery 2001].

There has been much empirical work carried out in the past. These studies have attempted to increase the measuring capability of GPS-R and enlarge its application scale. The experiments have been performed on bridges, balloons and aircraft, generally less than 25 kilometres in altitude. In 2003, ESA and Starlab reported the results of an experiment that used GPS-R L1 signals from low altitude aircraft to observe meso-scale eddies. This was based on the **P**Assive **R**eflectometry **I**nterferometric **S**ystem (PARIS) concept [Martin-Neira 1993]. Other empirical studies on ground or air-borne platforms have also confirmed GPS-R's potential ability for altimetry monitoring [Cardellach 2003] [Germain 2003] [Ruffini 2004]. For scatterometric research, in two air-borne GPS-R campaigns, researchers from the Purdue University collected GPS-R reflection data along the ground track of the Topex/Poseidon satellite [Garrison 2002]. The experimental results of this study, which were validated with ground truth data from Topex/Poseidon, demonstrated reliable extraction of wind conditions using correlated waveforms of GPS-R signals. The research also proposed the use of statistics to describe the properties of a rough sea surface.

[Armatys 2000] concentrated on GPS-R waveform research in the Delay domain. A Delay Mapping Receiver, developed by NASA Langley Research Centre (LaRC), was accommodated on an aircraft which flew over the coast area of North California. The Least-Square method was used to extract sea-surface wind information. The derived results were validated by ground truth data, such as wind measurements from the QuikSCAT satellite and local buoy data.

[Ruffini 2003] and [Soulat 2004] focused on modelling and analysis of data from the ESA/Starlab air-borne GPS-R experiment. **D**irectional sea-surface **m**ean square slope (DMSS) data was derived from GPS-R data-model fitting by using Least-Square method. This GPS-R DMSS output was also compared with the DMSS results from solar bi-static

reflection measurements (SORES). Both results observed higher amplitude slopes than the Gaussian predictions.

Due to the weak strength of reflected signals and the lack of observation platforms, there are few opportunities to carry out GPS-R experiments from a satellite altitude. The first space-borne GPS-R receiver, built by NASA Jet Propulsion Laboratory (JPL), successfully observed GPS reflections from the space in 2000. This onboard imaging radar (SIR-C), with a linear-polarized antenna of 38 dB gain, was capable of receiving L2 band signals from GPS reflections. A preliminary reflection waveform signature, obtained from the SRL-2 flight data, agreed with modelled equivalent. This signature could therefore be used for future altimetry and scatterometry applications [Lowe 2002a].

The UK-DMC satellite, built by Surrey Satellite Technology Limited (SSTL), is the next space-borne experiment able to detect reflected GPS signals. Scott Gleason from SSTL has successfully achieved GPS-R data collection and signal pattern acquisition from the ocean surface, sea ice and land [Gleason 2006]. This work has shown the potential of GPS-R applications in different areas of remote sensing. The UK-DMC GPS-R platform will be detailed further in section 2.4.

The theoretical models, needed to describe the relationship between GPS reflected signals and sea surface characteristics, fall into two categories: wave spectrum model and electromagnetic (EM) model. The wave spectrum model is used to describe wind conditions and wave spectrum distributions [Cox 1954] [Pierson 1964] [Elfouhaily 1997]. The EM model, however, characterises the relation between scattered GPS signals and ocean wave statistics [Clifford 1998][Zavorotny 2000][Elfouhaily 2002]. These models form the foundation upon which the simulation work of this research is based and therefore will be discussed in depth in Chapter 3.

2.4 UK-DMC GPS-R experiment

The UK-DMC satellite, launched in October 2003, is one of the standard-designed micro-satellites in the Disaster Monitoring Constellation (DMC), as seen in Figure 2-5. Several experimental platforms were onboard, such as a commercial internet router for communication, and a GPS-R bi-static receiver for GPS-R space-borne research. UK-DMC

can be scheduled to repeatedly measure reflected GPS signals from Low Earth Orbit (LEO) altitude.

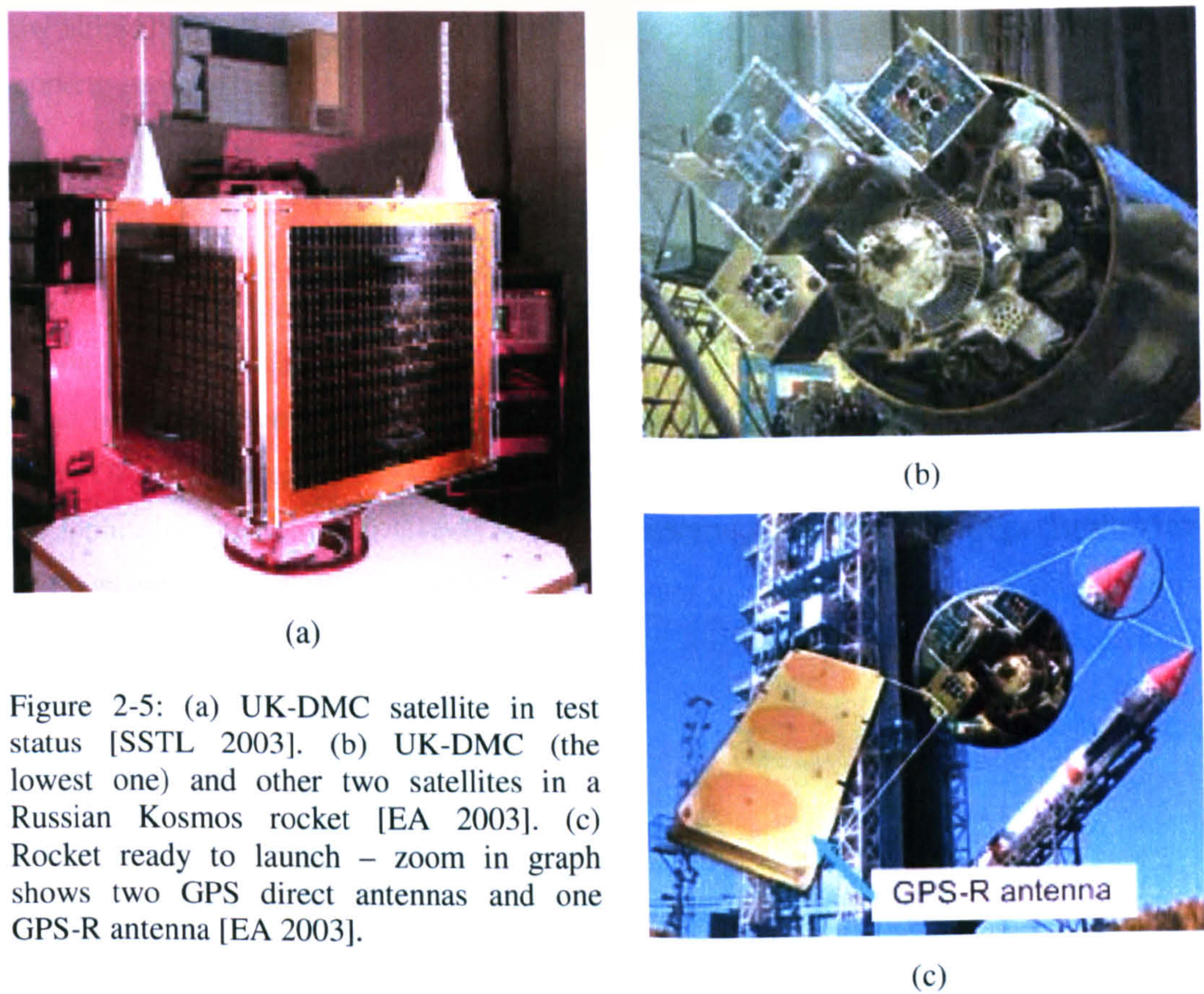


Figure 2-5: (a) UK-DMC satellite in test status [SSTL 2003]. (b) UK-DMC (the lowest one) and other two satellites in a Russian Kosmos rocket [EA 2003]. (c) Rocket ready to launch – zoom in graph shows two GPS direct antennas and one GPS-R antenna [EA 2003].

Three antennas are installed on the UK-DMC for GPS-R experiments. Two zenith looking Right Hand Circular Polarisation (RHCP) antennas receive direct GPS signals, and one nadir looking Left Hand Circular Polarisation (LHCP) antenna receives GPS-R L1 band reflections [Gleason 2005a] (Figure 2-5 (c)).

Figure 2-6 briefly summarises the data flow route for GPS-R experiment. The signals from each antenna are down-converted to IF and then are either, processed in real-time by the GPS receiver, or logged into a solid-state data recorder. When the satellite is in view of the ground station, the direct and reflected GPS data can be downloaded and post-processed off line. From October 2005, the data can be transmitted between all data storage units with more freedom via an internet router. This significantly increases the GPS-R data collection capability of the UK-DMC platform [Gleason 2006].

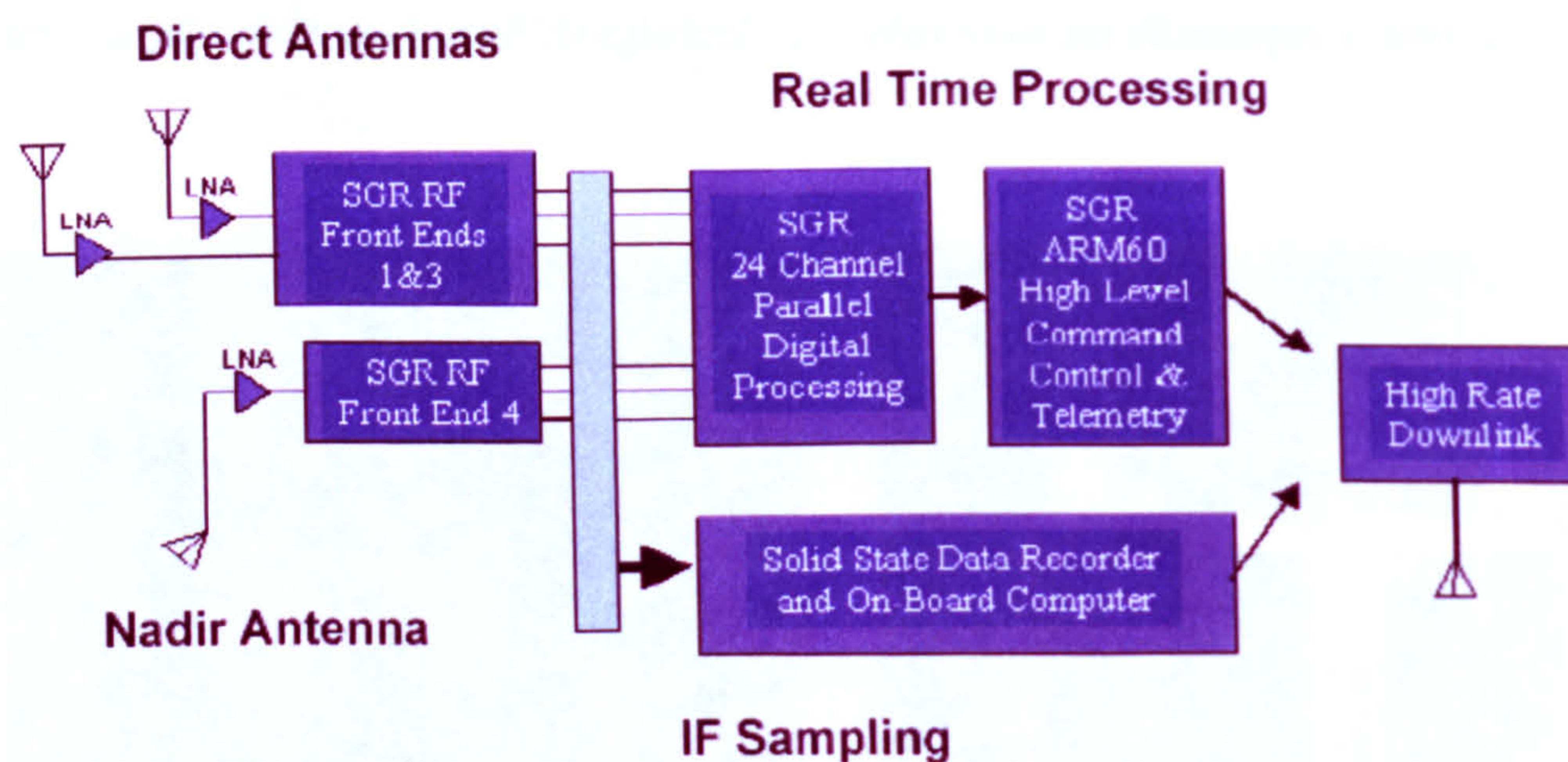


Figure 2-6: UK-DMC GPS reflectometry experiment set-up [Gleason 2006].

An example of raw GPS-R data cross-correlation results is presented below,

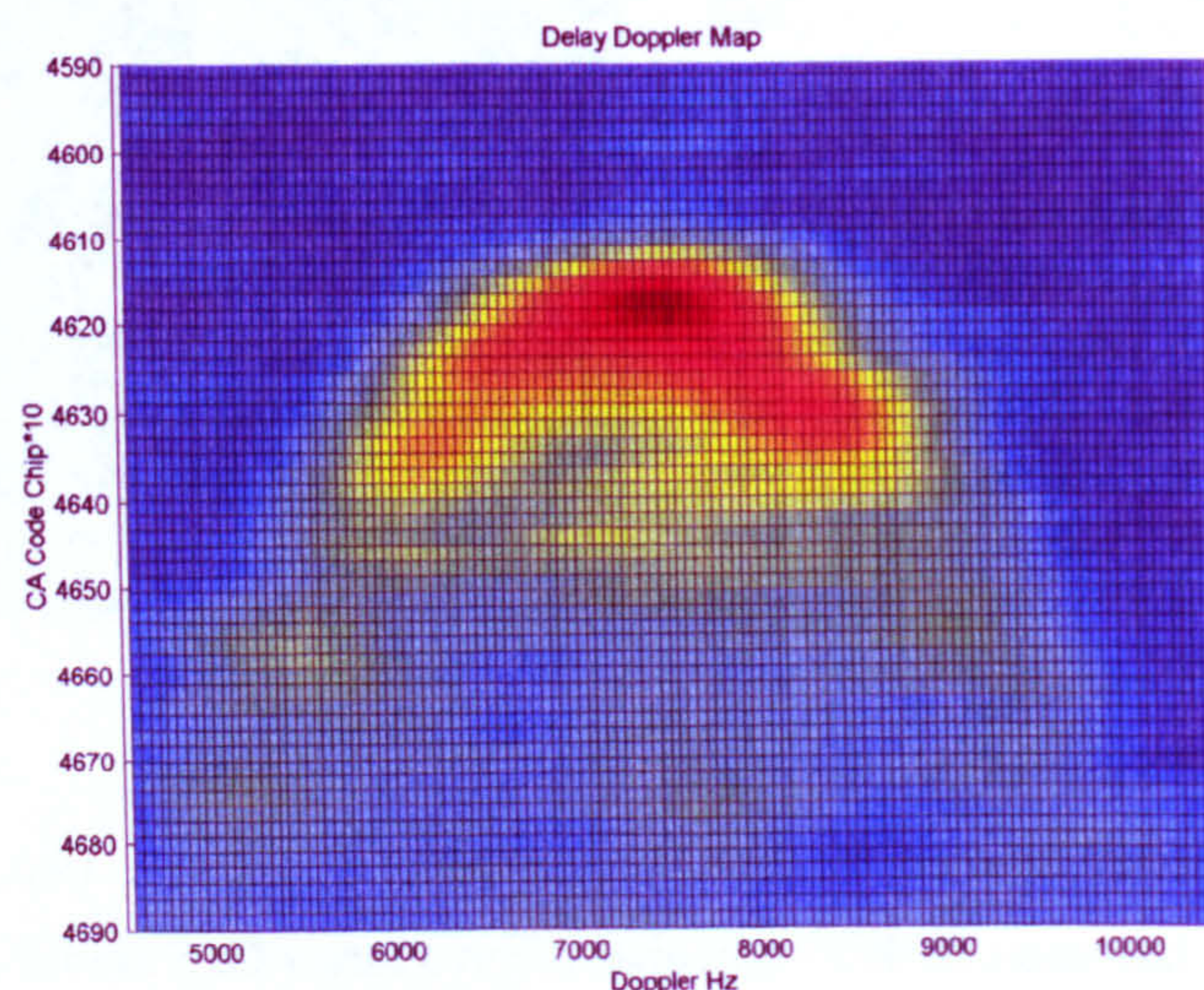


Figure 2-7: A Delay-Doppler Map from UK-DMC GPS reflection data [Gleason 2005b].

Figure 2-7 shows the typical horse-shoe pattern of GPS reflection signals on a Delay-Doppler Map (DDM). The Doppler frequency shift range (x axis) is from $\sim 5000\text{Hz}$ to $\sim 10000\text{Hz}$. The Delay measured in C/A code length (y axis) is from ~ 459 C/A code to ~ 469 C/A code. For convenient viewing, the Delay axis direction is normally reversed.

2.5 Summary

This chapter introduces the background knowledge and current research status of GPS-R oceanography in the remote-sensing field. Fundamental concepts of oceanography and GPS

technology are summarised in section 2.1 and 2.2. Section 2.3 briefly reviews previous empirical studies on GPS-R techniques, with most of the experiments being carried out from ground and air-borne level. The results of these experiments have proven that near-ground or low altitude GPS-R data do correlate with ocean altimetry, sea states, wind conditions, soil property and ice states.

The UK-DMC GPS-R platform, as introduced in section 2.4, represents the first practical space-borne GPS-R platform for remote sensing research. This platform and the preliminary result of earlier data processing are briefly described. Initial feasibility study has demonstrated the multiple possible applications of space-borne GPS-R. However, there is still a gap between the preliminary qualitative tests and the practical quantitative application of future GPS-R techniques. The aim of this research is to extend the previous investigation into the applications of UK-DMC GPS-R data, and further validate GPS-R in space. This research will concentrate on the modelling and interpretation of existing GPS-R data collected from the UK-DMC platform. Details relating to the theoretical research of GPS-R, with particular emphasis upon modelling technique of GPS scattered signals, will be discussed in the next chapter.

References

- [Anthoni 2000] J. F. Anthoni, Oceanography: waves, Seafriends Marine Conservation and Education Centre, <http://www.seafriends.org.nz/oceano/waves.htm>, 2000
- [Armatys 1999] M. Armatys, Receiver Algorithms for Estimation of Sea-Surface Parameters Using Reflected GPS Signals, PhD thesis, Aerospace Engineering, University of Colorado, Boulder, USA, 1999
- [Armatys 2000] M. Armatys, D. Masters, A. Komjathy et al., Exploiting GPS as a New Oceanographic Remote Sensing Tool, in the proceedings of the Institute of Navigation Technical Meeting, Anaheim, CA, January 2000
- [BBC 2006] First Galileo Signals Received. <http://news.bbc.co.uk/1/hi/sci/tech/4610452.stm> BBC website, January 2006.
- [BDStar 2007] Beijing BDStar Navigation, Ltd., <http://www.navchina.com/company-english/company-english.asp> , April 2007

- [Bisnath 2003] S. Bisnath, D. Wells, S. Howden, et al., The Use of a GPS-equipped Buoy for Water Level Determination, In Proceedings of OCEANS 2003, Vol. 3, pp. 1241-1246, September 2003
- [Blunt 2005] P. Blunt, T. Ebinuma, S. Hodgart, M. Unwin, A Demonstration of Galileo Transmitter/Receiver Architecture for Space Applications, In Proceedings of ION GNSS 2005, California, September 2005
- [Born 1994] G.H. Born, M.E. Parke, P. Axelrad, et al., Colorado Center for Astrodynamics Research, University of Colorado at Boulder, Calibration of the TOPEX Altimeter Using a GPS Buoy, Journal of GeoPhysical Research, Vol. 99, pp. 24517-24526, 1994
- [Cardellach 2003] E. Cardellach, G. Ruffini, D Pino and et al., Mediterranean Balloon Experiment: Ocean Wind Speed Sensing From the Stratosphere Using GPS Reflections, Remote Sensing of Environment, 88(2003), pp:351-362, 2003
- [CAST 2007] China Academy of Space Technology, <http://www.cast.cn/CastEn/index.asp>
- [Clifford 1998] S.F. Clifford, V.I. Tatarskii, A.G. Voronovich and V.U. Zavorotny, GPS Sounding of Ocean Surface Waves : theoretical assessment, Geoscience and Remote Sensing Symposium Proceedings, 1998, Vol. 4, July 1998
- [Cox 1954] C. Cox and W. Munk, Measurements of the Roughness of the Sea Surface From Photographs of the Sun Glitter, Journal of the Optical Society of America, Vol.44, pp:838-850, November 1954.
- [EA 2003] European Antennas, Surrey Satellite Technology Ltd. Choose European Antennas to Design a Nadia Antenna for the GPS Reflectometry Experiment On the UK-DMC Satellite, <http://www.european-antennas.co.uk/2003-11surreysat.htm> , November 2003
- [Ebuchi 2002] N. Ebuchi and S. Kizu, Probability of Surface Wave Slope Derived Using Sun Glitter Images from Geostationary Meteorological Satellite and Surface Vector Winds from Scatterometers, Journal of Oceanography, Vol. 58, pp: 477-486, 2002
- [Emery 2001] W.J. Emery, P. Axelrad, R.S. Nerem, et al., CCAR/Univeristy of Colorado at Boulder, Student Reflected GPS Experiment (SuRGE), Geoscience and Remote Sensing Symposium, 2001, IGARSS '01. IEEE 2001 International, Vol.3, pp.1518-1520, July 2001
- [Elfouhaily 1997] T. Elfouhaily, B. Chapron, K. Katsaros et al., A Unified Directional Spectrum for Long and Short Wind-Driven Waves, Journal of Geophysical Research, Vol.102, No.C7, pp:15781-15796, July 1997

- [Elfouhaily 2002] T. Elfouhaily, D. R. Thompson and L. Lindstrom, Delay-Doppler Analysis of Bistatically Reflected Signals from the Ocean Surface: Theory and Application, IEEE Transactions on Geoscience and Remote Sensing, Vol.40, No.3, March 2002
- [El-Rabbany 2006] Ahmed El-Rabbany, Introduction to GPS: The Global Positioning System, second edition, Artech House, Inc., 2006, ISBN 978-1596930162
- [Galileo 2005] European Space Agency-Galileo, <http://www.esa.int/esaNA/galileo.html>, December 2005
- [Garrison 1998] J.L. Garrison, S.J. Katzberg and M.I. Hill, Effect of Sea Roughness on Bistatically Scattered Range Coded Signals from the Global Positioning System, Geophysical Research Letters, Vol.25, No.13, pp:2257-2260, July 1998
- [Germain 2003] O. Germain, G. Ruffini, F. Soulat, et al., The Eddy Experiment II: GNSS-R Speculometry for Directional Sea Roughness Retrieval from Low Aircraft, Geophysical Research Letters, Vol.31, No.21, 2003
- [Gleason 2003] S.T. Gleason and M.J. Unwin, Development and Testing of a Remote Sensing Instrument Using GNSS Reflectometry Concepts, In Proceedings of the IEEE International Geoscience and Remote Sensing Symposium, Toulouse France 2003
- [Gleason 2004] S.T. Gleason, A Proposal for Preventing Marine Accidents Caused by Dangerous Seas Using Emerging Bistatic Radar Technology, American Geophysical Union Fall Meeting, San Francisco USA, 2004
- [Gleason 2005a] S.T. Gleason, S. Hodgart, Y. Sun et al., Detection and Processing of Bistatically Reflected GPS Signals from Low Earth Orbit for the Purpose of Ocean Remote Sensing, IEEE Transactions on Geoscience and Remote Sensing, Vol.43, No.6, pp.1229-1241, June 2005
- [Gleason 2005b] S.T. Gleason and M. Adjrad, An Attempt to Sense Ocean Winds and Waves Empirically Using Bistatic GNSS Reflections in Low Earth Orbit, In Proceedings of the IEEE International Geoscience and Remote Sensing Symposium, Seoul, South Korea, July 2005
- [Gleason 2006] S. Gleason, Remote Sensing of Ocean, Ice and Land Surface Using Bistatically Scattered GNSS Signals From Low Earth Orbit, PhD Thesis, University of Surrey, UK, December 2006
- [Gommenginger 2002] C. Gommenginger, M. Srokosz, P. Challenor et al., Development and Validation of Altimeter Wind Speed Algorithms Using an Extended Collocated Buoy/Topex Dataset. IEEE Transactions on Geoscience and Remote Sensing, Vol. 40, No. 2, February 2002

- [Hajj 2003] G.A. Hajj and C. Zuffada, Theoretical Description of a Bistatic System for Ocean Altimetry Using the GPS Signal, Radio Science, Vol. 38, No.5, 2003
- [Hall 1988] C. Hall and R. Cordey, Multistatic Scatterometry, In Proceedings of IEEE IGARSS '88, Edinburgh, Scotland 1988
- [Holben 2000] Jay Holben, Understanding and Utilizing the Secrets of Waves, Nautical Know How, Inc., <http://www.boatsafe.com/nauticalknowhow/waves.htm>, 2000,
- [Huler 2004] Scott Huler, Defining the Wind: The Beaufort Scale, and How a 19th-Century Admiral Turned Science Into Poetry, Three Rivers Press, ISBN-10 -1400048850, 2005
- [Issler 2003] Jean-Luc Issler, Gunter W. Heiner, et al., Galileo Frequency and Signal Design, GPS World, Vol. 14, No. 6, pp. 30-37, June 2003
- [Janssen 2004] Peter Janssen, The Interaction of Ocean Waves and Wind, Cambridge University Press, 2004, ISBN 0-521-46540-0
- [Kaplan 1996] Elliott D. Kaplan, Understanding GPS: Principles and Applications, Artech House, Inc., 1996, ISBN 0-890060793-7
- [Katzberg 2005] S.J. Katzberg, O. Torres, M.S. Grant et al., Utilizing Calibrated GPS Reflected Signals to Estimate Soil Reflectivity and Dielectric Constant: Results from SMEX 2, Remote Sensing of Environment 100, 17-28, 2005
- [Kinsman 1965] Blair Kinsman, Wind Waves: Their Generation and Propagation On the Ocean Surface, Prentice-Hall, Inc., New Jersey, 1965
- [Knowles 2004] C.E. Knowles, Introductory Oceanography, *Lecture Notes*, North Carolina State University, <http://www4.ncsu.edu/eos/users/c/ceknowle/public/chapter10/>, 2004
- [Krumvieda 2001] K. Krumvieda, P. Madhani, C. Cloman et al., A Complete IF Software GPS Receiver: A Tutorial About the Details, in Proceedings of ION GPS 2001, Salt Lake City, Utah, September 2001, www.datafusion.com/gps/baselinereceiver.pdf
- [Lemaire 1999] D. Lemaire, P. Sobieski and A Guissard, Full Range Sea Surface Spectrum in a Non-Fully Developed State for Scattering Calculations, IEEE Transactions on Geoscience and Remote Sensing, GE-37, pp: 1038-1051, March 1999
- [Levanon 2004] N. Levanon and E. Mozeson, Radar Signals, John Wiley & Sons, Inc., 2004, ISBN 0-471-47378-2
- [Lowe 2002a] S. Lowe, J.L. Labrecque, C. Zuffada, et al., First Spaceborne Observation of an Earth-Reflected GPS Signal, Radio Science, Vol.37, No.1, 2002

- [Lowe 2002b] S. Lowe, C. Zuffada, Y. Chao et al., 5-ms-Precision Aircraft Ocean Altimetry Using GPS Signals, *Geophysical Research Letters*, Vol.29, No.10, 2002
- [Martinez-Benjamin 2003] J.J. Martinez-Benjamin, M. Martinez-Garcia, A. Nunez Andres, et al., JASON-1 Calibration Campaign at the Ibiza Island Area, In *Proceedings of the Geoscience and Remote Sensing Symposium 2003*, Vol.2, pp. 1071 – 1073, July 2003
- [Martin-Neira 1993] M. Martin-Neira, A Passive Reflectometry and Interferometry System (PARIS): Application to Ocean Altimetry, *ESA Journal*, Vol. 17, 1993
- [Masters 2004] D. Masters, Surface Remote Sensing Applications of GNSS Bistatic Radar: Soil Moisture and Aircraft Altimetry, PhD Thesis, University of Colorado, US, 2004
- [Nave 2005] C.R. Nave, Ocean Waves – Their Energy and Power, Physics Lecture Notes, Department of Physics and Astronomy, Georgia State University, <http://hyperphysics.phy-astr.gsu.edu/hbase/waves/watwav2.html>
- [NDBC 2006] National Data Buoy Centre website, <http://www.ndbc.noaa.gov/>
- [Parkinson 1996] Bradford W. Parkinson and James J. Spilker Jr., *Global Positioning System: Theory and Applications Volume 1*, American Institute of Aeronautics and Astronautics, Inc., Washington DC, 1996
- [Pierson 1964] W.J. Pierson and L. Moskowitz, A Proposed spectral form for fully developed wind seas based on the similarity theory of S. A. Kitaigorodskii, *Journal of Geophysical Research*, vol. 69, pp. 5181-5190, 1964
- [Robinson 1994] I.S. Robinson, *Satellite Oceanography: An Introduction for Oceanographers and Remote Sensing Scientists*, John Wiley & Sons, Inc., 1994, ISBN 0-471-95424-1
- [Ruffini 2003] G. Ruffini, O. Germain, F. Soulat et al., GNSS-R: Operational Applications, In *Proceedings of the 2003 Workshop on Oceanography with GNSS Reflections*, Barcelona, Spain, 2003
- [Ruffini 2004] G. Ruffini, F. Soulat, M. Caparrini et al., The Eddy Experiment: Accurate GNSS-R Ocean Altimetry from Low Altitude Aircraft, *Geophysical Research Letters*, Vol.31, No.21, June 2004
- [SEAL 2003] SEAL project description – Moored GPS Buoy, The GeoForschungsZentrum Potsdam (GFZ), Germany, http://www.gfz-potsdam.de/pb1/op/seal/buoy/main_gpsbuoy.html
- [SeaWinds 2005] SeaWinds website, <http://winds.jpl.nasa.gov/aboutScat/index.cfm>
- [Shaw 1997] J.A. Shaw and J.H. Churnside, Scanning Laser Glint Measurements of Sea-Surface Slope Statistics, *Applied Optics*, Vol.36, No.18, pp: 4202-4213, June 1997

- [Sheridan 2007] John Sheridan, AINonline News, China Commits to Compass Satnav Project, http://ain.gcnpublishing.com/content/news/single-news-page/article/china-commits-to-compass-satnav-project/?no_cache=1&cHash=e89cb47fe8, March 2007
- [Sino 2007a] Compass Satellite Navigation Experimental System (BeiDou-1), Chinese Defence Today, <http://www.sinodefence.com/strategic/spacecraft/beidou1.asp>, February 2007
- [Sino 2007b] Compass Navigation Satellite System (BeiDou-2), Chinese Defence Today, <http://www.sinodefence.com/strategic/spacecraft/beidou2.asp>, February 2007
- [Soulat 2004] F. Soulat, Sea Surface Remote-sensing with GNSS and sunlight reflections, PhD thesis, University Politecnica de Catalunya / Starlab, 2004
- [SSTL 2003] British National Space Centre DMC Microsatellite, SSTL website, 2003, <http://www.sstl.co.uk/index.php?loc=113>
- [SSTL 2005] SSTL Space Missions: GIOVE-A, SSTL website, 2005, <http://www.sstl.co.uk/index.php?loc=111>
- [Steward 2005] Robert H. Stewart, Department of Oceanography Texas A&M University, USA, Introduction to Physical Oceanography, Open Source Textbook, September 2005, http://oceanworld.tamu.edu/resources/ocng_textbook/contents.html
- [Torres 2005] O. Torres and S. Katzberg, Investigation of Possible Sources of Uncertainty in GPS Reflections from Cultivated Fields, GNSS-05 Workshop, University of Surrey, UK, June 2005
- [Tsui 2002] J.B. Tsui, Fundamentals of Global Positioning System Receivers: A Software Approach, John Wiley & Sons, Inc., 2002, ISBN 0-471-38154-3
- [Willis 1934] N.J. Willis, Bistatic Radar, Artech House, Inc., 1934, ISBN 0-89006-427-X
- [Wong 2005] Ronald Wong, GPS Carrier Phase Multipath Mitigation by Spectral Analysis for LEO Satellite, PhD Thesis, University of Surrey, UK, 2005
- [Yoo 2004] Y. Yoo, D. Hou, N. Kouguchi, et al., Arrayed GPS-buoys Wave Observation JASON-1 Calibration Campaign at the Ibiza Island Area, OCEANS '04. MTS/IEEE TECHNO-OCEAN '04, Vol.3, pp. 1370 – 1375, November 2004
- [Zavorotny 2000] V.U. Zavorotny and A.G. Voronovich, Scattering of GPS Signals from the Ocean with Wind Remote Sensing Application, IEEE Transactions on Geoscience and Remote Sensing, Vol.38, pp: 951-964, March 2000
- [Zavorotny 2005] Zavorotny webpage, Remote Sensing of Sea Land and Ice Using GPS Reflected Signals, NOAA/ETL, <http://www.etl.noaa.gov/etl/wave/gps>

Chapter 3. PDF-based GPS-R scatterometric model

3.1 Introduction

Preliminary studies have proven the correlation between the pattern of received GPS-R signals and sea states. This research aims to further the investigation of GPS-R scatterometric applications and improve the interpretation of space-borne GPS-R data for the purpose of wave/wind extraction from ocean surfaces. To achieve this, we first need to model the effects of ocean surface features on GPS-R signal properties. With such a model we would then be able to analyse the similarities and diversities between simulations and truth data, such that the capacity of GPS-R scatterometry for ocean remote sensing may be assessed. Towards such ends, this chapter reviews the GPS-R scatterometric model. Related concepts and methodologies are also detailed. GPS-R simulation results will then be presented and discussed in Chapter 4.

The GPS-R scatterometric model predicts the interaction between GPS signals and the sea surface. This provides the fundamental theory with which we can simulate a Delay-Doppler Map, under different wind conditions and reflection geometry, from GPS-R signals. The basic model structure consists of a wave spectrum model and an electromagnetic (EM) model. The wave spectrum model determines the statistical characteristics of wave slopes, under certain sea surface condition. The EM model, which is an extended version of bi-static radar model, describes the relationship between GPS electromagnetic waves and ocean surface. The connection between these two models is represented by the Normalised Radar Cross Section (NRCS) σ_0 . NRCS is an essential parameter in the radar equation, which represents the reflection surface property. This parameter is related to the Probability Density Function (PDF) of wave surface slopes. Wave PDF modelling is a key concept, for indicating the likelihood of an ocean segment being a certain slope, which forms the base of our GPS-R scatterometric research.

The first section of this chapter focuses on wave spectrum theory and related concepts, and introduces several empirically-based wave spectrum models. The second section concentrates

on the EM model developed by Zavorotny and Voronovich. Finally, the principles of Delay-Doppler Map generation will be explained along with a brief introduction of the GPS Ambiguity Function concept.

3.2 Wave spectrum model

Wave spectrum models generate the spectral distribution of waves given certain sea surface properties, such as sea surface wind. This section will introduce some general notation and relevant concepts in wave modelling. Three experimental wave spectral models will then be briefly reviewed.

3.2.1 Theory

Non-linear wave model

Ocean waves are complex non-linear phenomenon. Early research defined the properties of a wave with finite amplitude [Stokes 1880]. The ocean surface displacement ζ can be expressed in a power series with the product of wave number k and wave amplitude a .

$$\zeta = a \cos(kx - \omega t) + \frac{1}{2} k a^2 \cos 2(kx - \omega t) + \frac{3}{8} k^2 a^3 \cos 3(kx - \omega t) + \dots \quad (3-1)$$

The combination of the cosine series forms waves with sharpened crests and flattened troughs, which is more realistic than a single sinusoid for ocean waves.

In recent hydrodynamics research [Hasselmann 1985] the equation of motion is applied with the energy balance theory to describe non-linear waves. Different boundary conditions and solving methods are suggested to solve the differential equation group of wave dynamics [Janssen 2004]. Such non-linear wave theory however, is beyond the scope of this thesis.

Linear wave model

Prior to introducing the wave spectrum concept, we must first consider the simplified linear wave theory. The following discussion ignores Earth curvature and Coriolis forces that result from Earth rotation. The waves are assumed to travel only along the x axis of a flat ground plane. The sea surface displacement ζ of a single sinusoid wave can be expressed using the linear wave equation:

$$\zeta = a \sin(kx - \omega t) \quad (3-2)$$

Wave description parameters include wave amplitude a , wave number k , angular frequency ω (rad/s), wave frequency f (Hz), wave period T (s) and wave length L (m). The following equation represents the general relations between these parameters.

$$\begin{cases} \omega = 2\pi f = \frac{2\pi}{T} \\ k = \frac{2\pi}{L} \end{cases} \quad (3-3)$$

The angular frequency ω is a function of wave number k , such that $\omega = f(k)$. This function is called the dispersion relation [Janssen 2004]. The linear wave model states that:

$$\omega^2 = g k \tanh(kd) \quad (3-4)$$

where g is the gravitational constant and d is the local water depth.

If we consider deep water case, where $d \gg L$ and $\tanh(kd) \approx 1$, then the dispersion relation can be simplified to:

$$\omega^2 = g k \quad (3-5)$$

Phase velocity c is the speed at which a particular phase of the wave propagates across the ocean. If this is defined as $c \equiv \frac{\omega}{k}$, then we have:

$$c = \sqrt{\frac{g}{k}} = \frac{g}{\omega} \quad (3-6)$$

The deep water phase speed c is dependent upon multiple wave properties. Longer waves have smaller angular frequency and travel faster. Deep water waves however, will contain different wavelengths, each travelling at different speeds. Such water waves are thus said to be dispersive. In shallow seas, where water depth d has similar scale to wavelength L , the phase speed c is merely related to water depth and therefore independent of wavelength. This allows multi-length-wave combination to have the same speed and be non-dispersive.

Group velocity c_g is the velocity at which the envelope of the wave group propagates across ocean. It is also thought of as the velocity at which energy is conveyed along waves. The group velocity can be defined through:

$$c_g \equiv \frac{\partial \omega}{\partial k} \quad (3-7)$$

For deep water, the group velocity can be seen as:

$$c_g = \frac{\partial \omega}{\partial k} = \left(\sqrt{gk} \right)'_k = \frac{\sqrt{g}}{2\sqrt{k}} = \frac{g}{2\omega} \quad (3-8)$$

Combining Equ.(3-8) with Equ.(3-6), we obtain:

$$c_g = \frac{c}{2} \quad (3-9)$$

Significant Wave Height (SWH) $H_{1/3}$, defined as the mean height of the highest 1/3 of waves, is another important concept in wave theory, although it makes the assumption that the waves are random in nature. SWH can be expressed as a function of the standard deviation of surface displacements, as seen below:

$$H_{1/3} = 4 \langle \zeta^2 \rangle^{1/2} \quad (3-10)$$

The standard deviation of surface displacement ζ is related to wave energy E by:

$$E = \rho_w g \langle \zeta^2 \rangle \quad (3-11)$$

where ρ_w is the water density and g is the gravitational constant.

Wave spectrum

The ocean surface is composed of waves with random amplitudes, frequencies, phases and travelling directions. It can be represented by a linear superposition of different cosine and sine waves, and therefore can be analysed by Fourier Transform. The ocean wave spectrum is a distribution of wave energy with different frequencies on sea surface. For continuous signals, the sea surface displacement equation can be written as:

$$\zeta(t) = \frac{a_0}{2} + \sum_{n=1}^{\infty} (a_n \cos 2\pi n f t + b_n \sin 2\pi n f t) \quad (3-12)$$

where the coefficients a_n and b_n can be computed from:

$$\begin{cases} a_n = \frac{2}{T} \int_{-T/2}^{T/2} \zeta(t) \cos 2\pi n f t dt \\ b_n = \frac{2}{T} \int_{-T/2}^{T/2} \zeta(t) \sin 2\pi n f t dt \end{cases} \quad (3-13)$$

Using exponential form, the above equation can be rewritten as:

$$\zeta(t) = \sum_{n=-\infty}^{\infty} Z_n \exp^{i2\pi n f t} \quad (3-14)$$

where Z_n is the Fourier Transform of $\zeta(t)$ [Stewart 2005].

For discrete wave sampling data ζ_j , Z_n can be calculated by Fast Fourier Transform (FFT):

$$Z_n = \frac{1}{N} \sum_{j=0}^{N-1} \zeta_j \exp[-i 2\pi j n / N] \quad (3-15)$$

where $j = 0, 1, \dots, N-1$ and $n = 0, 1, \dots, N-1$.

Wave spectrum S_n , also known as periodogram, can be computed from:

$$S_n = \frac{1}{N^2} \left[|Z_n|^2 + |Z_{N-n}|^2 \right] \quad n = 1, 2, \dots, (N/2 - 1) \quad (3-16)$$

where $S_0 = \frac{1}{N^2} |Z_0|^2$ and $S_{N/2} = \frac{1}{N^2} |Z_{N/2}|^2$.

The normalised periodogram is computed as:

$$\sum_{n=0}^{N/2} S_n = \sum_{j=0}^{N-1} |\zeta_j|^2 \quad (3-17)$$

Traditionally, 10 to 30 periodograms will be collected in-situ to produce an average spectrum S_M (measured in m^2/Hz) and therefore reduce spectral noise. Since the wave height variance is proportional to the wave energy, as seen in Equ.(3-11), S_M also represent the distribution of wave energy as a function of frequency.

There is natural connection between sea surface wind properties and wave energy distribution. For example, strong winds of long duration will generate large waves. In order to understand better this relationship the following section will describe several experimental wave spectrum models.

3.2.2 Experimental wave spectrum models

Pierson-Moskowitz spectrum

The Pierson-Moskowitz (P-M) wave spectrum model is one of the idealised empirical wind-wave models proposed by [Pierson 1964]. The model is based on a fully developed sea, which assumes that the energy transfer between winds and waves will reach an equilibrium status given a sufficient duration, fetch and steady wind. The P-M model was derived from accelerometer measurements over the North Atlantic Ocean. The model describes the relationship between wave spectral density and wind speeds, as in Figure 3-1.

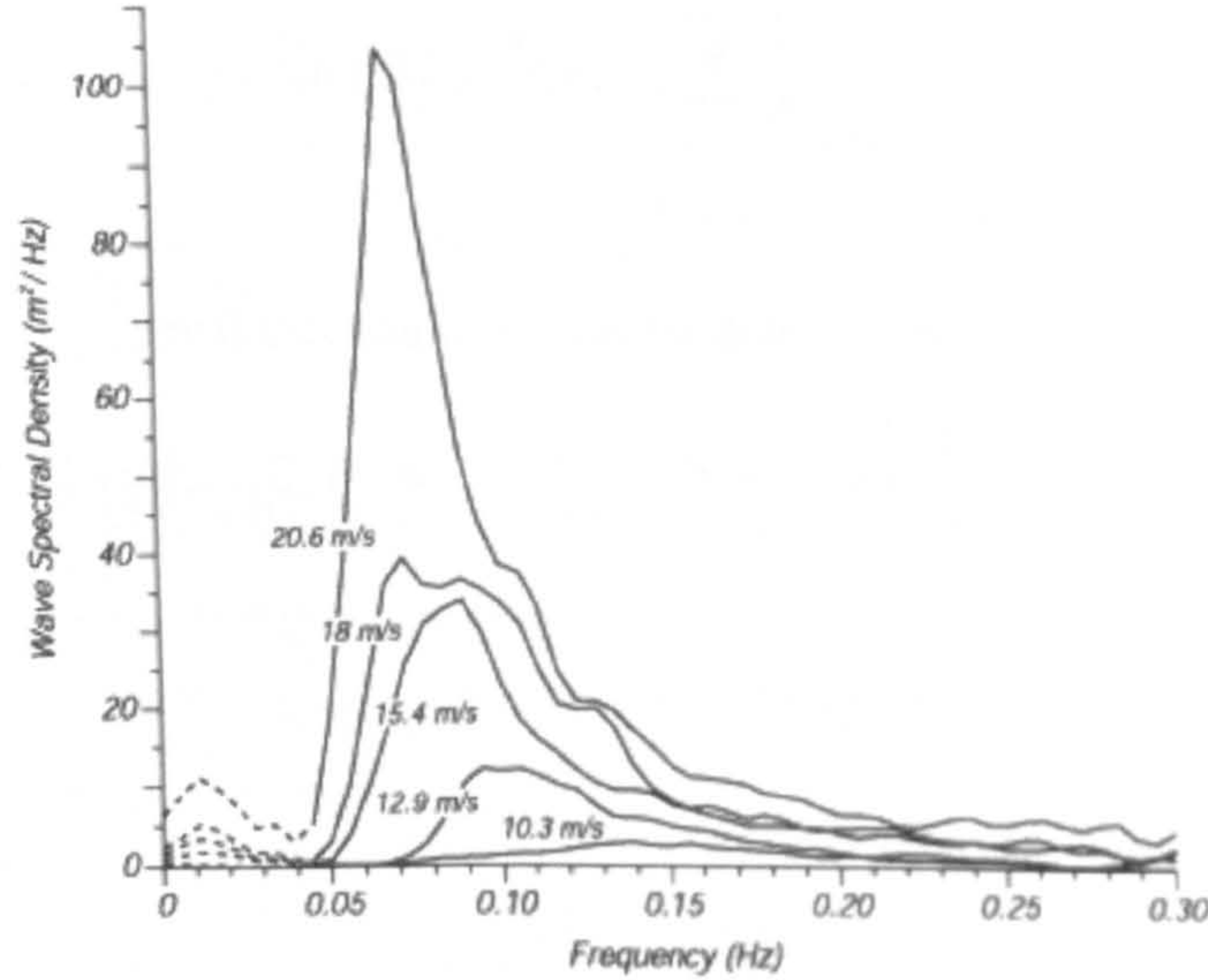


Figure 3-1: Wave spectra for different wind speeds by P-M model [Stewart 2005].

An empirical equation is proposed in [Pierson 1964] to fit the spectra lines as seen in the above figure.

$$S(\omega) = \frac{\alpha \cdot g^2}{\omega^5} \exp \left[-\beta \left(\frac{\omega_0}{\omega} \right)^4 \right] \quad (3-18)$$

Above ω is the wave angular frequency mentioned in Equ.(3-3). $\omega_0 = g/U_{19.5}$, related to wind speed $U_{19.5}$, which is measured at a height of 19.5 m above the sea surface. α , β and g are all constants. This equation will be used for geometric wave height field simulations in Chapter 7.

JONSWAP spectrum

[Hasselmann 1980] analysed the data collected during the Joint North Sea Wave Observation Project (JONSWAP) in 1973. They found that the ocean is unlikely to completely achieve the fully developed status. After the wind blows over a long distance (roughly 5000 wavelengths) and for a long time (roughly 10000 wave periods), non-linear wave-to-wave interactions will begin to hamper the formation of fully developed sea [Steward 2005]. As such, the spectrum equation of the P-M model is amended, with several new parameters introduced.

$$S(\omega) = \frac{\alpha \cdot g^2}{\omega^5} \exp \left[-\frac{4}{5} \left(\frac{\omega_p}{\omega} \right)^4 \right] \gamma^r \quad (3-19)$$

where the exponent r can be calculated from:

$$r = \exp \left[-\frac{(\omega - \omega_p)^2}{2\sigma^2 \omega_p^2} \right] \quad (3-20)$$

In Equ.(3-19) and (3-20), γ and σ are constants. α and ω_p are not only related to wind speed U_{10} , but also related to fetch F , which is defined as the distance over which the wind blows with a constant velocity.

The JONSWAP spectrum is derived from a fetch-limited wind-wave model and is well accepted among the wealth of theoretical and experimental studies on wind-wave spectra [Robinson 1994] [Elfouhaily 1997] [Janssen 2004].

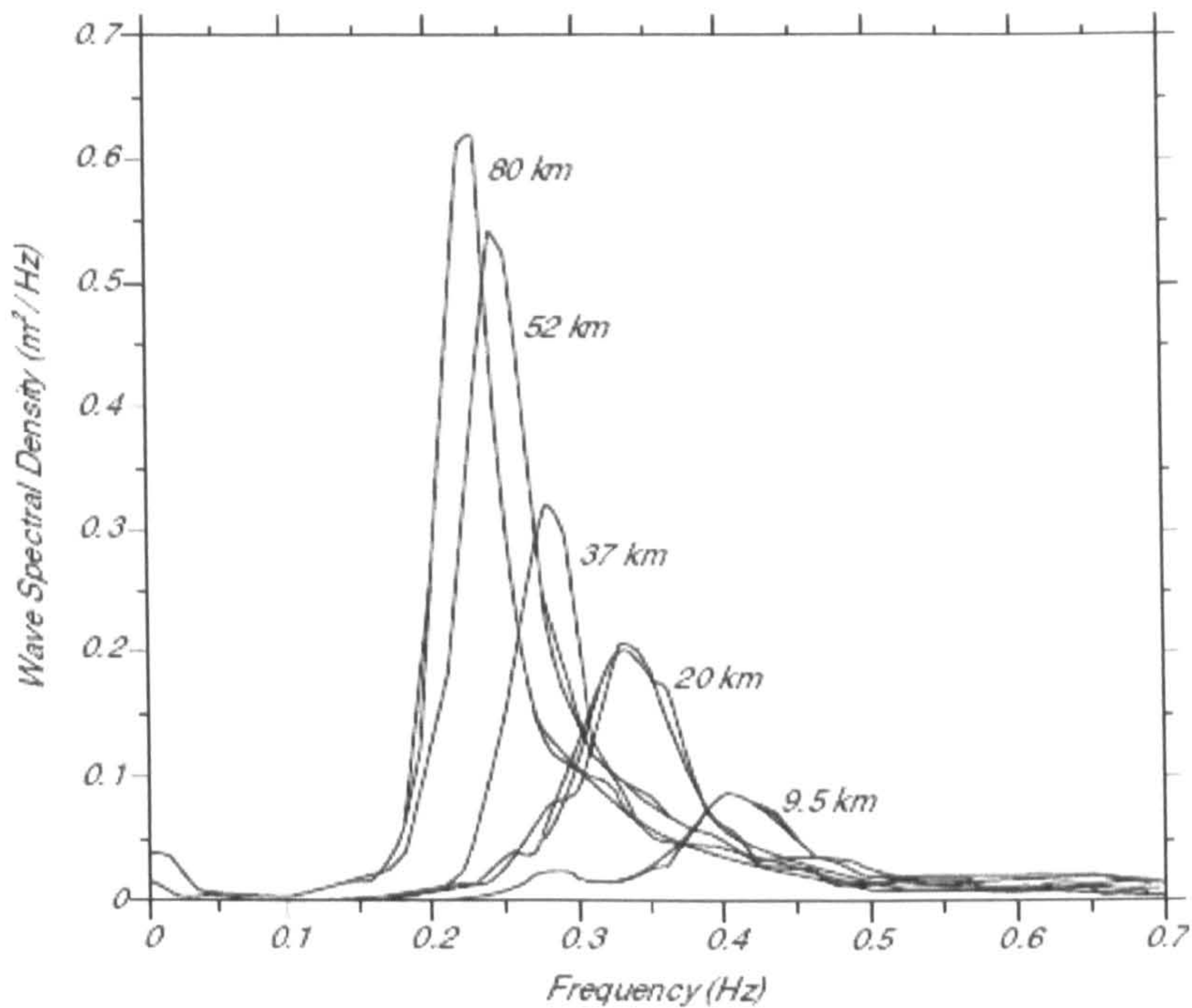


Figure 3-2: Wave spectra for different wind speeds by JONSWAP model [Stewart 2005].

Elfouhaily spectrum

Microwave radar signals that are scattered from the sea surface are a main object of study in ocean remote sensing research. Modelling the interactions between these radar signals and short-scale waves is an essential part of ocean scatterometry. Short waves however, are always coupled with intermediate and long-scale waves. A full range of wave frequencies therefore need to be considered to describe the wave spectrum more accurately. Several models that consider the above have been developed for scatterometric purposes [Bjerkaas 1979] [Donelan 1987][Apel 1994][Lemaire 1999]. The Elfouhaily model is one of the latest such models which consider a full range of wave numbers.

The Elfouhaily model describes a two-dimensional (2-D) wave spectrum that is valid for all wave frequency regions [Elfouhaily 1997]. This model adopts the long-wave regime of the

JONSWAP model and the short-wave regime model developed by [Kitaigorodskii 1983] and [Phillips 1985]. Although in the Elfouhaily model, wave spectral density is considered as a function of wave number, as seen in Figure 3-3, this is essentially equivalent to the wave frequency used in the JONSWAP model (Figure 3-2). The 2-D Wave Height Spectrum of a wind-driven sea surface can be expressed as the product of two spectral parts, as described below:

$$\Psi(k, \varphi) = \frac{1}{k} S(k) \cdot \Phi(k, \varphi) \tag{3-21}$$

where $S(k)$ is the Omni-directional Elevation Spectrum and independent of wave directions. This Elevation Spectrum is composed of a low frequency correction term $B_l(k)$ and a high frequency correction term $B_h(k)$ [Elfouhaily 1997][Zavorotny 2000][Sun 2004], as in:

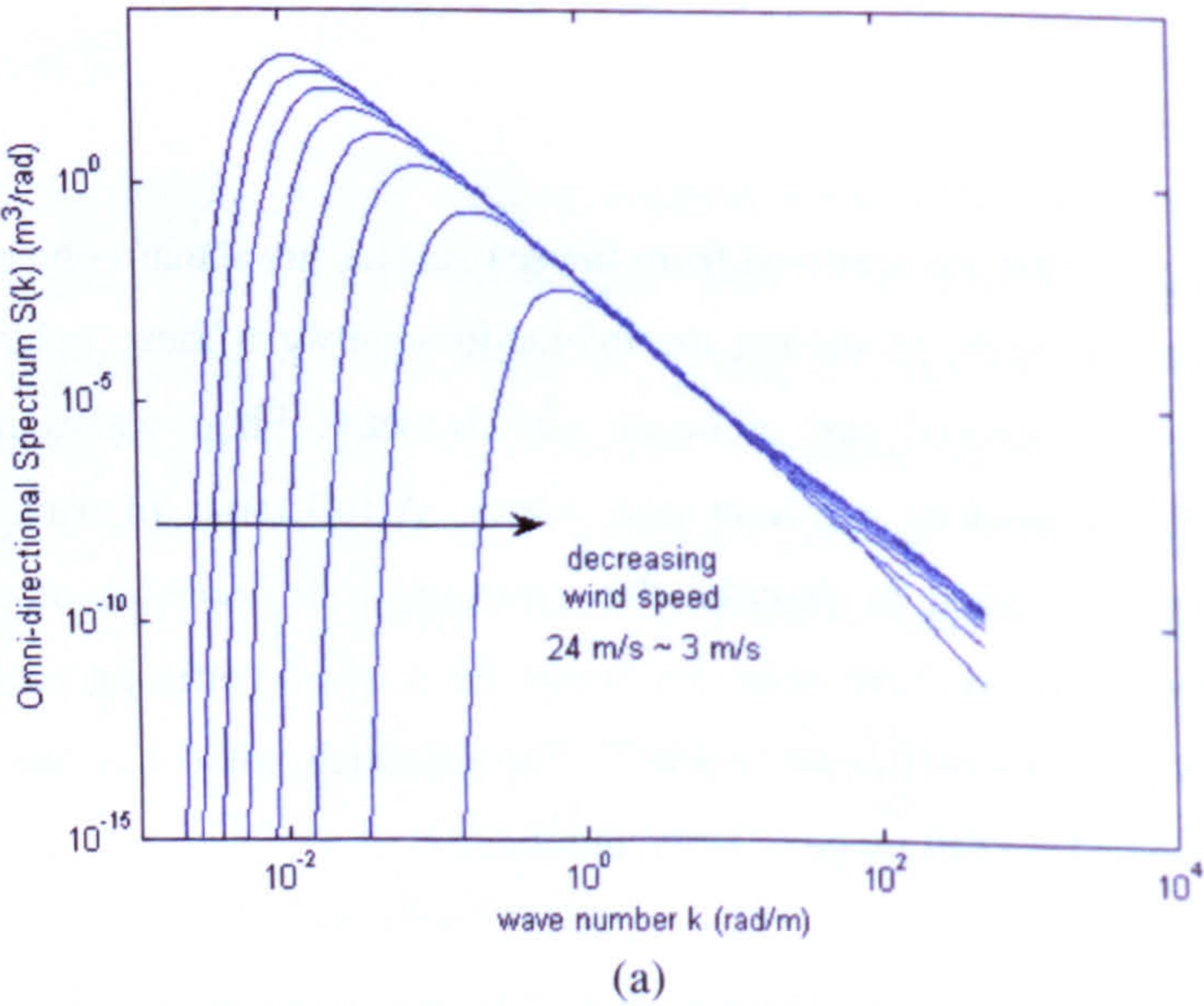
$$S(k) = k^{-3} [B_l(k) + B_h(k)] \tag{3-22}$$

The Saturation (also known as the Curvature spectrum) in Elfouhaily model corresponds to the sum of $B_l(k)$ and $B_h(k)$, and therefore will be referred to as $B(k)$:

$$B(k) = k^3 \cdot S(k) \tag{3-23}$$

From dimensional analysis, we find that $B(k)$ has a unit of $(m^3 / rad) \times (rad / m)^3 = rad^2$, which is equivalent to a dimensionless value.

In accordance with the theory of the Elfouhaily model, we simulated the Elevation Spectra $S(k)$ and Saturation Spectra $B(k)$ under different wind speeds, as shown in the figure below



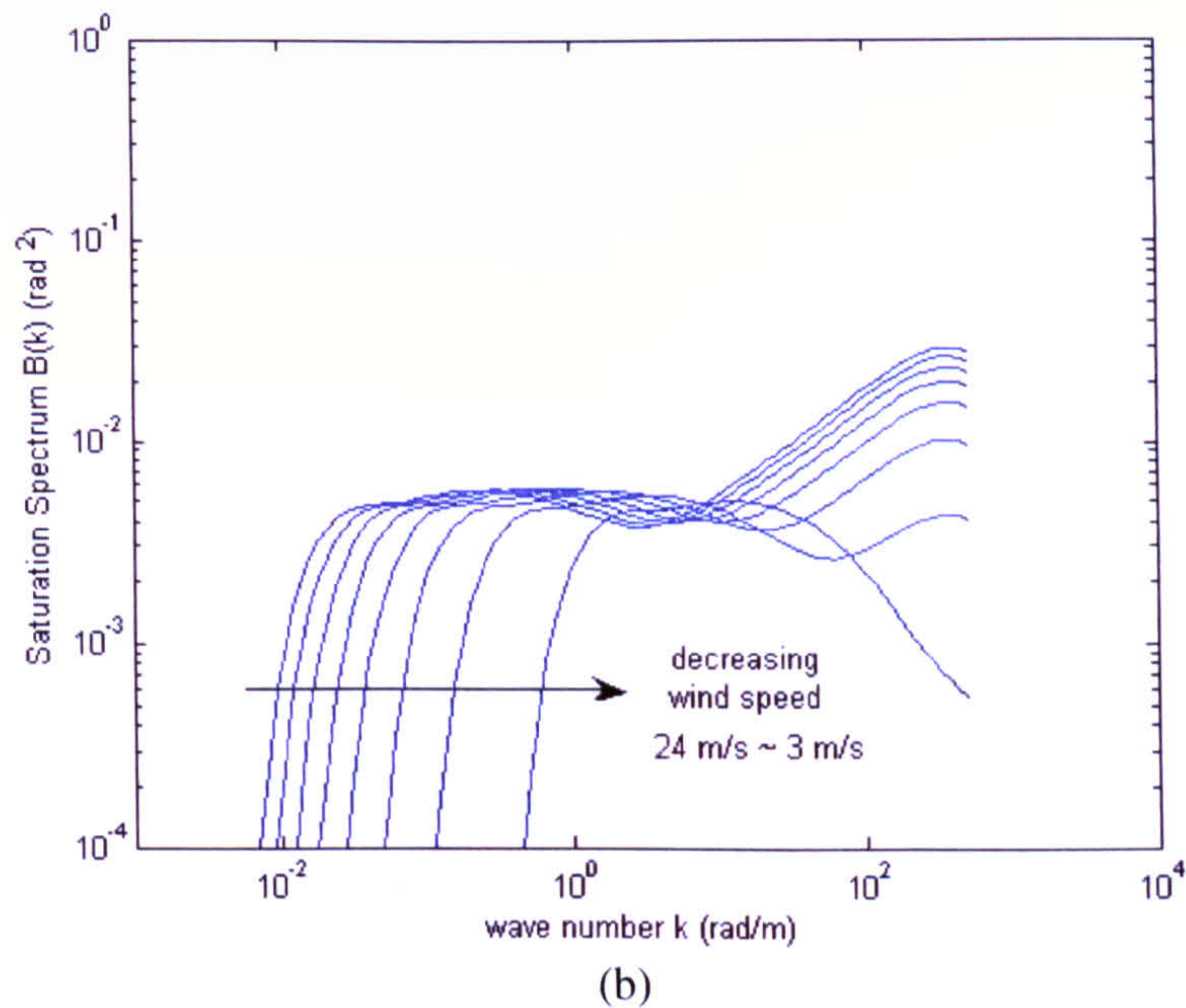


Figure 3-3: The Elevation Spectrum (a) and Saturation Spectrum (b) of the Elfouhaily wave spectrum model under 3 to 24 m/s wind speeds.

The simulation results show the wave spectra, which is independent of wind directions, under 3 m/s, 6 m/s, 9 m/s, 12 m/s, 15 m/s, 18 m/s, 21 m/s and 24 m/s wind speeds. In the Elevation Spectrum figure (Figure 3-3 (a)), when wind speed increases, the spectral range extends to lower wave number values and the spectral peak shifts to a lower wave number. This means that higher speed winds will transfer more energy to longer waves. In the Saturation Spectrum (Figure 3-3 (b)), with increasing wind speeds, the spectrum extends to lower wave numbers. The spectral signature of the highest wave number also increases in amplitude due to the effect of the higher wave-number correction term $B_h(k)$. For higher k values, the k^{-3} term in Equ.(3-22) reduces the influence of $B_h(k)$. Therefore, the high frequency segments of different wind speed spectra are almost identical, as seen in the Elevation Spectra figure (Figure 3-3 (a)).

In the above we have discussed the term $S(k)$ which refers to the elevation component in Equ.(3-21). We will now discuss the azimuth term $\Phi(k, \varphi)$, which can be seen as:

$$\Phi(k, \varphi) = \frac{1}{2\pi} [1 + \Delta(k) \cos 2(\varphi - \varphi_0)] \quad (3-24)$$

where φ is the azimuth direction of waves, ranging from $-\pi$ to π , and φ_0 is the wind direction in the observing baseline coordinate system.

Apart from defining the wave spectrum, the Elfouhaily model also proposes a method to calculate the statistical property of wave slopes, which is based on integration of the wave spectrum. The wave slope probability concept and the relevant calculation methodologies will be introduced in the following section.

3.3 Wave slope probability concept

3.3.1 Overview

Statistical models often prove to be useful tools for describing complex problems. As a random process, ocean waves have several interesting statistical properties worth studying, such as, the probability distribution of wave slopes. The statistical research of wave slopes was first inspired by sun glitters on the sea surface [Cox 1954][Schooley 1954]. By studying glitter patterns, it is possible to gain some knowledge of the local wave slope probability distributions, and furthermore, to relate sea states to local wind conditions. In addition to passive sun glitter observations, a laser has also been used to obtain active glint measurements, allowing extraction of sea surface slope statistics. The results of this laser experiment agree with Cox and Munk's approximation on wave slope probability density [Shaw 1997]. The Elfouhaily model proposed a similar connection between wave slope probability properties and reflected radar-wavelength signals [Elfouhaily 1997].

A standard mutual parameter, between the wave spectrum model and the EM model, to describe ocean waves in the field of scatterometry is the slope Probability Density Function (PDF). To introduce the wave slope PDF concept, we first need to assume that the sea surface plane is divided into a grid. Each grid square, referred to as a spatial "patch" in the following text, independently pivots around its centroid. With this, we can study the signal scattering phenomenon of the sea surface by analysing the reflection behaviour of each patch. Since we consider each patch reflection as a classical specular reflection, the analysis method we use in GPS-R modelling is called "quasi-specular" reflection. The pattern of the reflected signal, as obtained by the receiver, can be modeled as function of statistics parameters related to patch slope angle, with Gaussian and near-Gaussian distributions often being assumed.

Considering a 1-D quasi-specular reflection surface, as seen in Figure 3-4, an ideal mirror-flat surface will only give a specular reflection. Given such a surface, it is impossible to reflect signals from patches other than at the specular point. Geometrically, a given slope angle is

required to reflect signals from patches A and B, which are away from the specular point. The geometric relationship between emitter and receiver determines the required slope to reflect the signal from such patches. The further the patch is away from the specular point, the steeper the slope that will be required to reflect the incoming signal (such as with patch B relative to patch A). Wave slope statistics defines the probability of a sea surface patch having different slope angles. This distribution of slope probabilities is dependant upon sea roughness condition, with steeper slopes always being less likely. Such wave slope statistics can be expressed as a 1-D wave slope PDF that describes slope elevation angles or a 2-D PDF, which also describes wave azimuth angle. Gaussian and near-Gaussian distributions have been well accepted, by oceanography researchers, for representing a wave slope PDF [Cox 1954][Shaw 1997][Janssen 2004].

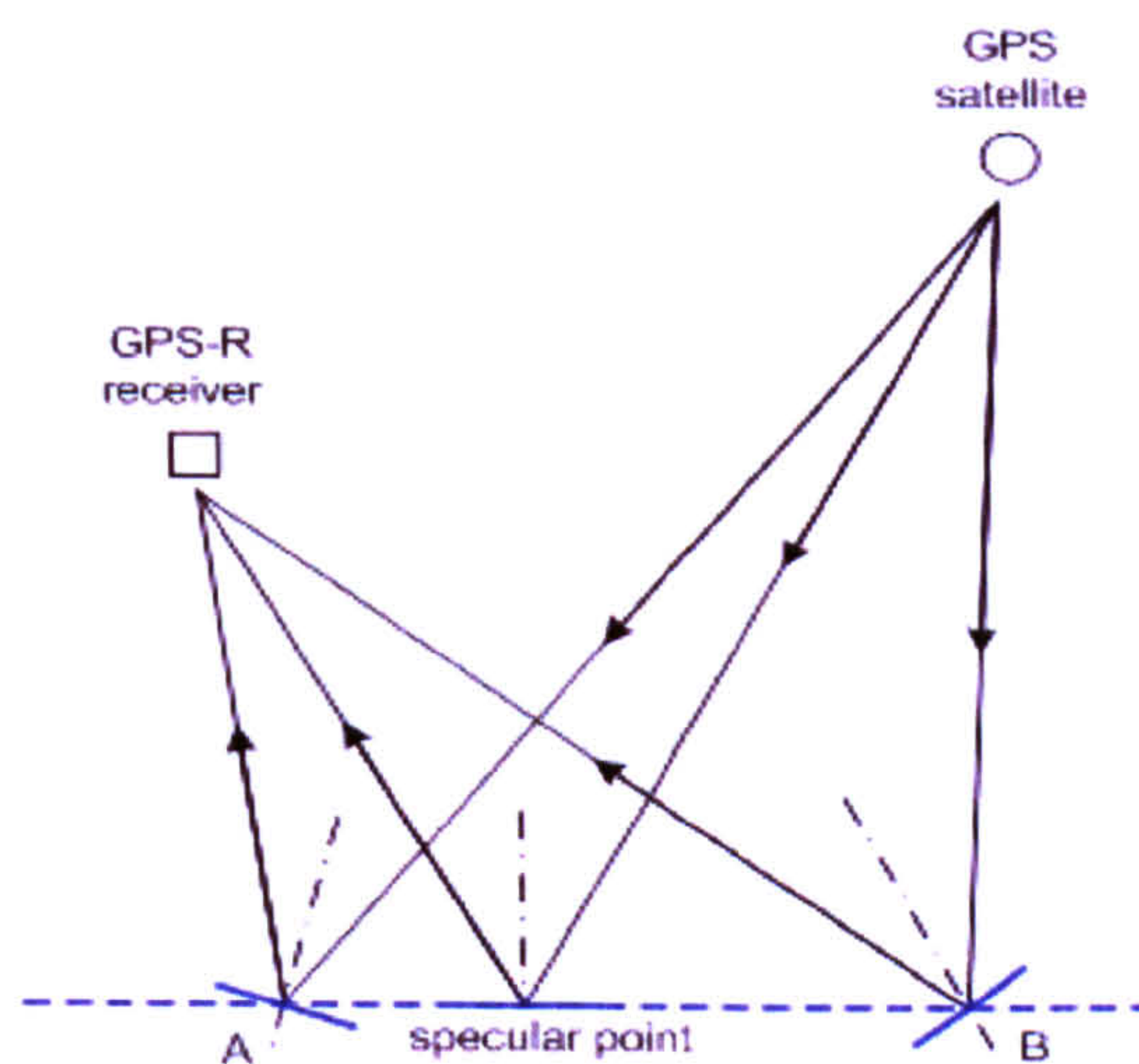


Figure 3-4: Quasi-specular reflection.

As seen in Figure 3-5, when the sea is an ideal mirror-flat surface, where only specular reflections exist, the receiver will not detect signals reflected from A. Given a moderately rough sea surface, however, patch A may have a 30% probability, for example, of reaching the required slope angle. With increasing wind speed, the probability of reflections from A will increase. The reflection area is therefore a function of sea surface roughness, such that with increasing wind speed the reflection boundary, defined through 3σ of the slope PDF, extends further from the specular point. Essentially, the stronger the wind and consequently rougher the sea surface, the larger the glistening zone, and the more likely it will be that patch A acquires the necessary slope angle.

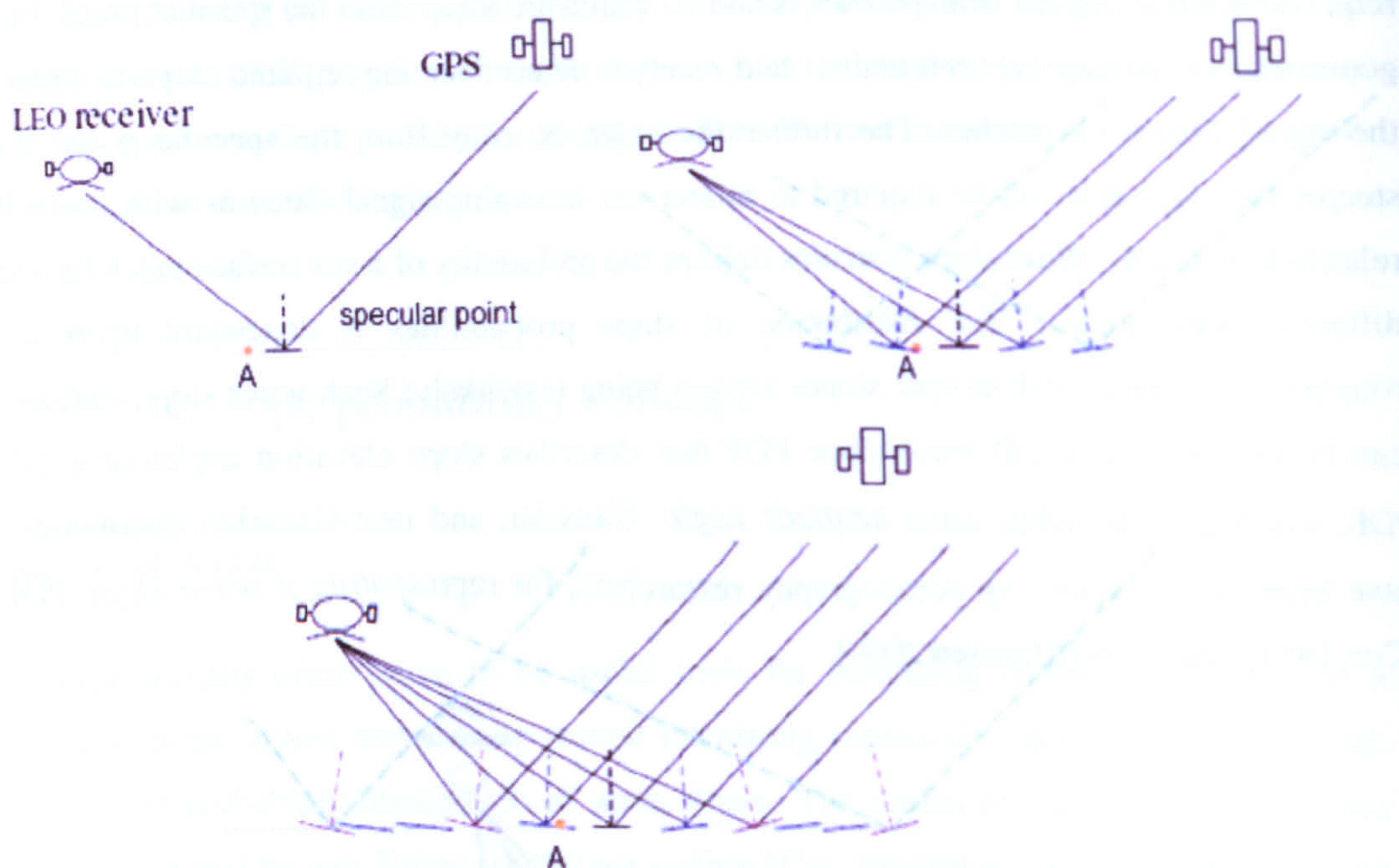


Figure 3-5: Quasi-specular reflection under different wave conditions.

3.3.2 Cox-Munk modelled slope PDF

Methodology

In [Cox 1954] a method was developed to interpret the sun glitter pattern on the sea surface in terms of wave slope statistics. The first phase of this method is to model the reflection geometry. For each small patch, the required slope angle to reflect sunlight into the camera is calculated. This angle is dependent upon the position of the patch relative to the emitter (sun) and receiver (camera). Figure 3-6 illustrates how sunlight is reflected of a sea surface patch that is inclined by such an angle. The blue plane $AB'C'D'$ represents part of a sea surface patch that is inclined from the flat sea surface plane $ABCD$. A ray of sunlight reaches the centre of this patch (A) and is reflected up into the camera. The elevation angle of the patch (β) is measured in the direction which gives the maximum angle. This direction also gives the azimuth angle α of the patch. With the elevation and azimuth angle we can obtain the x direction component (z_x) and y direction component (z_y) of the slope surface. These two angles are used to parameterise wave slope in the statistical models. \vec{z} is the normal vector of $AB'C'D'$ plane and bisects the angle (2ω) between the incident beam and the reflection.

The reflected ray is projected onto the camera plane and forms an image point P . The above geometry modelling method is also adapted into this GPS-R research.

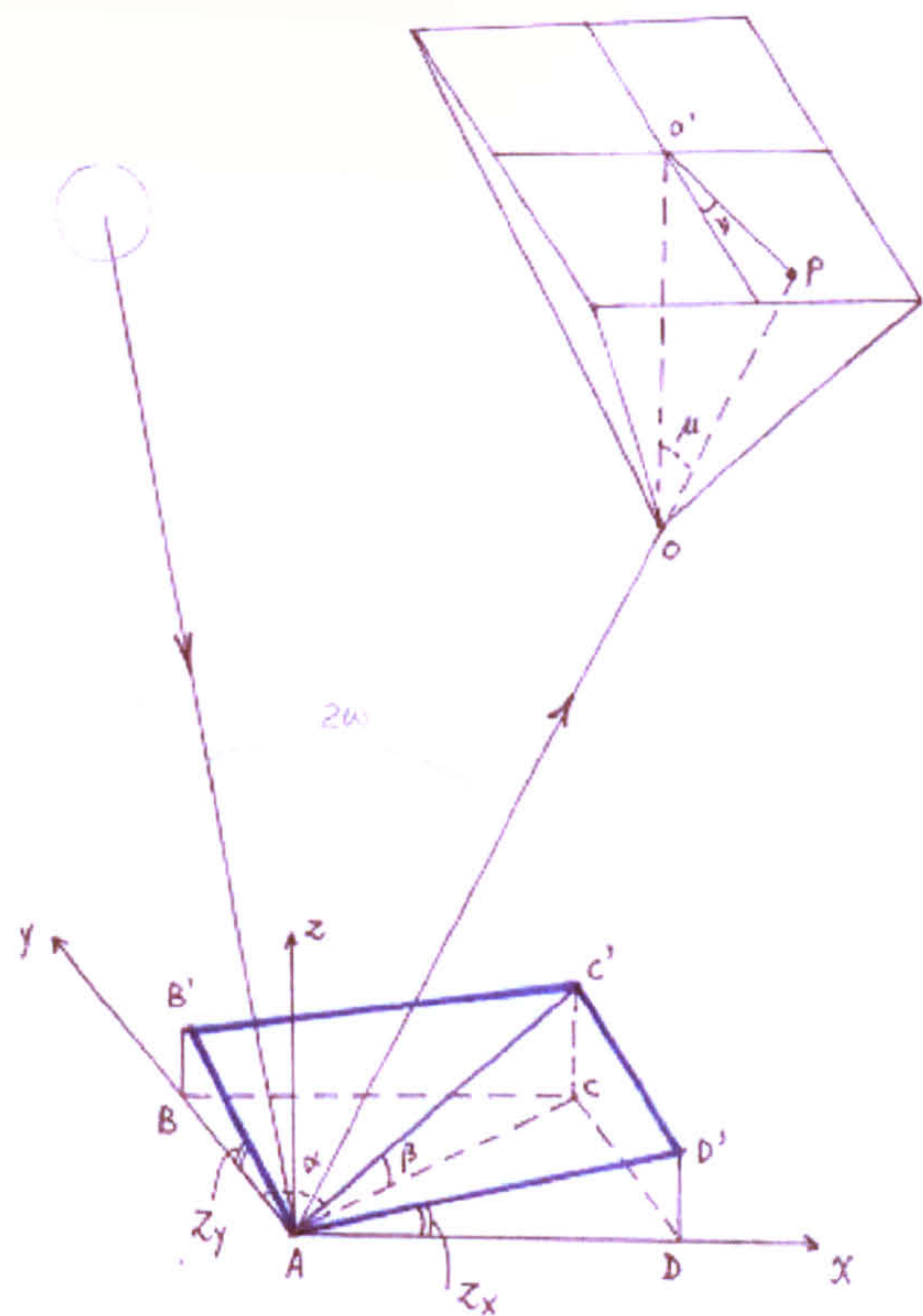


Figure 3-6: Sun glitter reflection geometry.

The second phase of the Cox-Munk method is to analyse the film density of the glitter photographs [Cox 1954] [Janssen 2004]. The film density D is related to the radiance of the sea surface in the line of sight(N):

$$N = C \cdot (\sec^4 \lambda) \cdot \tau^{-1} E(D) \tag{3-25}$$

The density D at each coordinate position ($\mu - \nu$) on the film plane can be measured by a densitometer. The exposure value $E(D)$ is known through the calibration of density D and C is a camera-hardware related parameter. λ is the angle between the principle axis of camera and the reflected ray. $\tau(\lambda)$ is the transmission coefficient of sea water.

If we consider the $\mu - \nu$ coordinate of image point P to be known, then we can obtain the α and β angle of its corresponding patch. The probability density p , which describes the likelihood of a patch being the required angle, can be expressed as a function of N .

$$p = 4\rho^{-1}(\cos^4 \beta)N \cos \mu H^{-1} \tag{3-26}$$

where ρ is the reflection coefficient and H represents the irradiance of the sea surface. By combining Equ. (3-25) and (3-26), the Cox-Munk model builds a connection between the wave slope probability p and photograph's film density D through the use of surface radiance N .

Statistics of slope distribution

Cox and Munk analysed sun glitter photos collected from an aerial platform and suggested that the wave slope PDF is a 2-D Gram-Charlier distribution. The Gram-Charlier distribution has a similar pattern to the Gaussian distribution, but with skewness and peakedness deviations [Cox 1954], which can be expressed as:

$$p = [2D \text{ Gaussian distribution}] \times \left[1 + \sum_{i,j=1}^{\infty} c_{ij} H_i(\xi) H_j(\eta) \right] \quad (3-27)$$

The correction term in Equ. (3-27) consists of the sum of Hermite polynomials H_i and H_j with wind-speed related coefficients c_{ij} . ξ and η corresponds to standardised slope components z_x and z_y , respectively. An example of a Cox-Munk modelled slope PDF is illustrated in Figure 3-7. This figure shows the two principal sections $p(z_x, 0)$ and $p(0, z_y)$, which are from a 2-D distribution under 10 m/s wind speed.

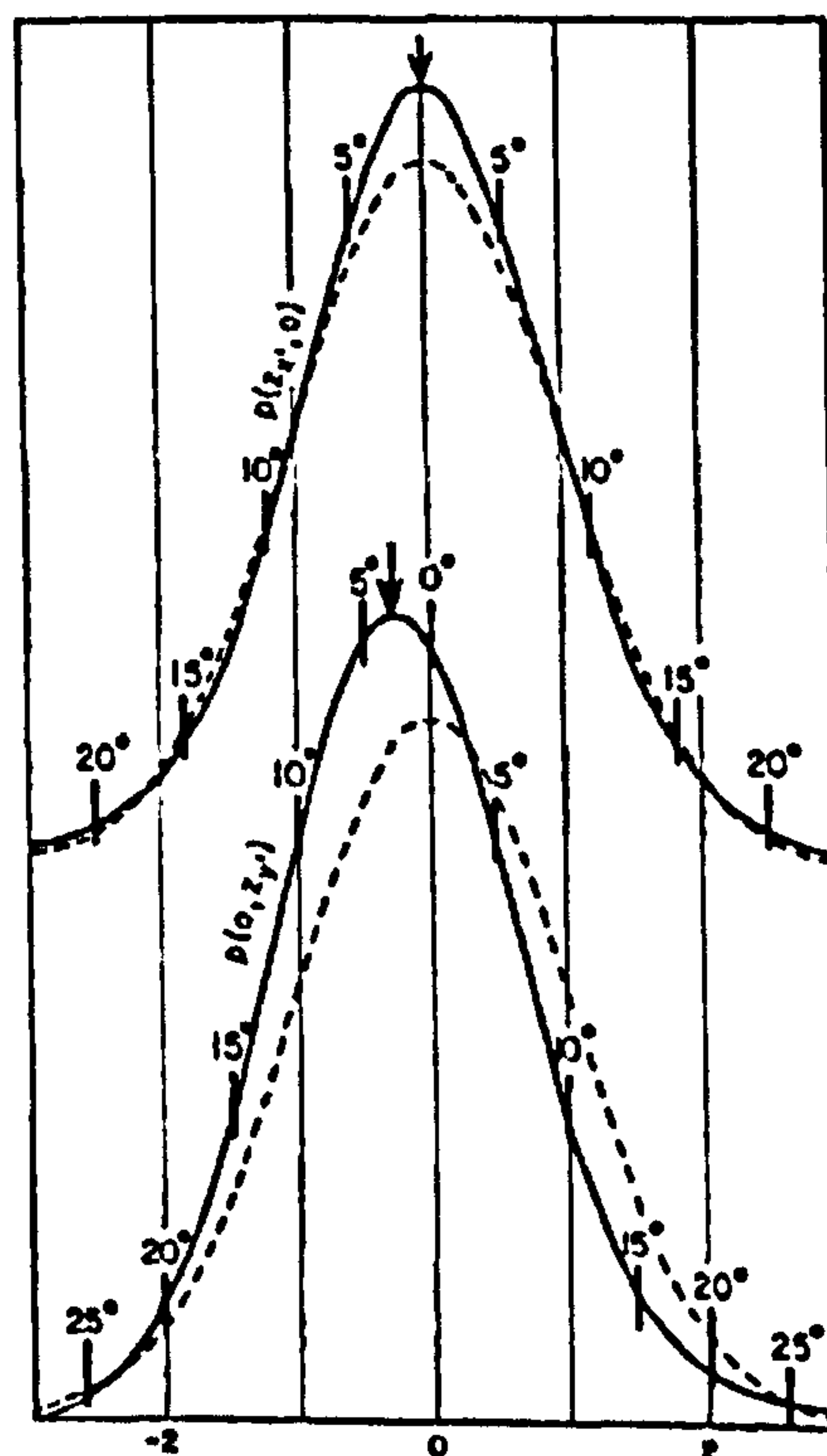


Figure 3-7: Gram-Charlier distribution of the sea surface slopes [Cox 1954].

The top curves of $p(z_x, 0)$ are along the crosswind direction and the bottom curves of $p(0, z_y)$ are along the up-downwind direction. The x axis of the figure represents the standardised components ξ and η for the top and bottom curves, respectively. The heavy vertical segments mark the probabilities of different elevations β (refer to Figure 3-6). The solid lines are the observed distributions (Gram-Charlier) and the dashed lines are the Gaussian equivalents. From this figure, we can see that the observed slope distribution is symmetric in the crosswind direction, but slightly more peaked than the Gaussian prediction. In the up-downwind direction the real slope distribution exhibits a peakedness and skewness that does not exist in the Gaussian distribution.

3.3.3 Elfouhaily modelled slope PDF

[Elfohaily 1997] models the PDF of ocean wave slopes as a standard Gaussian distribution. By integrating an Elfouhaily wave spectrum in both radial and azimuth dimensions, both variances and co-variance values can be obtained to determine the Gaussian slope PDF under certain wind conditions [Zavorotny 2000][Sun 2004]. This is shown below, where x_0 is along the up-downwind direction and y_0 along the crosswind direction:

$$\sigma_{sx_0}^2 = \int_0^\infty \int_{-\pi}^\pi k^2 \cos^2 \varphi \Psi(k, \varphi) k dk d\varphi \quad (3-28)$$

$$\sigma_{sy_0}^2 = \int_0^\infty \int_{-\pi}^\pi k^2 \sin^2 \varphi \Psi(k, \varphi) k dk d\varphi \quad (3-29)$$

$$b_{x_0 y_0} = \langle s_{x_0} s_{y_0} \rangle / (\sigma_{sx_0} \sigma_{sy_0}) \quad (3-30)$$

where

$$\langle s_{x_0} s_{y_0} \rangle = \int_0^\infty \int_{-\pi}^\pi k \cos \varphi \cdot k \sin \varphi \cdot \Psi(k, \varphi) k dk d\varphi \quad (3-31)$$

The variances of the PDF are mostly determined by the low-frequency region of the wave spectrum in the two-scale model. As such, the upper limit of the above wave-number integration can be defined as a wave-number boundary K_* , which is dependent upon the signal wavelength and incident angle ν [Sun 2004].

$$K < K_* = 2\pi \cos \nu / 3\lambda. \quad (3-32)$$

The GPS L1 carrier wavelength λ , which is used in GPS-R research, is 0.1905 m. When the incident angle ν increases, the integration range of the wave number will decrease allowing the shape of slope PDF to change somewhat.

In the satellite baseline frame, wind direction has an initial angle φ_0 with respect to the y axis. With this knowledge, the Gaussian PDF parameters measured in such a frame can then be derived from their equivalents in the wind-direction-frame.

$$\sigma_{sx}^2 = \sigma_{sx_0}^2 \cos^2 \varphi_0 + \sigma_{sy_0}^2 \sin^2 \varphi_0 \quad (3-33)$$

$$\sigma_{sy}^2 = \sigma_{sy_0}^2 \cos^2 \varphi_0 + \sigma_{sx_0}^2 \sin^2 \varphi_0 \quad (3-34)$$

$$b_{xy} = \langle s_x s_y \rangle / (\sigma_{sx} \sigma_{sy}) \quad (3-35)$$

where

$$\langle s_x s_y \rangle = (\sigma_{sy_0}^2 - \sigma_{sx_0}^2) \cos \varphi_0 \sin \varphi_0 \quad (3-36)$$

In summary, wind speed, wind direction and signal incident angle are the three inputs of the Elfouhaily wave model. By assuming that wave slope PDFs have bi-variate Gaussian distributions, which are centred about the origin, the Elfouhaily model is able to produce the variances $(\sigma_{sx}^2, \sigma_{sy}^2)$ and covariance (b_{xy}) that reflect the slope distribution. According to the definition of a bi-variate Gaussian distribution, the probability density value for a certain slope (s_x, s_y) can be expressed by the equation below [Wolfram 2002]:

$$p(s_x, s_y) = \frac{1}{2\pi\sigma_{sx}\sigma_{sy}\sqrt{1-b_{xy}^2}} \cdot \exp\left[-\frac{1}{2(1-b_{xy}^2)}\left(\frac{s_x^2}{\sigma_{sx}^2} - 2b_{xy}\frac{s_x s_y}{\sigma_{sx}\sigma_{sy}} + \frac{s_y^2}{\sigma_{sy}^2}\right)\right] \quad (3-37)$$

The whole procedure of Elfouhaily's modelling method, from initial wind conditions to wave-slope PDF generation, is illustrated in Figure 3-8.

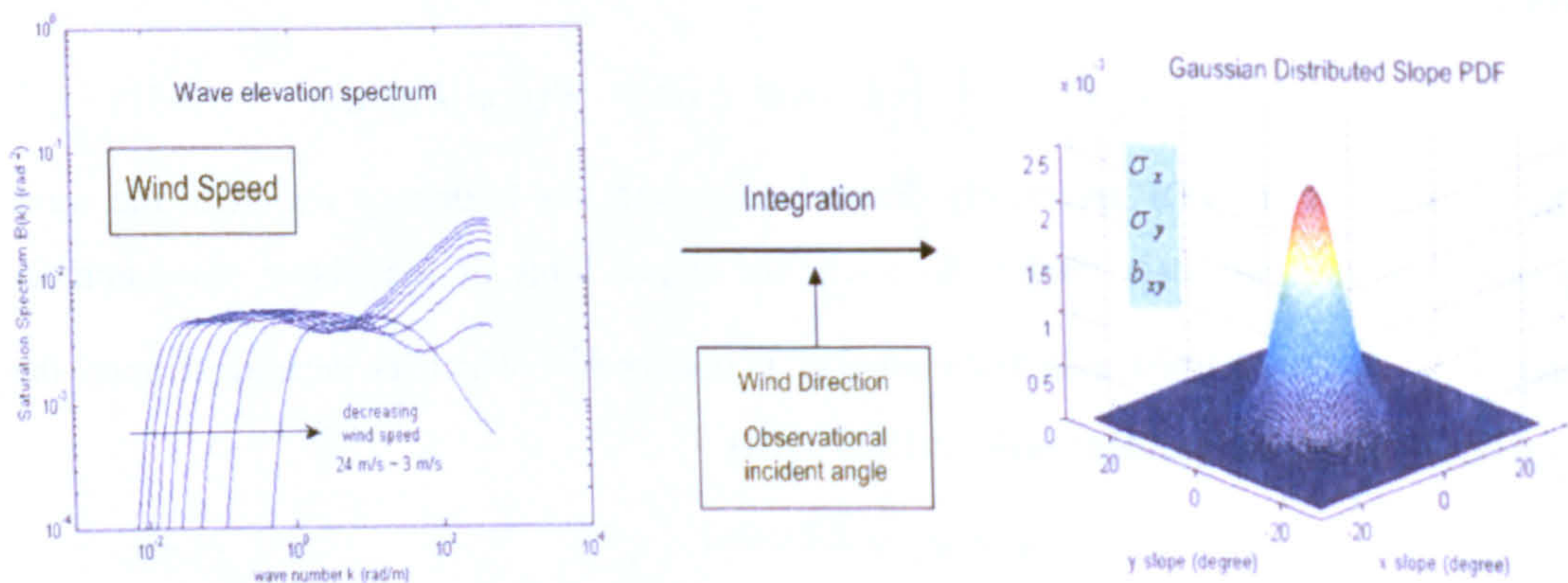


Figure 3-8: The Elfouhaily wave spectrum and slope PDF model structure.

For the above procedure, the Elfouhaily Elevation Spectrum, which is mainly depends on the given wind speed, is first calculated. Wind direction and observational incident angle are then

added into the integration process to determine the Gaussian slope distribution. These latter parameters are two minor factors when compared to wind speed. The sensitivity analysis of the Elfouhaily model will be detailed in Chapter 4.

3.4 Electromagnetic (EM) Model

While the wave spectrum model connects wind conditions and reflection geometry to local wave slope PDF, the EM model describes the relationship between slope PDF and received GPS reflections. The GPS-R EM model, developed by Zavorotny and Voronovich, incorporates the GPS PRN correlation function with the general bi-static radar equation. This EM model, also referred to as the Z-V model, is detailed below.

3.4.1 Z-V model

The Z-V model, which is based on the bi-static radar equation, describes the properties of forward-scattered GPS signals [Zavorotny 2000] [Sun 2004]. By separating the reflection area into patches and using an analysis method similar to the one described in Figure 3-6, the geometric attributes and reflected energy of these patches can be modelled numerically. The received signal power of each patch (dP_r) can be expressed as:

$$dP_r = \frac{P_T G_T G_R \lambda^2 \sigma_0}{(4\pi)^3 R_T^2 R_R^2} ds \quad (3-38)$$

. where: R_T - the range between the GPS satellite and the patch

R_R - the range between the patch and the GPS-R receiver

P_T - the transmitter power output

G_T - the transmitting antenna power gain

G_R - the receiving antenna power gain

λ - the GPS L1 carrier wavelength

ds - the patch area

σ_0 - the Normalised Radar Cross Section (NRCS)

The pattern propagation factors, system losses and noise constants in the original radar equation have been ignored [Sun 2004][Gleason 2006]. The NRCS is a key parameter related to wave characteristics and so is detailed in the next section.

3.4.2 NRCS calculation

In the Z-V model, NRCS is the only parameter related to the physical properties of sea surface patches. All other factors in Equ.(3-8) are calculated with respect to the geometric relation between emitter, receiver and patch location. NRCS can be expressed with the probability of required slope angle [Zavorotny 2000]:

$$\sigma_0(\vec{\rho}) = \frac{\pi |\mathcal{R}|^2 |q|^4}{q_z^4} p\left(-\frac{\vec{q}_\perp}{q_z}\right) \quad (3-39)$$

where \mathcal{R} is the geometric Fresnel coefficient.

p is the slope probability computed from the Elfouhaily modelled slope PDF.

$\vec{\rho}$ and \vec{q} are geometric vectors, as shown in Figure 3-9.

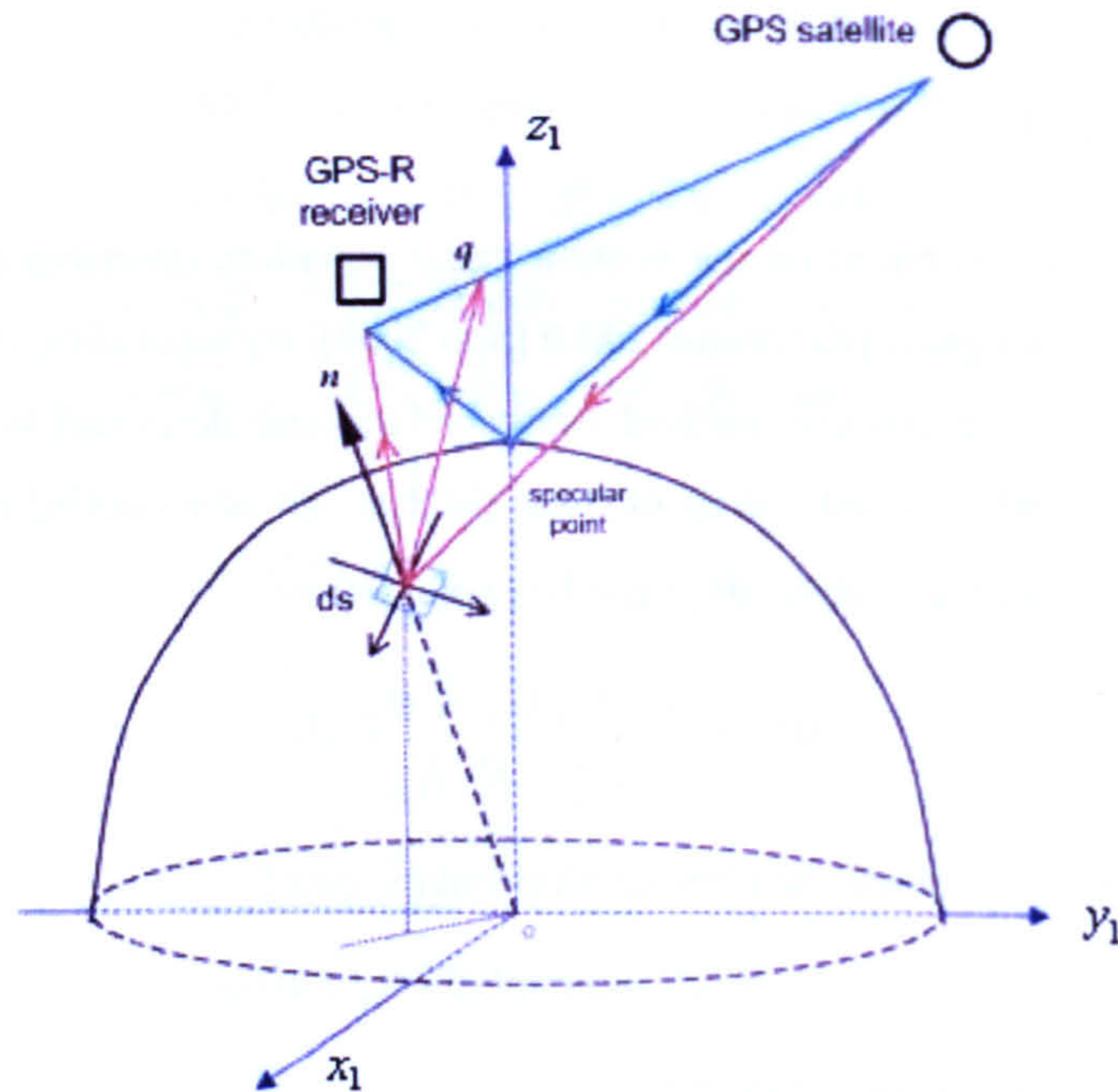


Figure 3-9: Geometric vector definitions in NRCS calculation.

In Figure 3-9, frame $x_1 y_1 z_1$ is rotated from the Earth-Centred Earth-Fixed (ECEF) frame such that the z_1 axis points towards the specular point and the y_1 axis is aligned with the satellite baseline. $\vec{\rho}$ is the location vector from the specular point towards the patch (not shown). \vec{n} is normal to the local sea surface. \vec{q} is normal to the sloped patch, such that it bisects the emitter-patch-receiver signal path. A certain slope angle is required to reflect the incident signal to the receiver. The necessary slope angle is different for each patch. The chance of the patch achieving this angle depends mainly on the local sea surface roughness and wind conditions. To estimate this required slope angle a convenient coordinate frame,

referred to as the local patch frame $x_2 y_2 z_2$, is chosen for the NRCS calculation. As seen in Figure 3-10, the x_2 axis is parallel to $\vec{\rho}$, the z_2 is aligned with the normal vector of the local sea surface (\vec{n}) and the y_2 axis is determined in the accordance with the right-hand rule. The slope-angle related factor in Equ.(3-39) can be expressed as:

$$\frac{\vec{q}_\perp}{q_z} = \frac{q_x + jq_y}{q_z} = \frac{q_x}{q_z} + j \frac{q_y}{q_z} = s_x + js_y \quad (3-40)$$

where q_z is the projection of \vec{q} along the z_2 direction.

\vec{q}_\perp is the projection of \vec{q} in the $x_2 y_2$ plane.

s_x and s_y are the normalised slope components in the x_2 and y_2 directions.

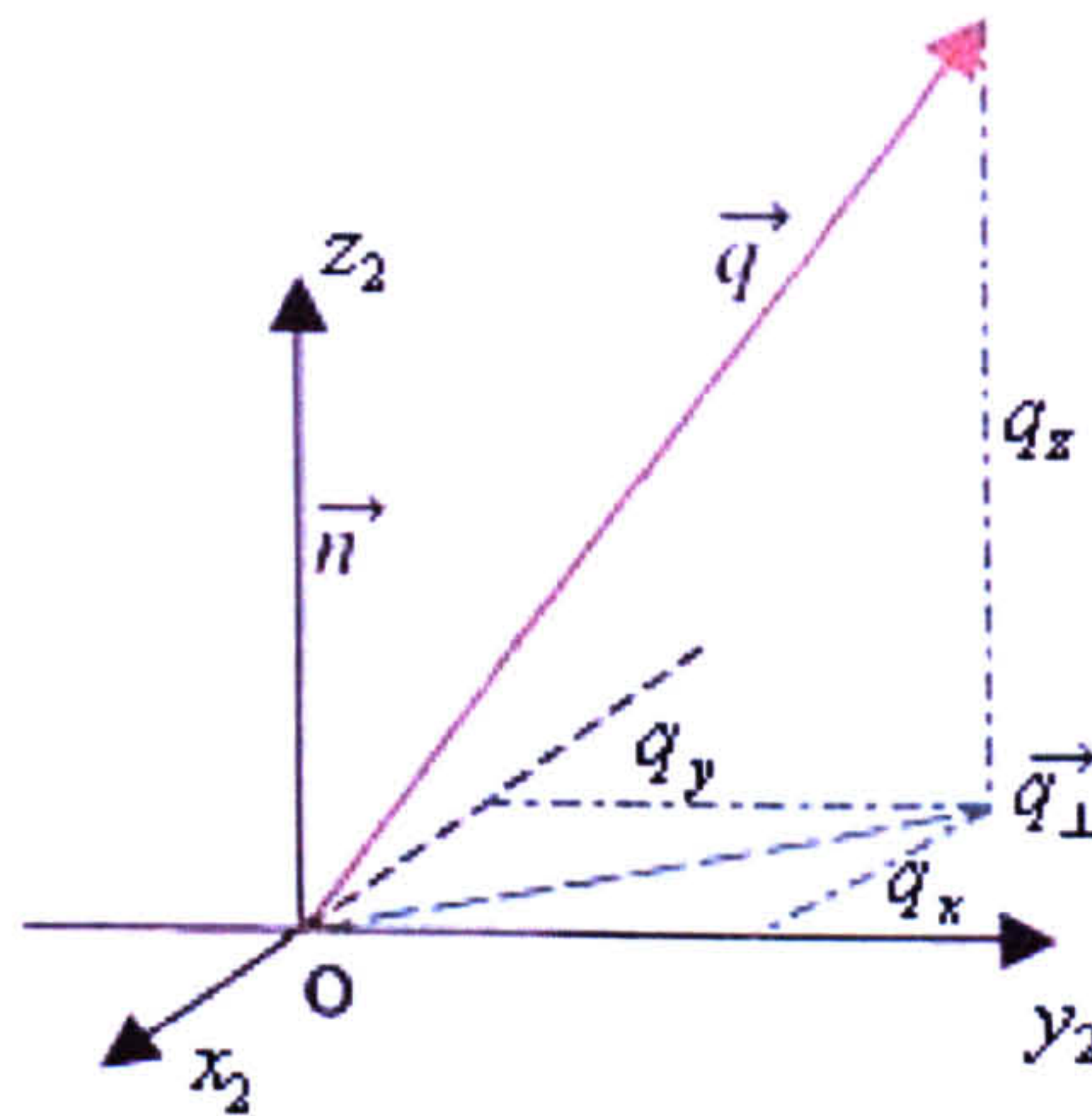


Figure 3-10: Decomposition of \vec{q} vector in the local frame of reflection patch.

The slope probability $p(-\frac{\vec{q}_\perp}{q_z})$ from Equ.(3-39) can be rewritten in terms of slope components s_x and s_y , in accordance with the definition of bi-variate Gaussian PDF such as in Equ.(3-37). The variances and co-variance parameters, which determine this 2-D Gaussian PDF, are outputs from the Elfouhaily wave spectrum model described in section 3.3.3.

In review of the GPS-R EM modelling procedure – firstly, reflection area is divided into a grid of patches. The geometry of each patch is then analysed to determine the require slope angle. We can estimate the probability of each patch achieving such angle with an Elfouhaily-modelled slope PDF, which is dependent upon wind conditions. The reflected signal power from the patches can then be calculated with the EM bi-static radar equation. From this modelling procedure, we can create a spatial energy distribution map of GPS reflections, in accordance with geometry and wind conditions.

3.5 Delay Doppler Map (DDM) generation

3.5.1 GPS signal acquisition procedure

GPS-R receivers share the same signal acquisition procedure with GPS direct signal receivers [Gleason 2006] (refer to section 2.2). When GPS signals arrive at the receiver, we can detect the delay time and Doppler shift in carrier frequency between the acquired signals and emitted signals. If we assume $PN(t)$ to be the original pseudo C/A code, which is modulated with carrier frequency, then the received signal $u(t)$ can be expressed as a delayed and Doppler shifted version of the original signal:

$$u(t) = PN(t + \tau)e^{-j2\pi f_d(t + \tau)} \tag{3-41}$$

where τ is the Delay and f_d is the Doppler shift.

In the GPS C/A code acquisition procedure, a series of Delay-Doppler searches are applied to the received PRN code. The search results can be plotted as an energy distribution map with Delay and Doppler axes. The location of the maximal value of this map indicates the Delay and Doppler of the received signal, as seen in Figure 3-11.

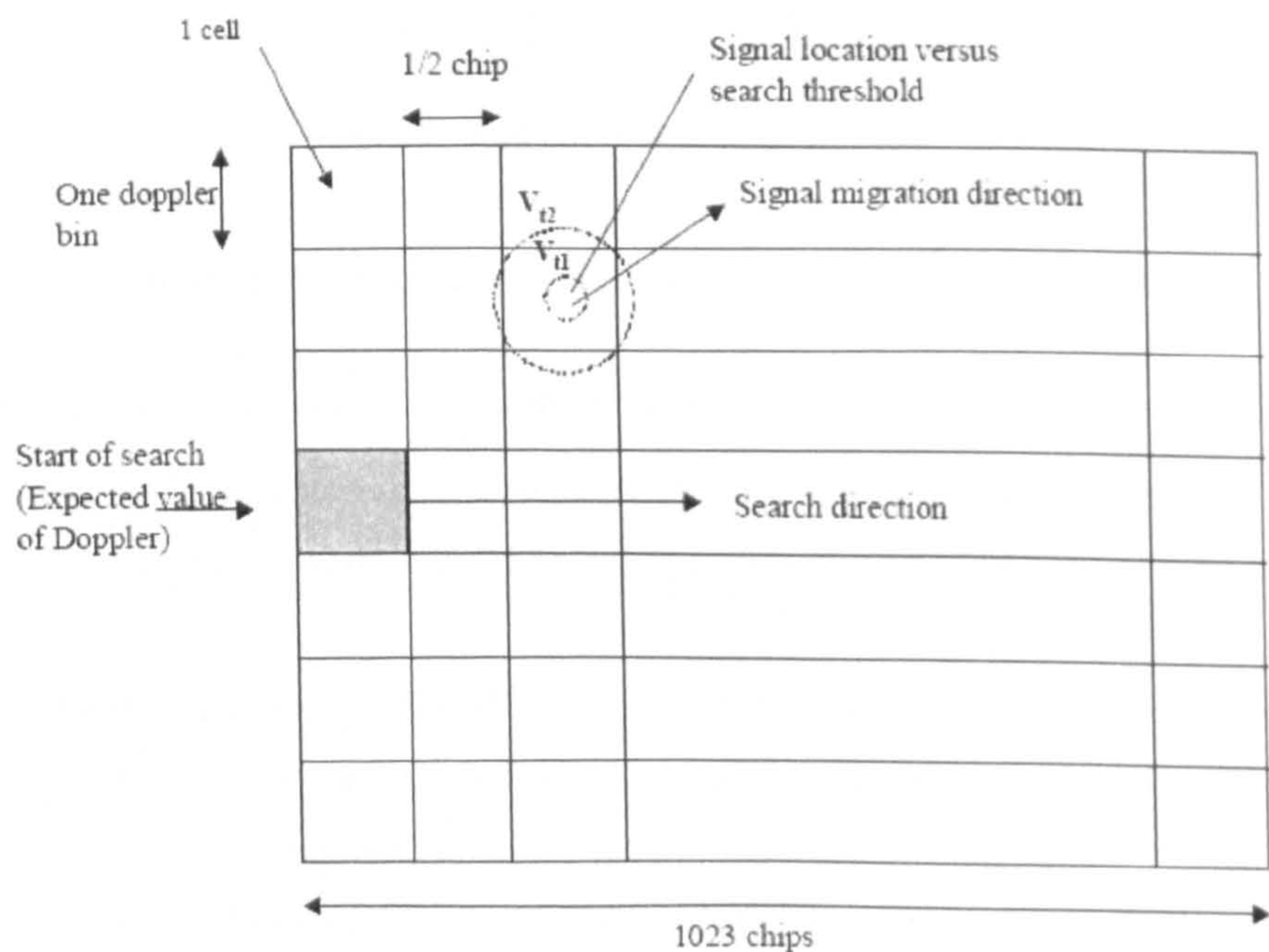


Figure 3-11: GPS signal acquisition searching in Delay and Doppler dimensions [Krumvieda 2000].

For direct GPS signals, the final correlation results show a single high peak on the Delay-Doppler Map (DDM), as seen in Figure 3-12(a). For GPS reflections however, the energy

distribution on the DDM is more complicated. A typical distribution for a GPS-R DDM is that of a horse-shoe pattern, as shown in Figure 3-12(b).

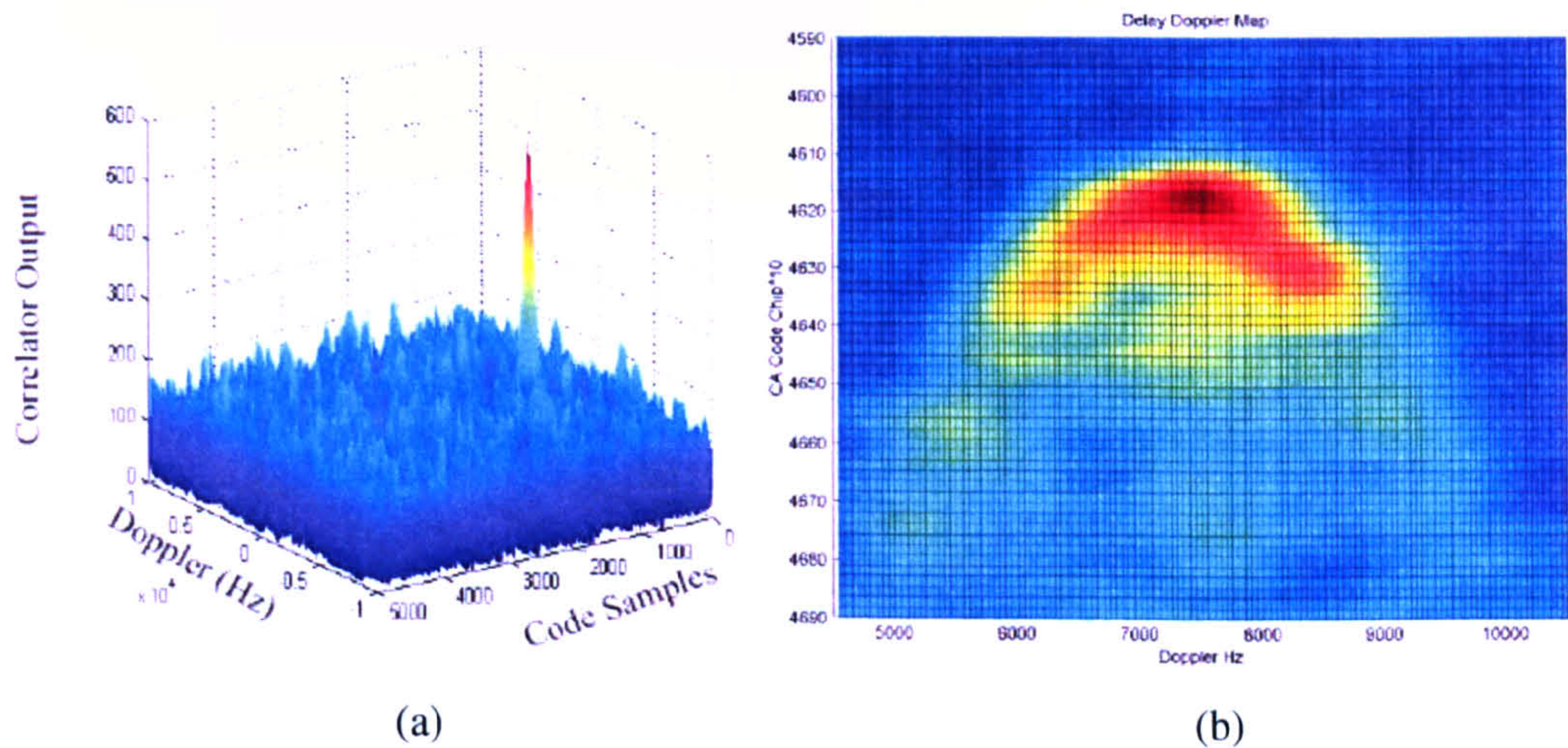


Figure 3-12: GPS signal correlation results (a) direct signal [Krumvieda 2000]. (b) GPS-R signal horseshoe pattern [Gleason 2005].

3.5.2 Creation of DDM from spatial energy distribution

Section 3.4 details the procedure for modelling a GPS-R spatial energy distribution. This is, however, not the final format in which the GPS-R receiver views the data. This section focuses on the conversion from spatial energy map to DDM.

The distribution of reflected signal power can be modelled as a function of each patch’s geometric coordinate, as well as a function of Delay (τ) and Doppler shift (f_d). Each patch on the sea surface has a unique Delay and Doppler signature, which is determined by its reflection geometry. The sensor resolution is such that, multiple patches may correspond to a single Delay-Doppler bin. The energy of the patches within the same Delay ring (red solid lines in Figure 3-13 (a)) and Doppler range (blue dash lines) is summed up to represent the magnitude of certain Delay and Doppler bin on a DDM. As shown in Figure 3-13, patch groups *A* and *B* are within the same Delay ring but in different Doppler ranges. Patch group *C* has a different Delay and Doppler signature to that of *A* and *B*.

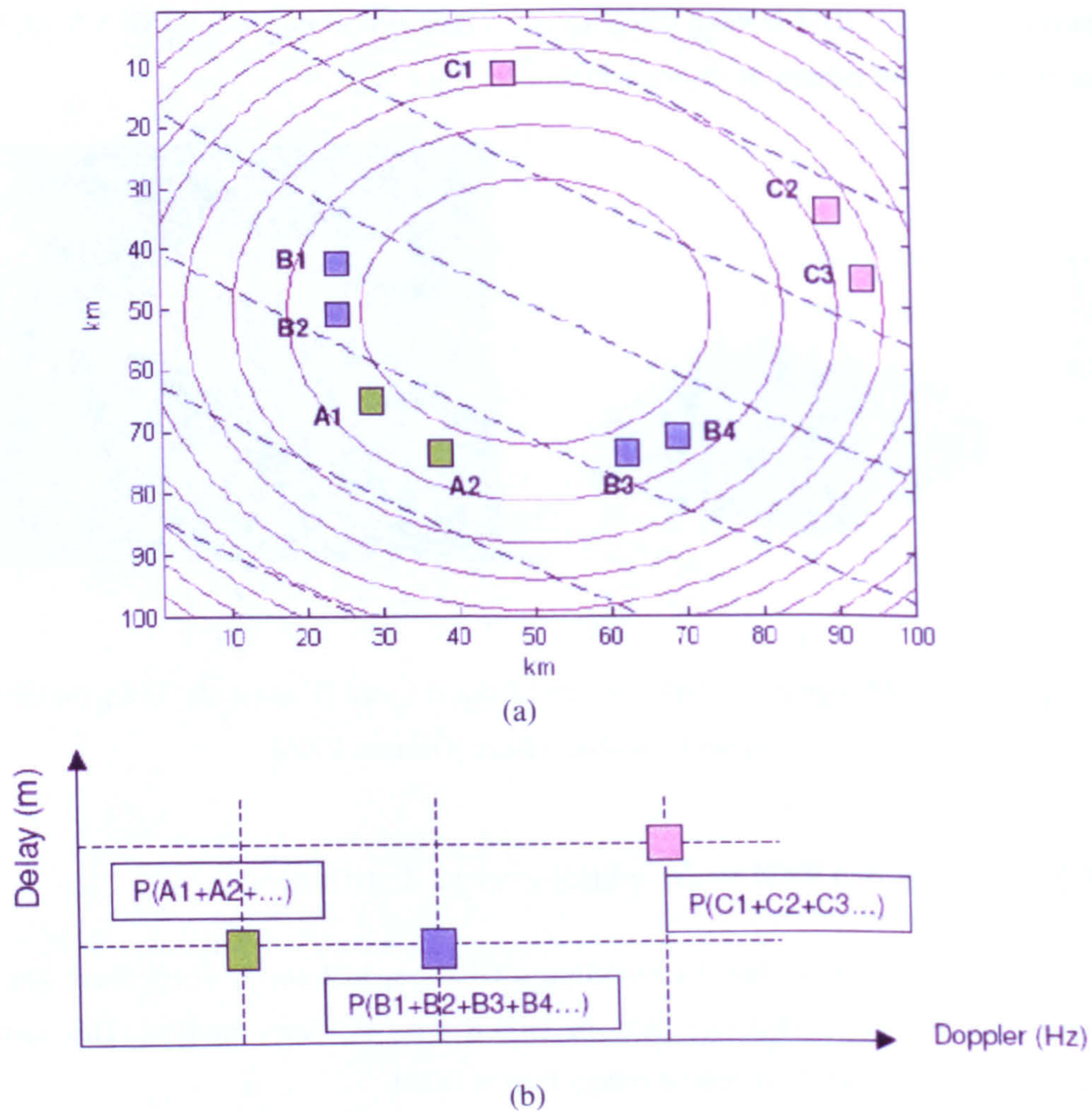


Figure 3-13: DDM generation from spatial energy map.

(a) Delay and Doppler contours (Delay – red solid line; Doppler– blue dash lines).

(b) Patch energy summed up to Delay-Doppler bin.

Figure 3-13 (b) represents the creation of a DDM from a spatial energy map. The sum of energy from each patch group (e.g., A , B or C) is binned as an individual element of the Delay-Doppler Map. While the term “Patch” refers to a spatial grid square on the ocean surface, “Bin” is used to represent each unit of a Delay-Doppler Map. One Delay-Doppler bin may correspond to several patches. Therefore, if we try to inverse a DDM back to a spatial map, there will be an inevitable ambiguous problem of how the energy from one bin is re-distributed among multiple patches. We will continue this discussion in Chapter 5 and 6.

3.5.3 GPS Ambiguity Function

The Ambiguity Function describes the effect of an uncompensated matched filter during the acquisition of finite-energy radar signals [Woodward 1980][Richards 2005]. The GPS

Ambiguity Function (AF) is introduced during the signal correlation procedure, which is performed in Delay-Doppler dimension [Pakinson 1996] [Kaplan 1996]. This function needs to be modelled to more accurately simulate a real DDM scenario. A 2-D GPS AF can be expressed as [Richards 2005]:

$$\chi(\tau, f_d) = \Lambda(\tau) \cdot S(f_d) \quad (3-42)$$

The two terms in the above equation are [Sun 2004]

$$\Lambda(\tau) = \chi(\tau, 0) = \frac{1}{T} \int_0^T PN(t + \tau) PN(t) dt = \begin{cases} 1 - |\tau|/\tau_c, & |\tau| < \tau_c(1 + \tau_c/T) \\ -\tau_c/T, & |\tau| > \tau_c(1 + \tau_c/T) \end{cases} \quad (3-43)$$

$$S(f_d) = \chi(0, f_d) = \int_0^T \exp(-i2\pi f_d t) dt = \frac{\sin(\pi f_d T)}{\pi f_d T} = \text{sinc}(\pi f_d T) \quad (3-44)$$

where τ is the time delay of reflected signals.

τ_c is one C/A code chip length, 1.023 μ s.

T is the coherent integration time, normally an integer factor of 20 ms.

f_d is the Doppler frequency shift of reflected signals.

Figure 3-14 shows the simulation of GPS C/A code Ambiguity Function $\chi(\tau, f_d)$, which is the combination of Delay term $\Lambda(\tau)$ and Doppler term $S(f_d)$.

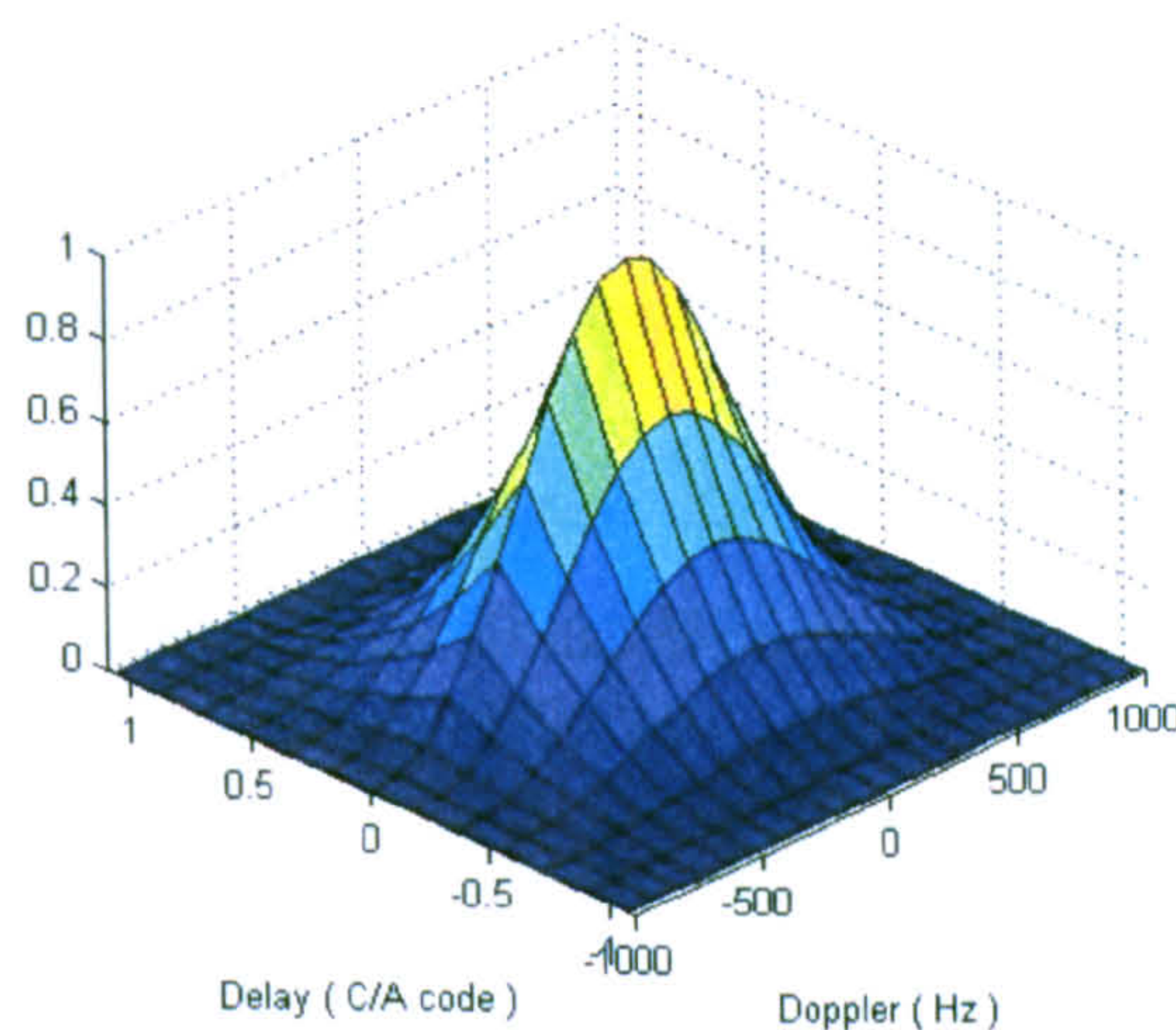


Figure 3-14: GPS C/A code Ambiguity Function.

Along the Delay direction, the GPS AF is a triangle function with two C/A codes length on the Delay axis (Equ.(3-43)). Along the Doppler direction the AF is a Sinc function, with only the main lobe considered in our GPS-R modelling (Equ. (3-44)). In Figure 3-14, the triangle shape and Sinc bell shape can be clearly seen in Delay and Doppler dimensions respectively.

Following conversion from a spatial energy map, a DDM becomes convoluted with the square of the 2-D GPS AF, to represent a more realistic DDM scenario, as expressed below:

$$\begin{aligned}
 Y(\tau, f_d) &= P_r(\tau, f_d) \otimes |\chi(\tau, f_d)|^2 = \iint (\sum_{\tau, f_d} dP_r) \cdot \left| \chi(\tau - \tau', f_d - f_d') \right|^2 d\tau' df_d' \\
 &= \iint (\sum_{\tau, f_d} dP_r) \cdot |\Lambda(\tau - \tau')|^2 |S(f_d - f_d')|^2 d\tau' df_d'
 \end{aligned}
 \quad (3-45)$$

3.6 Conclusions

This chapter details the relevant concepts and modelling methods of GPS-R scatterometry. The current GPS-R model includes a wave spectrum model, which associates sea surface slope PDF with local wind conditions, and a GPS EM model, which describes the relationship between reflected signal power and wave-slope statistics. By combining the wave spectrum model and the EM model, the reflected power of each sea surface patch can be written as:

$$P_r = \underbrace{p(-\frac{\bar{q}_\perp}{q_z})}_S \cdot \underbrace{\frac{G_R |\Re|^2}{R_T^2 R_R^2} \cdot \frac{q^4}{q_z^4} \cdot ds}_Q \cdot \underbrace{\frac{P_T G_T \lambda^2 \pi}{(4\pi)^3}}_T \quad (3-46)$$

This reflected power can be separated into three components:

$$P_r = S \cdot Q \cdot T \quad (3-47)$$

where S stands for the probability of a patch achieving the required slope to reflect GPS signal to the sensor; Q represents geometry-related factors, such as reflection path length and receiver antenna gain; T includes all parameters we assume constant along with a scale factor.

The Delay-Doppler Map simulation principle can be summarised in three steps, as seen in Figure 3-15:

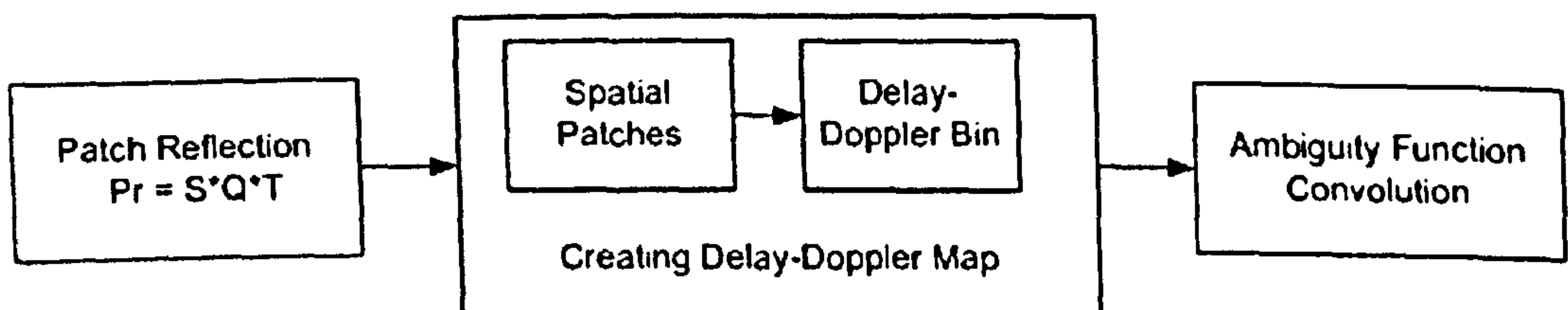


Figure 3-15: DDM simulation procedure

Chapter 3 outlines the GPS-R scatterometric model and associated parameters, from wind conditions to slope probability, from spatial reflection energy distribution to the final Delay-

Doppler Map. The next chapter will investigate the simulation of real GPS-R DDM scenarios. Case studies will be discussed in details, along with the sensitivity analysis of the above GPS-R scatterometric model.

References

- [Apel 1994] J.R. Apel, An Improved Model of the Ocean Surface Wave Vector Spectrum and Its Effects on Radar Backscatter, *Journal of Geophysical Research*, Vol.99, No. C8, pp. 16269-16291, 1994
- [Beckmann 1963] P. Beckmann and A. Spizzichino, *The Scattering of Electromagnetic Waves from Rough Surfaces*, New York Macmillan Co., New York, 1963
- [Bjerkaas 1979] A.Q. Bjerkaas and F.W. Riedel, Proposed Model for the Elevation Spectrum of a Wind-Roughened Sea Surface, Technical Memo, Laurel MD Applied Physics Lab, John Hopkins University, 1979
- [Cox 1954] C. Cox and W. Munk, Measurement of the Roughness of the Sea Surface from Photographs of the Sun Glitter, *Journal of Optical Society of America*, Vol.44, pp.838-850, November 1954
- [Donelan 1987] M.A. Donelan and W.J. Pierson, Radar Scattering and Equilibrium Ranges in Wind-Generated Waves with Application to Scatterometry, *Journal of Geophysical Research*, Vol. 92, No. C5, pp.4971-5029, 1987
- [Elfouhaily 1997] T. Elfouhaily, B. Charpon, K. Katsaro and D. Vandemark, A Unified Directional Spectrum for Long and Short Wind-driven Waves, *Journal of Geophysical Research*, Vol. 102, Issur C7, pp.15781-15796, July 1997
- [Gleason 2005] S.T. Gleason, S. Hodgart, Y. Sun et al., Detection and Processing of Bistatically Reflected GPS Signals from Low Earth Orbit for the Purpose of Ocean Remote Sensing, *IEEE transactions on Geoscience and Remote Sensing*, Vol.43, No. 6, pp. 1229-1241, June 2005
- [Hasselmann 1980] D.E. Hasselmann, M. Dunkel and J.A Ewing, Directional Wave Spectra Observed during JONSWAP 1973, *Journal of Physical Oceanography*, Vol. 10, Issure 8, pp. 1264-1280, August 1980

- [Hasselmann 1985a] S. Hasselmann and K. Hasselmann, Computations and Parameterizations of the Nonlinear energy transfer in a gravity-wave spectrum. Part 1 & 2. *Journal of Physical Oceanography*, No. 15, pp. 1369-1391
- [Janssen 2004] Peter Janssen, *The Interaction of Ocean Waves and Wind*, Cambridge University Press, 2004, ISBN 0-521-46540-0
- [Kaplan 1996] E.D. Kaplan, *Understanding GPS: Principles and Applications*, Artech House Publishers, February 1996, ISBN 0-890-06793-7
- [Kitaigorodskii 1983] S.A. Kitaigorodskii, On the Theory of the Equilibrium Range in the Spectrum of Wind-generated Gravity Waves, *Journal of Physical Oceanography*, Vol.13, pp. 816-827, 1983
- [Krumvieda 2000] K. Krumvieda, P. Madhani, C. Cloman et al., *A Complete IF Software GPS Receiver: A Tutorial about the Details*, Data Fusion Corporation, 2000, <http://www.datafusion.com/gps/baselinereceiver.pdf>
- [Lemaire 1999] D. Lemaire, P. Sobieski, Full-Range Sea Surface Spectrum in Nonfully Developed State for Scattering Calculations, *IEEE transactions on Geoscience and Remote Sensing*, Vol. 37, No. 2, March 1999
- [Parkinson 1996] B.W. Parkinson, J.J. Spilker, *Global Positioning System: Theory & Applications (Vol. One)*, AIAA, January 1996, ISBN 1-563-47106-X
- [Philips 1985] O.M. Philips, Spectral and Statistical Properties of the Equilibrium Range in Wind-generated Gravity Waves, *Journal of Fluid Mechanics*, Vol.156, pp. 505-531
- [Pierson 1964] W.J. Pierson and L. Moskowitz, A Proposed spectral form for fully developed wind seas based on the similarity theory of S. A. Kitaigorodskii, *Journal of Geophysical Research*, vol. 69, pp. 5181-5190, 1964
- [Richards 2005] M.A. Richards, *Fundamentals of Radar Signal Processing*, McGraw-Hill Inc., 2005, ISBN 0-071-44474-2
- [Schooley 1954] A.H. Schooley, A Simple Optical Method for Measuring the Statistical Distribution of Water Surface Slopes, *Journal of American Optical Society*, Vol.44, pp. 37-40, 1954
- [Shaw 1997] J.A. Shaw and J.H. Churnside, Scanning-laser Glint Measurements of Sea Surface Slope Statistics, *Applied Optics*, Vol.36, pp. 4202-4213, 1997
- [Stewart 2005] R.H. Stewart, *Introduction to Physical Oceanography*, Open Source Textbook, Department of Oceanography, Texas A&M University, US, 2005

http://oceanworld.tamu.edu/resources/ocng_textbook/chapter16/chapter16_04.htm#top

[Stokes 1880] G.G. Stokes, On the Theory of Oscillatory Waves, in G.G. Stokes, Mathematical and Physical Papers, Vol.1, Cambridge University Press, Cambridge, 1880

[Sun 2004] Y. Sun, Remote Sensing of Ocean Winds and Waves using Bi-static GPS reflections: Review, Technical Notes, Surrey Space Centre, University of Surrey, June 2004

[Ulaby 1986] F.T. Ulaby, R.K. Moore and A.K. Fung, Microwave Remote Sensing: Active and Passive, Vol. II, Artech House, 1986

[Wolfram 2002] Wolfram Mathworld website, Gaussian Function, December 2002, <http://mathworld.wolfram.com/GaussianFunction.html>

[Woodward 1980] P.M. Woodward, Probability and Information Theory with Applications to Radar, Artech House Publishers, December 1980, ISBN 0-890-06103-3

[Zavorotny 2000] V.U. Zavorotny, A.G. Voronovich, Scattering of GPS Signals from the Ocean with Wind Remote Sensing Application, IEEE transactions on Geoscience and Remote Sensing, Vol.38, Issue 2, pp.951-964, March 2000

Chapter 4. GPS-R Delay-Doppler Map Simulation

4.1 Introduction

Dozens of datasets have been received from the UK-DMC GPR-R platform since 2003. Earlier work concentrated on front-level data processing of GPS-R signals. This chapter continues the research on these data, focusing on the data simulation procedure and the evaluation of current modelling method.

While Chapter 3 describes the theoretic model for GPS-R scatterometry, Chapter 4 reviews the technical details in GPS-R simulation procedure. DDM simulations, which are based on wind information and reflection geometry of real scenarios, are compared to corresponding truth data from the UK-DMC GPS-R receiver. The correlations between simulated and real data will help us to validate the modelling technique used in this space-borne GPS-R research.

Six datasets are chosen for this data-model fitting experiment. Two of these datasets, R13 and R12, are presented in this chapter as case studies. While R13 represents a weak wind-speed case, R12 corresponds to a medium wind-speed case. While noise reduction processing is applied to real DDM data to enhance the signal, an image registration method is used to compensate for the mismatch in Delay-Doppler shift. The outcomes of the experiment prove the viability of the current GPS-R model. The results from model sensitivity analysis, however, highlight the limited scope of GPS-R for wind information extraction.

4.2 Simulation procedure

The GPS-R datasets received from UK-DMC have time tags. Information about the GPS emitter can be found by analysing the C/A code carried within GPS signals. The time tag can therefore indicate the instant positions and velocities of the UK-DMC and GPS satellite. With further analysis, we can find the signal scattering region and then rotate the Earth-centred coordinates system to a more convenient frame to model the reflection energy distribution in Delay-Doppler format. Ground-truth wind conditions are extracted from local buoy data and used to validate our GPS-R simulation

experiments. The following sections mainly look into the geometric modelling of GPS-R data scenarios as part of the simulation procedure framework. Other related technical aspects are also detailed in this chapter.

4.2.1 Searching for specular point

The reflection geometry can be determined with the time tag and GPS emitter information as extracted from the received GPS-R data. By using the SGP4 orbit propagation model, the ECEF positions and velocities of the UK-DMC and GPS satellite can be calculated. While the positions of the satellites are used for the purpose of calculating specular reflection geometry and the Delay values, the velocity vectors are used for computing the Doppler shift.



Figure 4-1: R10 geometry scenario - UK-DMC (blue) and GPS SVN-17 (purple).

Using the Satellite Tool Kits (STK) software, Figure 4-1 shows two satellite positions from GPS-R dataset R10. The UK-DMC satellite (blue) is around the Hawaii area. The reflection geometry in ECEF frame can be seen in Figure 4-2.

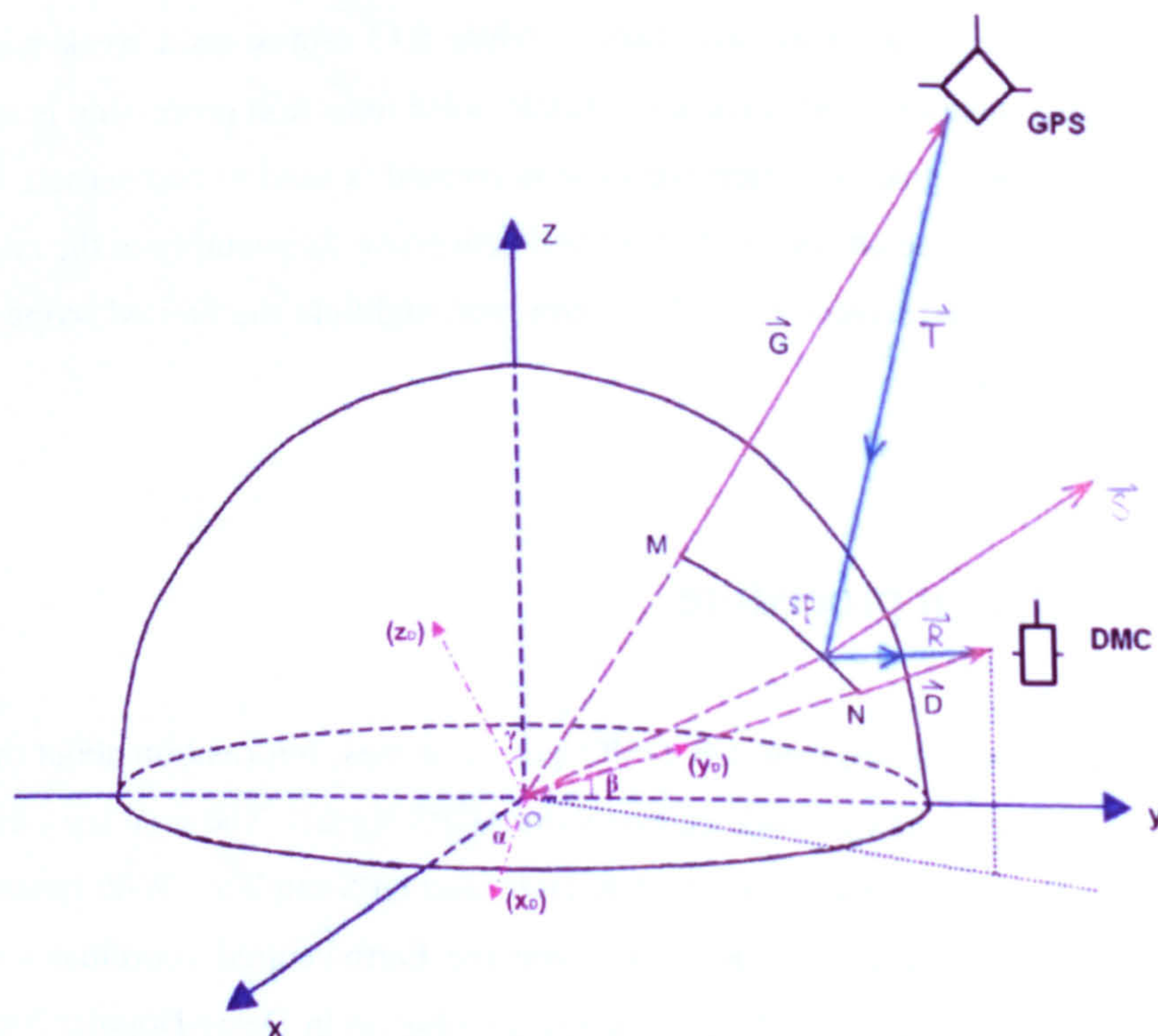


Figure 4-2: GPS-R reflection geometry in ECEF frame.

Compared to the MEO altitude of GPS satellites, the Low Earth Orbit (LEO) of UK-DMC is much closer to the Earth surface. The GPS reflection area is therefore always near the sub-satellite point of UK-DMC. As seen in Figure 4-2, the UK-DMC satellite and GPS emitter are defined as two known position vectors \vec{D} and \vec{G} relative to a spherical Earth. Under such condition we aim to find the ECEF coordinates of the specular point (SP). This specular point gives the shortest signal reflection path between emitter and receiver. The position of the specular point is used in GPS-R geometric modelling, and also dictates the proximity of the ground truth reference for our GPS-R DDM simulations.

To find the specular point, we first rotate the ECEF frame to a local frame $x_D y_D z_D$ (Figure 4-3), where y_D is aligned with the UK-DMC position vector \vec{D} and z_D is in the same plane with \vec{D} and \vec{G} . x_D , y_D and z_D naturally form a right-hand orthogonal system. The three steps used to rotate ECEF to the local frame $x_D y_D z_D$ are:

- 1) Rotate z axis to make y_D align with the projection of \vec{D} on the xy plane.
- 2) Rotate x_D axis to make y_D align with \vec{D} .
- 3) Rotate y_D to make z_D on the same plane with \vec{G} .

By using three rotation matrices we can therefore obtain the new vector coordinates of \vec{D} and \vec{G} in the local frame $x_D y_D z_D$.

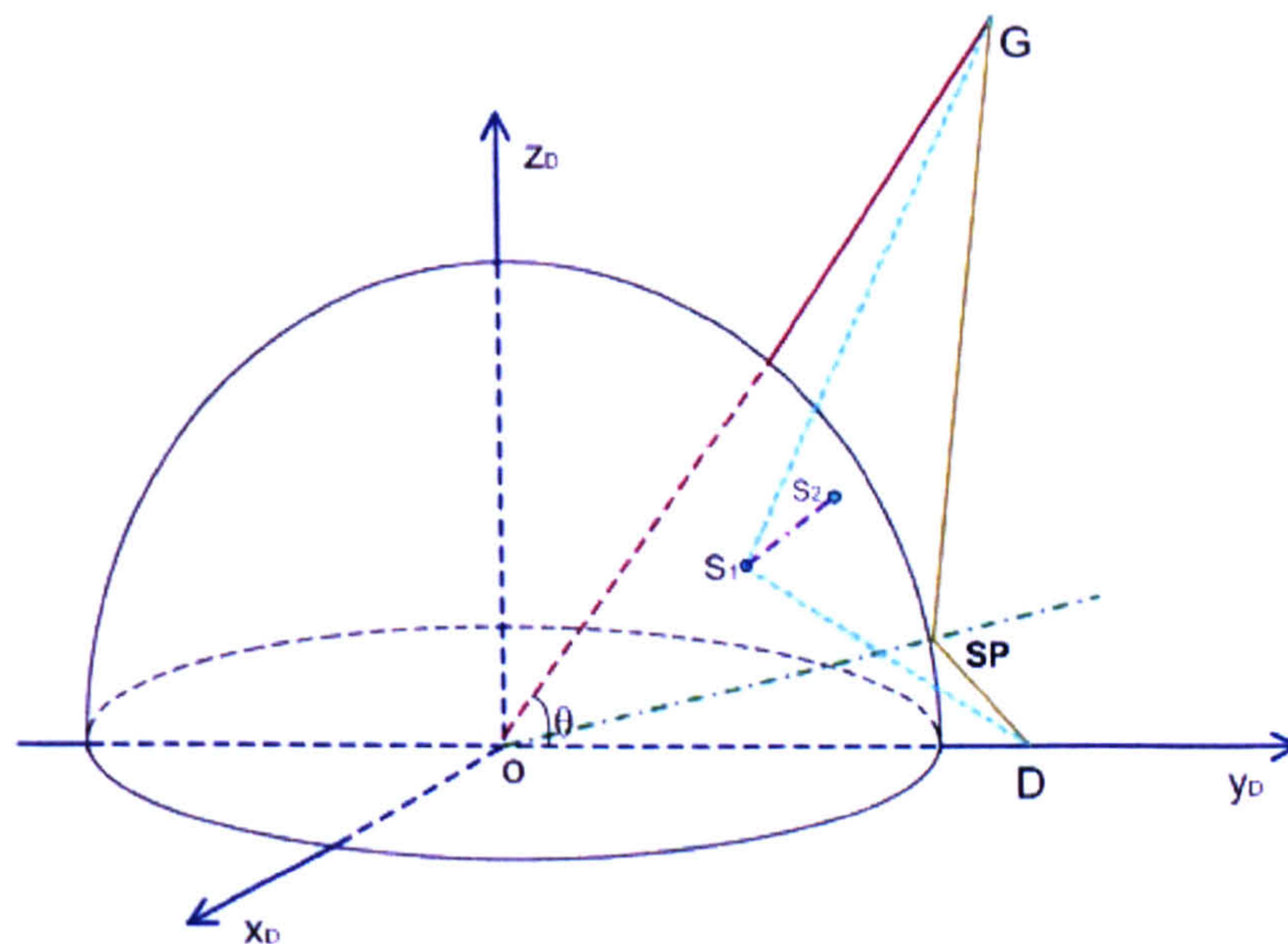


Figure 4-3: Minimum path length searching in the local frame.

In the $x_D y_D z_D$ frame, the specular point is assumed on the $y_D - z_D$ plane, which corresponds to our principal circumference of the Earth sphere (Figure 4-3), and lies between point G and D but closer

to D (UK-DMC). To explain the validity of the above assumption, we first find a reference point (SP point in Figure 4-3) on the principal circumference, between the sub-satellite points of G and D , that gives the minimum reflection path length among the the points along this circumference curve. An ellipsoid with foci G and D , as we image, is tangent to the Earth sphere at this point SP . If there is another point S_1 outside the $y_D - z_D$ plane, which forms a reflection path shorter than the one through SP , then another symmetric point S_2 can be found on the other side of the spherical Earth surface to achieve the same reflection path length. The ellipsoid with foci G and D will intercept the Earth sphere with point S_1 and S_2 at the same time. Actually this ellipsoid will intercept with the spherical Earth surface with infinite points. However, according to the physical meaning of reflection, one and only one specular point exists. The S_1 assumption is therefore invalid, which means, ideally there should not be any point other than SP to reflect the signal towards the receiver.

To investigate an analytical proof of this assumption, we abstract the geometric relation of O (Earth centre), G (GPS), D (UK-DMC) and S (Specular point) in Figure 4-4. The fact that, the shortest reflection path is via the specular point, is a key point for this discussion.

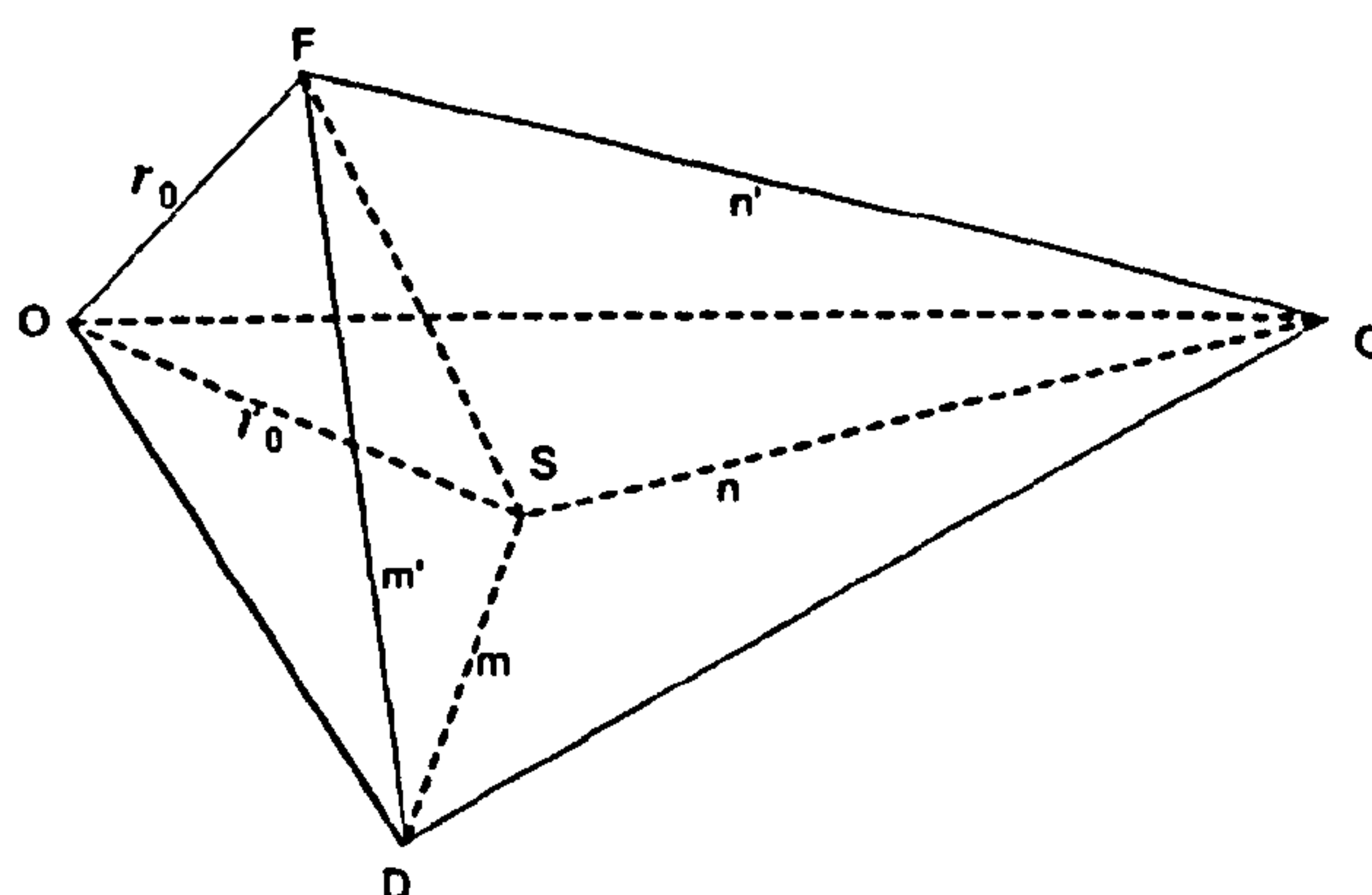


Figure 4-4: Abstract geometry model for specular point searching.

In $\triangle ODG$, the lengths of three sides $|OD|$, $|OG|$ and $|GD|$ are known. S is on the same plane with triangle $\triangle ODG$, where $|OS|$ equals to the Earth radius r_0 . Draw point F outside plane ODG , make $|OF|$ equal to $|OS|$, and define other line lengths as $|SD| \equiv m$, $|FD| \equiv m'$, $|SG| \equiv n$, $|FG| \equiv n'$. Our aim is to prove that, with such F point, $m' + n' > m + n$. The proving procedure following this model is complicated and drifting away from the main goal of this research. However, as an interesting question, it might be solved by further exploration of the above method or using spherical geometry to model the problem instead of traditional plane geometry.

Back to the topic, numerical method is used to search for the specular point position. In the local frame $x_D y_D z_D$ as seen in Figure 4-3, small steps of θ angle are set to find the minimum path length. Since the specular point is very close to the sub-track point of UK-DMC, there is no need to search the whole GD curve. To reduce the computing cost we can just choose a small range of θ around point D to search for the specular point.

In summary, the specular point searching procedure can be set into three steps:

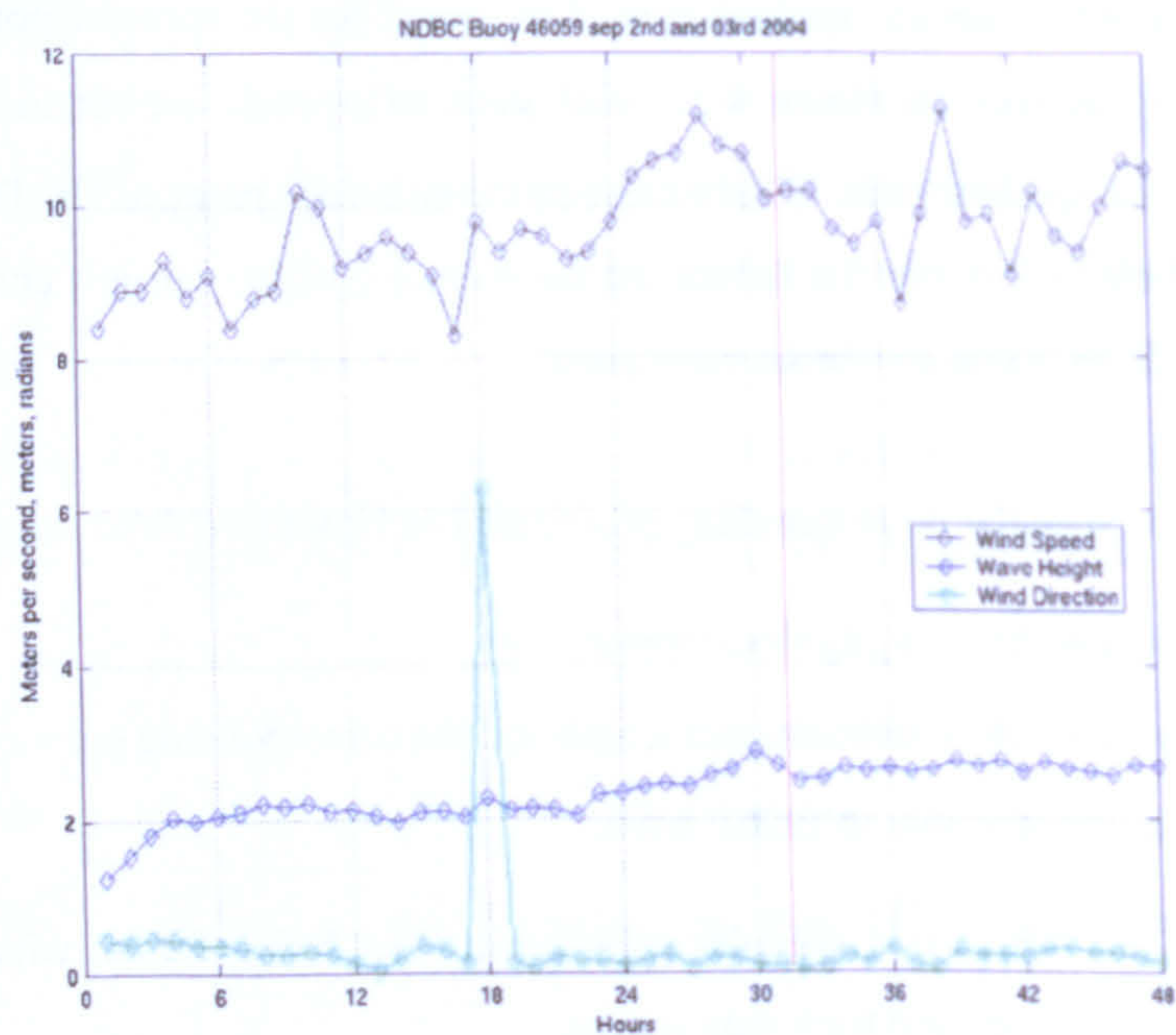
- 1) ECEF frame $\rightarrow x_D y_D z_D$ local frame.
- 2) Searching for the minimum path length and the corresponding point on GD curve.
- 3) $x_D y_D z_D$ local frame \rightarrow ECEF frame.

The output of this search is a specular point position in ECEF frame, with which we can choose reference buoys as the ground truth data source.

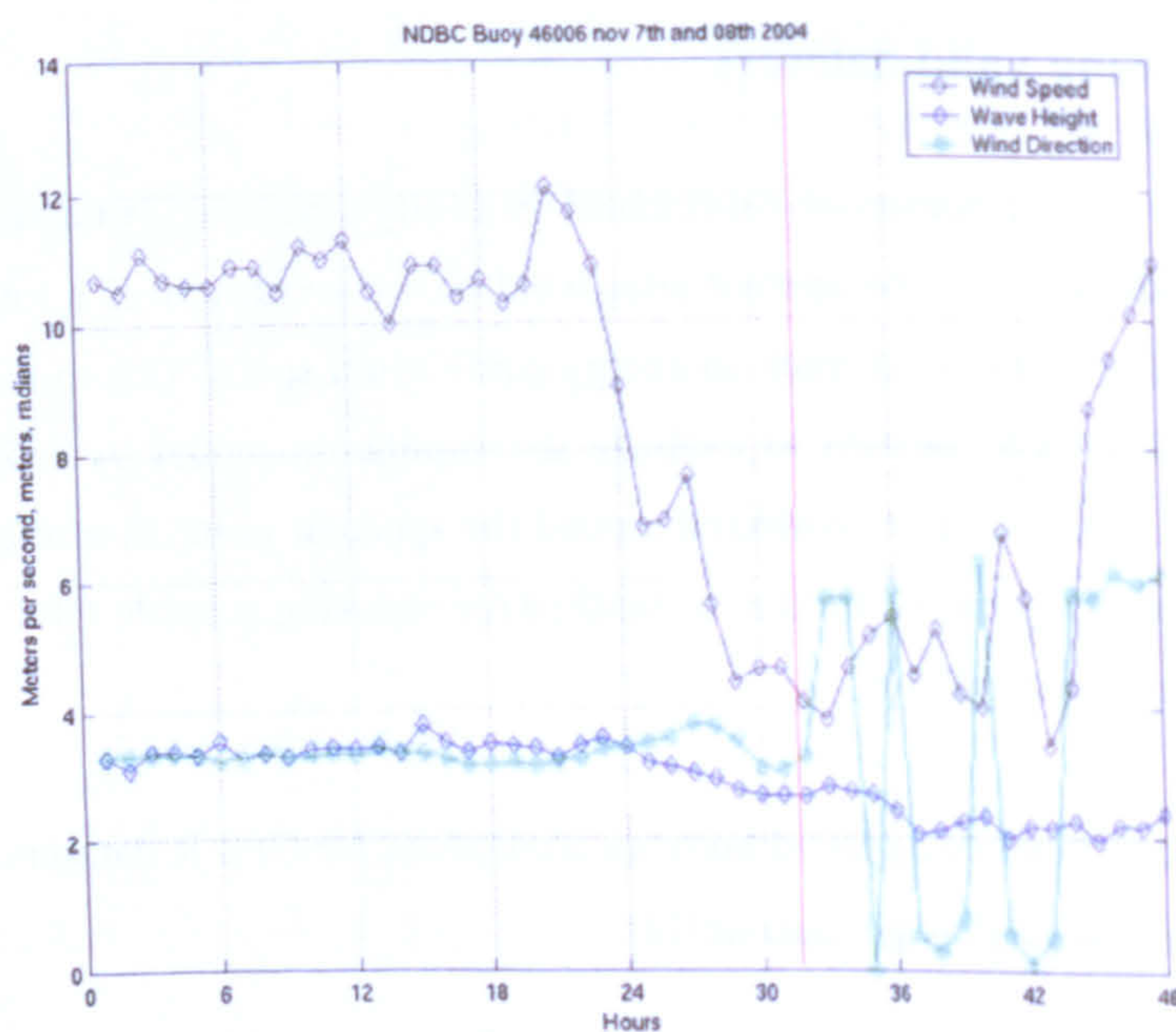
4.2.2 Choosing valid datasets

The Elfouhaily wave spectrum model is based on a fully developed sea assumption. It means that the Elfouhaily model can only be applied after wind blows steadily over a long fetch for a long time, where the sea states and wind reach an energy equilibrium status. Due to this restriction, we need to choose suitable GPS-R datasets to evaluate the simulation model by referring to the local buoy measurements. Buoy data are collected around the specular point as a reference of local wind and wave conditions. They can be used as a standard for choosing suitable GPS-R datasets which satisfy the fully develop sea condition.

Figure 4-5 below shows two typical buoy measurements for GPS-R datasets. While (a) is for a valid dataset R10, (b) is for an invalid dataset R11.



(a)



(b)

Figure 4-5: Buoy measurements for R10 (a) and R11 (b) datasets: wind speed (black), wind direction (green) and wave height (blue).

The vertical red lines indicate the time tags of received datasets. While R10 is valid due to the steadiness of wind and sea, R11 is invalid because of the sudden change in wind speed just before the signal acquisition. According to this criterion, six sets of data are chosen for the simulation experiment to evaluate the existing GPS-R scatterometric model in space application. These datasets are R10, R12, R13, R14, R15 and R18.

4.2.3 Coordinate system rotation

To apply the Z-V model in simulation, it is more convenient to consider the geometry in a local coordinate system $x_1 y_1 z_1$, as seen in Figure 4-6, than in ECEF (Figure 4-2).

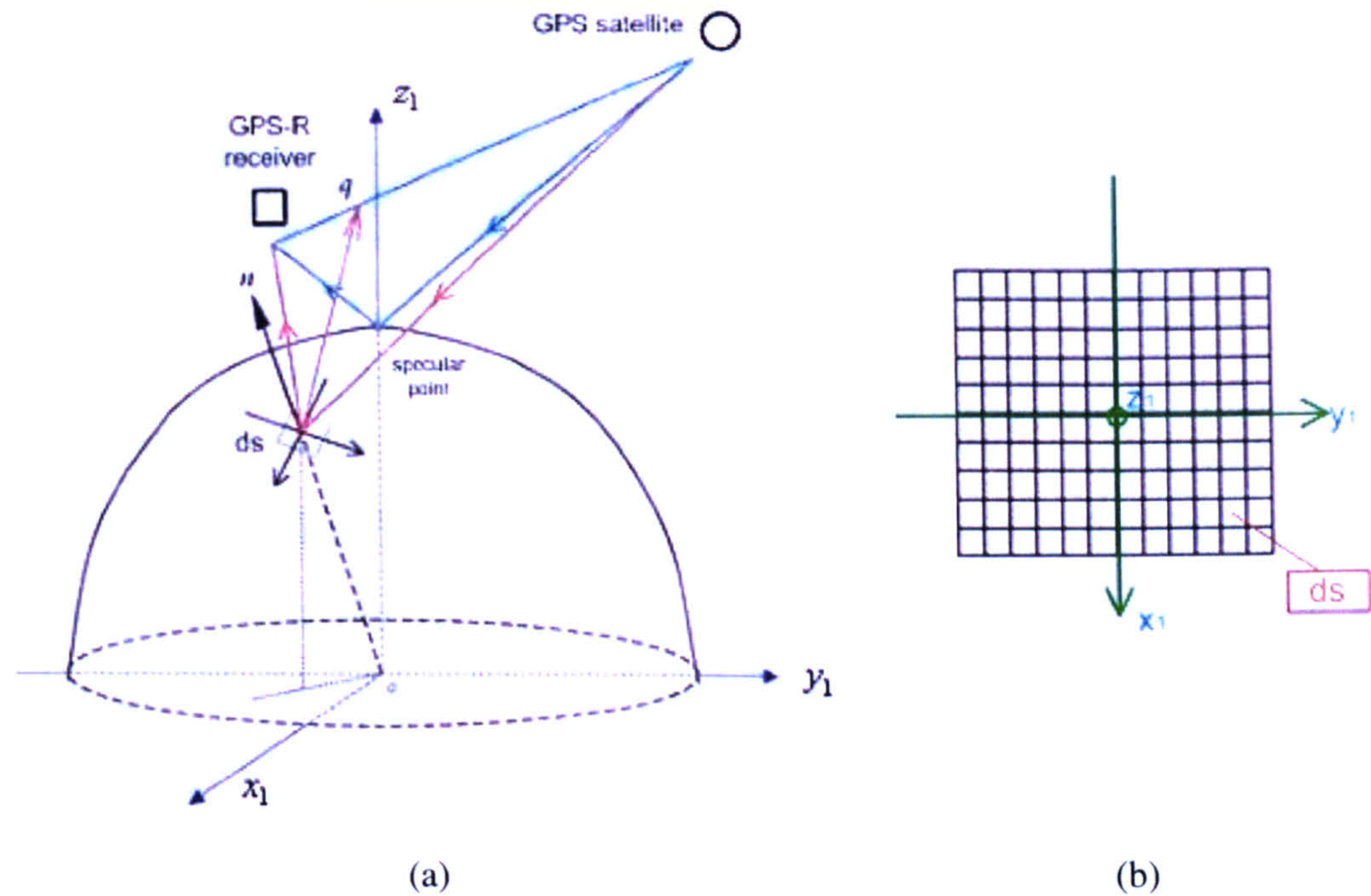


Figure 4-6: GPS-R reflection geometry description in the specular point frame.

In reference to Figure 4-6 (a), the new z_1 axis is aligned with the specular point vector, the UK-DMC and GPS satellite are both on the new y_1 axis, with z_1 bi-sectoring the reflection angle. The reflection area around the specular point is divided into a grid, as in Figure 4-6(b). For each patch, the Delay and Doppler properties are calculated individually, along with the reflected signal power, which is modelled from the Elfouhaily model and the Z-V model, as described in Chapter 3 (Equ. (3-38)).

4.2.4 Antenna pattern

Since the reflection area is much closer to UK-DMC than to GPS, the GPS emitter antenna pattern can be ignored, we have to however, consider the UK-DMC receiver antenna pattern as modelled in Figure 4-7 (a). In the local frame $x_1 y_1 z_1$, ds is the considered small patch. \vec{v} is the instant UK-DMC velocity vector of UK-DMC, representing the orientation of the satellite. The location of patch B forms angle α and β with A , which is the nadir point of UK-DMC. These two angles decide the antenna gain for the patch B , i.e., the G_R parameter in Equ. (3-38).

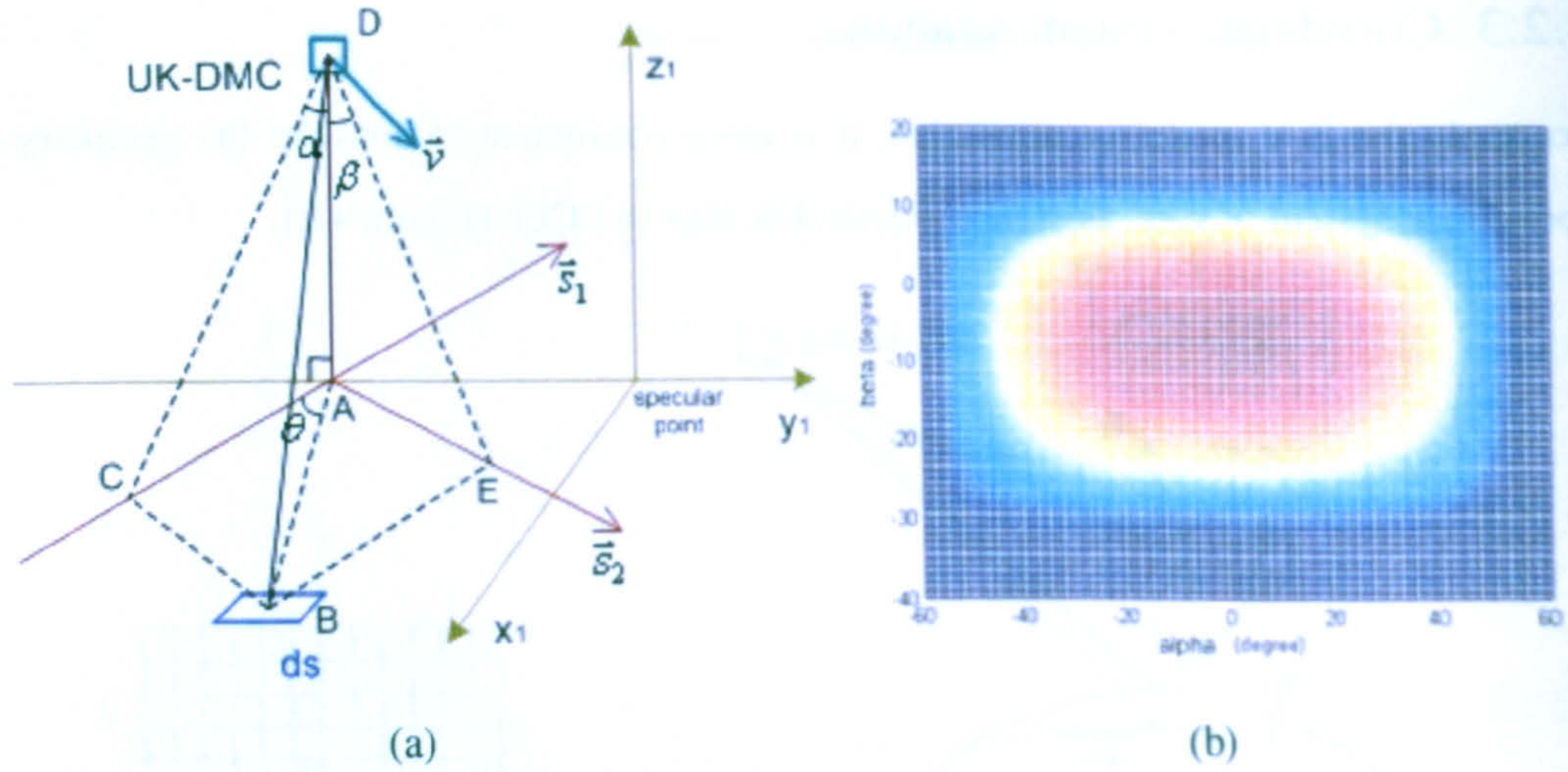


Figure 4-7: Antenna pattern calculation: (a) geometry, (b) antenna gain map.

Refer to Figure 4-7 (a), we have \vec{s}_1 and \vec{s}_2 axis definitions by vector cross product, as in the following equations:

$$\vec{s}_1 = \overrightarrow{AD} \times \vec{v} \quad (4-1)$$

$$\vec{s}_2 = \vec{s}_1 \times \overrightarrow{AD} \quad (4-2)$$

To calculate α and β angles of an individual patch, we can use:

$$\alpha = \arctan \frac{\overrightarrow{AB} \cdot \vec{s}_1}{|\vec{s}_1| \cdot |\overrightarrow{AD}|} \quad (4-3)$$

$$\beta = \arctan \frac{\overrightarrow{AB} \cdot \vec{s}_2}{|\vec{s}_2| \cdot |\overrightarrow{AD}|} \quad (4-4)$$

With patch geometric calculation, we can look up, for a certain patch, the corresponding antenna gain in the UK-DMC GPS-R antenna gain map, as shown in Figure 4-7 (b). This map shows a symmetry pattern on the α axis, however, the peak gain on the β axis shifts to -10° .

As an example, Figure 4-8 represents the antenna contour simulation of the R15 data scenario. A $200\text{km} \times 200\text{km}$ area is chosen as the reflection area around the specular point. According to the comparative positions of the specular point and UK-DMC, the centre of antenna gain is on the right edge of the reflection area. This will cause a typical unbalance-arm pattern in a horseshoe shape, as seen in the GPS-R DDMs in Appendix I.

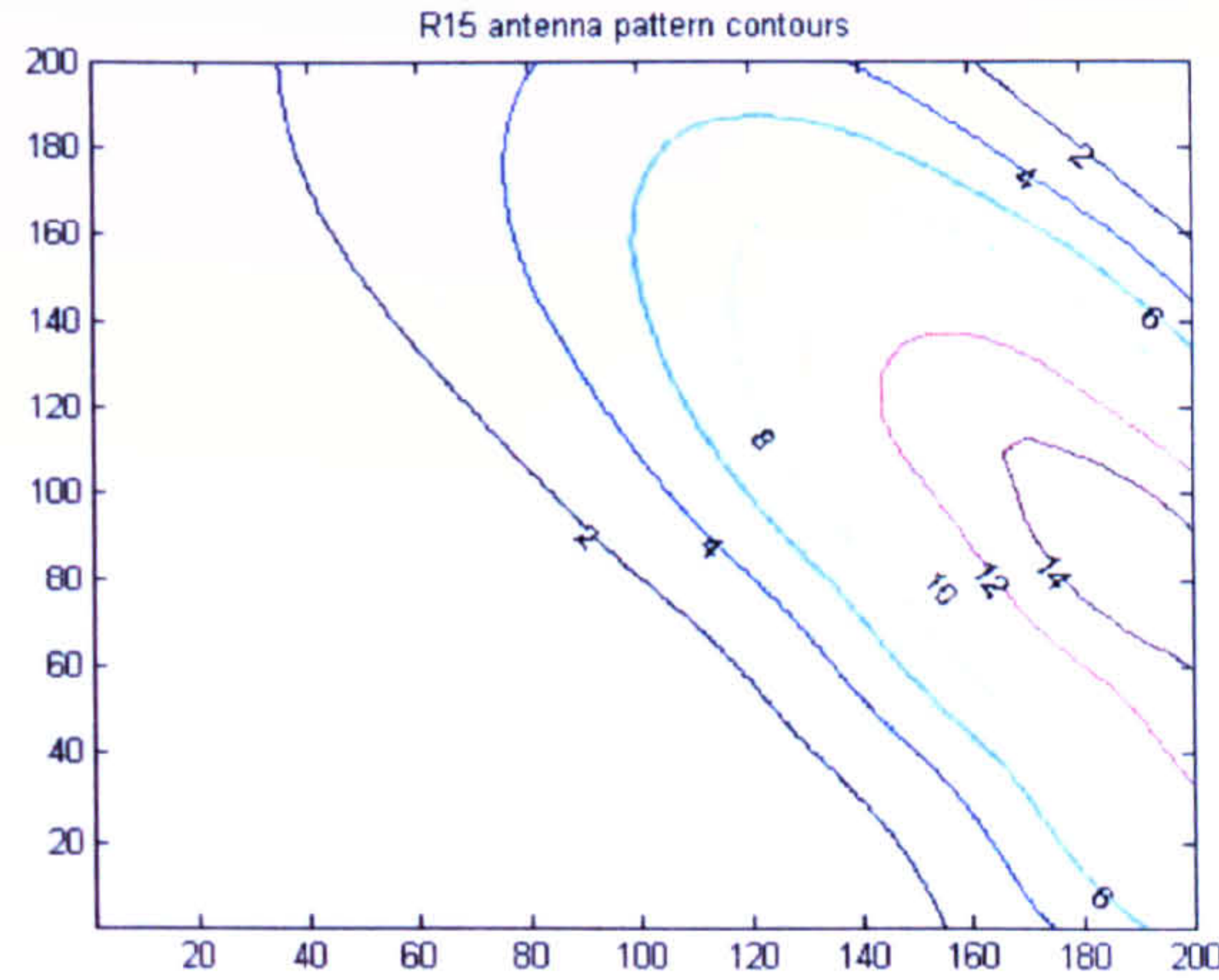


Figure 4-8: R15 antenna pattern contours on the reflection area.

4.2.5 Delay and Doppler calculation

To simulate a Delay-Doppler Map, we need to compute the Delay and Doppler properties of each patch. The Delay is comparatively easy to derive, by converting the reflection path length $R_T + R_R$ into the unit of GPS C/A code length.

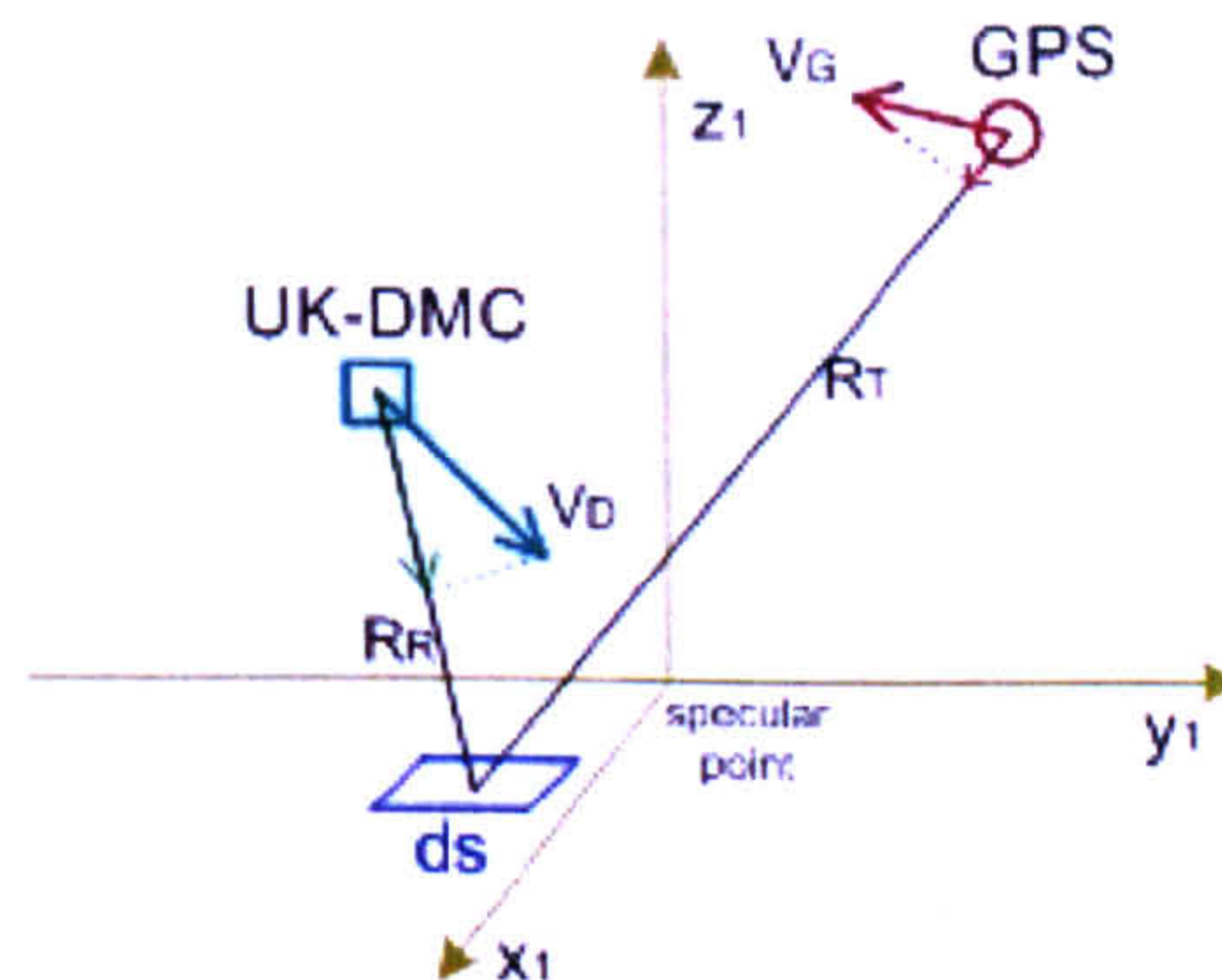


Figure 4-9: Delay and Doppler calculations for one patch.

The Doppler frequency shift can be expressed as a function of the reflection path length changing rate:

$$f_d = \frac{1}{\lambda} \left(\frac{dR_T}{dt} + \frac{dR_R}{dt} \right) \quad (4-5)$$

As seen in Figure 4-9, this changing rate is the sum of two scalars, one is the projection of UK-DMC velocity V_D along the R_R line, the other one is the projection of GPS velocity V_G along the R_T direction. The GPS-R signal receiving period for one Delay-Doppler Map is 1 second [Scott 2006]. During this time period, the Earth rotation movement and ocean wave movement are very small and ignorable when compared to the movement of LEO satellite (approximately 7 kilometres per second for UK-DMC). Therefore the velocity of GPS-R receiver satellite has the major contribution for the Doppler shift effect and both the Earth and ocean can be assumed stationary during one DDM

receiving, to simplify our GPS-R geometric modelling. Since the Doppler shift calculation **only** focus on the comparative movement between the stationary ocean surface, GPS and UK-DMC satellites, we can input either ECI or ECEF velocities of satellites into the Doppler calculation. These two reference frames give the same Doppler shift output according to our simulations.

4.2.6 UK-DMC DDM processing

GPS-R data received from the UK-DMC platform are with strong noise. Apart from the **noise** reducing processing in GPS signal acquisition procedure, bias reducing method is used here to reveal clearer signal patterns on real DDMs, to achieve better comparison results with the simulations.

The top boundary of horse-shoe pattern in DDM represents the signals with minimum reflection **path** length within different Doppler frequency band. Therefore the area above the horse-shoe pattern is considered as the signal bias reference. The mean value of each bias reference array is calculated as the noise floor value for its corresponding Doppler band.

With noise analysis in received DDMs, we find that the noise floor is different along the Doppler frequency axis, as shown in Figure 4-10 (b). In R18 dataset, the noise floor reaches its peak around 8000Hz. An obvious strip can be observed in the raw R18 DDM image (Figure 4-10 (a)). The possible reason for this phenomenon is the biased frequency response of the GPS-R receiver hardware in UK-DMC (refer to noise floor figures in Appen.I).

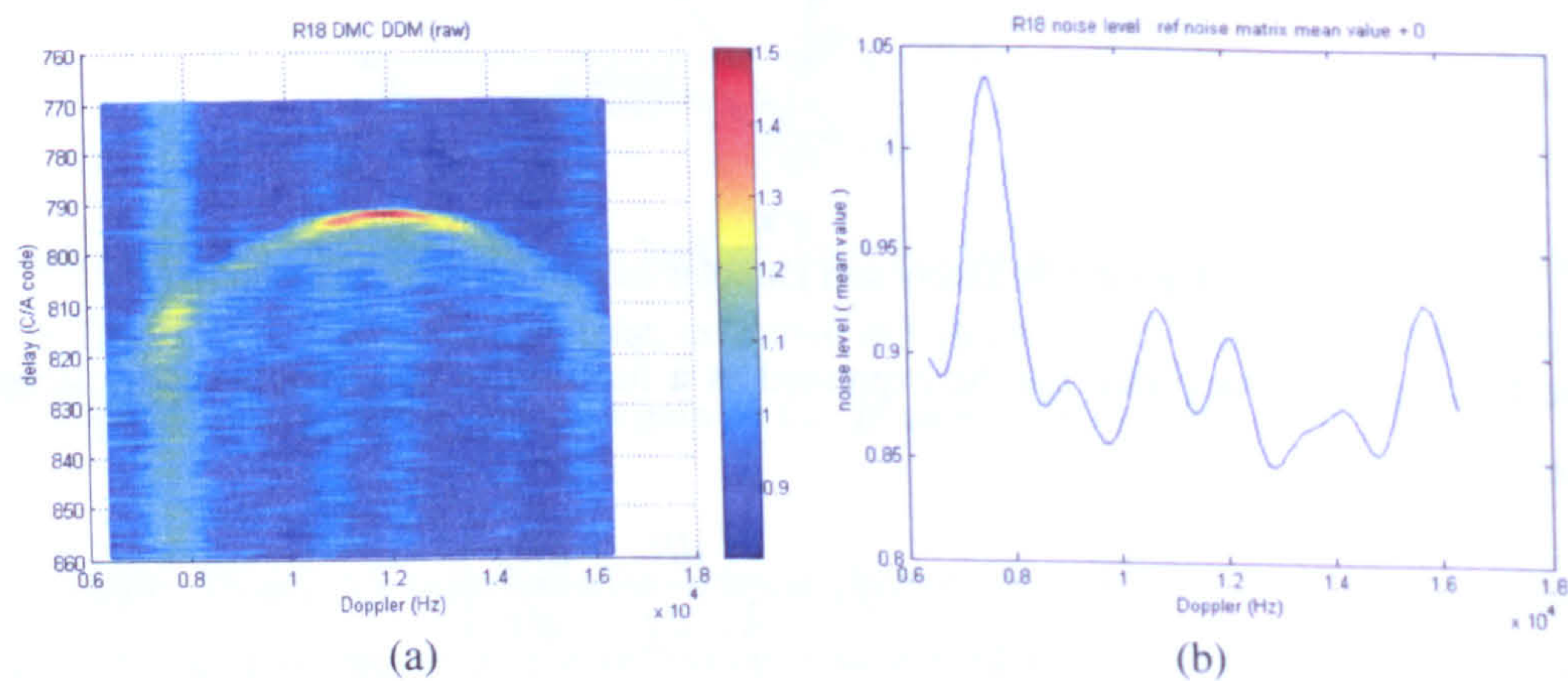


Figure 4-10: UK-DMC noise floor change. (a) R18 raw DDM. (b) R18 noise floor.

The peak power of the horse-shoe shape in the DDM is the strongest specular reflection from the centre of reflection area. Therefore, data above this horse-shoe shape should be invalid and considered as noise. Based on this assumption, the different noise floors, or bias, are calculated and removed from their corresponding Doppler band, as shown in Figure 4-11. The processed R18 DDM has a clearer pattern than the raw R18 DDM, especially around 8000Hz Doppler frequency where the strongest noise level was.

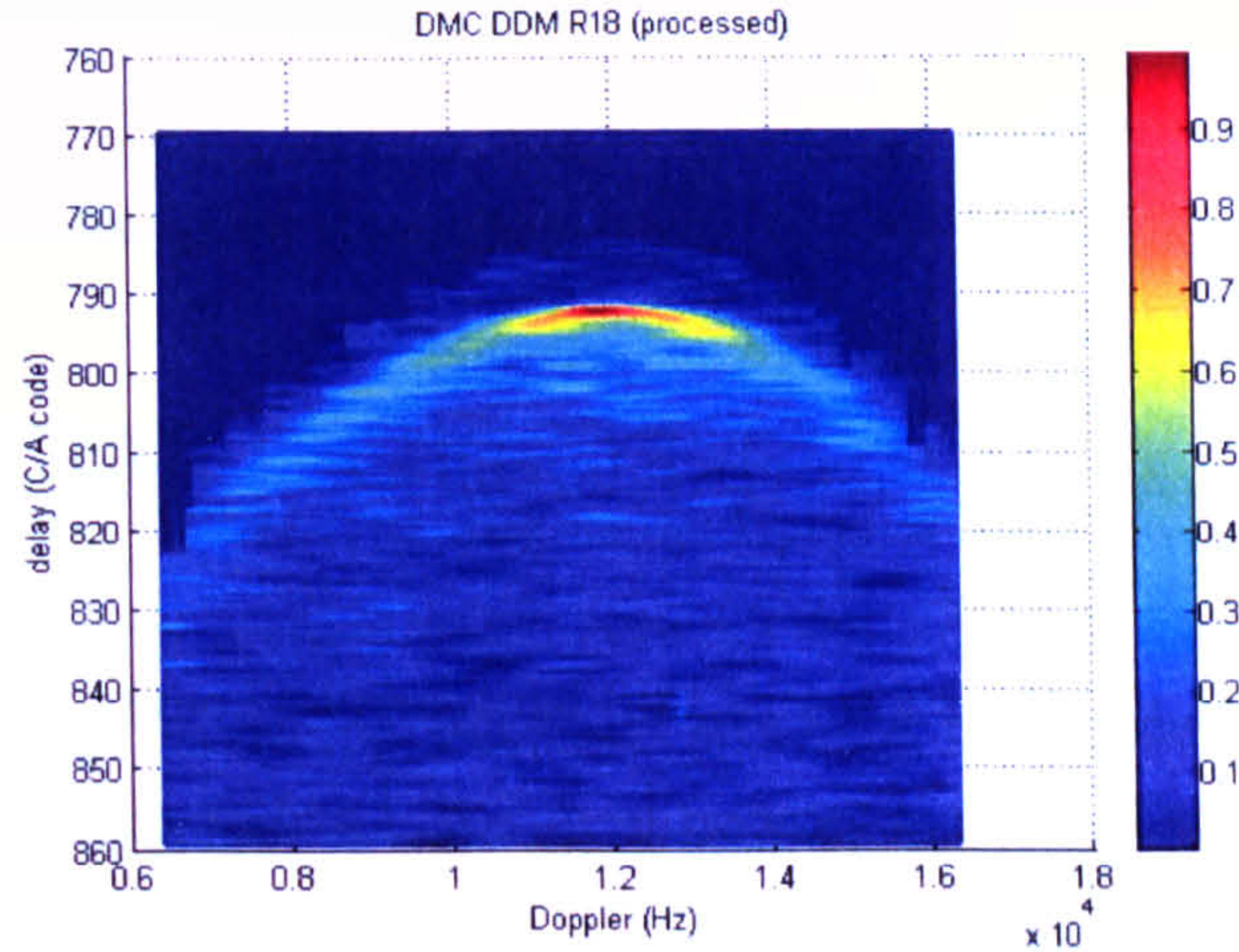


Figure 4-11: Processed and normalised R18 real DDM data.

4.2.7 Image correlation and geometrical compensation

The ideal spherical Earth assumption, which we use to predict the specular point position (section 4.2.1), introduces geometric error in our modelling. In addition, atmosphere, geoid and tide factors are not considered in our research. The estimation of reflection geometry therefore brings inevitable mismatch problem in the comparison between the real and simulated DDMs. To compensate this problem, the phase correlation method is applied to match the simulations and received DDMs.

Delay-Doppler Maps can be seen as images on Delay and Doppler dimensions instead of spatial dimensions. From the image processing viewpoint, if there is only spatial shift between two images, Fourier Transform (FT) and phase correlation algorithm can be used to remove the motion effect and improve the visual quality of images [De-Castro 1987] [Cafforio 1990].

To explain the algorithm, we consider two images g_1 and g_2 , where g_2 is a spatially shifted version from g_1 , i.e.,

$$g_2(x, y) = \alpha \cdot g_1(x - d_x, y - d_y) \quad (4-6)$$

where d_x, d_y are displacements on two spatial dimensions, and α represents a possible amplitude scalar factor.

The spectrum contents of two above images are G_1 and G_2 . For each 2-D frequency component (u, v) , the normalised cross power spectrum, with phase difference information, is defined as [Vu 2000]:

$$\exp(j(\phi_1(u, v) - \phi_2(u, v))) = \frac{G_1(u, v) \cdot G_2^*(u, v)}{|G_1(u, v) \cdot G_2^*(u, v)|} \quad (4-7)$$

where * denotes complex conjugation.

The phase correlation surface $P(x, y)$ can be obtained by applying an Inversed Discrete Fourier Transform (IDFT) on the normalised cross spectrum:

$$P(x, y) = F^{-1}(\exp(j(\phi_1(u, v) - \phi_2(u, v)))) = F^{-1}(\exp(j(ud_x + vd_y))) = \delta(x + d_x, y + d_y) \quad (4-8)$$

As seen in Equ.(4-8), if there is a spatial shift between two images, the phase correlation surface will ideally display a delta function at location $(-d_x, -d_y)$ and be zero everywhere else. The peak of the delta function indicates the displacement between image g_1 and g_2 .

When comparing simulated DDM to received data, two DDMs may have shifts on both Delay and Doppler dimensions. By applying phase correlation on these two images and using real DDM as reference, we can find the Delay-Doppler displacements of the simulated DDM. These displacement values can be feedback into the simulation procedure and partially compensate the error introduced by specular point estimation.

Figure 4-12 below shows the peak position of the delta function, derived from phase correlation, after the displacement compensation. Since the output from inversed Fourier Transform should be periodic, the peak value is valid at the start or at the end of the data array.

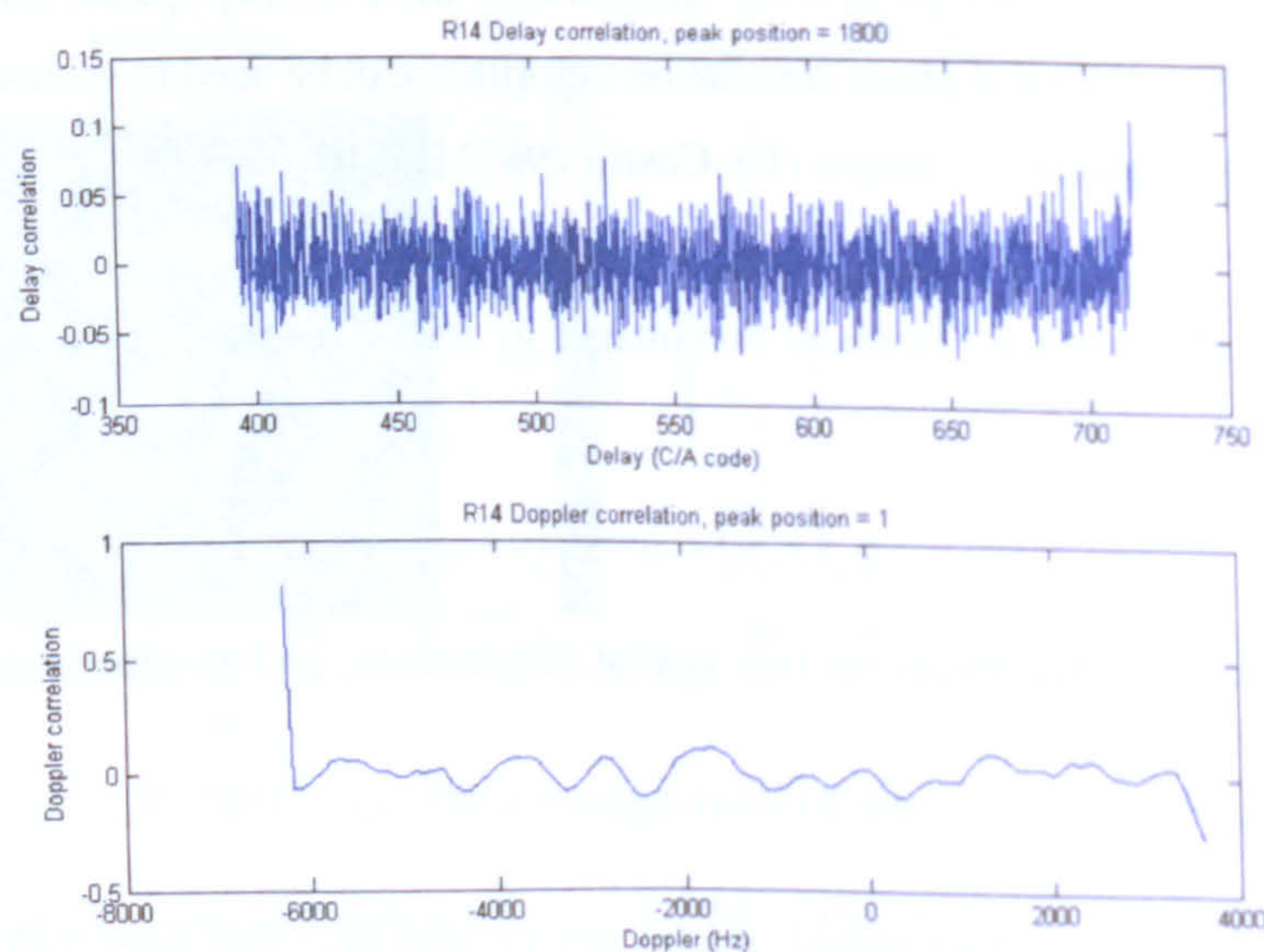


Figure 4-12: DDM phase correlation result after geometric compensation.

This phase correlation method can not completely cancel out geometric errors in our modelling, however, it can help to achieve a better DDM matching result than those uncompensated DDMs.

4.3 Case studies

This section demonstrates two DDM simulation cases. While one case is for R13 dataset with low wind speed, the other case is for R12 dataset with medium wind speed. After obtaining the geometry information from the datasets and slope PDF output from the Elfouhaily model, the Z-V model is applied to generate simulated DDMs. The data-model fitting is made by quantitative point-to-point comparison, whose results show a close match between the simulation and real data. Such results give much confidence in the modelling technique presented in previous chapters. However, the sensitivity analysis of R12 scenario reveals the limitation of current GPS-R wind measurement capacity. This sensitivity problem is the direct motivation for our following research, which will be described in Chapter 5 and 6.

4.3.1 R13 case

The R13 dataset was received in November 2004. The signals were reflected from the North Pacific Ocean between Hawaii and the West Shore of America. The ocean surface was fairly quiet with a 2.5 m/s local wind speed measured by buoys. The data facts of R13 are shown in the following table.

Table 2 UK-DMC GPS-R R13 data set facts

Data Set	R13
Signal source	SVN-47 GPS satellite
Time tag	26 November 2004 07:36:36 AM
Specular point position estimate	Lat 43:39:19N (43.6552°) Lon 132:8:22W (-132.1395°)
Wind conditions (from local buoy data)	2.5 m/s, -61°
UK-DMC DDM range	Delay axis 751~ 859 C/A code Doppler axis 5350 ~ 15250 Hz

The following figures show the raw and bias-reduced UK-DMC R13 data along with the simulated R13 DDM. Figure 4-13 (a) is the raw DDM after GPS-R signal acquisition. This raw image is processed to remove different biases in different Doppler bands, as in (b). A clear horse-shoe shape is presented on the processed real DDM (c). The two arms are slightly unbalanced due to the reflection geometry and antenna pattern calculation (refer to section 4.2.4). (d) is the simulated DDM under the same wind conditions (2.5m/s, -61°). These two normalized DDMs, (c) and (d) , visually match well.

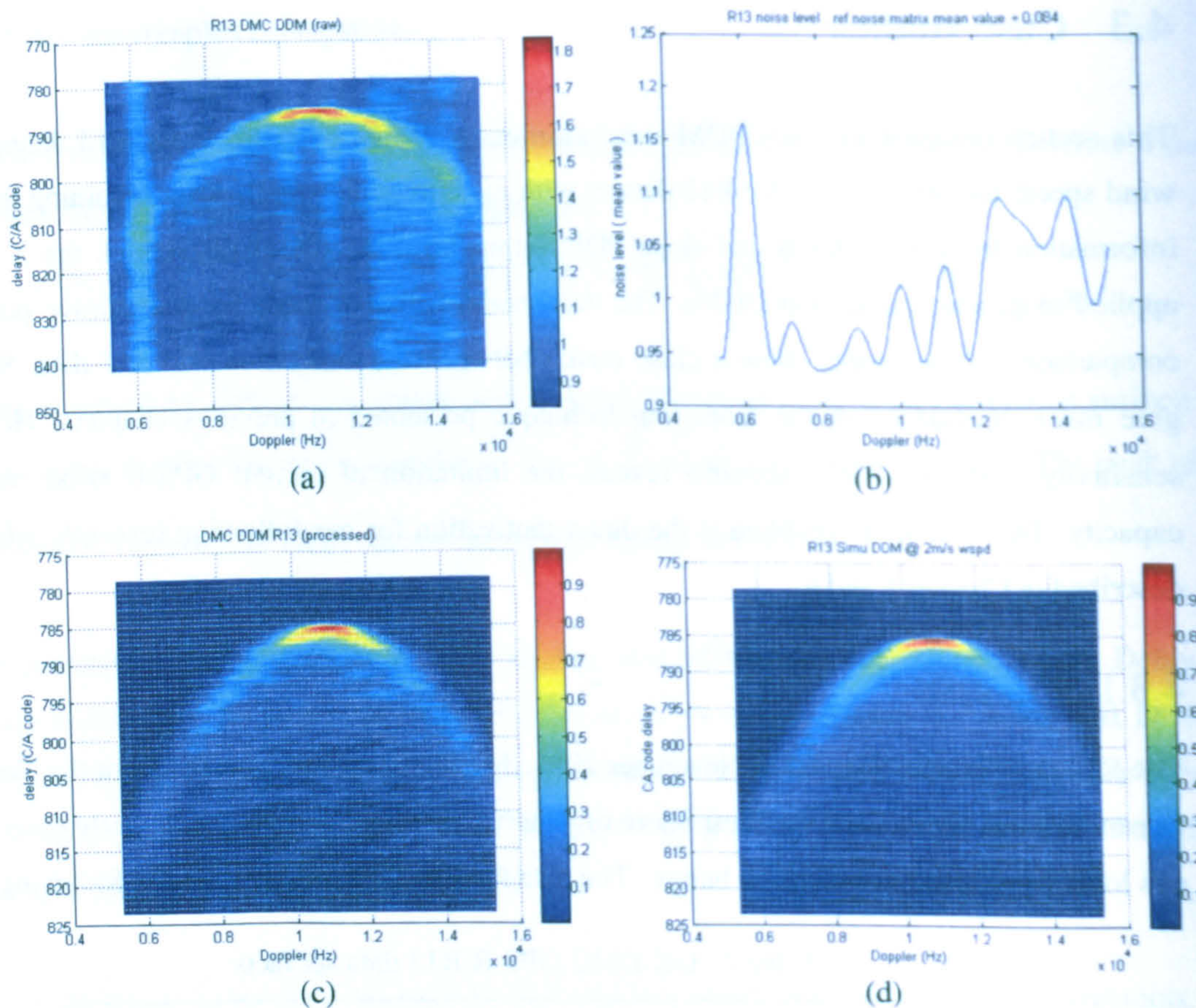


Figure 4-13: R13 DDM simulation.

- (a) Raw UK-DMC R13 DDM. (b) Bias difference in Doppler axis.
 (c) Processed UK-DMC R13 DDM. (d) Simulated R13 DDM.

To quantitatively compare Figure 4-13 (c) and (d), we plot the two images point against point. For example, while the amplitude of Delay-Doppler coordinates (x_0, y_0) in real DDM is D_1 , the equivalence in simulated DDM is D_2 . A point is then plotted on the position of (D_1, D_2) of an empty 2-D figure. After scanning two whole images, we can obtain a point distribution map, as seen in Figure 4-14, which indicates the correlation level of these two images. Ideally, if two DDMs are identical, the points will construct a straight line, with a gradient 1, going through the original point. Practically, the points will form certain level of linearisation, where a straight line can be fitted in by using the Least Square Method. Figure 4-14 illustrates the correlation result of the modelled R13 DDM (x axis) and UK-DMC R13 DDM (y axis).

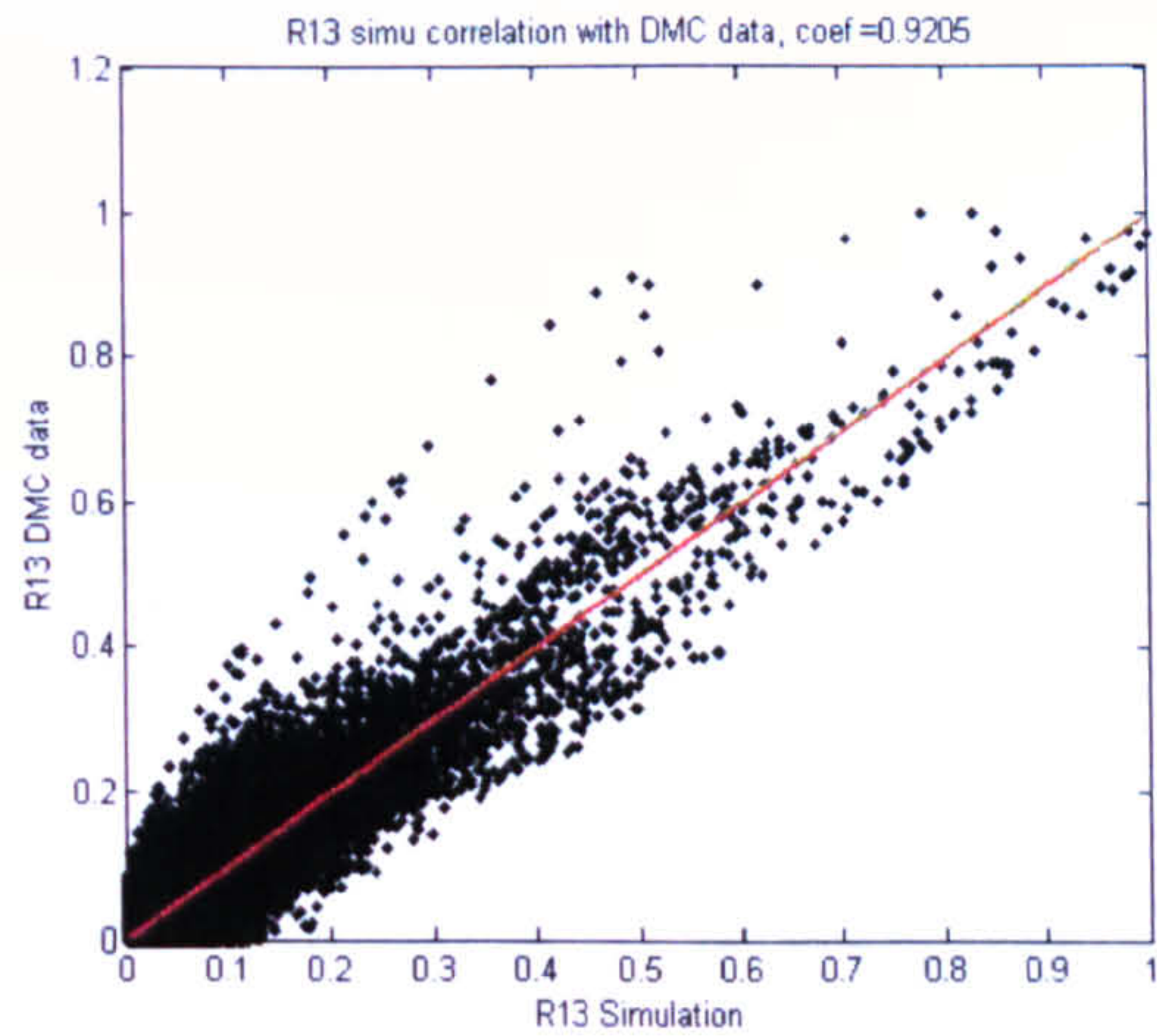
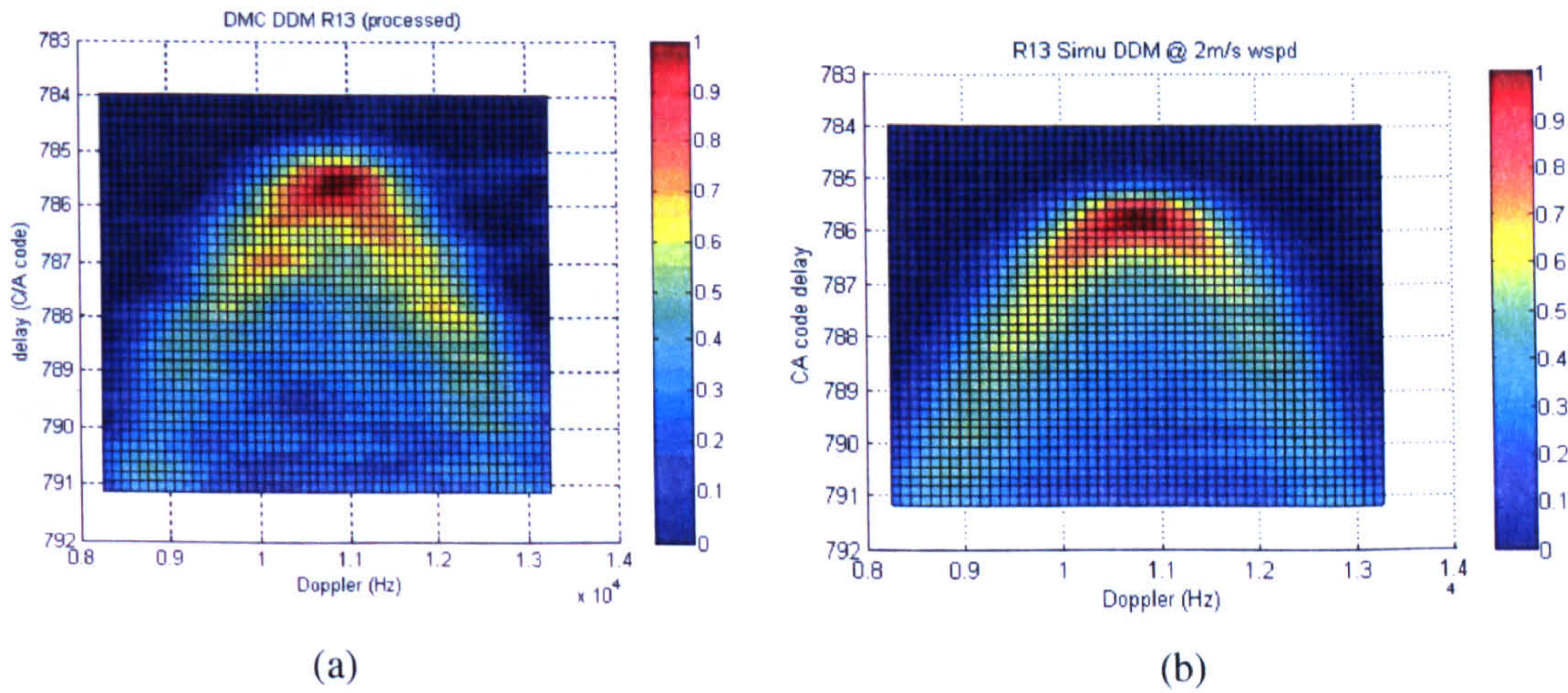


Figure 4-14: Point-to-point match between the simulated and real R13 data.

In Figure 4-14, while the green line (overlapped with the red line) has an ideal gradient of 1, the red one is the Least-Square fitted line from all points, with a 0.9205 gradient. The points form a linear pattern, there are however, some deviant points, among which the worst ones are around (0.5, 0.9).

The point-to-point correlation method can also be used in image sections, as seen in Figure 4-15 below. Figure 4-15 (c) gives a better view of the deviant points in Figure 4-14. These deviant points are within the strong reflection signal area of the horse-shoe shape, which suggests that the real DDM has slightly bigger strong reflection area than the simulated DDM.



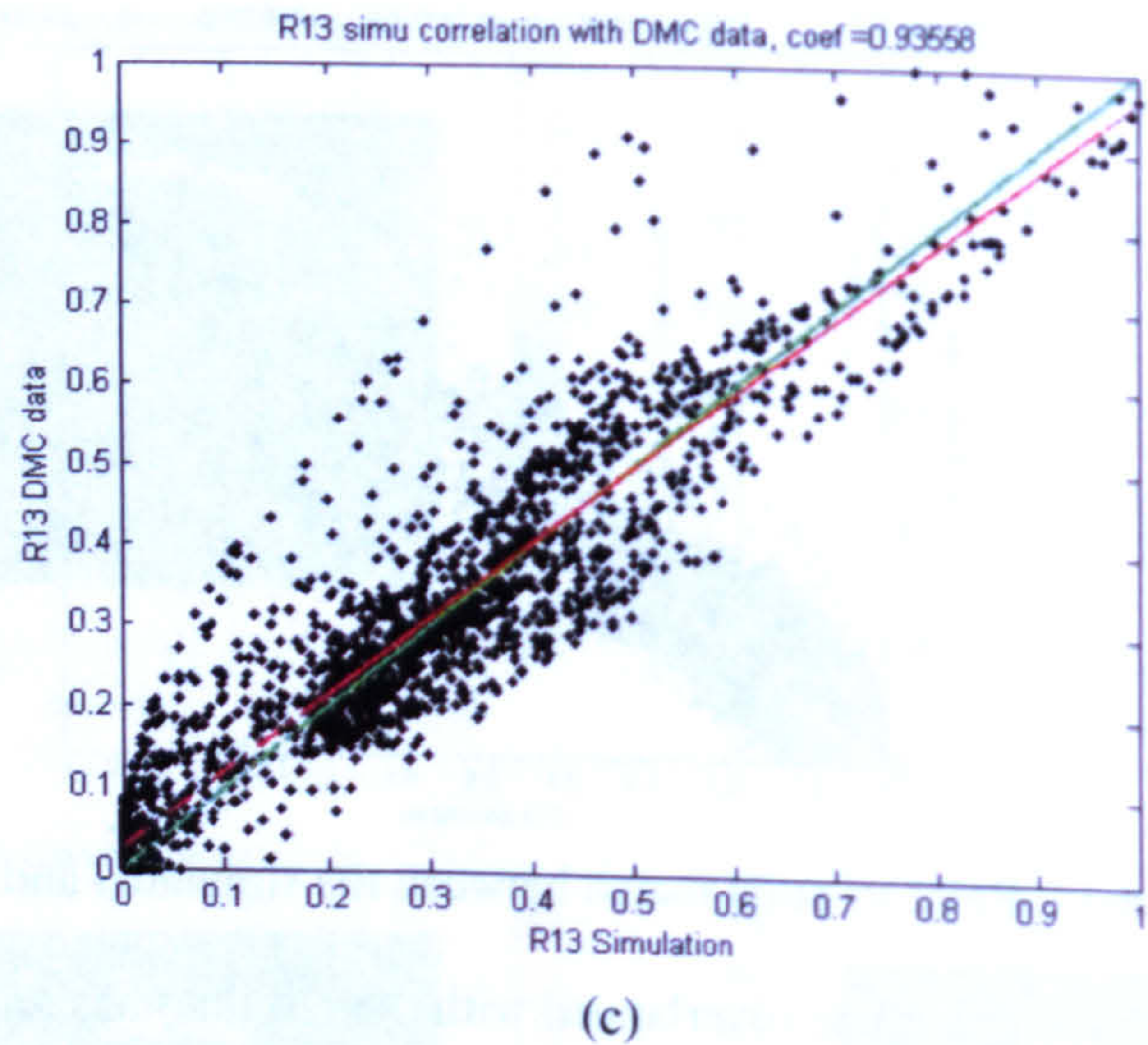


Figure 4-15: DDM strong signal area correlation.

(a) real R13 DDM. (b) simulated R13 DDM. (c) correlation result.

Similarly, we can observe the weak signal area in both DDMs, as seen in Figure 4-16. The different patterns in the simulated and real DDM represent the deviant data close to the original point in Figure 4-14.

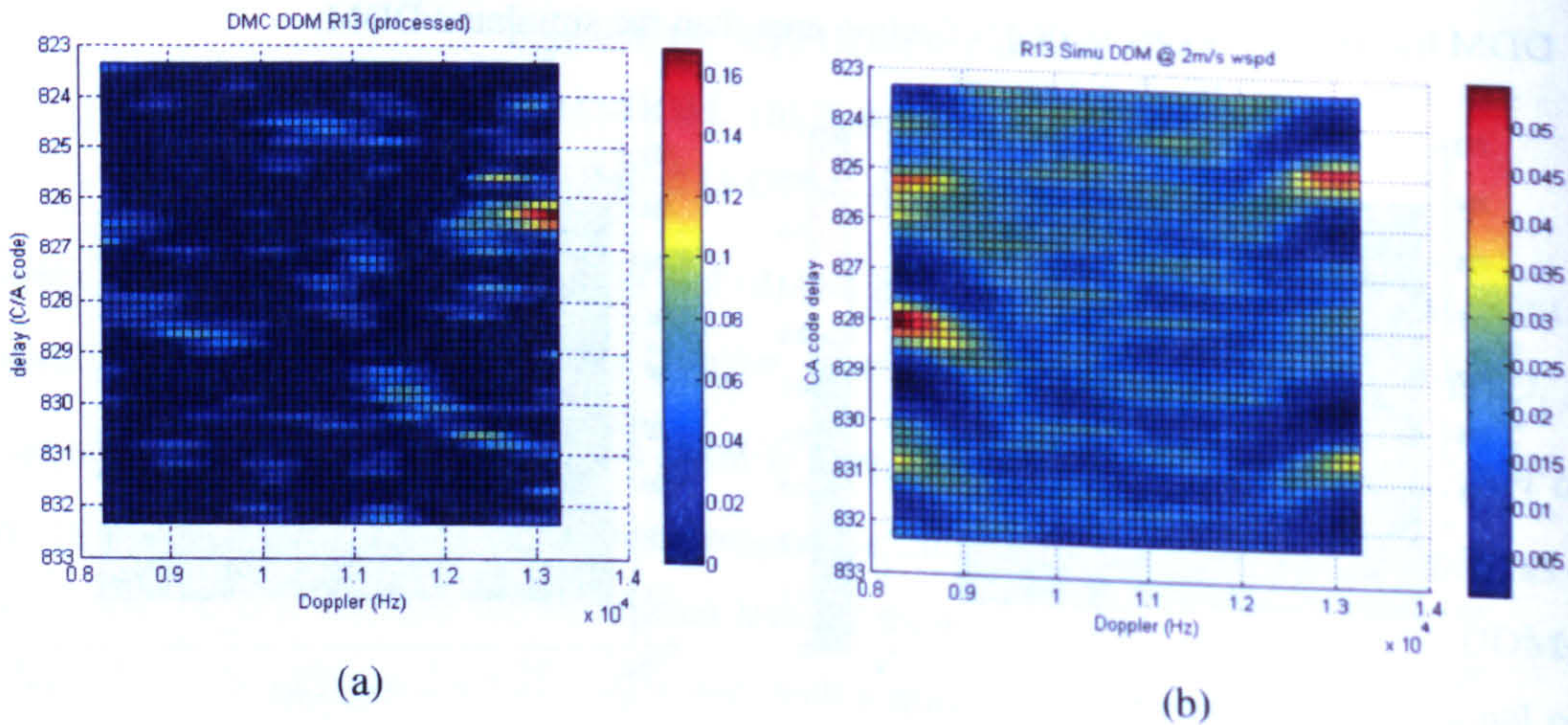


Figure 4-16: DDM weak signal area comparison. (a) real R13 DDM. (b) simulated R13 DDM.

When considering comparisons in Delay and Doppler dimensions respectively, DDMs can be summed up into Delay or Doppler waveforms.

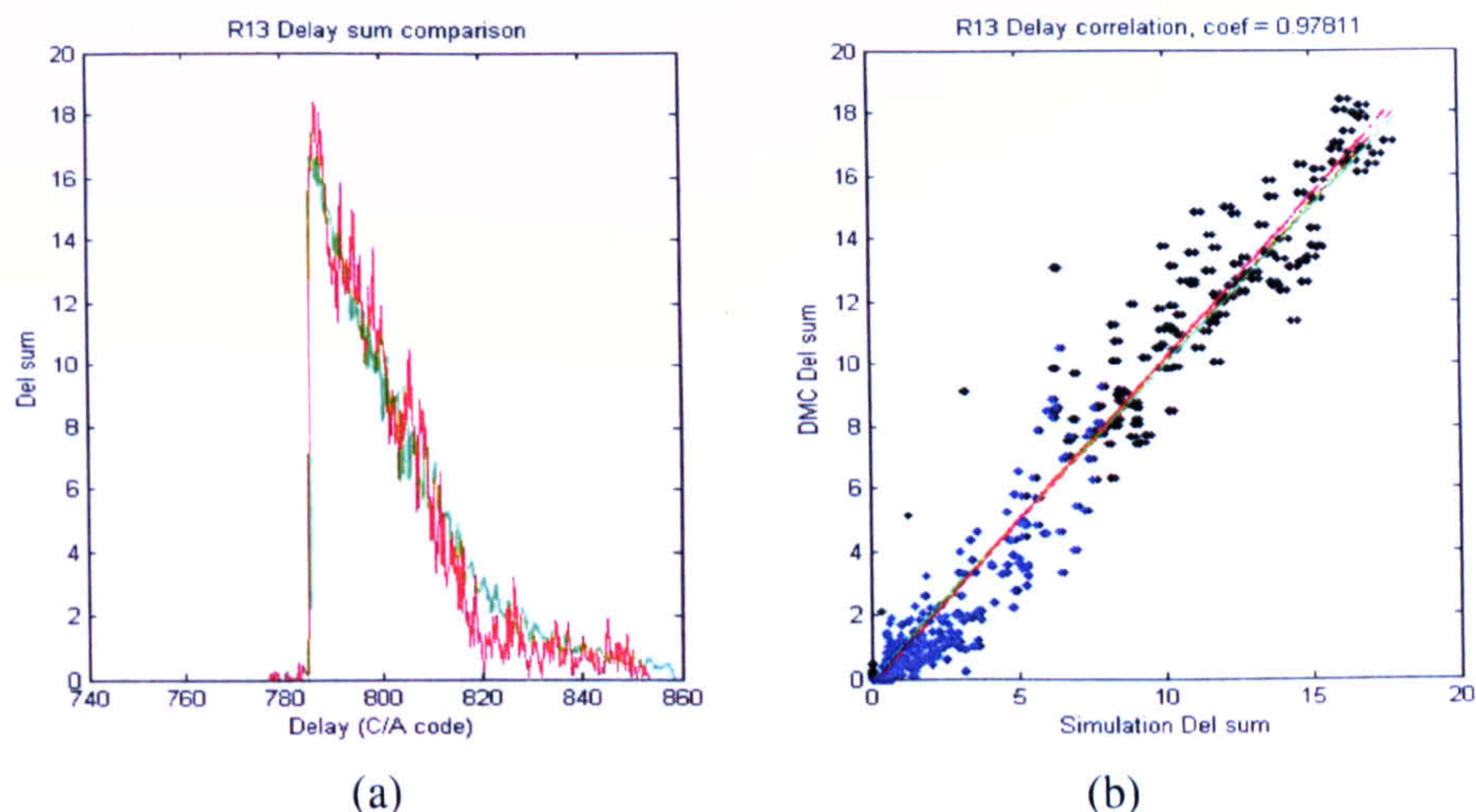


Figure 4-17: R13 Delay waveform comparison. (a) Delay waveforms (green - simulation, red - UK-DMC data). (b) Point-to-point correlation (green - 1:1, red - fitted).

Figure 4-17 shows a good match between Delay waveforms of the simulated and real R13 data. The point-to-point association of the waveforms is presented in Figure 4-17 (b). The fitted line has a good agreement with the 1:1 reference. The Doppler waveforms have similar shapes, however, a shift can be observed, as in Figure 4-18(a), between the two waveforms. The pattern on the point-to-point correlation figure (Figure 4-18 (b)) is due to the displacement between the two Doppler waveforms. The blue points represent the low Doppler region where the simulated Doppler waveform is higher than that of the real DDM, and the black points represent the high Doppler region where the real Doppler waveform is higher than the simulated one.

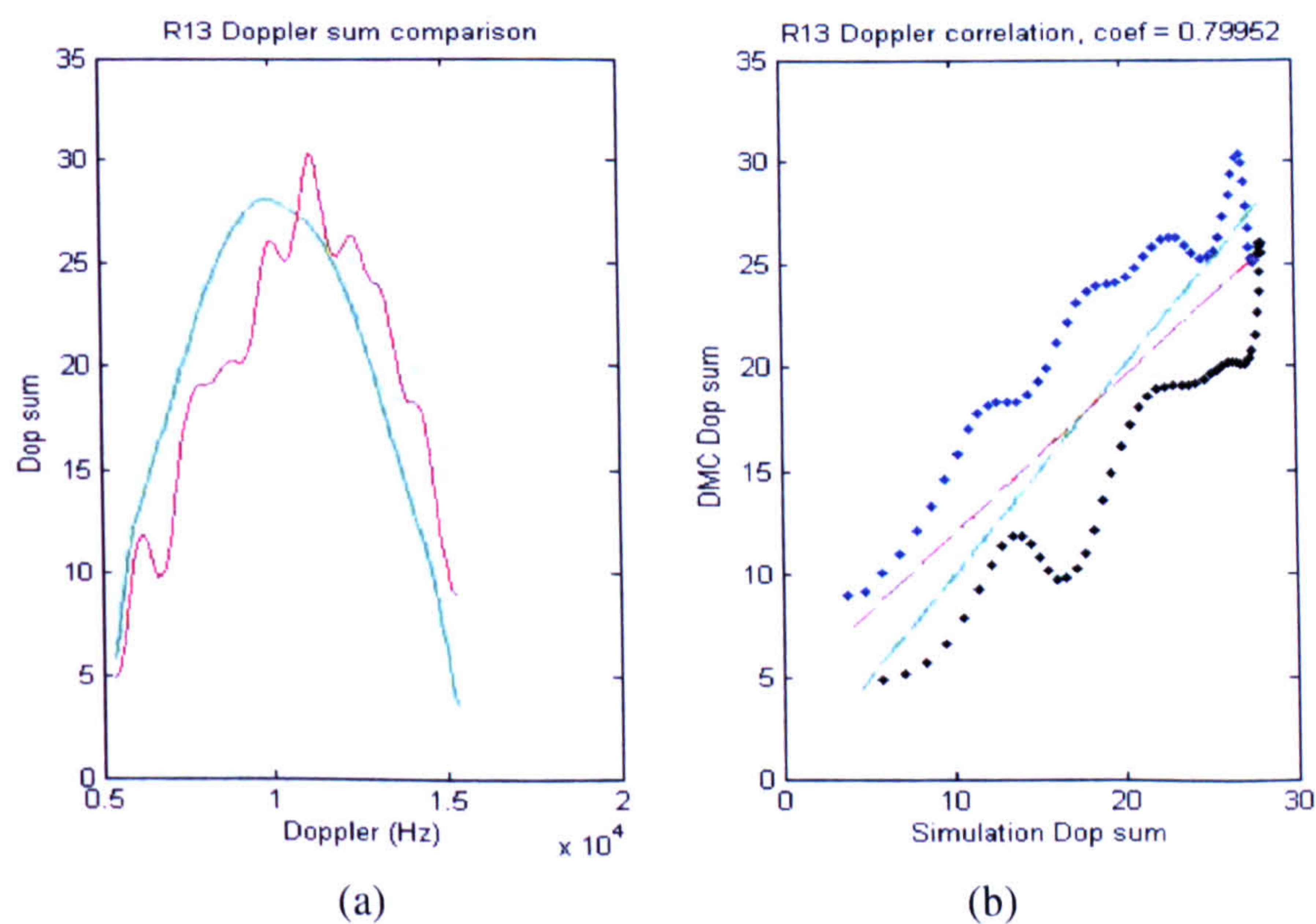


Figure 4-18: R13 Doppler waveform comparison. (a) Doppler waveforms (green - simulation, red - UK-DMC data). (b) Point-to-point matching (green - 1:1, red - fitted).

The Doppler waveform shift, as seen in Figure 4-18 (a), is likely due to the geometric modelling error. Instead of using the Doppler offset, calculated from phase correlation (about -150 Hz), to compensate the simulation, different Doppler offsets are employed in the experiment. The Doppler waveform comparison, as we expect, changes with the Doppler offset value.

Figure 4-19 presents the simulation results with a Doppler offset. For each patch on the reflection area, we inject a 3000 Hz offset value into its Doppler shift frequency. When assuming a frozen scenario during the DDM receiving, the Doppler offset value can be related to the geometry modelling error of the patch position. 3000 Hz value is chosen to emphasise the Doppler shift effect.

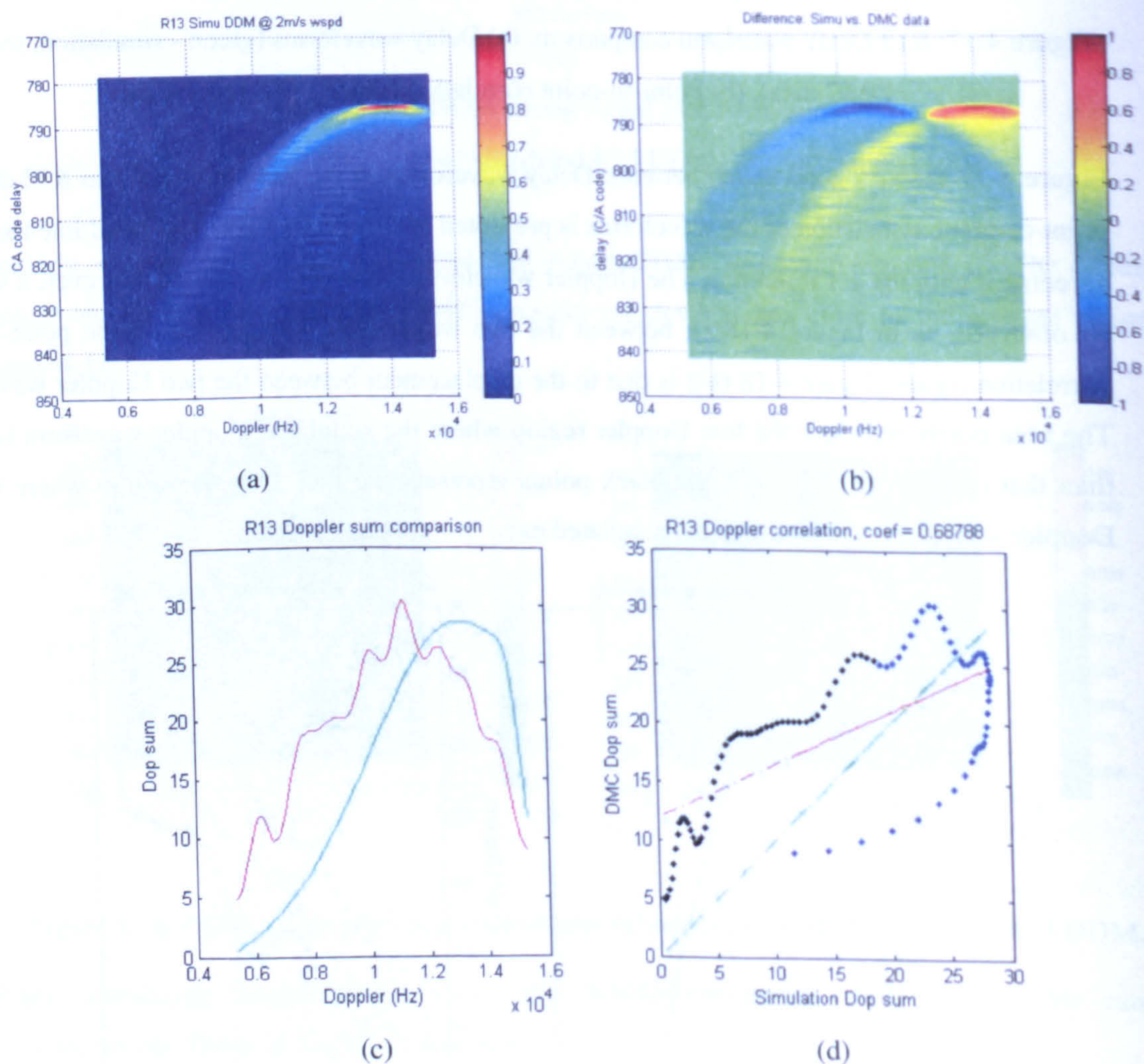


Figure 4-19: R13 Doppler waveform comparison with 3000 Hz Doppler offset.

(a) simulated DDM. (b) shift between simulated and real DDMs. (c) Doppler waveforms (green - simulation, red - UK-DMC data). (d) Point-to-point matching (green - 1:1, red - fitted).

Figure 4-19 (a) is the simulated DDM, shifted to the higher Doppler frequency side. (b) is the difference map between the simulated and real DDM. (c) is the Doppler waveform comparison

result, in which we can observe a large displacement between two waveforms with the large Doppler offset input. This displacement is opposite to the one in Figure 4-18 (a) due to the opposite Doppler offset.

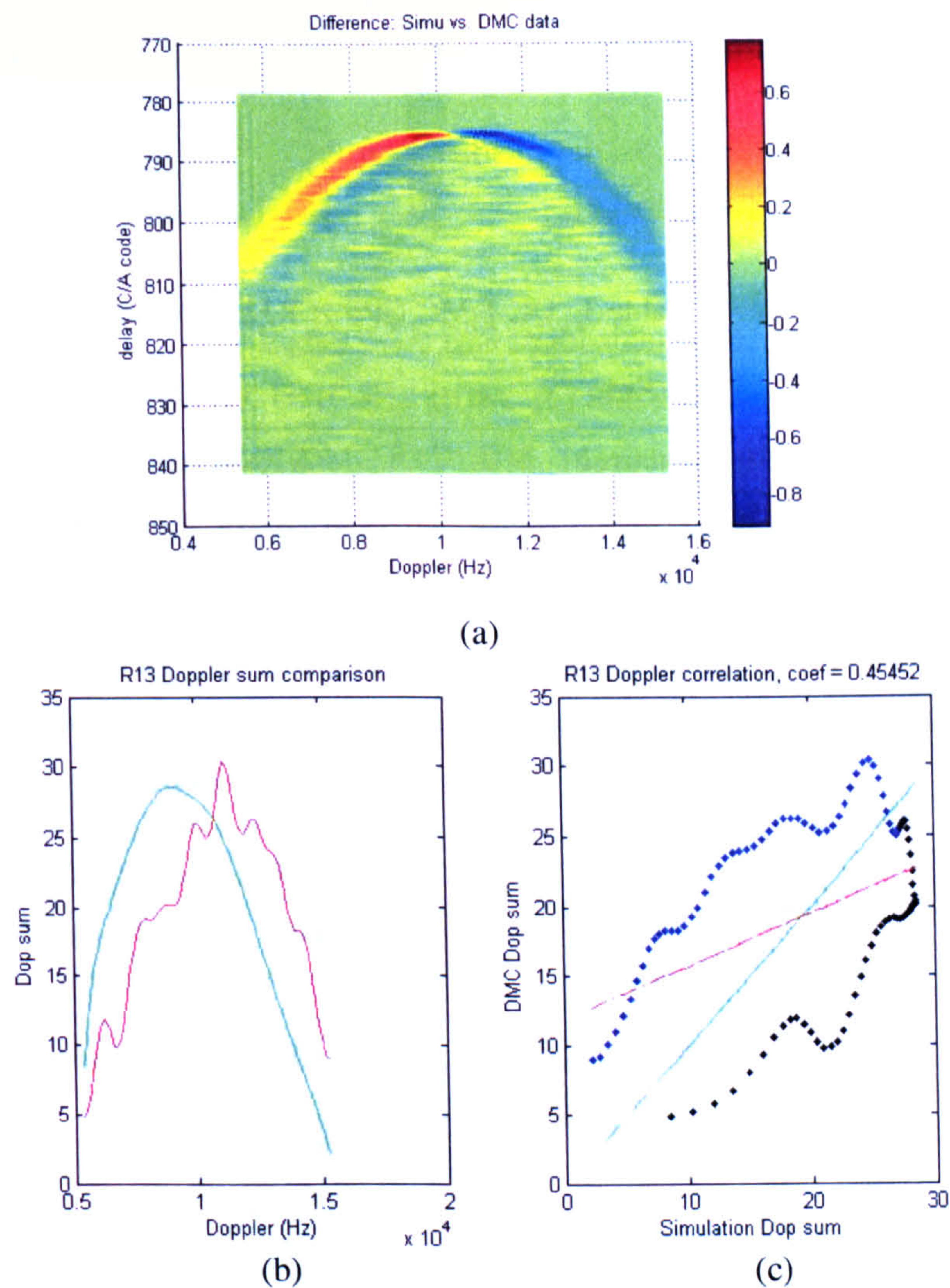


Figure 4-20: R13 Doppler waveform comparison with -1000 Hz Doppler offset.
 (a) shift between simulated and real DDMs. (b) Doppler waveforms (green - simulation, red - UK-DMC data). (c) Point-to-point matching (green - 1:1, red - fitted).

Figure 4-20 presents the simulation with a -1000Hz Doppler offset. Figure 4-20 shows a larger displacement between the Doppler waveforms, but in the similar pattern with Figure 4-18 (a). The blue and black point definition is similar to what we describe for Figure 4-18 (b).

The above experiments prove the connection between the final Doppler waveform position and patches' Doppler property. The error in Doppler calculation mainly comes from the modelling error in specular point position and other geometrical factors ignored in our modelling procedure, such as Earth rotation and tide movement. The phase correlation method, as mentioned in section 4.2.7, can

only partially counteract such geometry error. Further investigation is needed to model the geometry more accurately in this GPS-R space-borne research.

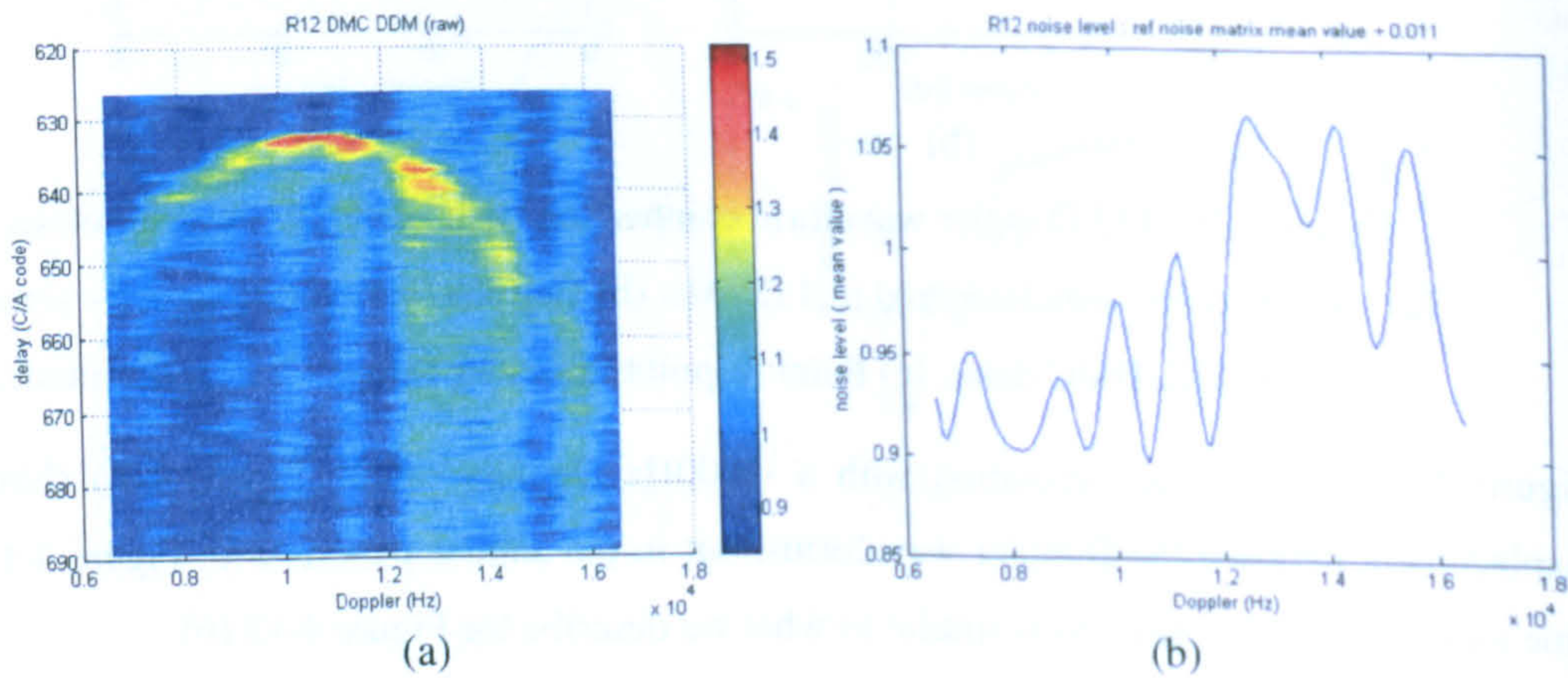
4.3.2 R12 case

The R12 dataset was received 10 days earlier than R13, and around the same area with the R13 dataset. Table 3 lists the R12 data facts.

Table 3 UK-DMC GPS-R R12 data facts

Data Set	R12
Signal source	SVN-47 GPS satellite
Time tag	16 November 2004 07:54:46 AM
Specular point position estimate	Lat 39:40:26N (39.6739°) Lon 138:15:40W (-138.2611°)
Wind conditions (from local buoy data)	8 m/s, -107°
UK-DMC DDM range	Delay axis 573~ 788 C/A code Doppler axis 6600 ~ 16500 Hz

The similar procedures of DDM processing and simulation, as we described in the R13 case, are employed in the R12 case. The results are shown below in Figure 4-21.



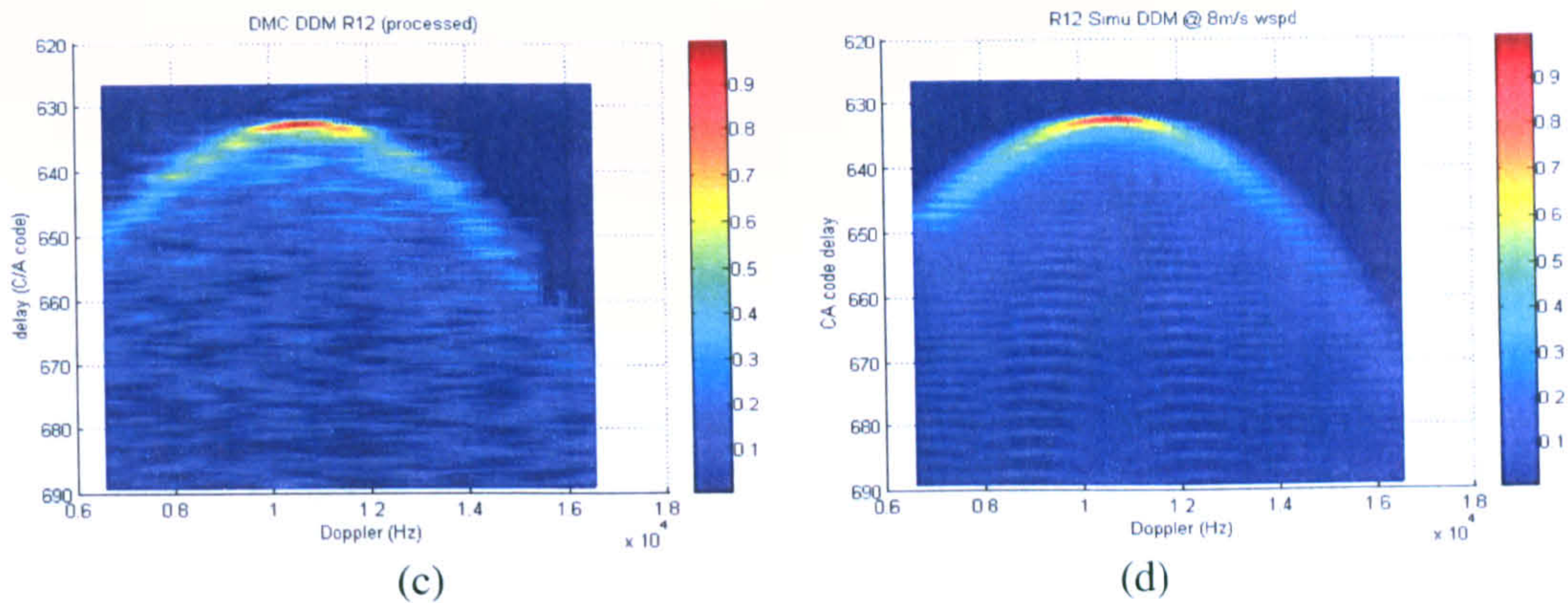


Figure 4-21: R12 DDM simulation.

- (a) Raw UK-DMC R12 DDM. (b) Bias in Doppler axis.
(c) Processed UK-DMC R12 DDM. (d) Simulated R12 DDM.

In Figure 4-21 (b), we notice that the bias is higher in 12000 ~ 16000Hz than in other frequency bands, akin to the bias pattern, around the same range, in the R13 case (Figure 4-13 (b)). This provides some evidence to support the hardware bias explanation for this Doppler bias variation phenomenon. By quantitatively comparing the simulated and real DDM, the point-to-point matching figure shows a good correlation, as seen in Figure 4-22 below:

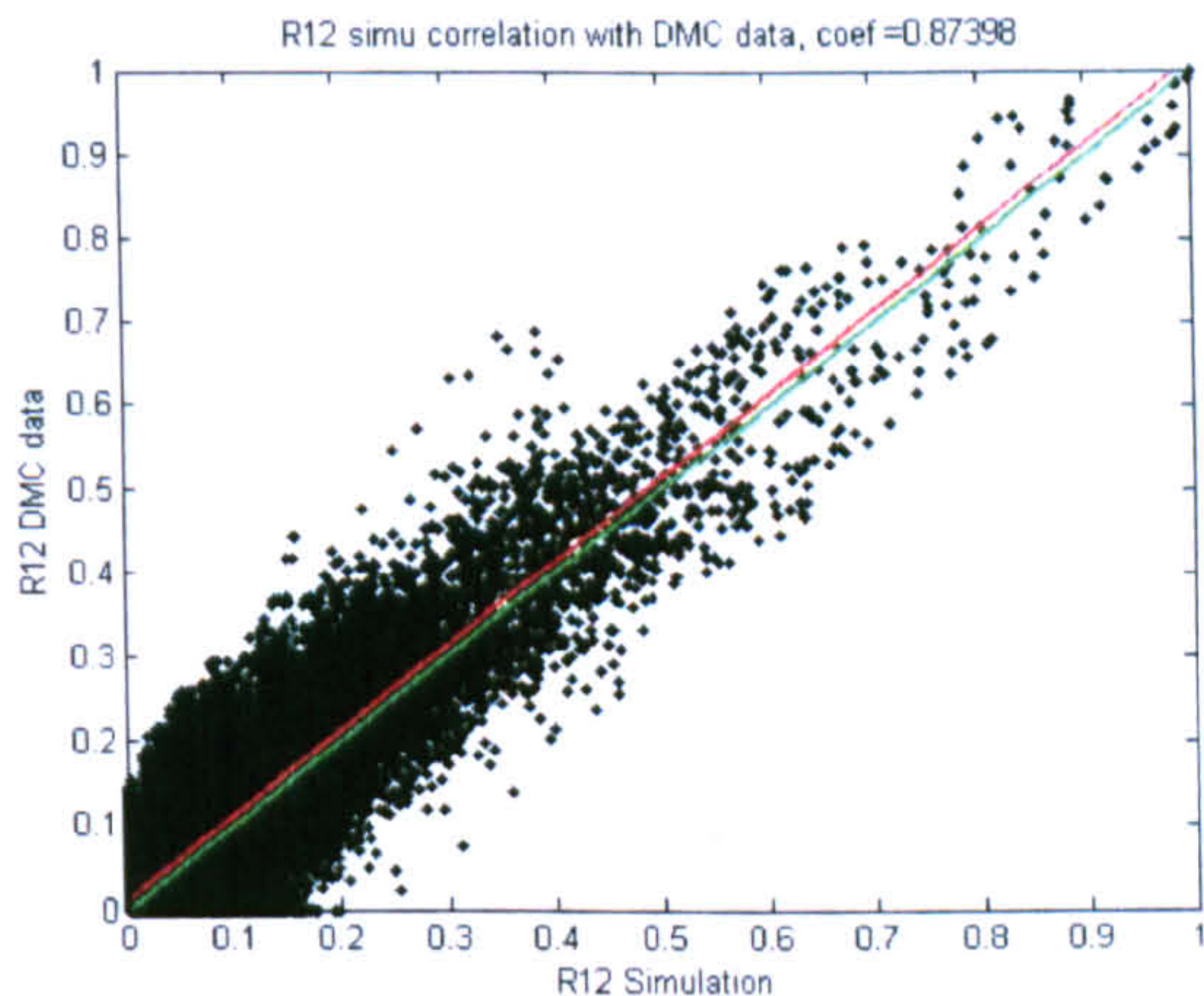


Figure 4-22: Point-to-point correlation between the R12 UK-DMC data and simulation.

The correlations of Delay and Doppler waveforms of the R12 case can be seen in Figure 4-23 and 4-24. In Delay waveform comparison, a bias is noticed between the fitted line and reference (Figure 4-23 (b)). This is due to the amount of points which are zero in the simulation but non-zero in the real DDM. Such points might be the residual noise after the bias-removing procedure in the real data.

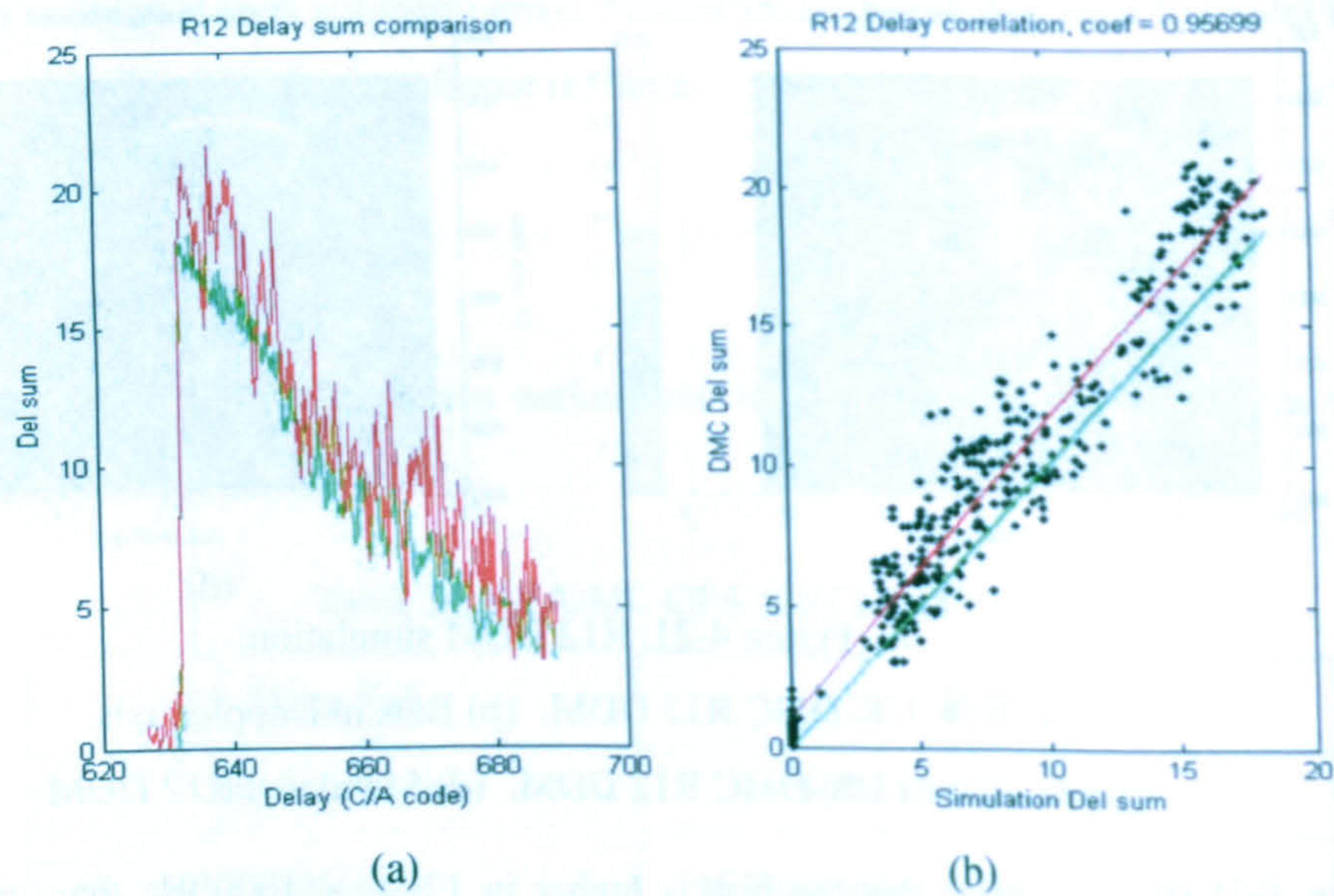


Figure 4-23: R12 Delay waveform comparison. (a) Delay waveforms (green – simulation, red - UK-DMC data). (b) Point-to-point matching (green - 1:1, red - fitted).

The Doppler comparison, as shown in Figure 4-24, exhibits a horizontal and a vertical displacement between the Doppler waveforms of the simulated and real DDM. The vertical displacement comes from the accumulation of residual noise in the real data. The horizontal shift might due to the error in geometric modelling, as we discussed in previous sections. The definition of blue and black point in Figure 4-24 (b) is as described for Figure 4-18 (b).

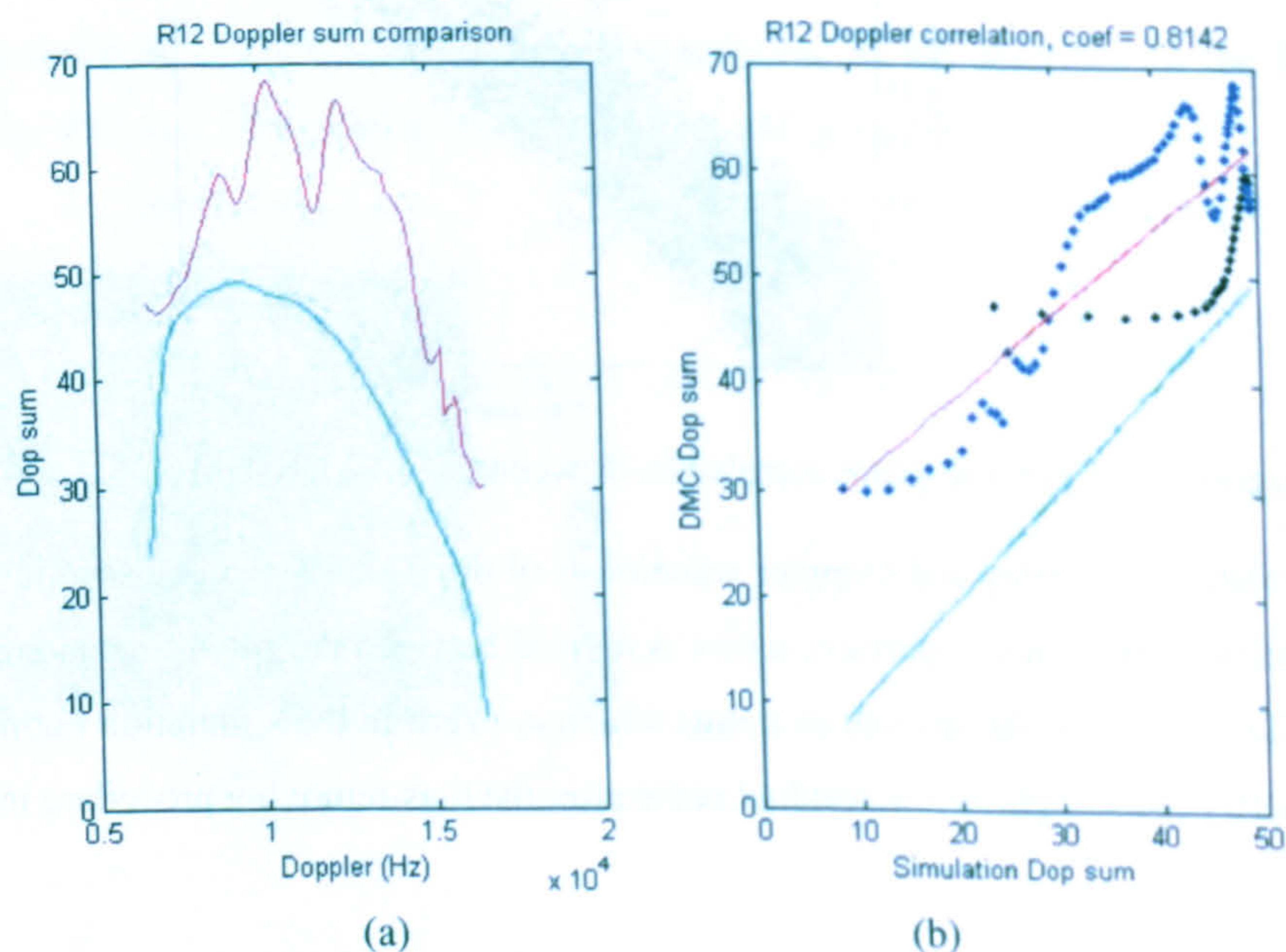


Figure 4-24: R12 Doppler waveform comparison. (a) Doppler waveforms (green - simulation, red - UK-DMC data). (b) Point-to-point correlation (green - 1:1, red - fitted).

4.3.3 Summary

Six sets of UK-DMC GPS-R data were processed and simulated, as shown in Appendix I. Among these datasets, R13 and R12 are presented as case studies in this section. Simulated DDMs and waveforms are compensated to achieve the best correlation results with corresponding UK-DMC data. Point-to-point matching figures give quantitative comparisons between the simulations and real data. DDMs match well in Delay-Doppler dimensions for low (R13) and medium (R12) wind speed case. Such results prove the viability of the modelling technique we use in this research, which combines the Elfouhaily and Z-V model. If considering Delay and Doppler waveforms separately, while correlation results show good matches in Delay dimension, displacements can be observed between Doppler waveforms. These displacements may either due to the inaccurate geometric modelling or the residual noise within the real DDM data, or the combination of both. From the R13 and R12 case, we can observe that higher wind speed and rougher sea surface reduce the linearisation of data-model correlation in GPS-R DDM research.

4.4 Sensitivity analysis of current GPS-R model

Practically, GPS-R technique should be applied in ocean remote sensing without a-priori wind or wave knowledge. By fitting real data with simulations under different conditions, it should be possible to derive the information of wind or waves from the real data. Therefore it is necessary to employ a “black-box” test in our GPS-R model evaluation. Such test takes an external perspective of test object and has little information about internal working principles of the object. Through this test, we can analyse the wind sensitivity of current GPS-R scatterometric model and evaluate its feasibility in practical level application of GPS-R space-borne remote sensing.

The R12 scenario is chosen for the “black-box” test. A series of noise-free simulated DDMs, which are under the same geometry (R12) but with different wind speed input, are correlated with a simulated DDM under 8 m/s wind speed. The quantitative point-to-point comparison method, as mentioned in section 4.3, is also applied here. Presumably the result from auto-correlation should give a 1:1 reference line. While the fitted lines from lower wind speed (< 8 m/s) correlations should be under this reference, the fitted lines of higher wind speed cases (> 8 m/s) should be above it. More deviant these lines are, more accurate the wind measurement would be. The real R12 DDM is also correlated with the simulated 8 m/s DDM. Ideally the fitted line from real DDM correlation should align with the reference 1:1 line, however, the noise in real data will affect the correlation result. The test outcomes are shown in Figure 4-21.

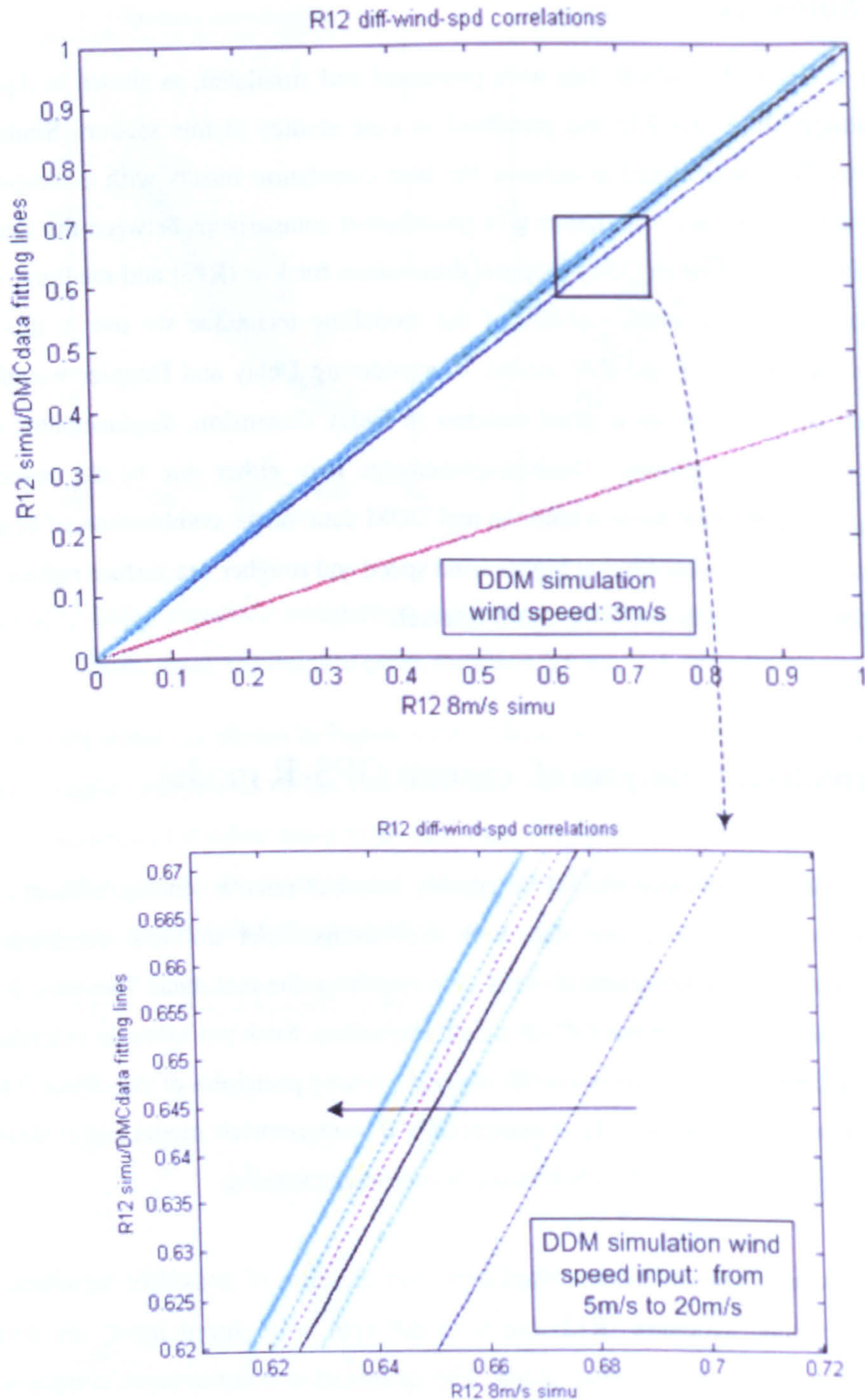


Figure 4-25: Correlations of different wind speed DDMs with an 8m/s simulated DDM.

As seen in Figure 4-25, the black line in the zoom-in figure is the fitted line from auto-correlation. The correlation between real data and reference DDM forms a line, just below the black line, with a gradient around 0.95. While the correlation results of 3m/s, 5m/s and 7m/s wind speed cases are below the black line, the results of other higher wind speed simulations are above the reference, as expected. However, Figure 4-25 shows that the correlation result lacks sensitivity to wind for medium and high wind speed cases. The fitted lines above the 8m/s DDM reference line are very

close to each other. When it is difficult to separate correlation results from simulations under ideal noise-free condition, it would be even more challenging to extract wind information, with strong noise in real GPS-R data, via the current GPS-R modelling technique.

To investigate the reason of the insensitivity problem, we need to review the principle of current GPS-R scatterometric model. As shown in Equ.(3-46), in the combination of Elfouhaily spectrum model and Z-V model, wave slope probability is the only parameter that connects wind-wave properties to modelled GPS reflection energy. The wind condition sensitivity of slope PDFs directly affects the accuracy of GPS-R scatterometric measurements, and is therefore in our concern. Several parameters are optional to represent the shape of a 2-D Gaussian distribution for PDF sensitivity analysis, such as the peak value of a zero-centred Gaussian PDF (as in Equ.(3-37)) is:

$$P = \frac{1}{2\pi\sigma_1\sigma_2\sqrt{1-b_{xy}^2}} \quad (4-9)$$

The half-peak width X_h along the s_y axis can be calculated from:

$$p(x,0) = \frac{1}{2} \cdot \frac{1}{2\pi\sigma_1\sigma_2\sqrt{1-b_{xy}^2}} \quad (4-10)$$

$$\exp\left(-\frac{1}{2} \cdot \frac{1}{1-b_{xy}^2} \cdot \frac{X_h^2}{\sigma_1^2}\right) = \frac{1}{2} \quad (4-11)$$

$$X_h = \sqrt{\left(\ln\frac{1}{2}\right)[-2(1-b_{xy}^2)]\sigma_1^2} = |\sigma_1| \cdot \sqrt{-\left(\ln\frac{1}{2}\right) \cdot 2 \cdot (1-b_{xy}^2)} \quad (4-12)$$

Similarly we have the half-peak width Y_k along the s_x axis as

$$Y_h = |\sigma_2| \cdot \sqrt{-\left(\ln\frac{1}{2}\right) \cdot 2 \cdot (1-b_{xy}^2)} \quad (4-13)$$

Ignoring the small effect of b_{xy} , we can see that the peak value of a slope PDF is related to both σ_1 and σ_2 , while the half-peak widths are only proportional to one of the parameters. The PDF peak value is therefore used to represent the overall shape of slope PDFs.

The Elfouhaily model has three inputs, which are wind speed, wind direction and observation incident angle. Figure 4-26 presents the effects of wind speed and incident angle on the shape of Gaussian slope PDFs, i.e., the peak values of the PDFs. The wind direction sensitivity analysis can be seen in Appendix II.

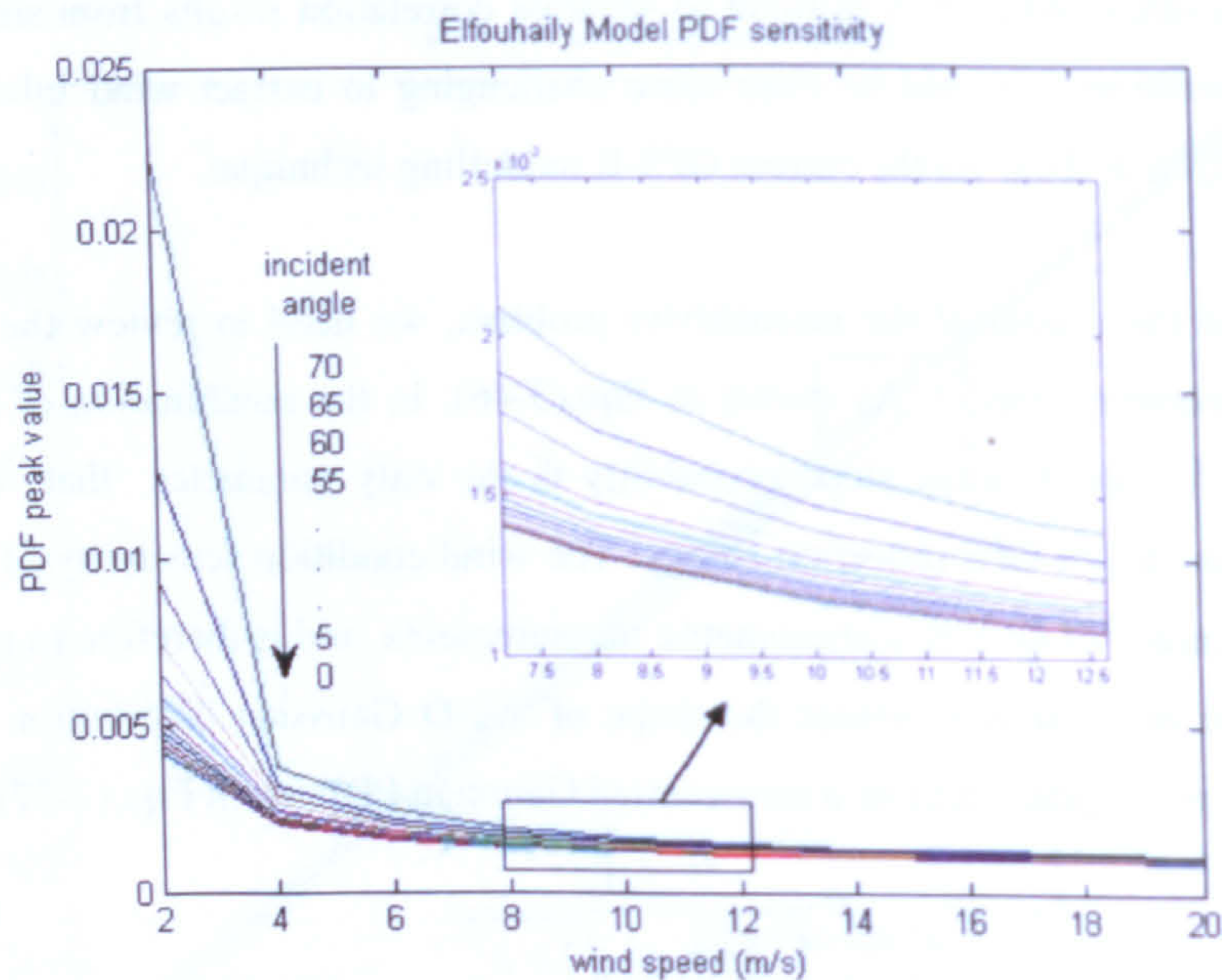


Figure 4-26: Wind speed and incident angle sensitivities of Elfouhaily modelled PDFs.

Figure 4-26 shows the peak values of Elfouhaily slope PDFs under different conditions of wind speeds and observing incident angles. The curves from top to bottom are from large incident angles to smaller ones. With a small incident angle, it is difficult to distinguish two adjacent PDFs, especially in the medium and high wind speed ranges. Even with a large incident angle, the slope PDF sensitivity to wind speed is not satisfactory beyond 10 m/s. Our simulations in Appendix II also show that the PDF sensitivity to wind directions is negligible.

4.5 Conclusions

This chapter details the GPS-R scatterometric modelling procedure, which is based on the Elfouhaily model and Z-V model described in Chapter 3. The DDM simulation procedure can be summarised in seven steps.

1. For each UK-DMC GPS-R dataset, estimate the specular point position in ECEF.
2. Check the validity of the dataset, according to its local wind/wave conditions from buoy measurements or other ground truth source.
3. If the dataset is valid, remove the bias in Doppler frequency domain to obtain a clear horse-shoe shape in the real DDM.
4. To simulate a DDM, rotate the coordinate system from ECEF to a specular-point-centred frame (Figure 4-6) and prepare patches on the reflection area.

5. Calculate reflection power of each patch according to the Elfouhaily and Z-V model combination as seen in Equ.(3-46), then convert the spatial energy distribution into a Delay-Doppler Map.
6. Estimate the geometric compensation from the image registration result of the bias-reduced UK-DMC data (output of step 3) and initial DDM simulation (output of step 5), and repeat step 5.
7. Compare a geometry-compensated DDM simulation to the corresponding real DDM.

Several UK-DMC datasets are chosen for this simulation experiment, for the purpose of evaluating the current GPS-R modelling method. Individual DDM data-model fitting shows a good match between the simulated and real data, that proves the viability of the model structure. The following “black-box” test, however, gave an unsatisfactory result. The insensitivity of slope PDFs to wind conditions induces the insensitivity problem of DDMs to wind conditions, which will narrow the disaster monitoring ability of GPS-R scatterometry using the above simulation procedure. Therefore we are motivated to find a new method to solve this problem. An empirical wave statistical model, which can be derived from UK-DMC GPS-R data, is proposed to replace the theoretical Elfouhaily model. The methodology is explained in Chapter 5.

References

- [Cafforio 1990] C. Cafforio, F. Rocca, S. Tubaro, Motion Compensated Image Interpolation, IEEE Trans. On Communication, Vol.38, No.2, February 1990.
- [De-Castro 1987] E. De-Castro and C. Morandi, Registration of Translated and Rotated Images Using Finite Fourier Transforms. IEEE Transactions on Pattern Analysis and Machine Intelligence, Vol. PAMI-9, No. 5, September 1987.
- [Gleason 2006] S. Gleason, Remote Sensing of Ocean, Ice and Land Surfaces Using Bistatically Scattered GNSS Signals From Low Earth Orbit, PhD Thesis, Surrey Space Centre, University of Surrey, UK, December 2006.
- [Vu 2000] M. Vu and M. Smulski, Motion Compensated Intermediate Viewpoint Image Interpolation, Project Report, Stanford Centre for Image Systems Engineering, Stanford University, 2000, <http://scien.stanford.edu/class/ee368/projects2000/project19/ee368proj.htm>

Chapter 5. Delay-Doppler Map Inversion Model

5.1 Introduction

From the discussion in Chapter 4, we have concluded that the wave spectrum model, which is insensitive to wind conditions, is the bottleneck of GPS-R scatterometric modelling technique. While reflection geometry dominates the GPS-R DDM simulation, wave conditions only play a minor roll in the simulation. Such problem limits the measuring capacity of GPS-R applications in oceanic remote sensing.

Due to the difficulty in finding an alternative of theoretic wind-wave model for GPS-R simulations, we are motivated to bypass this problem and find a solution to improve the accuracy of GPS-R measurements. Since it is the local wind or wave conditions that we want to obtain, it is reasonable to remove geometry factors from received DDMs to reveal the information related to wind and waves. The DDM inversion technique, which we discuss in this chapter, has exactly such aims. From the DDM generation procedure summarised in Figure 3-15, we can deduce a data processing procedure to inverse a DDM back to a spatial energy distribution map, from which a corresponding wave probability distribution can be obtained. The wave statistical attributes can be seen as an individual parameter to quantify sea states, and can also be associated with sea surface wind conditions.

This chapter will first identify the DDM inversion methodology. Then two steps of the inversion procedure will be detailed in the following sections, one is deconvolution, the other one is Bin-Patch searching. For deconvolution step, we compare several existing algorithms in the context of DDM simulation, and choose the one with the best performance for GPS-R DDM inversions. In Bin-Patch searching step, a new coordinates system is developed to represent local patch positions. This new frame simplifies the searching process when compared to the conventional Cartesian coordinate frame.

5.2 DDM inversion scheme

In the conclusion section of Chapter 3, Figure 3-15 outlines the principle procedure of GPS-R DDM simulation. To reveal wave slope probability information from GPS-R DDMs, we need to reverse this DDM simulation procedure, as shown in Figure 5-1:

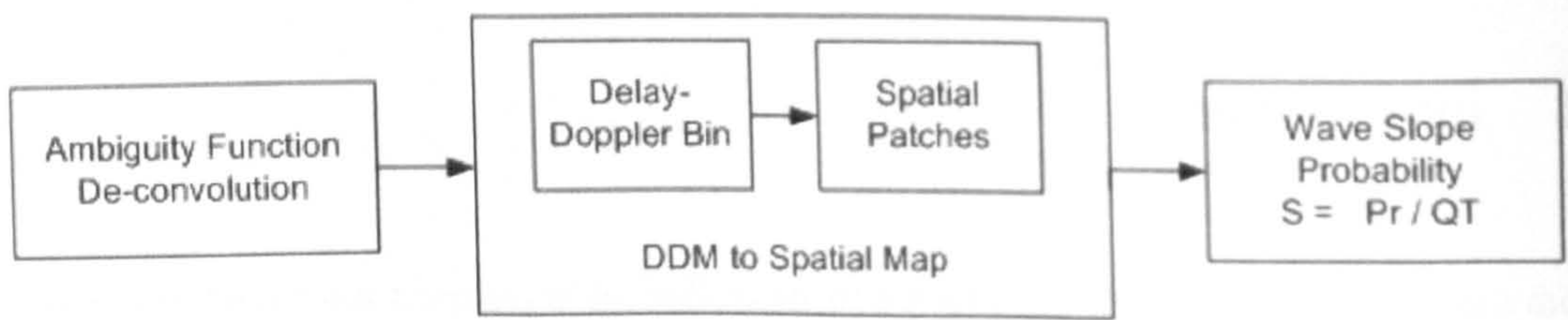


Figure 5-1: DDM inversion procedure.

The first step is to deconvolve the effect of GPS Ambiguity Function from a DDM. Then the energy distribution map can be converted from Delay-Doppler format to spatial format. From the spatial energy distribution of GPS reflections, we can estimate the statistical properties of local sea surface slopes by calculating S value from Equ. (3-47), i.e.,

$$S = P_r / (Q \cdot T) \quad (5-1)$$

where P_r is the reflected energy of a local patch. Q and T are corresponding geometric factors and constant factors.

The above methodology provides a solution to derive a wave statistical model empirically from UK-DMC GPS-R DDMs. As the literature review states in Chapter2, GPS-R satellites can provide high temporal and spatial coverage of the Earth surface. A continuous source of data therefore would be available for processing, to generate close estimations of an accurate wave statistical model. After systematically analysing DDM data and corresponding ground truth data, filtering techniques, such as the Kalman Filter, can be used in combination to adjust the empirical wave model.

A scheme structure is proposed to test the feasibility of the DDM inversion methodology, as seen in Figure 5-2. This flowchart represents the main research subject of Chapter 5 and 6.

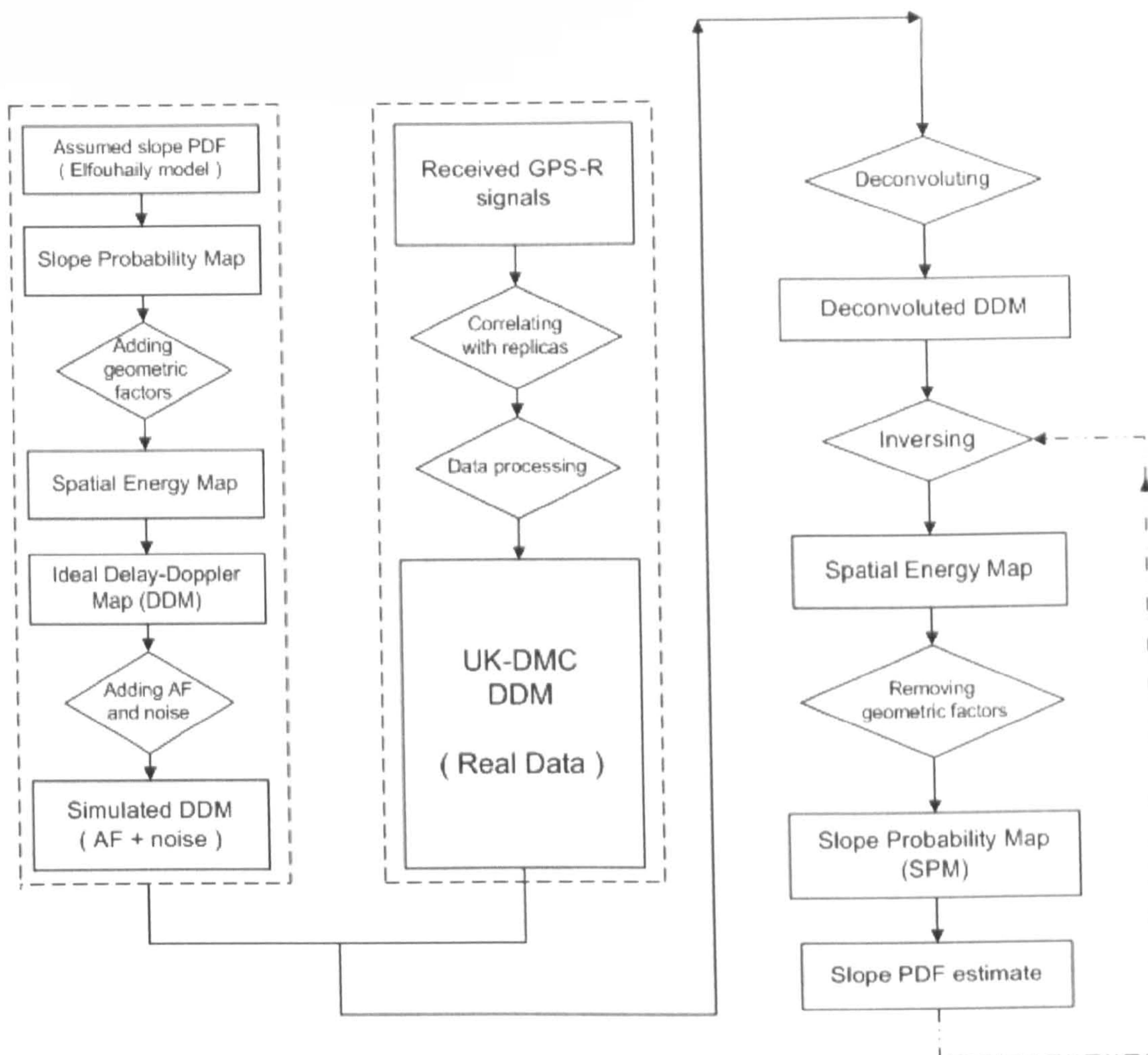


Figure 5-2: DDM inversion scheme flowchart.

As shown in Figure 5-2, while the left dash squares represent two types of DDM source, the flowchart on the right is the DDM inversion procedure. The first dash square is synthetic DDM data, for the purpose of validating key algorithms of the inversion scheme and analysing the inversing performance under noise. This procedure is similar to the DDM simulation method we described in Chapter 3 and 4. The only difference is that, while previous DDM simulations are noise-free, here a series of noise are added to the simulations to test the robustness of DDM inversion.

The inversion procedure flowchart on the right side of Figure 5-2 is an extended version of Figure 5-1. First a deconvolution algorithm is chosen to remove GPS Ambiguity Function effect from DDMs. Simulations show that the SNR quality of deconvolution results has significant effect on the following inversion procedure (section 5.3). In next step, the deconvoluted DDM is inversed back to a spatial energy map. An ambiguity problem is introduced by reversing Delay-Doppler bin power into several spatial patches. To overcome such problem several methods, based on certain assumptions, are investigated in Chapter 6.

The purpose of these inversion methods is not to get an analytical solution for the patch ambiguity, but to explore the possibilities of estimating the answer.

After obtaining a spatial energy map of reflected signals, we can calculate a wave slope probability value for each spatial patch by removing all geometric factors from its reflected power. In validation stage, the output Slope Probability Map (SPM) is compared with the original Gaussian SPM, which is the input of synthetic DDM generation. The correlation ratio between these two SPMs can evaluate the inversion quality of the method used. Iteration can be introduced into the procedure to decrease the patch ambiguity level and enhance the accuracy when necessary. If inversions of simulated DDMs have satisfactory results, we can apply the real UK-DMC DDMs (the second dash square in Figure 5-2) into the inversion experiment to get the first touch of an empirical wave slope probability model.

5.3 DDM deconvolution

5.3.1 Review

Deconvolution is a key area in a wide variety of signal and image processing problems [Proakis 1995][Jansson 1996] [Cornwell 1996]. For example, practical satellite images are often blurred due to the aperture effect of camera [Hanisch 1996][Jalobeanu 2000]. Many deconvolution algorithms have been developed to adapt to different situations.

The inversion problems, for most of the mathematical models of physical phenomena, are ill-conditioned. This means that the inversed results significantly depend on signal quality and very sensitive to noise, normally unstable in numerical analysis [Neelamani 2004]. The GPS-R signals are very weak due to the long reflection path and signal scattering on the sea surface. The noise problem is inevitable when processing DDMs.

Convolution and deconvolution can be simplified to scalar operations in Fourier domain, therefore Fourier analysis is naturally connected to deconvolution algorithms. For a non-ideal receiver system with input x , the output discrete signal y is:

$$y = (h * x) + \gamma \quad (5-2)$$

where input signal x is convolved with a transform function h and noise γ is then added to the system. The transfer function h is also known as Point Spread Function, or PSF, in image

processing field. The GPS Ambiguity Function, as the PSF, is known in our DDM inversion case, therefore this is not a blind deconvolution problem.

If we apply the Fourier Transform (FT) to y , we will have:

$$Y = H \cdot X + \Gamma \quad (5-3)$$

where Y, H, X, Γ are the frequency contents of y, h, x, γ respectively. The estimate of X can be written as:

$$\tilde{X} = \begin{cases} X + \frac{\Gamma}{H}, & \text{if } H > 0 \\ 0 & \text{otherwise} \end{cases} \quad (5-4)$$

An estimate of the original incoming signal \tilde{x} can be calculated by applying the Inversed Fourier Transform (IFT) on \tilde{X} . The noise, however, is significantly amplified around the cut-off frequency of H . To overcome such problem, different noise reduction methods are used in several deconvolution algorithms.

Three commonly used deconvolution methods are Wiener algorithm, Least-square algorithm and Richardson-Lucy (R-L) algorithm [Bertero 2000] [Starck 2002]. Another wavelet-based algorithm, which is developed for ill-posed deconvolution problems, is also discussed and tested. While this section briefly reviews the first three well known methods, the next section will focus on the new wavelet-based algorithm.

A Fourier shrinkage factor λ^f is introduced to attenuate the FT amplified noise in Equ. (5-4), as below:

$$\tilde{X}_{\lambda^f} = \frac{Y}{H} \cdot \lambda^f \quad (5-5)$$

The Wiener algorithm is a linear regularised method, which defines the shrinkage term λ^f as [Gonzalez 2003]:

$$\lambda_{Wiener}^f = \frac{|H|^2}{|H|^2 + \alpha \frac{N\sigma^2}{|X|^2}} \quad (5-6)$$

where N is the length of data array, σ^2 is noise variance of an assumed Gaussian noise, α is an adjustable regularisation parameter related to $|Y|^2$ and $|H|^2$.

The Least-square method is also a linear regularisation algorithm, which gives the minimum least square error between the estimates and true images. It also has the best possible

smoothness effect among the well-known algorithms [Neelamani 2004]. Assuming a flat signal spectrum $|X|^2$, the shrink term of the Least-square method, which is also known as Tikhonov-Miller regularisation term, can be expressed as [Starck 2002]:

$$\lambda_\tau = \frac{|H|^2}{|H|^2 + \tau} \quad (5-7)$$

with a positive value τ . τ is known as Tikhonov factor and can be written as σ_b^2 / σ_x^2 , in which σ_b is the standard deviation of convolved signal and σ_x is the standard deviation of original signal [Wiki 2008].

The Wiener method and the Least-square method are both standard Fourier-based regularisation algorithms. They can provide good quality estimates when input signal is smooth and its corresponding Fourier spectrum is limited. On signal singularities or image edges, where the signal spectrum spreads out in a wide range, the Fourier shrinkage is not as efficient as on smooth signals.

The Richardson-Lucy (R-L) method, also known as Maximum Likelihood algorithm, is a typical statistics-based deconvolution method [Lucy 1974] [Cornwell 1996]. It uses the Bayes rule and the law of total probability to analyse the maximum probability of estimations to real data. Such statistical relationship can be expressed as [Starck 2002] [Borman 2004]:

$$p(x|y) = \frac{p(y|x) \cdot p(x)}{p(y)} \quad (5-8)$$

With Poisson noise assumption in the R-L algorithm, the probability $p(y|x)$ is

$$p(y|x) = \prod \frac{(h * x)^y \exp(-h * x)}{y!} \quad (5-9)$$

The Maximum Likelihood solution can be found by maximising the density $p(y|x)$ over x , i.e.,

$$\frac{\partial \ln p(y|x)}{\partial x} = 0 \quad (5-10)$$

The Picard iteration and constraints (P_c) are used to achieve the numerical estimation of the analytical solution for the above equation [Starck 2002][Tiebaut 2004]. The $(n+1)$ th estimation of original signal can be written as:

$$x^{n+1} = P_c \cdot \left\{ x^n \cdot \left[\frac{y}{h * x^n} * h^* \right] \right\} \quad (5-11)$$

5.3.2 Fourier-Wavelet algorithm

Apart from Fourier and statistics-based algorithms, other methods, such as wavelet analysis and super-resolution, are also used to solve deconvolution problems [Neelamani 2004].

Wavelet technique provides a mathematical framework for multi-resolution processing. It is an economical representation for a diverse class of signals, especially for signals with singularities, such as image edges and point sources [Graps 1995][Rao 1998]. With a Discrete Wavelet Transform (DWT), the finite resolution estimate of a 1-D signal can be expressed by scalar function ϕ and wavelet functions ψ [Mallat 1999]. The J level approximation x^J of original signal x can be given by:

$$x^J(n) = \sum_{l=0}^{N_{j0}-1} s_{j0,l} \phi_{j0,l}(n) + \sum_{j=j0}^J \sum_{l=0}^{N_j-1} w_{j,l} \psi_{j,l}(n) \quad (5-12)$$

where N is the sampling number, j and l are the scale and location of the wavelets, respectively. Different levels of scalar function and wavelet can be expressed as below [Mallat 1999]:

$$\begin{cases} \phi_{j,l}(n) = 2^{j/2} \phi(2^j n - l) \\ \psi_{j,l}(n) = 2^{j/2} \psi(2^j n - l) \end{cases} \quad (5-13)$$

While ϕ corresponds to a low-pass filter, ψ is equivalent to a band-pass filter, which is shifted and expanded over the spectrum range of input signal. They satisfy Quadrature mirror filter conditions, which means, the power sum of two sets of filters is equal to 1 at every frequency range in concern [Torrence 1997]. The scalar function and wavelet pairs developed by [Haar 1909], [Daubechies 1988] and [Mallat 1999] all satisfy this orthogonal relationship. A typical three level DWT wavelets can be represented in frequency domain as Figure 5-3.

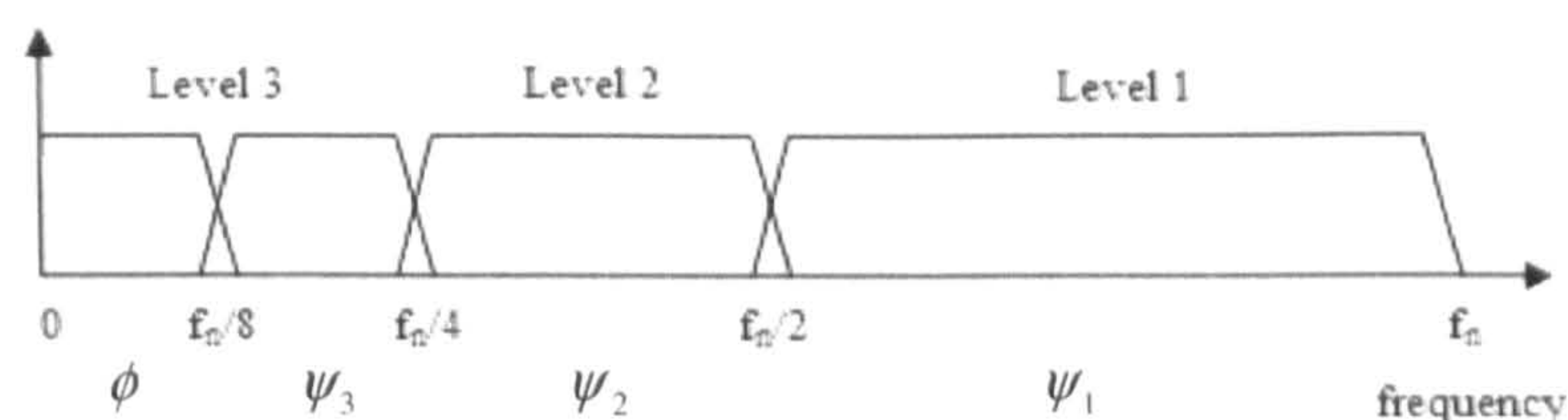


Figure 5-3: Three level DWT frequency domain representation [Rao 1998].

The **F**ourier-**W**avelet **R**egularised **D**econvolution (ForWaRD) method was developed by [Neelamani 2004]. In addition to the Fourier shrinkage term λ^f , a wavelet shrinkage term λ^w is introduced into the noise reduction procedure. The ForWaRD algorithm derives the optimal

balance between the Fourier and wavelet regularisations and is proven to be an efficient hybrid algorithm in a wide variety of ill-conditioned deconvolution problems. The ForWaRD deconvolution procedure can be seen in Figure 5-4:

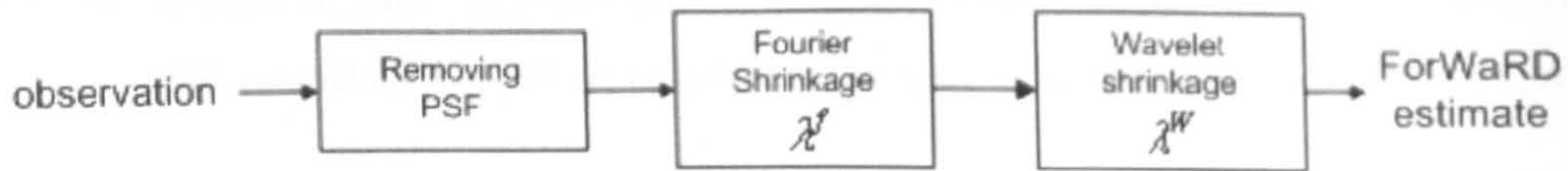


Figure 5-4: Fourier and wavelet noise shrinkage procedure in ForWaRD [Neelamni 2004].

The shrinkage term λ^w in wavelet domain is:

$$\lambda_{j,l}^w = \frac{|\tilde{w}_{j,l}|^2}{|\tilde{w}_{j,l}|^2 + \sigma_j^2} \quad (5-14)$$

where σ_j^2 is the variance of coloured noise at different wavelet scale j , and $\tilde{w}_{j,l}$ is the wavelet coefficients of the initial estimate for original signal.

To find the most suitable deconvolution algorithm in our DDM inversion procedure, a series of simulated DDMs of R12 scenario, with different noise levels, are created (refer to DDM simulation and R12 case study sections in Chapter 4) and input into the deconvolution experiment. The main purpose of this experiment is to evaluate the noise robustness of different deconvolution algorithms in the DDM inversion context. The comparisons of the ForWaRD algorithm to Fourier-based methods (Wiener and Least-Square) and statistical method (R-L) are presented in the following sections.

5.3.3 Wiener vs. ForWaRD

Received GPS-R signals have heavy noise [Gleason 2006], however, lack of reference makes it difficult to quantify the Signal-to-Noise Ratio (SNR) of real DDM data. To simulate the noise effect on DDM deconvolution, different levels of Gaussian noise is generated and added into DDM simulations. One of the deconvolution algorithms, with the best overall performance on all noise levels, will be chosen for our DDM inversion processing.

As the comparison standard for deconvolved results, a clear DDM, without GPS Ambiguity Function (AF) blurring, is first generated according to the wind conditions and reflection geometry of the R12 scenario, as seen in Figure 5-5. Then the square of GPS AF is convolved with this clear DDM, and different levels of Gaussian noise are added to the AF-blurred DDM afterwards.

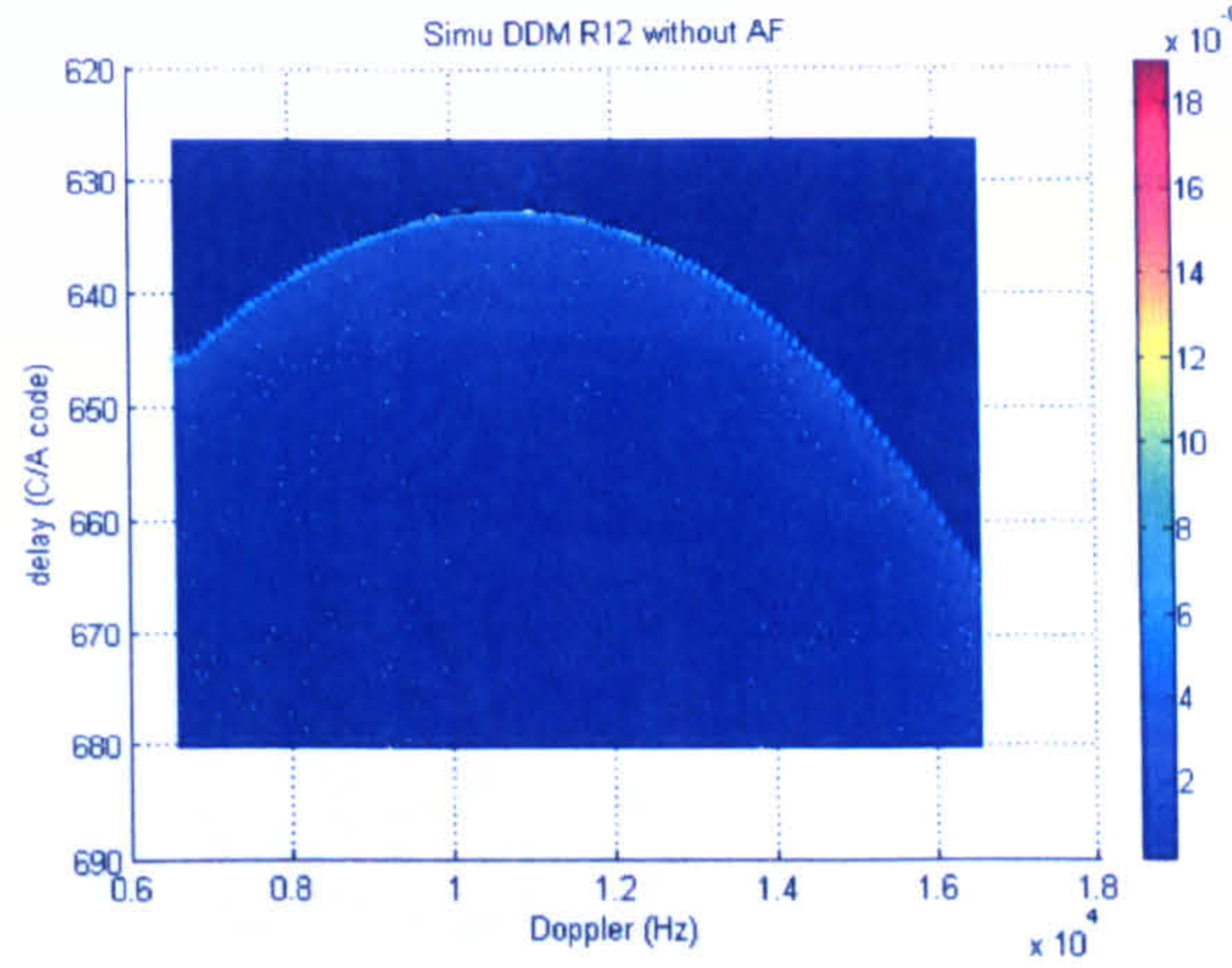


Figure 5-5: Simulated noise-free clear R12 DDM.

The Blurred SNR ($BSNR$) is used to describe the quality of noisy DDM before deconvolution [Neelamni 2004]:

$$BSNR = 10 \log_{10} \left(\frac{\sigma_s^2}{\sigma_N^2} \right) \quad (dB) \quad (5-15)$$

Where σ_s^2 is the root mean square (RMS) of original image (noise-free AF-blurred DDM, as in Figure 4-21(d)), and σ_N^2 is the noise RMS [Brooks 2003].

The quality of deconvolved image can be evaluated by the normal SNR or the Improvement in SNR ($ISNR$) parameter. SNR of digital image is normally defined as the ratio of mean pixel value to standard deviation of the pixel values [Young 1998], as in Equ. 5-16:

$$SNR = 10 \log_{10} \frac{\sum I_c^2}{\sum (I_c - I_D)^2} \quad (dB) \quad (5-16)$$

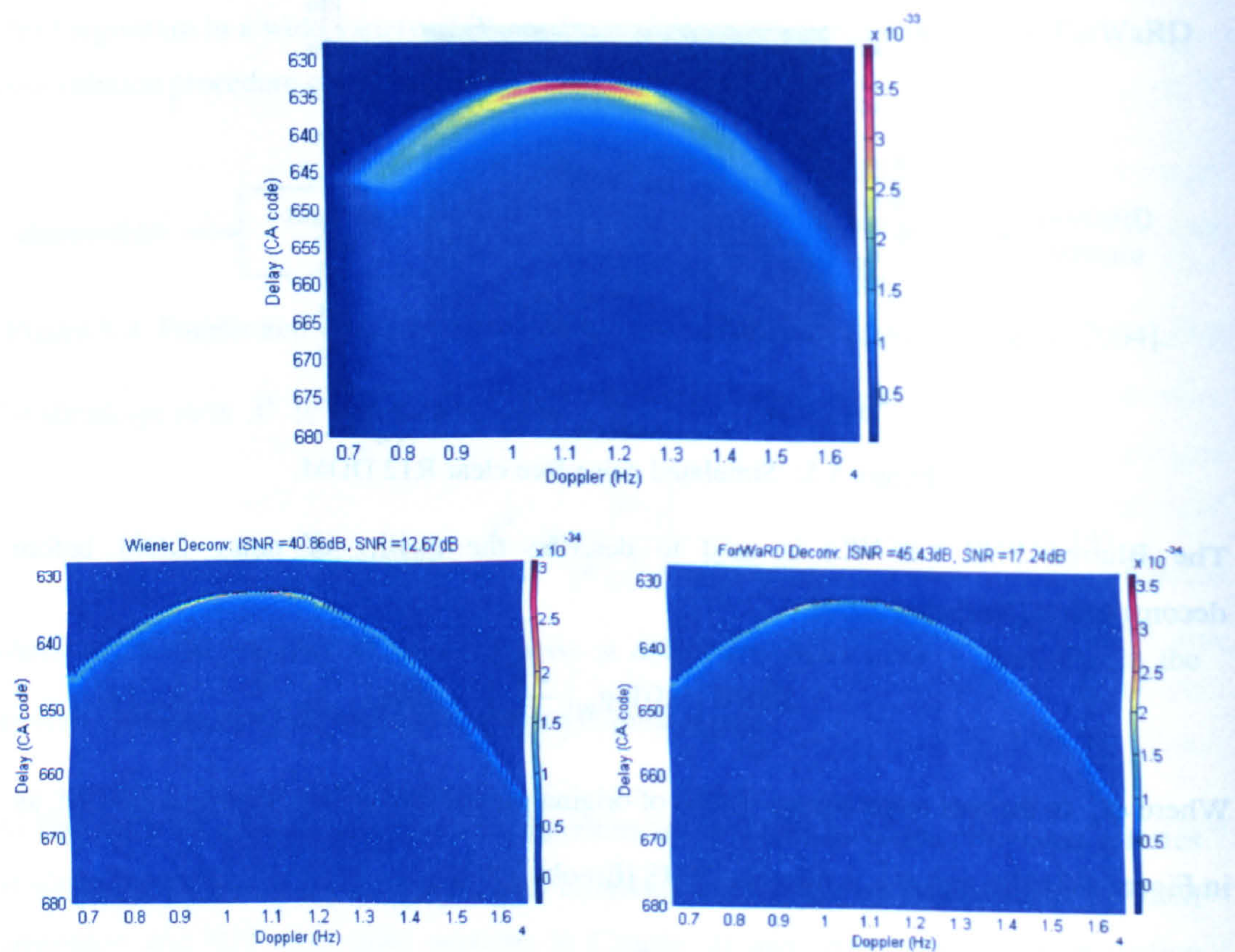
$ISNR$ can be defined as in Equ. 5-17:

$$ISNR = 10 \log_{10} \frac{\sum (I_c - I_B)^2}{\sum (I_c - I_D)^2} \quad (dB) \quad (5-17)$$

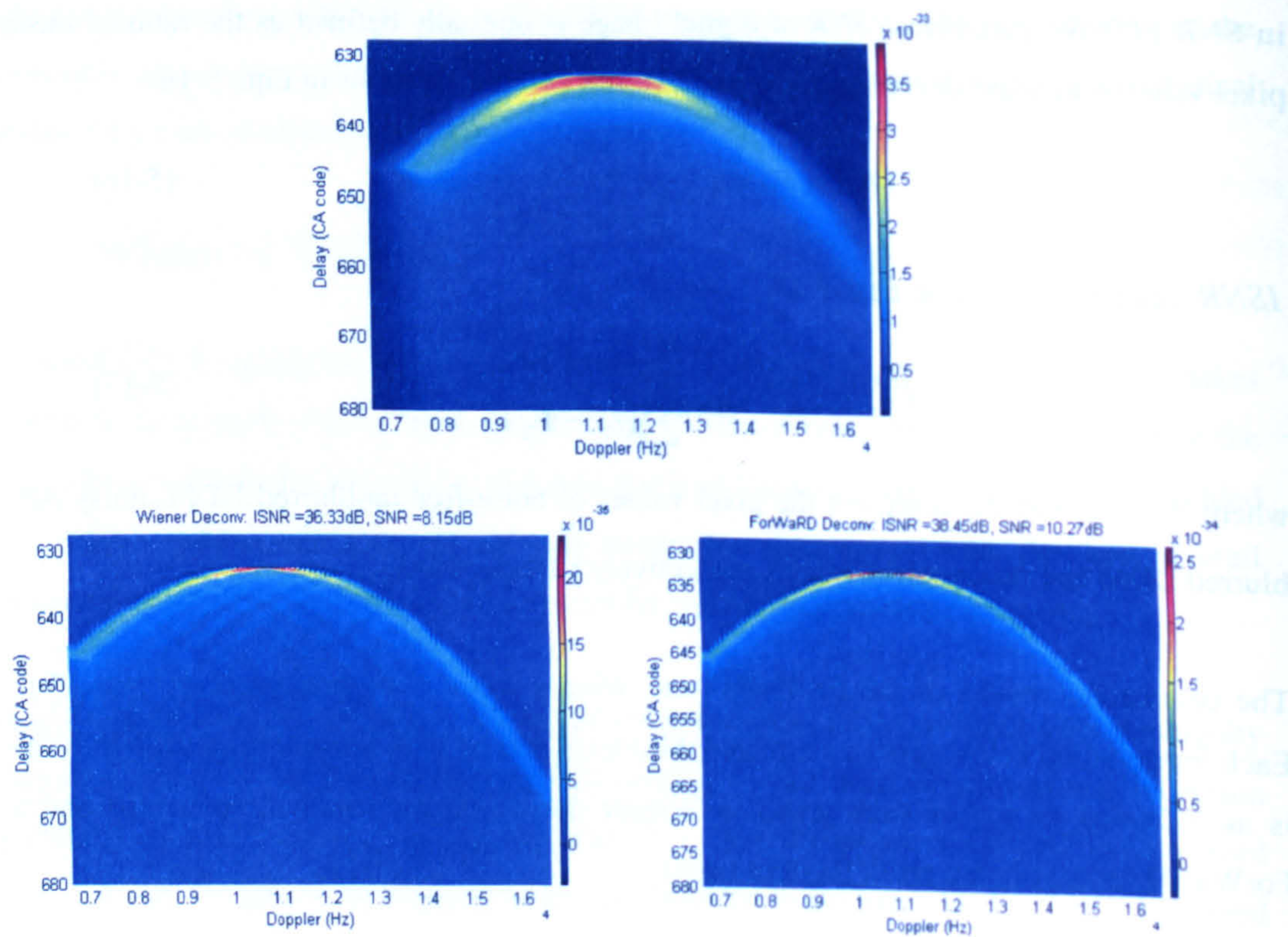
where I_c , I_B and I_D represent the pixel values of noise-free un-blurred DDM, noisy AF-blurred DDM and deconvolved image, respectively [Brooks 2003].

The comparison results of the ForWaRD and Wiener method are presented in Figure 5-6. Each image group below gives a simulated AF-blurred DDM with noise, whose $BSNR$ value is as indicated on top of each group, a Wiener deconvolution result (bottom left) and a ForWaRD deconvolution result (bottom right).

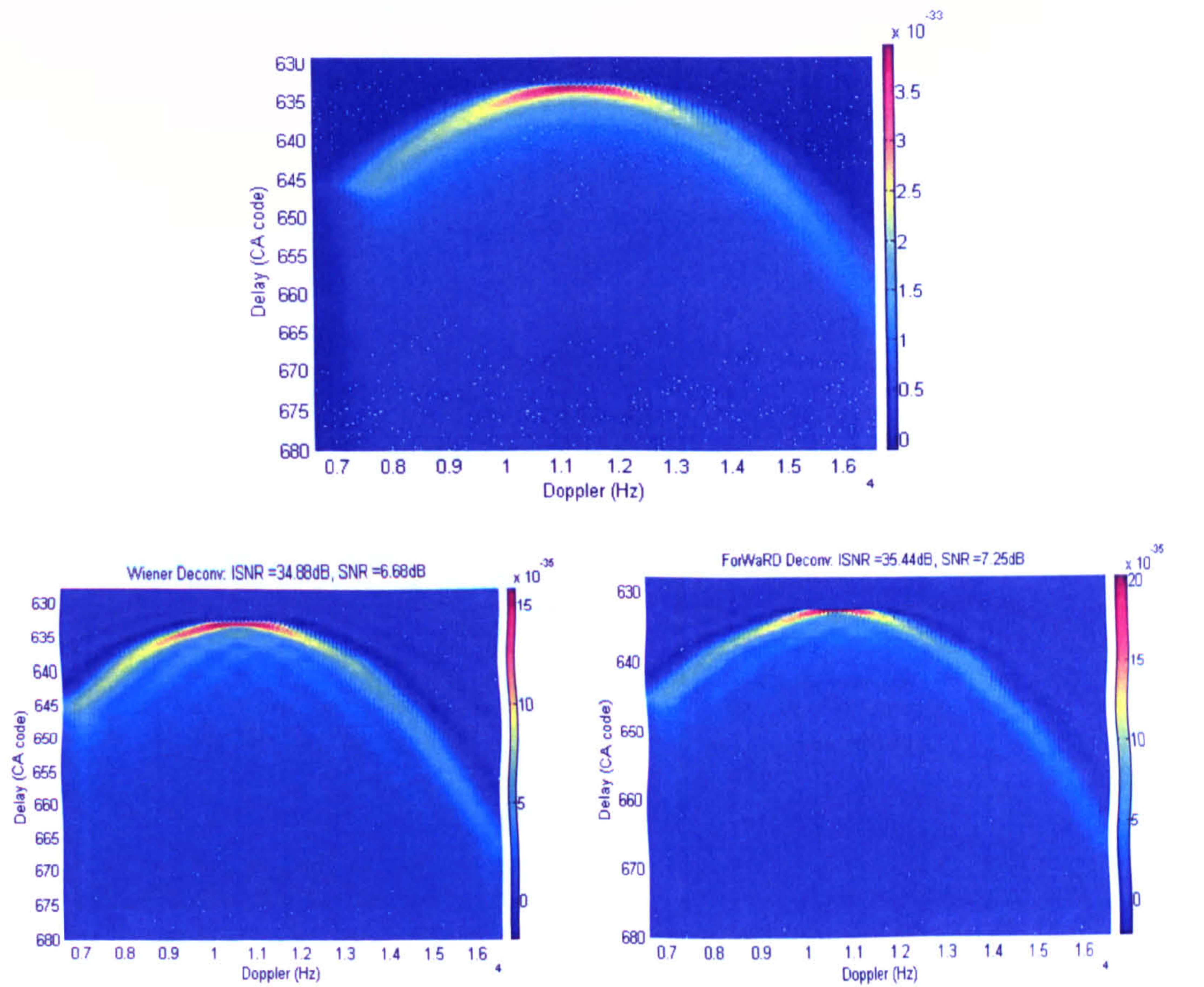
BSNR = 100 dB



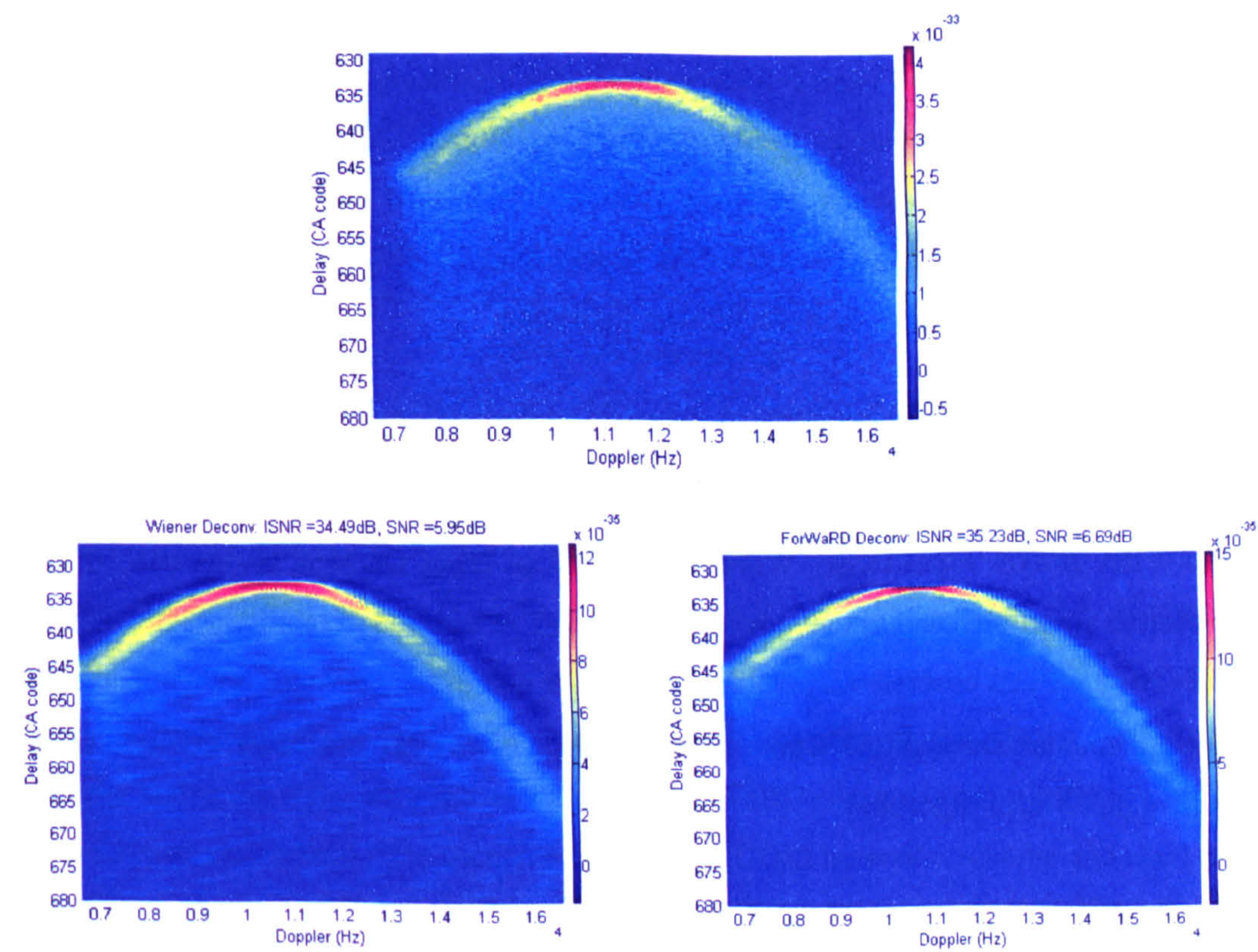
BSNR = 60 dB



BSNR = 20 dB



BSNR = 5 dB



BSNR = 3 dB

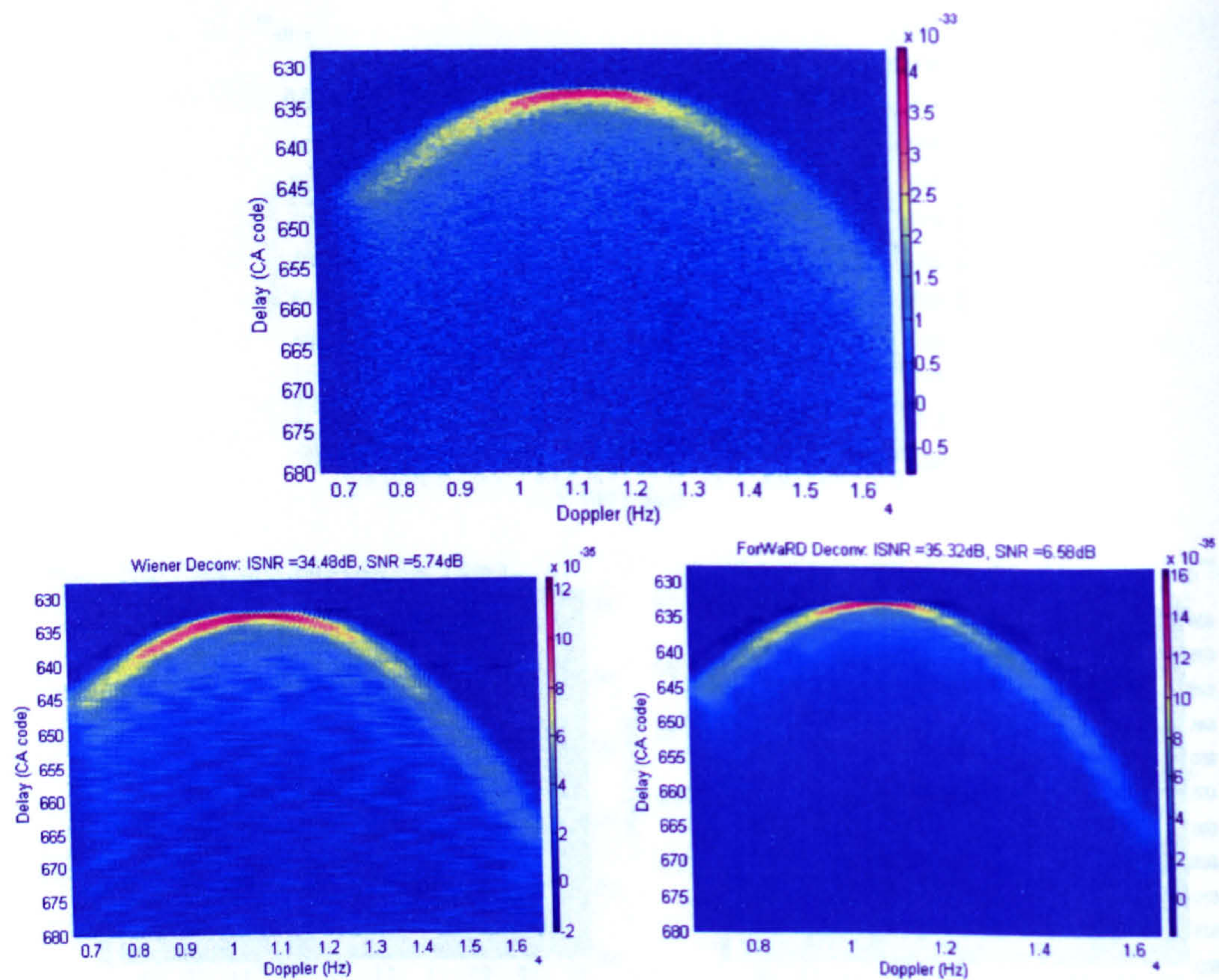


Figure 5-6: Wiener vs. ForWaRD for DDM deconvolution with different noise level.

This group of simulations in Figure 5-6 shows that, with increasing noise in synthetic DDMs, the quality of deconvolved outputs decrease. When the blurred DDM has a 100 dB *BSNR*, both Wiener and ForWaRD result are quite close to the original clear DDM, as shown in Figure 5-5. When the *BSNR* of blurred DDM is less than 10 dB, the ForWaRD algorithm visually has better performance than the Wiener algorithm.

We quantitatively compare the *SNR* and *ISNR* values of deconvolved DDMs from both algorithms, as shown in Figure 5-7. The top right part of each diagram is an amplified figure of 40 to 0 dB *BSNR* input range. When the *BSNR* of input DDM is lower than 10 dB, deconvolution algorithm can eliminate some of the noise in addition to removing PSF. That is the reason why we can observe *ISNR* increasing at the end of the curve for both Wiener and ForWaRD methods. Through the whole *BSNR* range, ForWaRD has better deconvolution quality than the Wiener algorithm.

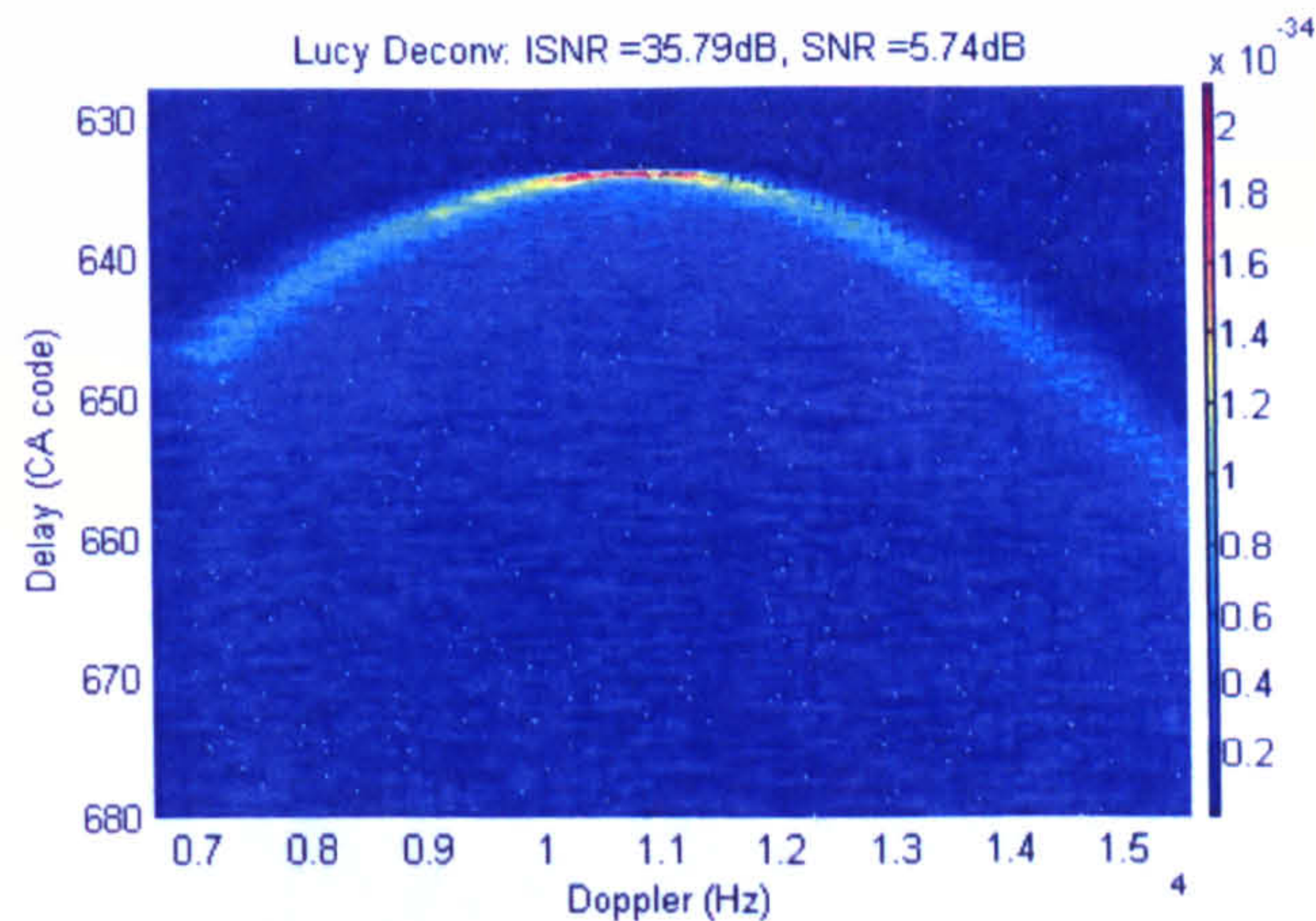


Figure 5-9: The performance of the R-L method in DDM deconvolution.

The *SNR* and *ISNR* comparisons between the Least-square, R-L and ForWaRD algorithm are shown in Figure 5-10 below:

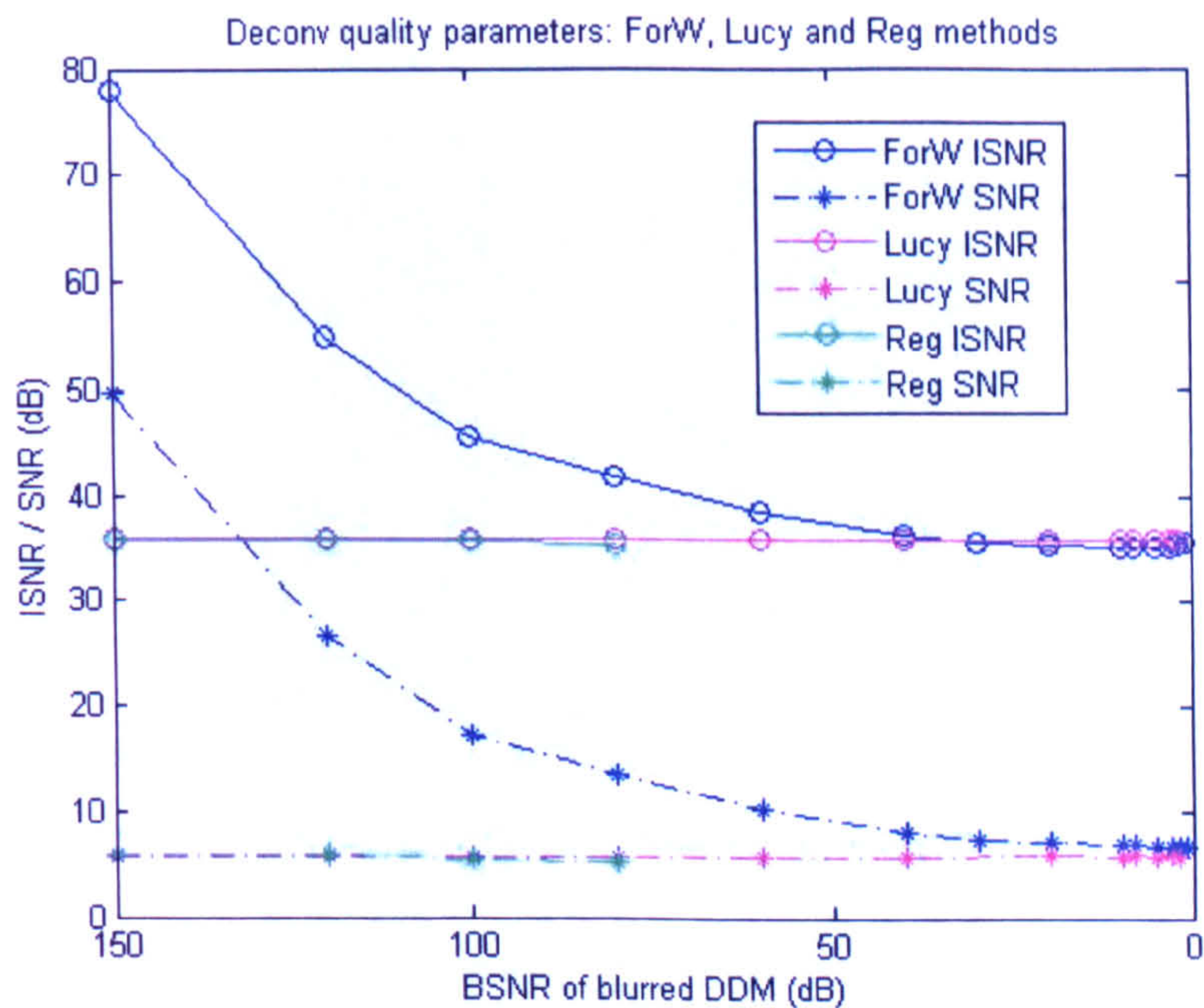
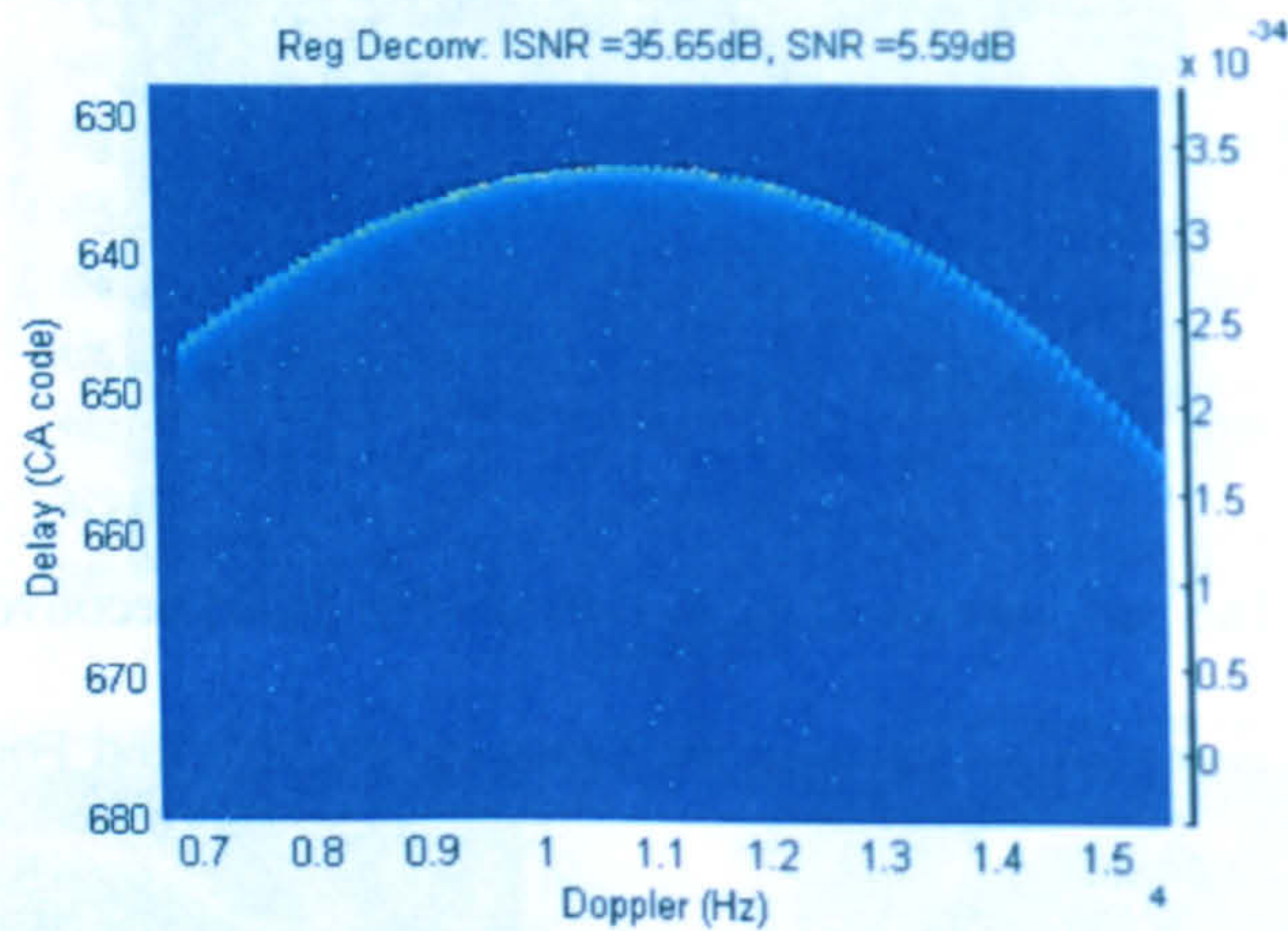


Figure 5-10: ForWaRD, Least-square (Reg) and R-L comparisons on SNR and ISNR.

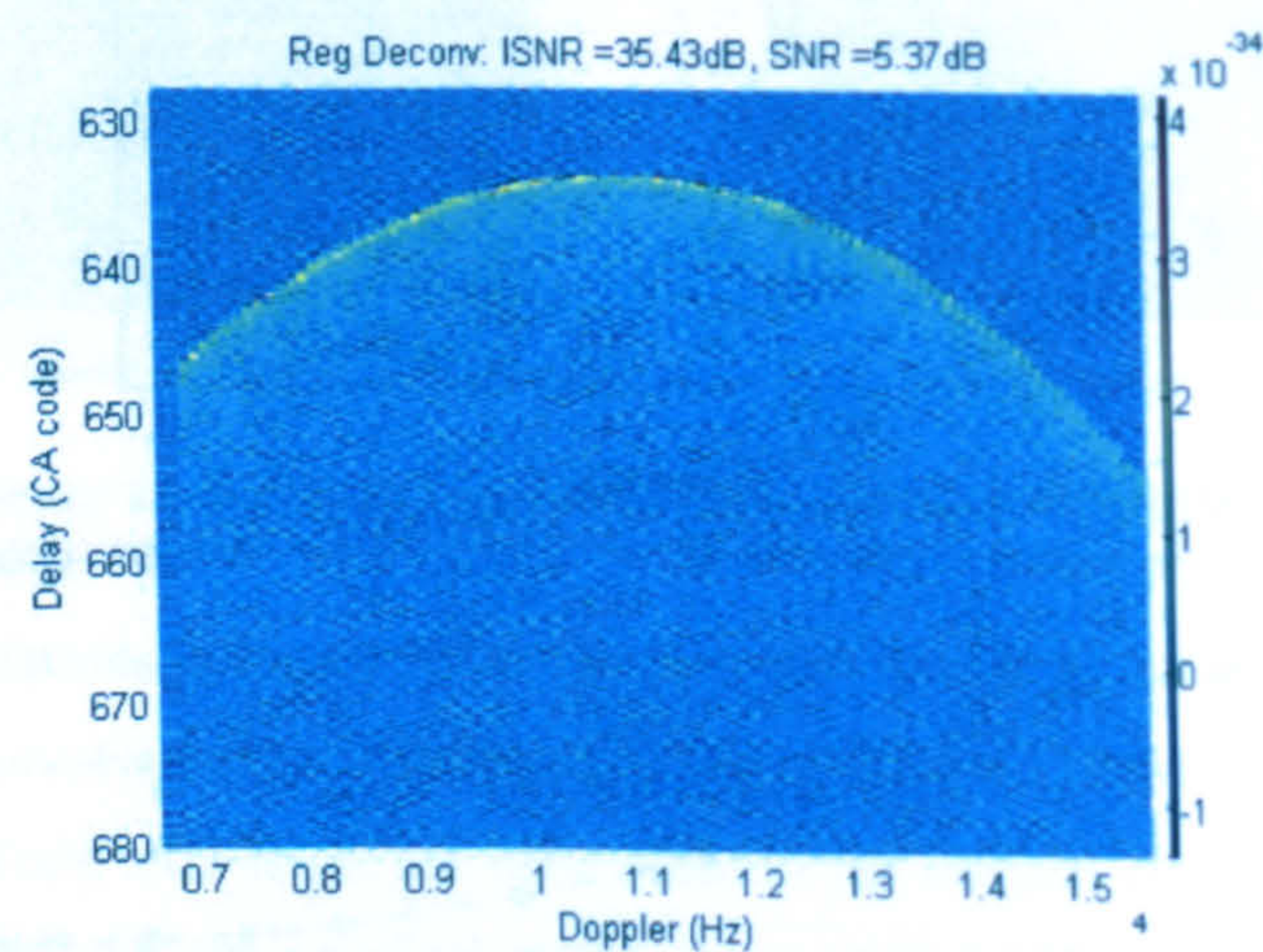
In Figure 5-7, we can observe that the output *SNR* and *ISNR* of the Wiener and ForWaRD method both vary with input DDM quality. As seen in Figure 5-10, however, the output of the R-L method is almost irrelevant to the input DDM *BSNR*. Though the R-L method has slightly better *ISNR* than ForWaRD under very noisy situation, ForWaRD has overall preferable performance on both *SNR* and *ISNR* values through the whole *BSNR* range. From the above analysis, we can conclude that ForWaRD outstands other methods in DDM deconvolution experiment. It is chosen as part of the DDM inversion scheme and used in our further research. We also notice the constant *SNR* and *ISNR* output from the R-L algorithm.

The figures below show the deconvolved DDMs from the Least-square method. This method does not perform well under heavy noise situation.

BSNR = 100 dB



BSNR = 80 dB



BSNR = 60 dB

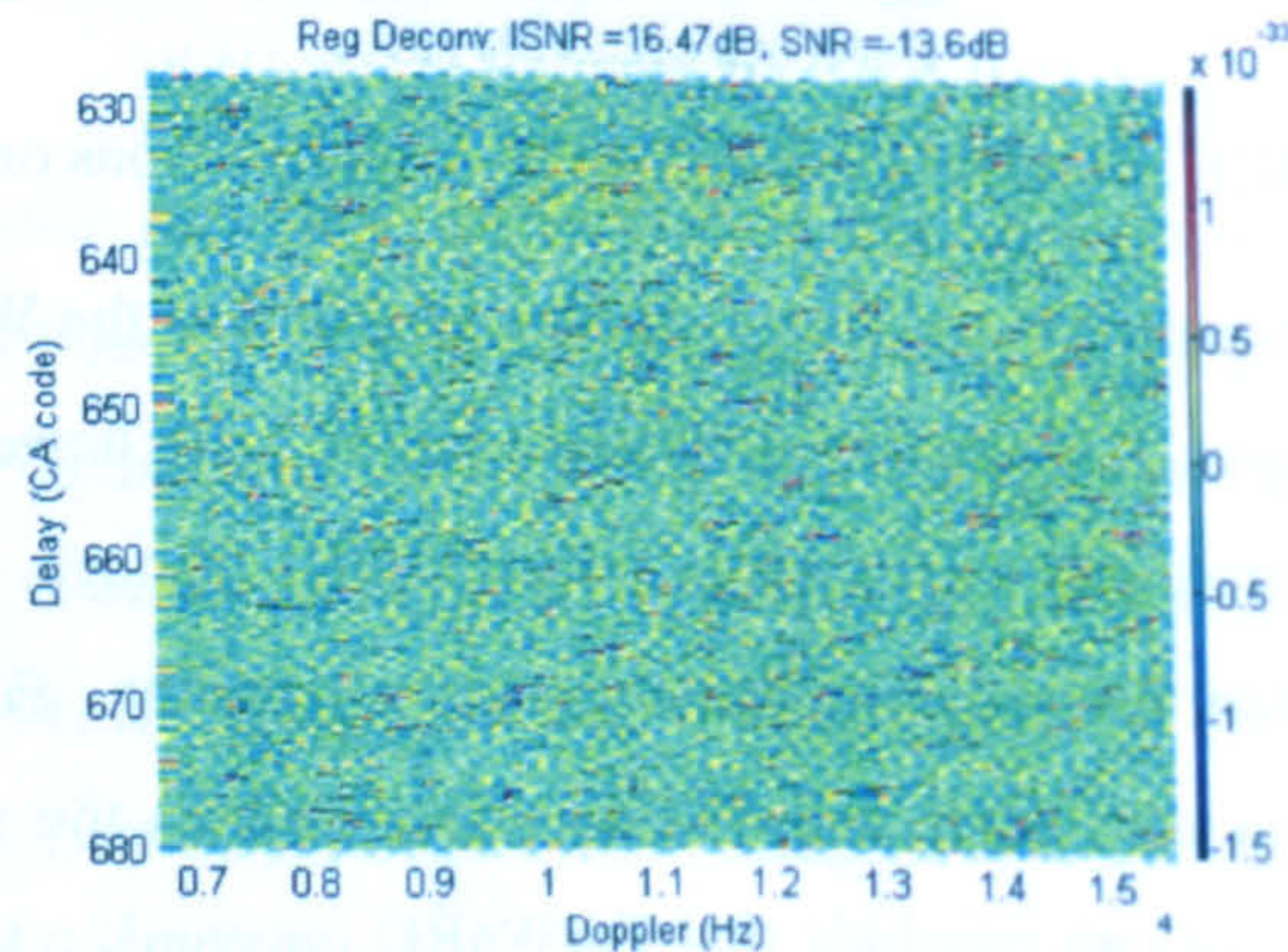
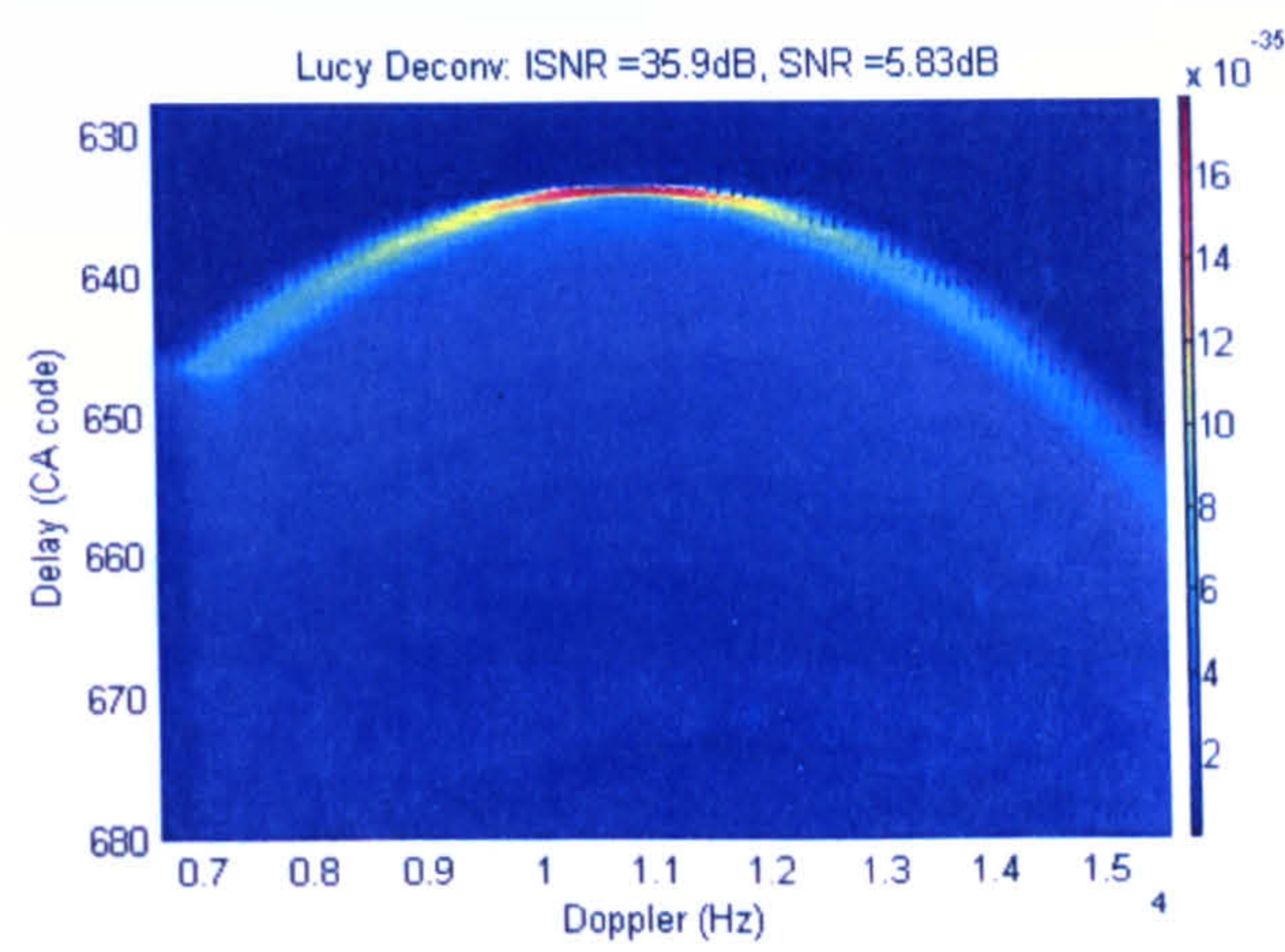


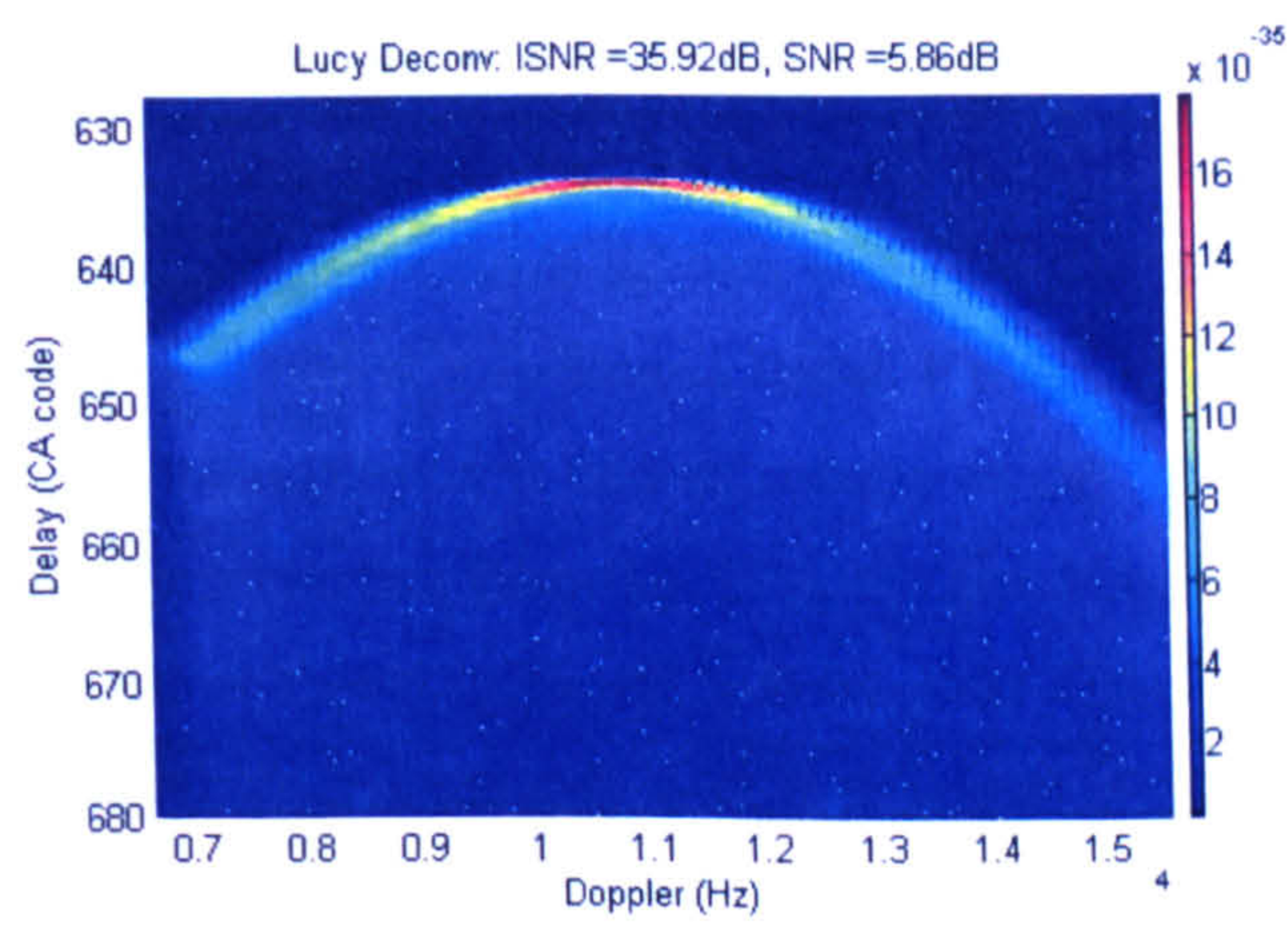
Figure 5-8: The performance of the Least-square method in DDM deconvolution.

The Richardson-Lucy algorithm has better robustness against noise than the Least-square method. The deconvolved DDM results are presented in figures below:

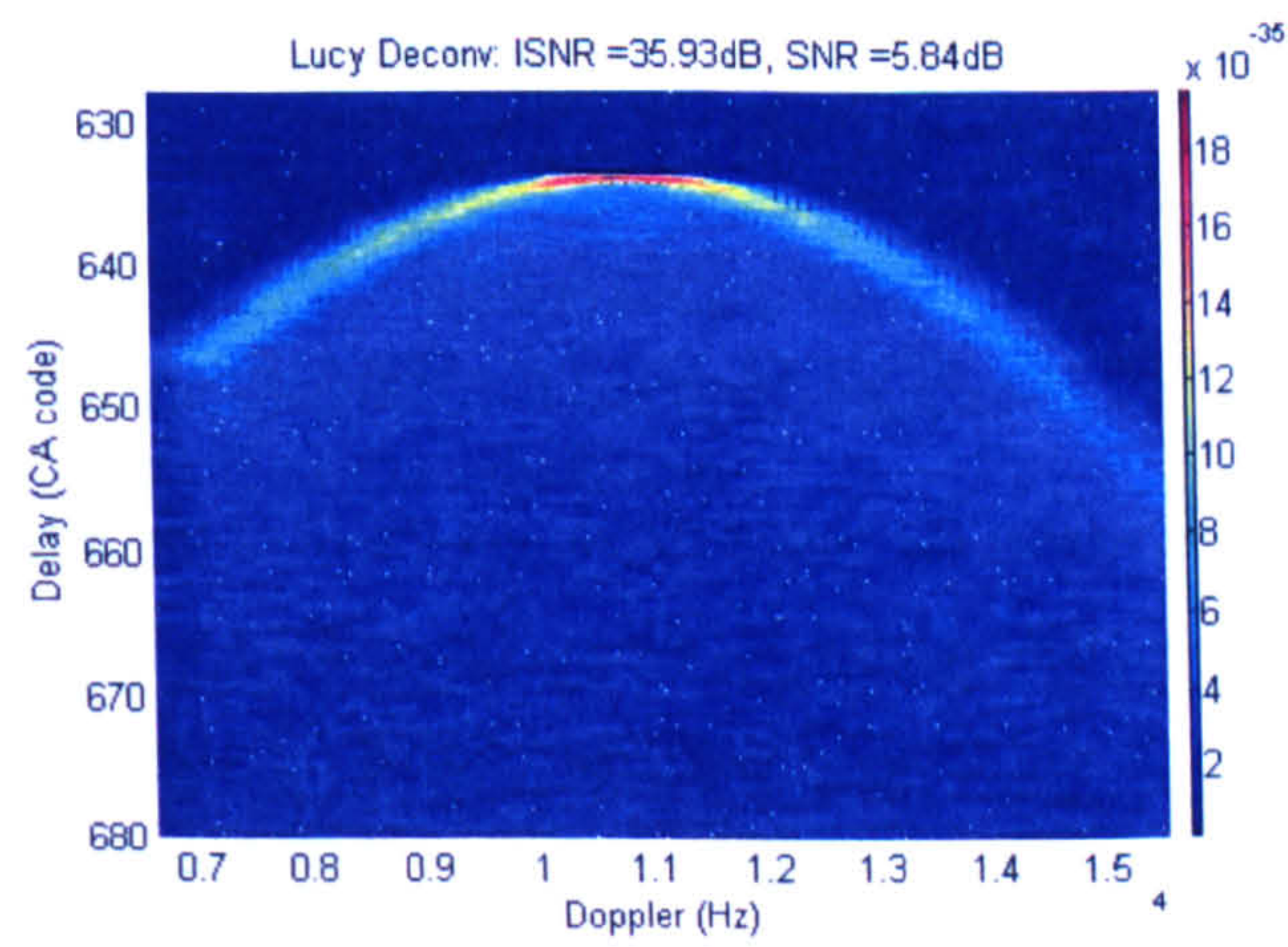
BSNR = 100 dB



BSNR = 20 dB



BSNR = 5 dB



BSNR = 2 dB

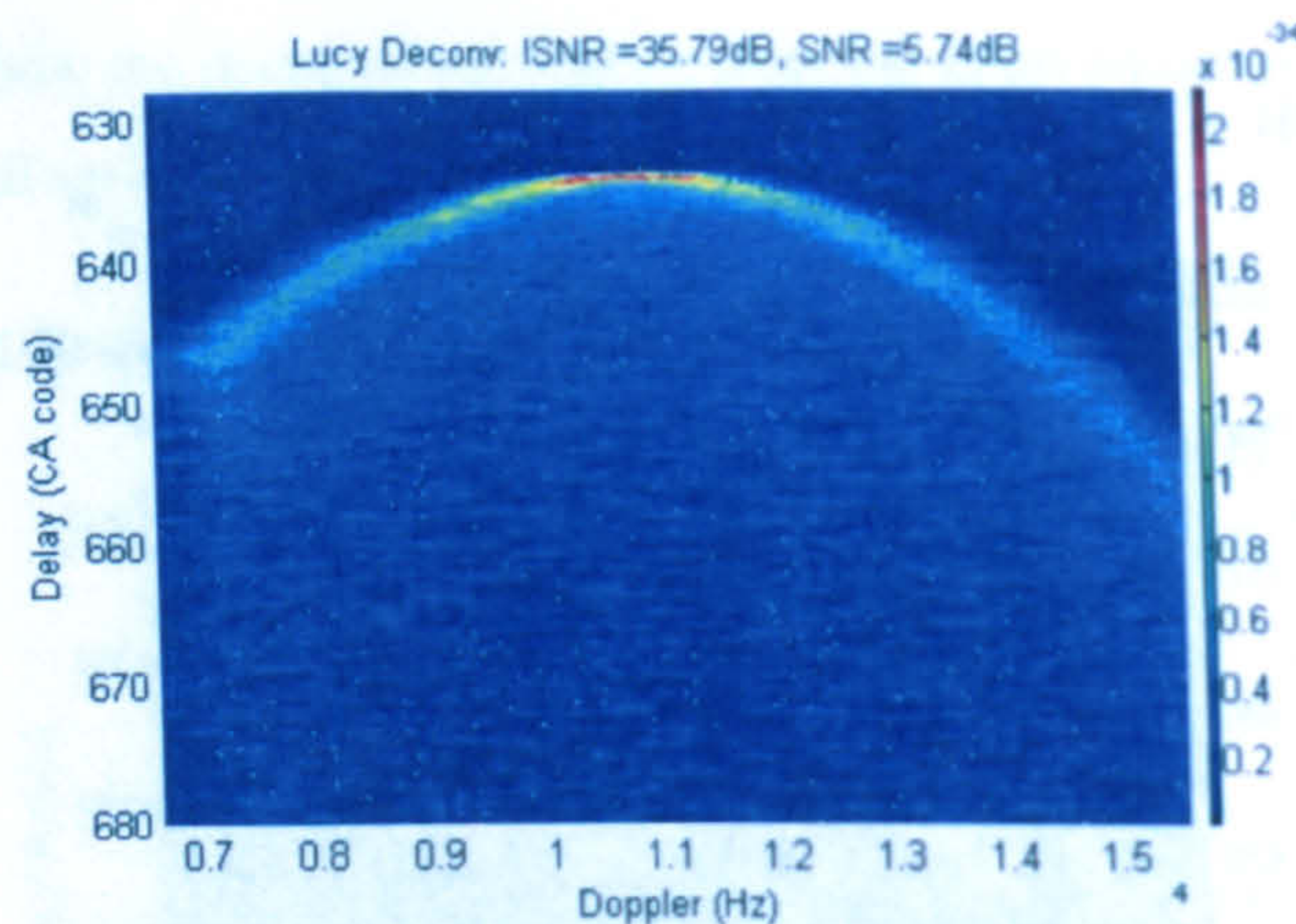


Figure 5-9: The performance of the R-L method in DDM deconvolution.

The SNR and $ISNR$ comparisons between the Least-square, R-L and ForWaRD algorithm are shown in Figure 5-10 below:

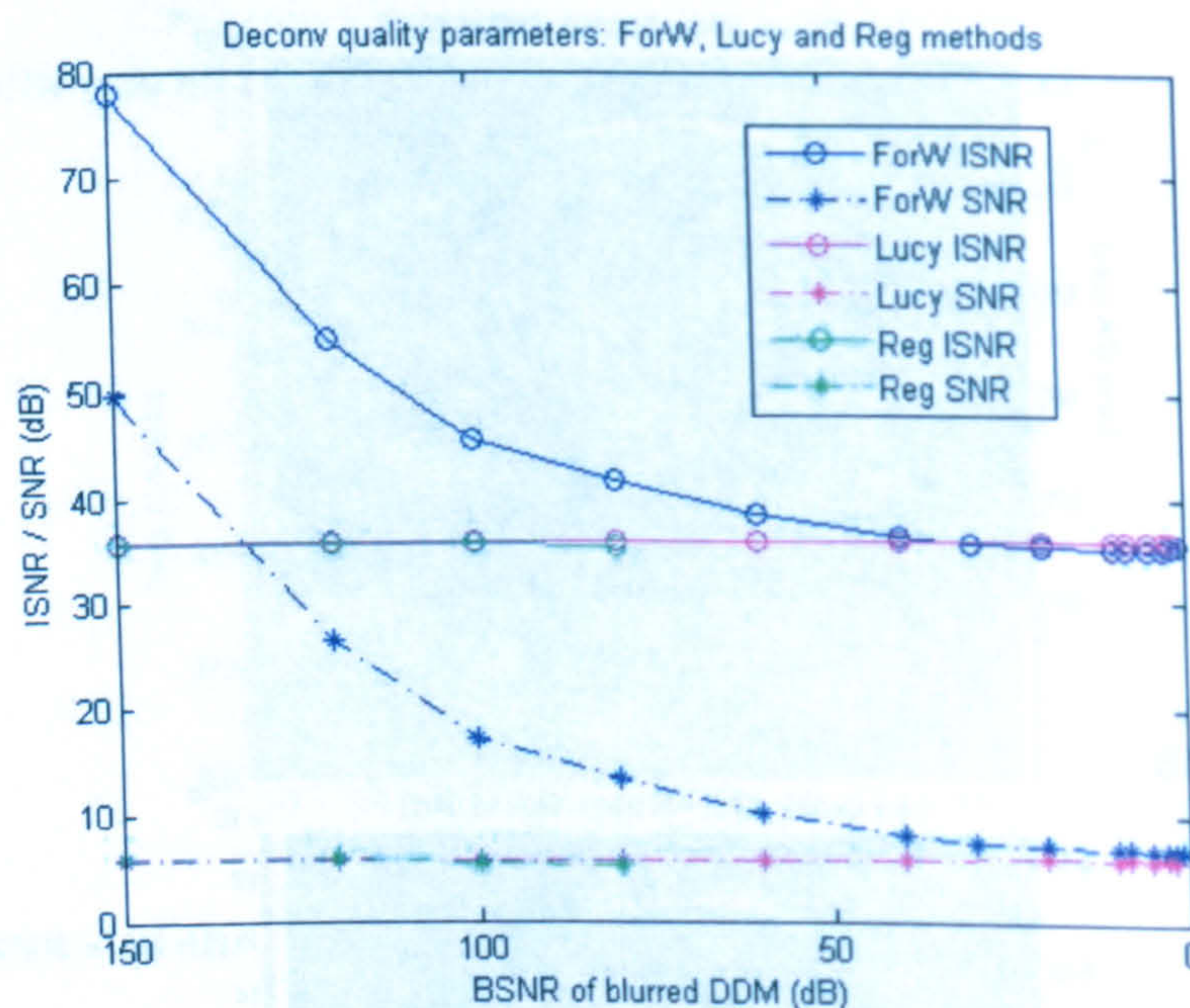


Figure 5-10: ForWaRD, Least-square (Reg) and R-L comparisons on SNR and ISNR.

In Figure 5-7, we can observe that the output SNR and $ISNR$ of the Wiener and ForWaRD method both vary with input DDM quality. As seen in Figure 5-10, however, the output of the R-L method is almost irrelevant to the input DDM $BSNR$. Though the R-L method has slightly better $ISNR$ than ForWaRD under very noisy situation, ForWaRD has overall preferable performance on both SNR and $ISNR$ values through the whole $BSNR$ range. From the above analysis, we can conclude that ForWaRD outstands other methods in DDM deconvolution experiment. It is chosen as part of the DDM inversion scheme and used in our further research. We also notice the constant SNR and $ISNR$ output from the R-L algorithm.

The deconvolved DDM image quality is independent of input image quality with the R-L method, which might be a useful analysing tool in the future study.

5.4 Spatial patch searching method

5.4.1 Cartesian vs. Polar

In the previous DDM simulation procedure, which is described in Chapter 4, we separate the reflection area into a Cartesian grid. In such coordinate system, the spatial patches in same row or same column unnecessarily have the same Delay and Doppler properties. However, when creating DDM simulations, the Cartesian Grid separation is straightforward and convenient.

The second step in DDM inversion scheme as seen in Figure 5-2, after deconvolution, is to generate a spatial energy distribution map from a DDM. For each Delay-Doppler bin, a 2-D searching procedure must be employed to find its corresponding patches on an initial empty spatial map (refer to Figure 3-13). In a Cartesian Grid, the matching patches are distributed in several rows and columns, as shown in Figure 5-11(a). Both Delay and Doppler indices of those patches have to be recorded separately with their spatial coordinates, which increases the complexity of matrix calculation. Another problem for the Cartesian Grid in DDM inversion is that, same size patches correspond to different resolutions of Delay-Doppler bins. For example, one patch might represent 1/5 bin size when it is close to specular point, but 1.5 bin size on the edge of reflection area. One possible solution for this problem is to increase the Cartesian Grid resolution of spatial energy map to suit for the Delay-Doppler bin resolution at the edge of reflection area. However, the inside area separating resolution is then too fine and become a waste in matrix calculation.

Based on the two problems stated above, we propose to use a Delay Contour Grid (DCG) to separate reflection area instead of the normal Cartesian Grid. In such a grid system, the reflection area is separated by Delay rings for each C/A code length, and each Delay ring is then divided into 360 patches, therefore 1° for each patch. By arranging iso-Delay patches in one column, the 2-D searching procedure for one Delay-Doppler bin can be simplified to 1-D searching, i.e., only looking for iso-Doppler patches in the same column as seen in Figure 5-11(b). The DCG separation also naturally solves the Delay resolution mismatch problem, which is introduced by the Cartesian grid.

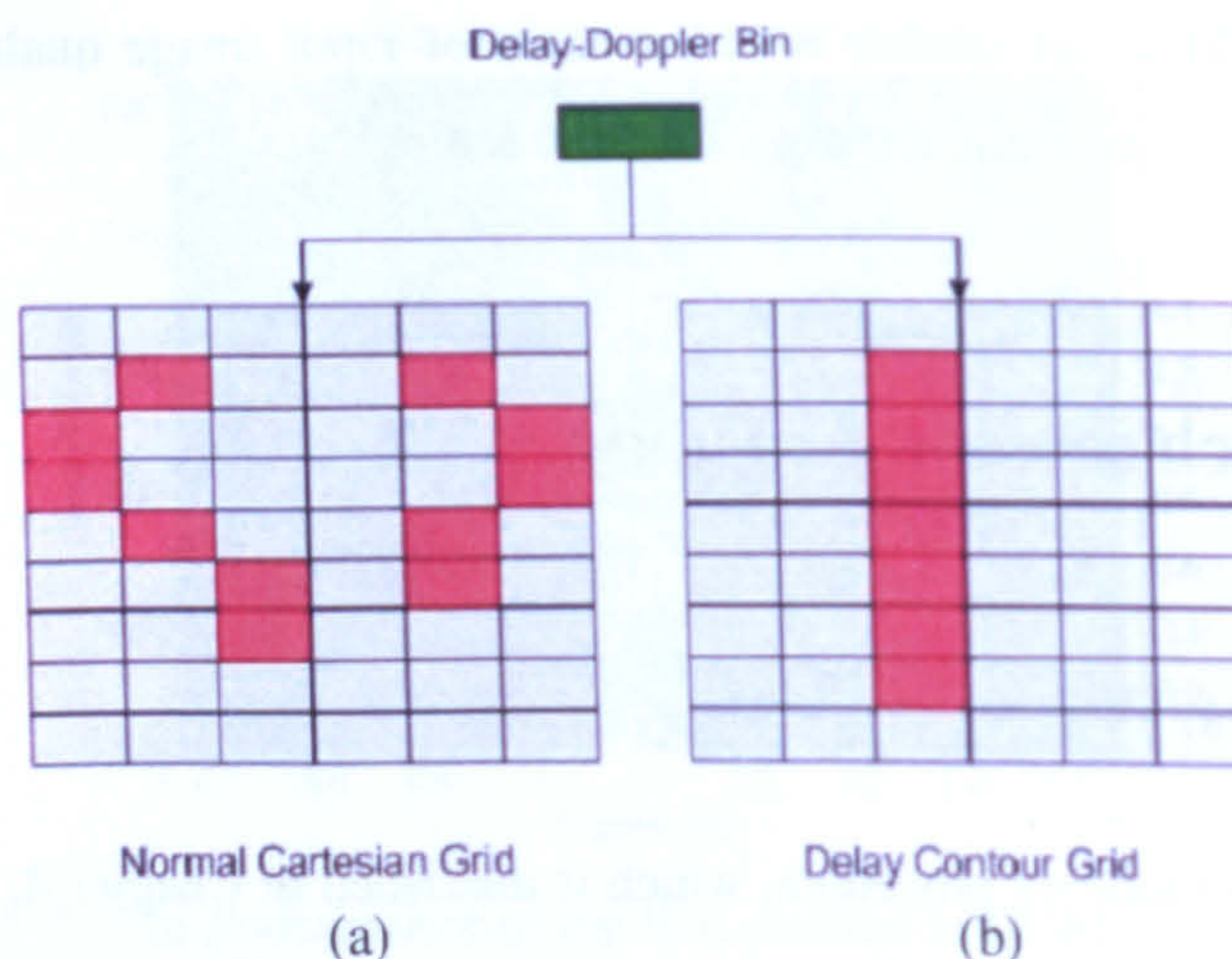


Figure 5-11: DCG simplifies the searching procedure in DDM inversion.

The Delay Contours Grid system is similar to a polar coordinate system. A detailed Delay Contours model, which gives the connection between Delay Contours and the spatial coordinates of patches, will be described in next section.

5.4.2 Delay Contour Grid model

Delay Contour Grid (DCG) is modelled in the local specular point frame (refer to Figure 4-6), where the y axis is aligned with satellite baseline and the z axis goes through the specular point. The GPS and UK-DMC coordinates are defined as $(0, p, s)$ and $(0, m, c)$, respectively, as seen in Figure 5-12.

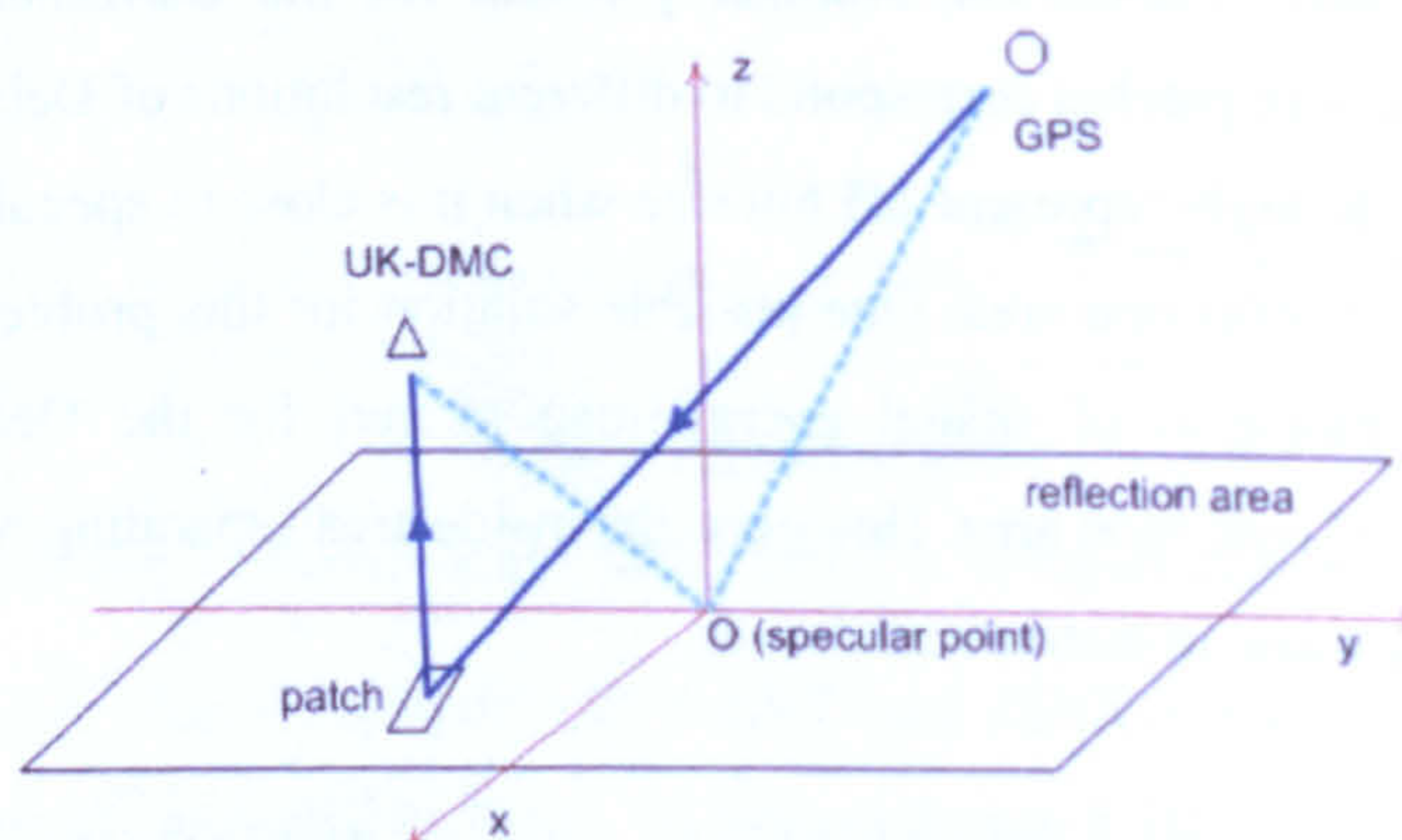


Figure 5-12: Delay Contour model geometry.

For a local patch at position $(x, y, 0)$, L is the reflection path length from GPS to the patch and then to UK-DMC. We aim to build an equation of variables x, y and constants p, s, m, c (satellite positions) with certain L . The reflection path length (Delay) L can be expressed as:

$$\sqrt{x^2 + (y - p)^2 + s^2} + \sqrt{x^2 + (y - m)^2 + c^2} = L \quad (5-18)$$

which is equivalent to

$$x^2 + y^2 - 2py + p^2 + s^2 = L^2 + x^2 + y^2 - 2my + m^2 + c^2 - 2L\sqrt{x^2 + (y-m)^2 + c^2} \quad (5-19)$$

If the reflection path length on two side is defined as $L_d^2 = m^2 + c^2$ and $L_g^2 = p^2 + s^2$, we will have

$$4L^2x^2 + 4L^2(y^2 - 2my + m^2) + 4L^2c^2 = [L^2 + 2(p-m)y + (L_d^2 - L_g^2)]^2 \quad (5-20)$$

i.e.,

$$4L^2x^2 + 4L^2y^2 - 8mL^2y + 4L^2(m^2 + c^2) = L^4 + 4(p-m)^2 + (L_d^2 - L_g^2)^2 + 2L^2(L_d^2 - L_g^2) + 4(p-m)L^2y + 4(p-m)(L_d^2 - L_g^2)y \quad (5-21)$$

i.e.,

$$4L^2x^2 + 4(L^2 - (p-m)^2)y^2 + [-4(p+m)L^2 - 4(p-m)(L_d^2 - L_g^2)]y = [L^2 + (L_d^2 - L_g^2)]^2 \quad (5-22)$$

To simplify Equ. (5-22), four new parameters are introduced in as

$$\begin{cases} w = 4L^2 \\ u = 4(L^2 - (p-m)^2) \\ v = (-8mL^2 - 4(p-m)(L^2 + L_d^2 - L_g^2)) \\ t = (L^2 + L_d^2 - L_g^2)^2 - 4L^2L_d^2 \end{cases} \quad (5-23)$$

Then Equ. (5-22) can be simplified as below:

$$wx^2 + uy^2 + vy = t \quad (5-24)$$

From Equ. (5-23) and the geometric definition in Figure 5-12, where $p > 0$ and $m < 0$, we can deduce that $w, u > 0$ and $v < 0$, then Equ. (5-24) shows an ellipse format as:

$$wx^2 + u\left(y + \frac{v}{2u}\right)^2 = t + \frac{v^2}{4u} \quad (5-25)$$

i.e.,

$$\frac{x^2}{\left(\frac{v^2}{4u} + t\right)/w} + \frac{\left(y + \frac{v}{2u}\right)^2}{\left(\frac{v^2}{4u} + t\right)/u} = 1 \quad (5-26)$$

Therefore, for a given reflection length (Delay) L , the iso-Delay patch positions can be expressed as:

$$\begin{cases} x = A \cdot \cos \alpha \\ y = B \cdot \sin \alpha - \frac{v}{2u} \end{cases} \quad (5-27)$$

The semi-major axis, semi-minor axis and centre of this Delay Contour ellipse are:

$$A = \sqrt{\frac{\frac{v^2}{4u} + t}{w}}, \quad B = \sqrt{\frac{\frac{v^2}{4u} + t}{u}}, \quad D = -\frac{v}{2u} \quad (5-28)$$

The shape of Delay Contour ellipses changes with L and the centre of the ellipses gradually shifts to the GPS side, along the y axis, with increasing L . The Delay contours on a spatial energy map are shown in Figure 5-13:

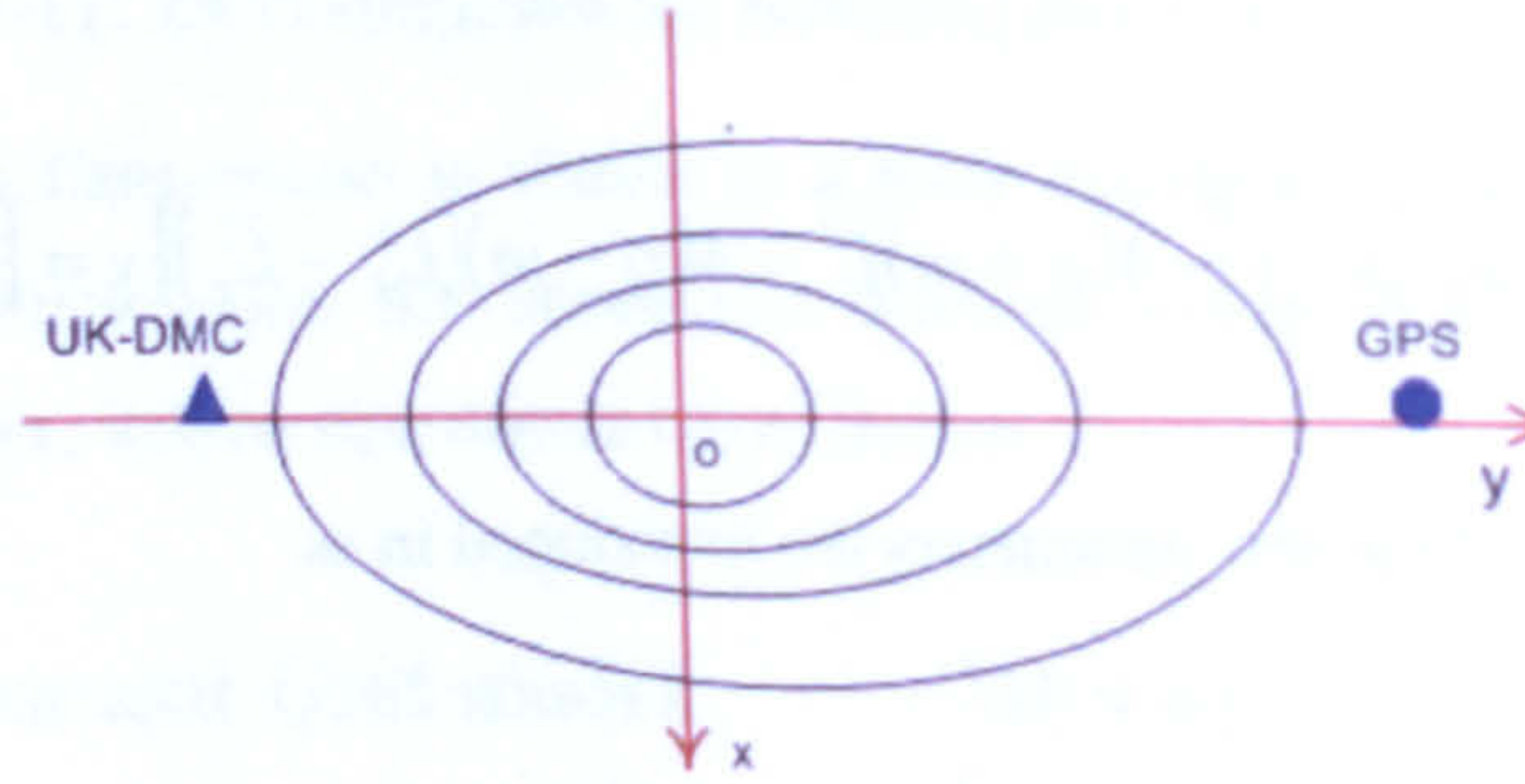


Figure 5-13: Delay contours in the specular point frame.

To estimate the ellipse centre shift, a typical set of geometry parameters from R12 scenario is used. By calculating a series of D value from Equ.(5-28), we find that the maximum ellipse centre shift between adjacent contours is about 1.7 m. Currently the received UK-DMC DDMs have around 100 C/A codes on the Delay axis, its corresponding spatial map should contain about 100 Delay contours. Therefore the most outside contour ellipse should have a centre shift less than 200m when compared to the central contour. Since reflection area is of tens of km^2 , the ellipse centre shifts are comparatively ignorable. Under such condition, if dividing the n^{th} Delay ring averagely into 360 patches, the patch area can be estimated as

$$ds = \frac{1}{2} \cdot 2\pi \cdot (A_{n+1}B_{n+1} - A_nB_n) / 360 \quad (5-29)$$

The patch position (Equ.(5-27)) and patch area estimate (Equ.(5-29)) are the essential parameters that we apply in the DDM inversion procedure.

The Delay Contour Grid system has another off-shot advantage. According to our previous DDM simulation study (refer to Appen.I, spatial energy map simulations), patches within one Delay contour have similar slopes and probability values. This is an important fact we will use to simplify DDM inversing procedure in Chapter 6.

5.5 Conclusions

The DDM simulation experiments in Chapter 4 reveals that the current GPS-R scatterometric model is not sensitive to wind information in medium and high wind speed range. Such problem motivates our DDM inversion research. This chapter proposes a detailed DDM inversion scheme and its validation approach. Furthermore it discusses the technical details of first two steps in the inversion procedure: deconvolution and spatial patch searching method.

For DDM deconvolution, we test the noise robustness of several deconvolution algorithms, in the context of DDM inversion, with different noise levels. The Fourier-Wavelet hybrid ForWaRD method has been proven to have better overall performance, in DDM deconvolution, than the Fourier-based algorithms (Wiener and Least-square) and Bayer-based algorithm (Richardson-Lucy). Therefore the ForWaRD algorithm is chosen for our DDM inversion scheme.

When trying to convert a DDM into spatial energy map, we propose the Delay Contour Grid method, instead of the Cartesian grid, to separate reflection area. The main advantages of DCG are:

- 1) Each column of spatial patch matrix represents the patches with same Delay. This reduces the Bin-to-Patch searching dimension from 2 to 1.
- 2) The resolutions of patches corresponding to each Delay Contour are unified. This reduces the complexity in matrix calculation.
- 3) The patches within one Delay Contour have similar slopes and probability values. This simplifies our future DDM inversion algorithm.

Next chapter will focus on converting deconvolved DDM bins into spatial patches via three different methods. Simulated and real UK-DMC DDMs will be inversed to evaluate those methodologies.

References

- [Bertero 2000] M. Bertero and P. Boccacci, Image Restoration Methods for the Large Binocular Telescope (LBT), *Astronomy and Astrophysics*, Vol.147, pp.323-332, September 2000, <http://www.disi.unige.it/person/BerteroM/papers-PDF/OSEM-2.pdf>
- [Borman 2004] S. Borman, The Expectation maximization Algorithm : A Short Tutorial, online tutorial, http://www.seanborman.com/publications/EM_algorithm.pdf, July 2004
- [Brooks 2003] Alan Brooks, Image Restoration codes in MATLAB, Northwestern University, March 2003, http://dailyburrito.com/m-files/ee420cmpAss1_v2.m
- [Cornwell 1996] T. Cornwell and A. Bridle, Deconvolution Tutorial, online source, National Radio Astronomy Observatory, <http://www.cv.nrao.edu/~abridle/deconvol/deconvol.html>, November 1996
- [Daubechies 1988] I. Daubechies, Ten Lectures on Wavelets, Cambridge University Press, July 1992, ISBN 0-8987-1274-2
- [Gleason 2006] S. Gleason, Remote Sensing of Ocean, Ice and Land Surfaces Using Bistatically Scattered GNSS Signals From Low Earth Orbit, PhD Thesis, Surrey Space Centre, University of Surrey, UK, December 2006
- [Gonzalez 2004] R. Gonzalez, R. Woods and S. Eddins, Digital Image Processing Using Matlab, Prentice Hall, February 2004, ISBN 0-1300-8519-7
- [Graps 1995] Amara Graps, An Introduction to Wavelets, IEEE Computational Science and Engineering, Vol.2, No.2, 1995, <http://www.amara.com/ftpstuff/IEEEwavelet.pdf>
- [Hanisch 1996] R. Hanisch, R. White and R. Gilliland, Deconvolution of Hubble Space Telescope Images and Spectra, *Deconvolution of Images and Spectra*, 2nd Edition, pp. 310-360, Academic Press Inc., U.S., September 1996
- [Haar 1910] A. Haar, Zur Theorie der orthogonalen Funktionensysteme, *Mathematische Annalen*, Vol.69, pp.331-371, 1910
- [Jalobeanu 2000] A. Jalobeanu, L. Blanc-Feraud, J. Zerubia, Satellite Image Deconvolution Using Complex Wavelet Packets, in *Proceedings of International Conference on Image Processing*, Vol.3, pp. 809-812, <http://ieeexplore.ieee.org/iel5/7221/19455/00899579.pdf>, September 2000,
- [Jansson 1996] P. Jansson (editor), *Deconvolution of Images and Spectra*, 2nd Edition, Academic Press, California, September 1996, ISBN 0-123-8-02229

- [Lucy 1974] L.B. Lucy, An Iterative Technique for the Rectification of Observed Distributions, *Astronomical Journal*, Vol.79, pp.745-757, June 1974
- [Mallat 1999] S. Mallat, A. Wavelet Tour of Signal Processing, Academic Press, 2nd Edition, September 1999, ISBN 0-1246-6606-X
- [Neelamani 2004] R. Neelamani, H. Choi and Ri. Baraniuk, ForWaRD: Fourier-Wavelet Regularized Deconvolution for Ill-Conditioned Systems, *IEEE Transactions on Signal Processing*, Vol.52, No.2, <http://www.dsp.rice.edu/publications/pub/neelshdecon.pdf>, February 2004. (open-source code : <http://dsp.rice.edu/software/ward.shtml>)
- [Proakis 1995] J.G. Proakis and D.K. Manolakis, *Digital Signal Processing: Principles and Algorithms and Applications*, 3rd Edition, Prentice hall, October 1995, ISBN 0-133-9-42899
- [Rao 1998] R.M. Rao and A.S. Bopardikar, *Wavelet Transforms: Introduction to Theory and Applications*, Prentice Hall, October 1998, ISBN 0-2016-3464-5
- [Starck 2002] J.L. Starck, E. Pantin and F. Murtagh, *Deconvolution in Astronomy: A Review*, *Publications of the Astronomical Society of the Pacific*, Vol.114, pp. 1051-1069, Oct. 2002, <http://www.journals.uchicago.edu/PASP/journal/issues/v114n800/202112/202112.web.pdf>
- [Tiebaut 2004] E. Tiebaut, Laurent Mugnier, *Convolution and Blind Deconvolution in Astronomy*, 2004, <http://jstarck.free.fr/Blind07.pdf>
- [Torrence 1997] C. Torrence and G.P. Compo, A Practical Guide to Wavelet Analysis, *Bulletin of the American Meteorological Society*, Vol. 79, No. 1, January 1997, http://atoc.colorado.edu/research/wavelets/bams_79_01_0061.pdf
- [Weisstein 2003a] E.W. Weisstein, Convolution, MathWorld – A Wolfram Web Resource, 2003, <http://mathworld.wolfram.com/Convolution.html>
- [Weisstein 2003b] E.W. Weisstein, Convolution Theorem, MathWorld – A Wolfram Web Resource, 2003, <http://mathworld.wolfram.com/ConvolutionTheorem.html>
- [Wiki 2008] “Tikhonov regularisation”, http://en.wikipedia.org/wiki/Tikhonov_regularization Wikipedia website, February 2008
- [Young 1998] I.T. Young, J.J. Gerbrands and L.J. van Vliet, *Fundamentals of Image Processing*, <http://www.qi.tnw.tudelft.nl/~lucas/education/et4085/sheets/ppt/FIP2.2.pdf>, Delft University of Technology, 1998

Chapter 6. DDM Inversion: From Bin to Patches

6.1 Overview

Chapter 5 introduces the structure of DDM inversion scheme, as seen in Figure 5-1 and Figure 5-2. After using the ForWaRD algorithm to remove the effect of GPS Ambiguity Function from DDM, we will convert the DDM into a spatial energy distribution map, from which we can derive the wave slope statistical parameters.

As a review of the DDM simulation procedure, the reflection power equation of patches is re-written here, in a simpler format of three factors as in Equ. (3-47).

$$P_r = S \cdot Q \cdot T \quad (6-1)$$

where

- P_r is the reflected energy of a small patch on reflection area.
- S is the slope probability value derived from a wave spectrum model. While the Cox-Munk model describes slope PDF as a Gram-Charlier distribution, the Elfouhaily model assumes that slope PDF is a bi-variate Gaussian distribution, which is related to wind speed, direction and observing incident angle.
- Q represents the geometry-related factors, such as reflection path length and antenna gain.
- T is the constant part, which includes not only the constant factors in radar equation, but also all other constant parameters from receiver hardware or data processing procedure.

For each patch, if its reflection energy P_r is known, its slope probability value S can be extracted from Equ.(6-1) by removing the geometry factor Q . Combining this inversion technique with data filtering method, it is possible to derive an empirical wave slope statistical model for GPS-R space-borne ocean applications.

When creating a DDM from a spatial energy map, the reflected energy of several spatial patches, which have same Delay and Doppler properties, is summed up to one Delay-Doppler bin.

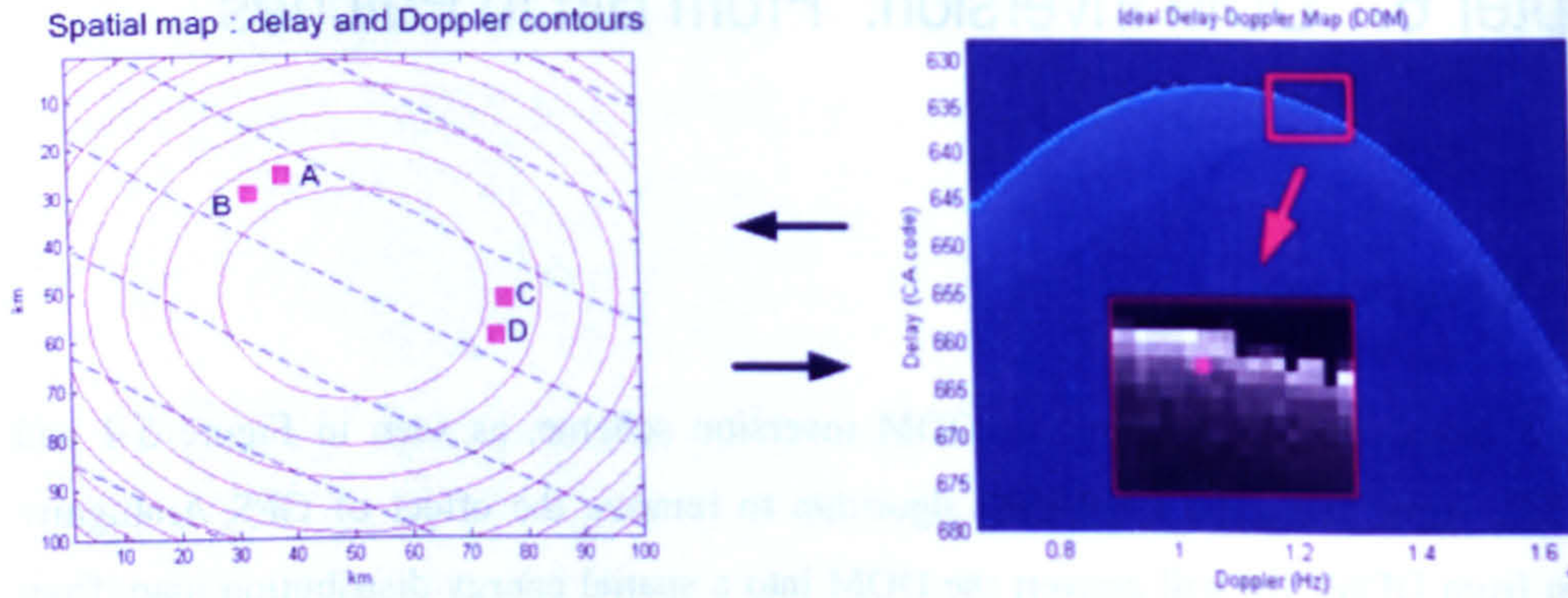


Figure 6-1: Spatial patches to Delay-Doppler bin.

Figure 6-1 shows a visual example of Delay-Doppler bin generation. The bin power (the pink square in the DDM) can be expressed as the totality of four spatial patches (A , B , C and D), within the same Delay ring and same Doppler range, as below:

$$P_b = T \cdot (S_A Q_A + S_B Q_B + S_C Q_C + S_D Q_D) \quad (6-2)$$

A vital step in DDM inversion processing is to assign the energy from one Delay-Doppler bin back to its corresponding patches, such patches have same Delay and Doppler attributes but probably different reflection power. The energy proportion that each patch contributes to a bin remains unknown. Without extra information and assumptions, this Bin-to-Patch inversion has ambiguity and can not be solved directly. Instead of solving the patch ambiguity and getting an analytical solution of slope statistical parameters, it is still possible to estimate wave slope probability distributions from processed DDMs. The estimation method is based on certain assumptions, which can be verified and corrected to adapt realistic situations with more real data and thorough understanding of GPS-R.

Three methods are proposed in this chapter to estimate spatial energy distributions and wave slope probabilities. They are all based on the bi-static radar equation from the Z-V model (refer to section 3.4.1) and the NRCS calculation (refer to section 3.4.2). The first method averages bin power into corresponding patches, therefore it is called the “Average Method”. The second method uses two adjacent bin power as the input and employs differentiation to solve the inversion ambiguity, as such it is called the “Differential Method”. Both methods aim to take full advantage of DDM information and obtain 2-D spatial maps. The third method sacrifices the information in Doppler dimension and outputs a 1-D slope probability distribution curve. Therefore it is named the “1-D Method” in our context. To validate these

methods, inversed spatial energy maps and slope probability maps under different noise conditions are compared to the original simulated inputs. Different methods have different levels of ambiguity and different performance against noise. The advantages and limitations of these methods are discussed alongside the presentation of inversion results.

After we have the first reasonable estimate of an empirical slope PDF, the initial estimate can be feedback into the inversing procedure again (Figure 5-2). This iteration processing is possible to remove more patch ambiguity in spatial energy map and obtain more accurate slope probability distributions. Filtering techniques, such as the Kalman Filter, might be a potential method to design this kind of iteration when GPS-R real DDMs are routinely processed and archived. This part of the work is not included in this research and will be discussed in the future work section.

6.2 The Average Method

6.2.1 Methodology

According to our previous DDM simulation experience, it is reasonable to assume that all patches, with same Delay and Doppler attributes, also have the same reflection power. As such we can average the power of one Delay-Doppler bin into its corresponding patches, then remove the geometric factor Q in each patch power and obtain the slope probability value (S) with the constant (T). The power relationship between a bin and one of its n patches is:

$$P_r = P_b / n \quad (6-3)$$

The slope probability for patch N is:

$$S_N = \frac{P_b}{n \cdot T \cdot Q_N} \quad (6-4)$$

According to the discussion on the Delay Contour Grid model (section 5.4.2), Delay contours can be seen as zero-centred ellipses. Due to the pattern of Delay-Doppler contours in DDMs as seen in Figure 6-1, the patches with same Delay and Doppler attributes, are normally separated into two groups (A, B and C, D). They are along the Doppler contour direction and roughly symmetric against the vertical direction of Doppler contours. Therefore, the inversed energy map from this method is also symmetric against the vertical direction of the Doppler Contours and can not represent the whole spatial energy distribution. When original spatial map has a smooth distribution, the symmetry in inversion result does not have a great effect. If sharp edge or singularities exist in original spatial map, however, the symmetric

inversion result is not trustworthy. The next section will present results of simulated DDM inversions via this Average Method.

6.2.2 Synthetic DDM inversion

Without Noise

The Average Method is initially applied in a noise-free DDM inversion test. The R12 scenario is again chosen for this experiment. The main purpose of this test is to validate the feasibility of whole DDM inversion scheme.

First of all an original slope probability map and a spatial reflection energy map are created according to the wind condition and reflection geometry of R12. A DDM, generated from the spatial energy map, is then convolved with the square of GPS AF. Without noise added in, the AF-blurred DDM is then deconvolved and inversed back to a spatial energy map. By removing geometric factors, an inversed slope probability map with constant T can be obtained. The constant T is removed by calibrating the peak values of the original and inversed slope probability distribution. These two probability maps are plotted against each other, as we discussed before in section 4.3. The linearisation level of point-to-point matching represents the correlation level of these two maps and the quality of the inversion scheme.

Figure 6-2 below shows the result of our first noise-free DDM inversion experiment. The left column represents the R12 DDM simulation procedure and the right column illustrates the DDM inversion procedure. The DDM simulation on the left column is based on the Gaussian wave slope PDF assumption, as shown in the simulated slope probability map (Figure 6-2 (a)). The ForWaRD algorithm is used to deconvolve the GPS AF effect from AF-blurred DDM as mentioned in section 5.3, and Delay Contour Grid, as discussed in section 5.4, is applied in the spatial patch searching step. The inversed slope probability map (Figure 6-2 (e)) has two empty areas on two sides of the image, which is due to the cut-off Doppler frequencies on two ends of the R12 DDM (Figure 6-2 (c)).

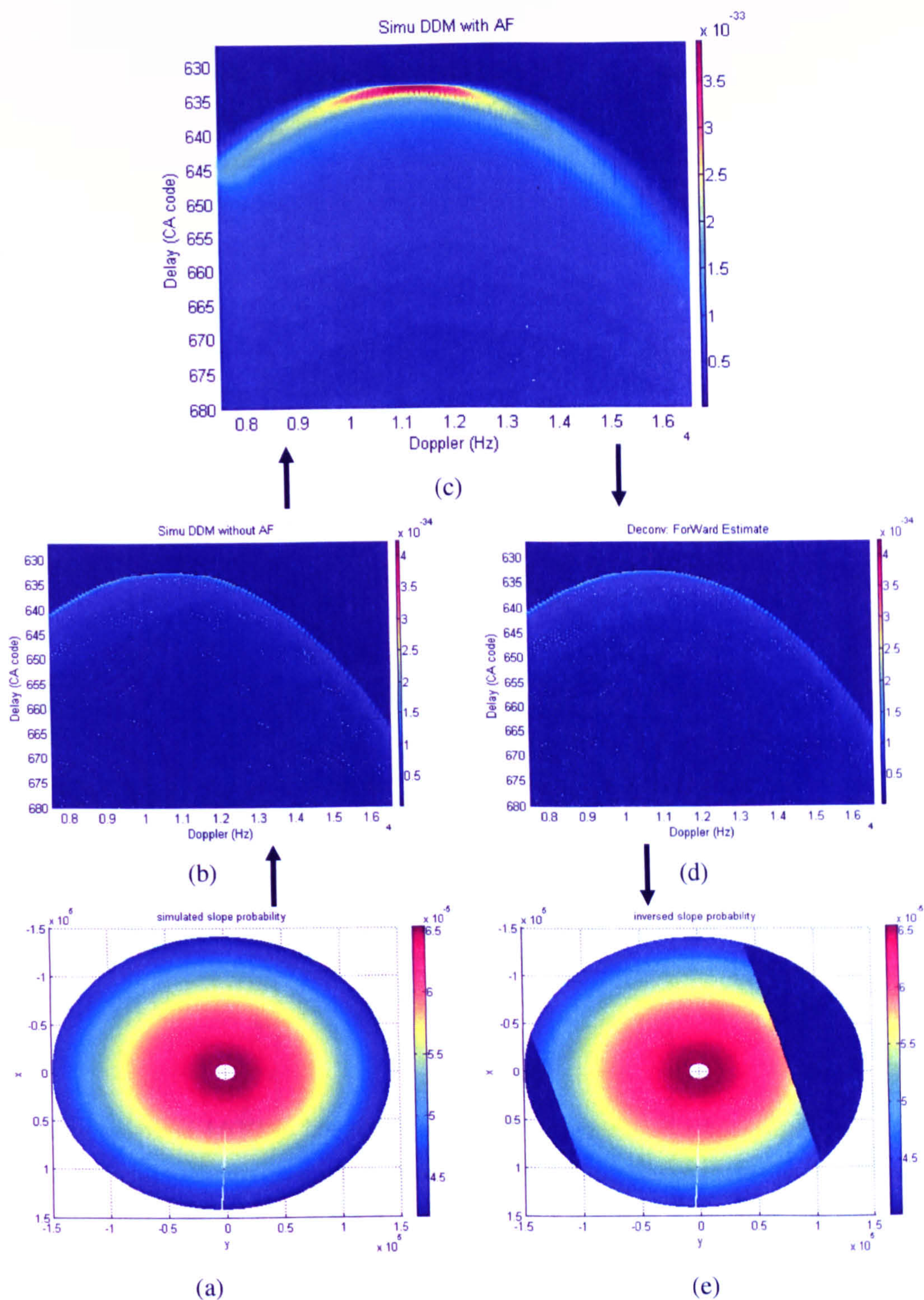


Figure 6-2: Inversion experiment of simulated noise-free R12 DDM.

(a) slope probability map. (b) clear DDM. (c) AF-blurred DDM.

(d) deconvolved DDM. (e) inversed slope probability map.

By correlating the original (a) and inversed probability map (e), we find that even with patch ambiguity from the Average Method, the point-to-point match still shows a clear linearisation feature, as seen in Figure 6-3. The matching points along the x axis are due to the correlations

between the empty areas of the inversed slope probability map and their corresponding non-zero points on the original map. The matching result suggests that the iso-patch-power assumption for the Average Method is valid under current geometric modelling technique, and patch ambiguity has minor effect in this simulated noise-free experiment. The exact spatial energy distribution map can not be obtained from the DDM inversion procedure, due to the symmetry along the Doppler Contour direction. However, we can still have an initial estimate of how slope probability changes with patch positions.

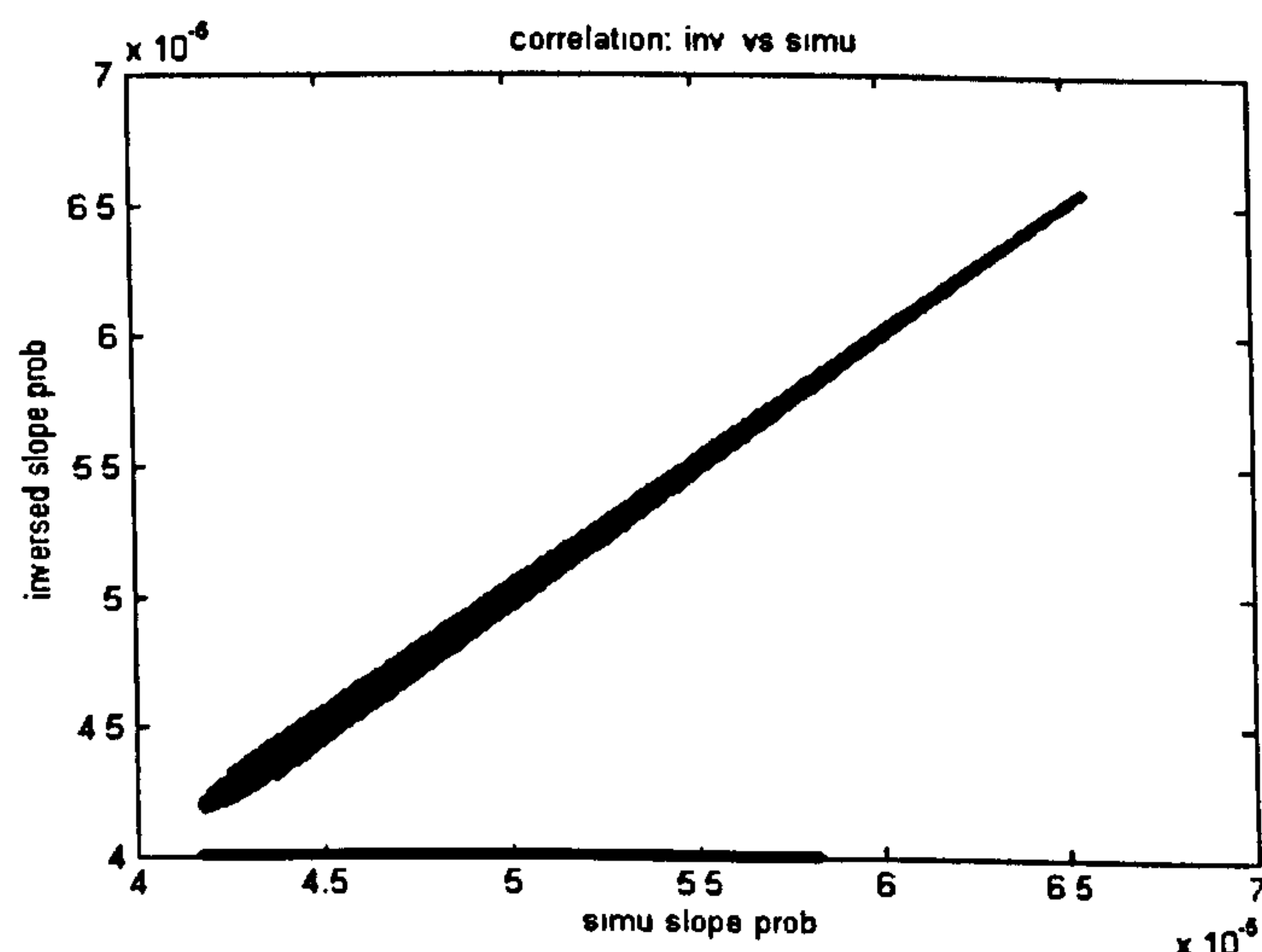


Figure 6-3: Point-to-point matching between original and inversed slope probability map from the simulated inversion test of noise-free R12 DDM.

This noise-free inversion simulation is too ideal for real noisy GPS-R cases. However, the clear linear matching result of this initial test gives us some confidence in the DDM inversion scheme.

With Noise

This section continues the discussion on the Average Method in DDM inversion scheme. Different levels of noise are added to an AF-blurred DDM, for the purpose of robustness test for this inversion method.

From the discussion of deconvolution algorithms in Chapter 5, we have observed that, when simulated DDM has low *BSNR*, deconvolution algorithms have unsatisfactory performances (Figure 5-7 and Figure 5-10). The deconvolution quality plays a significant roll in spatial energy map inversing. Figure 6-4 below portrays the Average Method inversion experiment of a simulated noisy R12 DDM.

BSNR = 150 dB

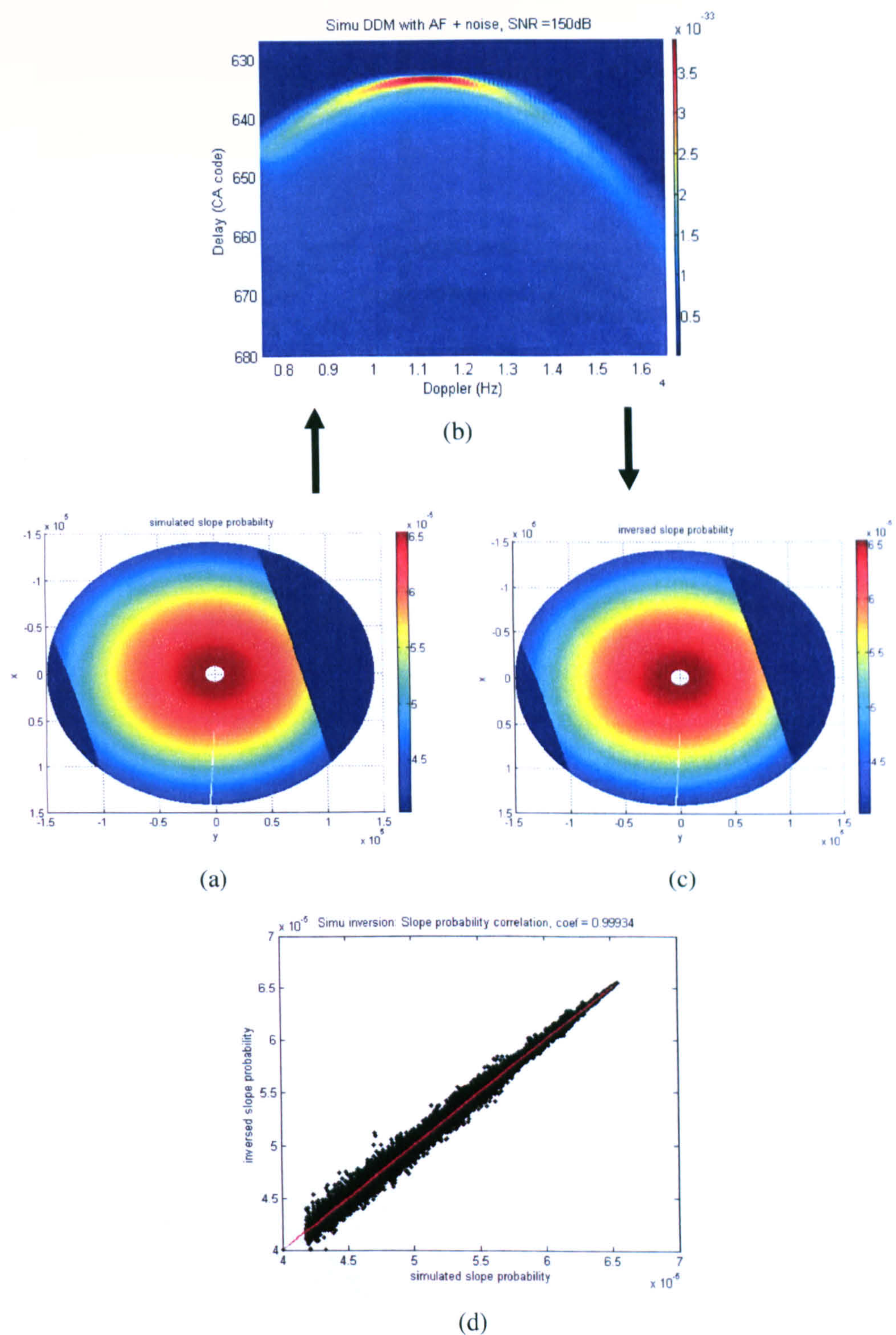


Figure 6-4: Inversion experiment of a simulated noisy DDM via the Average Method.
(a) simulated slope probability. (b) AF-blurred noisy DDM. (c) inversed slope probability.
(d) correlation of two slope probability maps.

The red line in Figure 6-4 (d) is the data fitting line, which ideally should have a gradient of 1 and zero offset. Two sets of parameters are used to evaluate the correlation result under noise.

One is the Correlation Coefficient (CC), indicating the deviation of data points. Another set includes two data, representing the gradient and offset of the correlation line, as $p = [\text{gradient}, \text{offset}]$. When $\text{BSNR} = 150 \text{ dB}$, the matching result of above case shows that $\text{CC} = 0.99934$ and $p = [0.9997, 0]$. The fitting points have a good linearization pattern, with a gradient close to 1 and zero offset.

When stronger noise is added to the simulated DDM, the linearization and data deviation of fitted lines start to get worse, as shown in the figures below:

BSNR = 120 dB

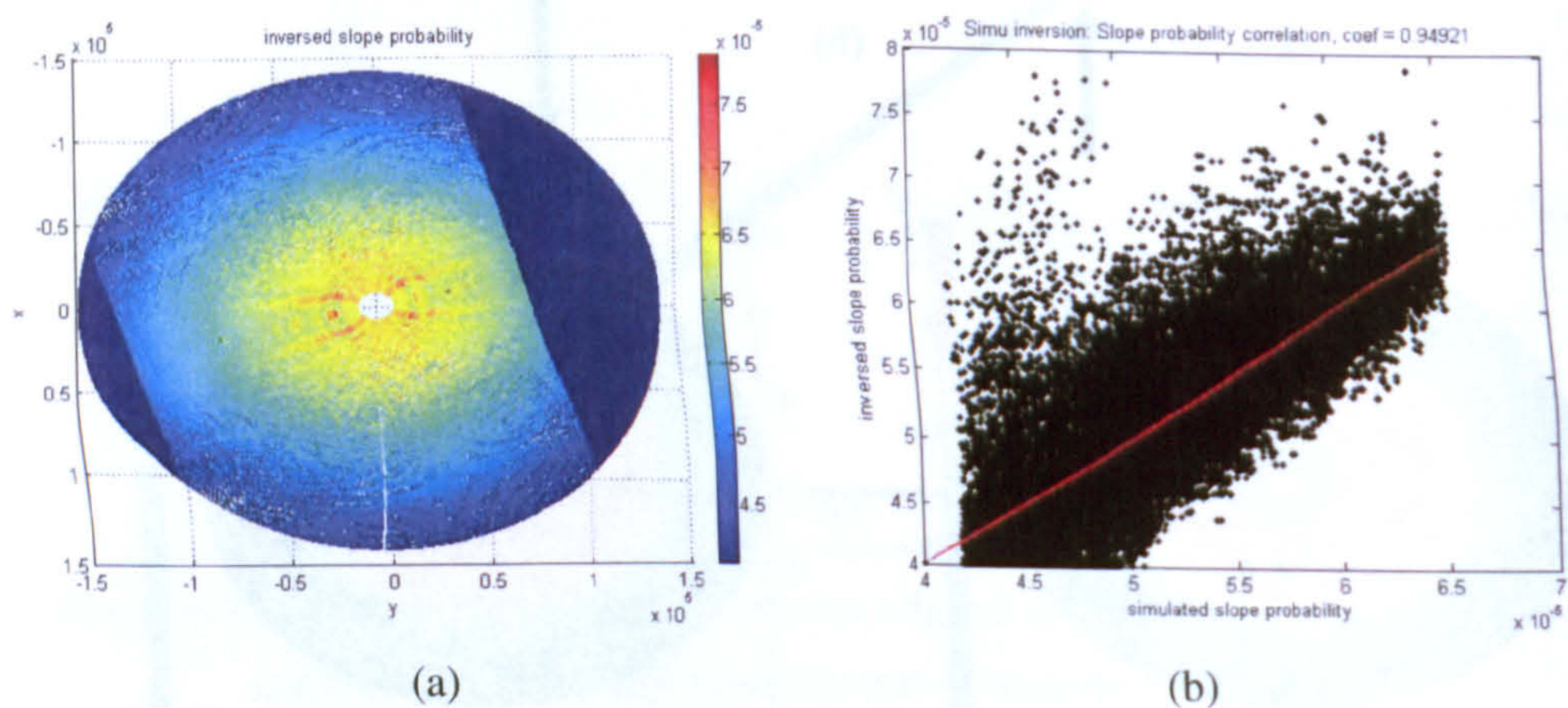


Figure 6-5: Inversion experiment of simulated 120 dB BSNR DDM. (a) inversed probability map. (b) point-to-point matching result $\text{CC} = 0.94921$, $p = [0.9943, 0]$.

BSNR = 100 dB

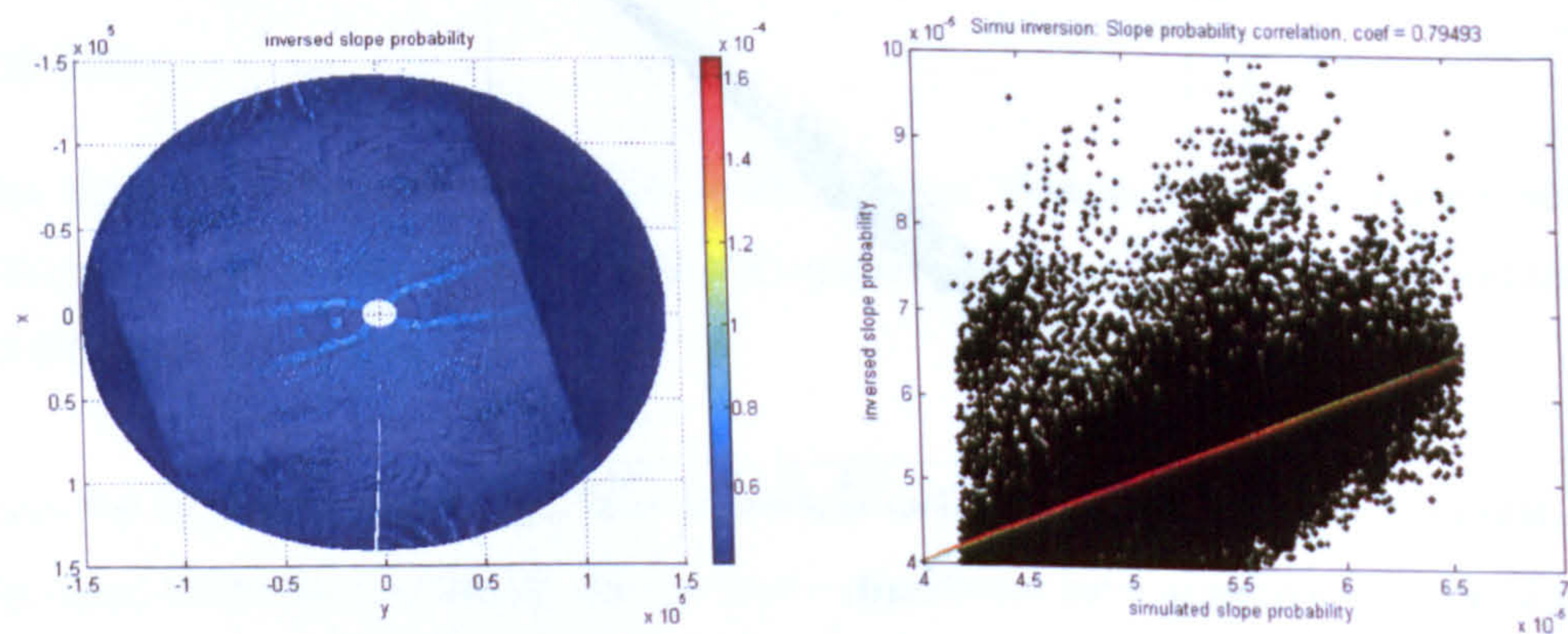


Figure 6-6: Inversion experiment of simulated 100 dB BSNR DDM. (a) inversed probability map. (b) point-to-point matching result $\text{CC} = 0.79493$, $p = [0.9715, 0]$.

BSNR = 60 dB

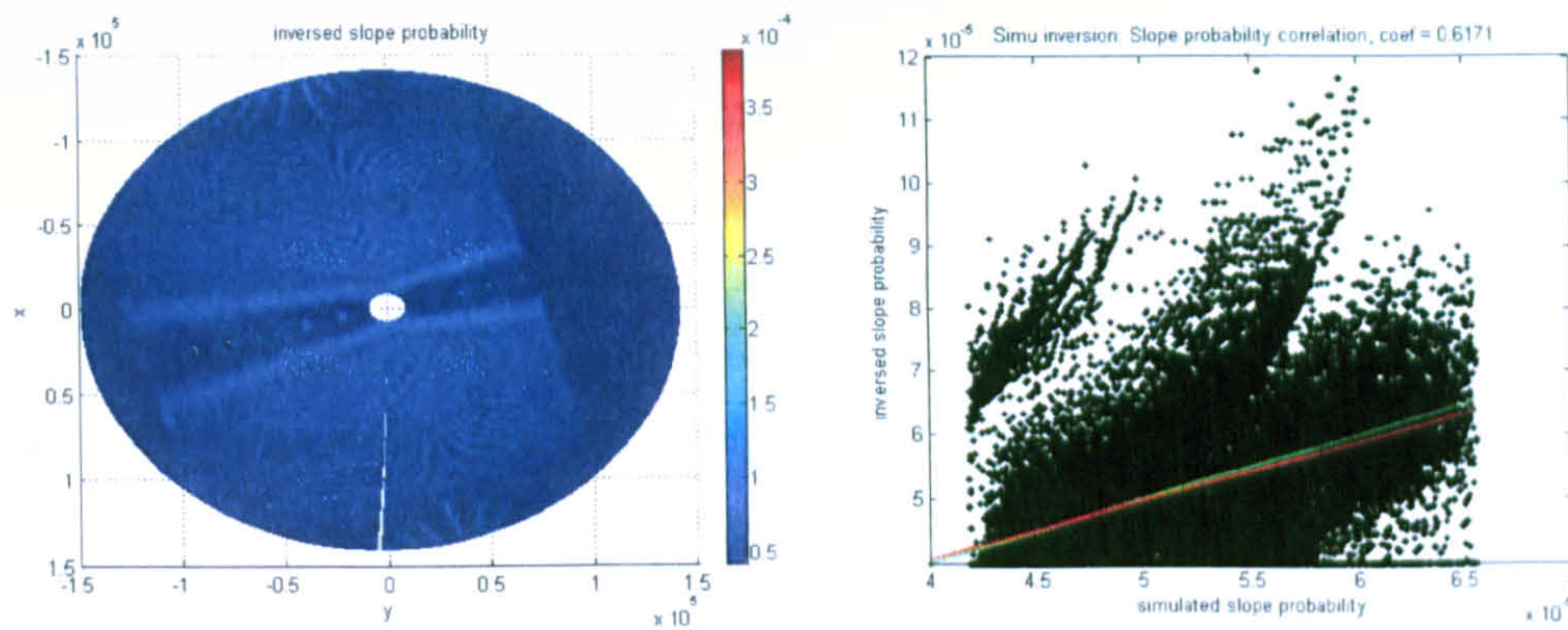


Figure 6-7: Inversion experiment of simulated 60 dB BSNR DDM. (a) inversed probability map. (b) point-to-point matching result $CC = 0.6171$, $p = [0.9093, 0]$.

BSNR = 20 dB

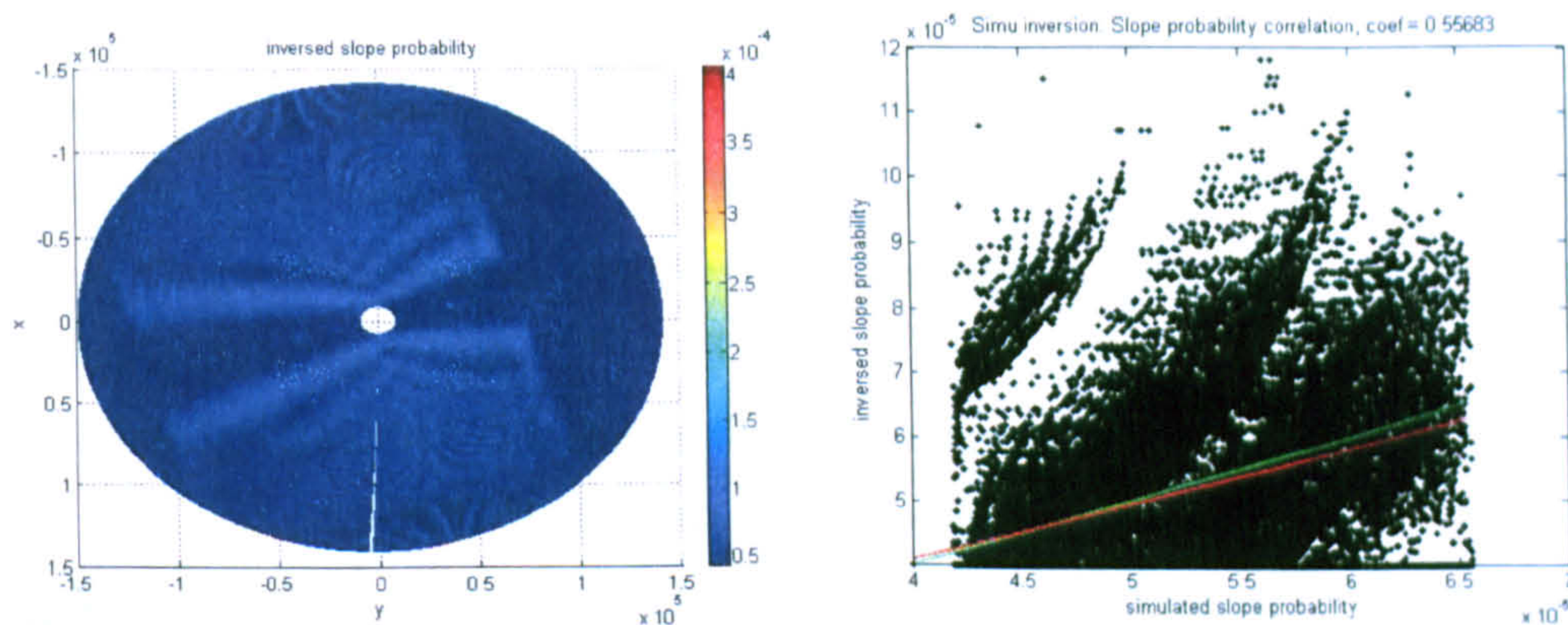


Figure 6-8: Inversion experiment of simulated 20 dB BSNR DDM. (a) inversed probability map. (b) point-to-point matching result $CC = 0.55683$, $p = [0.8702, 0]$.

As seen in the above results, the quality of inversed slope probability maps seems decreasing quickly with increasing noise. However, when looking at the correlation lines on point-to-point matching figures, we find that the inversed probability maps actually correlate well with the original assumed probability maps under different noise conditions. This feature suggests that, with more noise in DDM, though more singularities will appear in the inversed result, the majority of the inversed points are still valid and represent a good estimation of the original slope probability map. This valid point pattern cannot be seen in Figure 6-5 (a) to Figure 6-8 (a) due to the scaling problem in MATLAB plotting, and is hidden under scattered singularities in point-to-point correlation maps (Figure 6-5 (b) to Figure 6-8 (b)). However, the good correlation fitting results reveal the high density of valid points.

There are two possible solutions to remove singularities, or “outliners”, from the inversed results. One is to change the normalisation method. Instead of normalising both DDMs (real

data and simulation) to their peak value, we can normalise them to some controlled level, such as the mean 3σ standard deviation of the data. The other solution is to apply some outlier removing algorithm on DDM inversion result, such as RANSAC (Figure 6-9). RANSAC stands for RANdom SAMple Consensus algorithm, which is an iterative method to remove outliers and help to estimate parameters of a mathematical model more accurately [Fischler 1981][Fisher 2002]. This algorithm has been proven efficient in different data processing areas, such as computer vision [Konouchine 2005] and astrodynamics [Kojima 2007], and should be beneficial for our DDM inversion study in the future.

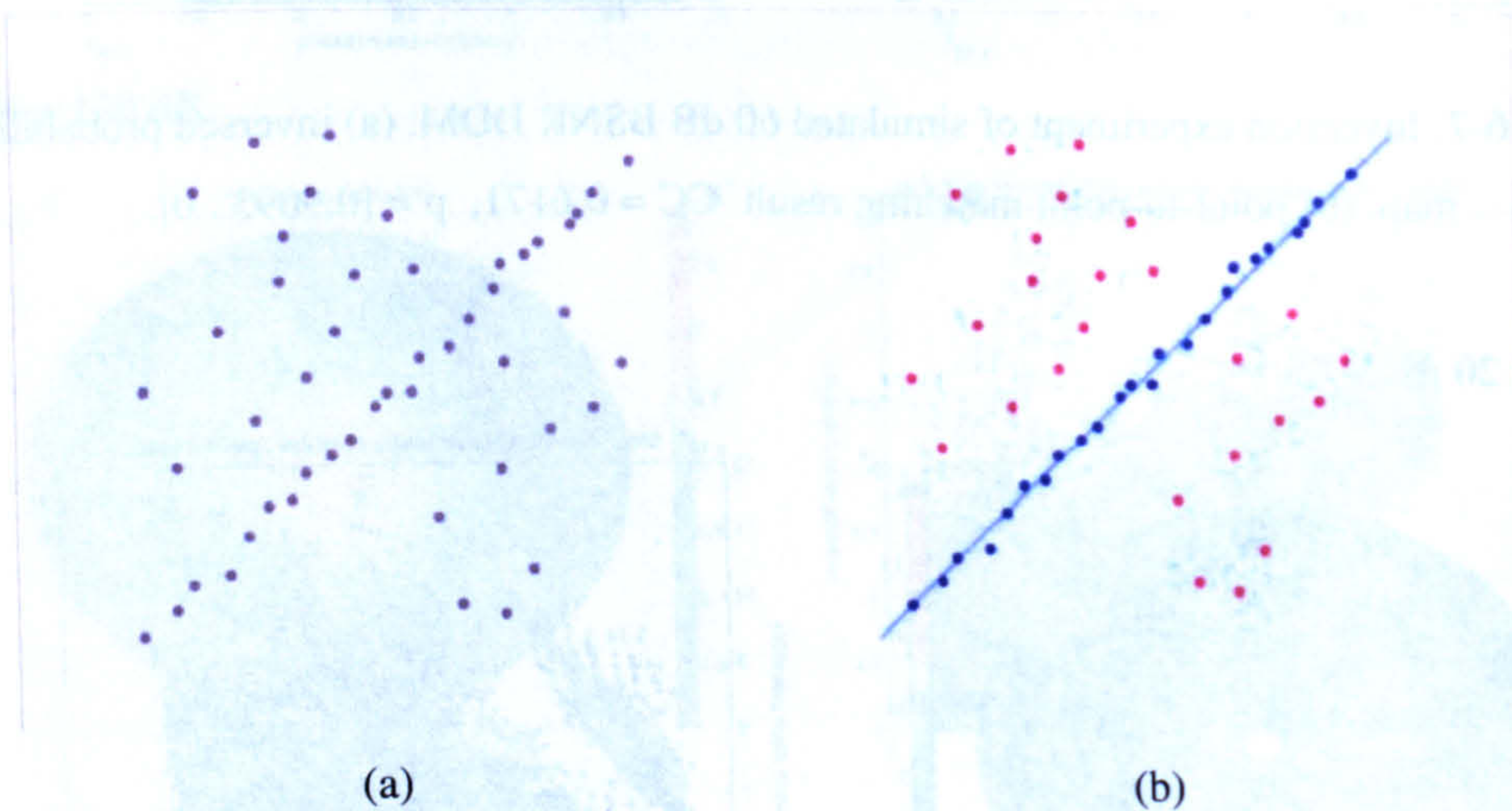


Figure 6-9: (a) a dataset with many outliers. (b) Fitted line with RANSAC algorithm, outliers have no influence on the result.[Wiki 2008]

This section only presents the test results of simulated noisy DDMs via the Average Method. The real UK-DMC DDMs, which are under heavy noise and lack of verification knowledge, are not considered for the Average Method test at the moment.

6.3 The Differential Method

The Differential Method uses two or more Delay-Doppler bins to calculate the energy of their corresponding spatial patches. This method takes advantage of adjacent bins' information from DDM and is supposed to have better noise robustness than the Average Method.

6.3.1 Two-bin Differential Method

The two-bin Differential Method aims to estimate a 2-D slope probability distribution by inputting two bins' information into the inversion procedure each time, instead of one bin each time as in the Average Method. To explain the principles of this method, a 2-D

probability estimation can be seen as an extension of a 1-D case, which is presented below in Figure 6-10:

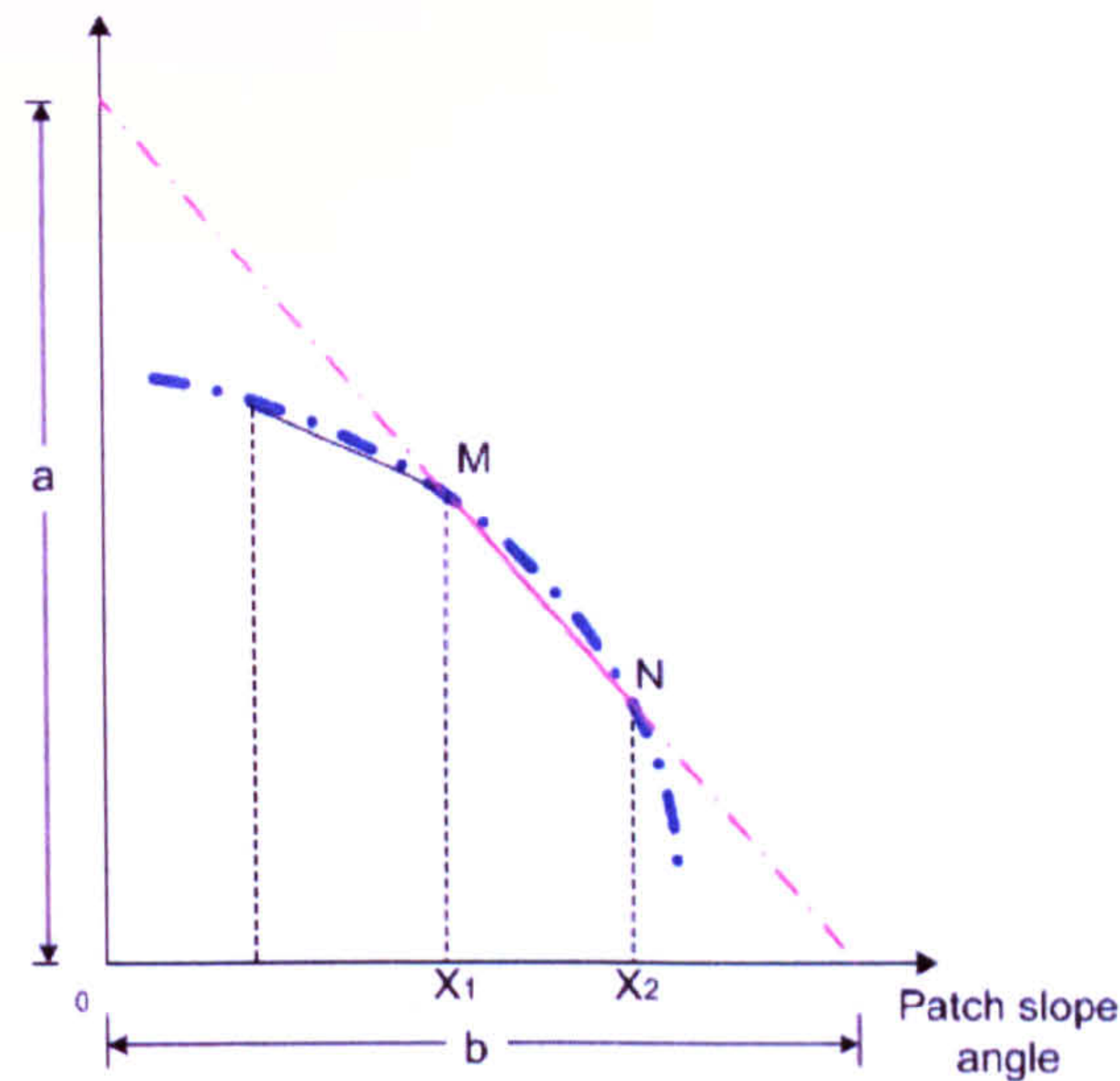
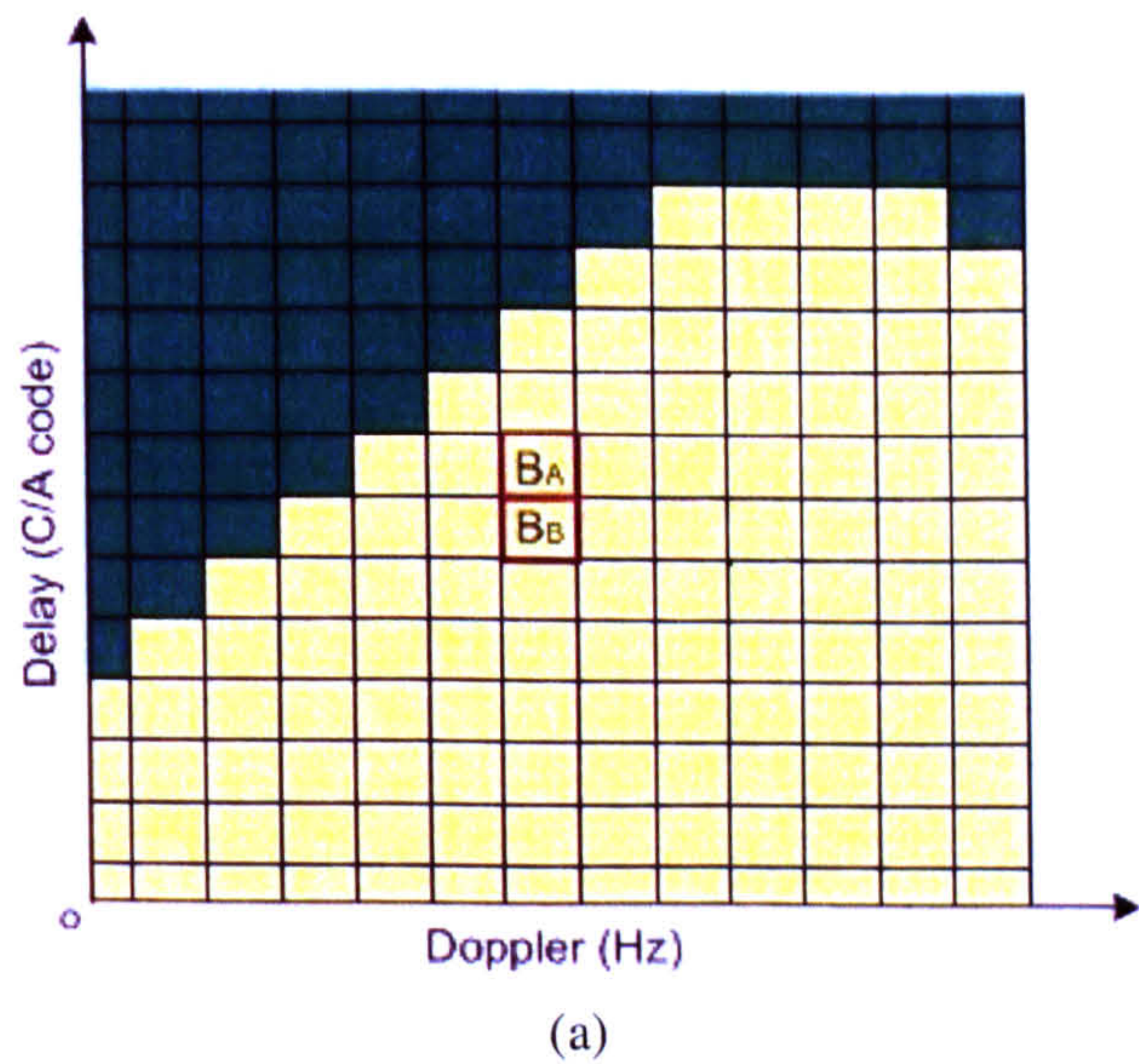


Figure 6-10: Estimation of 2-D slope probability curve.

If a probability distribution curve (blue line) is divided into small sections, a series of straight lines can be used to estimate the probability curve. Each small section, such as MN in Figure 6-10, is elongated to intercept with two axes. Then two lengths a and b can be used to express this MN line:

$$\frac{x}{b} + \frac{y}{a} = 1 \text{ , i.e., } y = -\frac{a}{b}x + a \tag{6-5}$$

As shown in Figure 6-11(a), two adjacent bins are along the Delay dimension, where bin B has longer Delay time than bin A.



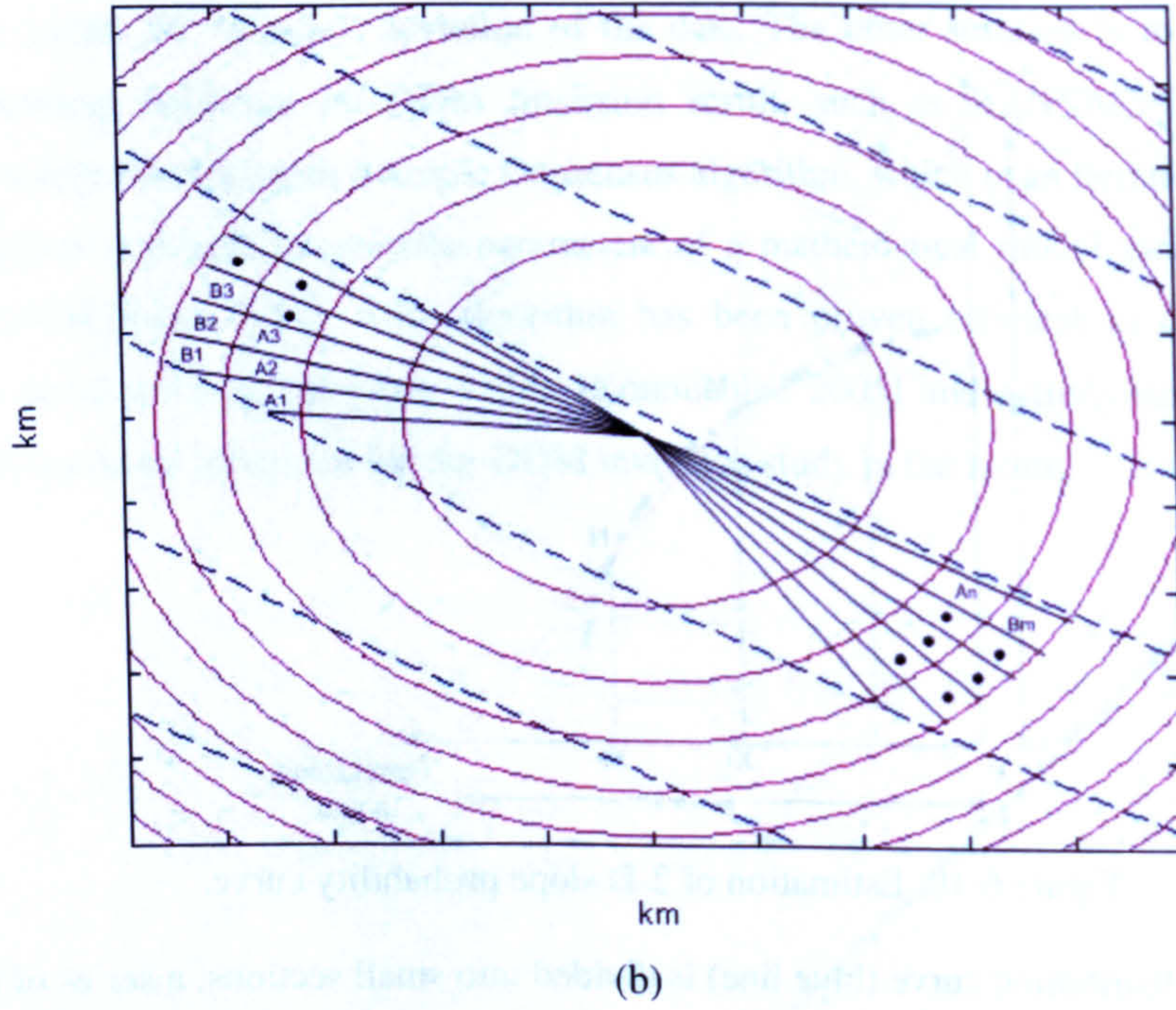


Figure 6-11: Adjacent bins on DDM (a) and their corresponding patches in spatial map (b).

In our Delay Contour Grid frame, bin A corresponds to patch $A_1, A_2, A_3, \dots, A_N$ and bin B corresponds to patch $B_1, B_2, B_3, \dots, B_M$, as seen in Figure 6-11 (b). The slope angles of these patches are defined as $e_{A1}, e_{A2}, e_{A3}, \dots, e_{AN}$ and $e_{B1}, e_{B2}, e_{B3}, \dots, e_{BM}$. According to our previous discussion in section 5.4, slope angles and probabilities of patches in each group are similar, therefore we assume they are within the same straight line estimation region MN . The slope probability values (S value in Equ. (6-1)) of these slope angles can be estimated with the same parameters a and b .

$$\begin{cases} S_{An} = -\frac{a}{b}e_{An} + a \\ S_{Bm} = -\frac{a}{b}e_{Bm} + a \end{cases} \quad (6-6)$$

P_r is used to represent the reflection power of one patch. For patches groups A and B, the reflected power of each patch can be written as:

$$\begin{cases} \Pr_{An} = T \cdot Q_{An} \cdot S_{An} & n = 1, 2 \dots N \\ \Pr_{Bm} = T \cdot Q_{Bm} \cdot S_{Bm} & m = 1, 2 \dots M \end{cases} \quad (6-7)$$

The power of bin A is summed up from patch group A, as in Equ.(6-8):

$$\begin{aligned}
P_{BinA} &= \sum_{n=1}^N T \cdot Q_{An} \cdot S_{An} = \sum_{n=1}^N T \cdot a \cdot \left[Q_{An} \cdot \left(-\frac{1}{b} e_{An} + 1 \right) \right] \\
&= T \cdot a \cdot \left(-\frac{1}{b} \cdot \sum_{n=1}^N Q_{An} \cdot e_{An} + \sum_{n=1}^N Q_{An} \right)
\end{aligned} \tag{6-8}$$

Similarly for bin B,

$$P_{BinB} = T \cdot a \cdot \left(-\frac{1}{b} \cdot \sum_{m=1}^M Q_{Bm} \cdot e_{Bm} + \sum_{m=1}^M Q_{Bm} \right) \tag{6-9}$$

The ratio of two bin power can cancel out constant T and one unknown a , as in:

$$\frac{P_{BinA}}{P_{BinB}} = \frac{-\frac{1}{b} \sum_{n=1}^N Q_{An} \cdot e_{An} + \sum_{n=1}^N Q_{An}}{-\frac{1}{b} \sum_{m=1}^M Q_{Bm} \cdot e_{Bm} + \sum_{m=1}^M Q_{Bm}} \tag{6-10}$$

To solve another unknown b , we extend the above equation as:

$$-\frac{P_{BinA}}{b} \cdot \sum_{m=1}^M Q_{Bm} \cdot e_{Bm} + P_{BinA} \cdot \sum_{m=1}^M Q_{Bm} = -\frac{P_{BinB}}{b} \cdot \sum_{n=1}^N Q_{An} \cdot e_{An} + P_{BinB} \cdot \sum_{n=1}^N Q_{An} \tag{6-11}$$

i.e.,

$$\left(P_{BinB} \cdot \sum_{n=1}^N (Q_{An} \cdot e_{An}) - P_{BinA} \cdot \sum_{m=1}^M (Q_{Bm} \cdot e_{Bm}) \right) \cdot \frac{1}{b} = P_{BinB} \cdot \sum_{n=1}^N Q_{An} - P_{BinA} \cdot \sum_{m=1}^M Q_{Bm} \tag{6-12}$$

Therefore b can be calculated as:

$$b = \frac{P_{BinB} \cdot \sum_{n=1}^N (Q_{An} \cdot e_{An}) - P_{BinA} \cdot \sum_{m=1}^M (Q_{Bm} \cdot e_{Bm})}{P_{BinB} \cdot \sum_{n=1}^N Q_{An} - P_{BinA} \cdot \sum_{m=1}^M Q_{Bm}} \tag{6-13}$$

We can not extract a from these equations, however, the power proportion of each patch contributed to the bin can be calculated as:

$$\frac{P_{rAn}}{P_{BinA}} = \frac{T \cdot a \cdot Q_{An} \cdot \left(-\frac{1}{b} e_{An} + 1 \right)}{T \cdot a \cdot \left(-\frac{1}{b} \sum_{n=1}^N (Q_{An} \cdot e_{An}) + \sum_{n=1}^N Q_{An} \right)} = \frac{Q_{An} \cdot \left(-\frac{1}{b} e_{An} + 1 \right)}{-\frac{1}{b} \sum_{n=1}^N (Q_{An} \cdot e_{An}) + \sum_{n=1}^N Q_{An}} \tag{6-14}$$

therefore the power of group A patch can be expressed as:

$$P_{rAn} = P_{BinA} \cdot \frac{Q_{An} \cdot \left(-\frac{1}{b} e_{An} + 1 \right)}{-\frac{1}{b} \sum_{n=1}^N (Q_{An} \cdot e_{An}) + \sum_{n=1}^N Q_{An}} \tag{6-15}$$

Similarly we can derive the power contributions of group B patches. For each patch, we can calculate the probability value S with the constant T , according to Equ.(6.1).

6.3.2 Three-bin Differential Method

To explore a more general solution for three unknowns T , a and b , as seen in Equ.(6-8) and (6-9), we extend the Differential Method from two-bin to three-bin input. As seen in Figure 6-12, three adjacent bins are chosen together to calculate the slope probabilities of their corresponding patches.

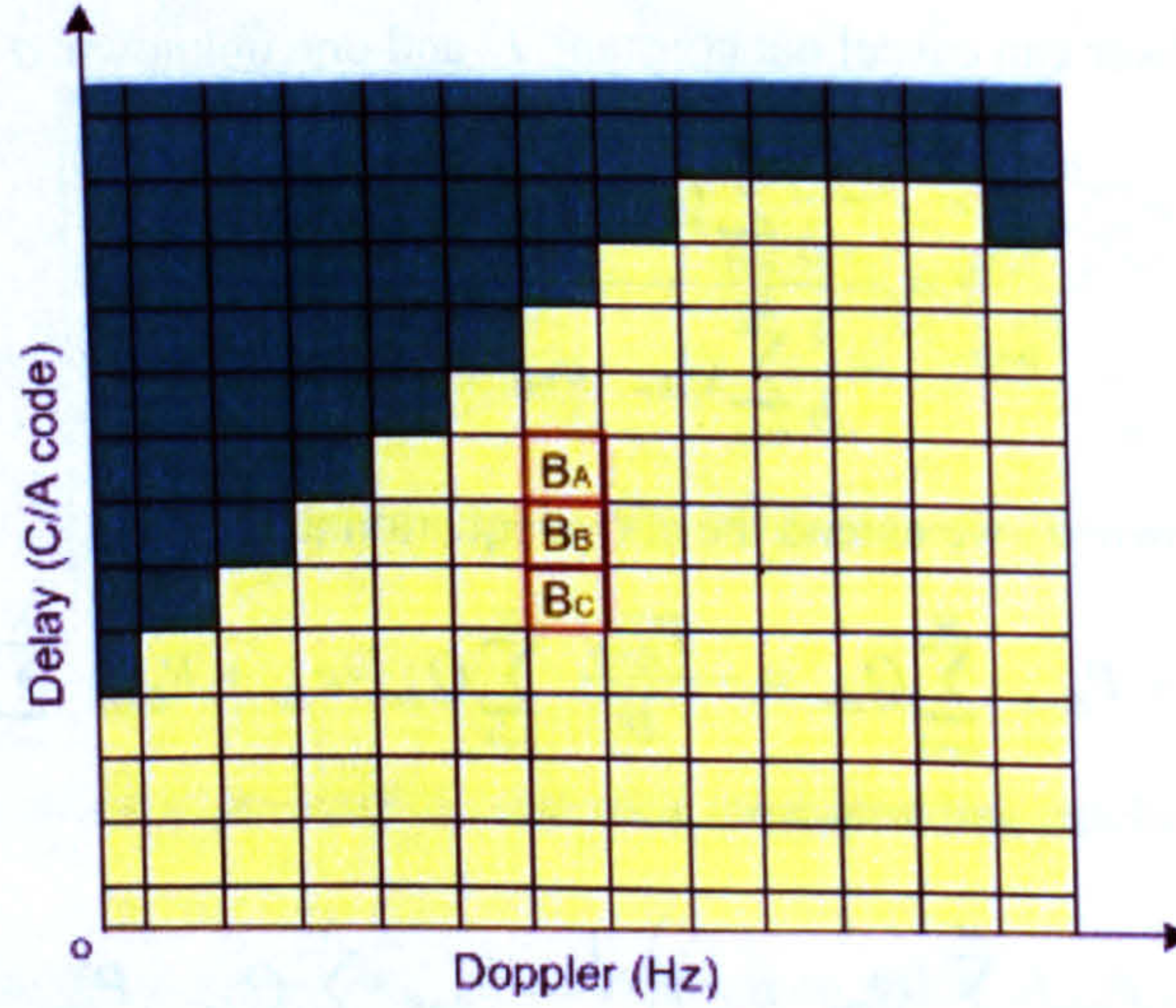


Figure 6-12: Three adjacent bins on DDM for differential calculation.

Here we apply a similar analysis as in the two-bin Differential Method. The slope angles of these three corresponding patch groups are $e_{A1}, e_{A2}, e_{A3}, \dots, e_{AN}$, $e_{B1}, e_{B2}, e_{B3}, \dots, e_{BM}$ and $e_{C1}, e_{C2}, e_{C3}, \dots, e_{CI}$. Slope-intercept format, instead of intercept format, is used to express the small section MN , which has a gradient $-a$ and a shift b , as in:

$$y = -ax + b \quad (6-16)$$

The slope probabilities and power of patches in three groups can be expressed respectively as:

$$\begin{cases} S_{An} = -ae_{An} + b & n = 1, 2 \dots N \\ S_{Bm} = -ae_{Bm} + b & m = 1, 2 \dots M \\ S_{Ci} = -ae_{Ci} + b & i = 1, 2 \dots I \end{cases} \quad (6-17)$$

and

$$\begin{cases} \text{Pr}_{An} = T \cdot Q_{An} \cdot S_{An} & n = 1, 2 \dots N \\ \text{Pr}_{Bm} = T \cdot Q_{Bm} \cdot S_{Bm} & m = 1, 2 \dots M \\ \text{Pr}_{Ci} = T \cdot Q_{Ci} \cdot S_{Ci} & i = 1, 2 \dots I \end{cases} \quad (6-18)$$

The power of three Delay-Doppler bins can be written as:

$$\begin{cases} P_{BA} = \sum_{n=1}^N \Pr_{A_n} = T \cdot \sum_{n=1}^N (Q_{A_n} \cdot (-a \cdot e_{A_n} + b)) \\ P_{BB} = \sum_{n=1}^N \Pr_{B_m} = T \cdot \sum_{m=1}^M (Q_{B_m} \cdot (-a \cdot e_{B_m} + b)) \\ P_{BC} = \sum_{n=1}^N \Pr_{C_i} = T \cdot \sum_{i=1}^I (Q_{C_i} \cdot (-a \cdot e_{C_i} + b)) \end{cases} \quad (6-19)$$

i.e.,

$$\begin{cases} P_{BA} = T \cdot \left[-a \cdot \sum_{n=1}^N (Q_{A_n} \cdot e_{A_n}) + b \cdot \sum_{n=1}^N Q_{A_n} \right] \\ P_{BB} = T \cdot \left[-a \cdot \sum_{m=1}^M (Q_{B_m} \cdot e_{B_m}) + b \cdot \sum_{m=1}^M Q_{B_m} \right] \\ P_{BC} = T \cdot \left[-a \cdot \sum_{i=1}^I (Q_{C_i} \cdot e_{C_i}) + b \cdot \sum_{i=1}^I Q_{C_i} \right] \end{cases} \quad (6-20)$$

which can be rewritten in a simpler format as:

$$\begin{cases} (w_1 x + u_1 y) \cdot z - v_1 = 0 & (f_1) \\ (w_2 x + u_2 y) \cdot z - v_2 = 0 & (f_2) \\ (w_3 x + u_3 y) \cdot z - v_3 = 0 & (f_3) \end{cases} \quad (6-21)$$

where x , y and z are used to replace the unknowns a , b and T .

Theoretically, it is possible to solve three unknowns (T , a and b) from these three non-linear equations. To test whether Equ.(6-20) is solvable by the Newton method, the Jacobian matrix determinant of Equ. (6-21) is concerned as:

$$\det(J) = \begin{vmatrix} \frac{\partial f_1}{\partial x} & \frac{\partial f_1}{\partial y} & \frac{\partial f_1}{\partial z} \\ \frac{\partial f_2}{\partial x} & \frac{\partial f_2}{\partial y} & \frac{\partial f_2}{\partial z} \\ \frac{\partial f_3}{\partial x} & \frac{\partial f_3}{\partial y} & \frac{\partial f_3}{\partial z} \end{vmatrix} = \begin{vmatrix} w_1 z & u_1 z & w_1 x + u_1 y \\ w_2 z & u_2 z & w_2 x + u_2 y \\ w_3 z & u_3 z & w_3 x + u_3 y \end{vmatrix} \quad (6-22)$$

therefore we have

$$\begin{aligned} \det(J) &= w_1 u_2 \cdot z^2 (w_3 x + u_3 y) + w_2 u_3 \cdot z^2 (w_1 x + u_1 y) \\ &+ w_3 u_1 \cdot z^2 (w_2 x + u_2 y) - w_1 u_3 \cdot z^2 (w_2 x + u_2 y) \\ &- w_2 u_1 \cdot z^2 (w_3 x + u_3 y) - w_3 u_2 \cdot z^2 (w_1 x + u_1 y) \end{aligned} \quad (6-23)$$

i.e.,

$$\begin{aligned} \det(J) &= z^2 \cdot (w_1 u_2 w_3 x + w_1 u_2 u_3 y + w_1 w_2 u_3 x + w_2 u_1 u_3 y \\ &+ w_2 w_3 u_1 x + w_3 u_1 u_2 y - w_1 w_2 u_3 x - w_1 u_2 u_3 y \\ &- w_2 w_3 u_1 x - w_2 u_1 u_3 y - w_1 w_3 u_2 x - w_3 u_1 u_2 y) \\ &= 0 \end{aligned} \quad (6-24)$$

Since the determinant of Jacobian matrix is 0, the above equations are linearly dependent and can not be solved by the Newton method. As such, the two-bin differential solution is used to carry on the inversion experiments on simulated DDMs.

6.3.3 Synthetic DDM inversion

The inversion test for the Differential Method is applied on simulated R12 and R13 scenarios. The simulated R12 DDM inversion is presented in this section, and the R13 case can be seen in Appen. III. The below Figure 6-13 (b) shows the inversed spatial energy distribution of R12 DDM with light noise.

BSNR = 200 dB (deconvolved SNR = 98.95 dB)

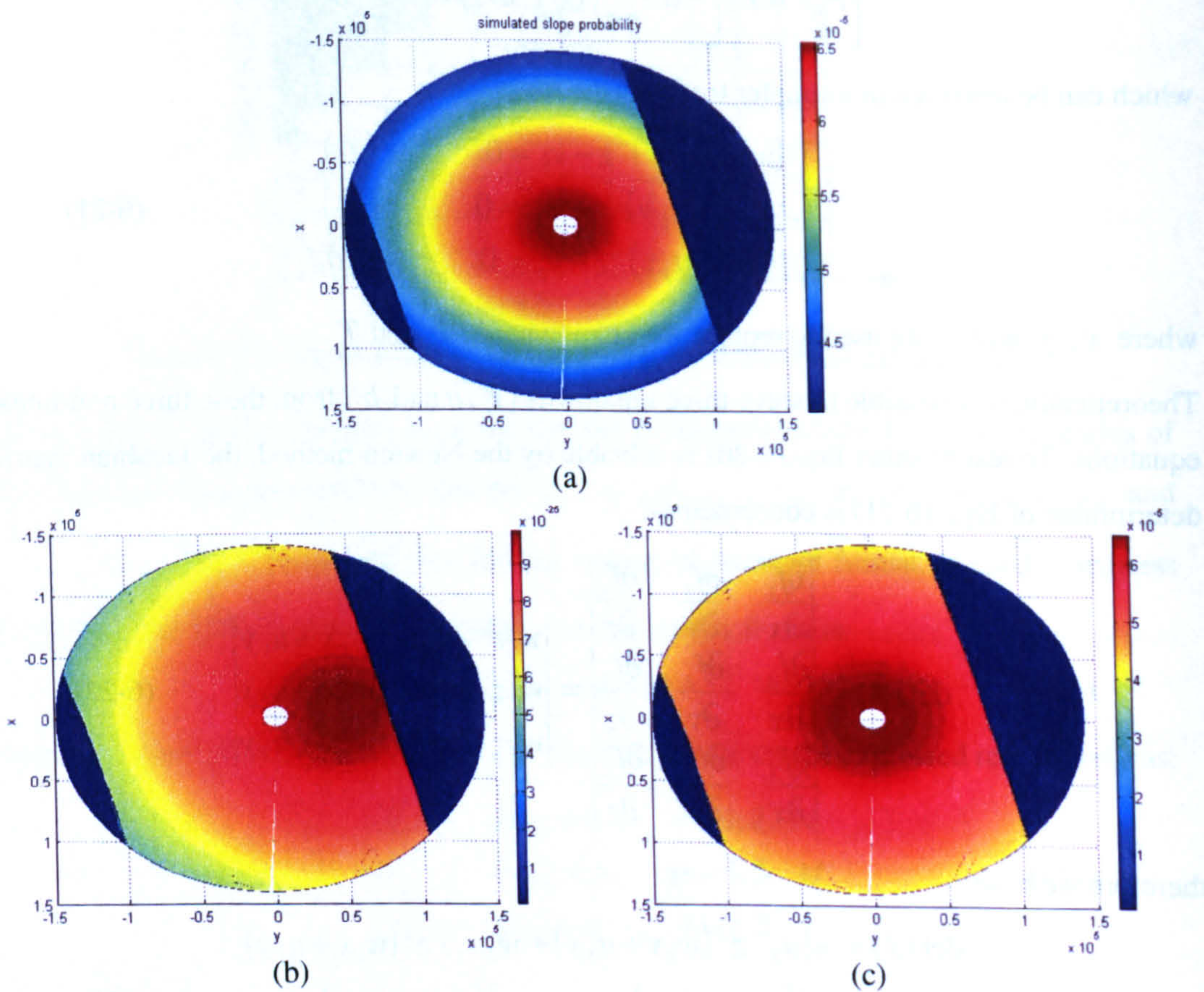


Figure 6-13: The Differential Method inversion test on R12 simulation. (a) simulated slope probability map. (b) inversed spatial energy map. (c) inversed slope probability map.

Due to the antenna pattern, the energy more concentrates on the right side of reflection area, where there has lower Doppler shift. This matches the real UK-DMC R12 DDM pattern as seen in Figure 4-21 (c), with stronger arm on the low Doppler side. Figure 6-13 (c) is the inversed slope probability map, which has a similar pattern and scale with the simulated

probability map (Figure 6-13 (a)). The inversion result from the Differential Method has good correlation with the original probability map, when the simulated noise is not strong.

BSNR = 150 dB (deconvolved SNR = 49.72 dB)

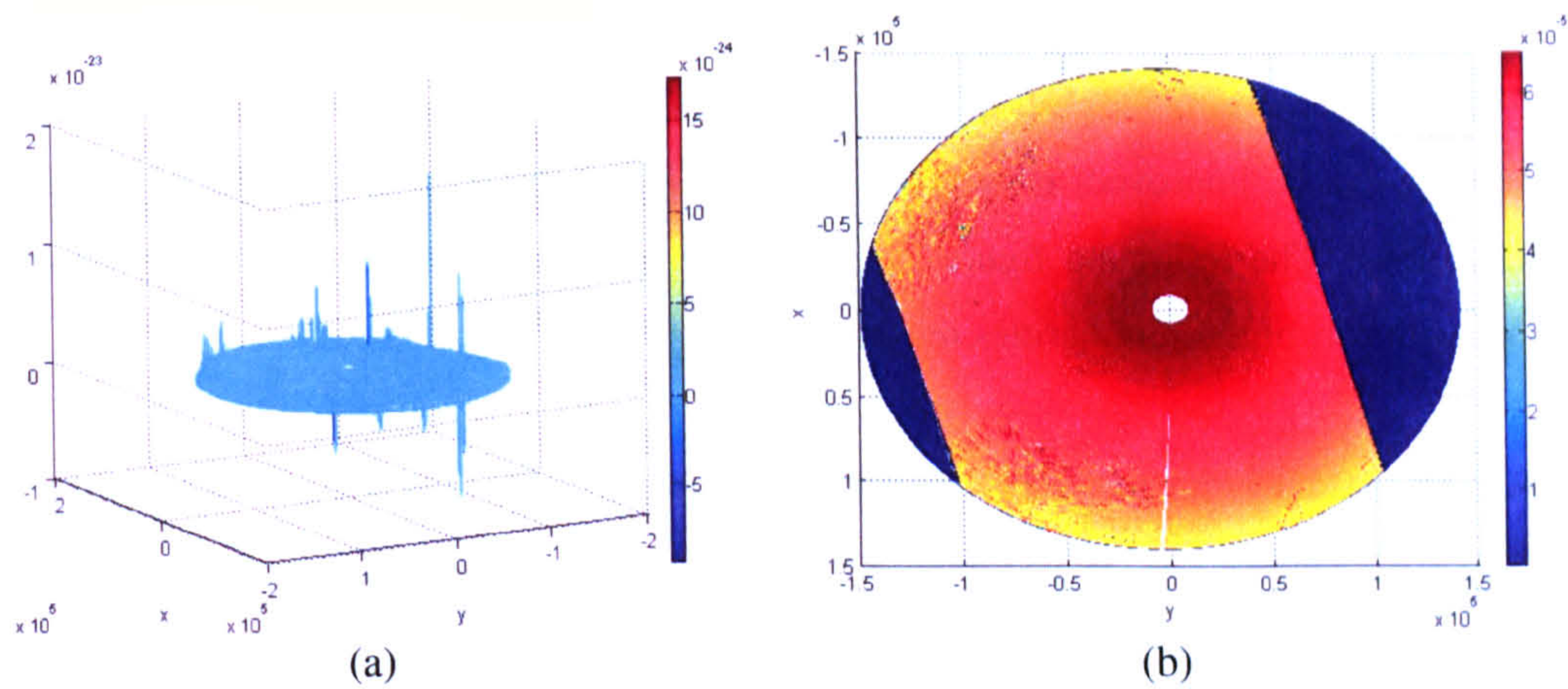


Figure 6-14: Inversed spatial energy map (a) and probability map (b) of simulated R12 test.

Figure 6-14 represents the inversed results of a 150dB BSNR R12 DDM. (a) is the inversed spatial energy map, which shows a typical pattern of the inversion results from the Differential Method when noise increases. The noisier the blurred DDM is, the more singularities there will be in the inversed spatial map. The two largest singularities always correspond to the edgy Delay rings in DDMs, such as in case R12, around the 646th and 665th Delay rings as shown in Figure 6-15:

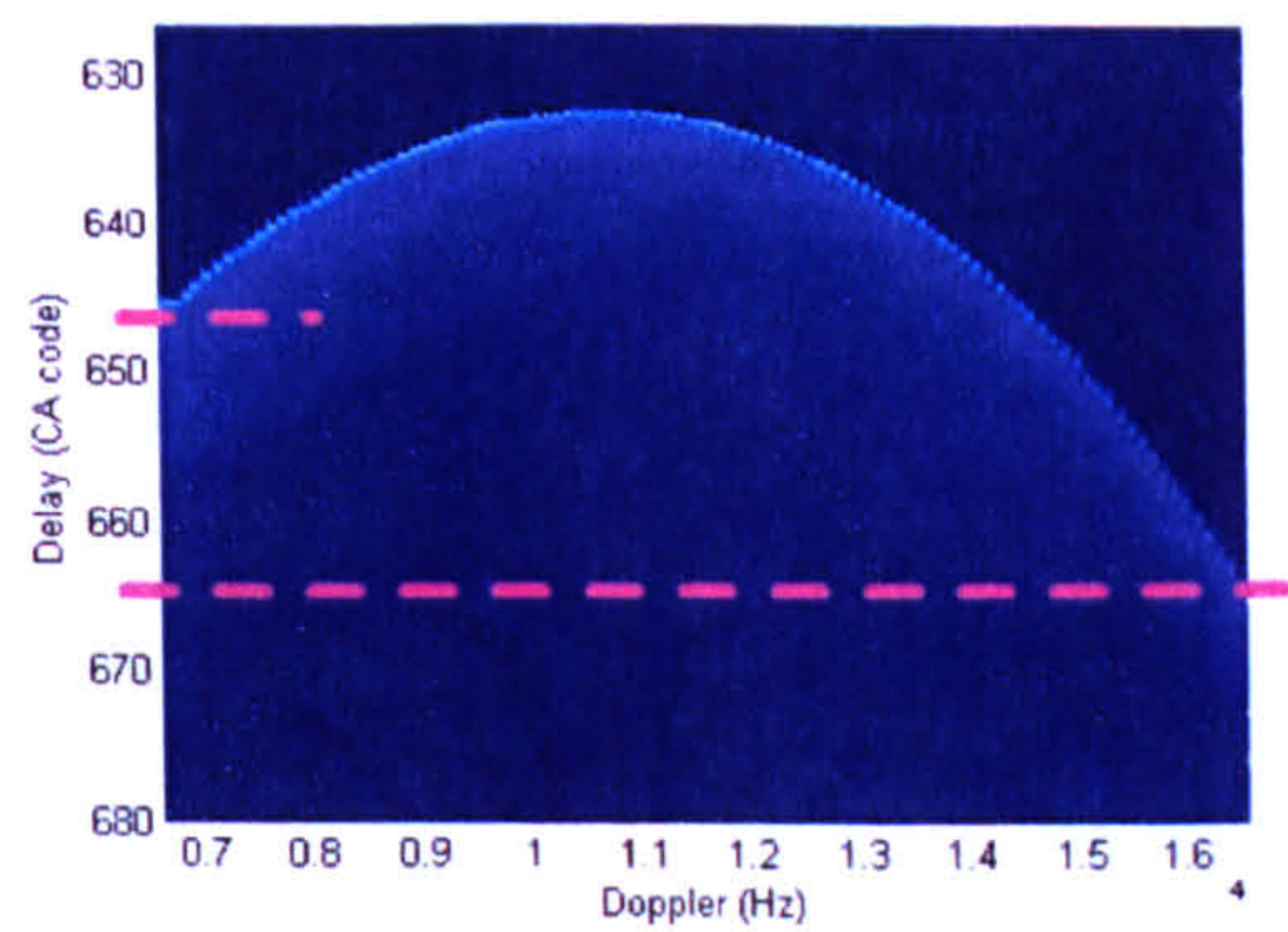


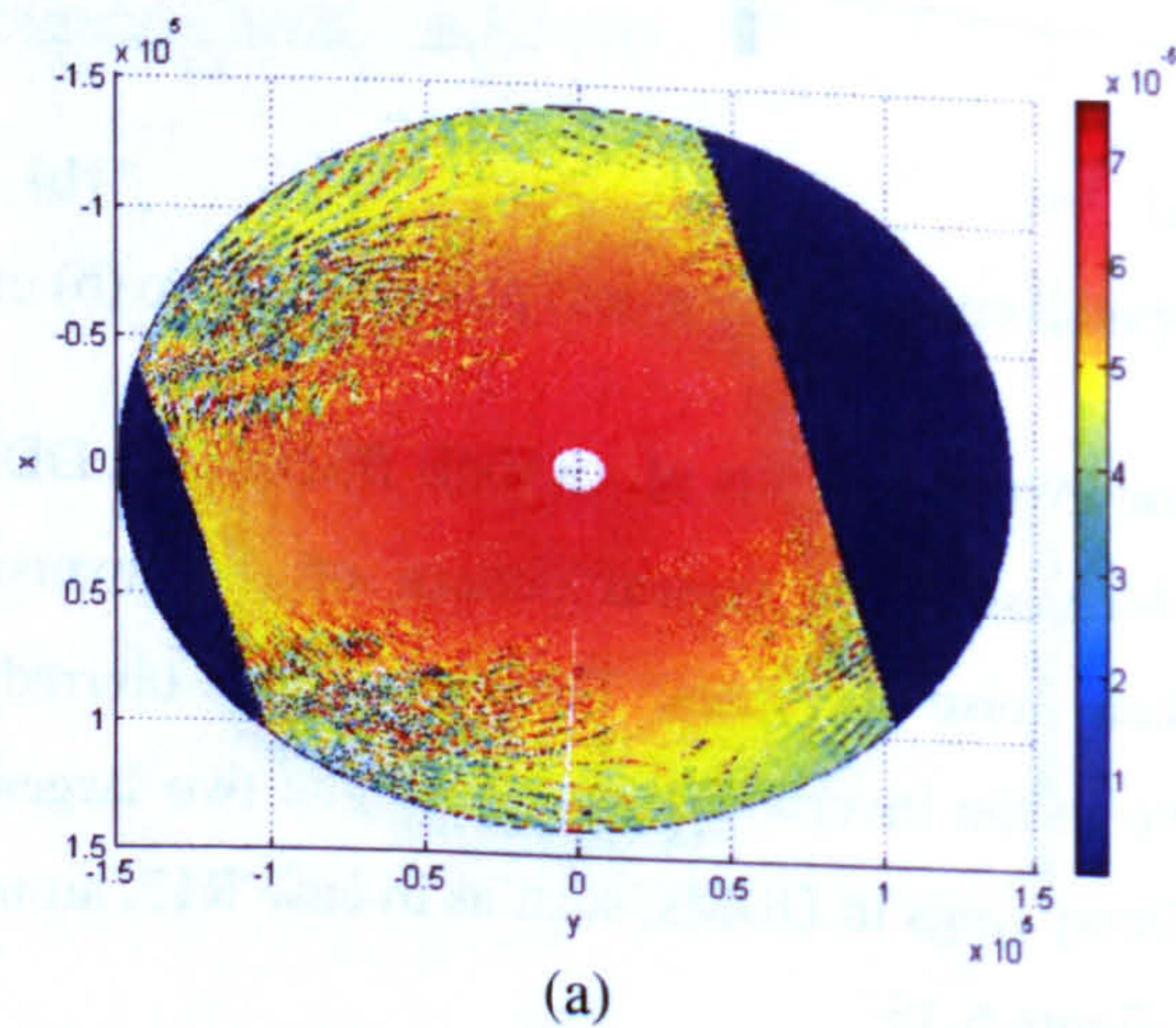
Figure 6-15: Cut-off Delay edges of R12 DDM.

In Figure 6-14(b), we can also observe a symmetry pattern of singularities distributed along the Doppler contour direction, as mentioned in our discussion of inversion ambiguity problem in section 6.2.1. Both the Average Method and Differential Method have this obstacle. In Figure 6-14(b), the singularity points are much denser on the lower Doppler side. This is because the R12 DDM has stronger power on the low Doppler cut-off frequency as seen in Figure 6-15. The DDM energy on the high Doppler cut-off frequency is much weaker than

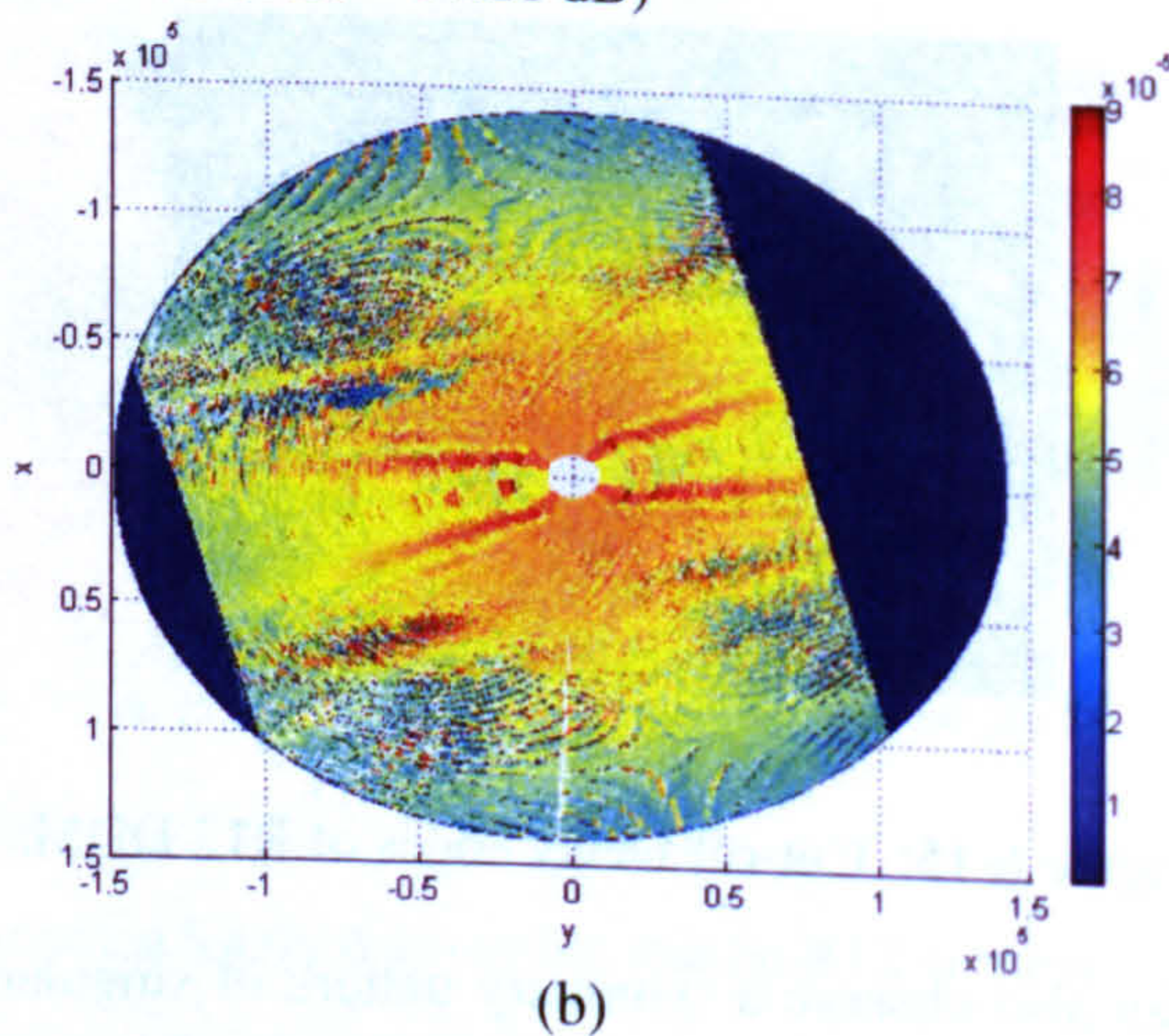
the low Doppler side, as such there are few singularity points on the right side of the inversed probability map. This analysis on inversion noise pattern suggests that, for the purpose of DDM inversing, GPS-R receivers should enlarge their bandwidth and avoid DDM cut-off frequency at strong signal area.

By manually removing large singularities on edgy Doppler positions, the quality of inversed spatial maps can be improved. However, the inversion results are still significantly affected by DDM noise. The following figures show the DDM inversion result by the Differential Method, with part of the singularities removed.

BSNR = 120 dB (deconvolved SNR = 26.61 dB)



BSNR = 100 dB (deconvolved SNR = 17.21 dB)



BSNR = 80 dB (deconvolved SNR = 13.36 dB)

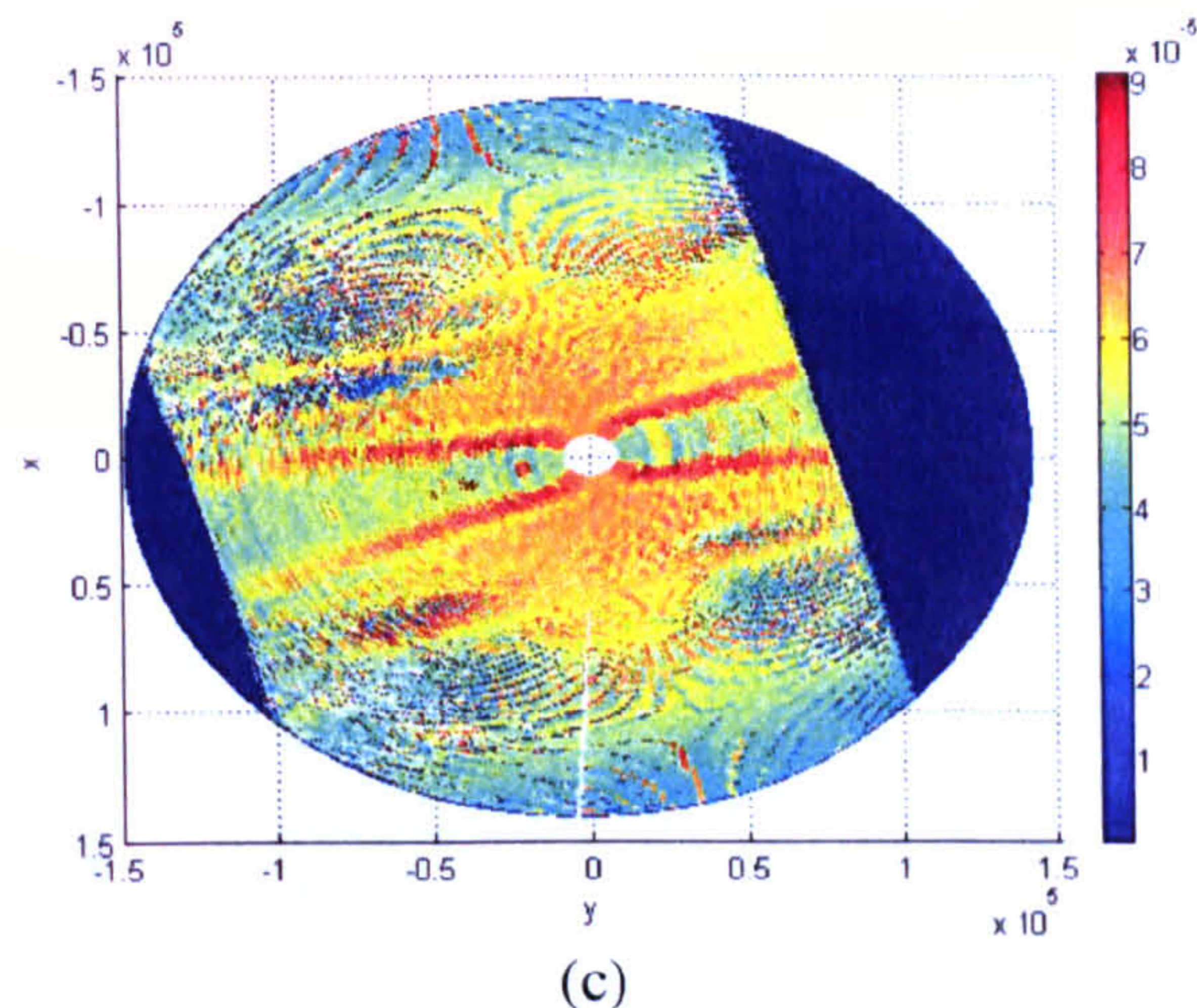


Figure 6-16: Inversed R12 slope probability maps via the Differential Method.

From Figure 6-16, we can observe that DDM inversion performance, from the Differential Method, declines quickly when noise increases. The symmetric pattern across the Doppler contour direction gradually dominates spatial energy maps and destroys the correlation level of inversed probability maps with the original ones. This is similar to the Average Method performance.

6.3.4 UK-DMC DDM inversion

The Differential Method test does not show good robustness against strong noise, however, an initial look at the real DDM data inversion is necessary for evaluating of the whole inversion scheme. This section presents the first data inversion experiment of R12 UK-DMC DDM using the two-bin Differential Method. The R12 DDM, which is input into the inversion procedure, has been processed to remove the bias in different Doppler frequencies (refer to section 4.2.6).

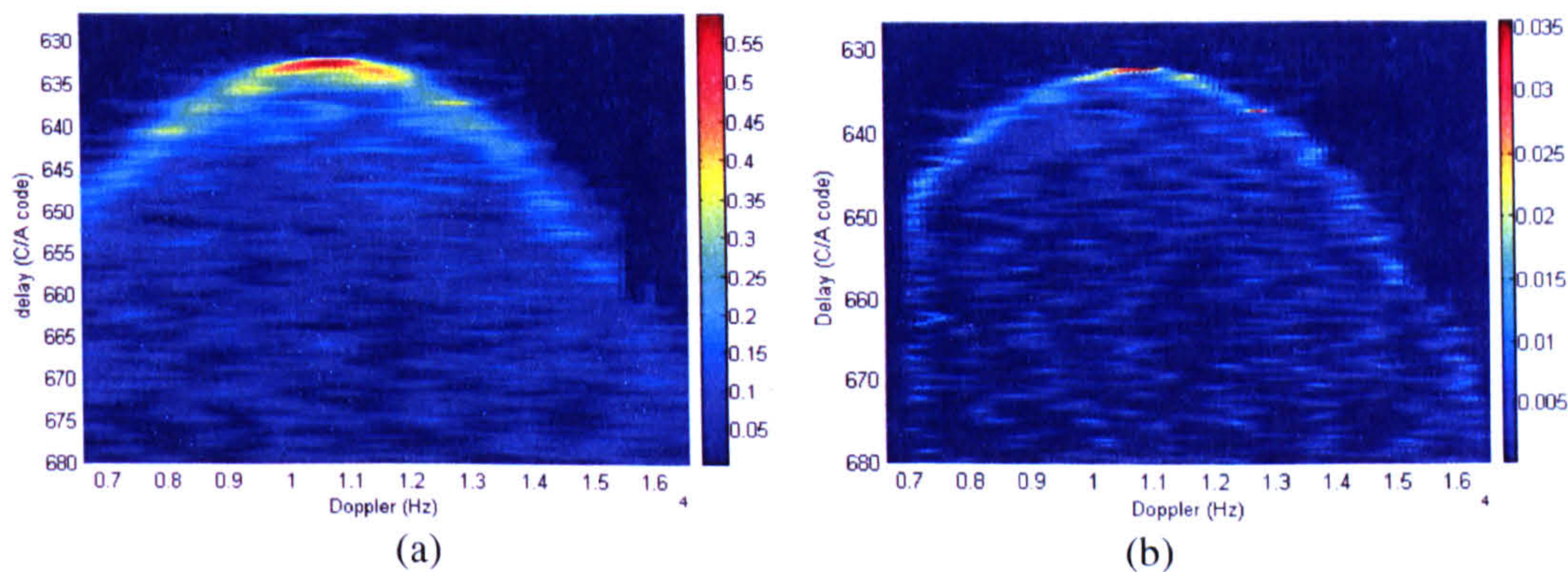


Figure 6-17: UK-DMC R12 DDM deconvolution.
(a) bias-removed real DDM. (b) deconvolved DDM.

If we apply the two-bin Differential Method on the deconvolved DDM (Figure 6-17 (b)), the inversed slope probability map (S with constant T) is as below:

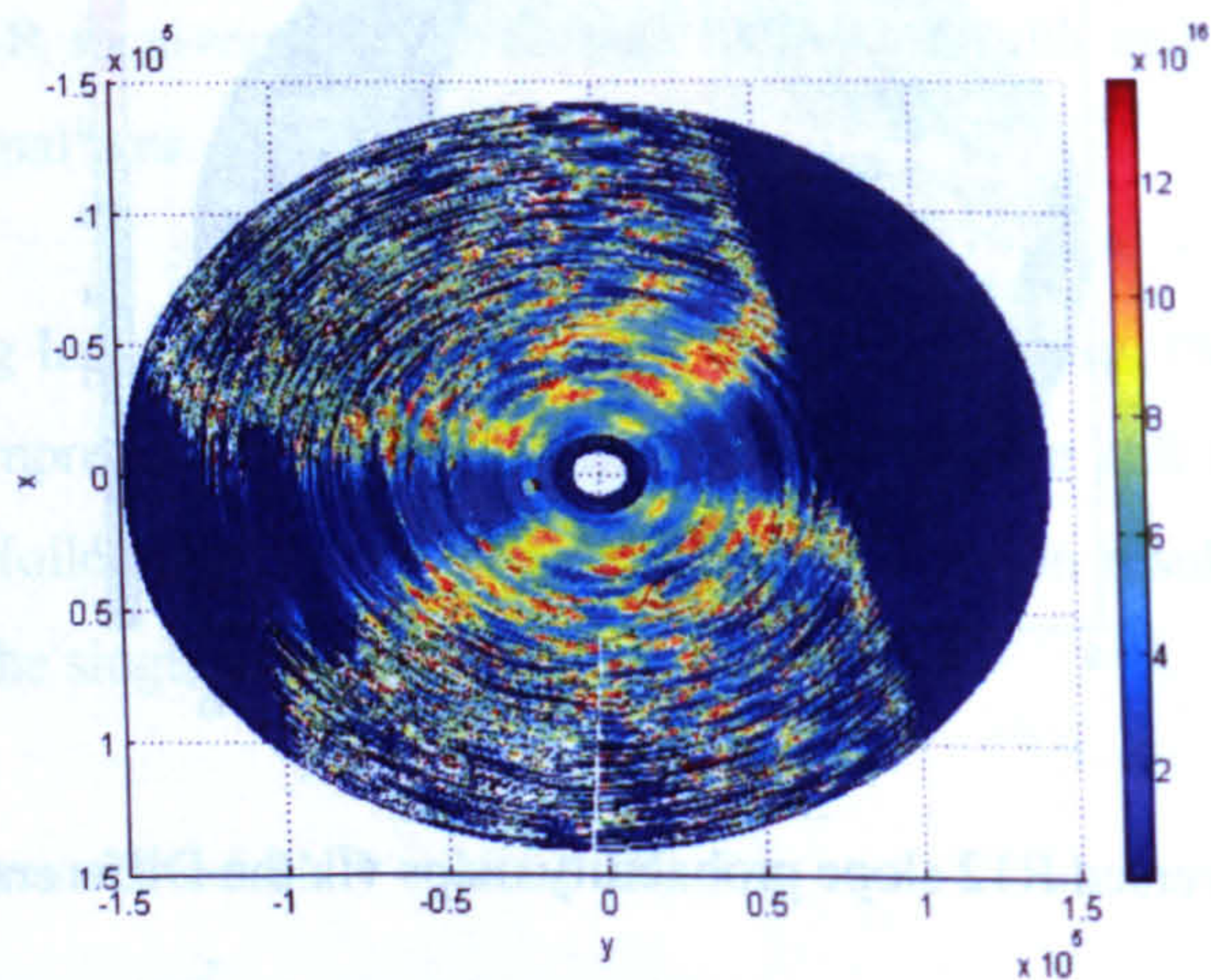


Figure 6-18: Spatial slope probability map inversed from UK-DMC R12 DDM.

A slope probability map can be derived from Figure 6-18. By averaging every 10 adjacent values within the same Delay ring, we can smooth the probability map as in Figure 6-19:

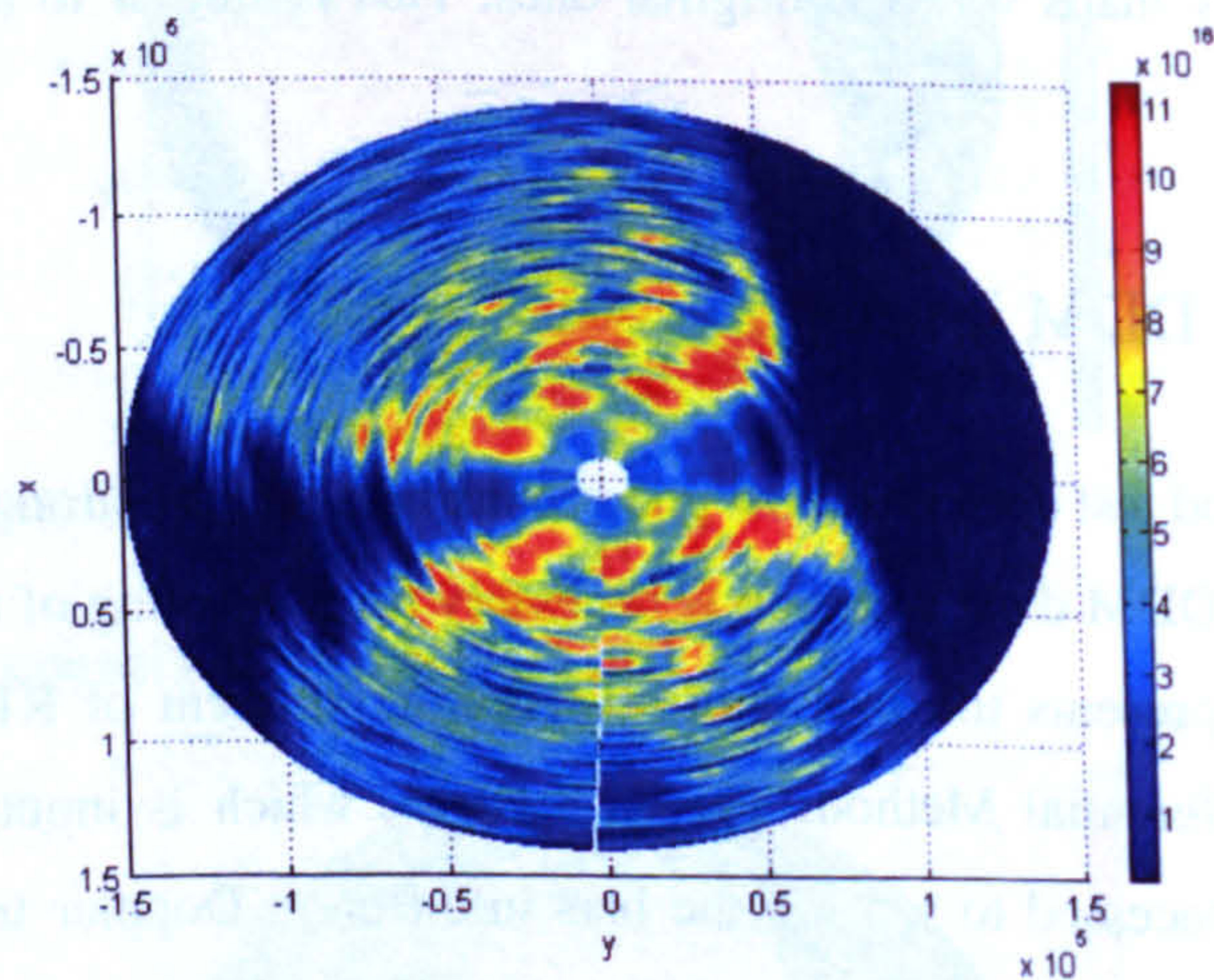


Figure 6-19: Filtered spatial slope probability map of UK-DMC R12 scenario.

The inversed slope probability map from real R12 DDM displays a basic Gaussian-like distribution pattern. The probability values are larger with low slope angles around the centre area and decreases towards the edge area, with growing slope angles. A strong symmetric pattern across the Doppler contour direction can also be observed, which is similar to our synthetic DDM inversion results under heavy noise. The result of real DDM inversion shows the validity of our DDM inversion study. Further research is needed to reduce the noise from reflected signals and improved the inversion algorithms.

6.4 1-D Probability Inversion

6.4.1 Methodology

From our DDM simulation experiments, we find that the required slope angles within same Delay contours are similar. It is therefore reasonable to assume that all iso-Delay patches have the same slope probabilities in DDM inversion. The sum of patch power within one Delay ring can be expressed as:

$$\sum_{\text{delay}} P_{rbin} = \sum_{\text{delay}}^k S \cdot T \cdot Q_k \quad (6-25)$$

Then the average slope probability value within the Delay ring is:

$$S = \sum_{\text{delay}} P_{rbin} / T \cdot \sum_{\text{delay}}^k Q_k \quad (6-26)$$

The above method simplifies the 2-D slope probability inversion to 1-D. It is expected to be more robust to inversion noise by sacrificing the information of Doppler dimension. Theoretically we can not extract slope direction information as 2-D probability inversions, however, it is still worthwhile to derive a slope amplitude statistical model in this initial research status of GPS-R DDM inversion.

6.4.2 Synthetic DDM 1-D inversion

To test the feasibility of 1-D probability inversion, we carry out the similar R12 synthetic experiment as in the previous two methods. Through the test, this 1-D inversion is proven to have better performance, than the Average Method and two-bin Differential Method, under strong noise.

The below figures provide a good example of 1-D probability inversion when the blurred DDM has a low BSNR. Figure 6-20(a) is the original simulated slope probability map, based on the Elfouhaily wave spectrum model with an 8m/s wind speed input. Figure 6-20(b) is the simulated noisy AF-blurred DDM, with an 8 dB BSNR. Figure 6-20(c) is the deconvolved DDM using the ForWaRD algorithm, with a SNR of 6.88 dB. Figure 6-20(d) is the inversed slope probability map.

BSNR = 8 dB

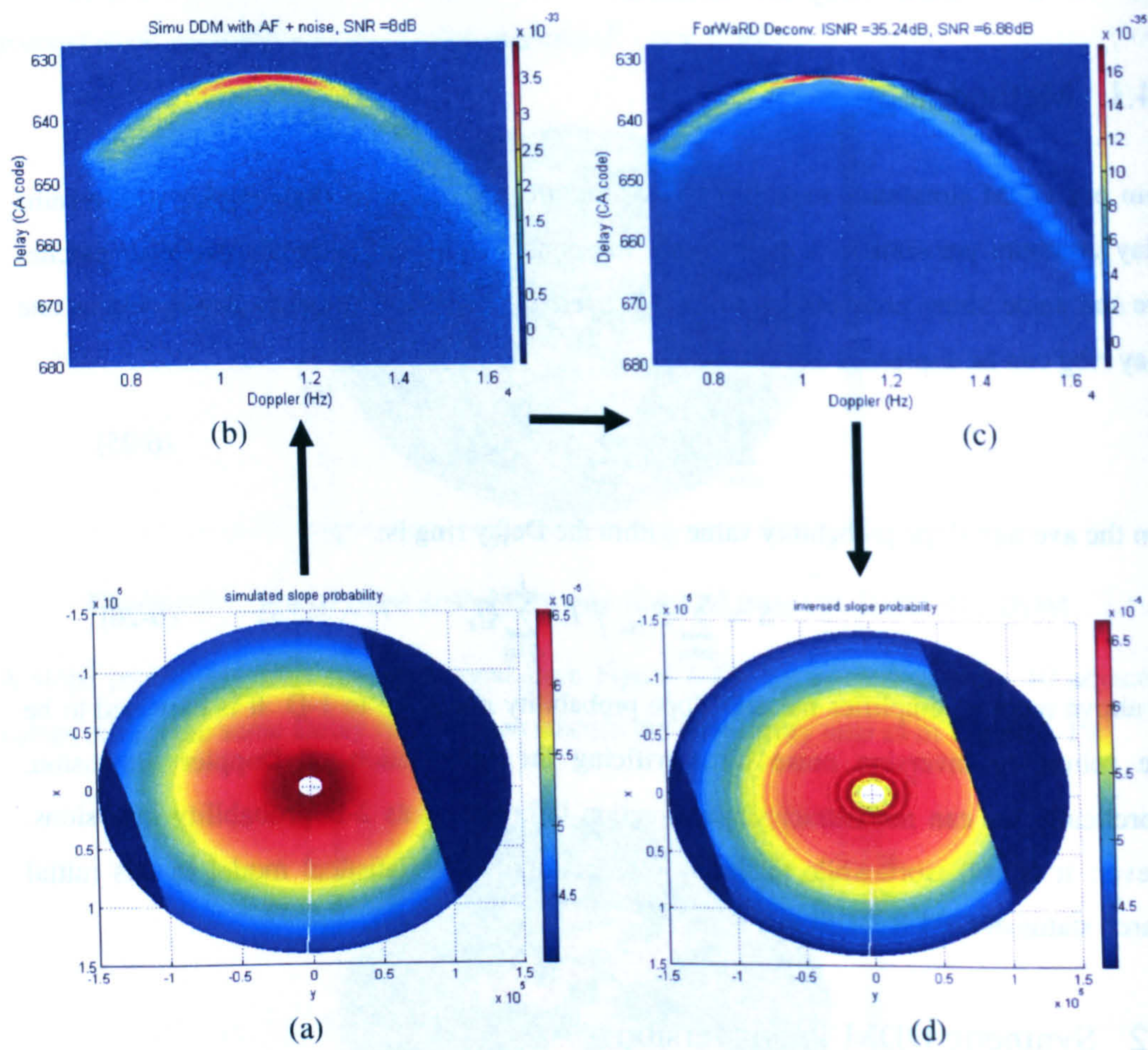


Figure 6-20: R12 synthetic experiment of 1-D probability inversion.

Since we assume the same slope probability within each Delay ring, the inversed probability map has a 360° ambiguity. The correlation of the inversed result (d) and original probability map (a) are shown below.

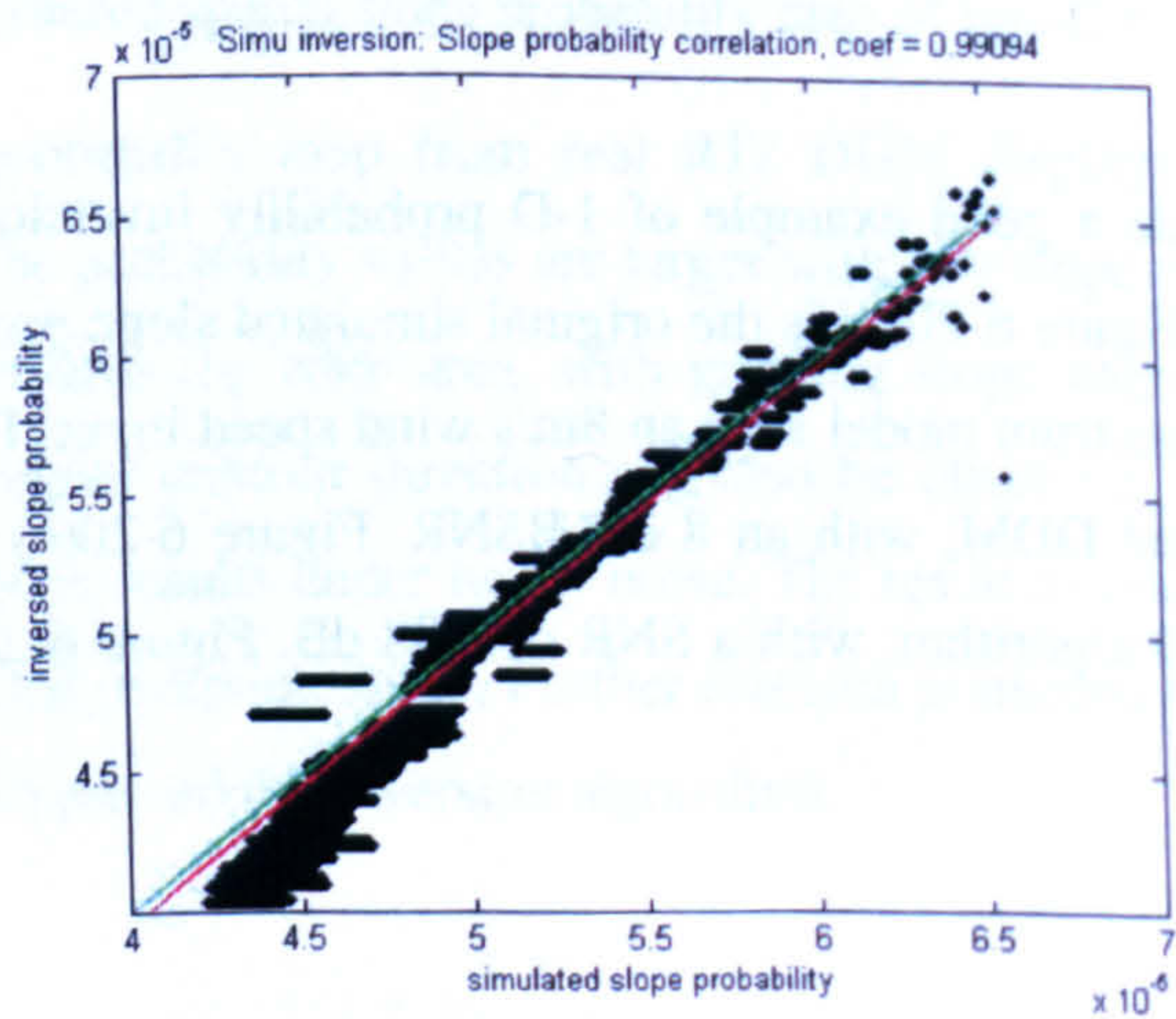


Figure 6-21: Correlation of the inversed and original R12 slope probability map.

The Correlation Coefficient of matching points, between Figure 6-20 (a) and (d), is 0.99094, and the gradient of the fitted line is 1.0024. This shows a good correlation between the two probability maps. The deviant data around $4.5\text{e-}5$ is due to the cut-off Doppler frequency of the R12 DDM.

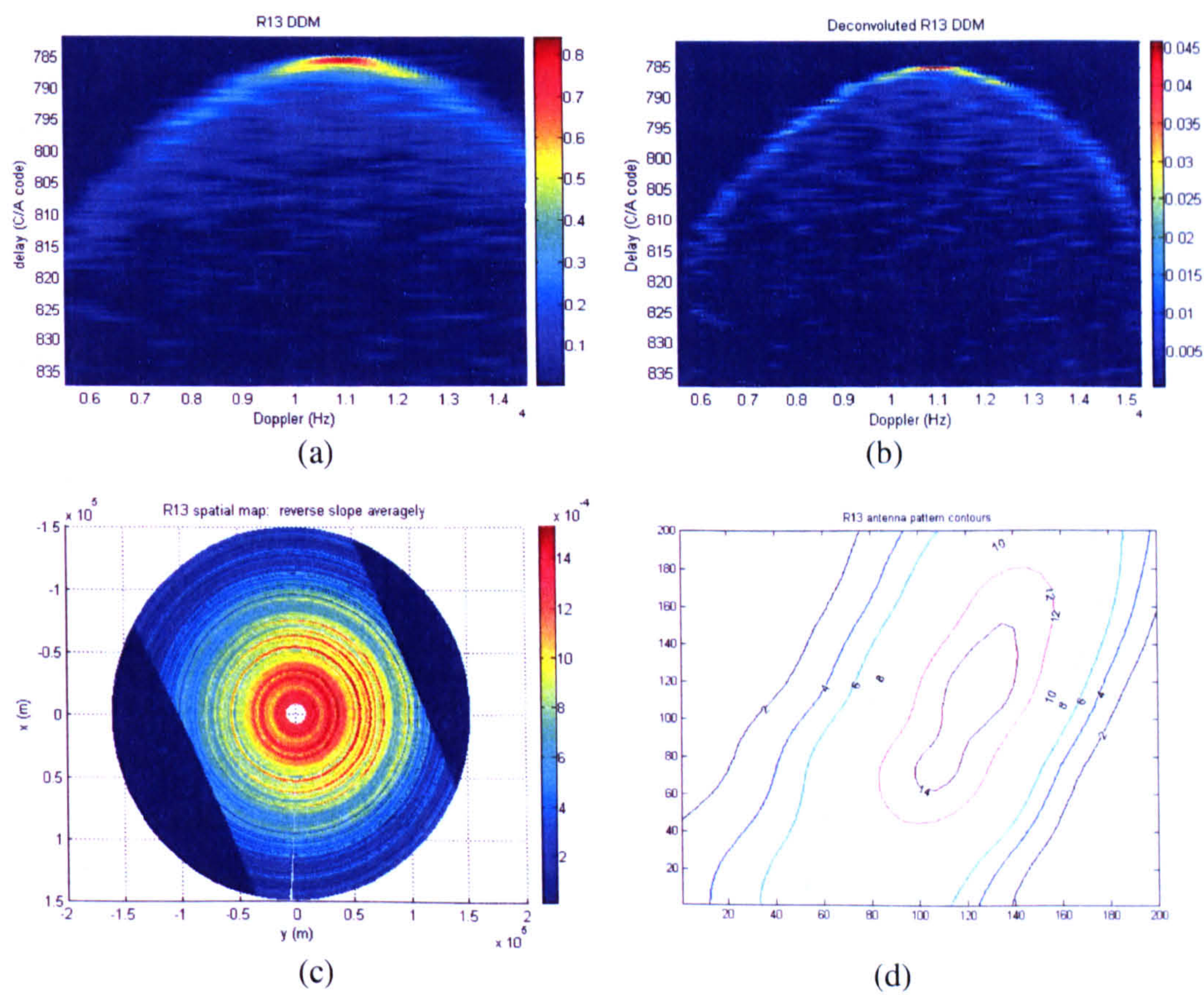
From the result above, we can conclude that, when using the 1-D Inversion Method, DDMs can be inversed into 1-D Slope Probability Maps (SPM) under heavy noise. As such this method will be applied on our real DDM inversions in next section.

6.4.3 UK-DMC DDM 1-D inversion

Six sets of UK-DMC data (R13, R18, R15, R12, R14 and R10) are available for the 1-D inversion experiment. From the local buoy measurements, these datasets can be arranged in order of wind speed:

$$\mathbf{R13} \text{ (2.5 m/s)} < \mathbf{R18} \text{ (7 m/s)} , \mathbf{R15} \text{ (7.3 m/s)} , \mathbf{R12\&R14} \text{ (8 m/s)} < \mathbf{R10} \text{ (10 m/s)}$$

The R13 inversion is presented as below.



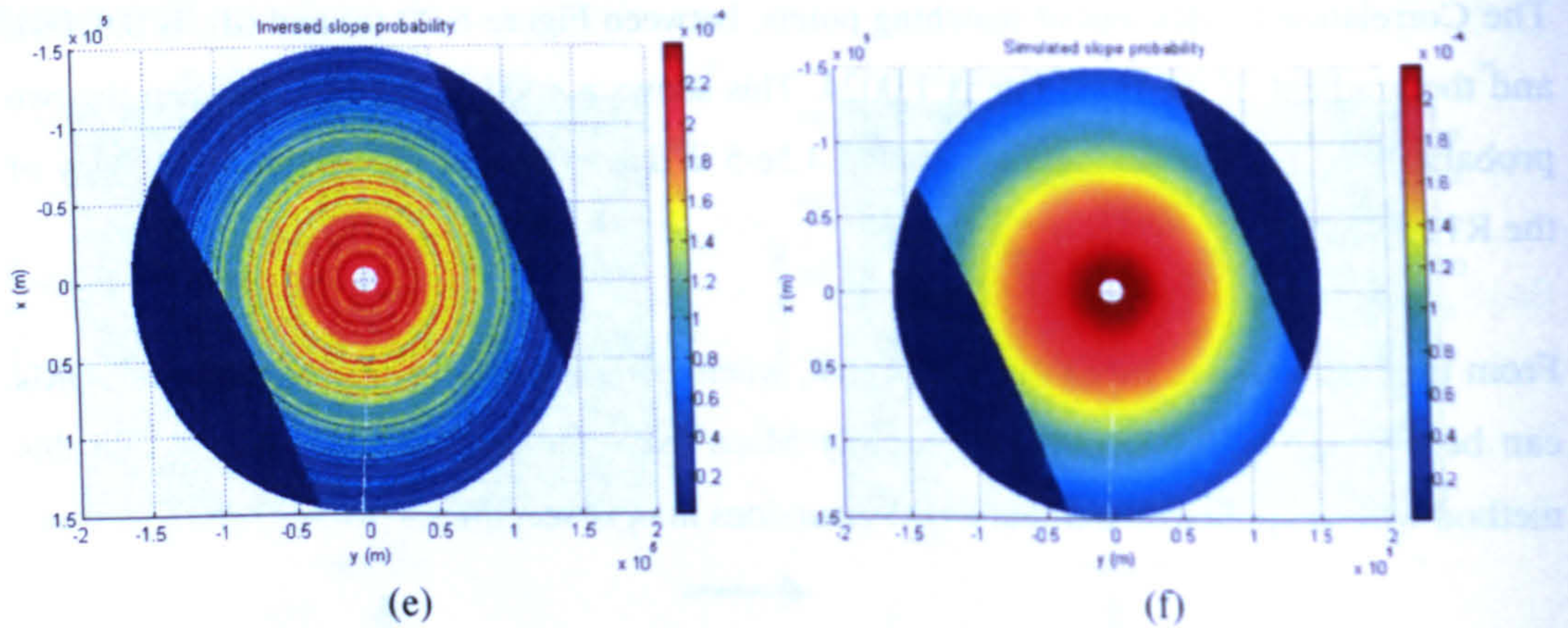


Figure 6-22: UK-DMC R13 DDM inversion experiment.

- (a) bias-removed UK-DMC R13 DDM. (b) deconvolved UK-DMC R13 DDM.
 (b) inversed R13 spatial energy map (with antenna pattern effect). (d) antenna pattern.
 (e) inversed R13 spatial slope probability map. (f) simulated R13 slope probability map.

As seen in Figure 6-22, (a) is the processed R13 data, from which the Doppler bias has been removed. (b) is the deconvolved DDM via the ForWaRD algorithm. After applying the 1-D Inversion Method on (b), we obtain a spatial energy distribution map as (c). Since the antenna pattern is not symmetric, as shown in the simulation (d), more energy concentrates on the right side of the spatial energy map (c). After all geometric factors are removed from the spatial energy map, we finally get the inversed slope probability map (e), with a 360° ambiguity. (f) is the simulated R13 slope probability map, based on the Gaussian slope PDF assumption.

Before the discussion on comparison, it is necessary to review the problem of constant T in this experiment (refer to Equ.(6-1)). The simulated 1-D inversion result does not consider the constant T , since T is assumed 1 in the DDM generation procedure. In real DDM inversion experiment, however, the results have the factor T in inversed Slope Probability Maps. Therefore a reference needs to be chosen to calibrate the inversion output. R13 is the low wind speed dataset, which has a good correlation result in previous DDM simulation experiment (refer to section 4.3.1-R13 DDM simulation case study). R13 DDM, as shown in Figure 6-22 (a), also has cut-off Doppler frequencies in weak signal region, and is supposed to have little inversing noise in the result. As such the R13 inversion output is used as a calibration reference, which means, a constant is calculated from the peak ratio of the R13 real data inversion result and simulated slope probability map. This constant value is used to compensate the R13 real data inversion result, to make two curves match in peak value as shown in Figure 6-23 (b). In the following experiments, the same constant are applied in all

dataset inversion results. Without further mentioning, all the inversion results presented in this chapter are with such calibration.

By comparing the inversion result (e) with the Elfouhaily modelled slope probability map (f) of Figure 6-22, we have the correlation result as in Figure 6-23:

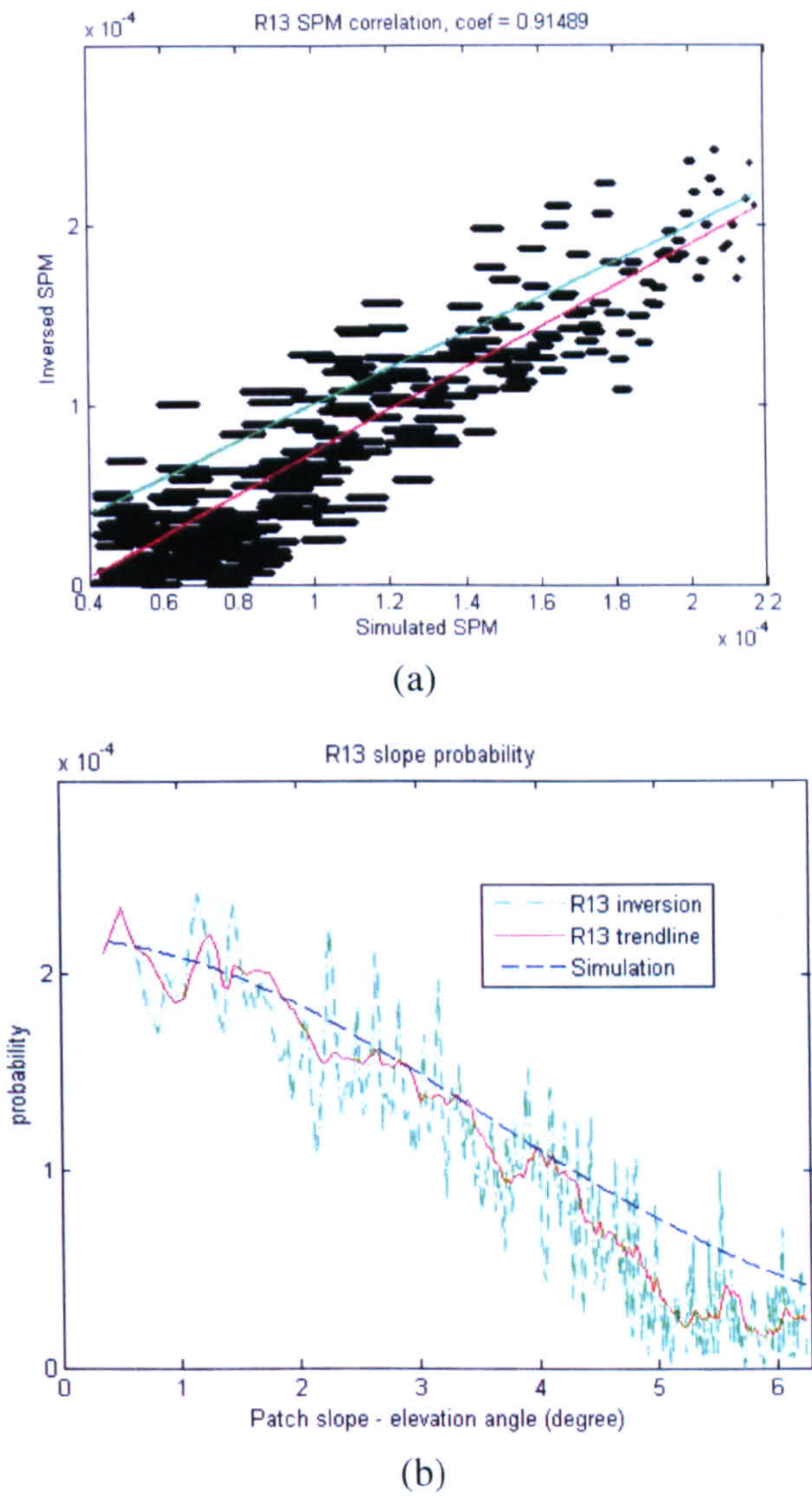


Figure 6-23: UK-DMC R13 slope probability comparison.

- (a) correlation of the inversed and simulated slope probability map with fitted line (green).
- (b) 1-D slope probability curve comparison between the real data and Gaussian simulation.

Figure 6-23 (a) is the point-to-point matching result of two Slope Probability Maps. The data points form a linearization pattern. The Correlation Coefficient is 0.9149 and the gradient of the data points fitted line (green) is 1.1580, close to the reference line (red). Figure 6-23 (b) plots the Gaussian slope probability distribution (blue) and trend line (red) of 45° direction data from the inversed probability map (Figure 6-22(e)). Since the 1-D inversion result has a

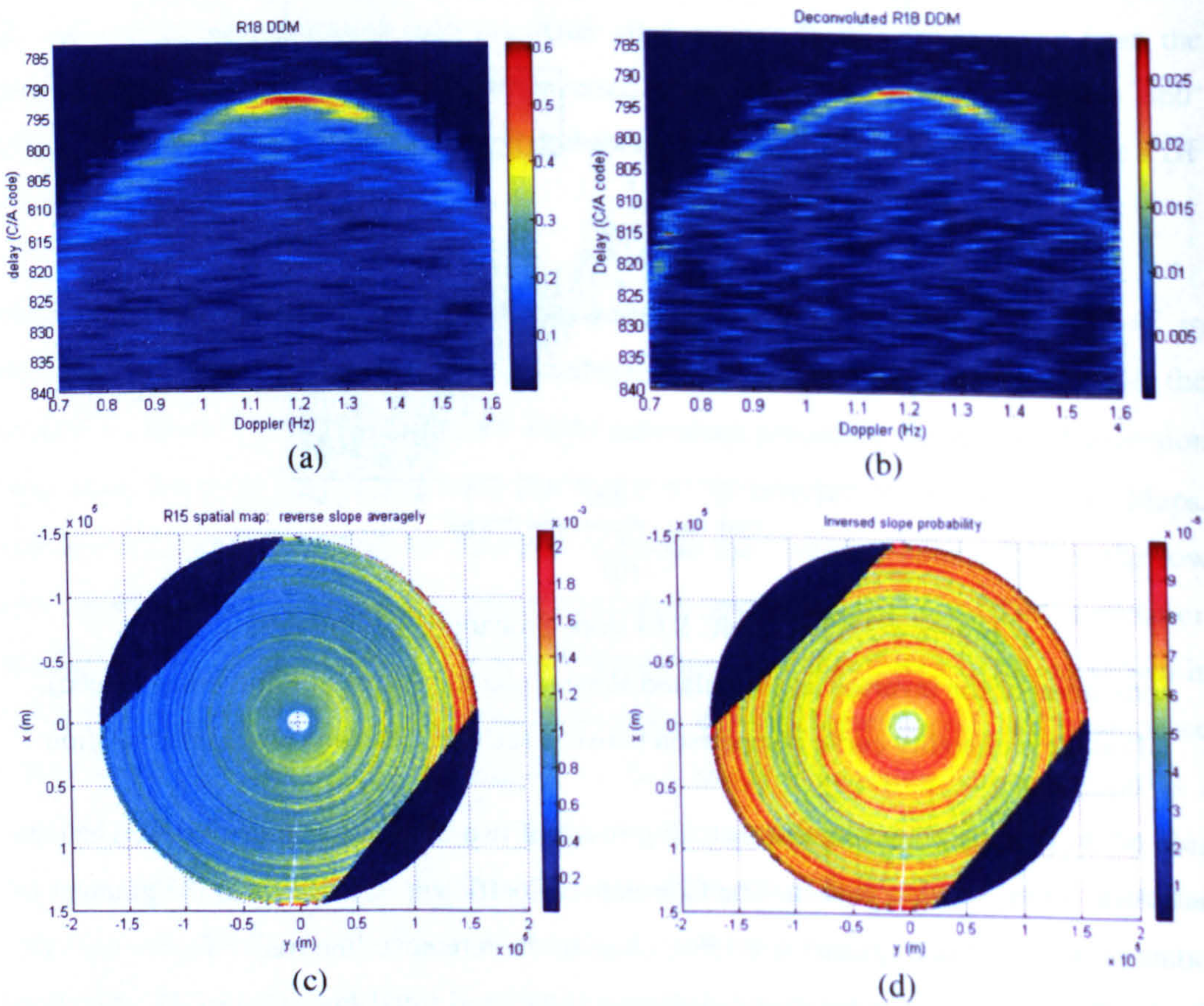
360° ambiguity, all directions should have the same result. However, 45° direction has more data points than the others, therefore it is chosen for display. The green dash line is the original inversion output, which has been simply filtered to reduce the RMS of the data. The trend line (red solid line) and the Gaussian simulation (blue dash line) show a close match.

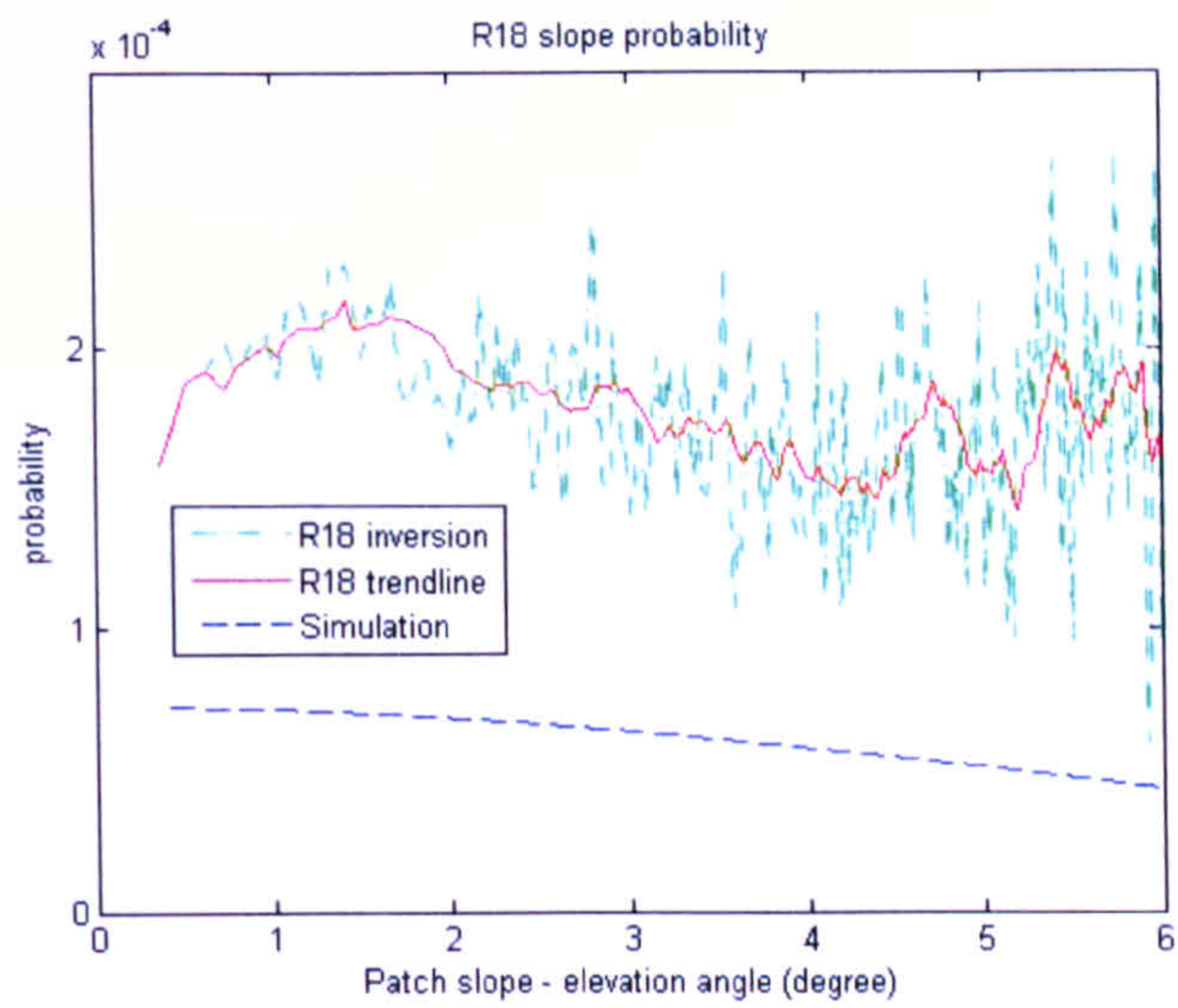
R18, R15, R12 and R14 data are within the medium wind speed range. The basic data facts are shown in Table 4.

Table 4 UK-DMC GPS-R R18, R15, R12 and R14 data facts

	R18	R15	R12	R14
Signal source	SVN-27	SVN-43	SVN-47	SVN-43
Time tag	08:28:50AM 04 March 2005	09:05:21AM 30 January 2005	07:54:46 AM 16 November 2004	10:23:58 AM 14 January 2005
Wind conditions (from local buoy)	7 m/s, 108°	7.3 m/s, 69°	8 m/s, -107°	8 m/s, 52°
Incident angle	28.0	35.1°	15.2°	1.8°

The inversion of R18 dataset is as in Figure 6-24 below.





(e)

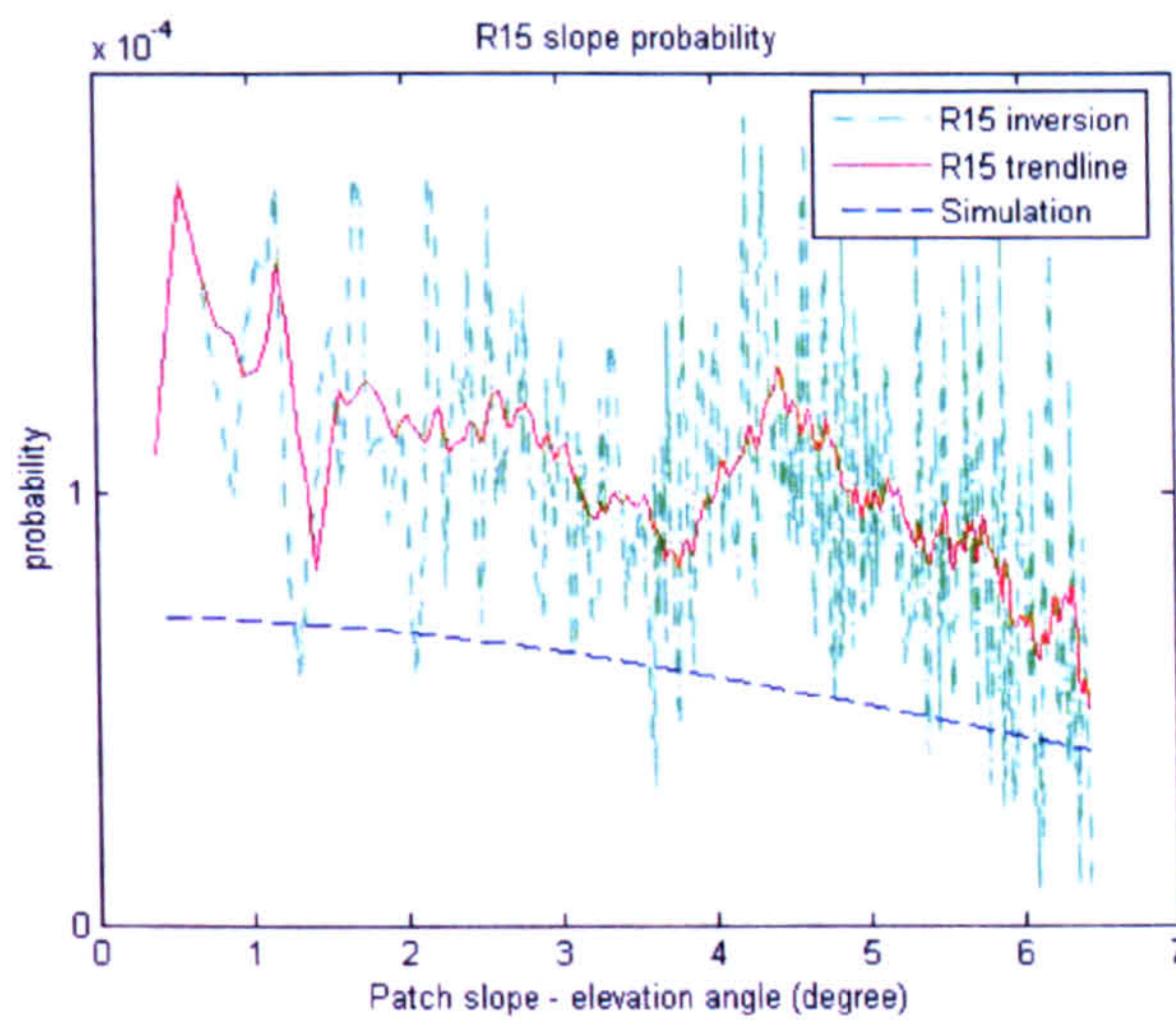
Figure 6-24: UK-DMC R18 DDM inversion and comparison.

(a) Doppler-bias removed R18 DDM. (b) deconvolved R18 DDM.

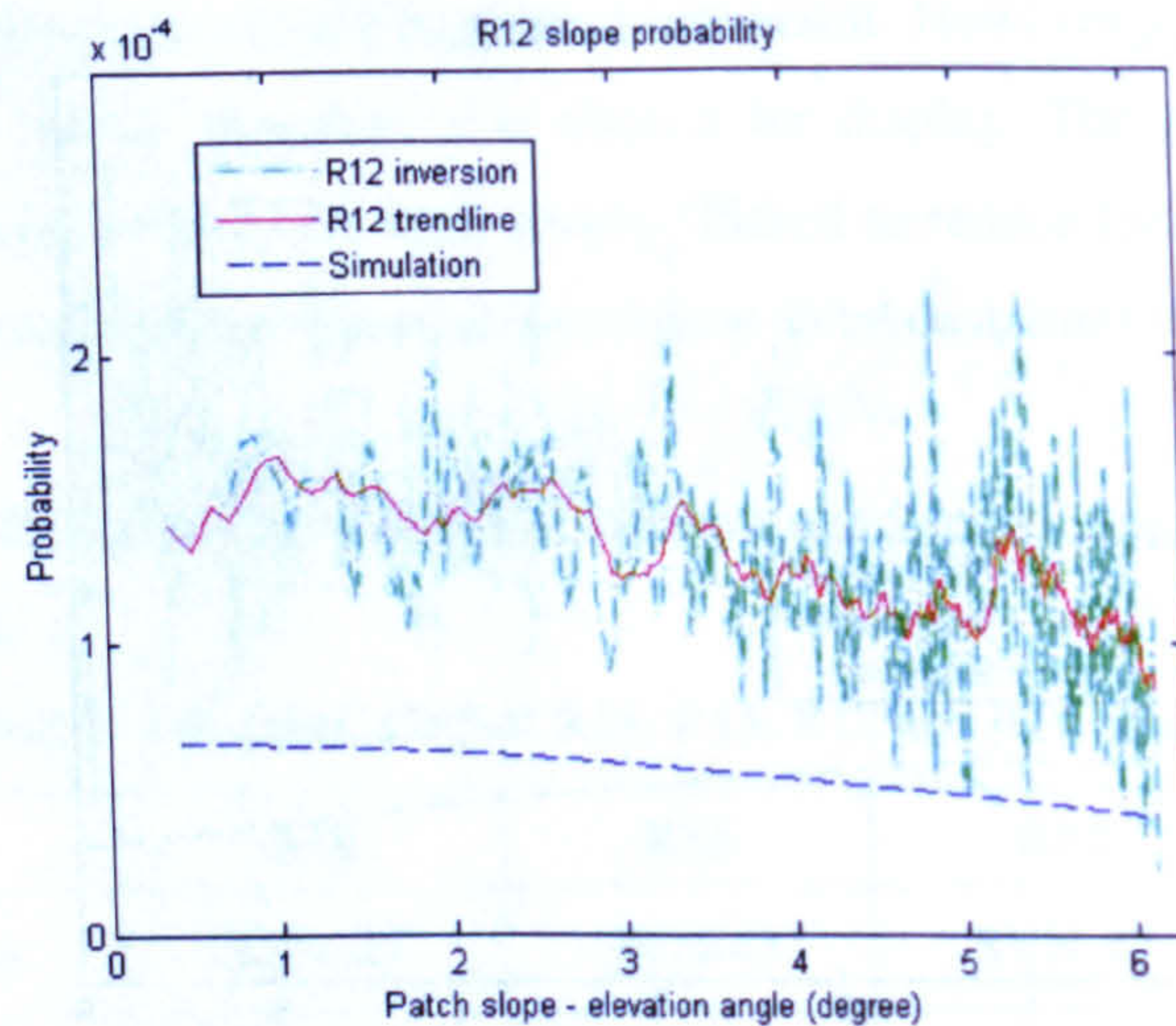
(b) inversed spatial energy map (with antenna pattern). (d) inversed slope probability map.

(e) slope probability comparison between the R18 inversion output and Gaussian simulation.

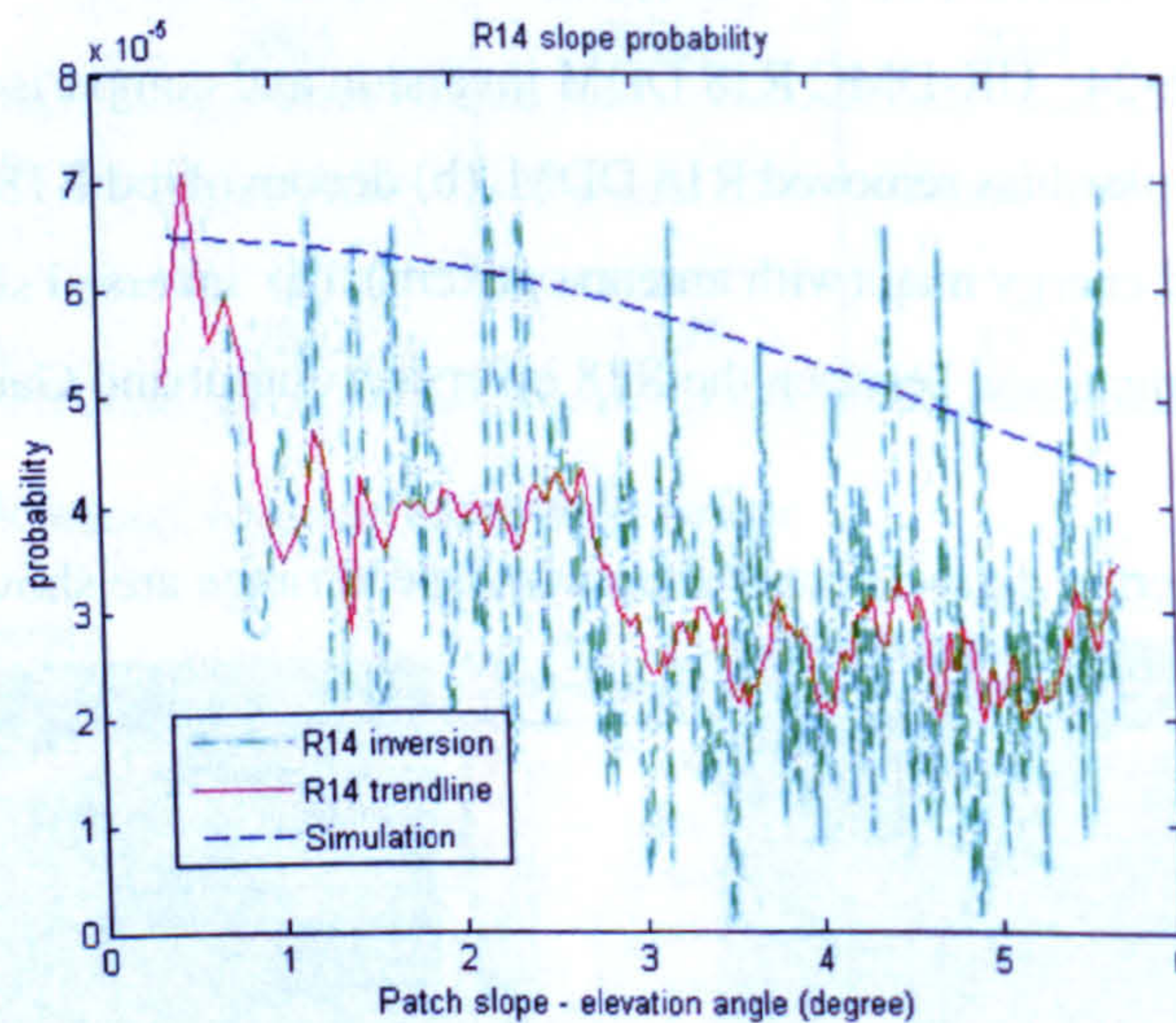
The inversion results of other datasets in medium wind speed range are shown in Figure 6-25.



(a)



(b)



(c)

Figure 6-25: 1-D inversion results of R15 (a), R12 (b) and R14 (c).

R18, R15, R12 and R14 datasets have similar wind speed condition, around 7 to 8 m/s. As seen in Figure 6-24(e) and Figure (6-25), the inversion probability curves of R18, R15 and R12 are all above the Elfouhaily Gaussian predictions. This phenomenon agrees with the conclusion in [Soulat 2004], which states that the Gaussian assumption is more conservative than the experimental derivation of slope statistics. Nevertheless, as an exception, the R14 inversion is lower than the expected value, as seen in Figure 6-25 (c). One possible explanation for this is the difference in observing incident angles between R14 and other datasets. Refer to Table 4, the incident angle of R14 is only 1.8 degrees, much smaller than the incident angles of R18, R15 and R12 (20 ~ 30 degrees). It was identified earlier that the wind sensitivity of the Elfouhaily model depends on incident angle (Figure 4-26). For larger incident angles, less short wavelength waves are visible to receiver and the slope PDF parameters slightly decrease, however, the effect is very small and ignorable in our DDM

simulation study. The above results from real data inversion, in this early state, suggest that the incident angle or other observing conditions may have greater effect on GPS-R measurements. If this assumption is true, specially selected observation conditions can be predefined to enhance the sensitivity of sea states derivation in GPS-R technique. This question is open to future research. More DDM inversions and finer geometric modelling could help to find the answer.

For the R10 dataset, with a 10 m/s wind speed, the specular point area seems to reflect more energy than predicted.

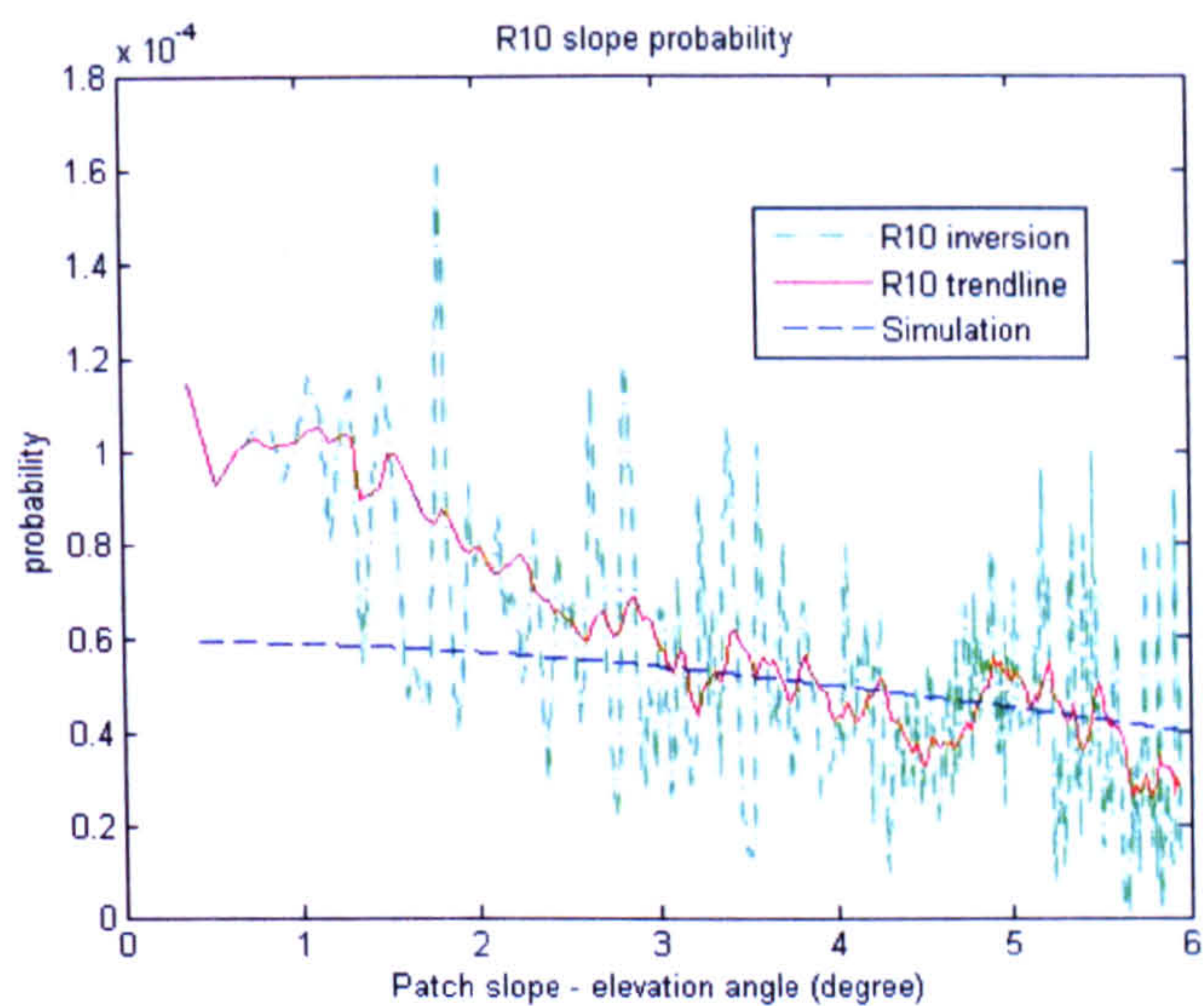


Figure 6-26: 1-D inversion result of R10.

Currently, the inversion results of only several real datasets can not conclude what type of statistical distribution pattern is correct for GPS-R scatterometric model. More data analysis and filter technique are necessary for the extraction of an empirical slope statistical model.

6.5 Conclusions

Chapter 5 overviews the whole proposed DDM inversion methodology and describes first two steps in DDM inversion. This chapter follows the discussion in Chapter 5, focusing on the inversion procedure from Delay-Doppler bins to spatial patches.

Three methods are proposed to solve the Bin-to-Patch inversion problem. The Average Method assumes that the patches with same Delay and Doppler attributes have the same slope probability, the energy of one Delay-Doppler bin is therefore averaged into its corresponding patches. This method performs well, however, further outlier removing algorithm needs to be applied on inversed results to reveal the valid points. The Differential Method uses two bins

as input and a set of algorithm is established to calculate their corresponding patch energy. The discussion on this method focuses on the inversion noise problem from another viewpoint. The initial simulated inversion test shows the considerable effect of the Doppler cut-off frequency in strong signal area. These two methods both can output 2-D spatial slope probability map. The results have good correlations with the original inputs. With an outlier removing algorithm in the future we should be able to remove the singularities in DDM inversions automatically and reveal the original slope probability truth.

The 1-D Inversion Method, sacrifices the information in Doppler dimension and only consider the statistical properties of slopes' elevation angle. This method has better robustness against noise in simulations than the first two methods, therefore more UK-DMC real DDMs are applied in inversion experiment with this method, and a low wind speed dataset is chosen to calibrate the results of other inversions. In the medium wind speed range, the inversed slope probability curves with $20^{\circ}\sim 30^{\circ}$ incident angles are generally higher than the Gaussian expectations. One dataset with an exceptional small incident angle has the opposite outcome, which suggests the observing geometry may weight more in the GPS-R slope statistical model. The inversion of 10 m/s wind speed case shows the disagreement of slope probability curves around specular point area, but has better correlation outside the central area.

The simulated and real DDM inversion experiments, presented in this chapter, prove that the DDM inversion is a possible solution to extract a wave slope statistical model, empirically from GPS-R observations.

References

[Fischler 1981] M.A. Fischler and R.C. Bolles, Random Sample Consensus: A Paradigm for Model Fitting with Applications to Image Analysis and Automated Cartography, Comm. of the ACM Vol.24, pp 381-395, June 1981

[Fisher 2002] R.B. Fisher, The RANSAC (Random Sample Consensus) Algorithm, May 2002, http://homepages.inf.ed.ac.uk/rbf/CVonline/LOCAL_COPIES/FISHER/RANSAC/

[Kojima 2007] H. Kojima, K.Kimoto and Y. Usuda, Corresponding Point Detection by Harris Corner Detector and RANSAC, and Attitude Variation Estimation by Eight Point Algorithm, AAS 07-350, AAS Astrodynamics Specialist Conference, August 2007

[Konouchine 2005] A. Konouchine, V. Gaganov and V. Vezhnevets, AMLESAC: A New Maximum Likelihood Robust Estimator, Graphicon-2005, 2005

[Soulat 2004] F. Soulat, Sea Surface Remote-sensing with GNSS and sunlight reflections, PhD thesis, University Politecnica de Catalunya / Starlab, 2004

[Wiki 2008] RANSAC, Wikipedia website, <http://en.wikipedia.org/wiki/RANSAC>, January 2008

Chapter 7. Geometric Modelling of Wave Slope PDF

7.1 Introduction

Previous chapters have described how to generate a DDM from a slope probability distribution (Chapter 3 & 4), and how to inverse a DDM back to the slope probability map (Chapter 5 & 6). From the DDM simulations, we have concluded that the current wave probability model is not accurate enough for GPS-R scatterometric technique. Therefore a novel method is proposed to inverse DDMs to spatial slope probability maps, for the purpose of deriving an empirical wave statistical model. Our study has proved the validity of the DDM inversion scheme. However, to extract a practical wave slope model, which can be employed in GPS-R applications, a large amount of effort is still needed in data collecting, archiving and analysing. This will be part of the future work proposed to continue the research. Meanwhile, lack of local ground truth reference, at exact position and time of GPS-R received data, introduces difficulties in validating empirical derivations. Due to these constrains, we are motivated to explore some new directions for our wave slope statistical research. This chapter is dedicated in modelling wave slope distribution from a new viewpoint.

The time-variable buoy measurements are used as ground truth to validate some slope probability functions, such as the Elfouhaily slope PDF. When applying the Z-V model to calculate the NRCS parameter, we also consider the time-varying slope probability property for each patch. All patches within reflection area are assumed to follow the same temporal slope probability distribution. As above reasons, we can conclude that our previous discussion mainly concentrates on the temporal slope probability attribute. However, the random nature of ocean waves makes it reasonable to assume that the temporal and spatial statistical distributions of wave slopes are similar, which means, slope probability distribution of all patches within the reflection area at one time instance should be similar to the time-variant slope statistical property of one patch during a period of time. If this assumption is valid, we can alternatively study the spatial wave slope distributions, which is easier to simulate and analyse than temporal distributions.

This chapter proposes a geometric modelling method to calculate statistical properties of sea surface slopes under different wind conditions. According to the basic definition of discrete probability distribution, the probability density value of one certain slope angle equals to the number of slopes with certain angle divided by the total population. In other words, the probability of a wave slope angle can be “counted” straightforwardly from a spatial sea surface simulation field, instead of being derived from wave spectrum. Nowadays, spatial sea surface simulation technique, such as ocean scenario special effects in films and animations, is developing quickly in computer graphic (CG) applications. If these modelling and simulation techniques can be used to study the wave slope statistical characters, they may provide another solution to validate empirical GPS-R wave models and bringing fresh opinions in ocean scatterometric research.

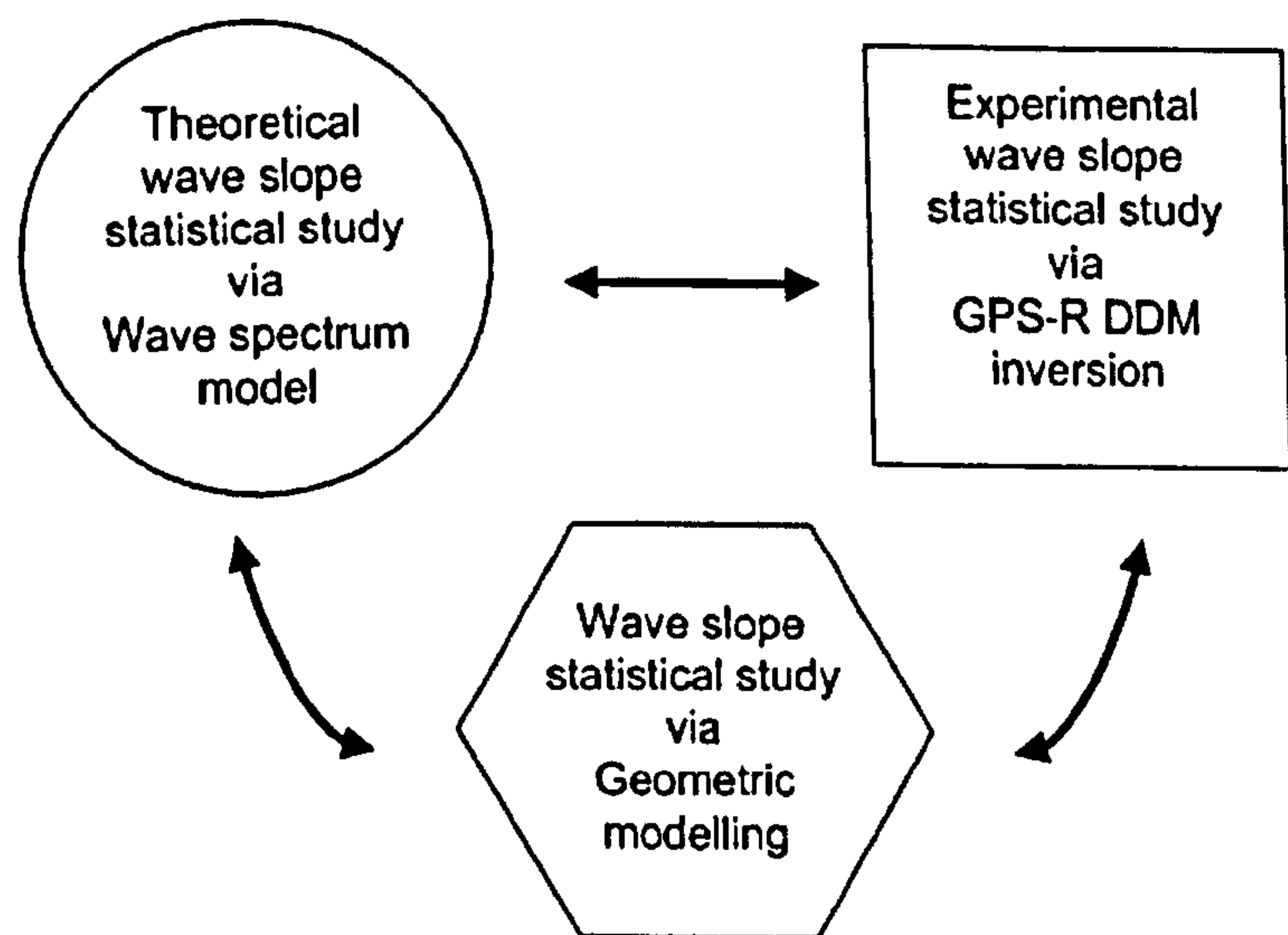


Figure 7-1: Three aspects of wave slope statistical study.

As shown in Figure 7-1, theoretical wave slope PDF simulations and experimental slope statistical research, via GPS-R DDM inversions, have been discussed in Chapter 3 & 4 and Chapter 5 & 6 respectively. The third approach, extracting wave slope statistical properties via geometric modelling, provides another viewpoint to interpret the roughness of sea surface. Such method takes advantage of existing techniques to simulate the visual effect of ocean surface. By analysing the spatial wave slope distribution with different wind conditions and under different geometry cases (which may not be easy to access from real data), we can have better understanding of real reflection data. Based on such knowledge, we can either adjust the theoretical wave slope model by adding more factors, or modifying the weights of current parameters in the model.

In the following sections, we will first discuss the modelling technique of wave height field simulation and slope probability estimation. Secondly we will look into the sensitivity analysis, which concerns the effects of wind speed and wave direction, as compared to the Elfouhaily modelled slope PDFs. Finally we will model the effect of observing incident angle in GPS-R reflections.

7.2 Geometric modelling methodology

7.2.1 Wave height field modelling

The Pierson-Moskowitz (P-M) wave spectrum model, as mentioned in section 3.2.2, is one of the ideal empirical wind-wave models based on a full developed sea condition. The P-M model is used to simulate wave height field as in [Hill 2001]. A P-M spectrum is first generated, with a wind speed input, to filter the frequency content of a 2-D white noise image. Then the result is attenuated in certain directions to simulate the linear wave phenomenon. This technique was originally developed to render ocean scenes, in which three wind speed spectra were summed up together with additive noise to generate a more realistic sea wave scenario. For our modelling research, we only use single wind speed input and noise-free frequency domain images to generate wave height field, as shown in Figure 7-2 (a). Figure 7-2 (b) is the amplified detail figure of a small area in (a).

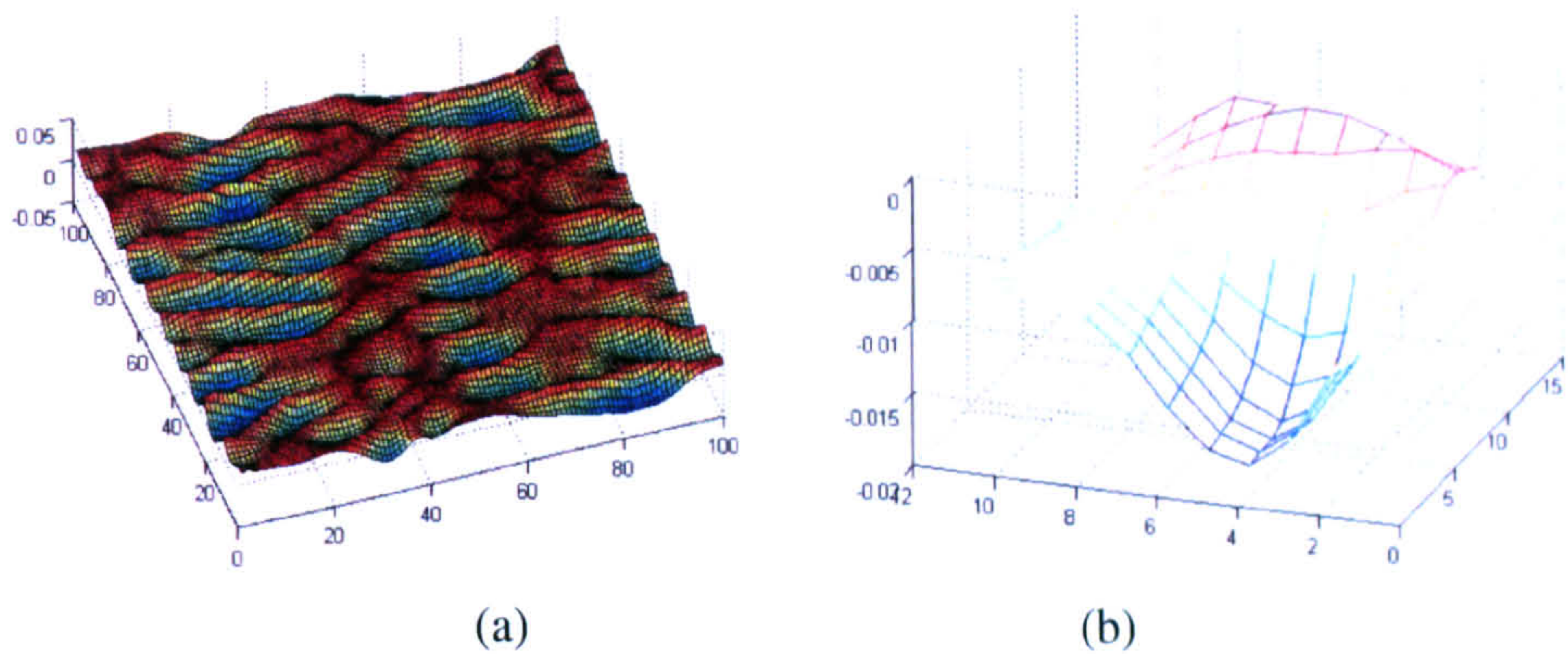


Figure 7-2: Wave height field simulation under 8 m/s wind speed.

(a) overall field. (b) partial details.

7.2.2 Slope angle estimation

Wave height field simulation naturally gives a grid feature with patches, as shown in Figure 7-2(b). However, the four adjacent points are not necessary on the same plane. We have to find a general solution to estimate the slope angle for each patch. The key step in estimation is

to find the normal vector of the grid surface. If we define a parameterised plane $\Phi(u, v)$, its normal vector can be expressed as the cross product of two tangent vectors [Nykamp 2005], as modelled in Figure 7-3.

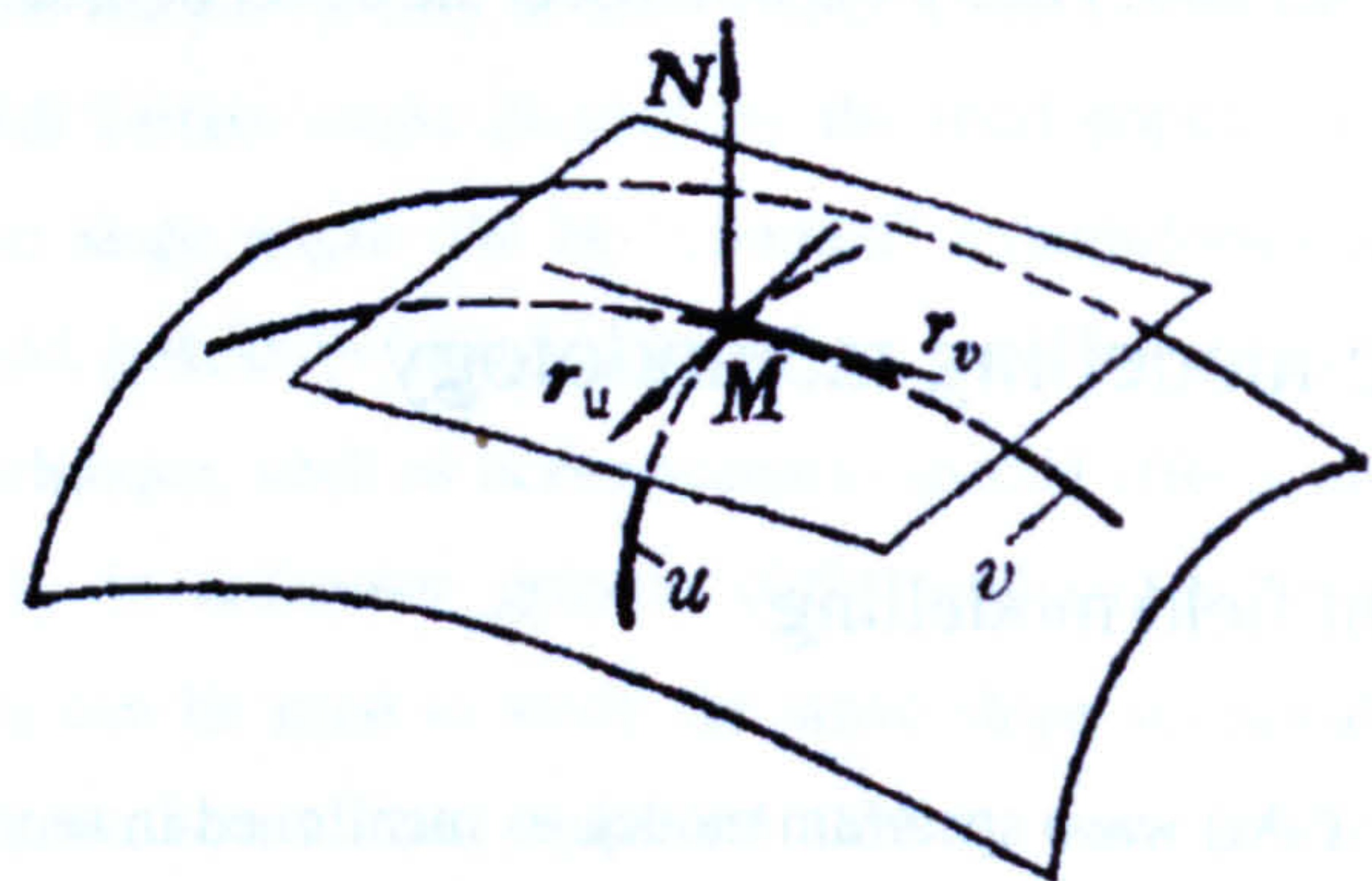


Figure 7-3: Normal vector calculation for a curve surface [Croft 2003].

The description in Figure 7-3 can be summarised in:

$$\vec{N} = \frac{\partial \Phi}{\partial u} \times \frac{\partial \Phi}{\partial v} \tag{7-1}$$

Figure 7-4 below zooms in the details of one grid of the wave height field in Figure 7-2 (b):

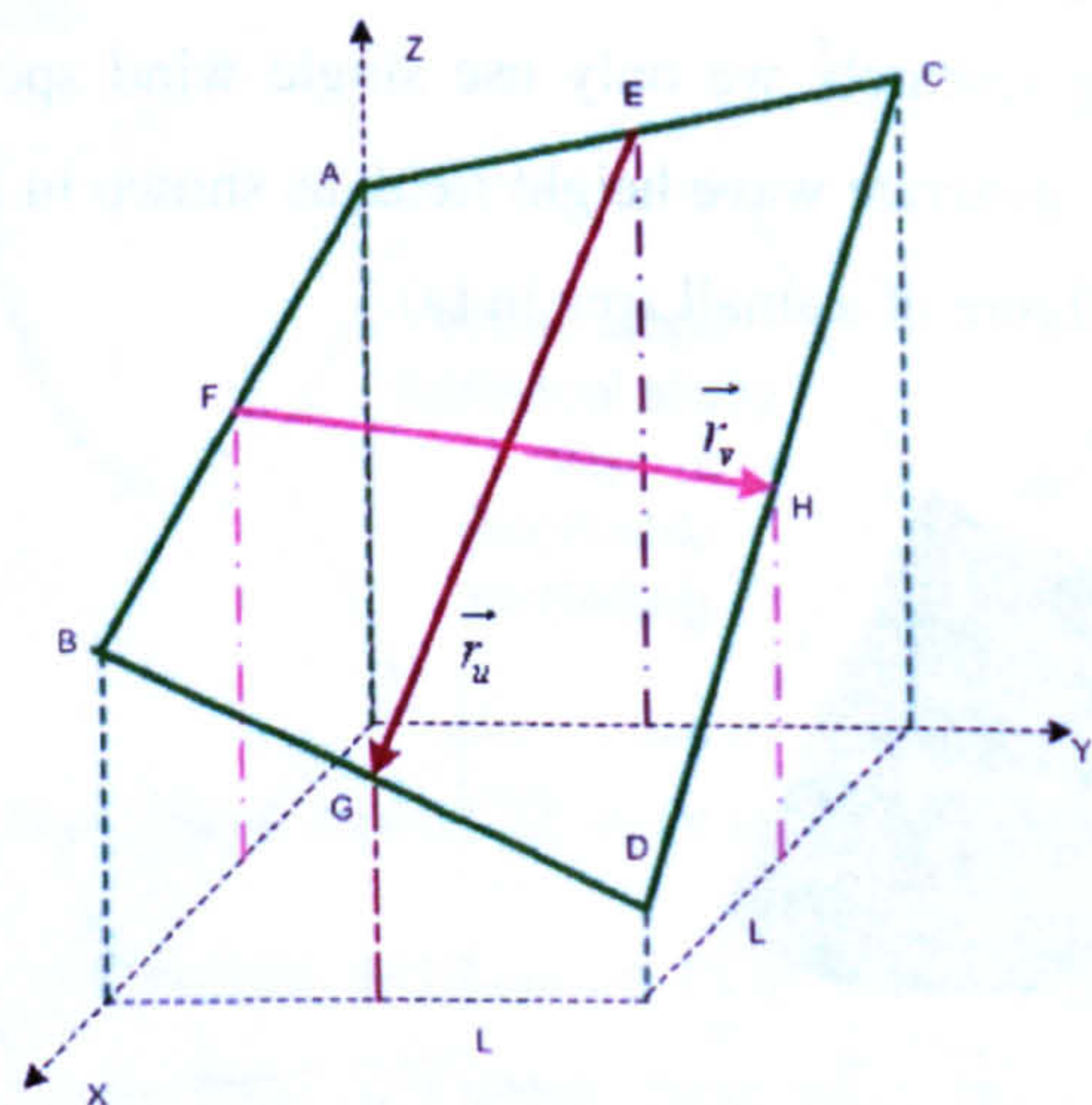


Figure 7-4: Normal vector estimation for one patch on wave height field.

In Figure 7-4, A, B, C, D are four wave height points created from the simulation, not on the same plane. E, F, G, H are four middle points for four edge lines (green solid lines). To estimate the normal vector, we define $\vec{r}_u \equiv \overrightarrow{EG}$ and $\vec{r}_v \equiv \overrightarrow{FH}$, then the unit normal vector for curved surface \overline{ABCD} can be expressed as:

$$\hat{N} \approx \frac{\vec{r}_u \times \vec{r}_v}{|\vec{r}_u \times \vec{r}_v|} \tag{7-2}$$

We use A_z, B_z, C_z and D_z to represent the magnitudes of four boundary points (green dash lines) and E_z, F_z, G_z, H_z as the magnitudes of four middle points (magenta and brown dash lines). L is the length of patch grid. The projection area of one square wave patch on x, y plane is L^2 . According to Figure 7-4, we have vector definitions as:

$$\begin{cases} \vec{r}_u = (L, 0, G_z - E_z) \\ \vec{r}_v = (L, 0, H_z - F_z) \end{cases} \quad (7-3)$$

Their cross product can be written as:

$$\begin{aligned} \vec{r}_u \times \vec{r}_v &= (r_{uy} \cdot r_{vz} - r_{uz} \cdot r_{vy}) i + (r_{uz} \cdot r_{vx} - r_{ux} \cdot r_{vz}) j + (r_{ux} \cdot r_{vy} - r_{uy} \cdot r_{vx}) k \\ &= (-r_{uz} \cdot r_{vy}) i + (-r_{ux} \cdot r_{vz}) j + (-r_{uy} \cdot r_{vx}) k \\ &= -(G_z - E_z) \cdot L i + -(H_z - F_z) \cdot L j + L^2 k \end{aligned} \quad (7-4)$$

The slope elevation angle can be expressed with the components of the vector in Equ. (7-4), i.e.,

$$\begin{aligned} S &= \arctan \left(\frac{\sqrt{(G_z - E_z)^2 L^2 + (H_z - F_z)^2 L^2}}{L^2} \right) \\ &= \arctan \left(\frac{\sqrt{(G_z - E_z)^2 + (H_z - F_z)^2}}{L} \right) \end{aligned} \quad (7-5)$$

The slope angles along x and y directions will be

$$\begin{cases} S_x = \arctan \frac{-(G_z - E_z)}{L} \\ S_y = \arctan \frac{-(H_z - F_z)}{L} \end{cases}, \text{ where } \begin{cases} E_z = (A_z + C_z)/2 \\ F_z = (A_z + B_z)/2 \\ G_z = (B_z + D_z)/2 \\ H_z = (C_z + D_z)/2 \end{cases} \quad (7-6)$$

According to the above modelling procedure, we can estimate the slope angles, along x and y axes, for each patch in the wave height field. Statistically, a 2-D slope probability density map can be generated by counting all possible slope angles on a simulated wave height surface, which is similar to the way of generating histogram of an image. An example of wave height field simulation and its corresponding slope PDF is presented in Figure 7-5 below, under a 14 m/s, 30° wind condition and with an area of 25*25 m².

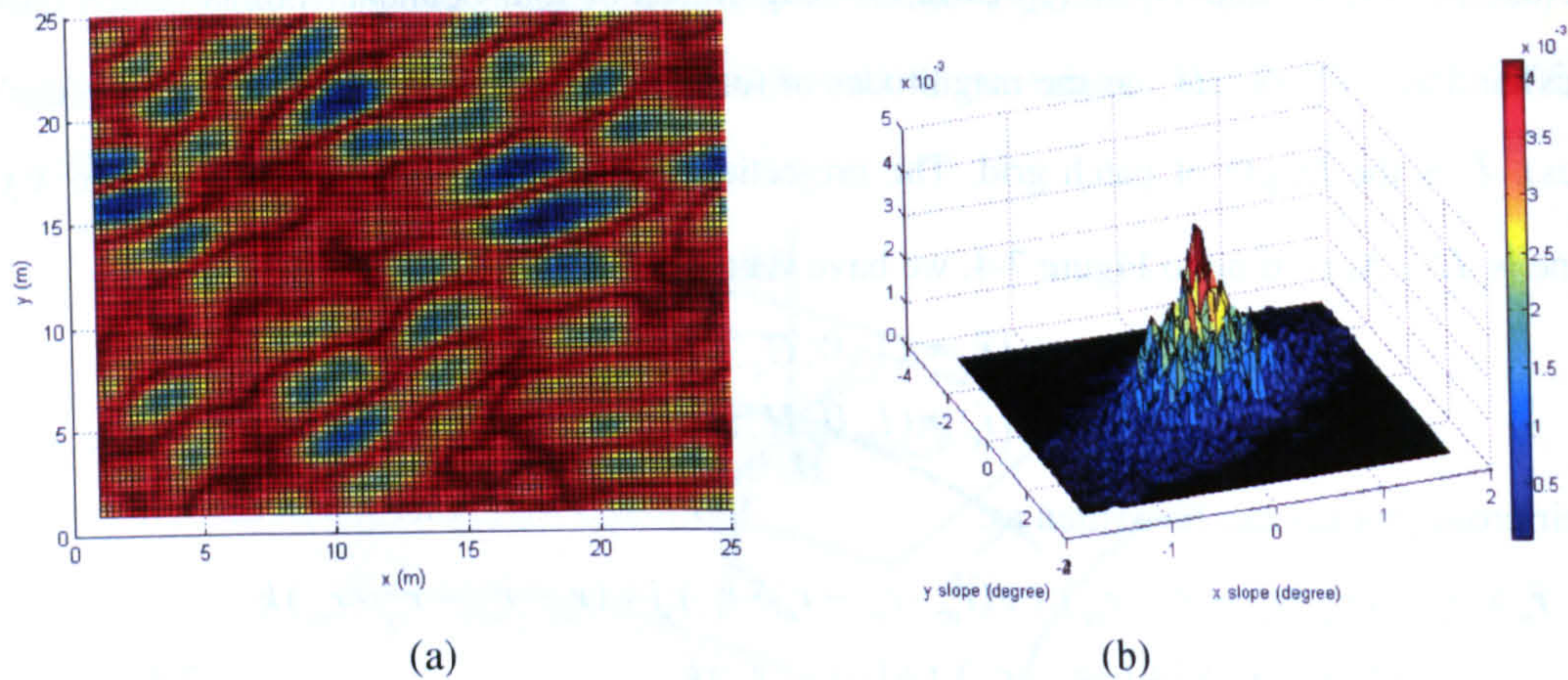


Figure 7-5: P-M modelled wave height field (a) and the corresponding slope PDF (b).

7.3 Sensitivity analysis of geometric slope PDF model

The geometric slope PDF simulation, is based on random numbers, therefore the experiments under same conditions can output similar but not identical results. Since the P-M modelled wave simulation is initially for the purpose of visual effect demonstrations, the grid size variable L can be defined by users. However L has considerable effect on the absolute slope calculation. As the reasons above, all following discussions are only qualitative analysis. The absolute slope angle values and probability properties are meaningless, due to the uncertainty of L . In all simulations below, if not mentioned individually, the whole wave area is temporarily set to $25 \times 25 \text{ m}^2$. By defining 10000 patches in such area, the grid length $L = 0.25 \text{ m}$.

The following sections focus on building a comparative relationship between wind conditions and slope probability maps, which are derived from geometric simulations. To compare with the Elfouhaily modelled slope PDFs, three aspects are considered in the geometric simulation experiments: wind speed, wind direction (or directional waves) and observing incident angle. They are the only three inputs for generating an Elfouhaily modelled slope PDF, in which wind speed is the dominant element, when wind direction and observing incident angle both are minor factors, as we previously mentioned in section 3.2.2 and section 4.4.

7.3.1 Wind speed effect

Chapter 4 has discussed the possibility of using peak values to analyse the wind sensitivity of Gaussian PDF shape. For Elfouhaily modelled slope PDFs, their peak values decrease when

wind speed grows (Figure 4-26). The P-M modelled slope PDFs, which we have derived so far, all have Gaussian-like distribution pattern, but we have not yet confirmed whether it is Gaussian distribution or not. To simplify the problem, however, we still use peak value to analyse the sensitivity of P-M modelled PDFs. For each wind speed input, we simulate 15 wave height fields and calculate their slope PDFs. The averaged PDF peak values are plotted against wind speed in the figure below.

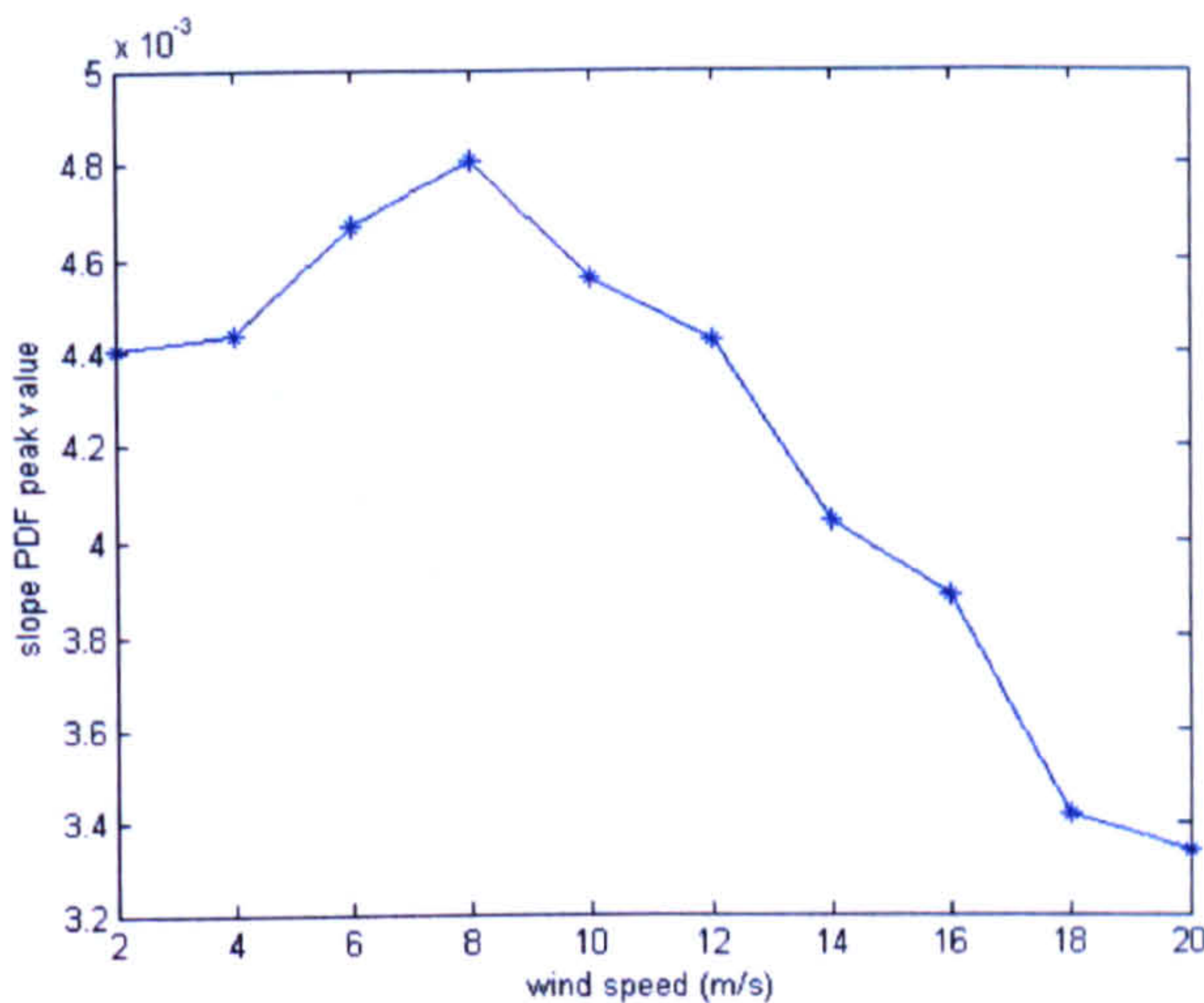


Figure 7-6: Peak value of geometric modelled slope PDF vs. wind speed.

According to Figure 7-6, slope PDF peak increases when wind speed is under 8 m/s and decreases beyond 8 m/s wind. The peak value of slope PDF represents the percentage of flat patches. According to the above result, within low wind speed range (< 8 m/s), the flat patch number increases with more windy condition. An initial guess for this phenomenon is that the ripple pattern on sea surface changes with light wind. When wind speed increases, ocean waves will have narrower crests and flatter troughs, as seen in Figure 7-7. Therefore flat patch percentage might increase in total.

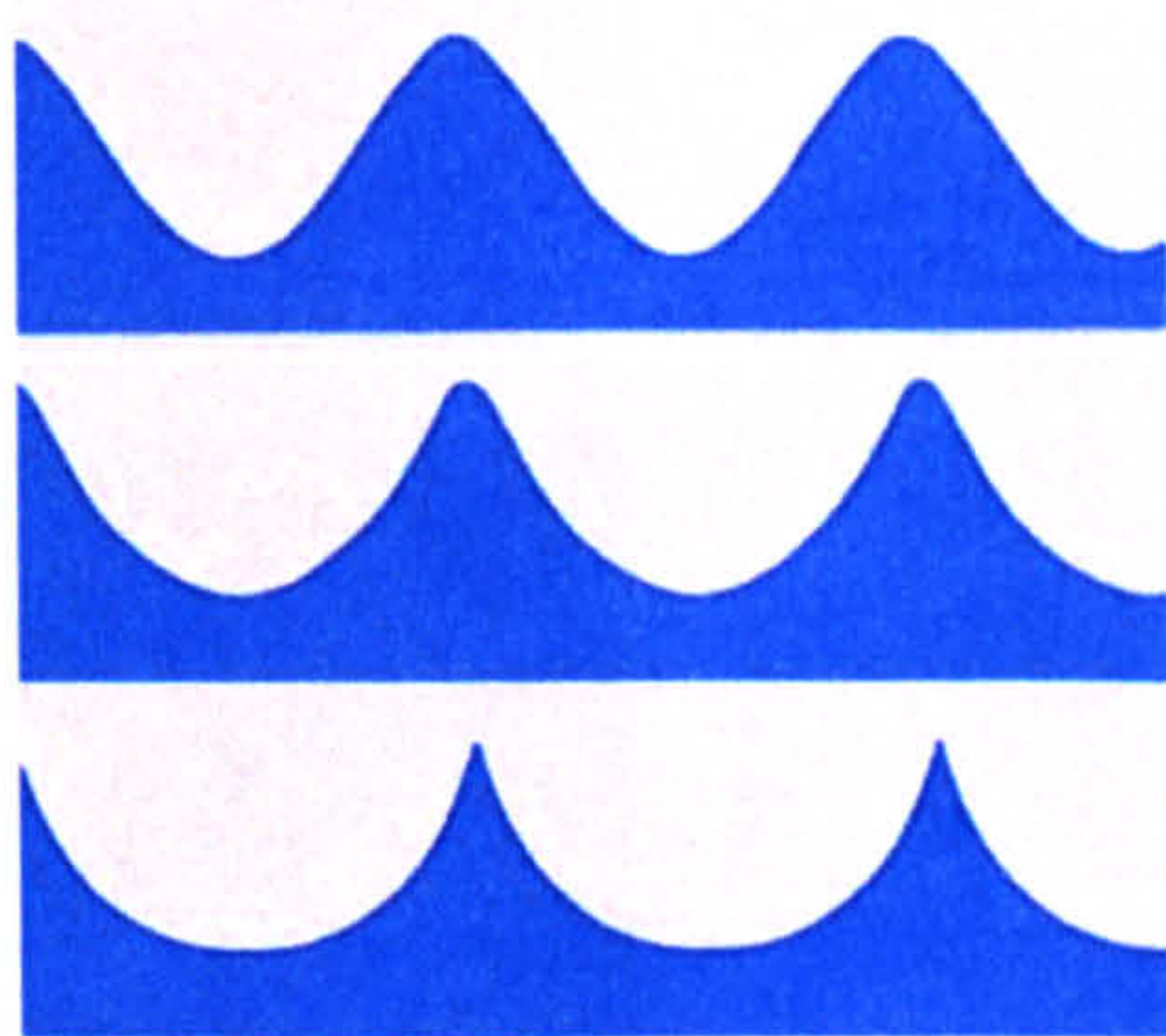


Figure 7-7: Wave pattern changing with increasing wind speed [Nave 2005].

When wind speed is above 8 m/s, the sea surface will form gravity waves, different from ripple patterns. As such the flat patch percentage will have a negative correlation with wind speed.

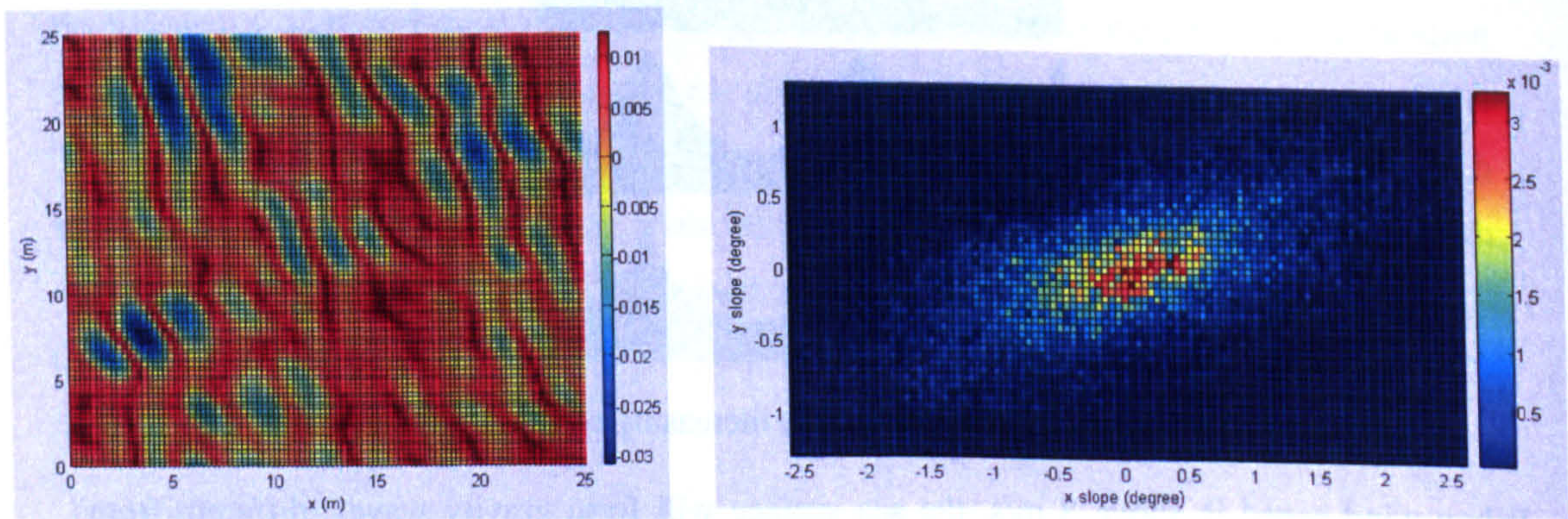
The discussion above is only for emphasising the difference between two types of slope PDFs, which are derived from the Elfouhaily model and from the geometric model respectively. Using geometric wave model to statistically characterise ocean waves is a novel direction in scatterometric field, more aspects of this topic, such as the shape and boundary information of slope PDFs, should be investigated in future studies.

7.3.2 Directional wave effect

Visually open water waves have directional phenomenon due to the wind direction effect. A 2-D slope distribution PDF should be able to reflect this effect. From the previous sensitivity analysis in Chapter 4, we have observed that the Elfouhaily modelled slope PDF changes little with different wind direction input. However, the geometric simulation experiments give different outputs. With a fixed wind speed, the peak value of slope PDF has no obvious changes, but the PDF shape and orientation are significantly affected by wave direction in our geometric wave simulations, as clearly presented in Figure 7-8.

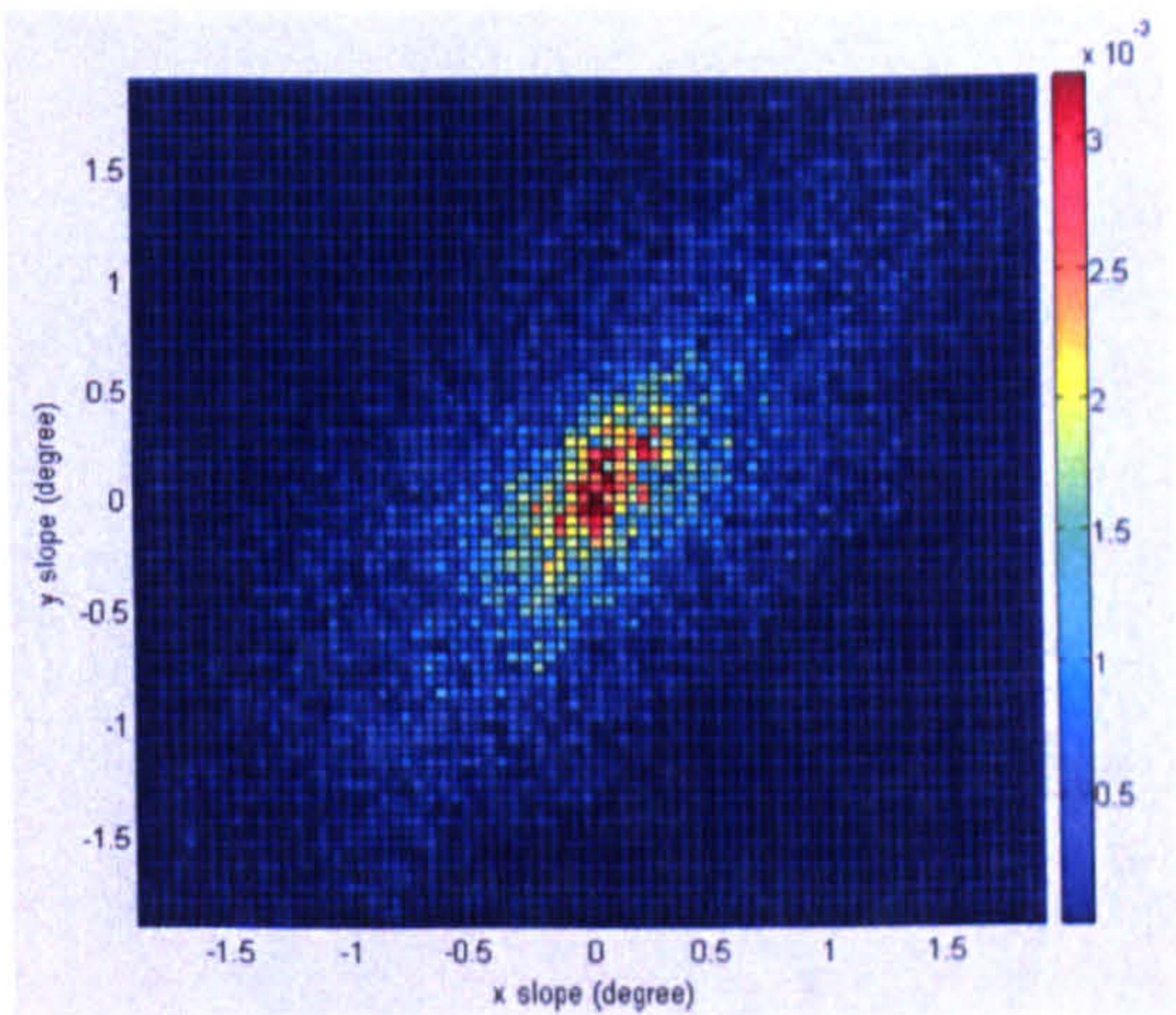
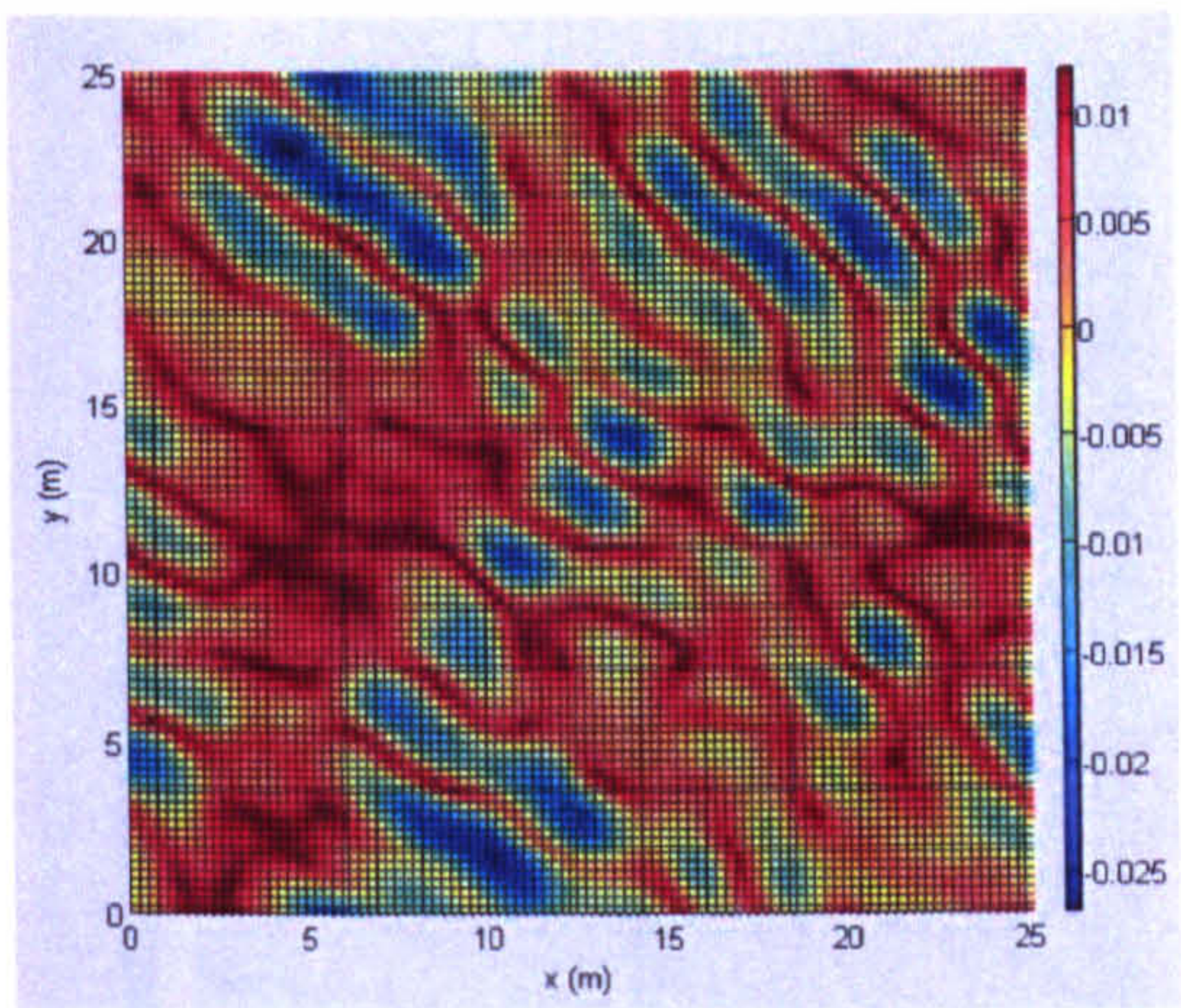
In this experiment, the wind speed is set to 14 m/s. The whole wave field area is $25 \times 25 \text{ m}^2$ and patch size is $0.25 \times 0.25 \text{ m}^2$. No extra noise is added in the wave height simulation. The x and y slope angle ranges, given below with the figures, show different slope scales on x and y directions and different shapes of the PDFs. Since the slope angle calculation involves the definition of patch length variable L , the absolute PDF values are meaningless. Our discussion focuses on the comparative variations of slope PDFs under different wave direction conditions.

Wave direction: -85°



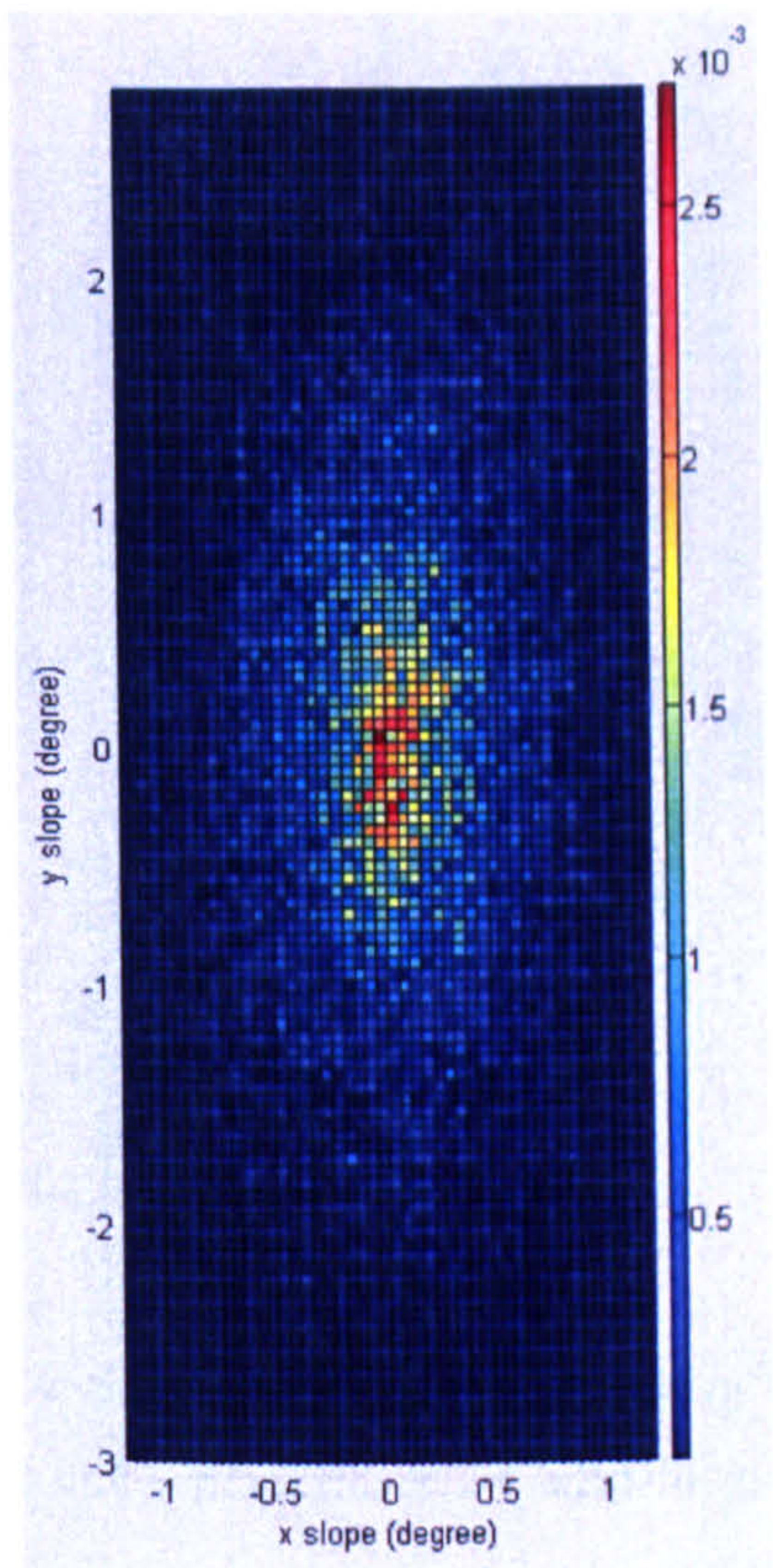
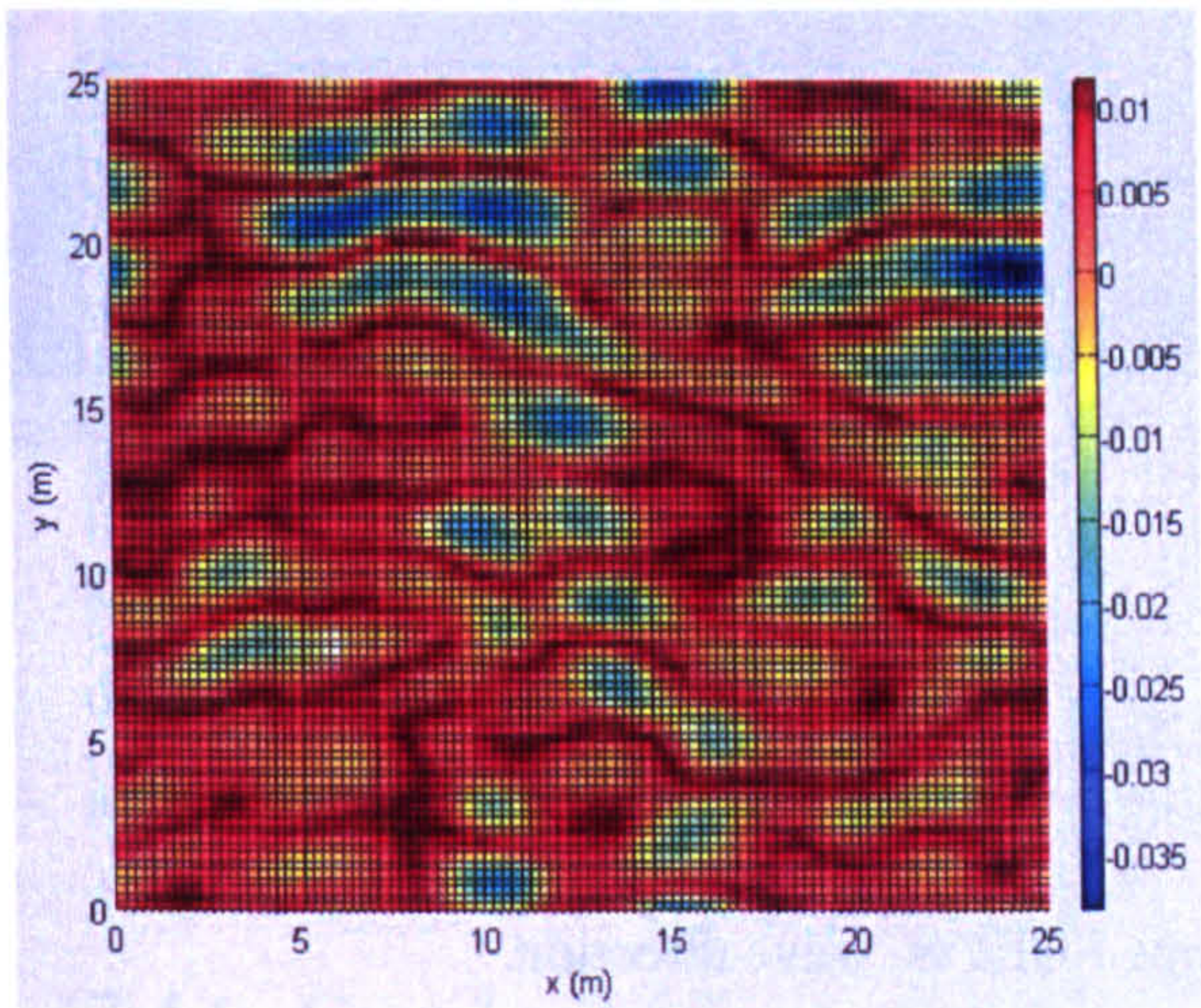
x slope range -2.6877° to 2.8916° , 112 bins, 0.05° step
 y slope range -1.4268° to 1.6146° , 61 bins, 0.05° step

Wave direction: -45°



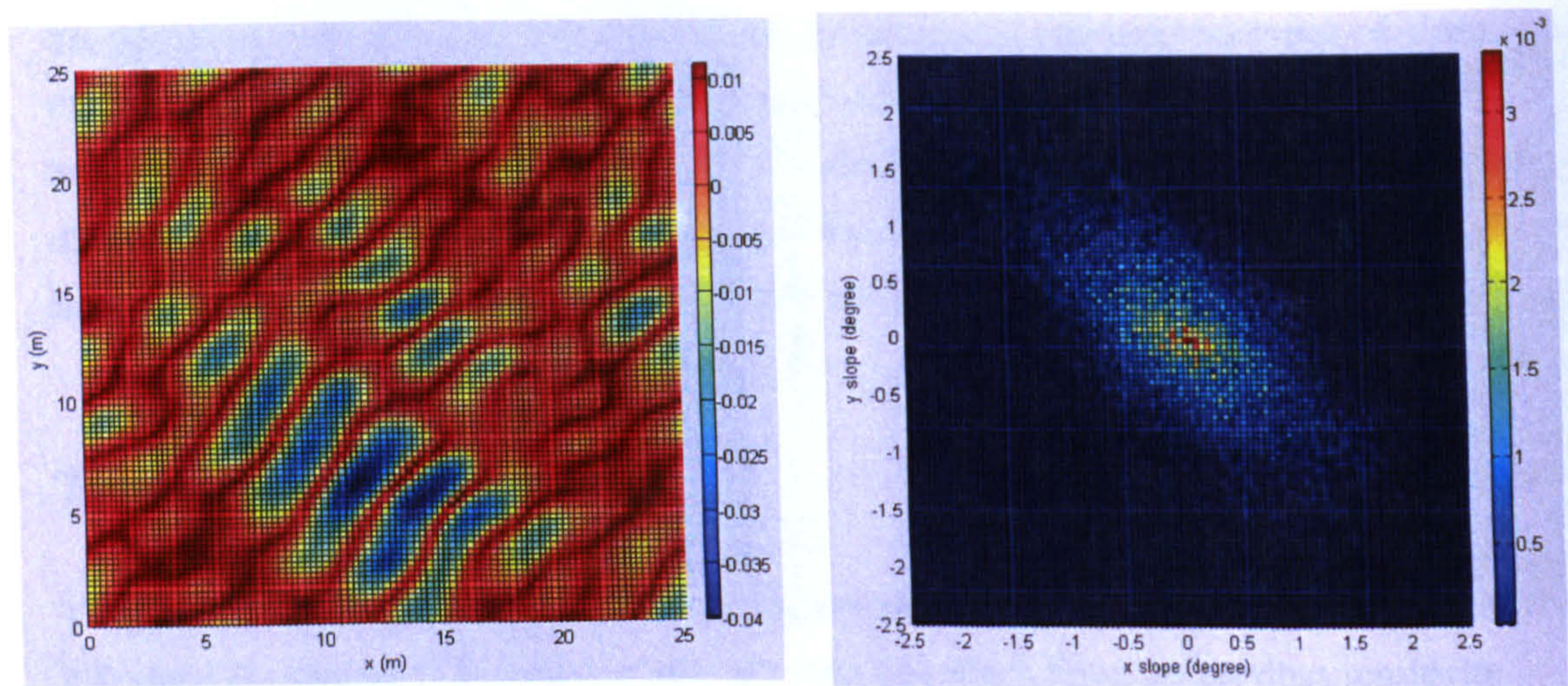
x slope range -2.1222° to 1.9568° , 82 bins, 0.05° step
y slope range -2.1057° to 2.0062° , 82 bins, 0.05° step

Wave direction: 0°



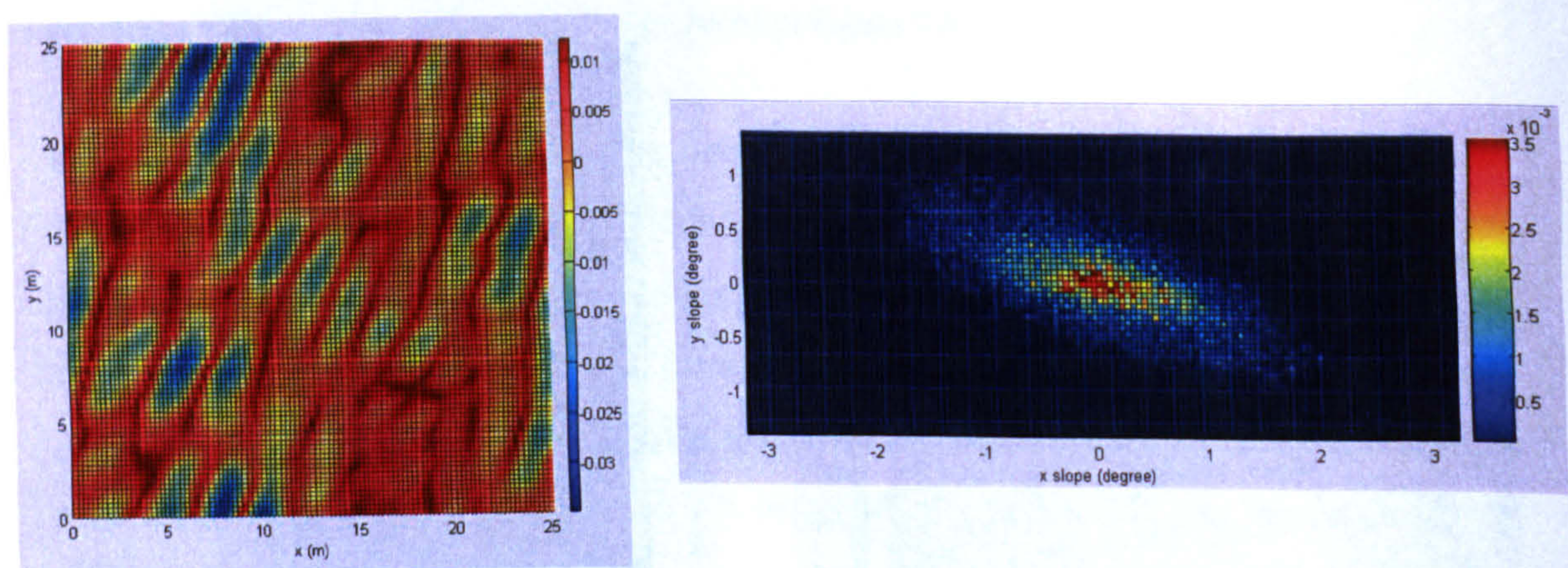
x slope range is from -1.4325° to 1.2681° , 54 bins, 0.05° step
y slope range is from -3.0454° to 2.8414° , 118 bins, 0.05° step

Wave direction: 45°



x slope range is -2.8227° to 2.5609° , 108 bins, 0.05° step
y slope range is -2.5107° to 2.6674° , 104 bins, 0.05° step

Wave direction: 85°



x slope range is -3.2292° to 3.2795° , 130 bins, 0.05° step
y slope range is -1.4350° to 1.4069° , 57 bins, 0.05° step

Figure 7-8: Geometric modelled slope PDFs vs. wave direction.

In above figures, the slope PDF rotates with wave direction. The shape of PDF is more elongated against the wave direction when the waves are along the x or y axis. Wind-driven linear wave phenomenon, as seen in our simulations, has important impact on the shape and orientation of slope PDFs. In current theoretical wave statistical models the directional wave factor has not been considered yet. This might be one of the aspects we can improve in GPS-R modelling technique in the future.

7.4 Observant incident angle effect in reflection geometry

The Elfouhaily wave spectrum model uses observing incident angle, as an input factor, to calculate an upper limit wave number for wave spectrum integration. The sensitivity analysis, as seen in section 4.4, concludes that this incident angle has only small effect on final slope PDF shape. When using P-M model for geometric slope PDF research, the slope probability is counted from spatial wave height field, independent of observing conditions. However, the observing incident angle does have effect in reflected signal pattern, which are obtained by GPS-R receivers.

For each patch in reflection area, different observing condition requires different slope angle to reflect signal into the receiver. If we define the boundary of reflection area, by setting a small value as the limit of slope probability, the size of reflection area and received energy distribution are both related to the observing incident angle. For example, if sea states and wave statistical property stay the same, the patches, which have 0.5% probability to reflect signals, are defined as the boundary of reflection area, different observing geometry then gives different boundaries and cause various patterns in received signals. We geometrically model the relationship between incident angle and required slope for a certain patch, which has a distance d to the central specular point. It is possible to use the modelling result to optimise the scheduling of GPS-R receiver to enhance the received power.

The following discussion, separated with the previous two sections, focused on developing a 1-D geometric model to connect observing incident angle and reflection area size. With the knowledge of required slope contours, the 1-D model can be easily extended to 2-D. Three different geometric situations, described in following sections, are divided into two cases according to whether the considered patch is on the side of GPS or the GPS-R receiver.

7.4.1 Case 1 - Patch on receiver's side

Figure 7-9 below describes the geometric model of required angle for a certain patch on a 1-D sea surface, with a varying observing incident angle α .

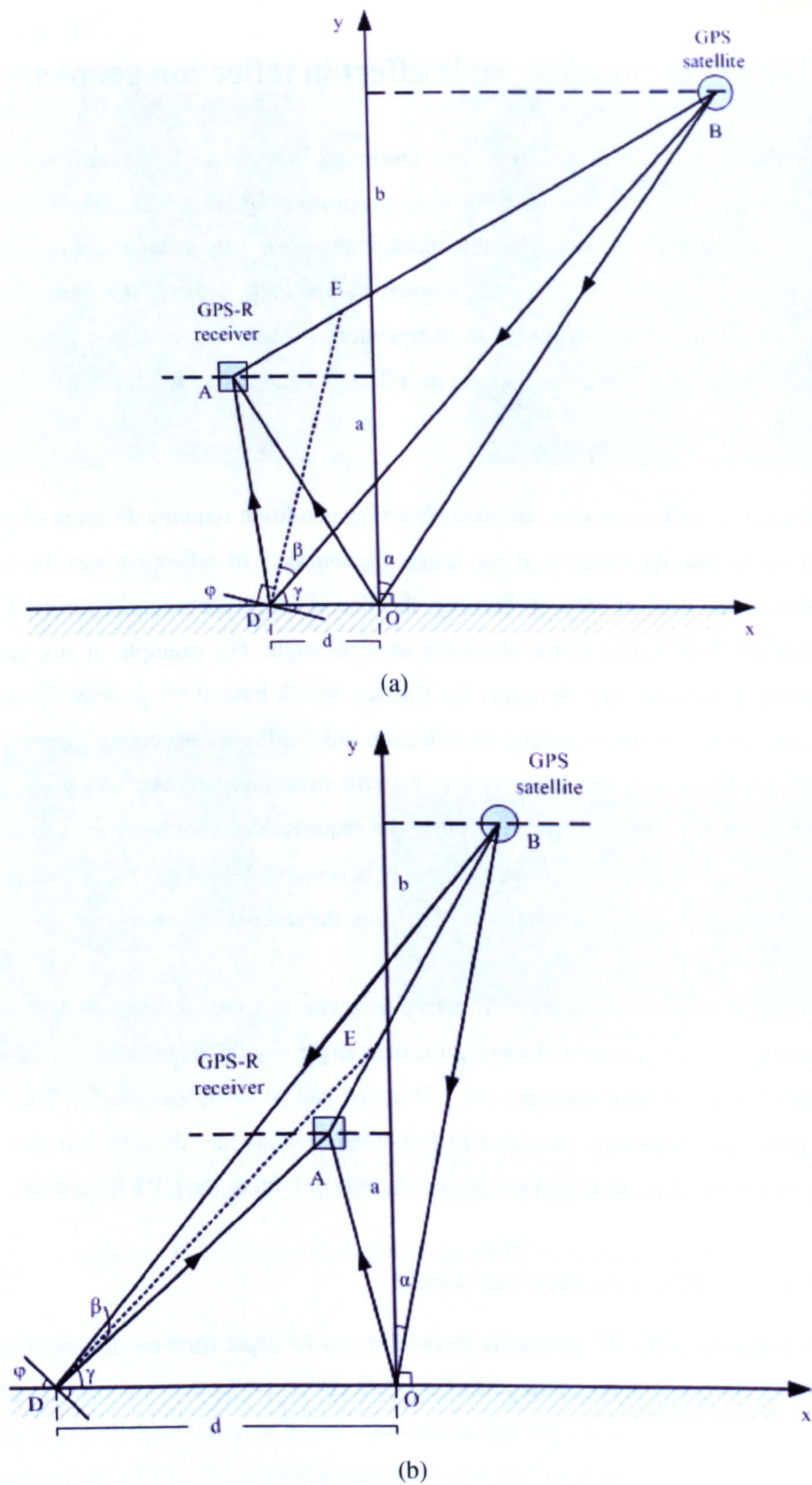


Figure 7-9: GPS-R 1-D reflection geometric model: Case 1.

The GPS and UK-DMC satellite are defined on the $x - y$ plane, with the specular point O defined as original point on the x axis. The height of UK-DMC above the sea level is a and

the GPS satellite height is b . The concerned patch D has a distance d with the specular point O . When the observing incident angle of specular point O is α , the local incident angle of patch D is β . Angle φ is the required slope angle for patch D to reflect signal to the receiver. The sum of angle β , γ and φ equals to 90° . The aim of this model is to connect the required slope φ with incident angle α , when satellite heights (a, b) and patch distance d are all constant. While Figure 7-9 (a) shows the geometry where $0 < d < a \cdot \tan \alpha$, Figure 7-9 (b) represents another situation where $d > a \cdot \tan \alpha$. These two cases, similar in vector expressions, are considered together mathematically.

As seen in Figure 7-9 above, we have the specular point O at $(0, 0)$ and key vectors $\overrightarrow{OA} (-a \cdot \tan \alpha, a)$, $\overrightarrow{OB} (b \cdot \tan \alpha, b)$ and $\overrightarrow{OD} (-d, 0)$. Therefore we have:

$$\overrightarrow{AD} = \overrightarrow{OD} - \overrightarrow{OA} = (a \cdot \tan \alpha - d, -a) \quad (7-7)$$

$$\overrightarrow{BD} = \overrightarrow{OD} - \overrightarrow{OB} = (-b \cdot \tan \alpha - d, -b) \quad (7-8)$$

m, n are defined as:

$$\begin{cases} m \equiv |\overrightarrow{AD}| = \sqrt{(a \cdot \tan \alpha - d)^2 + a^2} \\ n \equiv |\overrightarrow{BD}| = \sqrt{(b \cdot \tan \alpha + d)^2 + b^2} \end{cases} \quad (7-9)$$

\overrightarrow{DE} bisects $\angle BDA$ in $\triangle ADB$. According to Sine law in $\triangle EDB$ and $\triangle EDA$, we have:

$$\frac{|\overrightarrow{AE}|}{\sin \beta} = \frac{|\overrightarrow{AD}|}{\sin \angle AED} \quad (7-10)$$

and

$$\frac{|\overrightarrow{EB}|}{\sin \beta} = \frac{|\overrightarrow{BD}|}{\sin \angle DEB} \quad (7-11)$$

From Equ. (7-10), we can derive:

$$\frac{|\overrightarrow{AE}|}{|\overrightarrow{AD}|} = \frac{|\overrightarrow{EB}|}{|\overrightarrow{BD}|} \rightarrow \frac{|\overrightarrow{AE}|}{|\overrightarrow{EB}|} = \frac{|\overrightarrow{AD}|}{|\overrightarrow{BD}|} \rightarrow \frac{|\overrightarrow{AE}|}{|\overrightarrow{AB}|} = \frac{|\overrightarrow{AD}|}{|\overrightarrow{AD}| + |\overrightarrow{BD}|} \quad (7-12)$$

Also we have:

$$\overrightarrow{AB} = \overrightarrow{OB} - \overrightarrow{OA} = ((a+b) \cdot \tan \alpha, b-a) \quad (7-13)$$

$$\therefore \overrightarrow{AE} = \overrightarrow{AB} \cdot \frac{|\overrightarrow{AD}|}{|\overrightarrow{AB}| + |\overrightarrow{BD}|} = ((a+b) \tan \alpha, b-a) \cdot \frac{m}{m+n} \quad (7-14)$$

Therefore the bisector \overrightarrow{DE} can be expressed as:

$$\overrightarrow{DE} = \overrightarrow{AE} - \overrightarrow{AD} = \left((a+b)\tan\alpha \cdot \frac{m}{m+n} - a\tan\alpha + d, (b-a) \cdot \frac{m}{m+n} + a \right) \quad (7-15)$$

Since \overrightarrow{DE} is perpendicular to patch D , it is the normal vector for this inclining patch. The two components of \overrightarrow{DE} in x and y directions are:

$$\begin{cases} \overrightarrow{DE}_x = (a+b)\tan\alpha \cdot \frac{m}{m+n} - a\tan\alpha + d \\ \overrightarrow{DE}_y = (b-a) \cdot \frac{m}{m+n} + a \end{cases} \quad (7-16)$$

The corresponding slope angle φ can be expressed as:

$$\frac{1}{\tan(\beta + \nu)} = \frac{\overrightarrow{DE}_x}{\overrightarrow{DE}_y} = \tan\varphi \quad (7-17)$$

$$\varphi = \tan^{-1} \frac{(a+b)\tan\alpha \cdot \frac{m}{m+n} - a\tan\alpha + d}{(b-a) \cdot \frac{m}{m+n} + a} \equiv \tan^{-1} t \quad (7-18)$$

To consider the monotonic property of Equ. (7-18) with the parameter a , we need to study the sign of the function's first derivative with a :

$$\frac{d\varphi}{d\alpha} = \frac{1}{1+t^2} \cdot \frac{dt}{d\alpha}, \text{ written as } \varphi'_\alpha = \frac{1}{1+t^2} \cdot t'_\alpha \quad (7-19)$$

$1+t^2$ is always positive, therefore we only need to consider the sign of t'_α .

$$t = \frac{(a+b) \cdot m \cdot \tan\alpha - a \cdot (m+n) \cdot \tan\alpha + d \cdot (m+n)}{(b-a) \cdot m + am + an} = \frac{(bm - an) \cdot \tan\alpha + d \cdot (m+n)}{bm + an} \quad (7-19)$$

$$t'_\alpha = \frac{\left[(bm - an) \cdot \tan\alpha + d \cdot (m+n) \right]_\alpha \cdot (bm + an)}{(bm + an)^2} - \frac{\left[(bm - an) \cdot \tan\alpha + d \cdot (m+n) \right] \cdot (bm + an)'_\alpha}{(bm + an)^2} \quad (7-20)$$

To simplify the calculation, we can define $t'_\alpha \equiv t_A/t_B$. The denominator $t_B = (bm + an)^2$ is positive, the sign of the numerator therefore decides the monotone of function $\varphi(\alpha)$.

$$t_A = \left[(bm' - an') \cdot \tan\alpha + (bm - an) \cdot \sec^2\alpha + d \cdot (m' + n') \right] \cdot (bm + an) - \left[(bm - an) \cdot \tan\alpha + d \cdot (m+n) \right] \cdot (bm' + an') \quad (7-21)$$

m and n are defined in Equ.(7-9), we have their first derivative of α as in:

$$\begin{cases} m'_\alpha = \frac{a \cdot \sec^2 \alpha}{m} \\ n'_\alpha = \frac{b \cdot \sec^2 \alpha}{n} \end{cases} \quad (7-22)$$

Apply Equ.(7-22) into Equ.(7-21), then we have:

$$t_A = \sec^2 \alpha \cdot \left[\frac{(bm^2 - an^2)}{m \cdot n} \cdot (d \cdot (b - a) - 2ab \cdot \tan \alpha) + (b^2 m^2 - a^2 n^2) \right] \quad (7-23)$$

Define $t_A = \sec^2 \alpha \cdot T$, where

$$T \equiv \frac{(bm^2 - an^2)}{mn} \cdot (d \cdot (b - a) - 2ab \cdot \tan \alpha) + (b^2 m^2 - a^2 n^2) \quad (7-24)$$

The sign of $T(\alpha)$ is the same as the sign of $\phi'_\alpha(\alpha)$

$$\frac{T}{|T|} = \frac{t_A}{|t_A|} = \frac{t'_\alpha}{|t'_\alpha|} = \frac{\phi'_\alpha}{|\phi'_\alpha|} \quad (7-25)$$

The function of T is very complex. As such, instead of obtaining an analytical solution, we try to find a numerical estimate which we can use directly in our applications. The UK-DMC and GPS satellite altitudes are set to $a = 700 \text{ km}$ and $b = 22000 \text{ km}$. The simulation result of T is shown as below:

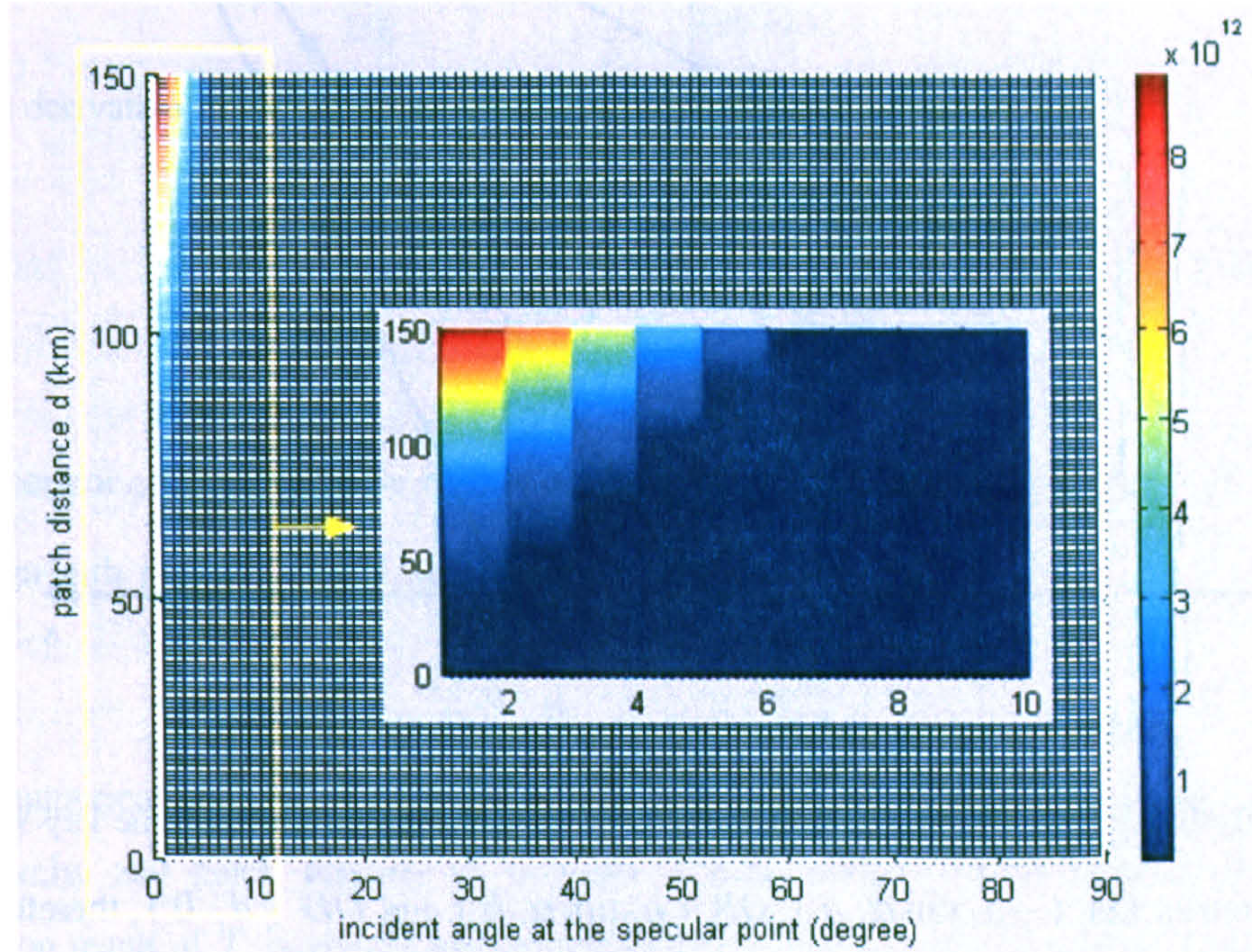


Figure 7-10: Numerical estimation of T for Case 1.

Figure 7-10 considers the sign change of T with different incident angle α and patch distance d . Negative values, which are set to 0 (deep blue colour), are the majority of this 2-

D map. This result suggests, in most of reflection cases, the required slope for a certain patch has a negative correlation with the incident angle at specular point. We also notice that a small group of values, in the left corner of the matrix, are still positive. In these situations, when incident angle α is below a value α_0 and patch distance d is more than 50 km, the required slope of one such patch will rise with the increasing α . This boundary value α_0 is related to satellite altitudes in this model. When tested by the UK-DMC orbit height (650 km ~ 700 km) and the GPS orbit height (18000 km ~ 22000 km), α_0 varies from 6° to 7° .

7.4.2 Case 2 - Patch on GPS emitter's side

When patch D is on the side of GPS, we have to consider a different geometry situation, as shown in Figure 7-11 below.

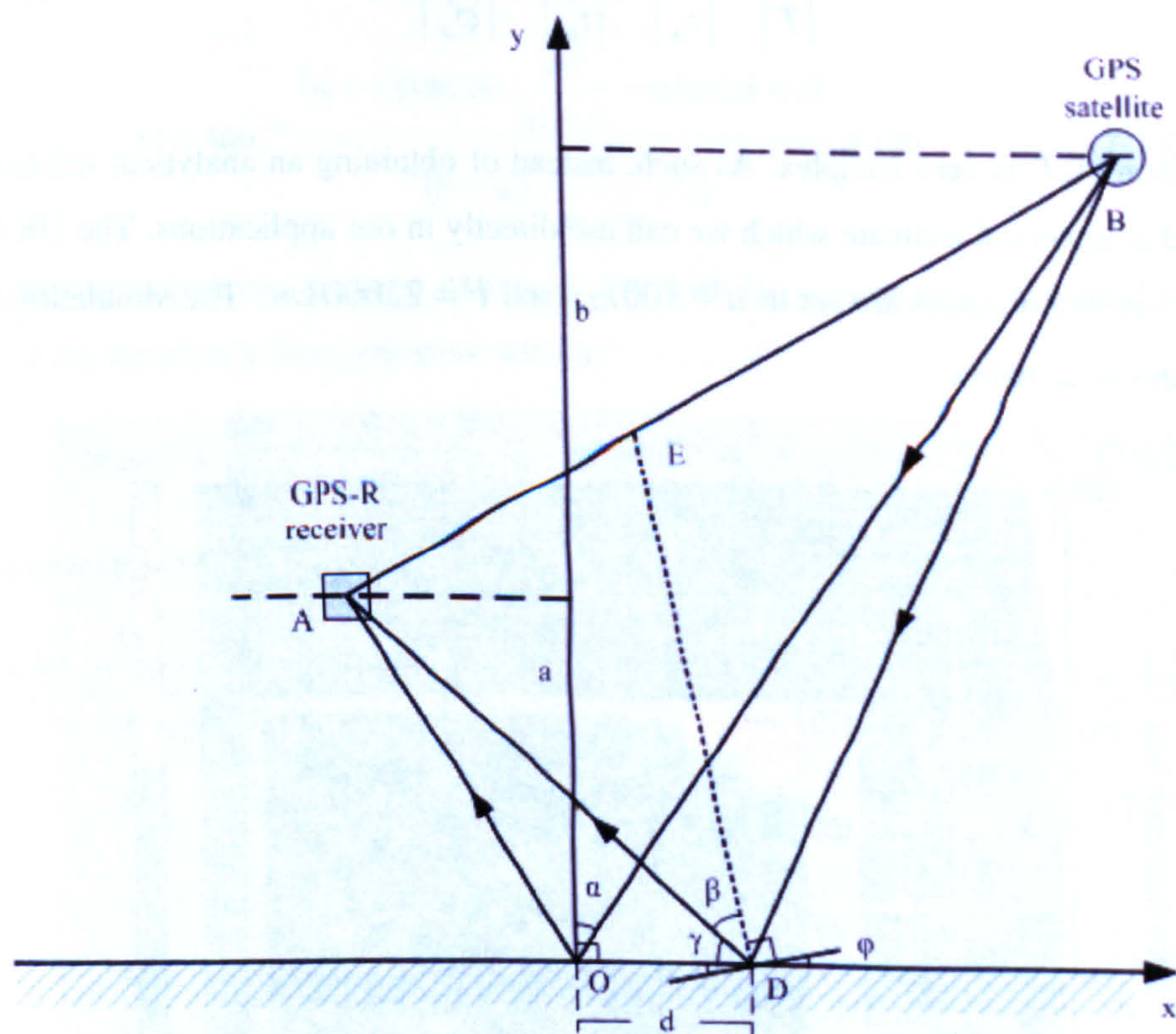


Figure 7-11: GPS-R 1-D reflection geometric model – Case 2

Similar analysis is employed here as in Case 1. If d is still defined positive, the key vectors can be written as $\overrightarrow{OA} (-a \cdot \tan \alpha, a)$, $\overrightarrow{OB} (b \cdot \tan \alpha, b)$ and $\overrightarrow{OD} (d, 0)$, therefore we have:

$$\overrightarrow{AD} = \overrightarrow{OD} - \overrightarrow{OA} = (a \cdot \tan \alpha + d, -a) \quad (7-26)$$

$$\overrightarrow{BD} = \overrightarrow{OD} - \overrightarrow{OB} = (-b \cdot \tan \alpha + d, -b) \quad (7-27)$$

Similarly we define m and n as:

$$m \equiv |\overrightarrow{AD}| = \sqrt{(a \cdot \tan \alpha + d)^2 + a^2} \quad (7-28)$$

$$n \equiv |\overrightarrow{BD}| = \sqrt{(b \cdot \tan \alpha - d)^2 + b^2} \quad (7-29)$$

According to Sine law in $\triangle EDB$ and $\triangle EDA$, we have:

$$\overrightarrow{AE} = \overrightarrow{AB} \cdot \frac{|\overrightarrow{AD}|}{|\overrightarrow{AB}| + |\overrightarrow{BD}|} = ((a+b)\tan \alpha, b-a) \cdot \frac{m}{m+n} \quad (7-30)$$

The bisector \overrightarrow{DE} can be expressed as:

$$\overrightarrow{DE} = \overrightarrow{AE} - \overrightarrow{AD} = \left((a+b)\tan \alpha \cdot \frac{m}{m+n} - a \tan \alpha - d, (b-a) \cdot \frac{m}{m+n} + a \right) \quad (7-31)$$

whose two elements can be written as:

$$\begin{cases} \overrightarrow{DE}_x = (a+b)\tan \alpha \cdot \frac{m}{m+n} - a \tan \alpha - d \\ \overrightarrow{DE}_y = (b-a) \cdot \frac{m}{m+n} + a \end{cases} \quad (7-32)$$

According to the geometry of Case 2 in Figure 7-11, $\overrightarrow{DE}_x < 0$ and $\varphi > 0$, so we have:

$$\tan \varphi = \frac{-\overrightarrow{DE}_x}{\overrightarrow{DE}_y} = \frac{-(bm - an) \cdot \tan \alpha + d \cdot (m+n)}{bm + an} \equiv t \quad (7-33)$$

The first derivative of t with respect to α is:

$$t'_\alpha = \frac{[-(bm - an) \cdot \tan \alpha + d \cdot (m+n)]'_\alpha \cdot (bm + an)}{(bm + an)^2} - \frac{[-(bm - an) \cdot \tan \alpha + d \cdot (m+n)] \cdot (bm + an)'_\alpha}{(bm + an)^2} \quad (7-34)$$

The numerator of t'_α can also be written in the format of $(1 + \sec^2 \alpha) \cdot T$, where T has the same sign with φ'_α .

$$T = \frac{bm^2 - an^2}{mn} \cdot (d(b-a) + 2ab \cdot \tan \alpha) - (b^2m^2 - a^2n^2) \quad (7-35)$$

In our numerical analysis, we set altitudes of UK-DMC and GPS to 700km and 22000km respectively, and patch distance d is from 1km to 200km. Under such condition, the simulation result of T is always negative as shown in Figure 7-12. This result suggests that, when the considered patch is on the GPS's side, the required slope of the patch always decreases with the increasing incident angle α .

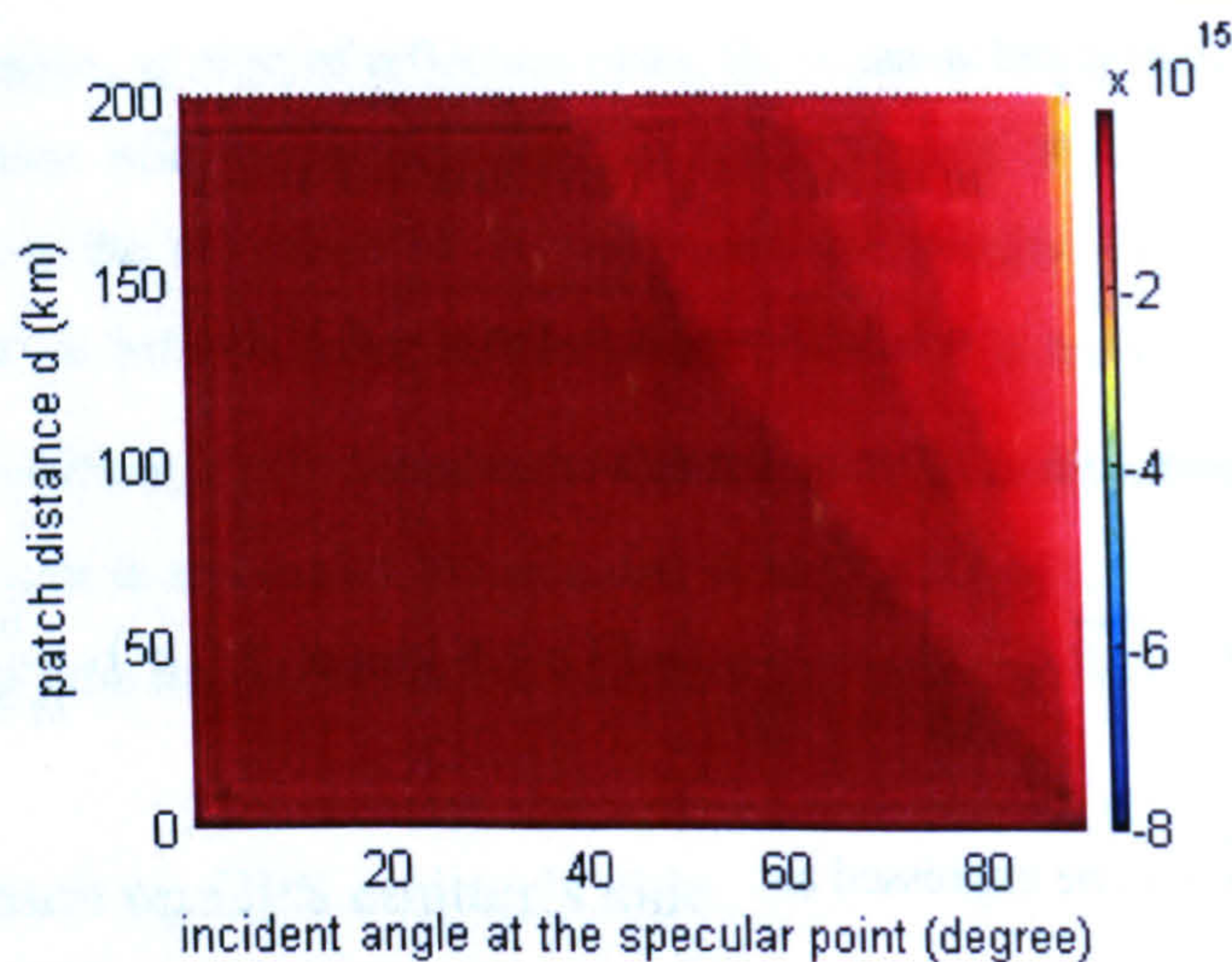


Figure 7-12: Numerical simulation of T for Case 2

7.4.3 Summary

Section 7.4 models the 1-D GPS-R reflection geometry in two cases. Generally, when the specular point incident angle α exceeds 10° , the required slope angle of a certain patch always decreases with the enlargement of α . This means, with constant sea states, a patch is likely to reflect more energy into receiver when the observing incident angle is larger. If we combine the slope contours computation with this knowledge, we can extend this from 1-D to 2-D. Such analysis suggests that, the received reflection energy, within the limited Delay and Doppler ranges, can be enhanced by choosing large incident angle (equivalent to low glazing angle). However, if observing incident angle is smaller than 7° , the above conclusion is not valid for patches which are 50 km or more away from the centre.

The real R14 DDM inversion result, as mentioned in Chapter 6, is lower than the Gaussian prediction, when the results of other datasets under the similar wind conditions are above the Gaussian output. Due to the data fact, the observing incident angle of R14 is only 1.8° , much lower than the 7° boundary. From the above geometric analysis, we believe that very small observing incident angle may reduce the reflection signal power. The weight of observing incident angle should be magnified in current GPS-R scatterometric modelling technique.

7.5 Conclusions

This chapter focuses on a geometric modelling method of wave slopes. The Pierson-Moskowitz model provides an opportunity to simulate wave height field, where we can count different slope angles and obtain the slope probability distributions. Though we can only

analysis the comparative distributions at the moment, it still gives an alternative viewpoint to model the wave slope statistics.

The sensitivity analysis of the geometric slope PDF model is separated into two sections. Wind speed effect shows a different pattern with the Gaussian slope PDF model. This phenomenon may be due to the change of wave patterns, where more detailed studies are needed. The simulations of wave direction effect illustrate that linear waves have great effect on the shape and orientation of wave slope PDFs. The wind and wave direction element should be weighted more in the ocean scatterometric research.

A separated section of this chapter is dedicated to model the effect of observing incident angle on reflections. The detailed analysis concludes that, within the limited Delay and Doppler ranges, a larger observing incident angle can increase the received GPS-R signal power. The increasing in reflection signal power can improve the accuracy of GPS-R scatterometric measurement and benefit the DDM inversion processing.

References

- [Croft 2003] A. Croft and R. Davison, Mathematics for Engineers: A Modern Interactive Approach, Prentice Hall, 2nd edition, December 2003, ISBN 0-1312-0193-X
- [Hill 2001] M. Hill and G. Kwan, Rendering Ocean Scenes, Stanford Graphics Lab 2001 Rendering Competition project, March 2001, http://graphics.stanford.edu/courses/cs348b-competition/cs348b-01/ocean_scenes/
- [Nykamp 2005] D. Nykamp, Normal Vector of Parameterised Surfaces, Online document for Multivariable Calculus and Vector Analysis, November 2005, <http://www.math.umn.edu/~nykamp/m2374/readings/surfnorm/index.html>
- [Stewart 2005] R.H. Stewart, Introduction to Physical Oceanography, Open Source Textbook, Department of Oceanography, Texas A&M University, 2005, http://oceanworld.tamu.edu/resources/ocng_textbook/contents.html
- [Nave 2005] C.R. Nave, Hyper-Physics, Department of Physics and Astronomy, Georgia State University, <http://hyperphysics.phy-astr.gsu.edu/hbase/hframe.html>

Chapter 8. Conclusions and Future Work

8.1 Conclusions

As compared to mono-static radars, GPS-R receivers have higher spatial-temporal sampling rate and are more affordable. These advantages make it a possible additional remote sensing tool for ocean disaster monitoring and long term ocean observations. Several earlier GPS-R air-borne experiments have shown correlations between received signals and sea states. The latest GPS-R experimental platform, on the UK-DMC satellite, provides a unique chance to evaluate the GPS-R technique in space applications. Early analysis of received datasets proves the feasibility of using GPS-R data to detect sea surface wind conditions, sea ice status and land humidity.

The first goal of this research is to assess the existing GPS-R scatterometric model for the space-borne application of ocean remote sensing. We aim to further the initial modelling research into the practical measurement level. Several datasets, in low and medium wind speed range, are applied in this study. The combination of the Elfouhaily spectrum model and Z-V EM model gives reasonable Delay-Doppler Map simulations, which match well with the received UK-DMC DDMs. The agreement between simulations and real data proves validity of the existing GPS-R scatterometric model, however, the sensitivity problem is revealed through the analysis. The Elfouhaily modelled wave slope PDF is not sensitive enough to wind conditions, in medium and high wind speed range, for the purpose of deriving accurate wind and wave information. The other two minor factors, wind direction and observing incident angle, also have inconsiderable effects on final reflection signal pattern.

Motivated to solve the insensitivity problem in current GPS-R model, we propose a novel processing scheme to inverse Delay-Doppler Maps to spatial energy distributions, for the purpose of extracting statistical properties of local waves. In DDM inversion scheme, the Fourier-Wavelet hybrid algorithm outperforms other algorithms in the DDM deconvolution test. Compared to the Cartesian frame, the Delay Contour Grid frame simplifies the Bin-to-Patch searching procedure and solves the mismatch problem in patch resolution.

The inversion from Delay Doppler bin to corresponding patches on a spatial energy map is an important phase in the DDM inversion scheme. Three Bin-to-Patch inversion algorithms are developed and tested. These algorithms do not aim to solve the ambiguity problem in energy distribution, but to estimate the spatial reflection energy distribution under certain assumptions. There are trade-offs between the noise robustness and the wave information we can derive. The Average Method and the Differential Method both can output 2-D slope PDFs. The inversion test of synthetic noise-free DDMs proves the validity of both algorithms. Under different noise conditions, the inversed results correlate well with the assumed slope probability map input, however, the valid data pattern is hidden behind scattered singularities. The Doppler cut-off frequency, in strong signal region, also introduces considerable singularity points in the inversed results. The 1-D DDM Inversion Method sacrifices the Doppler domain information for the purpose of achieving more noise robustness. This method assumes that the required slope angles of patches, within one Delay ring, are the same. Such assumption has been justified by the inversion experiments of simulated noisy DDMs. As expected, the 1-D Inversion Method does have better performance under heavy noise, in comparison with the other two inversion methods. Therefore this algorithm is employed in real UK-DMC DDM inversions, to explore the potential of its practical applications.

The UK-DMC DDM inversion experiments use a low wind speed dataset as the calibration reference. The inversed slope probability curves, from real DDM data, are compared with the Gaussian slope PDFs from the Elfouhaily model. The inversed results of several datasets, with a medium wind speed and a 20° ~ 30° incident angle, are all above the Gaussian expectations. One exception, R14 dataset, has a similar wind condition but with very small observing incident angle, which might be the reason of the phenomenon.

In the final chapter, a comprehensive analysis is performed for wave slope PDF study from a geometric viewpoint. Inspired by visual effect simulations of ocean scenarios, this modelling method provides another way to look into wave statistical attributes, besides theoretical models and empirical observations. The effects of wind speed and wave direction deviate from the outputs of Gaussian slope PDF model. The observing incident angle in bi-static geometry is independent of sea states, but also has effect on received reflection energy. The effect of this element is modelled and analysed. The result concludes that, generally GPS-R observation with large incident angle can enhance the received reflection energy, and the possible SNR increasing in received signals is able to improve the quality of real DDM inversions.

8.2 Future work

The research for upgrading GPS-R receiver platform is now ongoing. This aims in coupling GPS-R data receiving and pre-processing onboard the satellite, for more and better quality GPS-R measurements. The present development of enhanced GPS signals and the Galileo constellation are also expected to provide a wide range of perspectives for the whole field of GPS-R research. More in-depth data interpretation and modelling work should catch up with these experimental achievements. The GPS-R data-model fitting and inversion experiments in this PhD study have raised a lot of questions for future studies.

8.2.1 Derivation of an empirical wave slope PDF model

The Delay-Doppler Map inversion scheme, as we proposed, has been initially justified by several UK-DMC DDM datasets. A forward step in this research direction is to systematically schedule, archive and process GPS-R data from the UK-DMC platform, for the purpose of extracting an accurate wave slope or wind-related model for GPS-R space-borne applications. By either decreasing the noise level in received data, or using filter techniques to generate more accurate estimates, we should be able to derive a useful empirical wave slope PDF model which can be used practically.

Noise is a significant factor to weaken the efficiency of the inversion algorithm. Improving the quality of received GPS-R signals is a straightforward way to enhance the performance of DDM inversions. The earlier error analysis in [Gleason 2006] shows that the quality of received signals can only rise to a certain level by amplifying the gain of receiver antenna. The trade-off, between incoherent time integration and dynamic measurement capacity of the system, also limits the development of GPS-R technique. Either improving the GPS-R receiver hardware, or promoting the signal processing algorithms, will considerably benefit the GPS-R technique.

Filter techniques have been long applied in data processing and system control engineering. The Kalman Filter, as one of the most commonly used filters, is efficient in modelling dynamic systems from incomplete and noisy measurements. It might be an ideal solution for this empirical GPS-R modelling research. As a pure time domain recursive filter, the Kalman Filter first gives an estimation of the current system status, based on the previous time step measurement. Then the current measurement updates the estimation, which is more likely towards the truth [Kalman 1960][Kalman 1961]. By combining the Kalman Filter with

continuous input of GPS-R Delay-Doppler data and reference ground truth, an experimental wave slope statistical model can be derived with a high accuracy. With such a model GPS-R can be used practically, to measure sea states and forecast extreme ocean disasters, via the space-borne platforms.

8.2.2 Ocean reflection rendering based on geometric wave model

Our geometric modelling for slope PDFs, as described in Chapter 7, is based on an ocean wave rendering simulation within the area of computer graphics research. Computer visual effect and animation techniques have been developed into a high level in recent years, thanks to the huge entertaining market of movies and games. A very interesting question for the future researchers will be, whether or not, we can apply some of these sea surface simulations into our GPS-R ocean remote sensing research. [Hill 2001] illustrates an ocean surface rendering program which simulate the diffusion of sky light from the sea surface. If sun glitter rendering can be modelled based on the geometric simulation of wave height field, the GPS-R signal scattering phenomenon would be possible to be simulated in a similar way. The achievement in this research direction will provide a valuable reference for our theoretical and empirical studies in GPS-R scatterometric field.

Reference

[Gleason, 2006] S.T. Gleason, "Remote Sensing of Ocean, Ice and Land Surfaces Using Bistatically Scattered GNSS Signals From Low Earth Orbit", PhD Thesis, University of Surrey, 2006.

[Hill 2001] M. Hill and G. Kwan, Rendering Ocean Scenes, Stanford Graphics Lab 2001 Rendering Competition project, March 2001, http://graphics.stanford.edu/courses/cs348b-competition/cs348b-01/ocean_scenes/

[Kalman, 1960] R.E. Kalman, "A New Approach to Linear Filtering and Prediction Problems", Transactions of the ASME - Journal of Basic Engineering, Vol. 82, 1960.

[Kalman and Bucy, 1961] R.E. Kalman and R.S. Bucy, "New Results in Linear Filtering and Prediction Theory", Transactions of the ASME - Journal of Basic Engineering, Vol. 83, 1961.

Appendix I

Delay-Doppler Map Simulation Experiments

1. R10 Dataset

GPS emitter satellite	SVN-17
Time tag	03 September 2004 07:25:05 AM
Wind condition (local buoy data)	10 m/s, 5°
Significant wave height (SWH)	2.8 m
UK-DMC DDM data facts (normalised)	
Map size : 1000 (Delay) * 100 (Doppler) Delay axis : 250 ~ 429 C/A code Doppler axis : 7600 ~ 17500 Hz Peak position : 345.0 C/A code , 12400 Hz	
DDM simulation (normalised)	
GPS ECF position : [-6776639, -17101054, 19641978] m GPS ECF velocity : [2287.7, 797.1, 1424.8] m/s DMC ECF position : [-3914248, -4256014, 4053233] m DMC ECF velocity : [-4145.8, -1960.3, -6058.6] m/s Predict specular point ECF position : [-3323828.61, -3889912.75, 3795299.02] m Specular point position (latitude/longitude) : [36.6589 , -130.5130] degree Observing incident angle : 22.4963 ° Patch resolution : 200 km * 200 km reflection area (200*200 patches) Delay/Doppler offset : 129.91 C/A code, 865.48 Hz <u>Elfouhaily slope PDF</u> Conditions : wind speed 10 m/s, direction 5°, incident angle 22.4936° Gaussian parameters: $\sigma_x = 0.013623$, $\sigma_y = 0.013169$, $b_{xy} = -0.0029893$ <u>UK-DMC DDM and simulation comparison</u> DDM correlation : $p = [0.9914 , 0.0016]$ (fitted line $y = 0.9914x + 0.0016$) Correlation coefficient : $c = 0.73435$ (Figure I-9) Delay dimension correlation : $p = [1.0600, -0.0974]$ Correlation coefficient : $c = 0.91667$ (Figure I-10) Doppler dimension correlation : $p = [1.1217 , -3.2554]$ Correlation coefficient : $c = 0.85461$ (Figure I-11)	

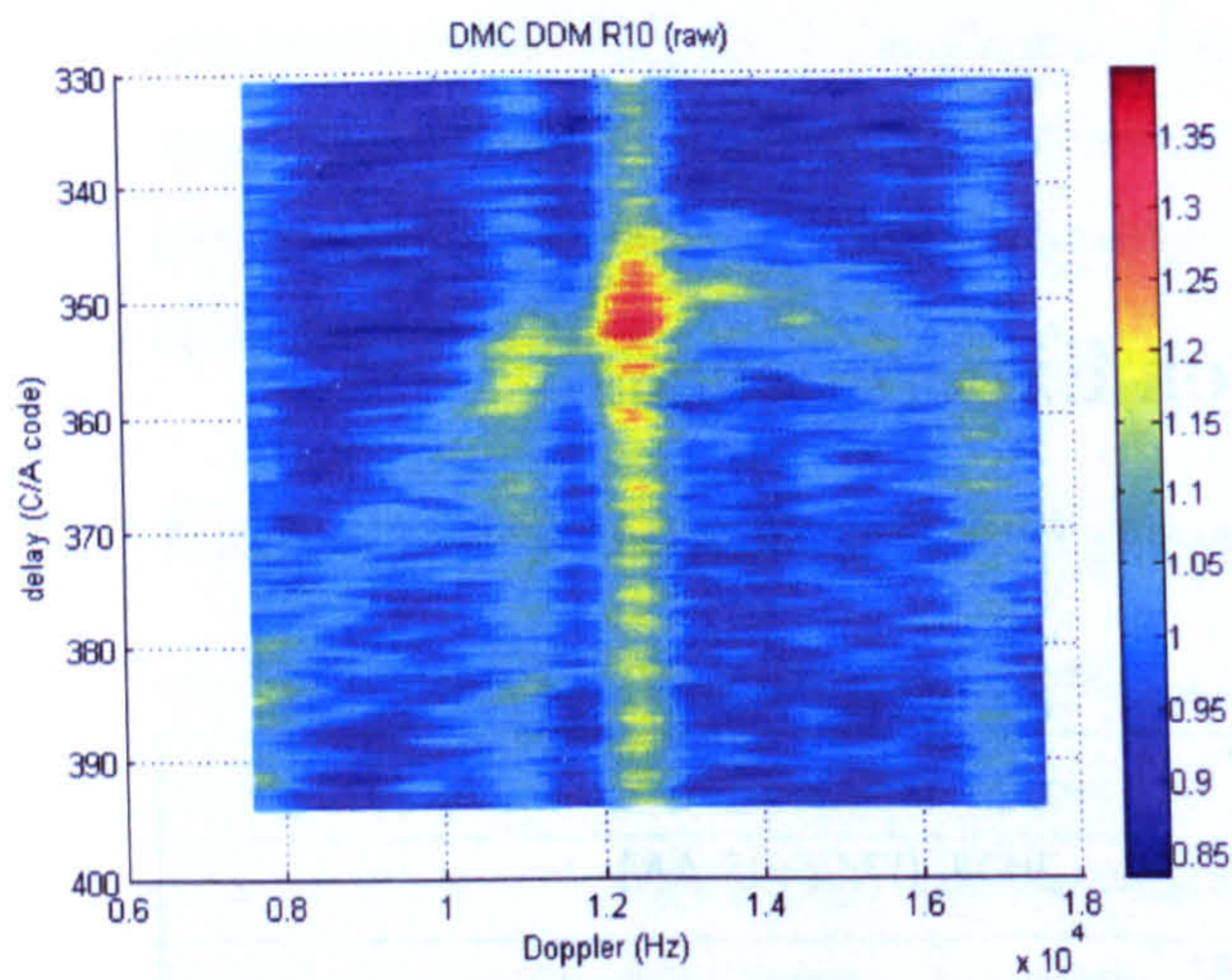


Figure I-1 : UK-DMC R10 DDM data (raw)

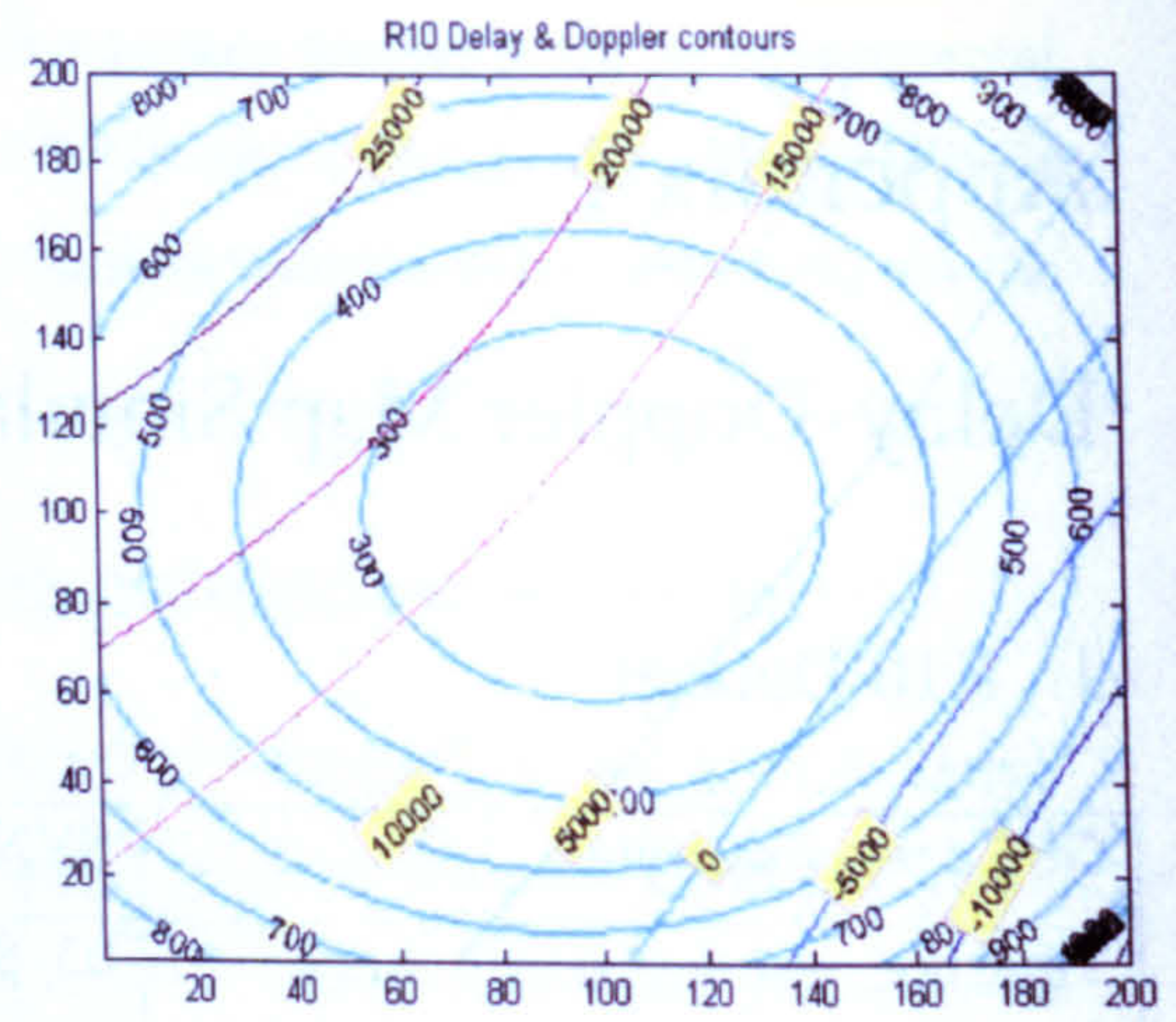


Figure I-4 : Simulated R10 Delay-Doppler contours

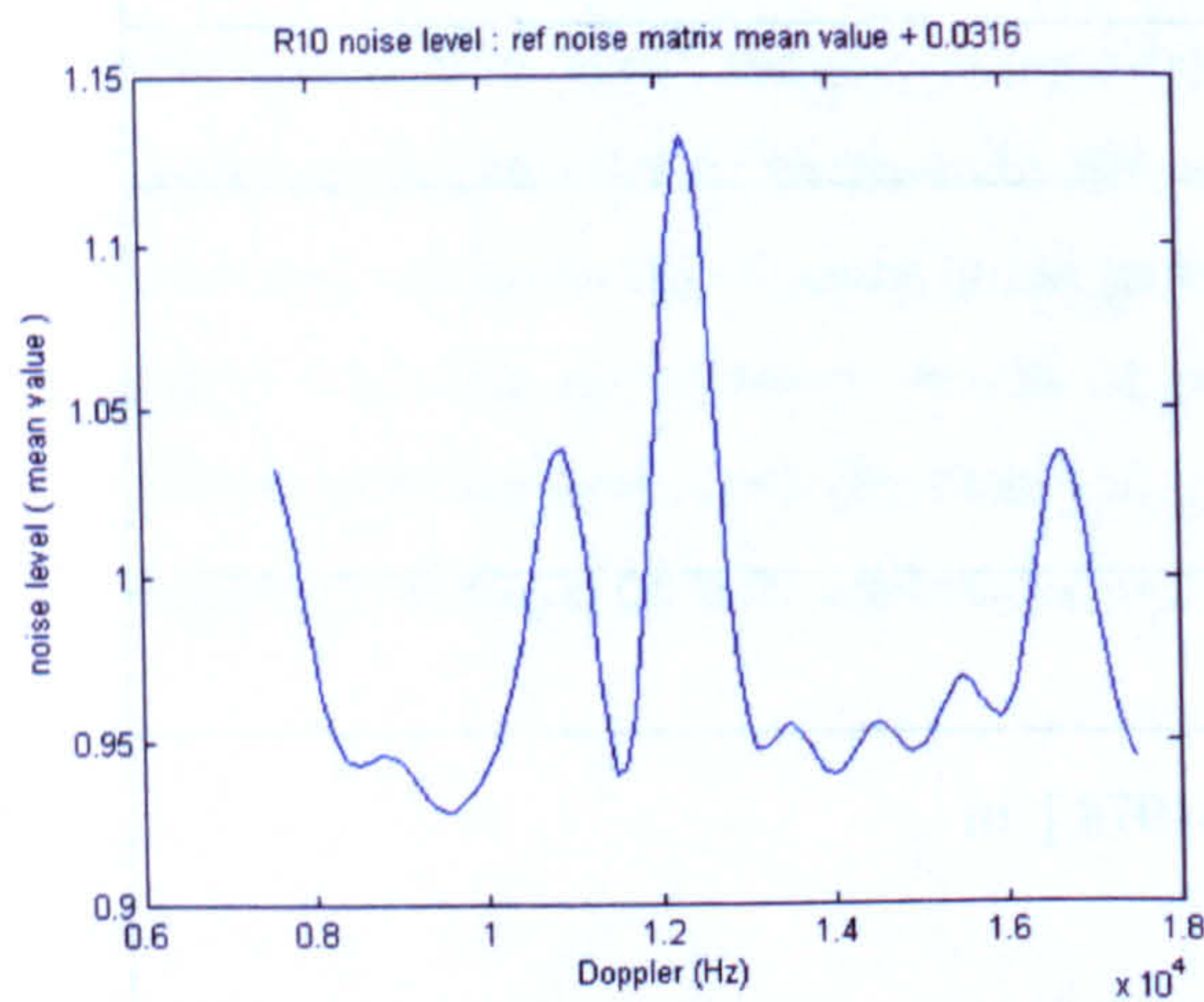


Figure I-2 : UK-DMC R10 DDM bias

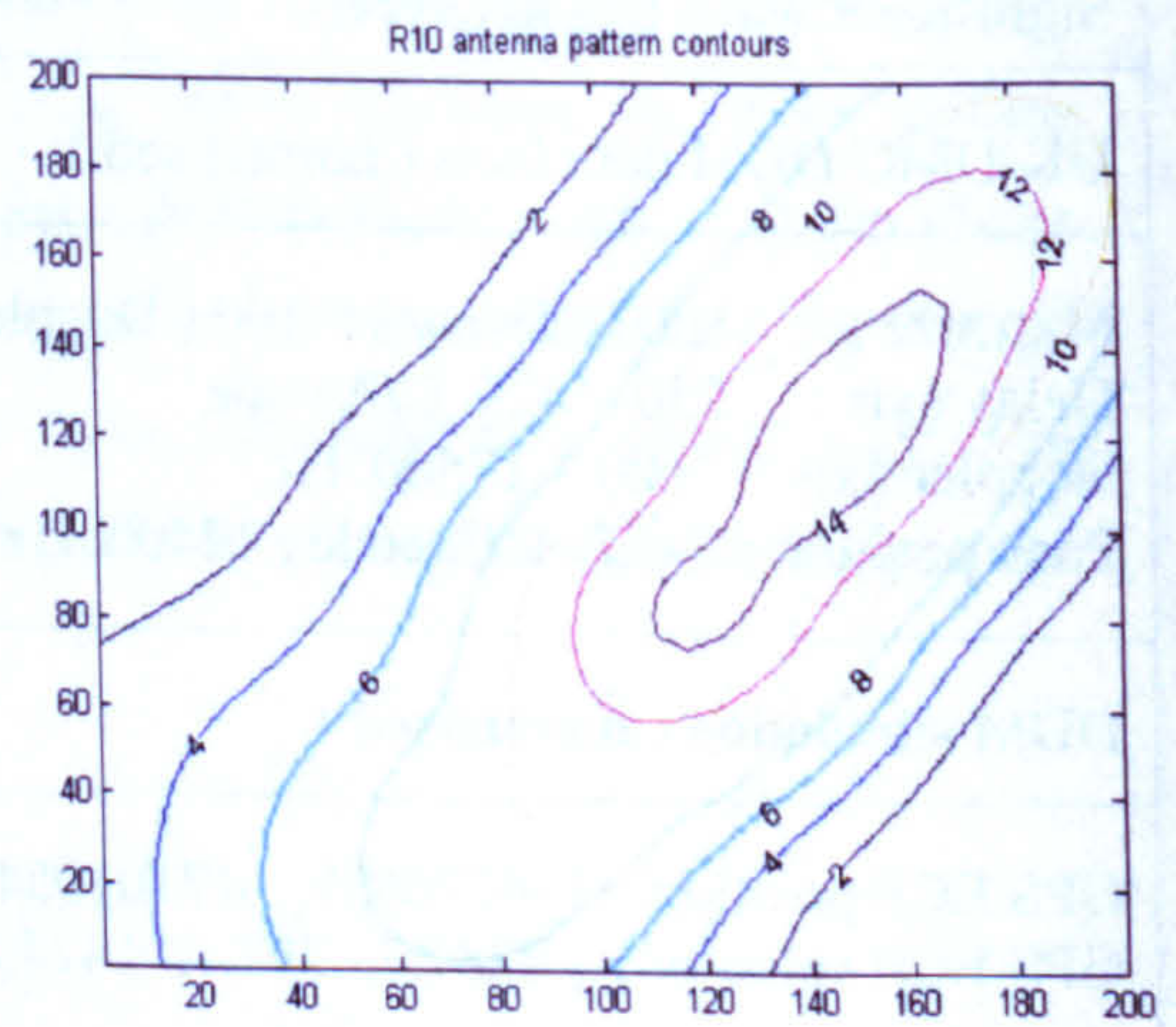


Figure I-5 : Simulated R10 antenna pattern

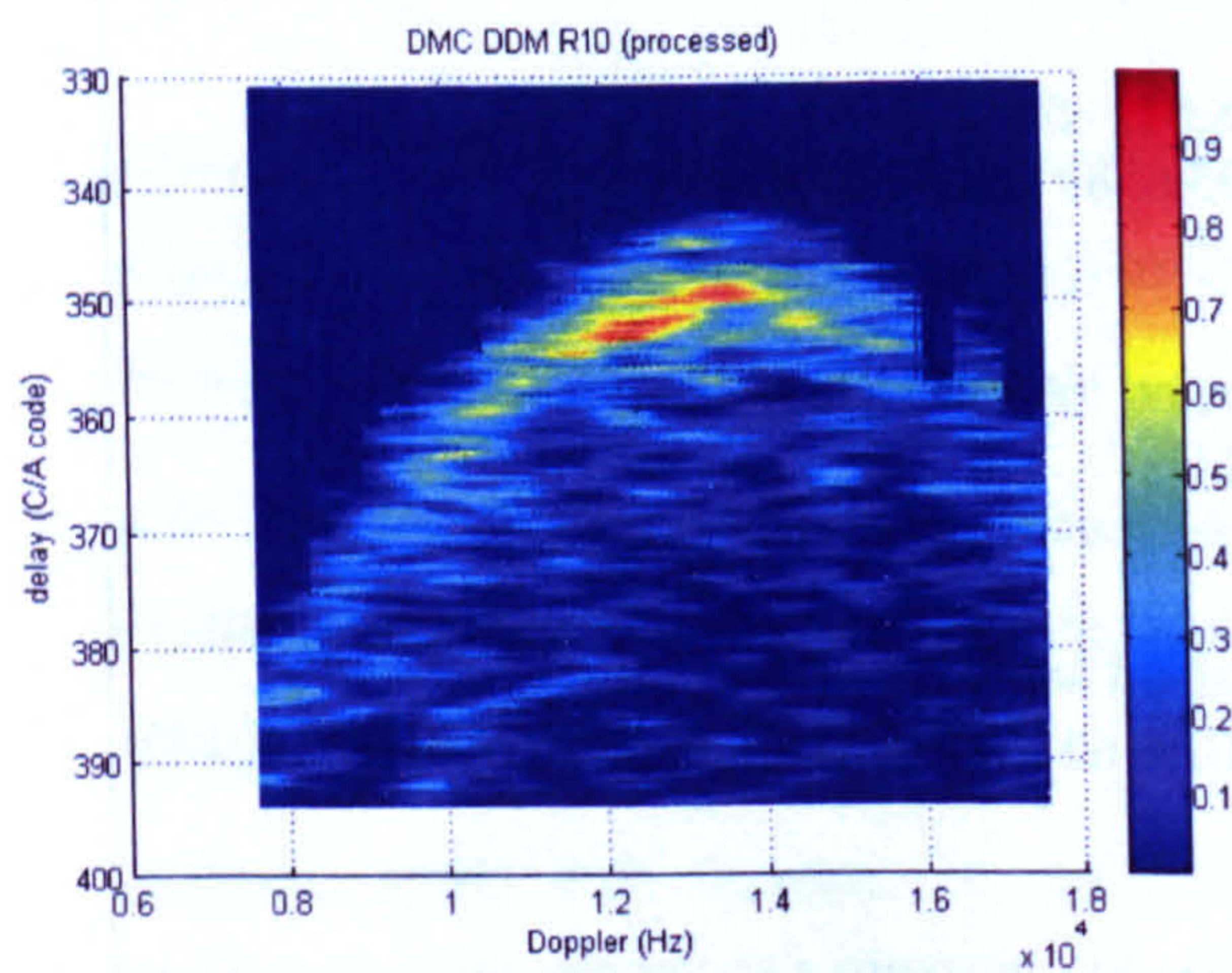


Figure I-3 : UK-DMC R10 DDM data (processed)

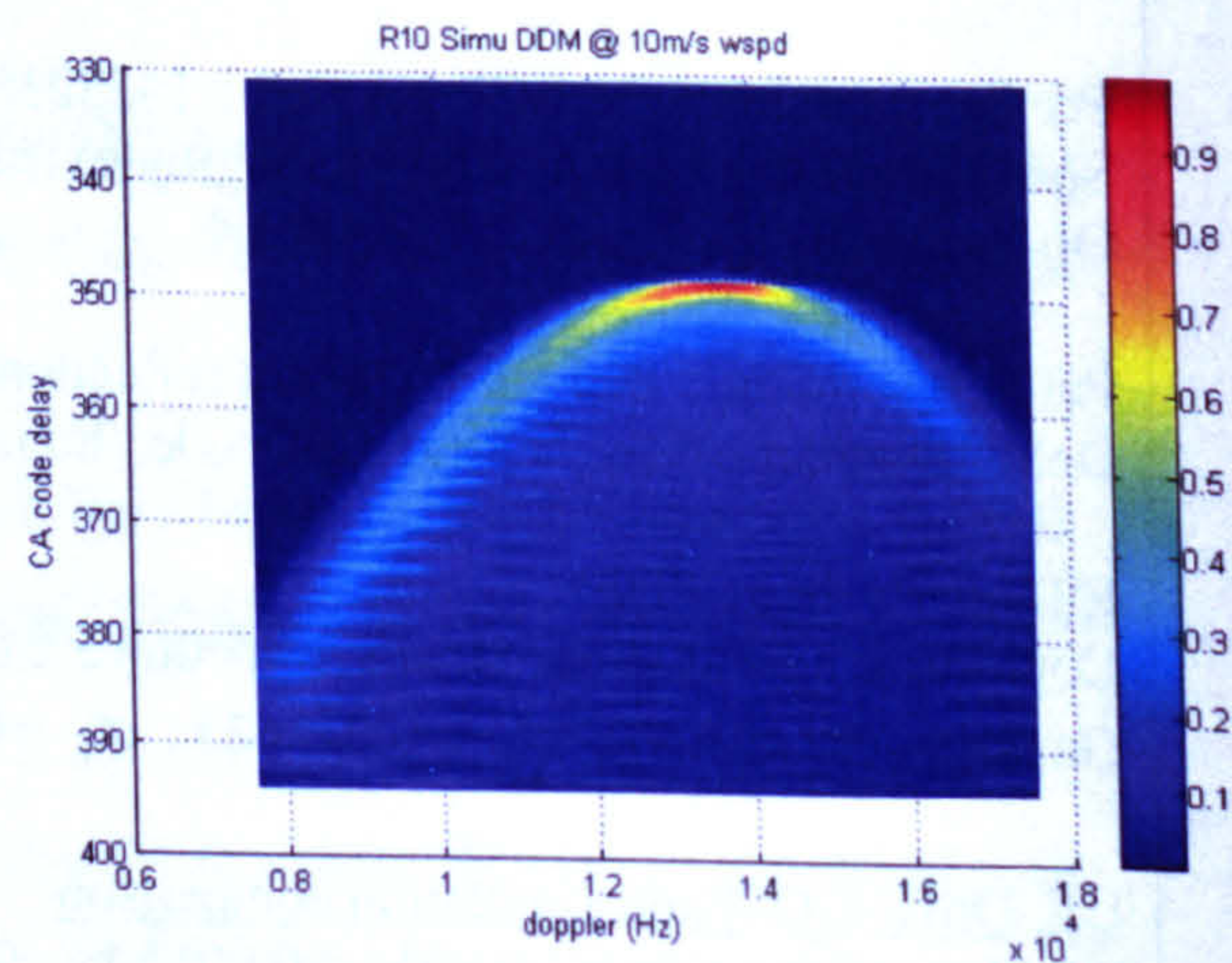


Figure I-6 : Simulated R10 DDM

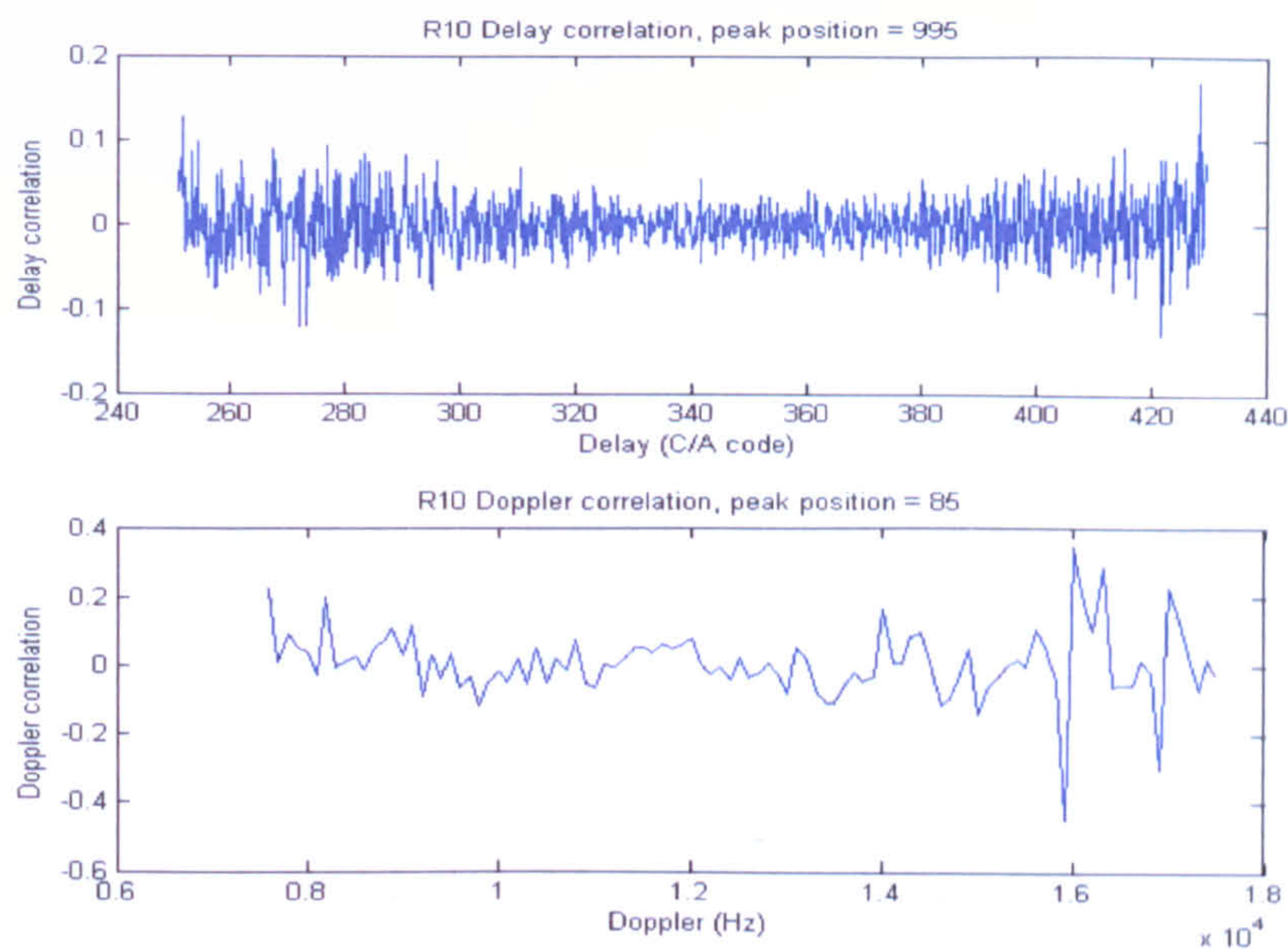


Figure I-7 : DDM registration in Delay and Doppler dimensions

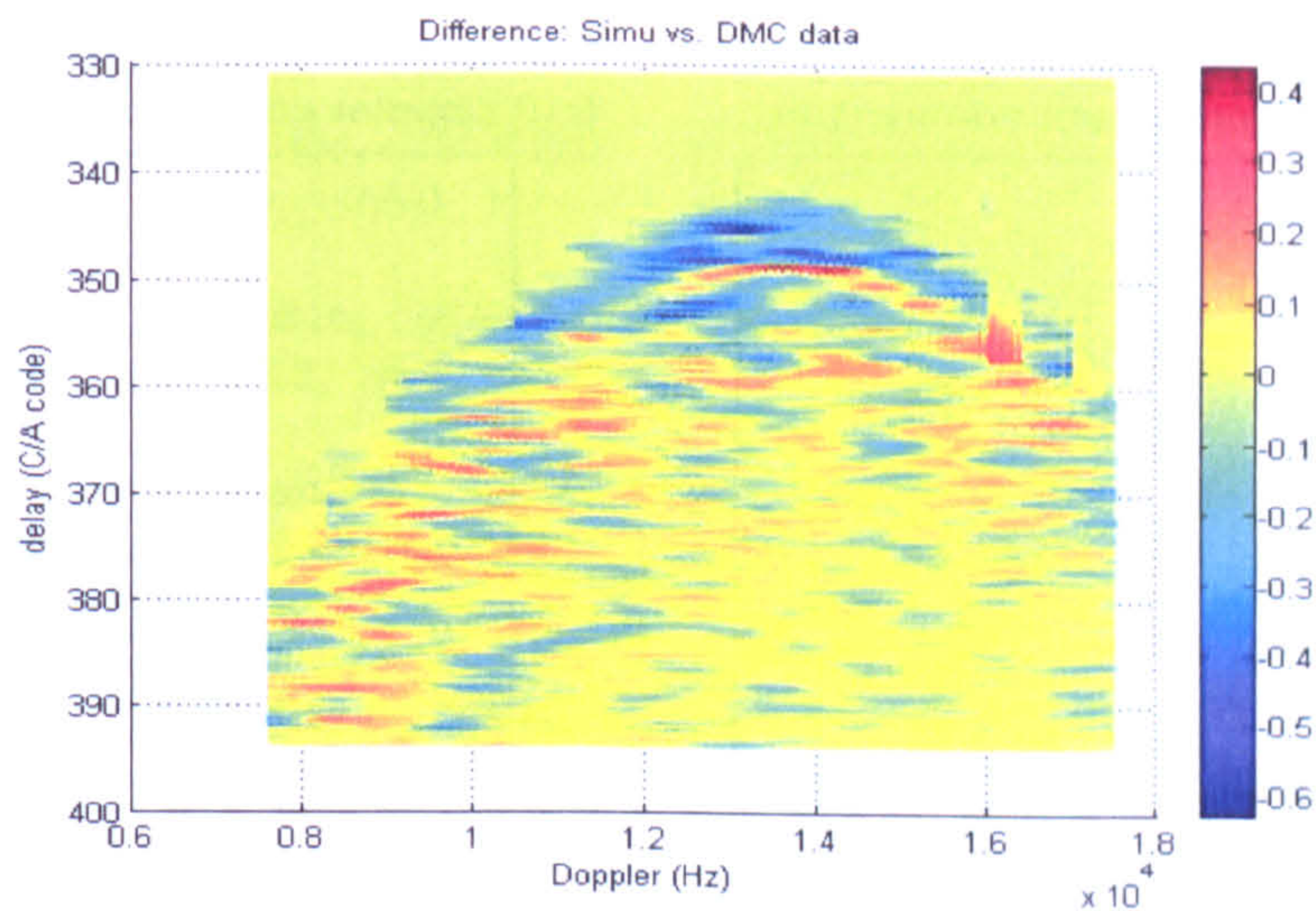


Figure I-8: Difference between UK-DMC R10 DDM and the Simulation

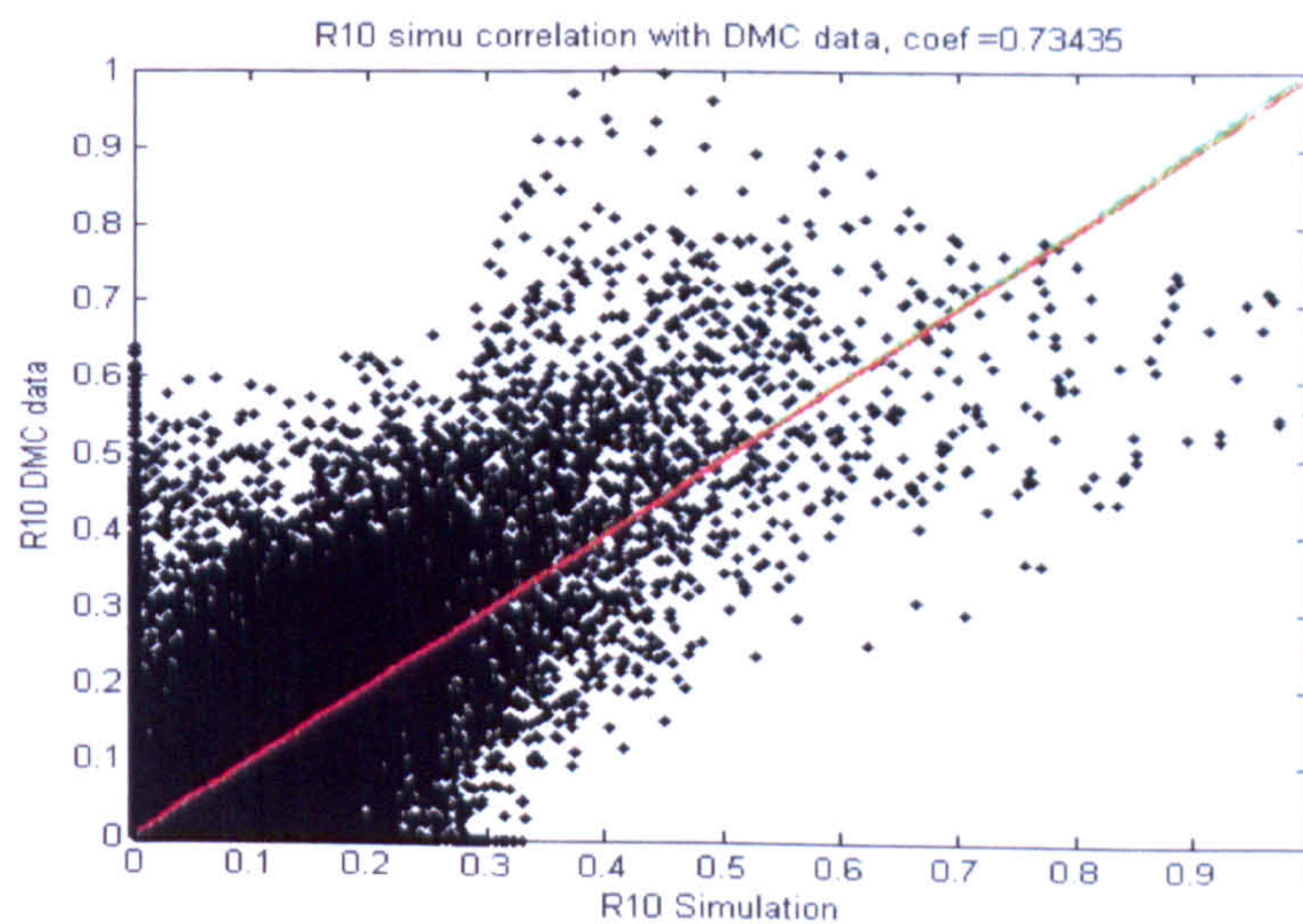


Figure I-9 : The point-to-point correlation of UK-DMC R10 DDM and the Simulation

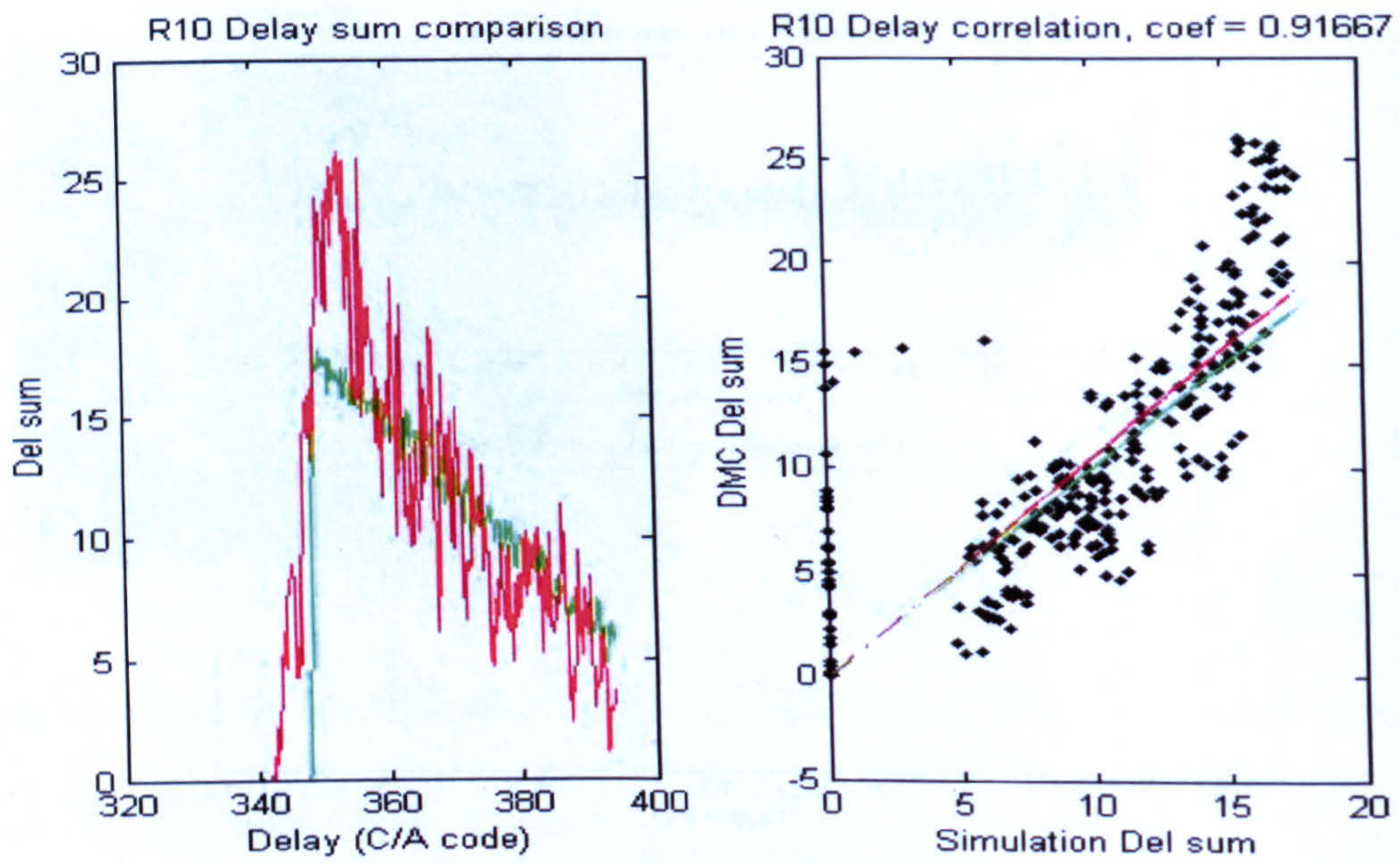


Figure I-10 : Delay dimension correlation

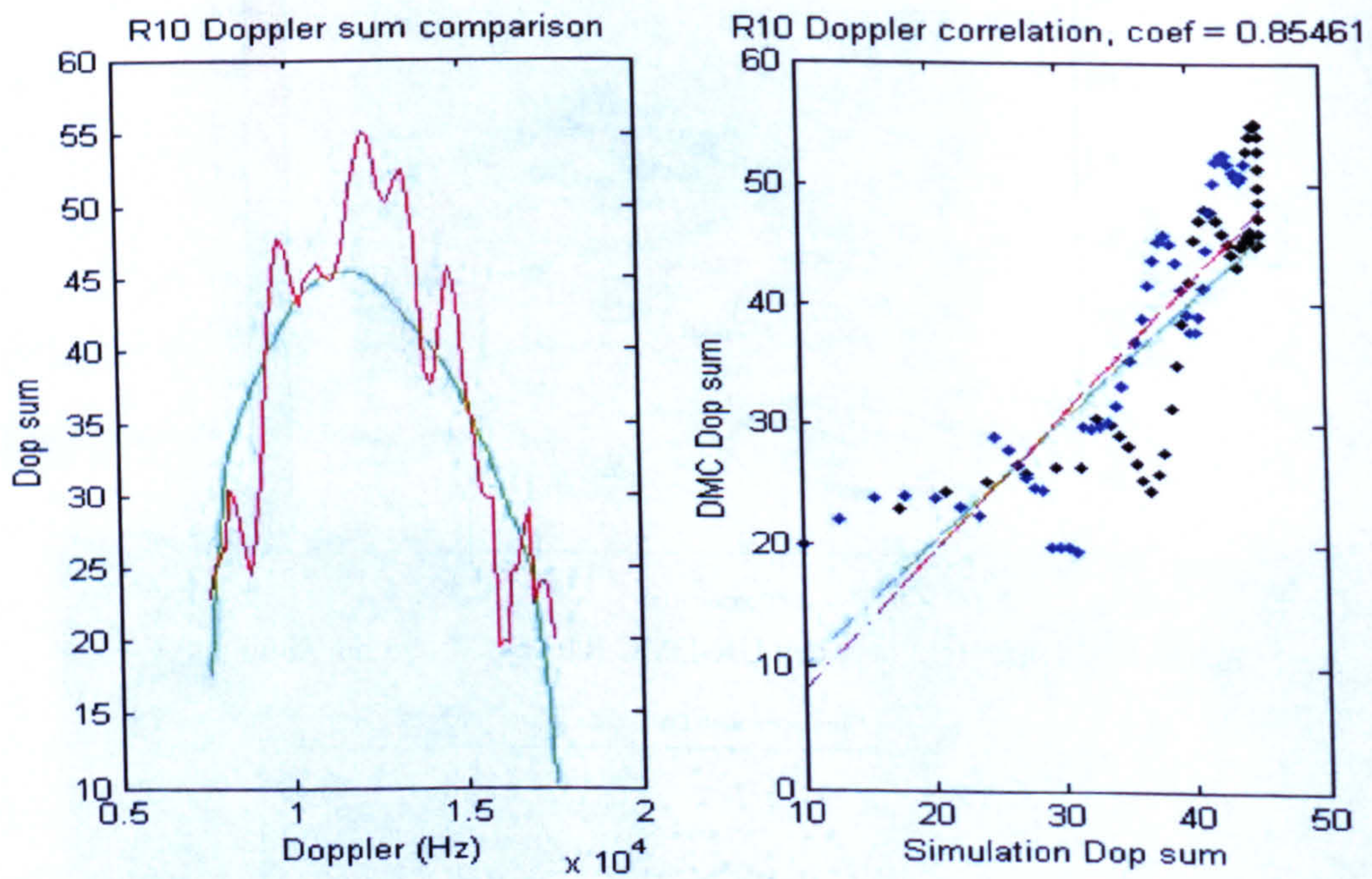


Figure I-11 : Doppler dimension correlation

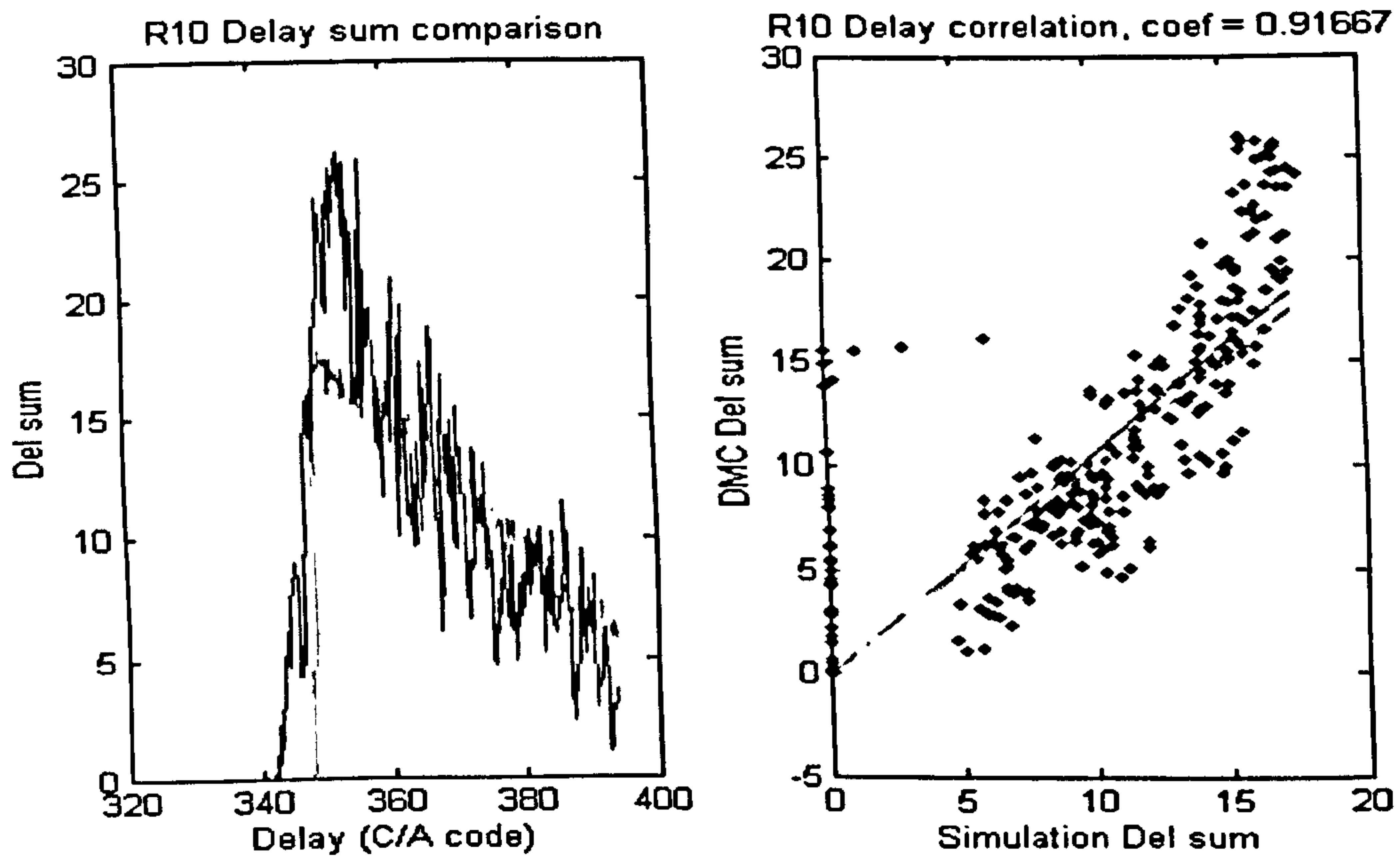


Figure I-10 : Delay dimension correlation

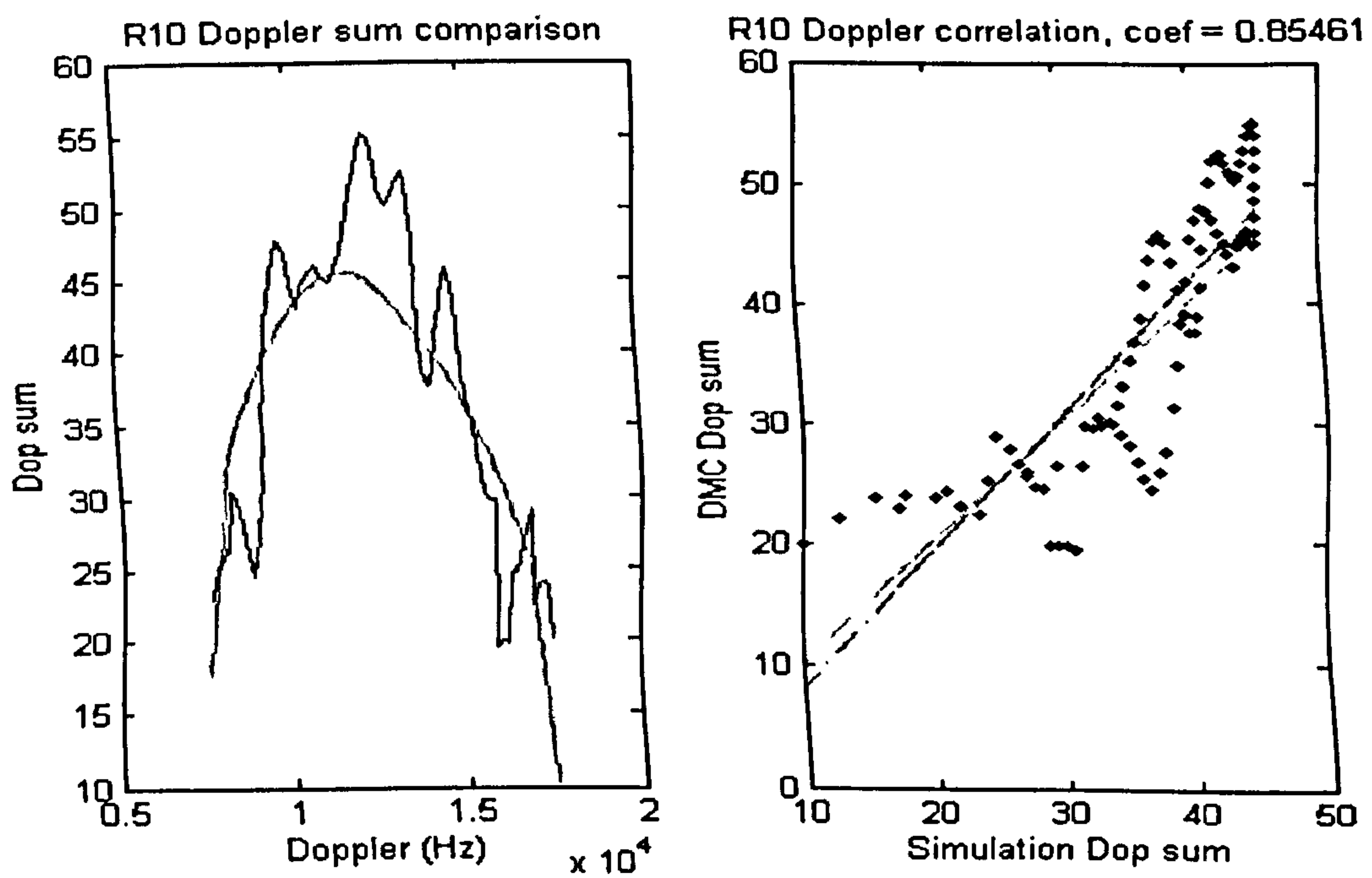


Figure I-11 : Doppler dimension correlation

2. R12 Dataset

GPS emitter satellite	SVN-47
Time tag	16 November 2004 07:54:46 AM
Wind condition (local buoy data)	8 m/s, -107°
Significant wave height (SWH)	2.8 m
UK-DMC DDM data facts (normalised)	
Map size : 1200 (Delay) * 100 (Doppler) Delay axis : 572.91 ~ 787.57 C/A code Doppler axis : 6600 ~ 16500 Hz Peak position : 632.17 C/A code , 10500 Hz	
DDM simulation (normalised)	
GPS ECF position : [-11107734, -13170262, 20372705] m GPS ECF velocity : [2526.9, -366.0, 1151.9] m/s DMC ECF position : [-4196816, -3630173, 4372866] m DMC ECF velocity : [-4619.2, -1667.9, -5791.2] m/s Predict specular point ECF position : [-3663167.61, -3268232.68, 4058262.20] m Specular point position (latitude/longitude) : [39.6739, -138.2611] degree Observing incident angle : 15.1509 ° Patch resolution : 200 km * 200 km reflection area (200*200 patches) Delay/Doppler offset : -63.449 C/A code, 265.01 Hz <u>Elfouhaily slope PDF</u> Conditions : wind speed 8 m/s, direction -107°, incident angle 15.1509°) Gaussian parameters: $\sigma_x = 0.011952$, $\sigma_y = 0.012306$, $b_{xy} = -0.0098426$ <u>UK-DMC DDM and simulation comparison</u> DDM correlation : p = [1.0009 , 0.0122] Correlation coefficient : c = 0.87398 (Figure I-20) Delay dimension correlation : p = [1.0566, 1.0415] Correlation coefficient : c = 0.95699 (Figure I-21) Doppler dimension correlation : p = [0.7893 , 23.0084] Correlation coefficient : c = 0.81420 (Figure I-22)	

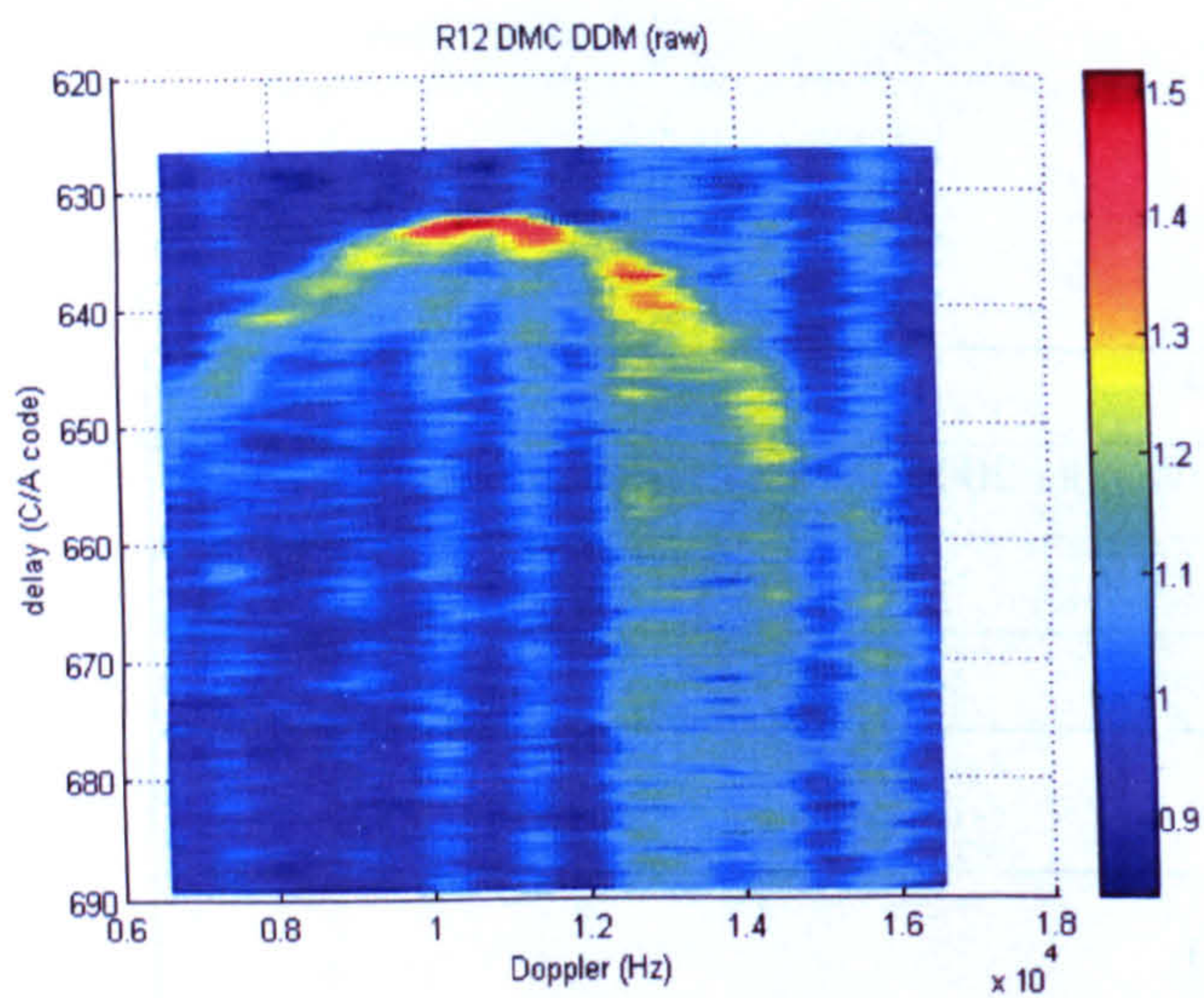


Figure I-12 : UK-DMC R12 DDM data (raw)

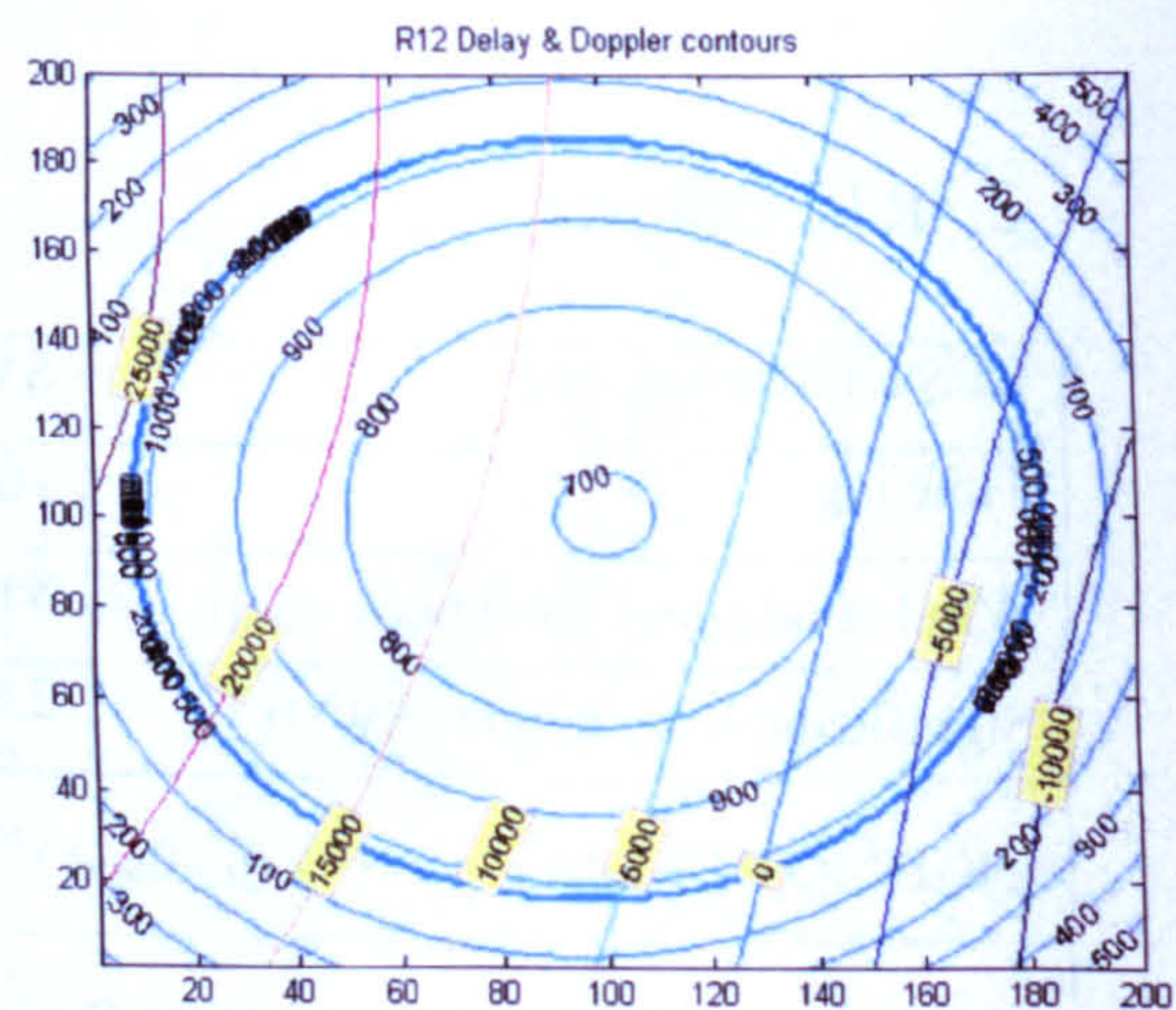


Figure I-15 : Simulated R12 Delay-Doppler contours

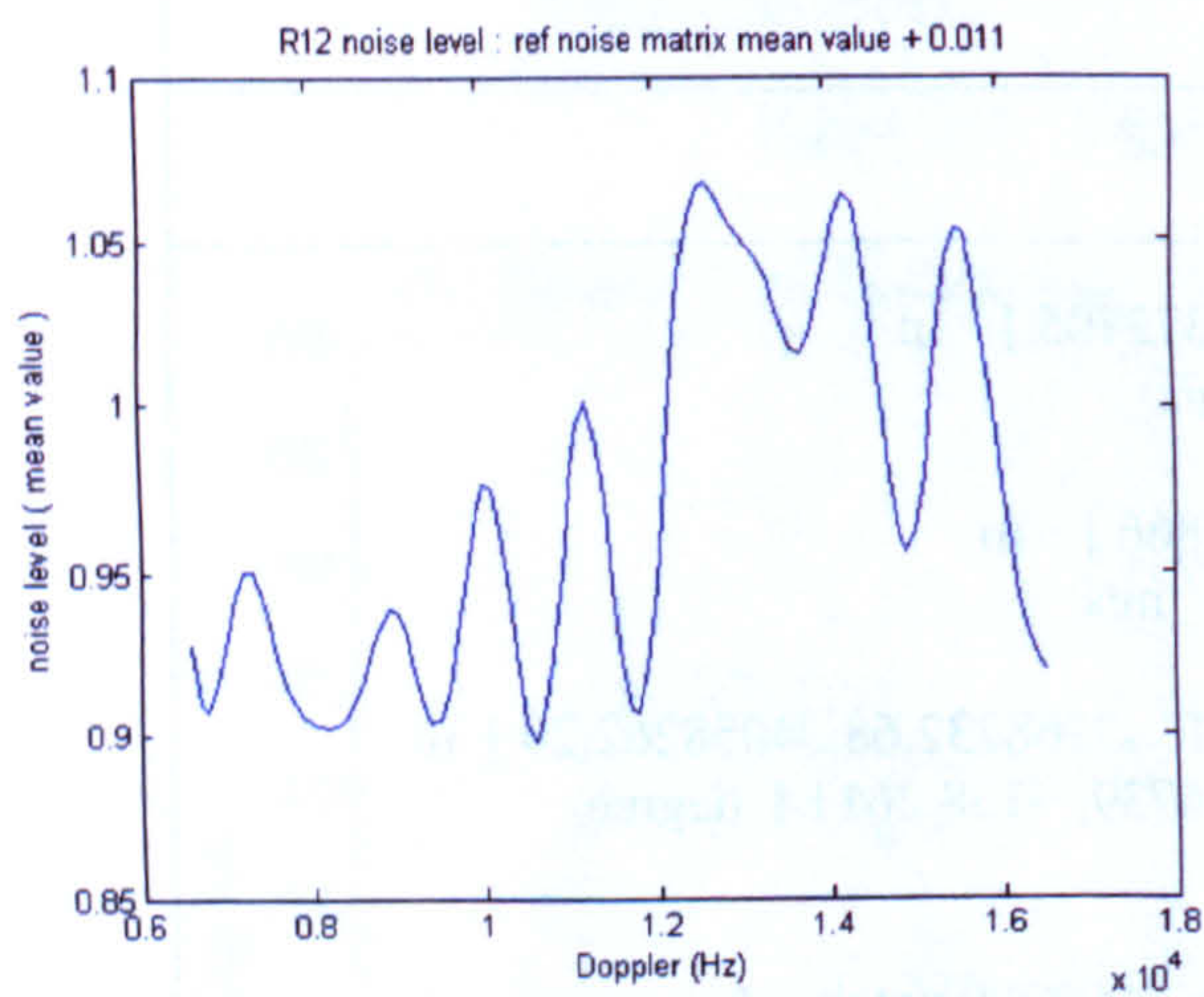


Figure I-13 : UK-DMC R12 DDM bias

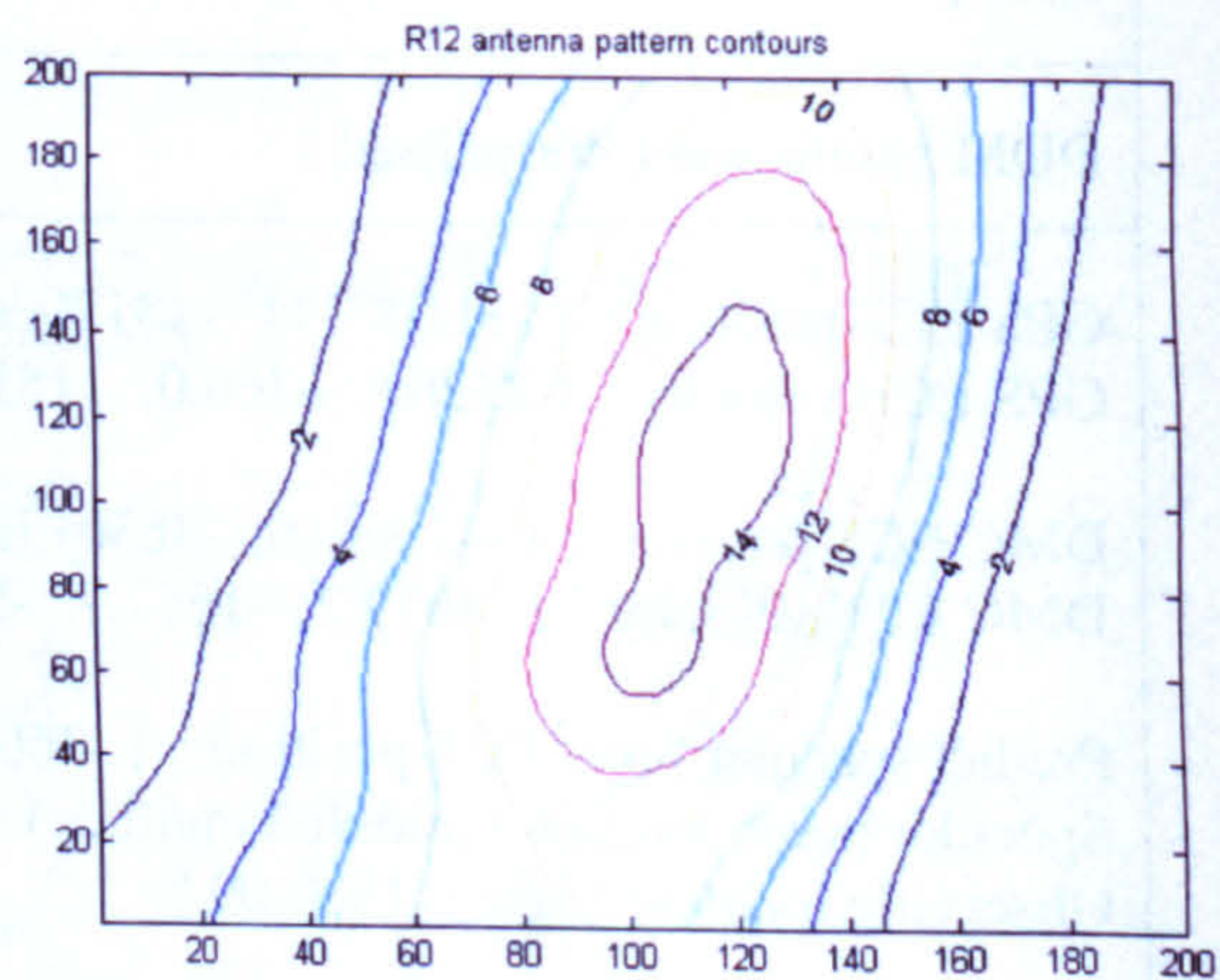


Figure I-16 : Simulated R12 antenna pattern

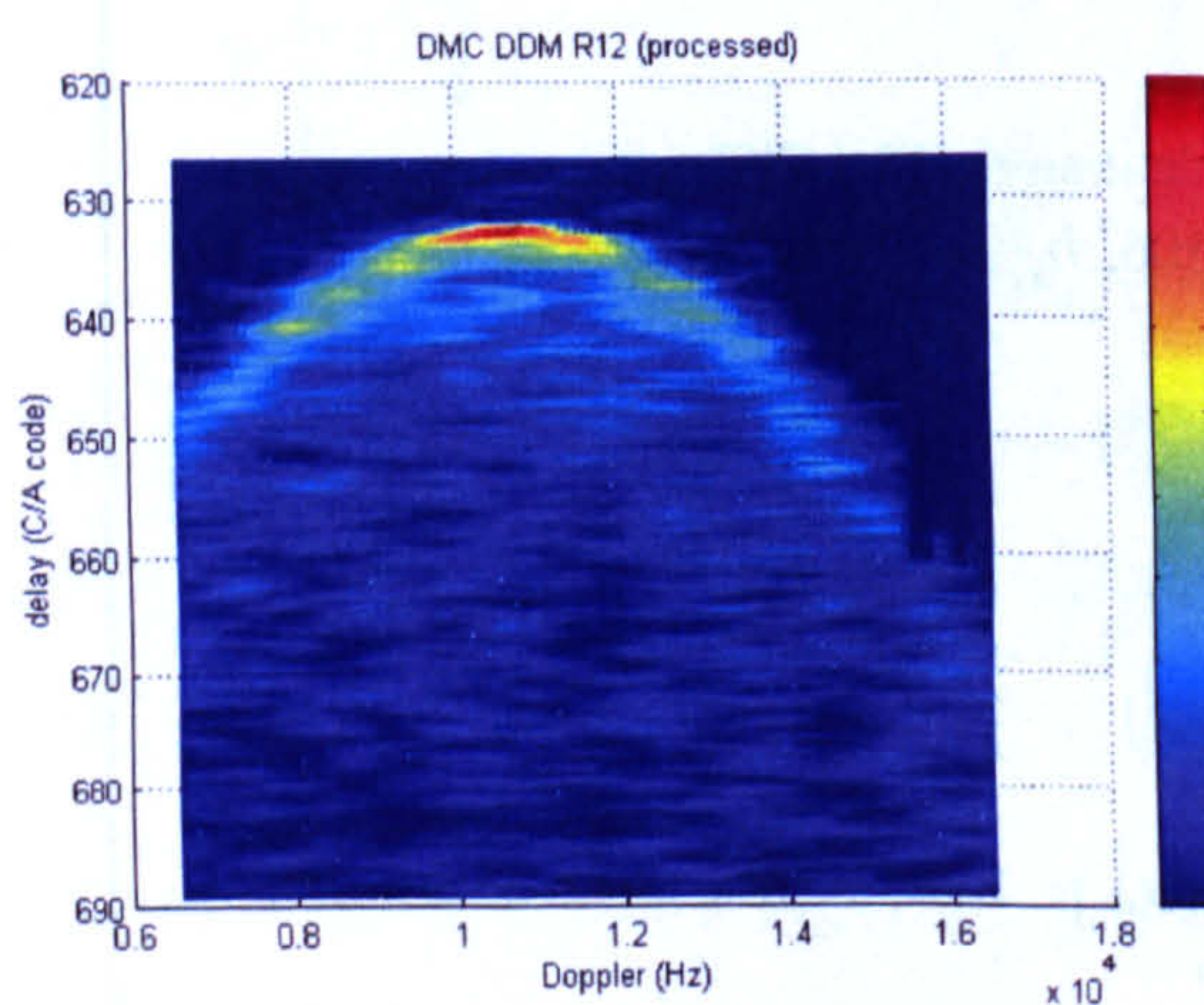


Figure I-14 : UK-DMC R12 DDM data (processed)

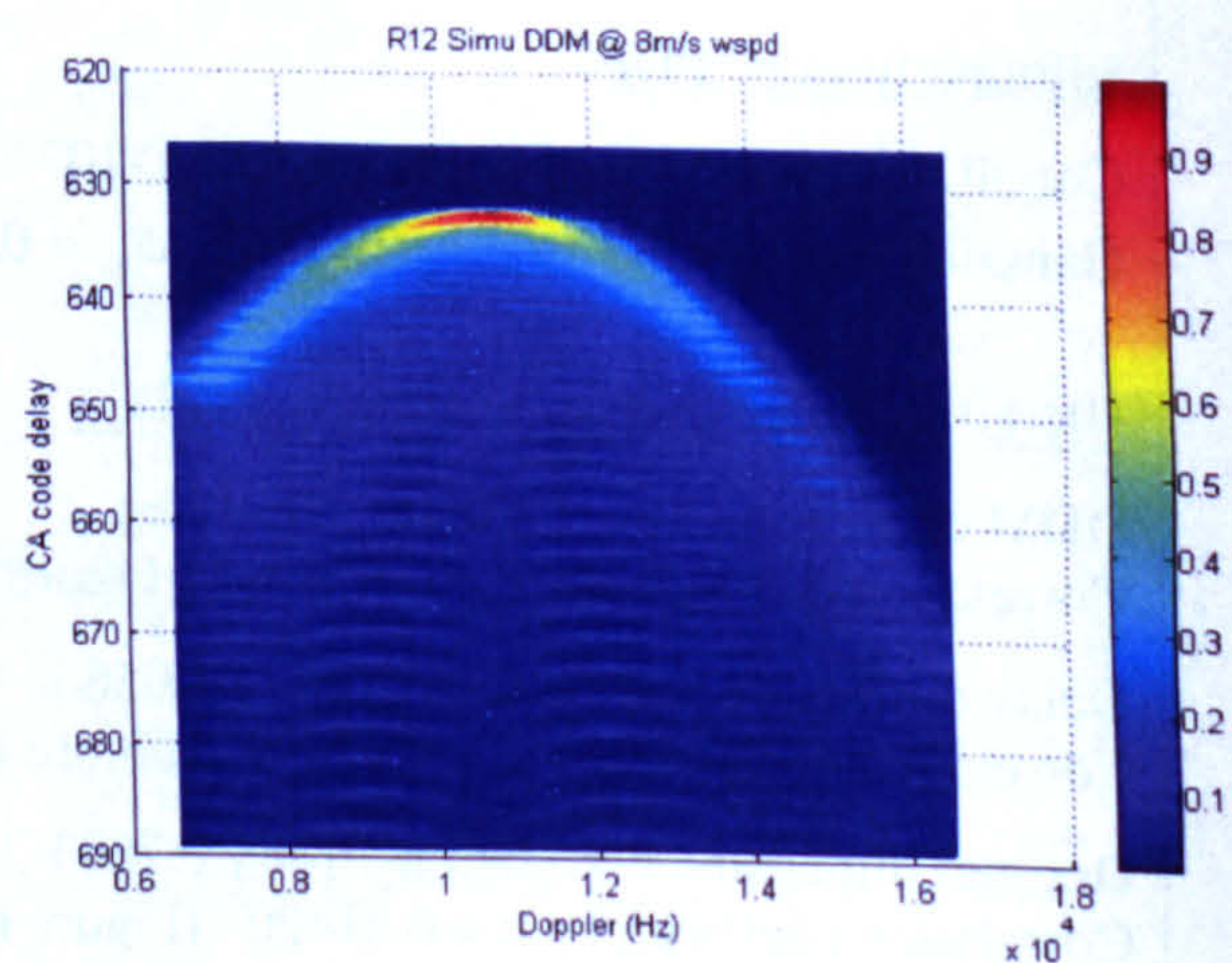


Figure I-17 : Simulated R12 DDM

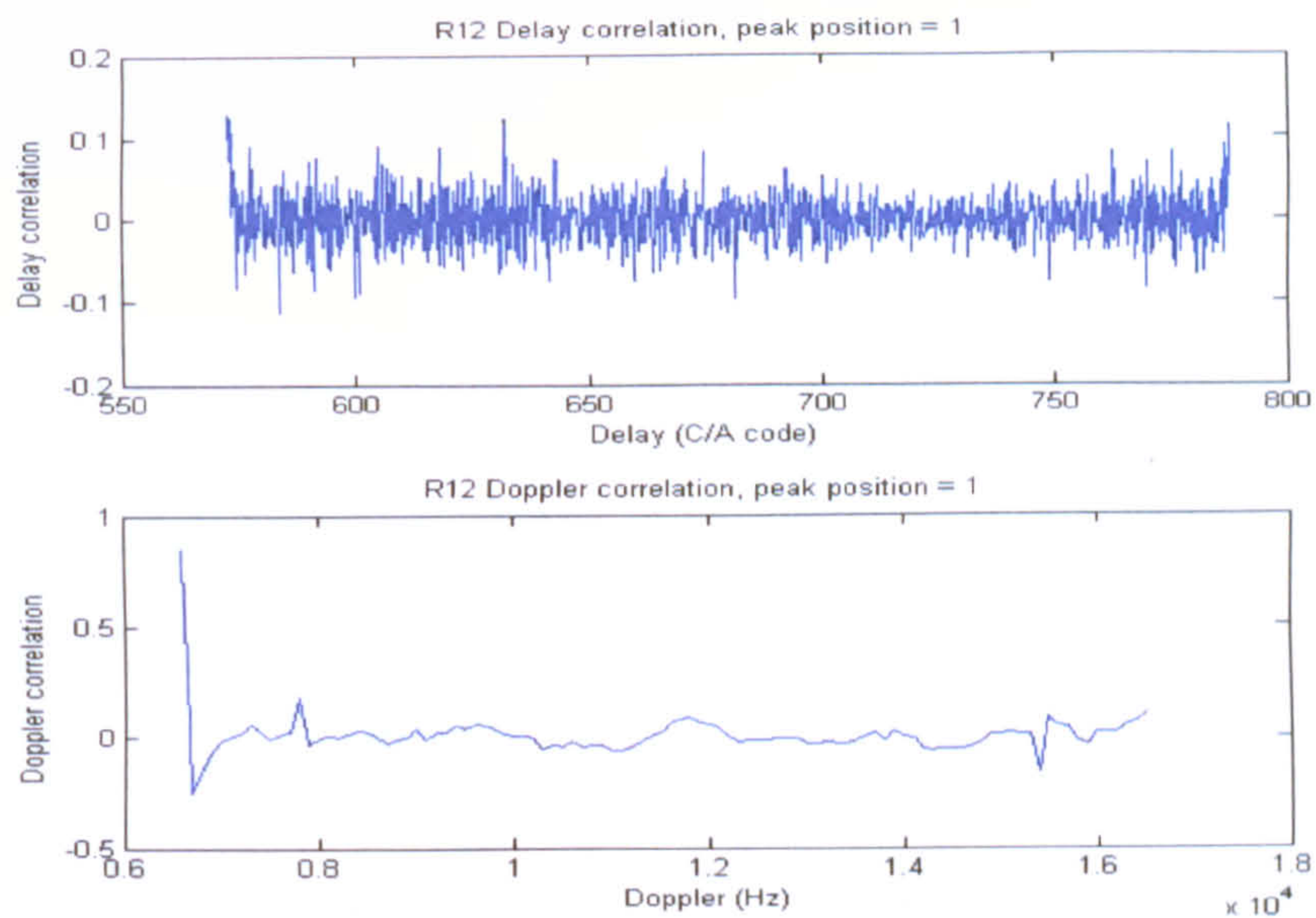


Figure I-18 : DDM registration in Delay and Doppler dimensions

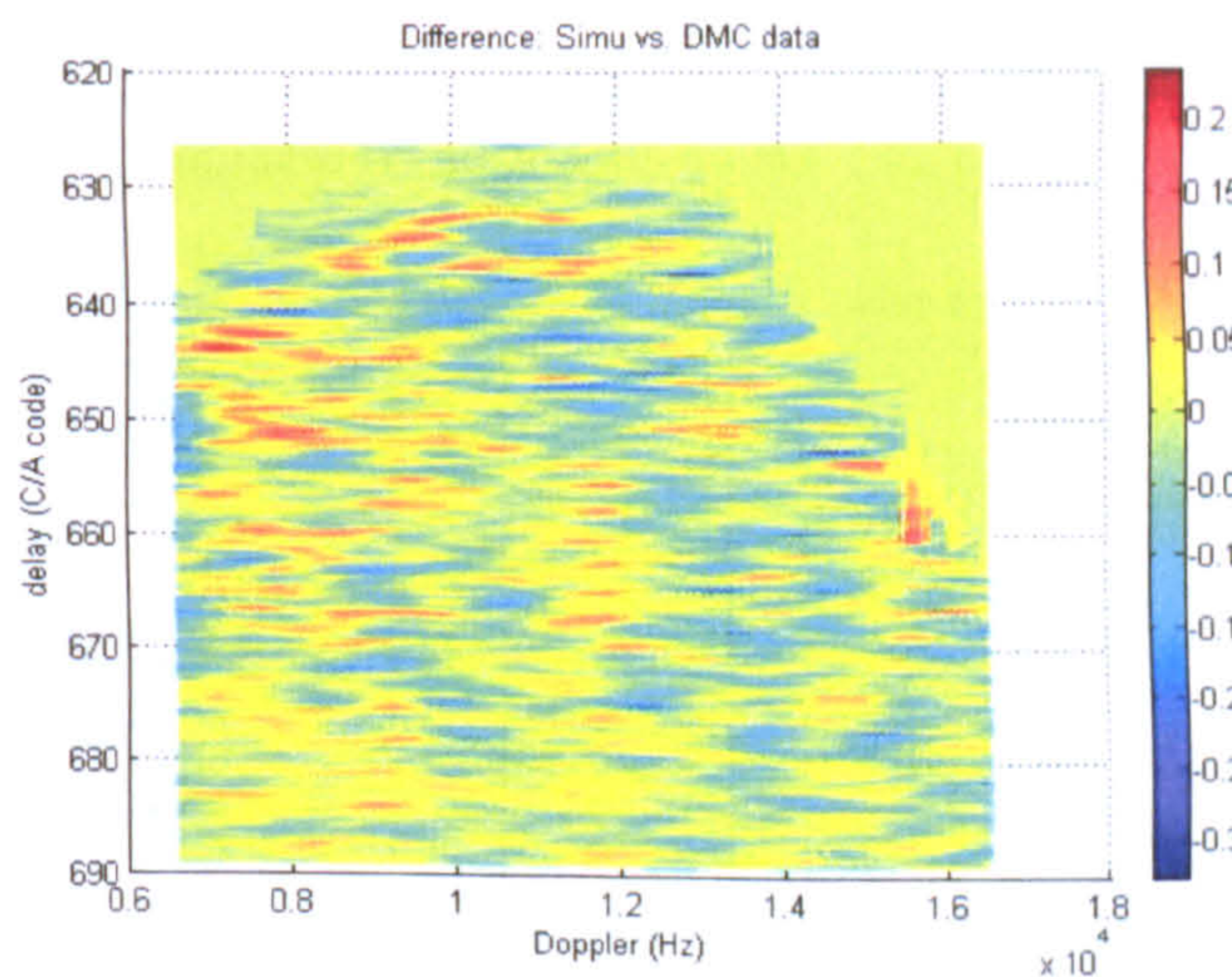


Figure I-19 : Difference between UK-DMC R12 DDM and Simulation

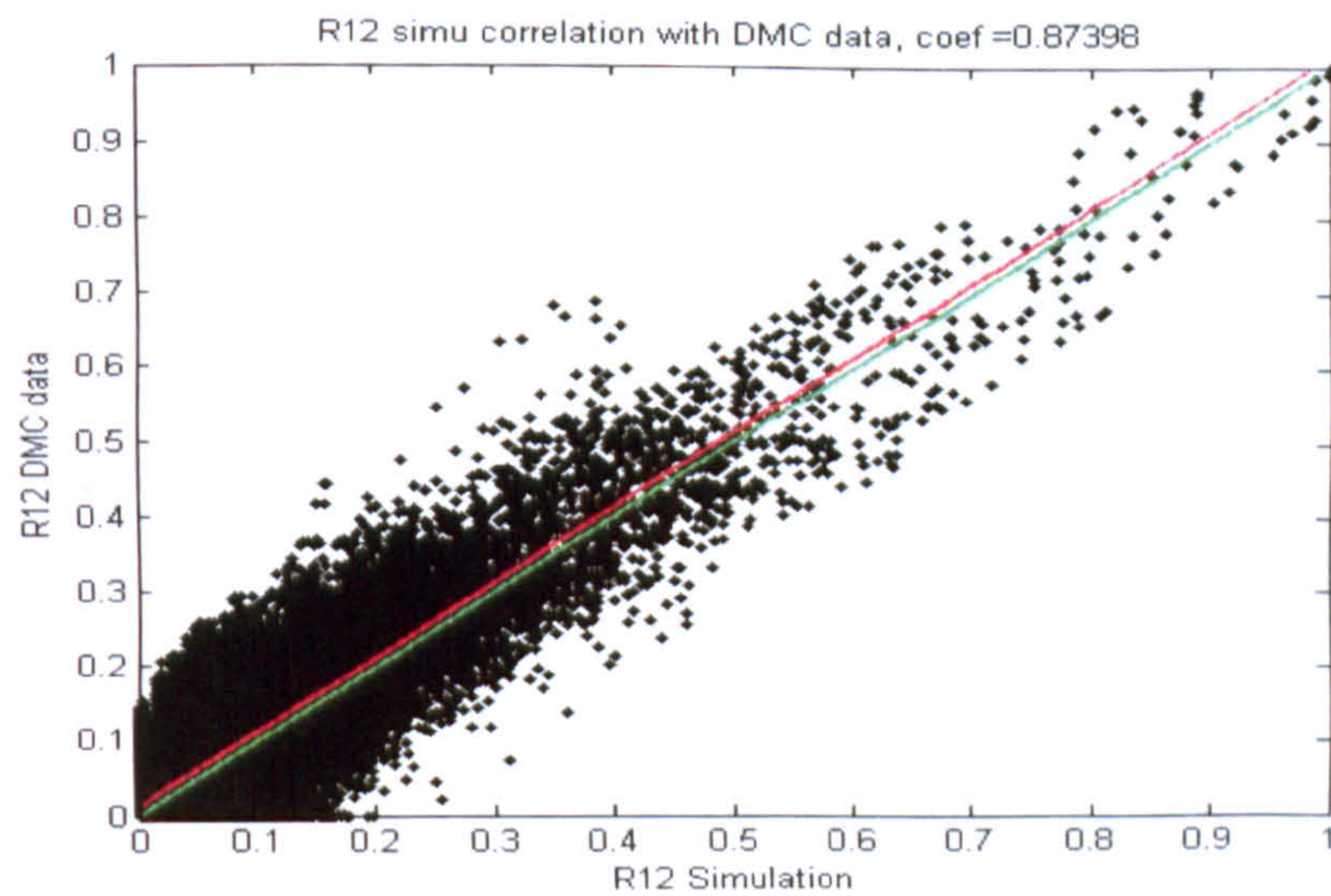


Figure I-20 : The point-to-point correlation of UK-DMC R12 DDM and Simulation.

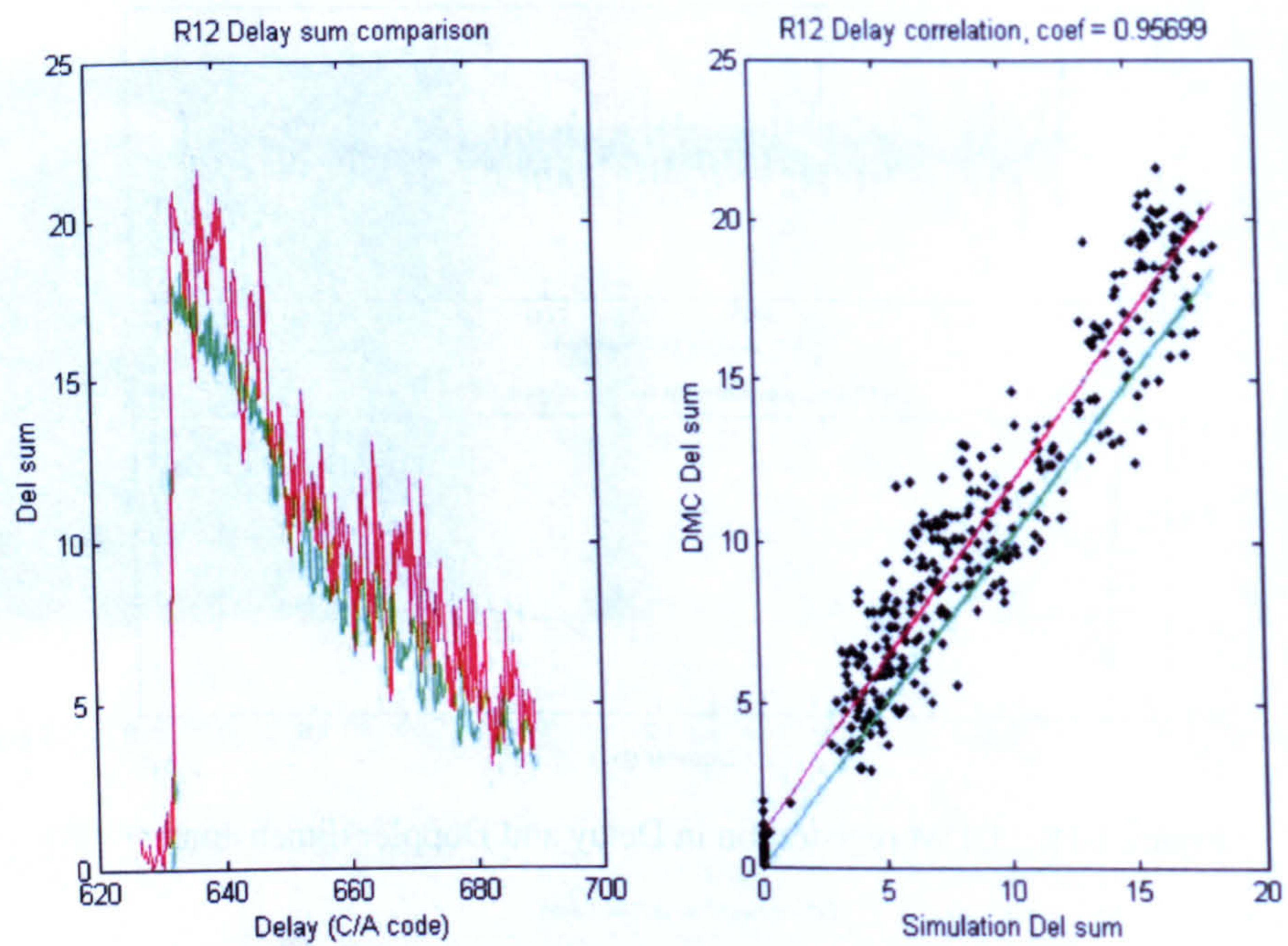


Figure I-21 : Delay dimension correlation

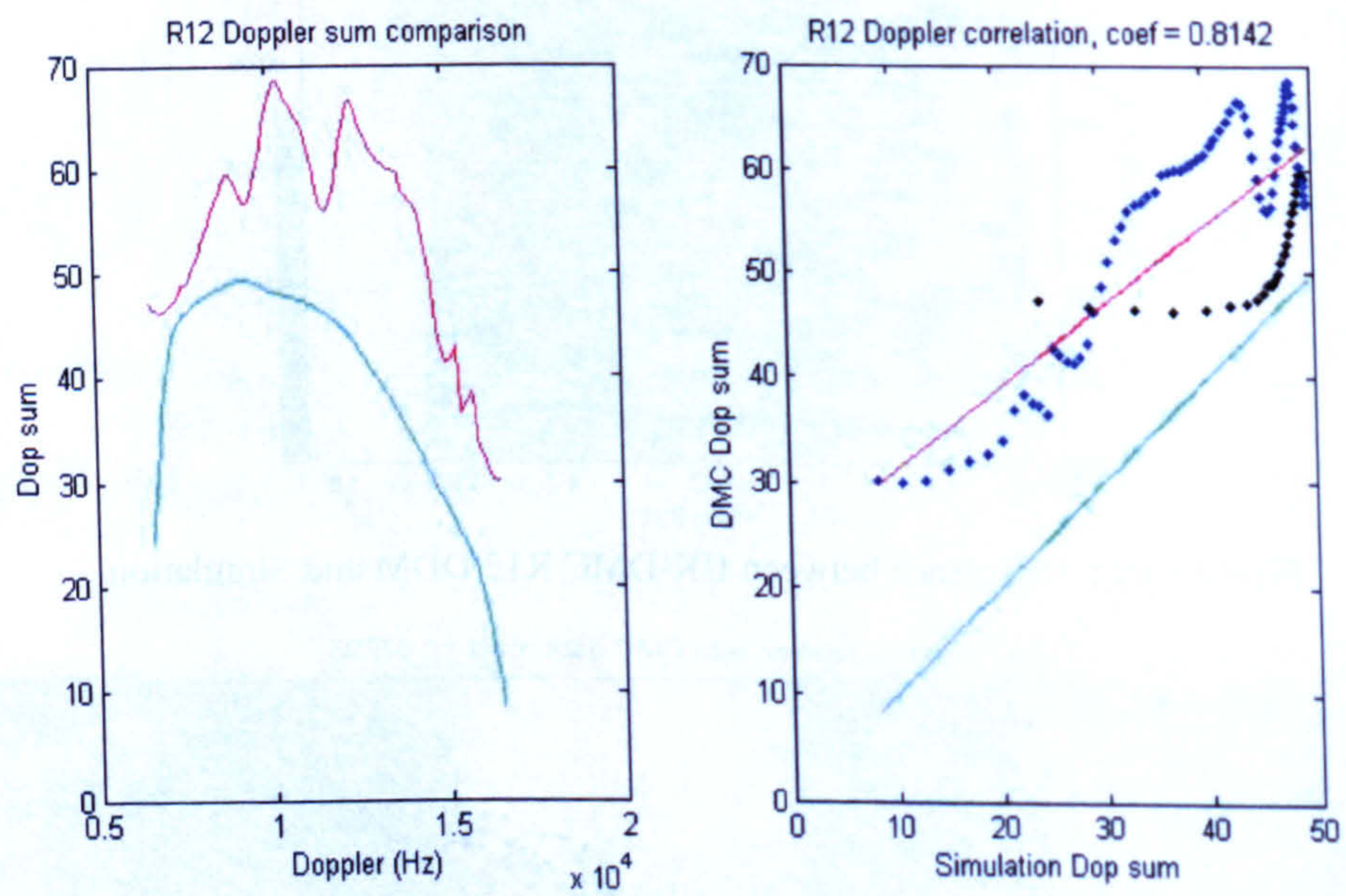


Figure I-22 : Doppler dimension correlation

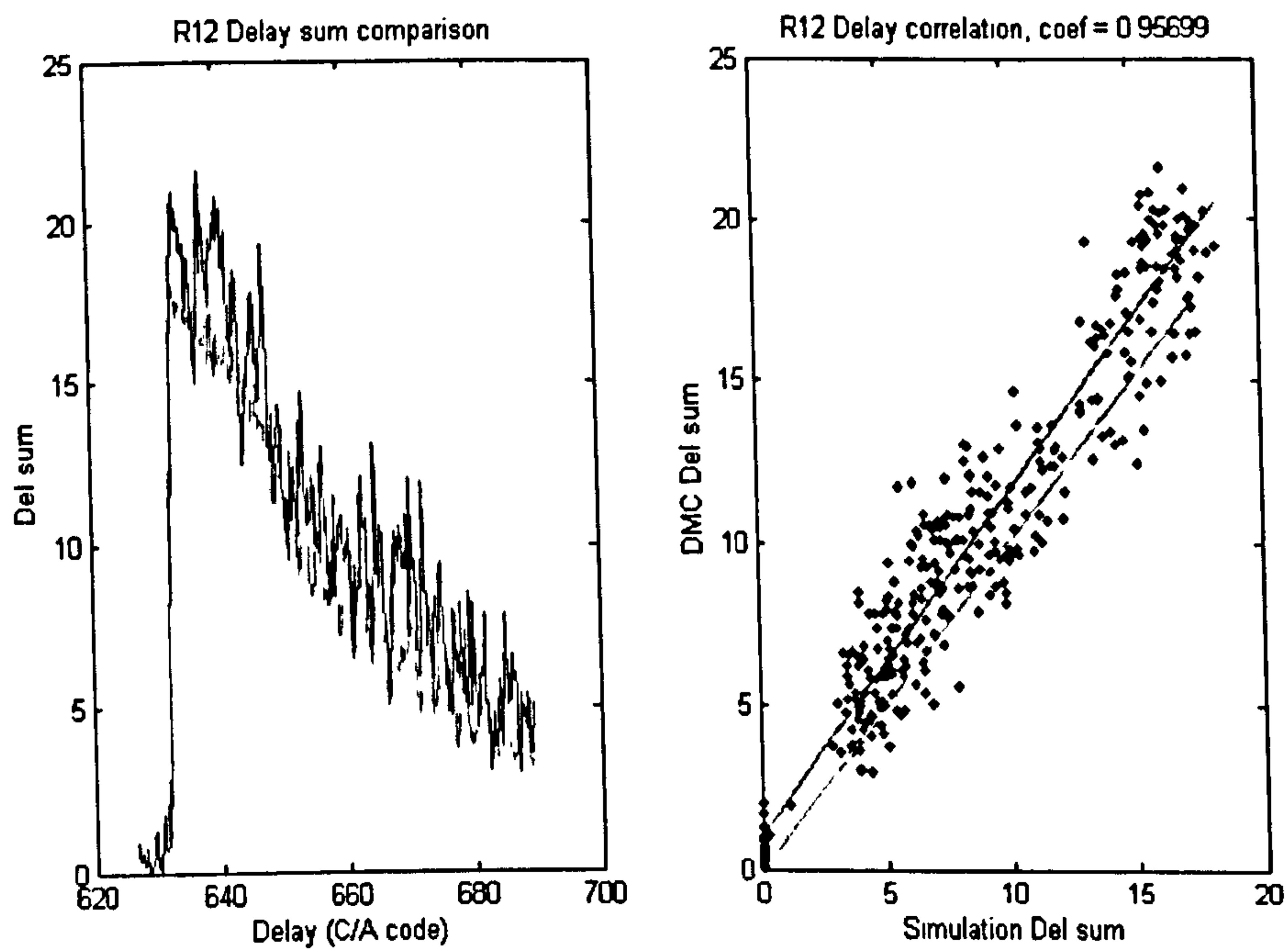


Figure I-21 : Delay dimension correlation

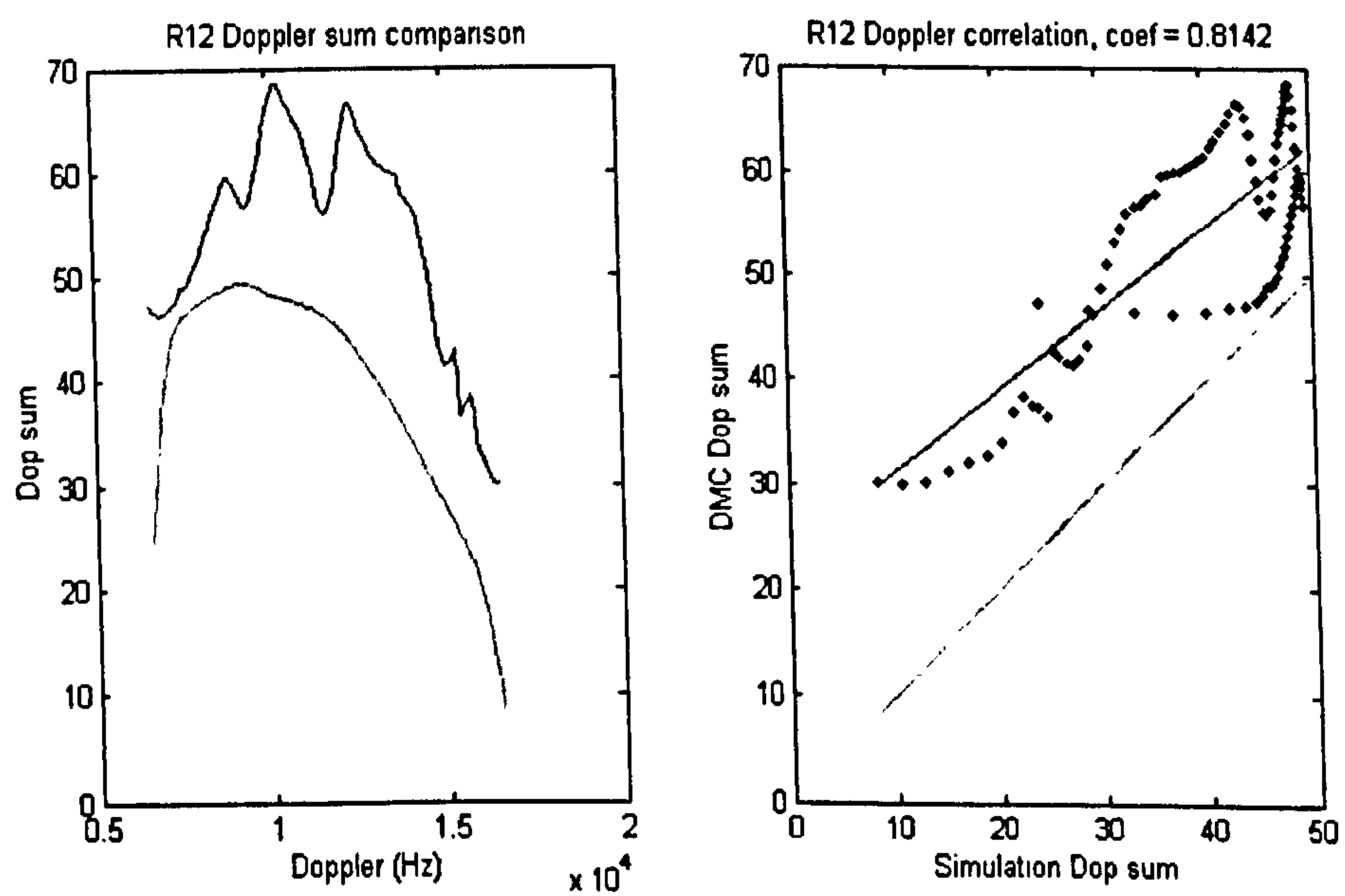


Figure I-22 : Doppler dimension correlation

3. R13 Dataset

GPS emitter satellite	SVN-47
Time tag	26 November 2004 07:36:36 AM
Wind condition (local buoy data)	2.5 m/s , -61°
Significant wave height (SWH)	3.0 m
UK-DMC DDM data facts (normalised)	
Map size : 600 (Delay) * 100 (Doppler) Delay axis : 751 ~ 859 C/A code Doppler axis : 5350 ~ 15250 Hz Peak position : 785.42C/A code , 10850 Hz	
DDM simulation (normalised)	
GPS ECF position : [-7643586, -13809837, 21522958] m GPS ECF velocity : [2630.0, -590.7, 560.8] m/s DMC ECF position : [-3608745, -3798358, 4742386] m DMC ECF velocity : [-4730.4, -2339.5, -5454.1] m/s Predict specular point ECF position : [-3096126.88, -3421811.69, 4388172.36] m Specular point position (latitude/longitude) : [43.6552 , -132.1395] degree Observing incident angle : 17.3045 ° Patch resolution : 200 km * 200 km reflection area (200*200 patches) Delay/Doppler offset : -150.3 C/A code, -376.33 Hz <u>Elfouhaily slope PDF</u> Conditions: wind speed 2.5 m/s, direction -61°, incident angle 17.3045° Gaussian parameters: $\sigma_x = 0.0035998$, $\sigma_y = 0.0036894$, $b_{xy} = 0.019684$ <u>UK-DMC DDM and simulation comparison</u> DDM correlation : p = [0.9958 , -0.0007] Correlation coefficient : c = 0.9205 (Figure I-31) Delay dimension correlation : p = [1.0415, -0.2172] Correlation coefficient : c = 0.97811 (Figure I-32) Doppler dimension correlation : p = [0.7532 , 4.4331] Correlation coefficient : c = 0.79952 (Figure I-33)	

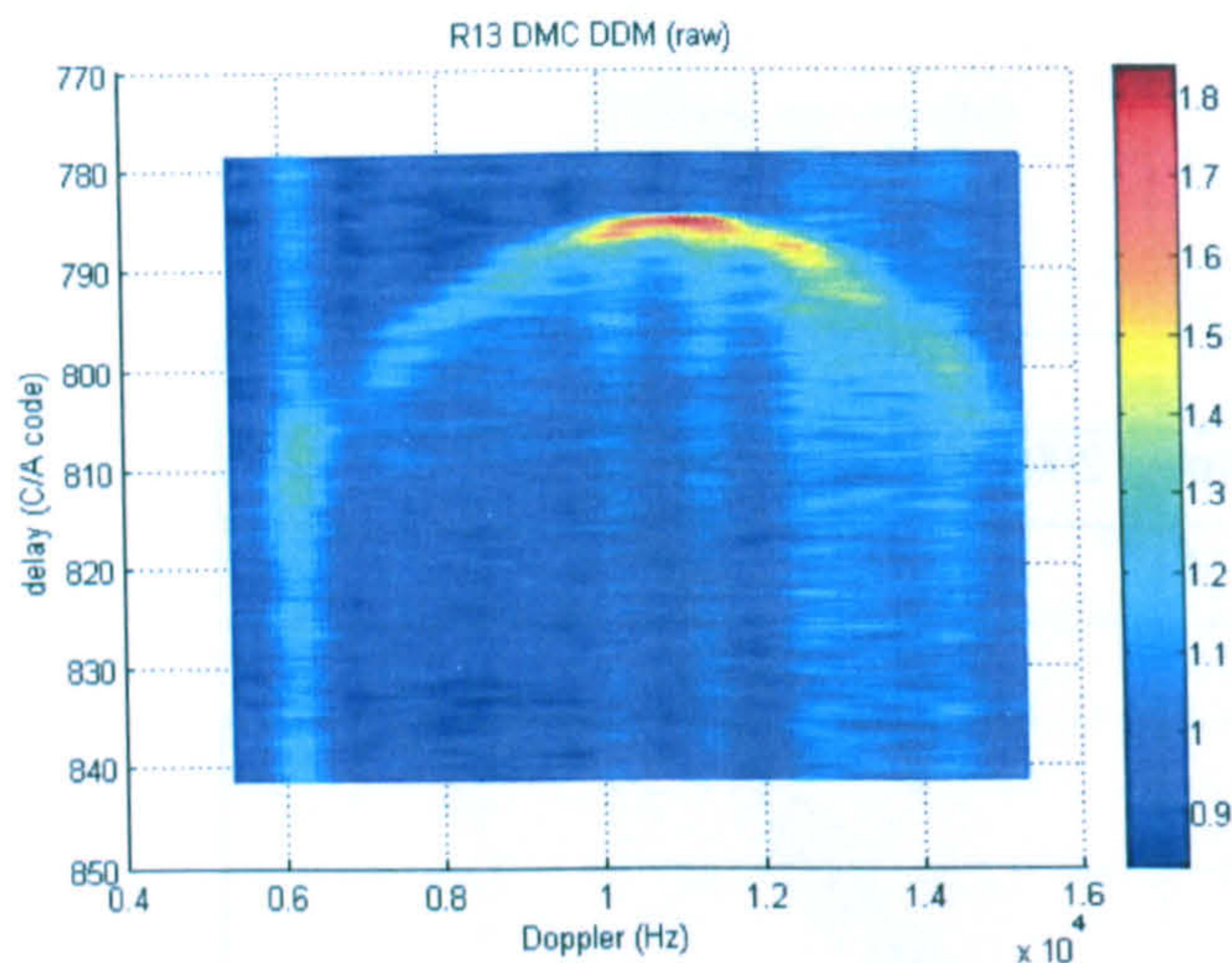


Figure I-23 : UK-DMC R13 DDM data (raw)

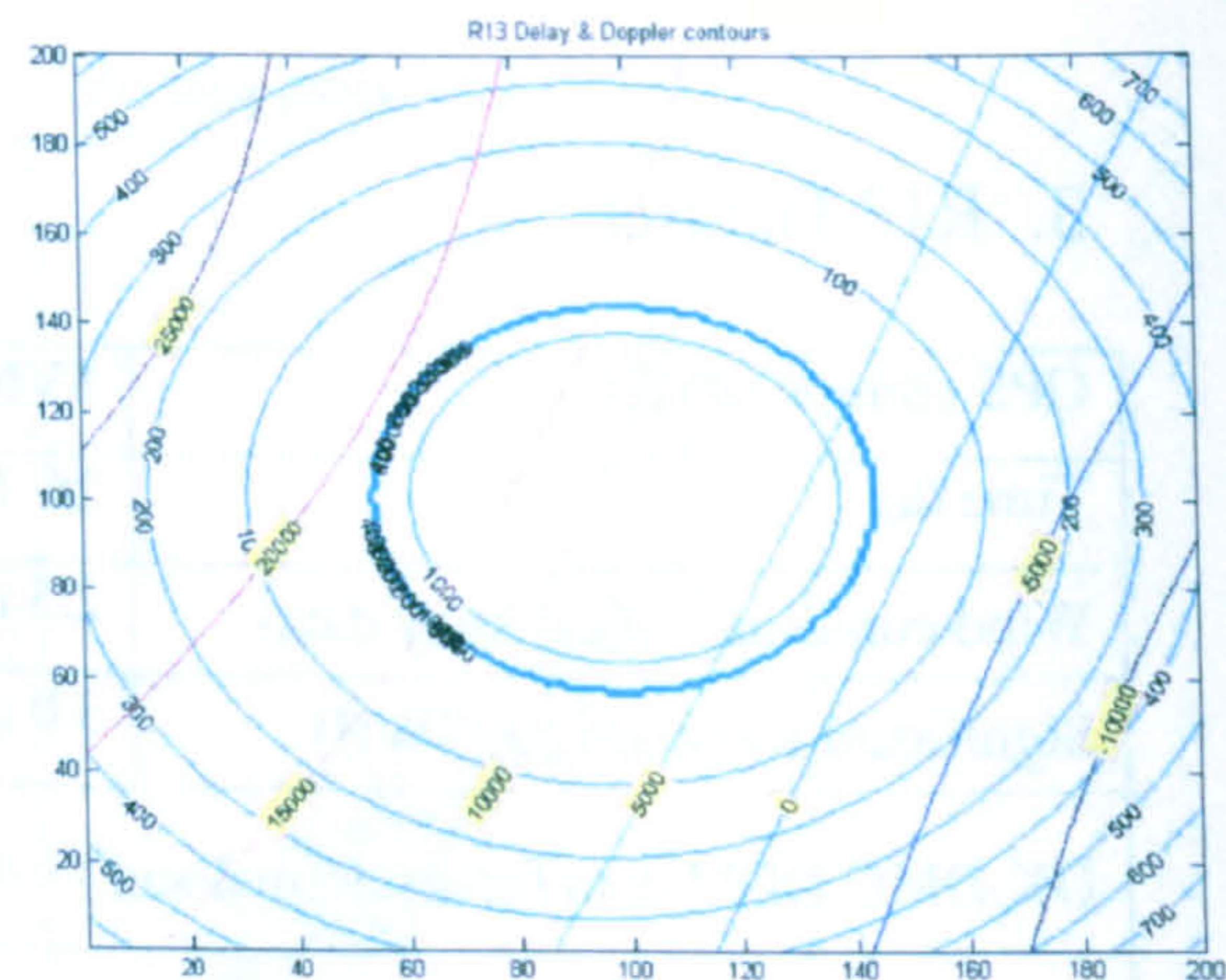


Figure I-26 : Simulated R13 Delay-Doppler contours

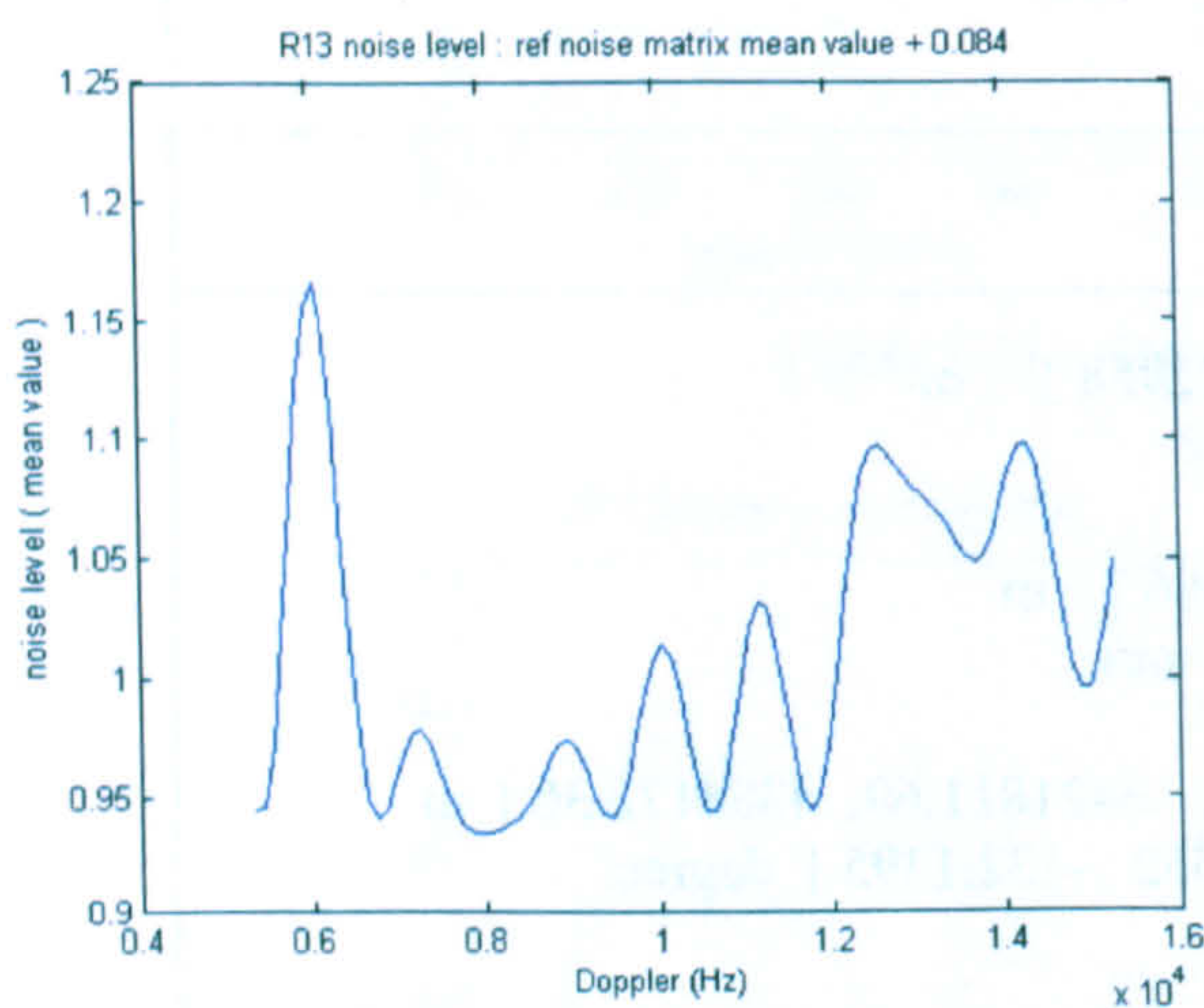


Figure I-24 : UK-DMC R13 DDM bias

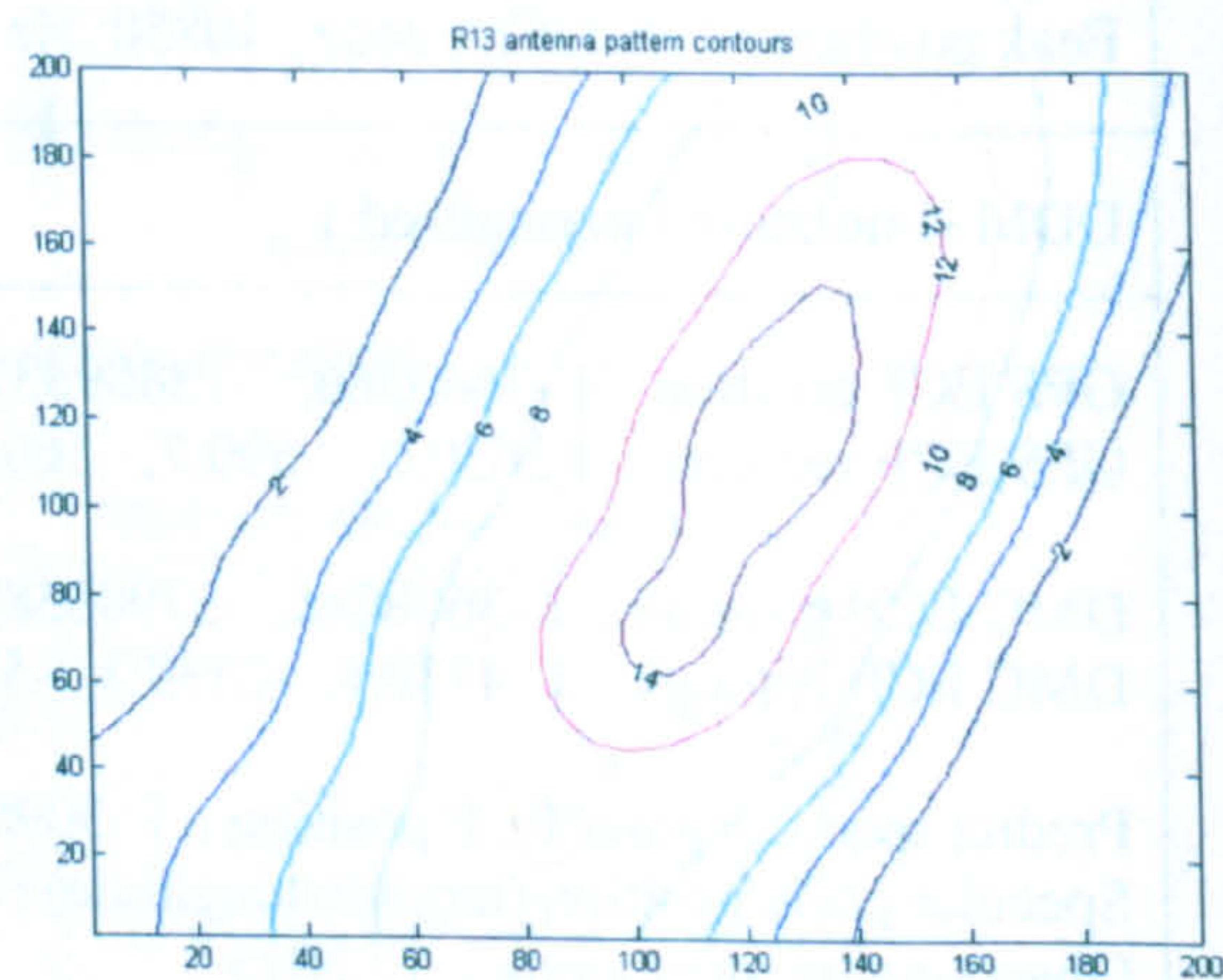


Figure I-27 : Simulated R13 antenna pattern

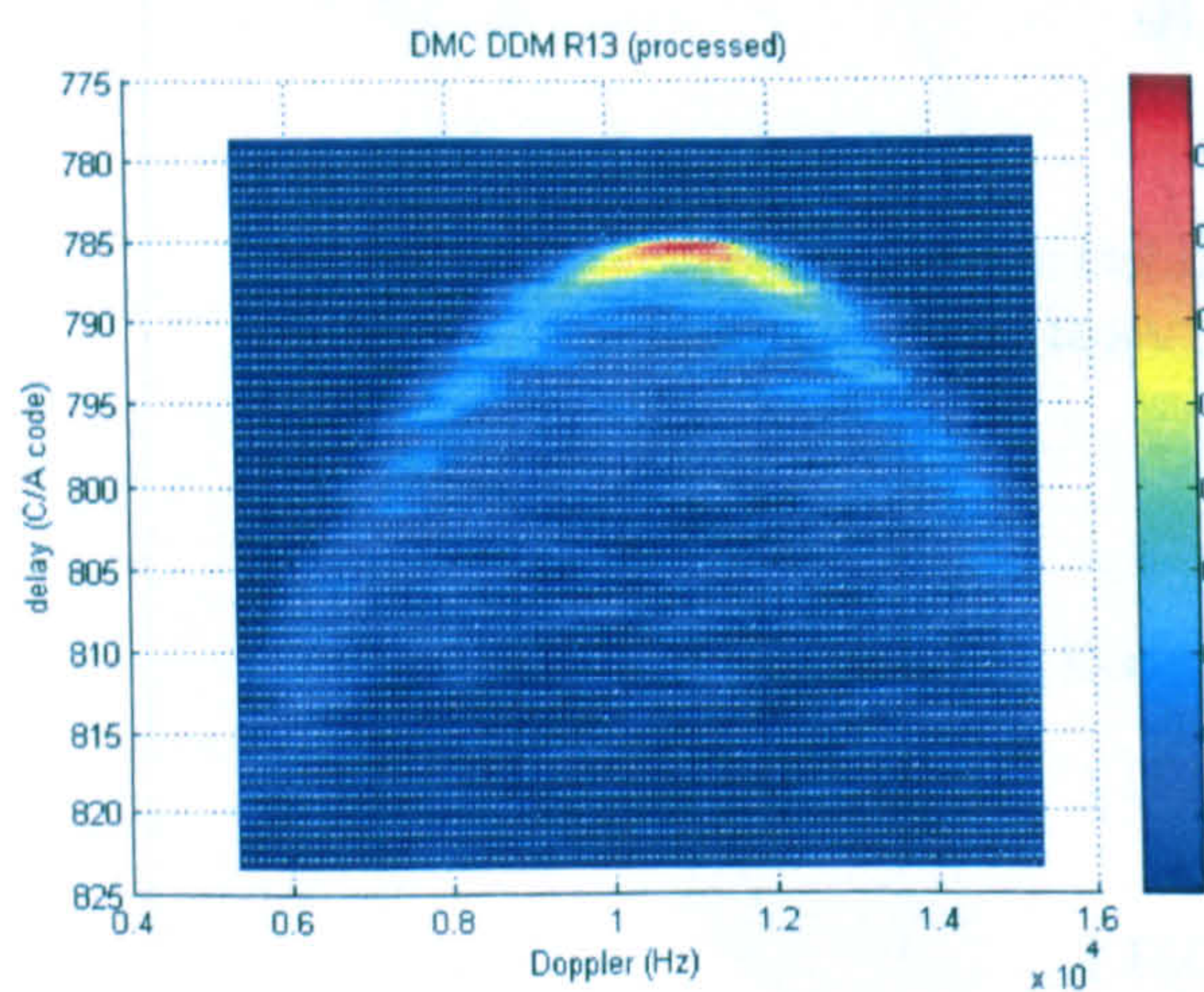


Figure I-25 : UK-DMC R13 DDM data (processed)

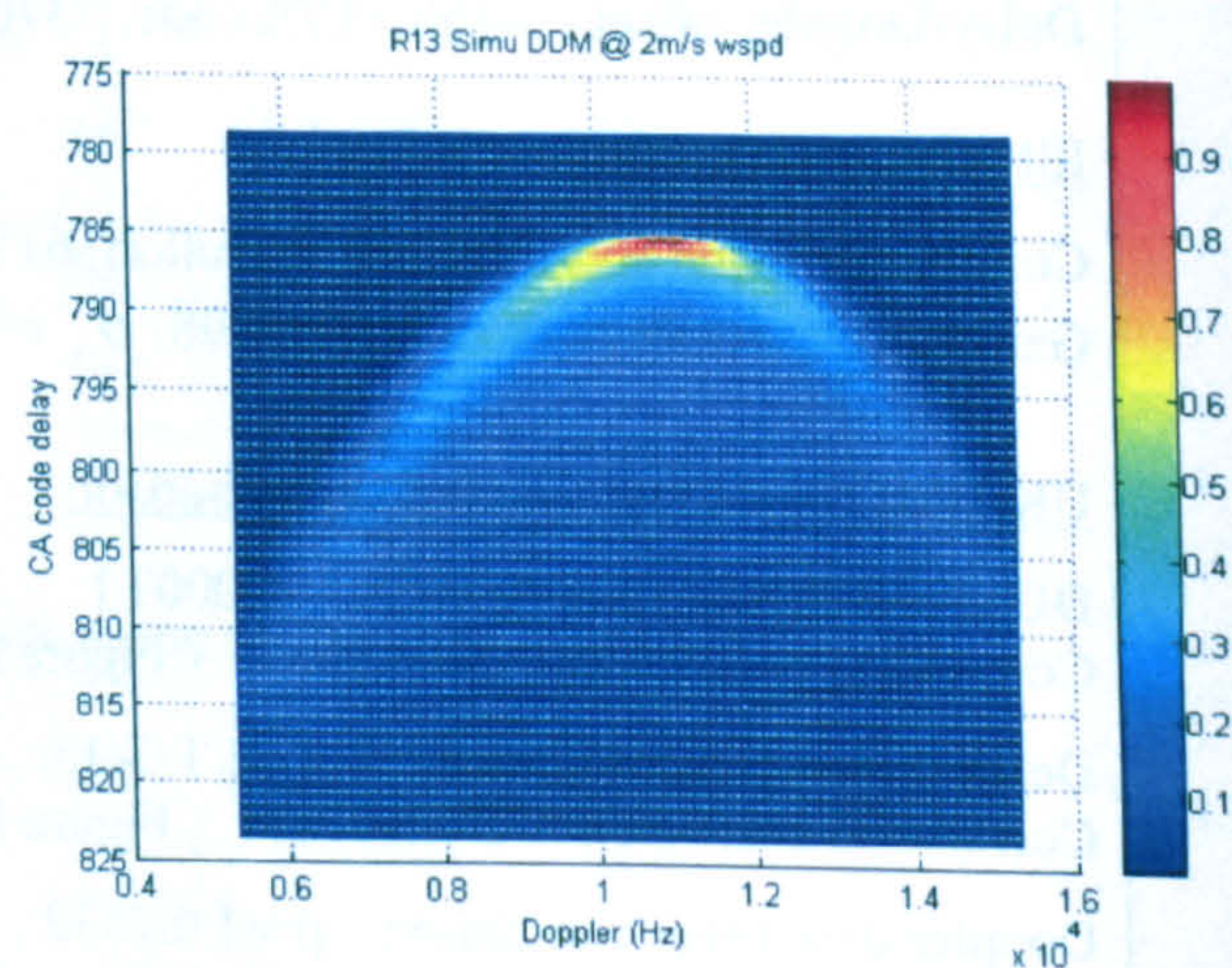


Figure I-28 : Simulated R13 DDM

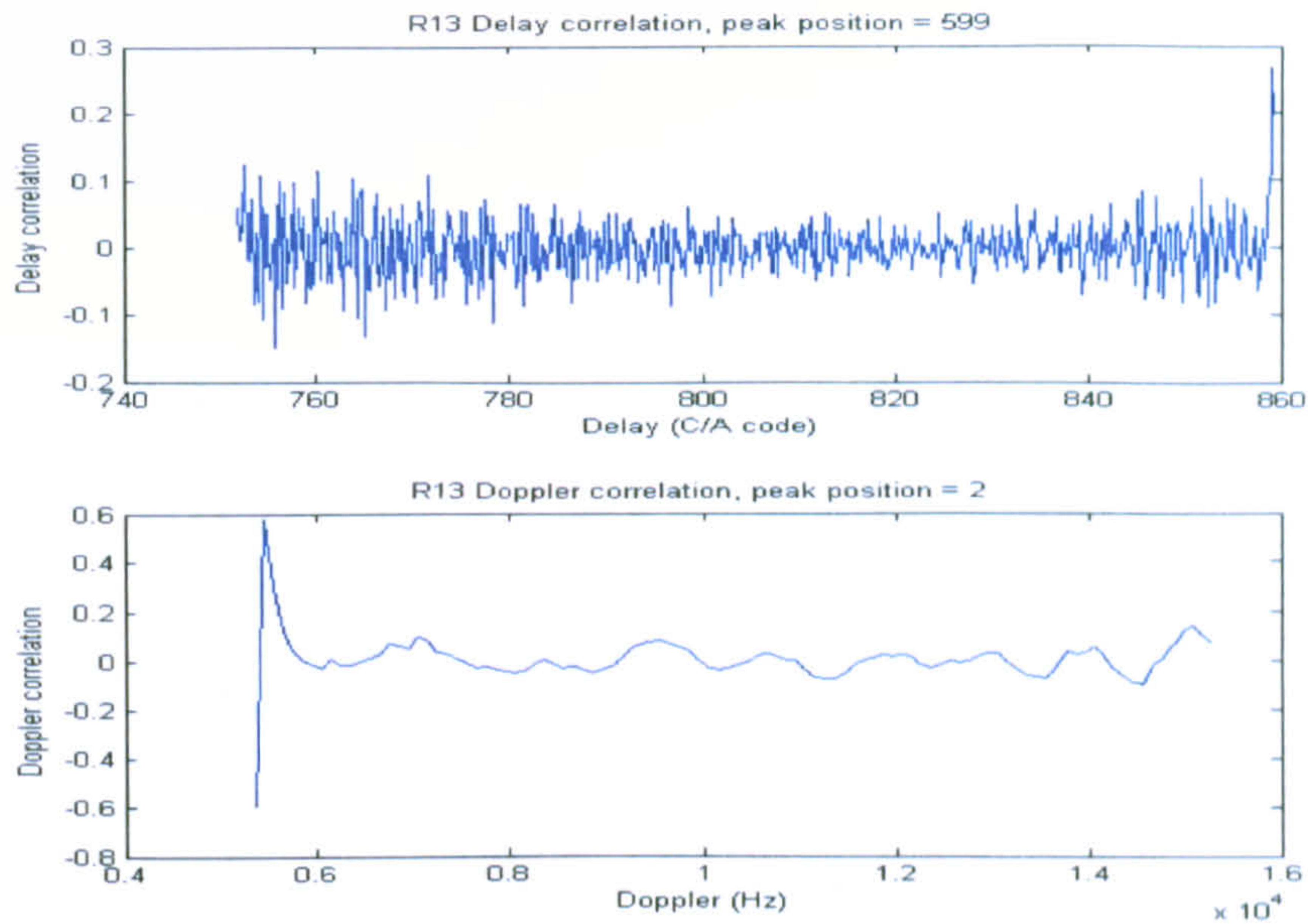


Figure I-29 : DDM registration in Delay and Doppler dimensions

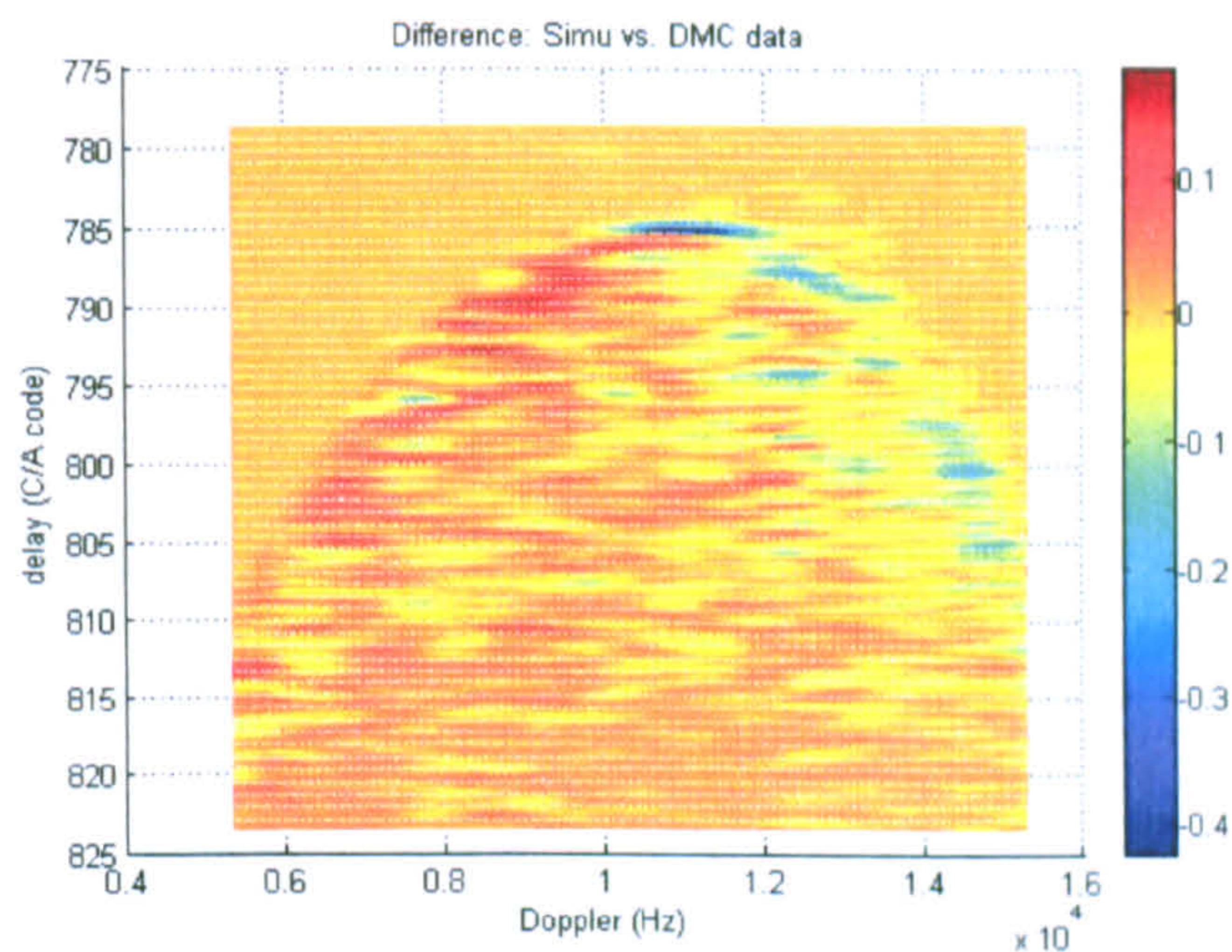


Figure I-30 : Difference between UK-DMC R13 DDM and the Simulation

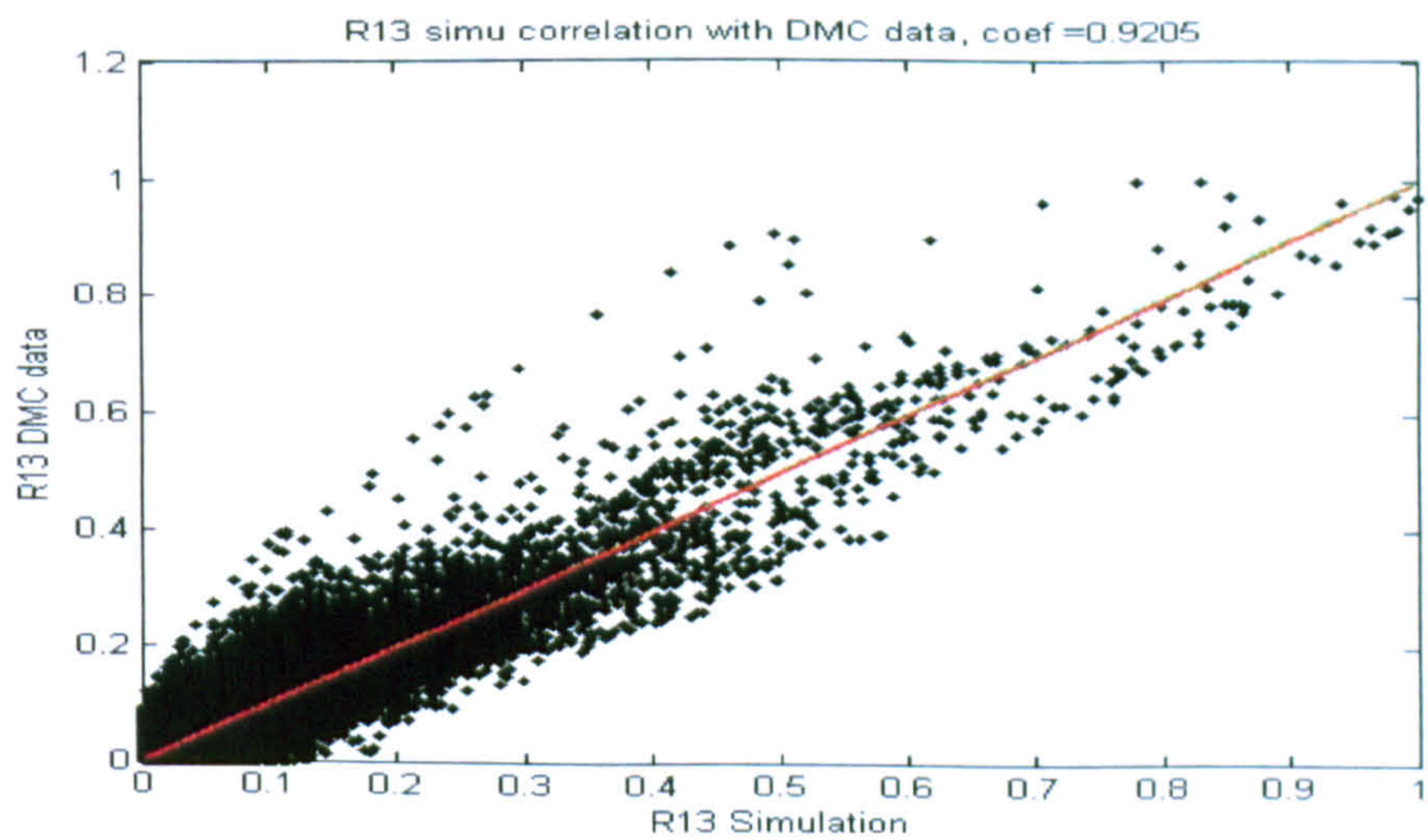


Figure I-31 : The point-to-point correlation of UK-DMC R13 DDM and the Simulation.

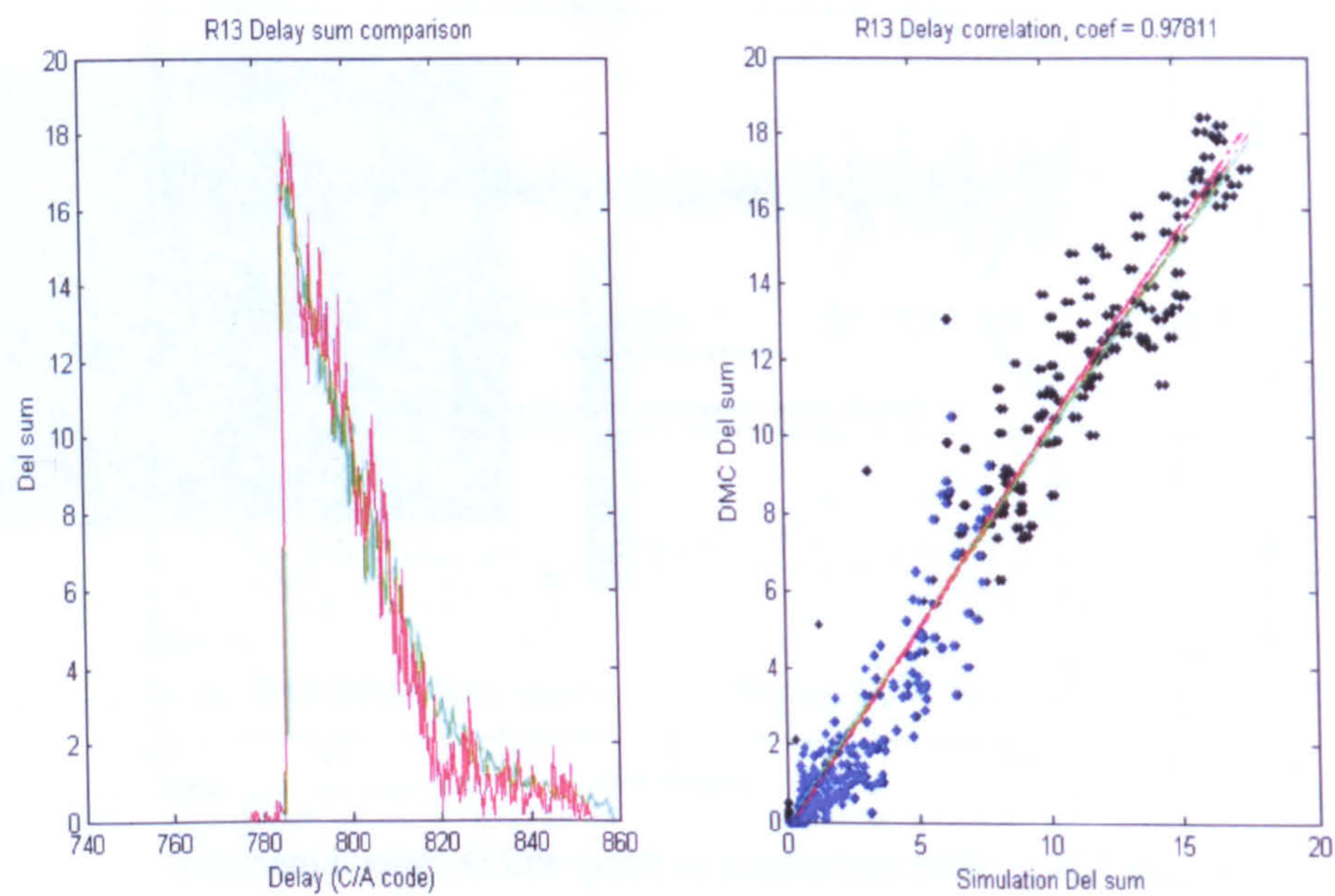


Figure I-32 : Delay dimension correlation

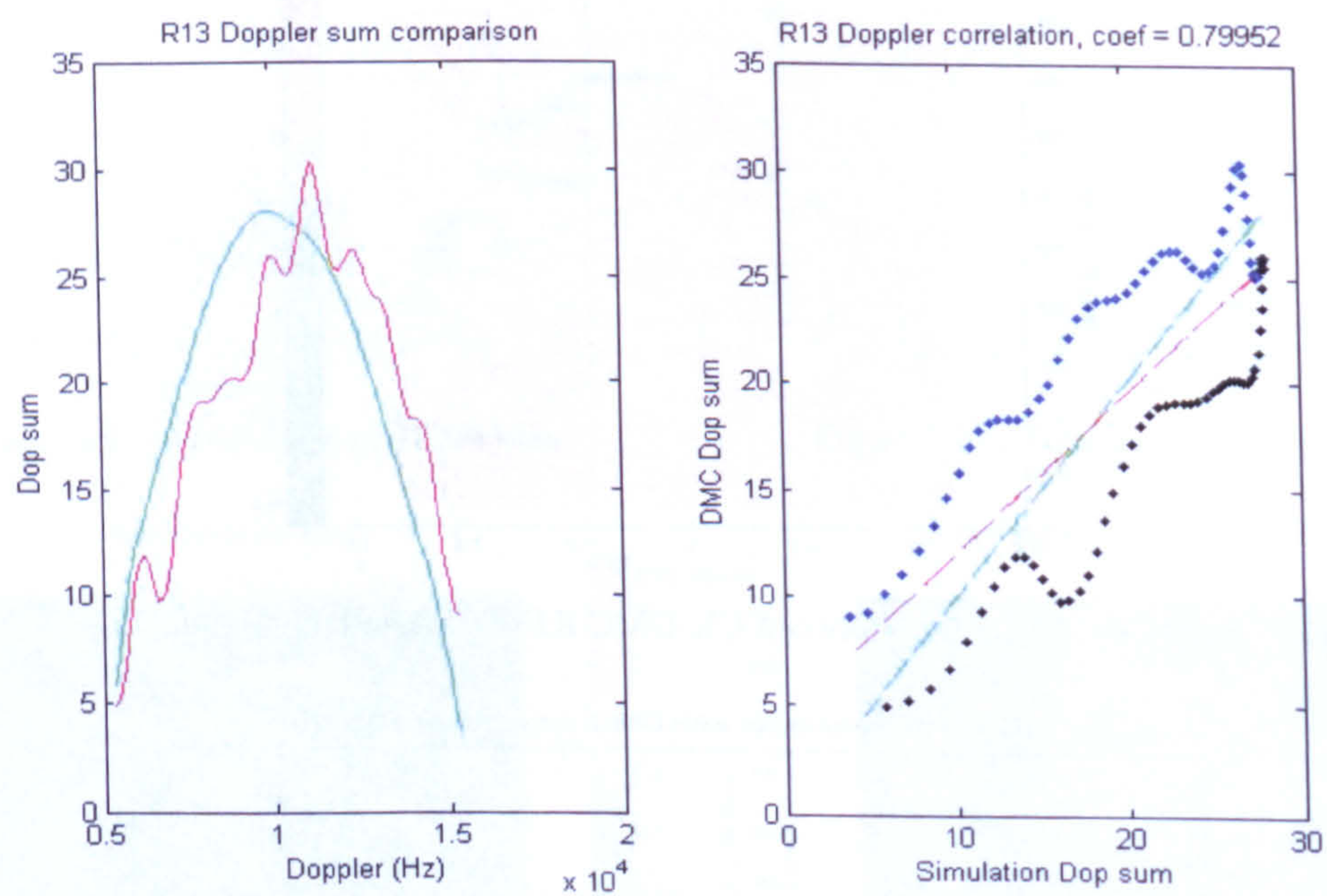


Figure I-33 : Doppler dimension correlation

4. R14 Dataset

GPS emitter satellite	SVN-43
Time tag	14 January 2005 10:23:58 AM
Wind condition (local buoy data)	8 m/s, 52°
Significant wave height (SWH)	3.1 m
UK-DMC DDM data facts (normalised)	
Map size : 1800 (Delay) * 100 (Doppler) Delay axis : 393.8747 ~ 715.9568 C/A code Doppler axis : -6300 ~ 3600 Hz Peak position : 499.5047 C/A code, 500 Hz	
DDM simulation (normalised)	
GPS ECF position : [-11107734, -13170262, 20372705] m GPS ECF velocity : [2526.9, -366.0, 1151.9] m/s DMC ECF position : [-4330955.515, -587985.058, 5535606.211] m DMC ECF velocity : [-5968.491, 248.197, -4535.098] m/s Predict specular point ECF position : [-3925196.84, -525578.48, 4982959.48] m Specular point position (latitude/longitude) : [51.6176, -172.3735] degree Observing incident angle : 1.8143 ° Patch resolution : 200 km * 200 km reflection area (200*200 patches) Delay/Doppler offset : 92.754 C/A code, 1342.4 Hz <u>Elfouhaily slope PDF</u> Conditions: wind speed 8 m/s, direction 52°, incident angle 1.8143 ° Gaussian parameters: $\sigma_x = 0.012157$, $\sigma_y = 0.012261$, $b_{xy} = -0.017047$ <u>UK-DMC DDM and simulation comparison</u> DDM correlation : p = [0.7617 , 0.0578] Correlation coefficient : c = 0.57432 (Figure I-42) Delay dimension correlation : p = [0.8076, 5.6947] Correlation coefficient : c = 0.70794 (Figure I-43) Doppler dimension correlation : p = [0.4323 , 115.3047] Correlation coefficient : c = 0.71303 (Figure I-44)	

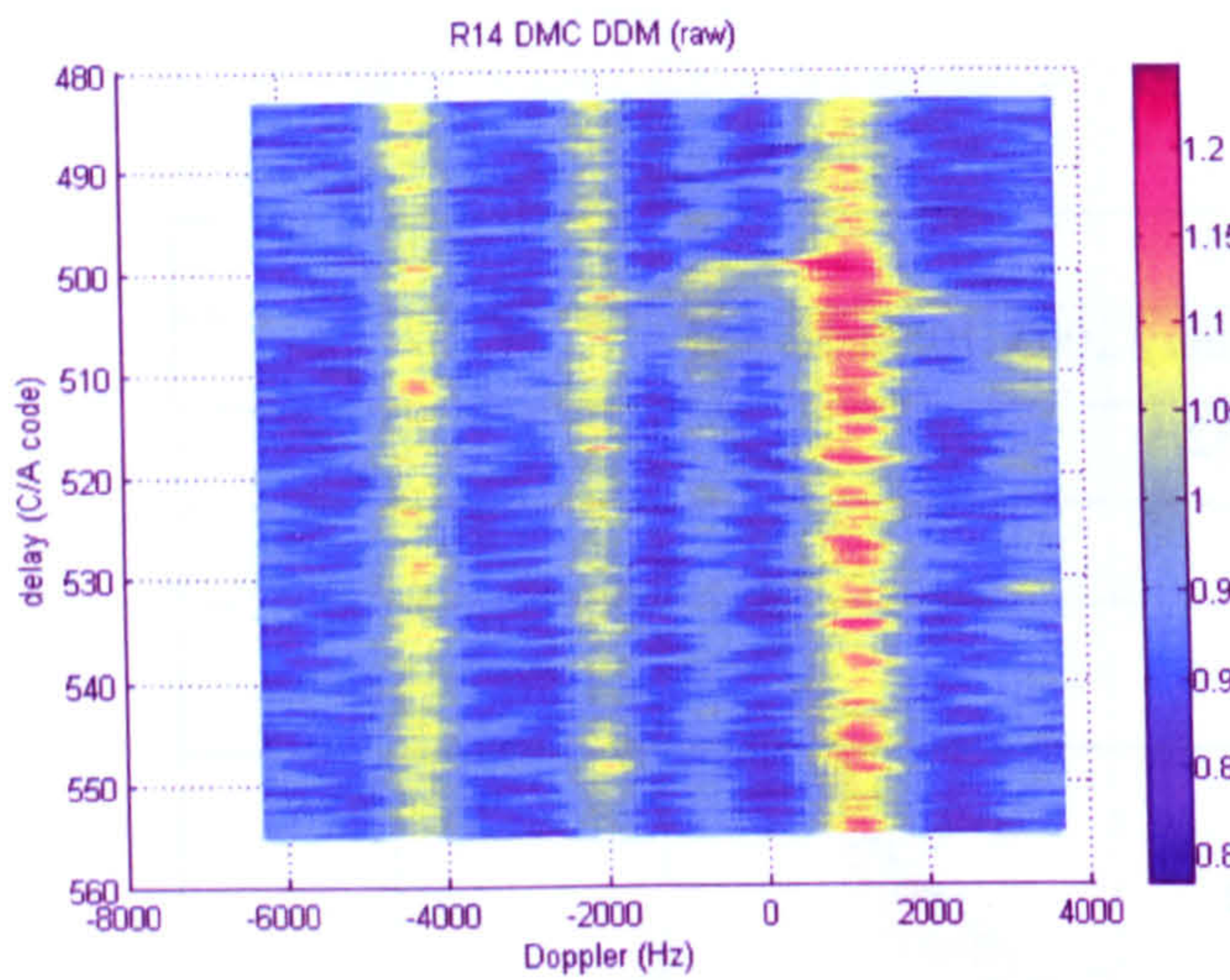


Figure I-34 : UK-DMC R14 DDM data (raw)

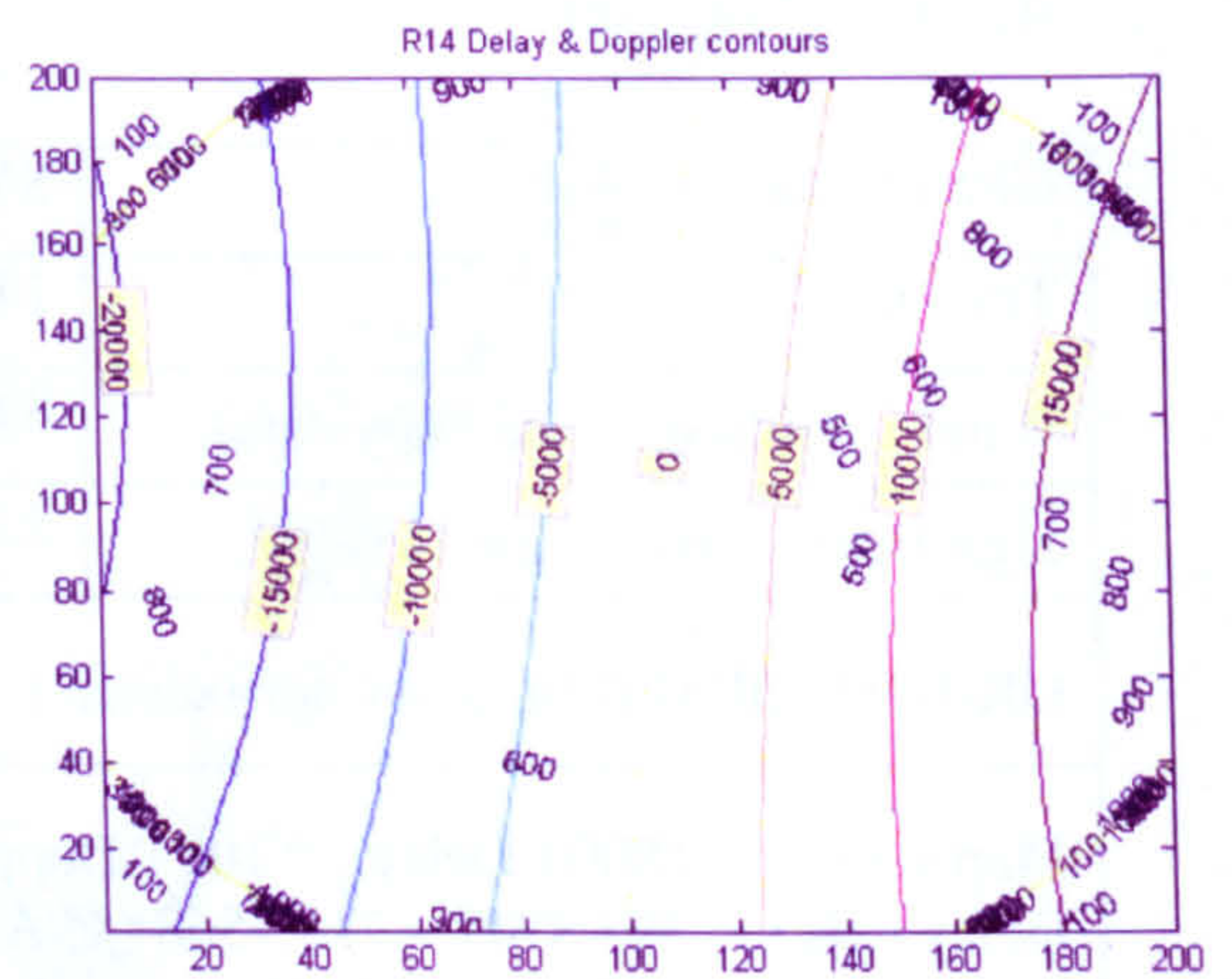


Figure I-37 : Simulated R14 Delay-Doppler contours

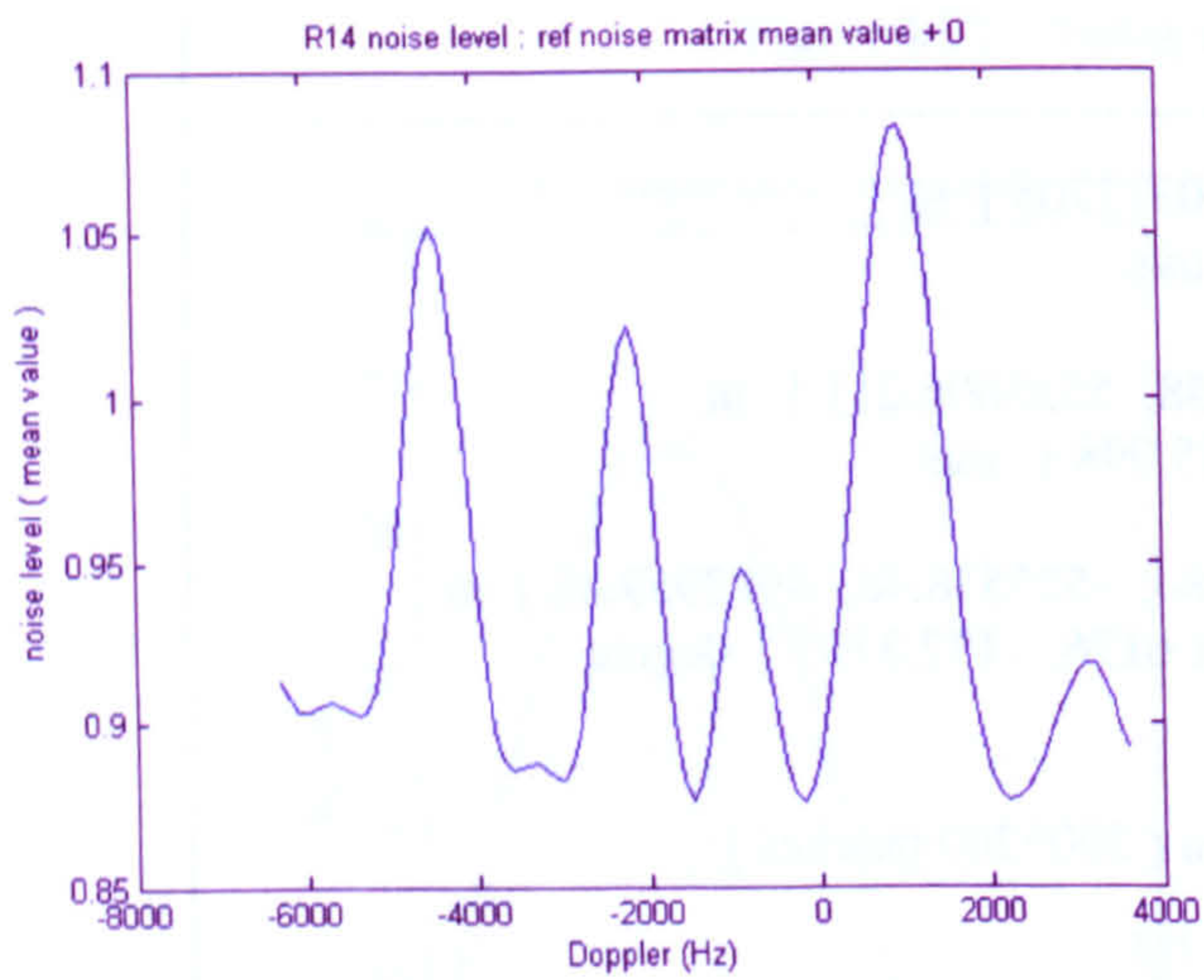


Figure I-35 : UK-DMC R14 DDM bias

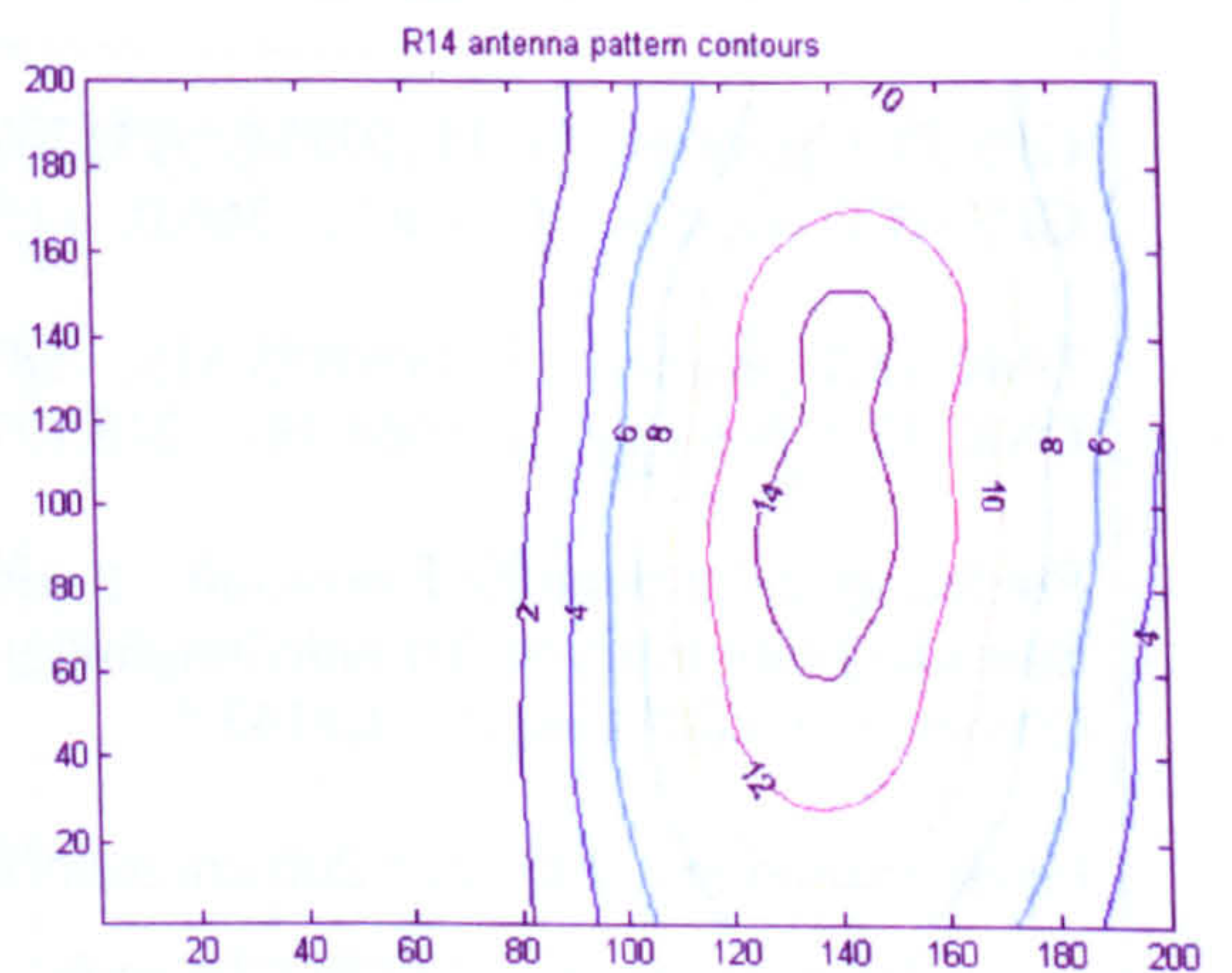


Figure I-38 : Simulated R14 antenna pattern

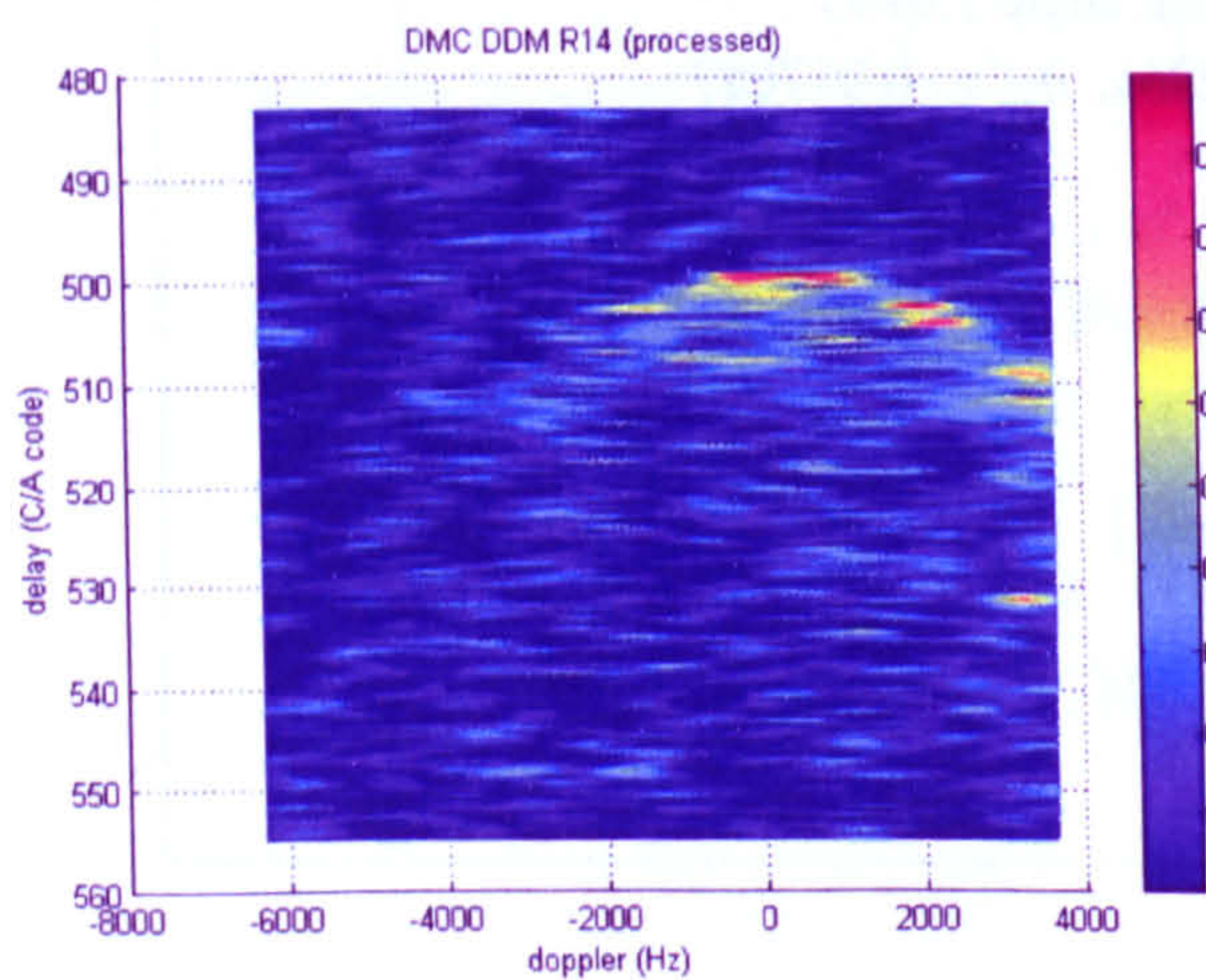


Figure I-36 : UK-DMC R14 DDM data (processed)

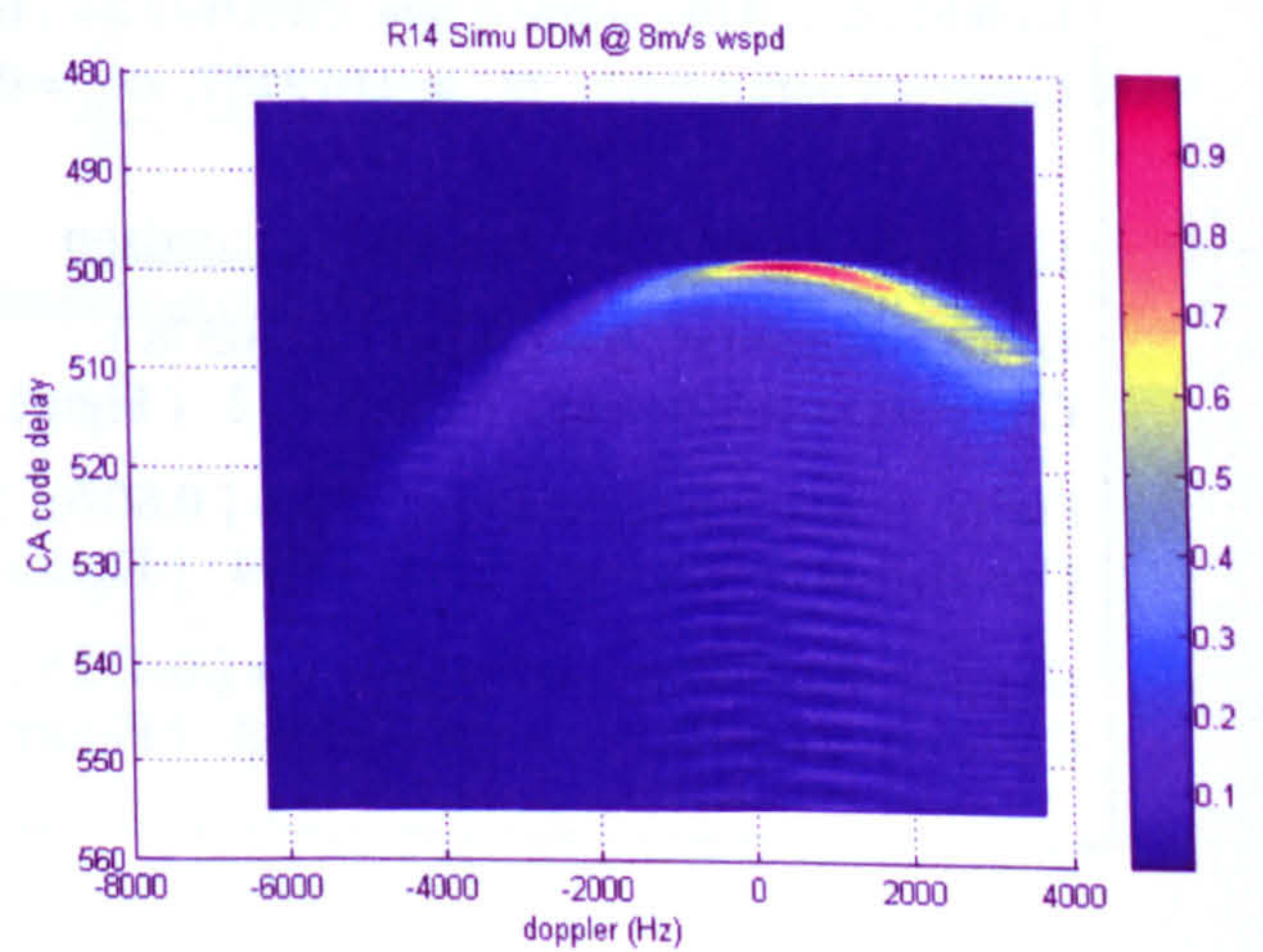


Figure I-39 : Simulated R14 DDM

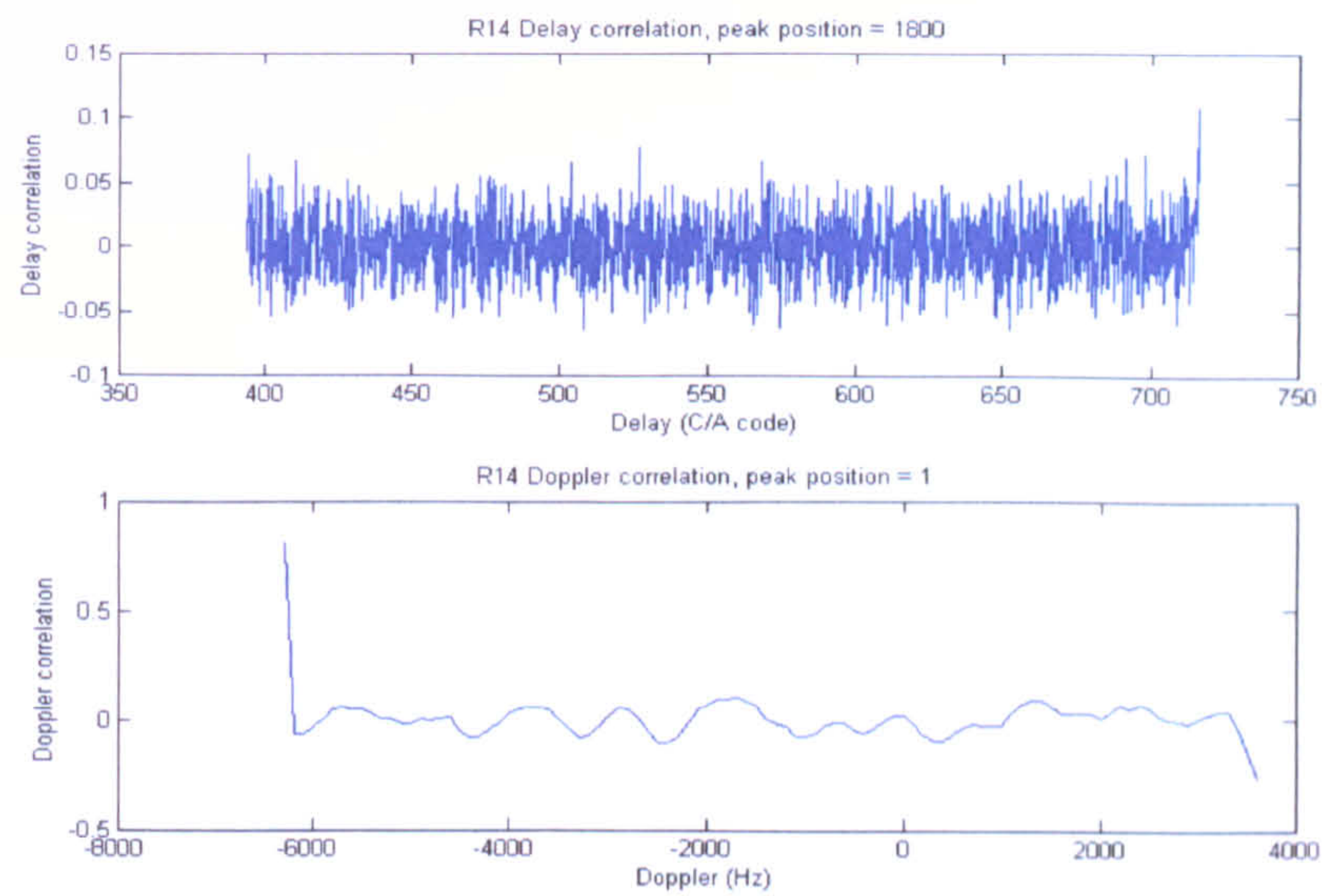


Figure I-40 : R14 DDM registration in Delay and Doppler dimensions

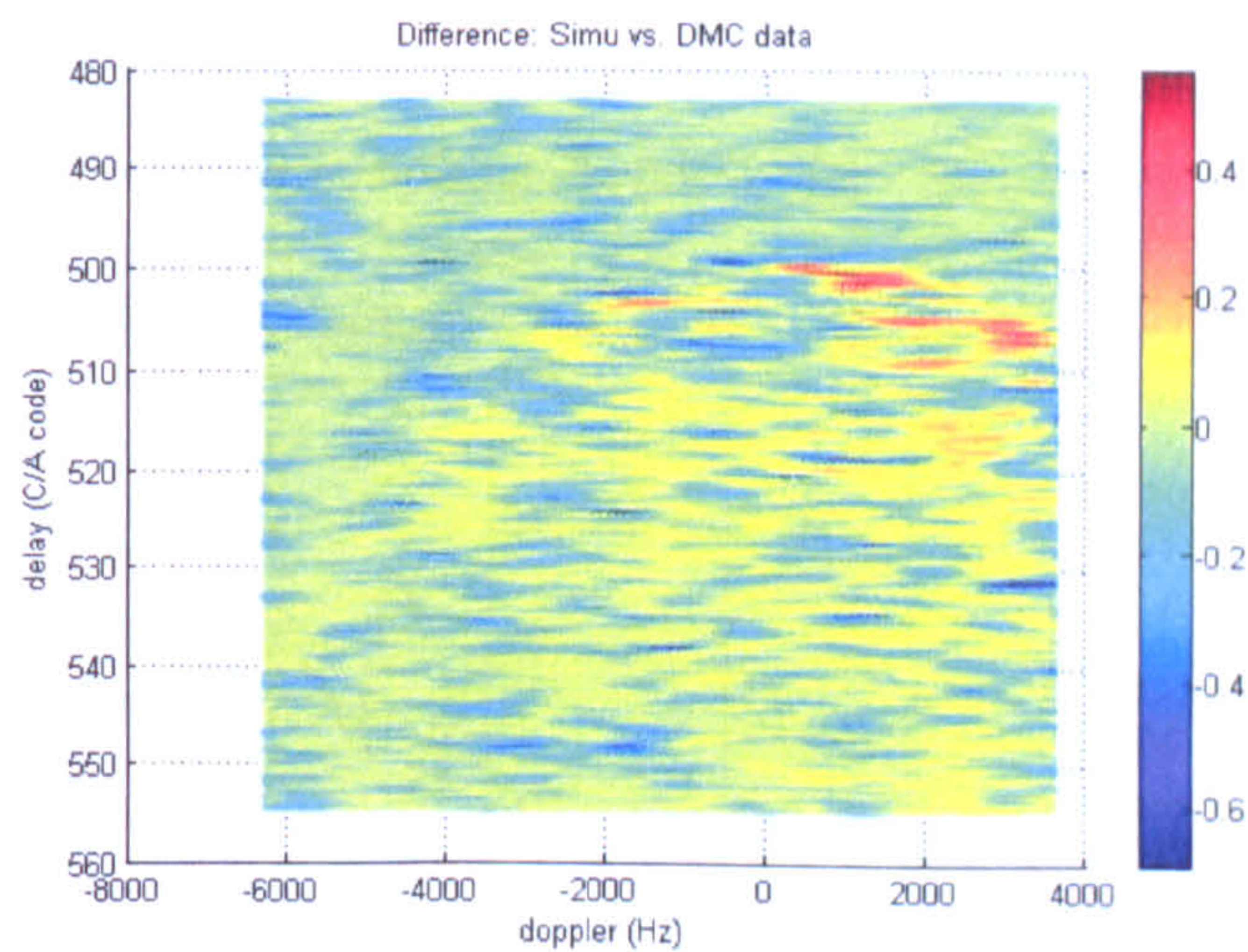


Figure I-41 : Difference between UK-DMC R14 DDM and the Simulation

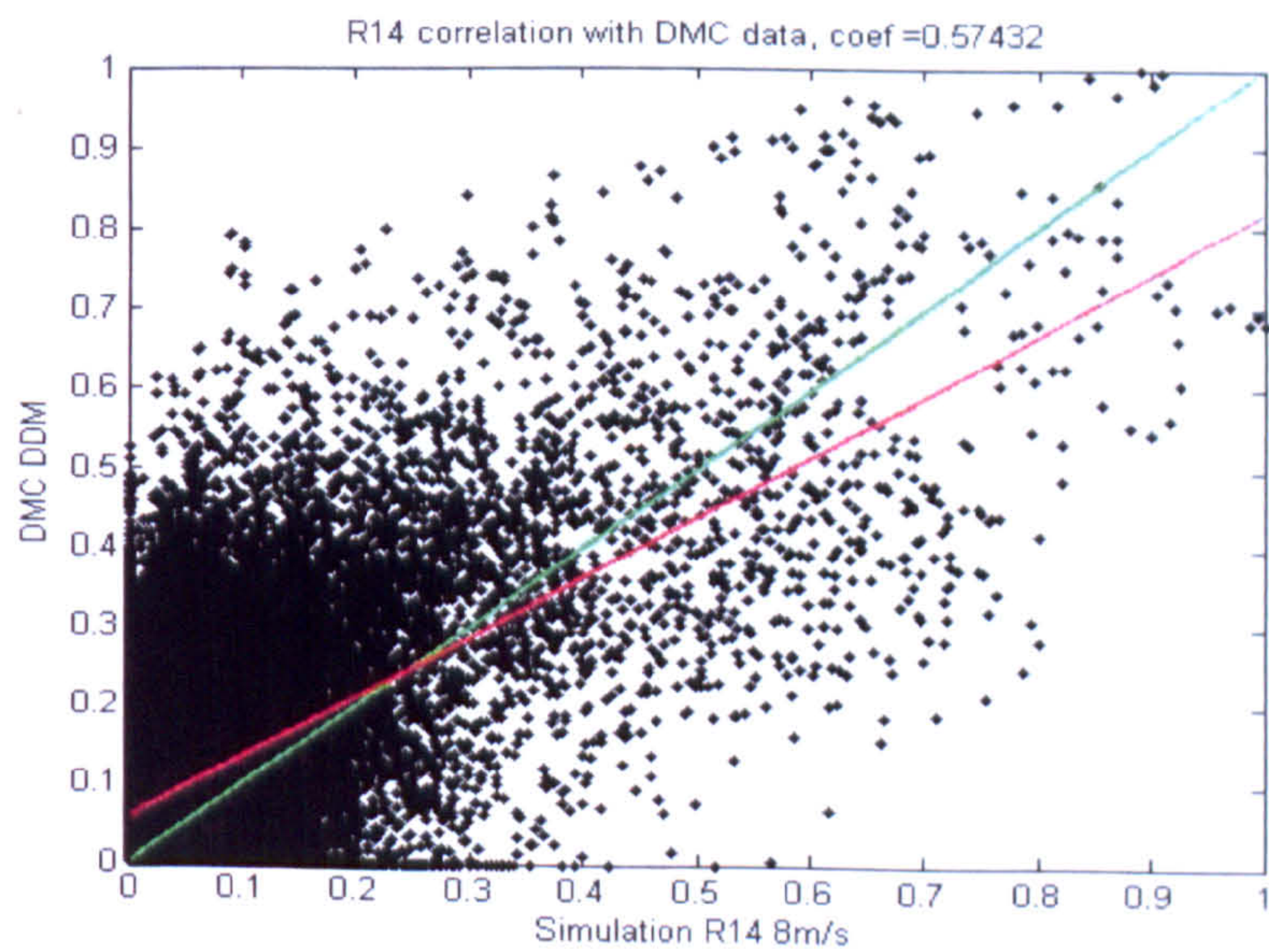


Figure I-42 : The point-to-point correlation of UK-DMC R14 DDM and the Simulation

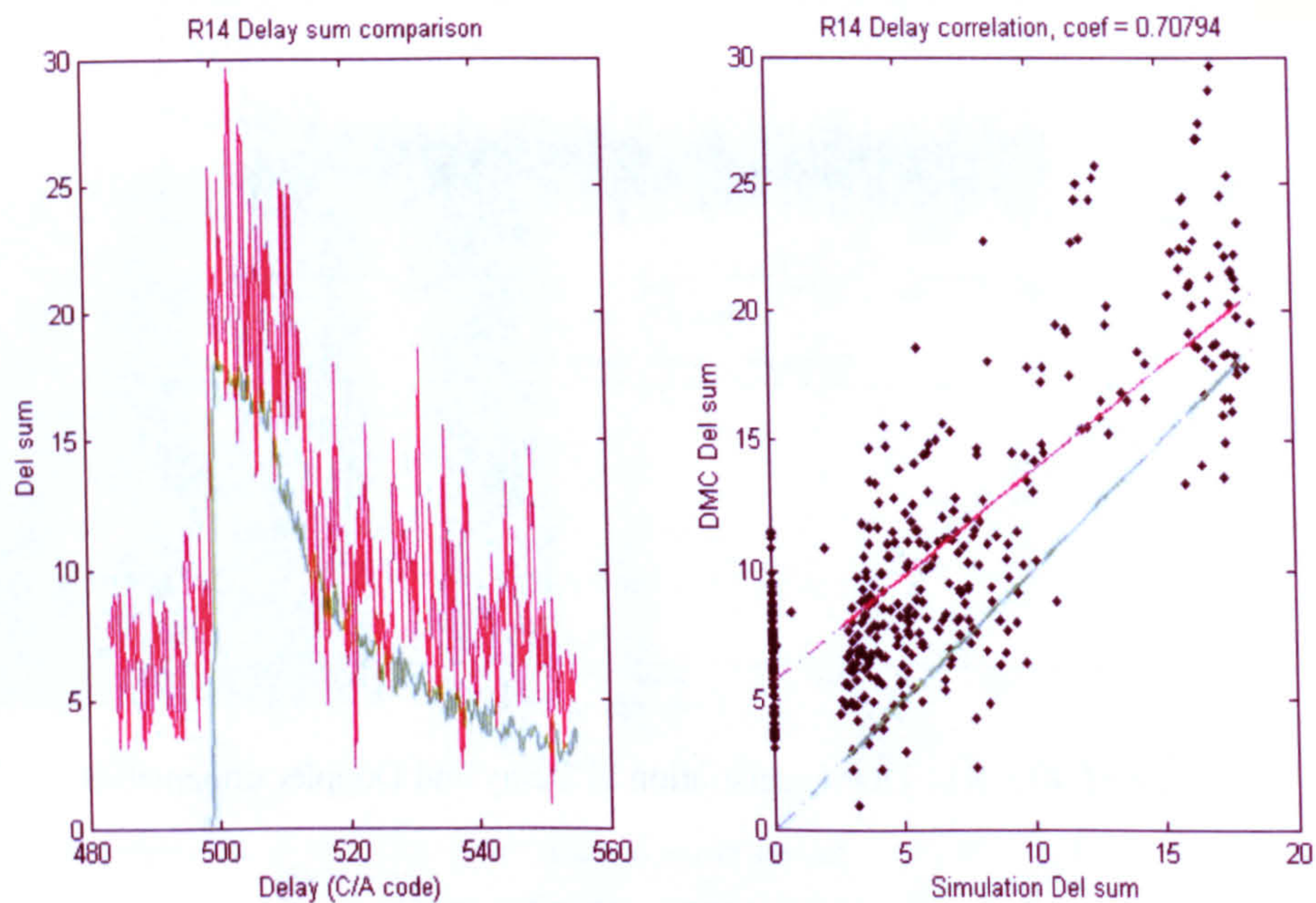


Figure I-43 : R14 Delay dimension correlation

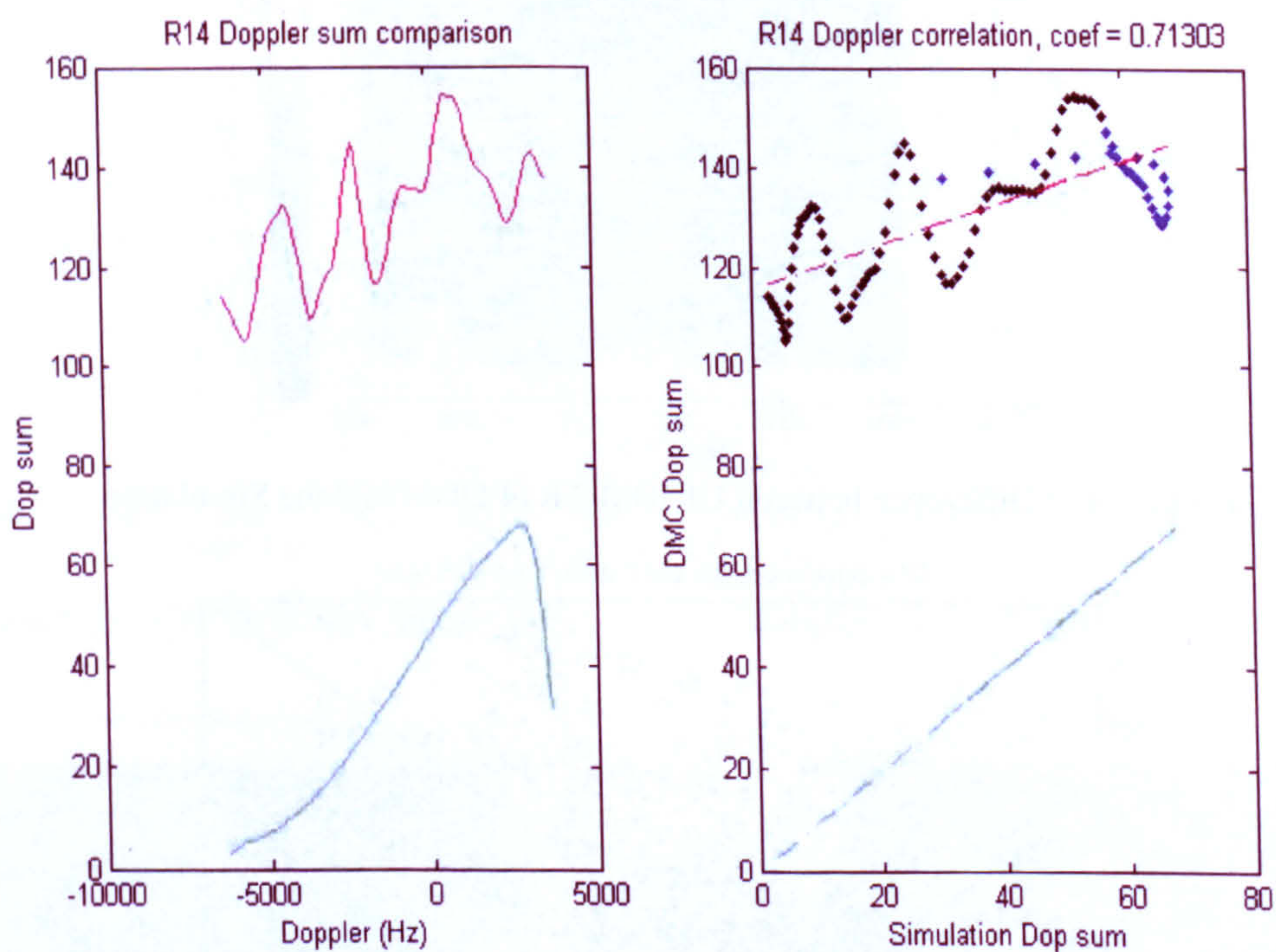


Figure I-44 : R14 Doppler dimension correlation

5. R15 Dataset

GPS emitter satellite	SVN-43
Time tag	30 January 2005 09:05:21 AM
Wind condition (local buoy data)	7.3 m/s, 69°
Significant wave height (SWH)	3.15 m
UK-DMC DDM data facts (normalised)	
Map size : 714 (Delay) * 100 (Doppler) Delay axis : 895.1698 ~ 1022.8209 C/A code Doppler axis : 13350 ~ 23250 Hz Peak position : 920.95 C/A code , 17250 Hz	
DDM simulation (normalised)	
GPS ECF position : [-18175565, -509440, 19279338] m GPS ECF velocity : [1727.9, -1748.2, 1585.0] m/s DMC ECF position : [-6256440, -2258389, 2353554]m DMC ECF velocity : [-2894.4, 673.0, -7006.1] m/s Predict specular point ECF position : [-5580528.55, -1827066.91, 2481663.23] m Specular point position (latitude/longitude) : [22.9793 , -161.8715] degree Observing incident angle : 35.0878 ° Patch resolution : 200 km * 200 km reflection area (200*200 patches) Delay/Doppler offset : 23.756 C/A code, 972.57 Hz <u>Elfouhaily slope PDF</u> Conditions: wind speed 7.3 m/s, direction 69°, incident angle 35.0878 ° Gaussian parameters: $\sigma_x = 0.0110$, $\sigma_y = 0.0113$, $b_{xy} = -0.01203$ <u>UK-DMC DDM and simulation comparison</u> DDM correlation : p = [0.9821 , 0.0392] Correlation coefficient : c = 0.77466 (Figure I-53) Delay dimension correlation : p = [1.1493, 3.1285] Correlation coefficient : c = 0.91327 (Figure I-54) Doppler dimension correlation : p = [0.8611 , 32.1040] Correlation coefficient : c = 0.83277 (Figure I-55)	

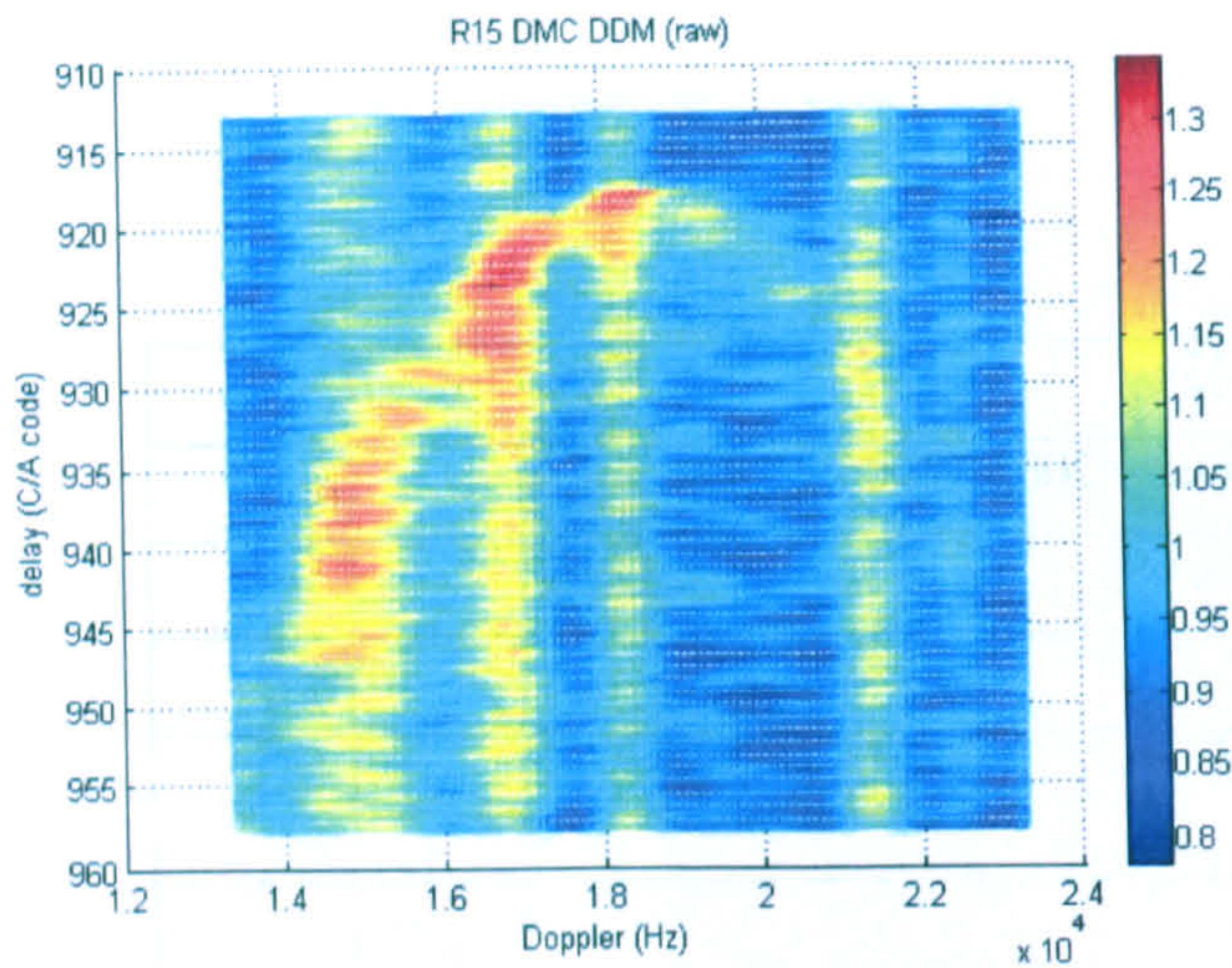


Figure I-45 : UK-DMC R15 DDM data (raw)

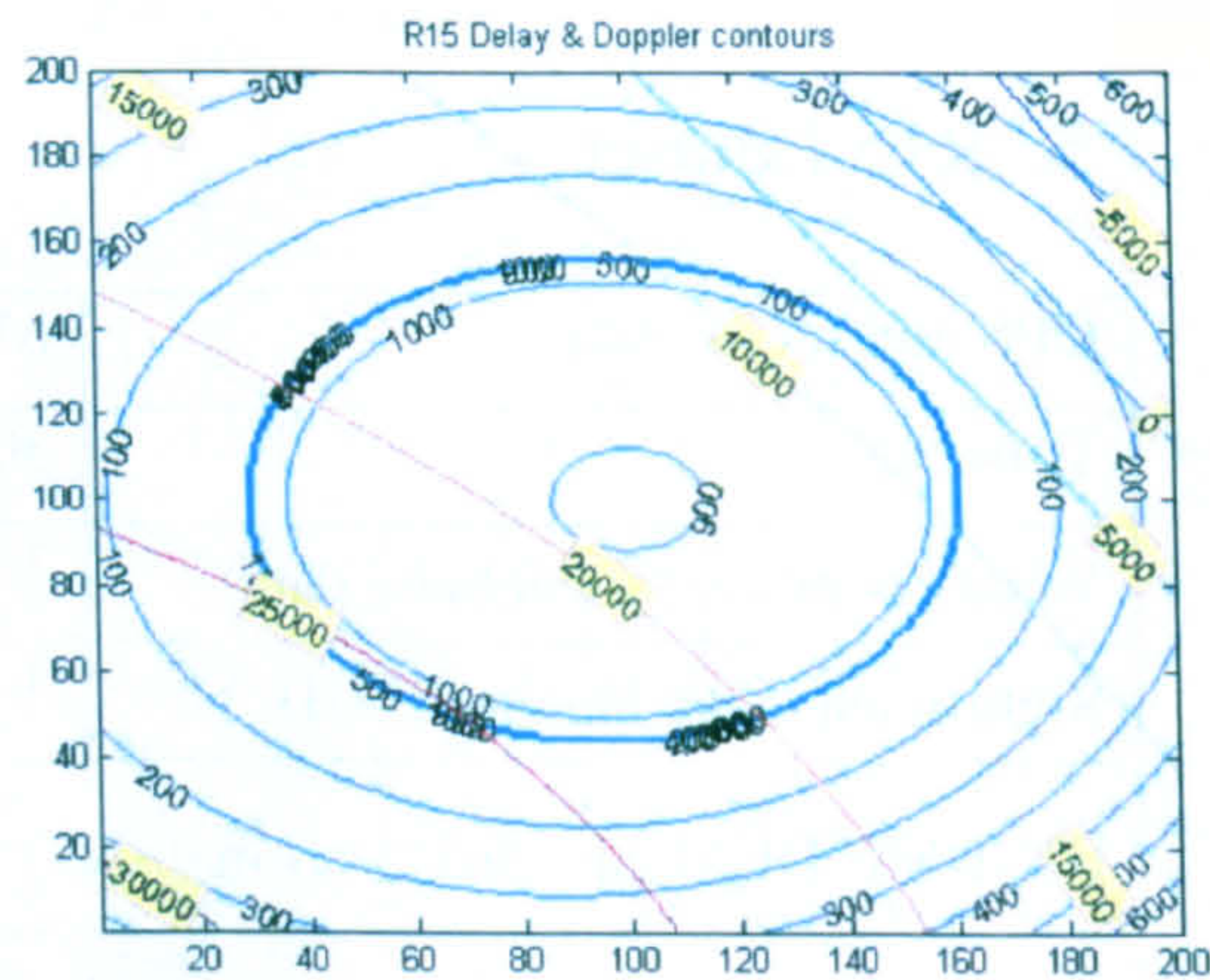


Figure I-48 : Simulated R15 Delay-Doppler contours

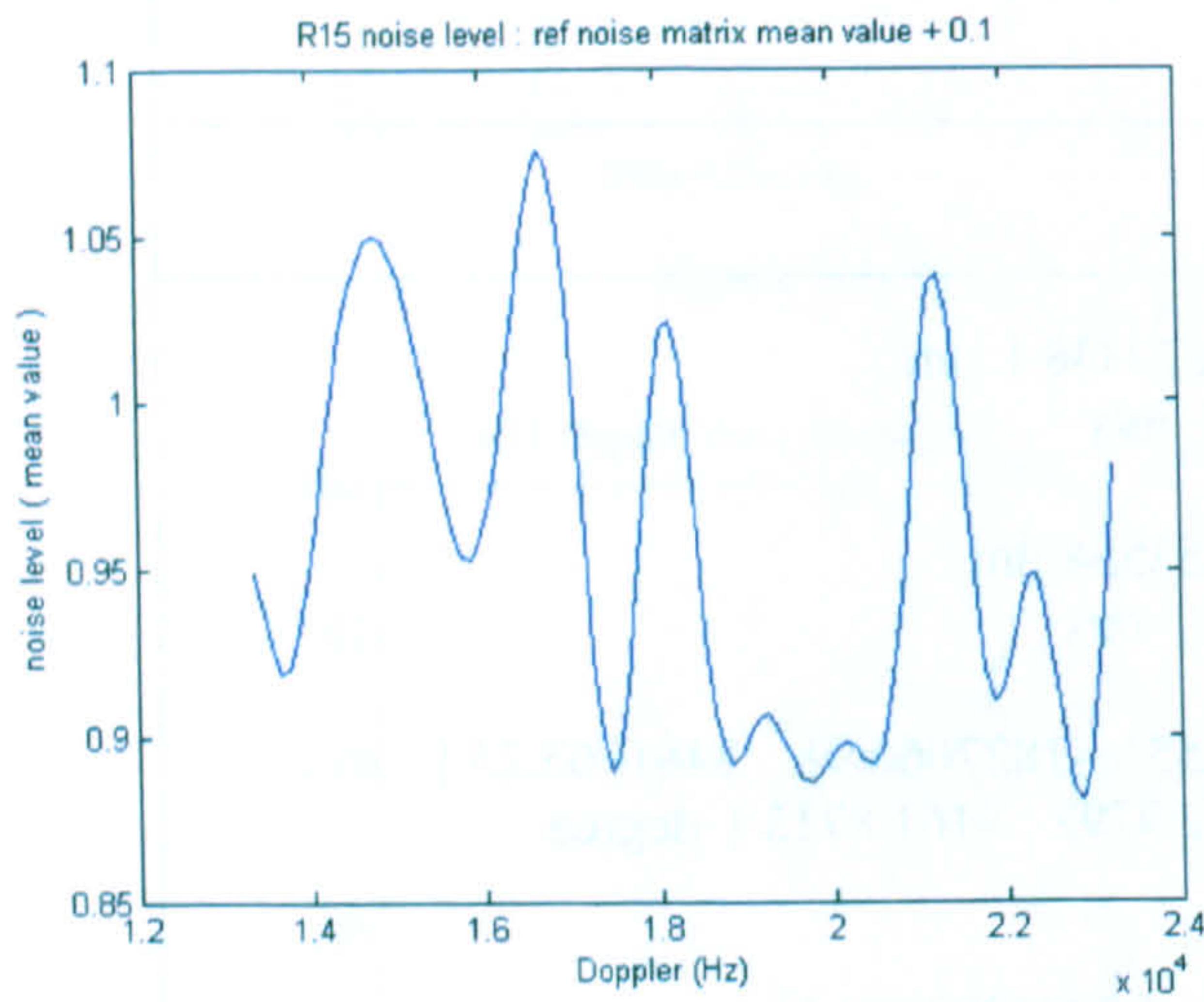


Figure I-46 : UK-DMC R15 DDM bias

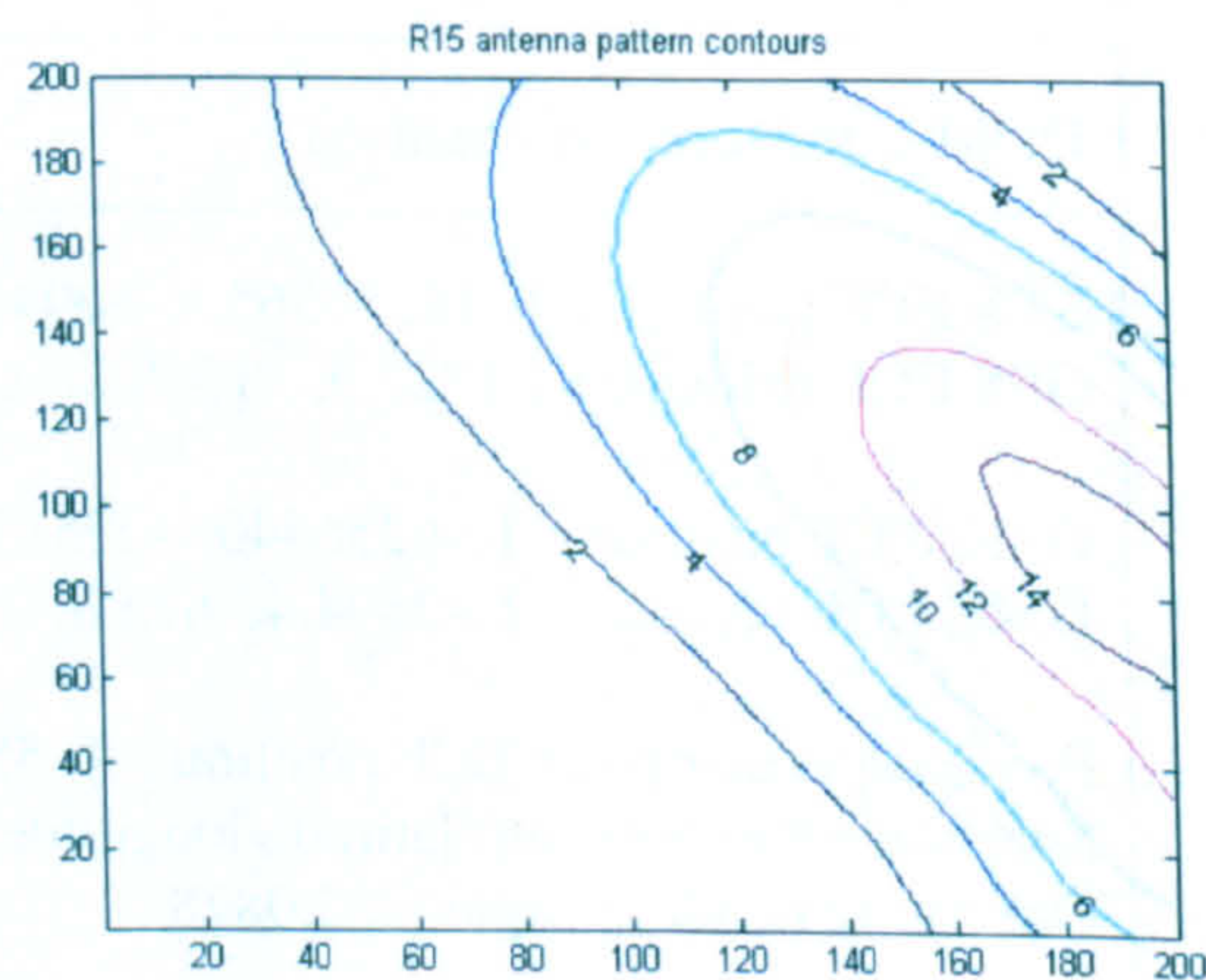


Figure I-49 : Simulated R15 antenna pattern

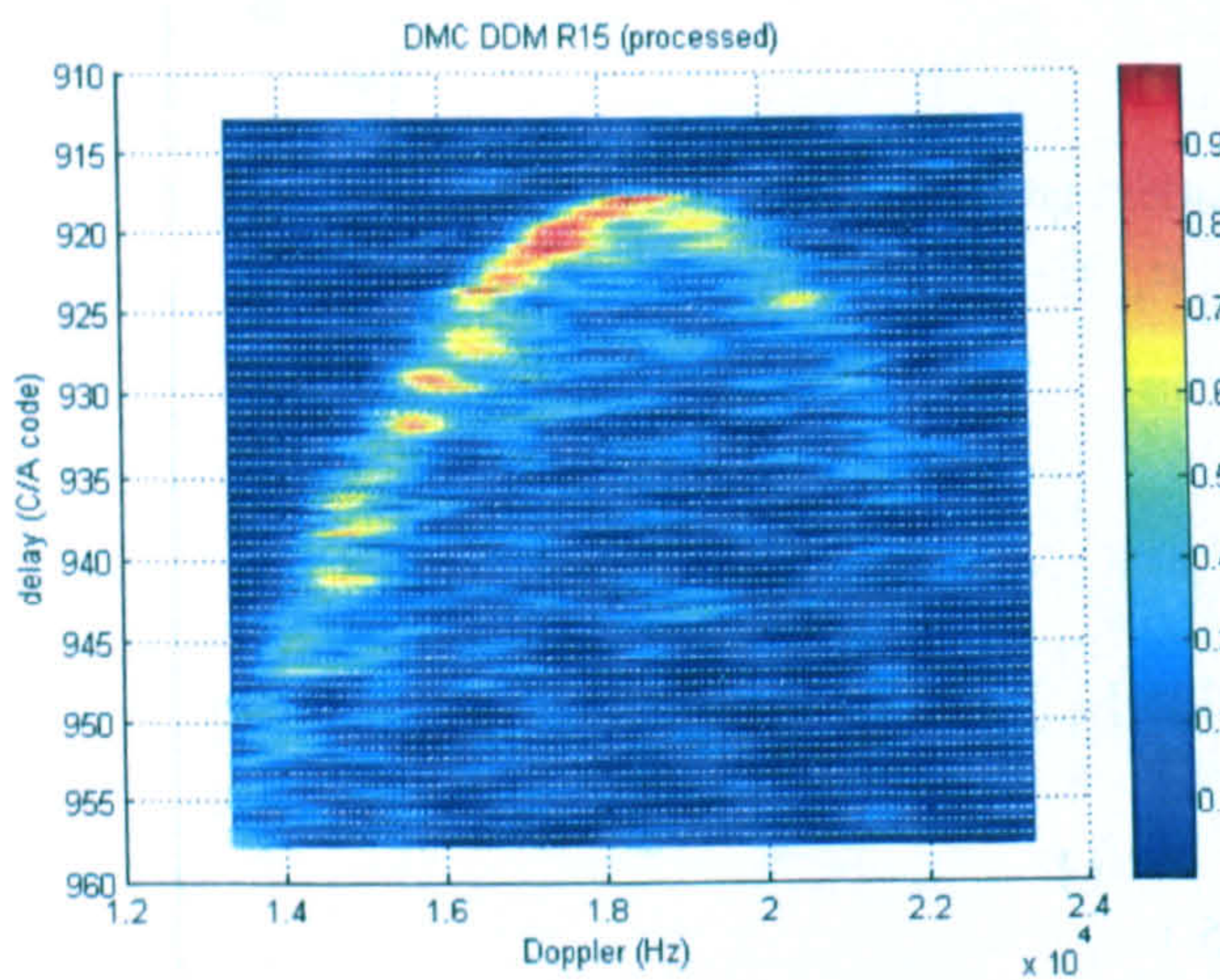


Figure I-47 : UK-DMC R15 DDM data (processed)

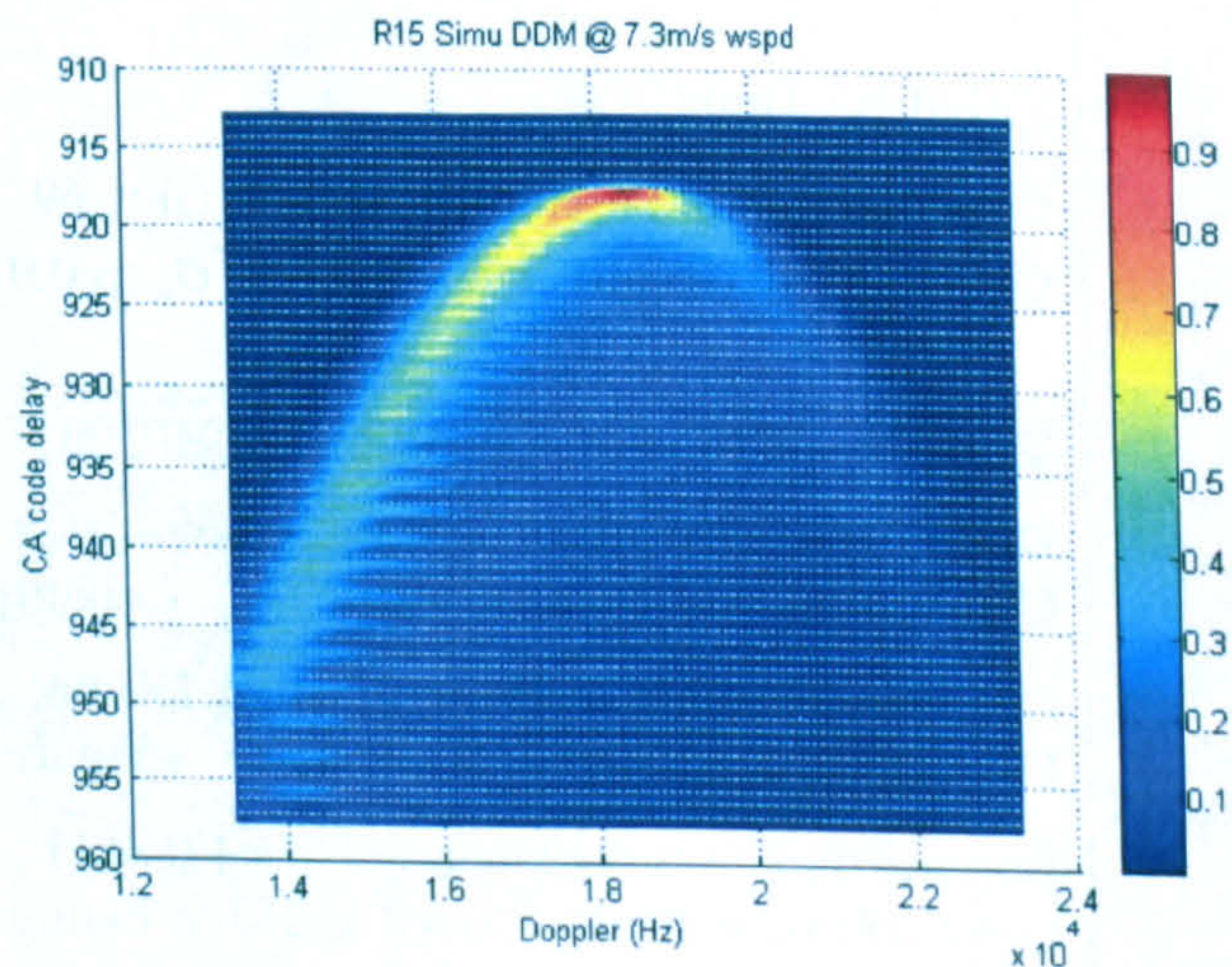


Figure I-50 : Simulated R15 DDM

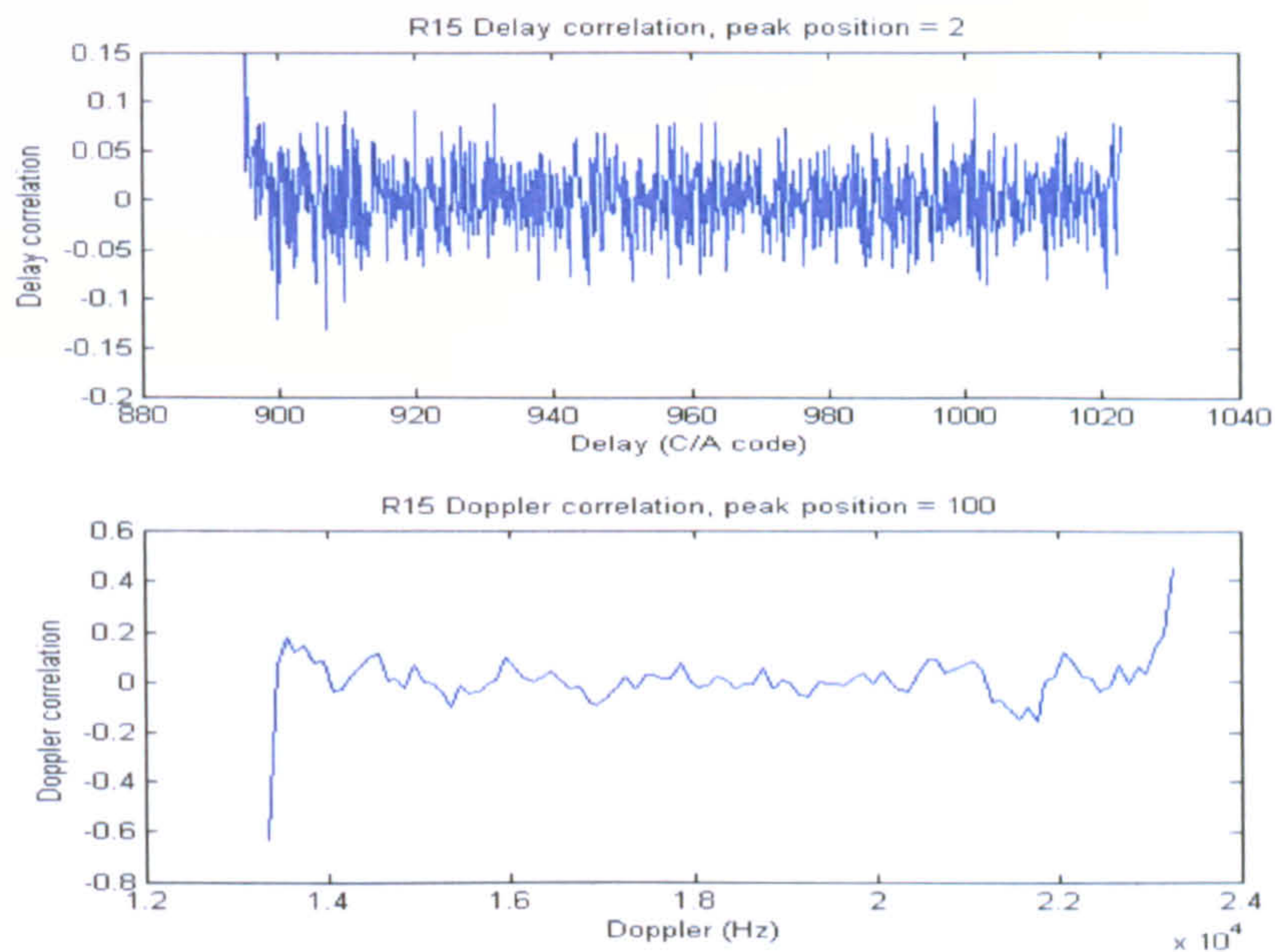


Figure I-51 : R15 DDM registration in Delay and Doppler dimensions

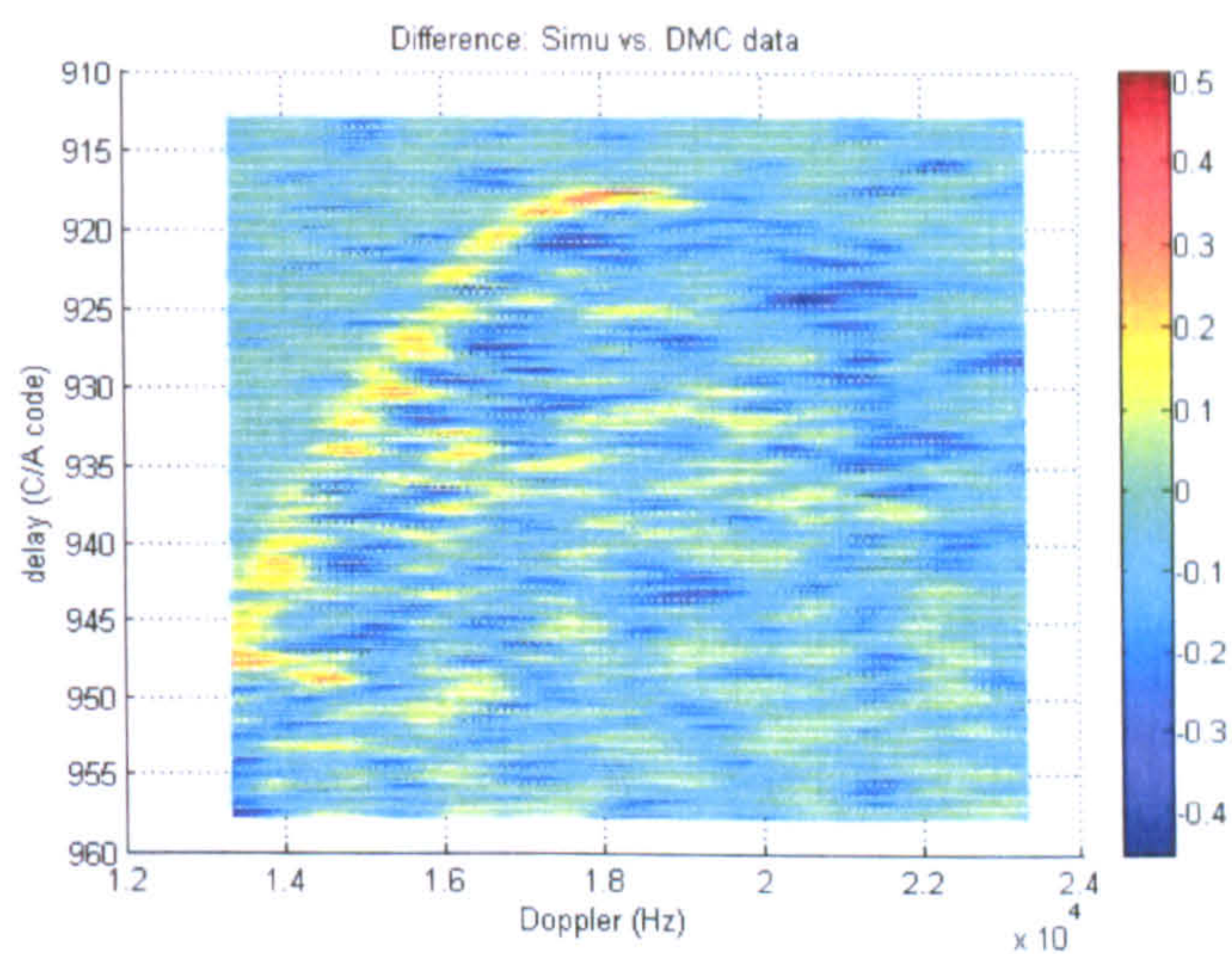


Figure I-52 : Difference between UK-DMC R15 DDM and the Simulation

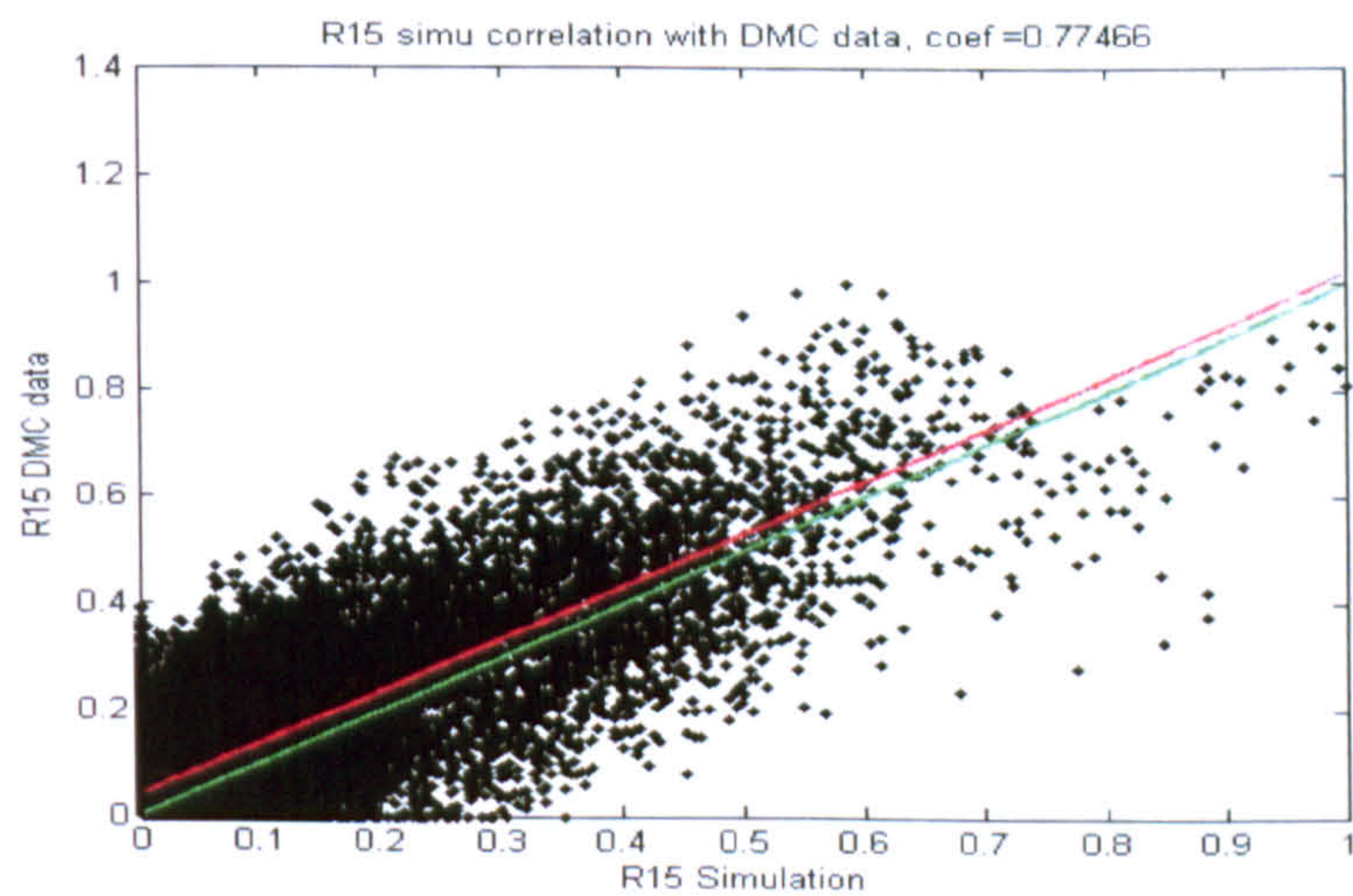


Figure I-53 : The point-to-point correlation of UK-DMC R15 DDM and the Simulation.

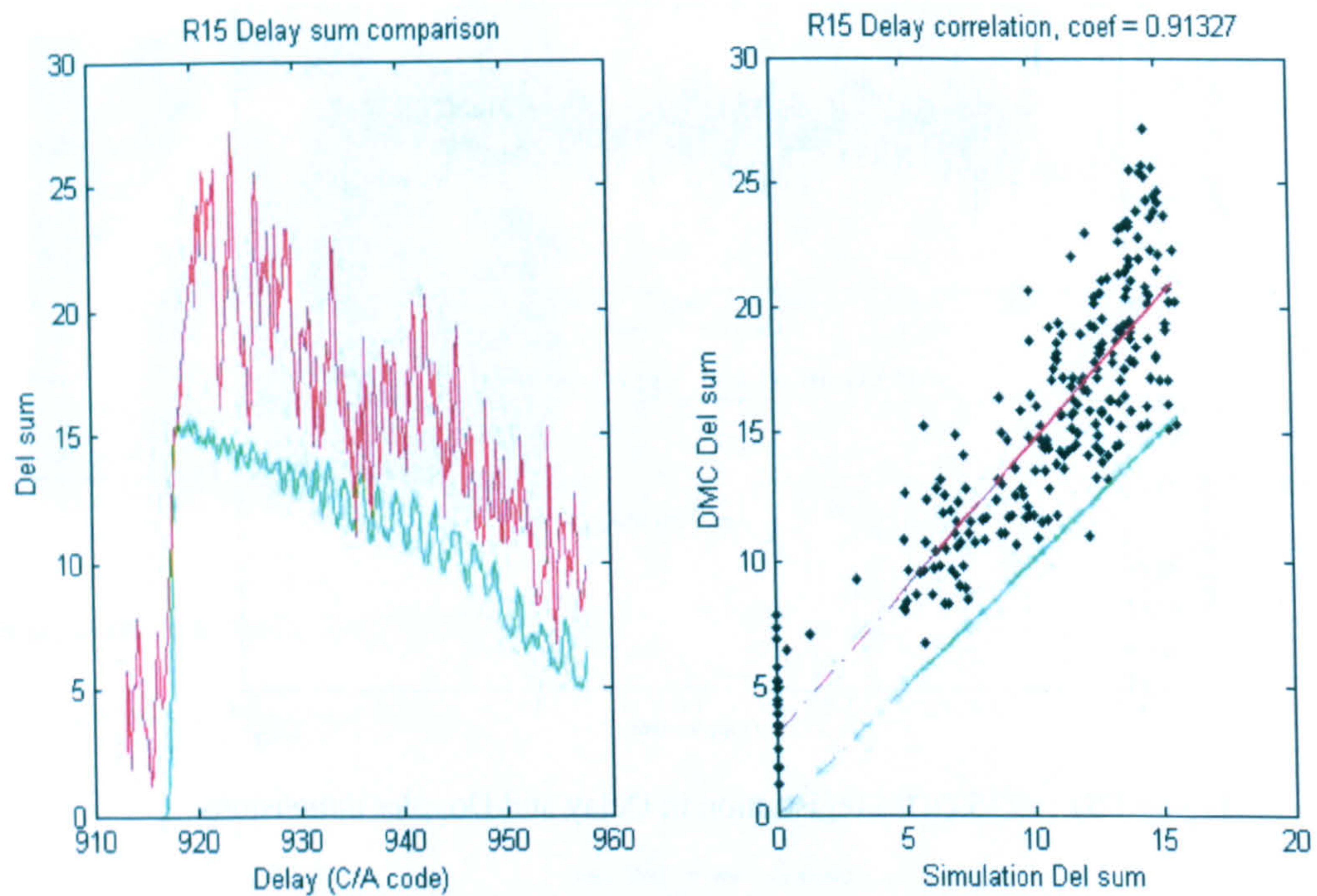


Figure I-54 : R15 Delay dimension correlation

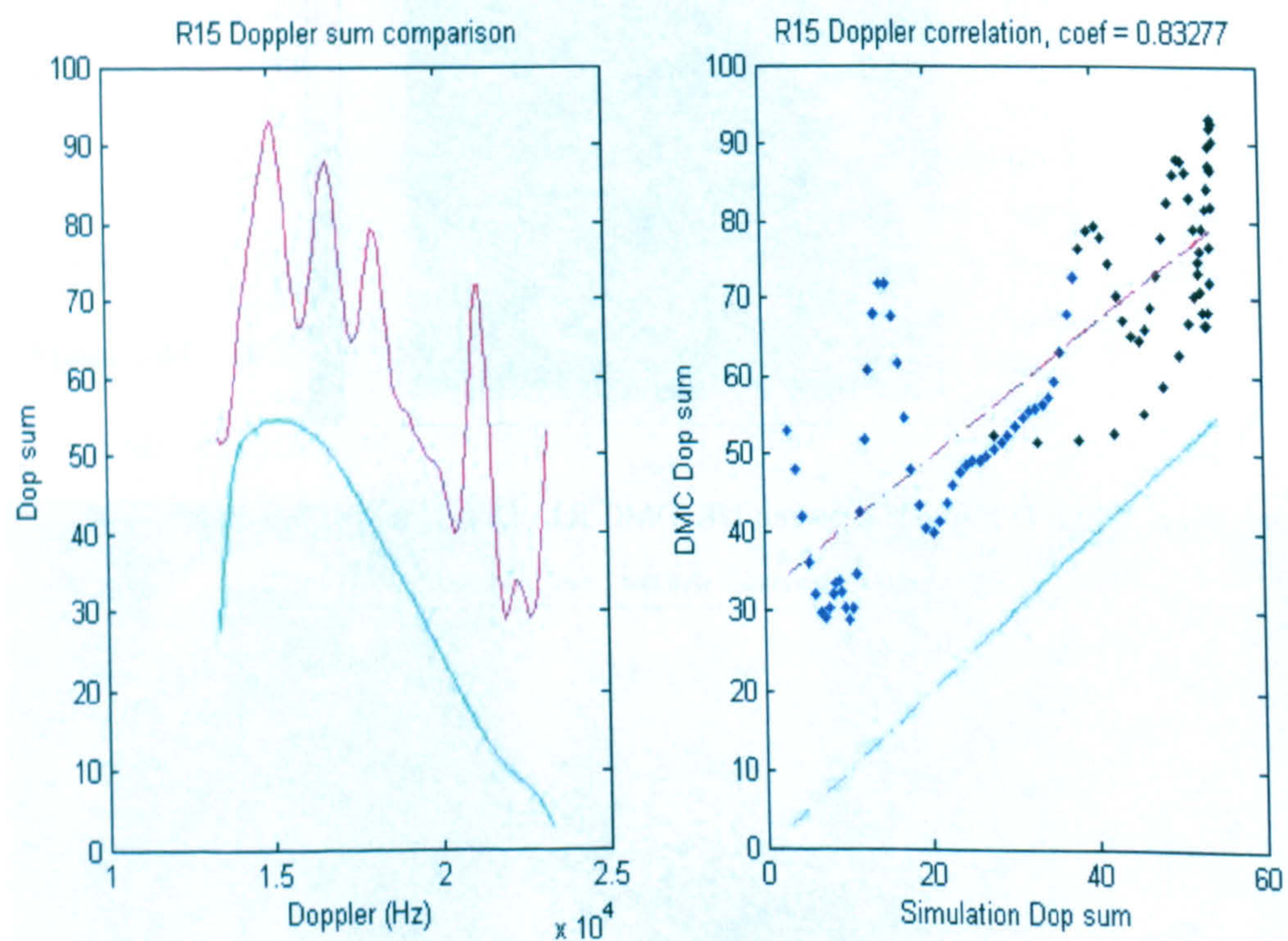


Figure I-55 : R15 Doppler dimension correlation

6. R18 Dataset

GPS emitter satellite	SVN-27
Time tag	04 Mar 2005 08 : 28 : 50 AM
Wind condition (local buoy data)	7 m/s, 108°
Significant wave height (SWH)	2.6 m
UK-DMC DDM data facts (normalised)	
Map size : 1000 (Delay) * 100 (Doppler) Delay axis : 769.8460 ~ 948.7009 C/A code Doppler axis : 6400 ~ 16300 Hz Peak position : 792.2252 C/A code / 11700 Hz	
DDM simulation (normalised)	
GPS ECF position : [-22201281.876; -5782738.093; 14290344.758] m GPS ECF velocity : [1634.578; -531.643; 2373.631] m/s DMC ECF position : [-6159670.054; -3226546.904; 1282705.602] m DMC ECF velocity : [-1943.693; 775.077; -7302.496] m/s Predict specular point ECF position : [-5571419.78 -2747913.10 1440452.31] m Specular point position (latitude/longitude) : [13.0971 -153.7467] degree Observing incident angle : 27.978 ° Patch resolution : 200 km * 200 km reflection area (200*200 patches) Delay/Doppler offset : 362.98 C/A code, -2505.8 Hz <u>Elfouhaily slope PDF</u> Conditions: wind speed 7 m/s, direction 108°, incident angle 27.978 ° Gaussian parameters: $\sigma_x = 0.01085$, $\sigma_y = 0.01117$, $b_{xy} = 0.010582$ <u>UK-DMC DDM and simulation comparison</u> DDM correlation : p = [0.9447 , 0.0390] Correlation coefficient : c = 0.84416 (Figure I-64) Delay dimension correlation : p = [1.0622, 3.4671] Correlation coefficient : c = 0.9280 (Figure I-65) Doppler dimension correlation : p = [0.6322 , 50.6745] Correlation coefficient : c = 0.69251 (Figure I-66)	

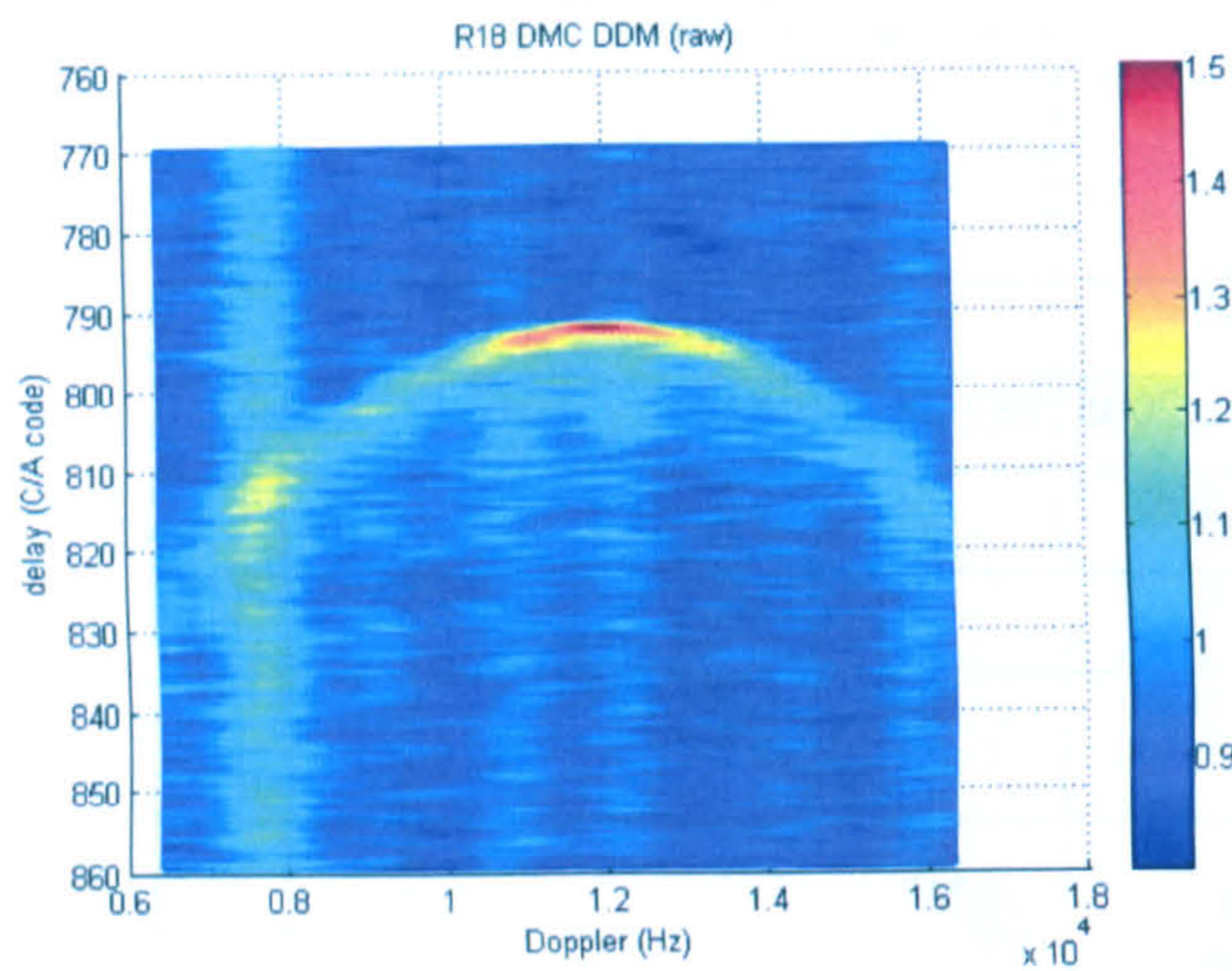


Figure I-56 : UK-DMC R18 DDM data (raw)

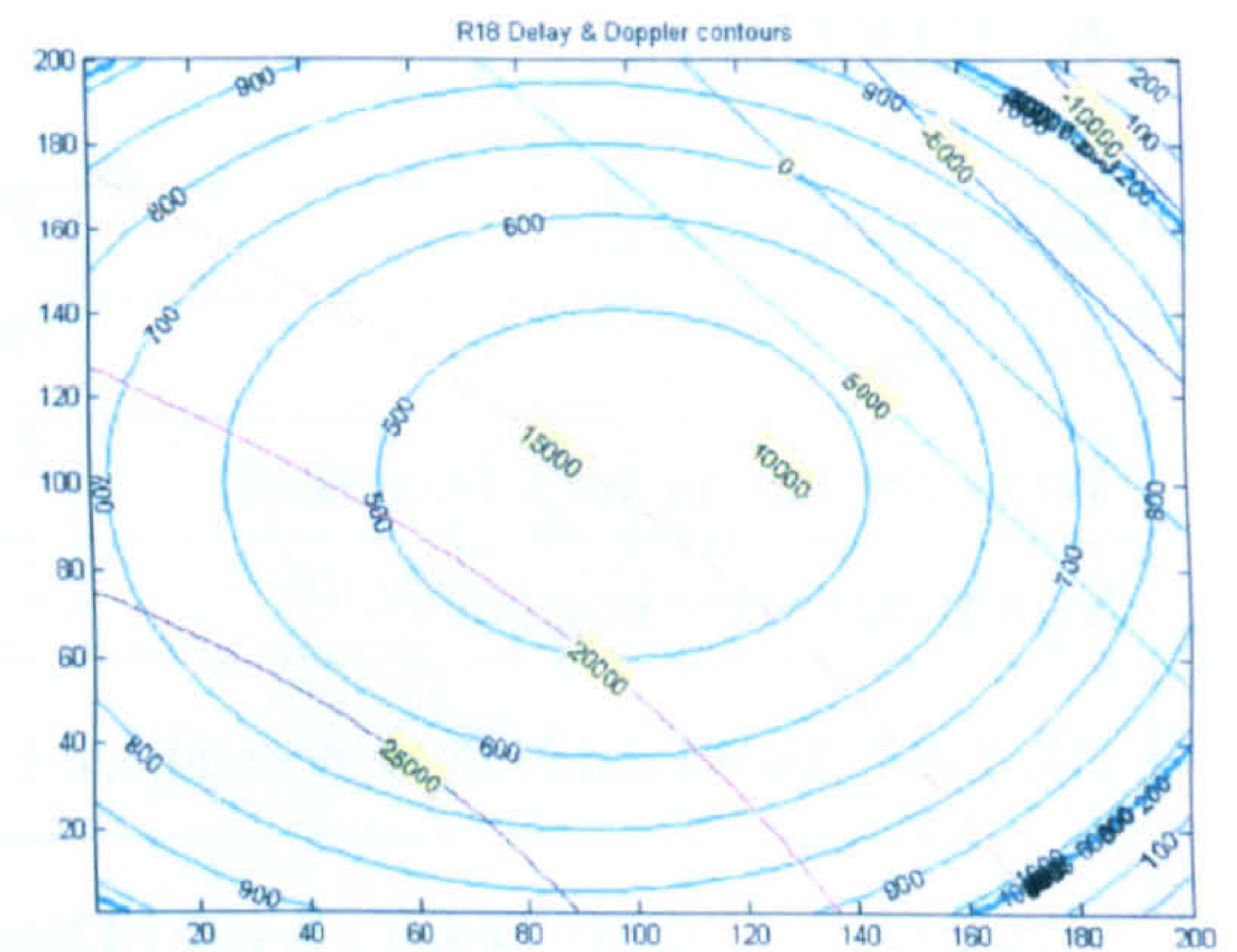


Figure I-59 : Simulated R18 Delay-Doppler contours

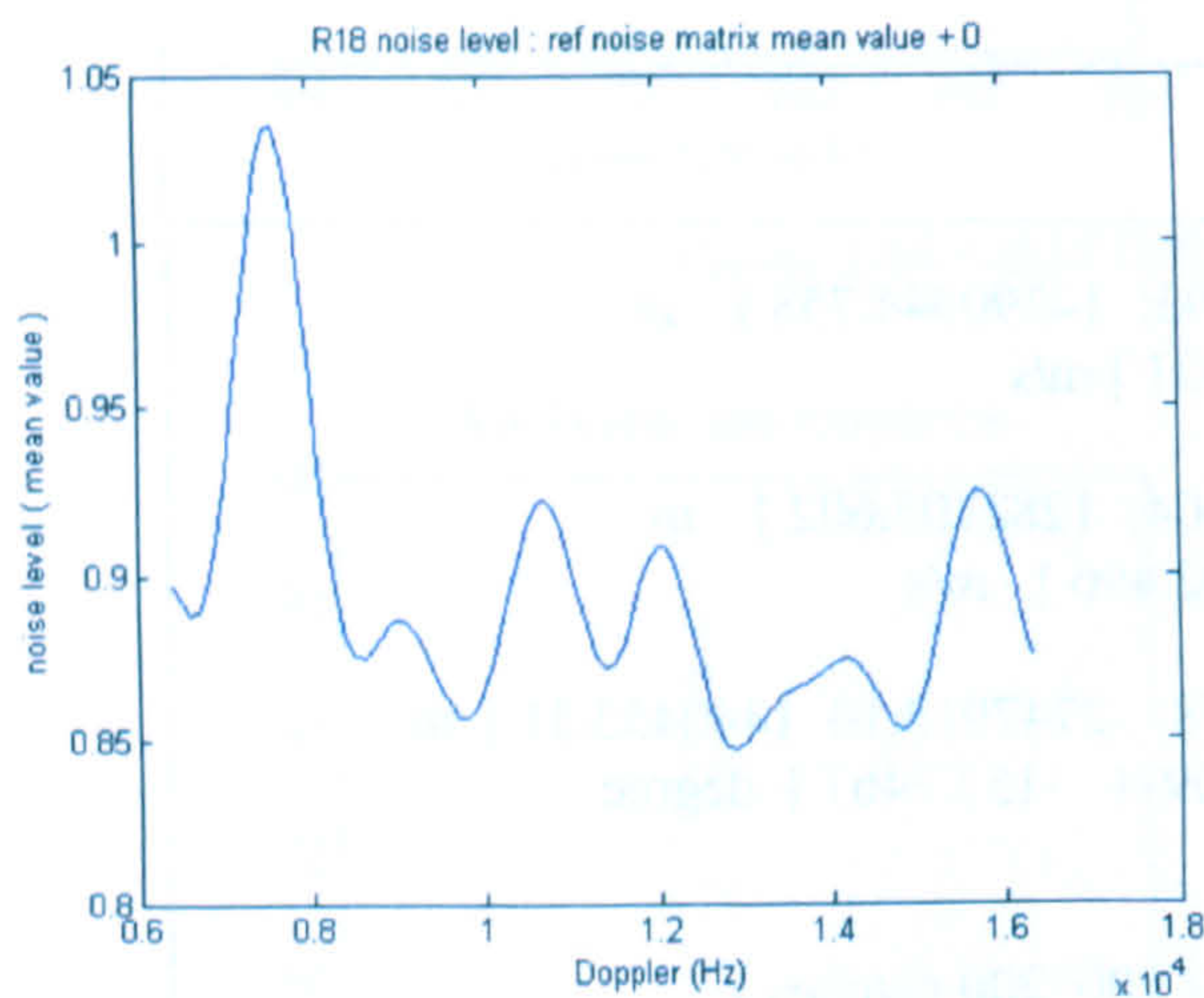


Figure I-57 : UK-DMC R18 DDM bias

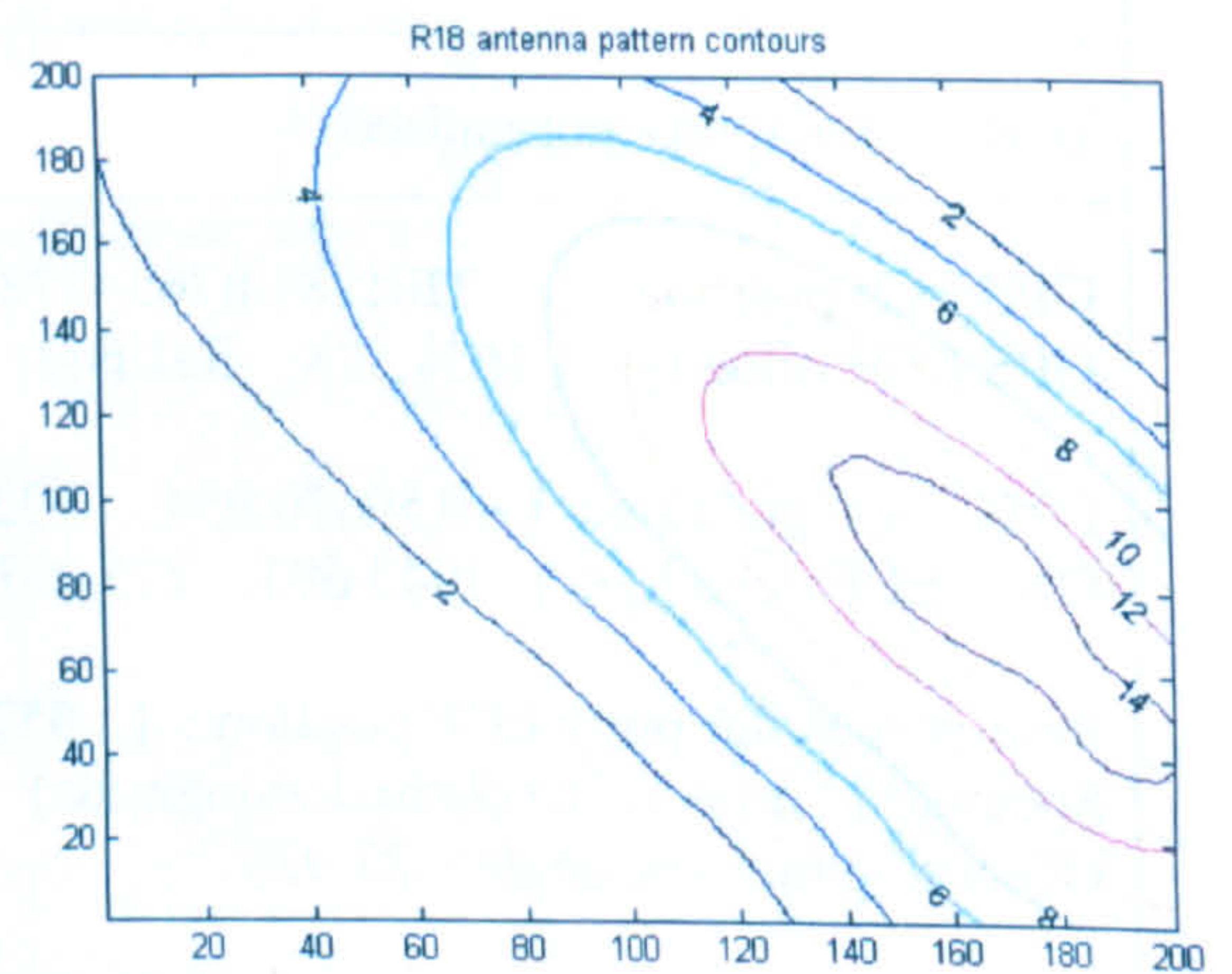


Figure I-60 : Simulated R18 antenna pattern

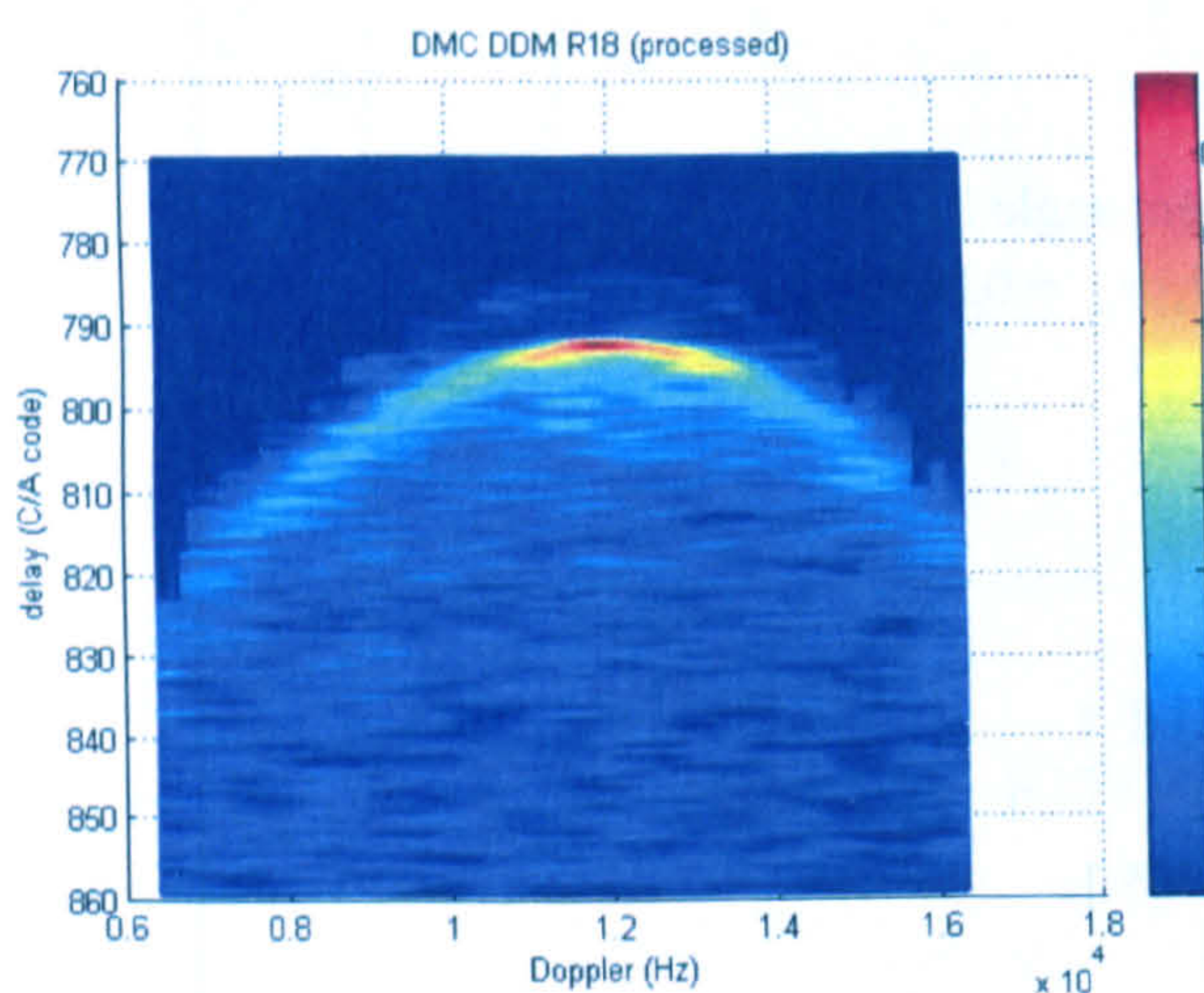


Figure I-58: UK-DMC R18 DDM data (processed)

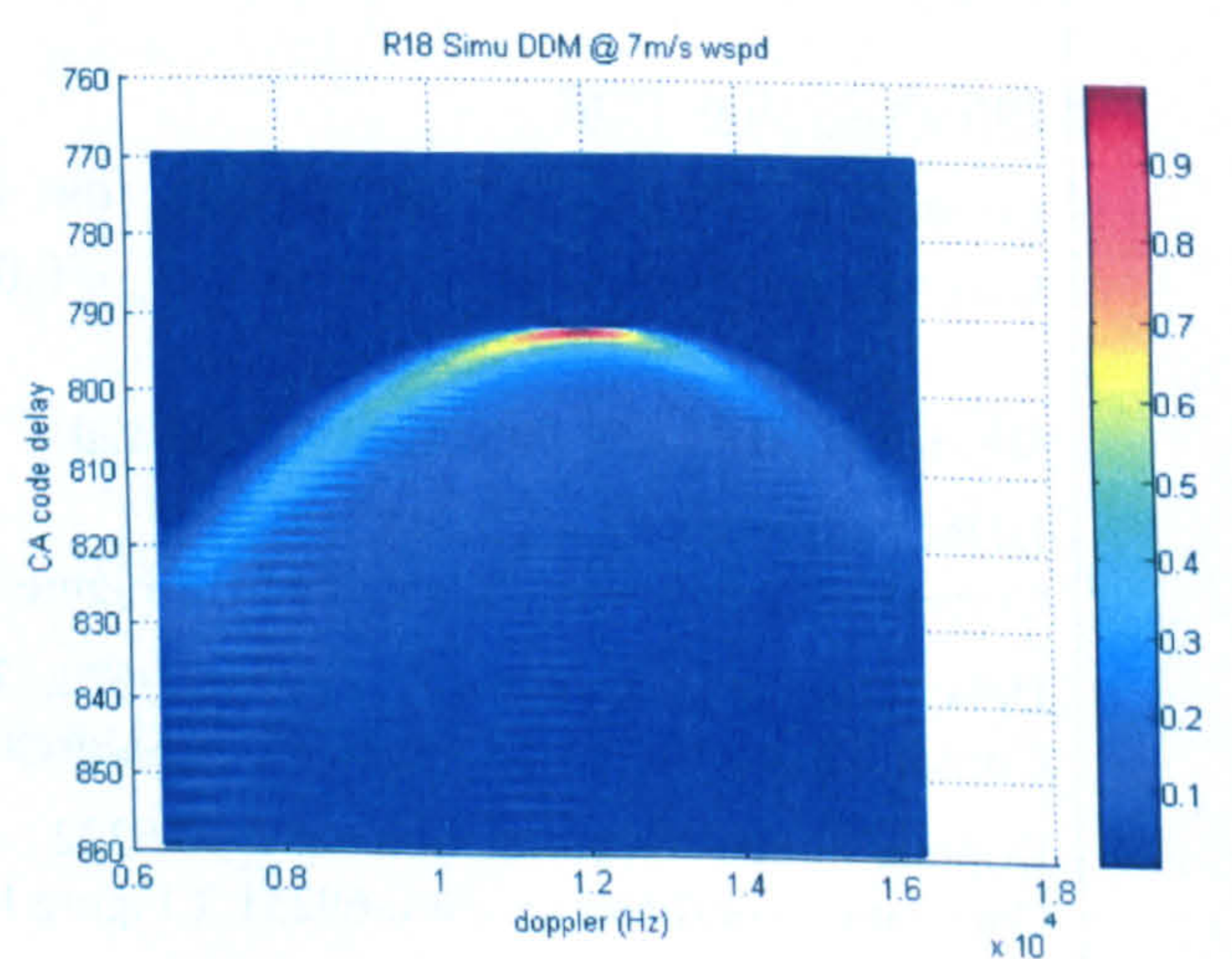


Figure I-61 : Simulated R18 DDM

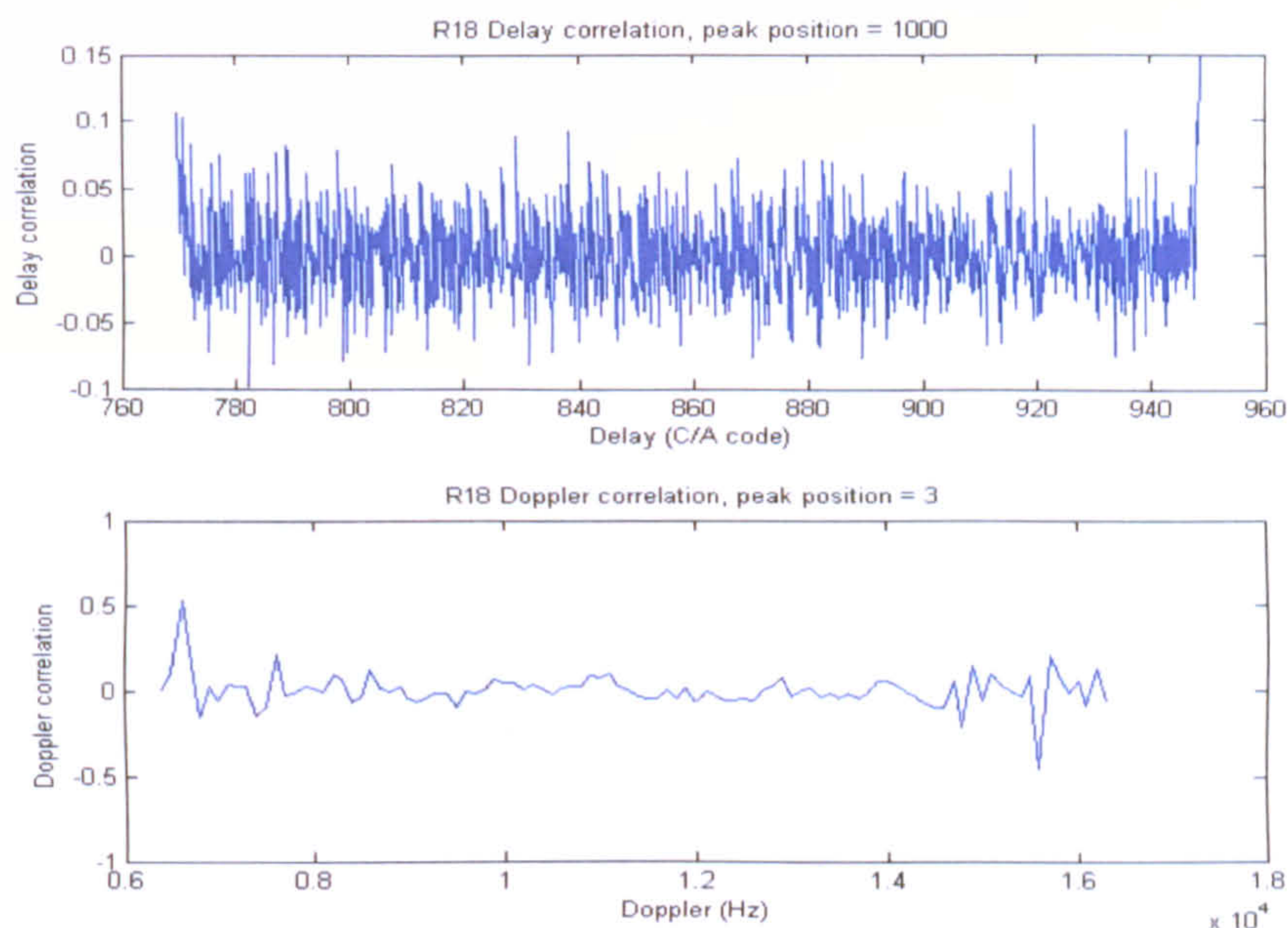


Figure I-62 : R18 DDM registration in Delay and Doppler dimensions

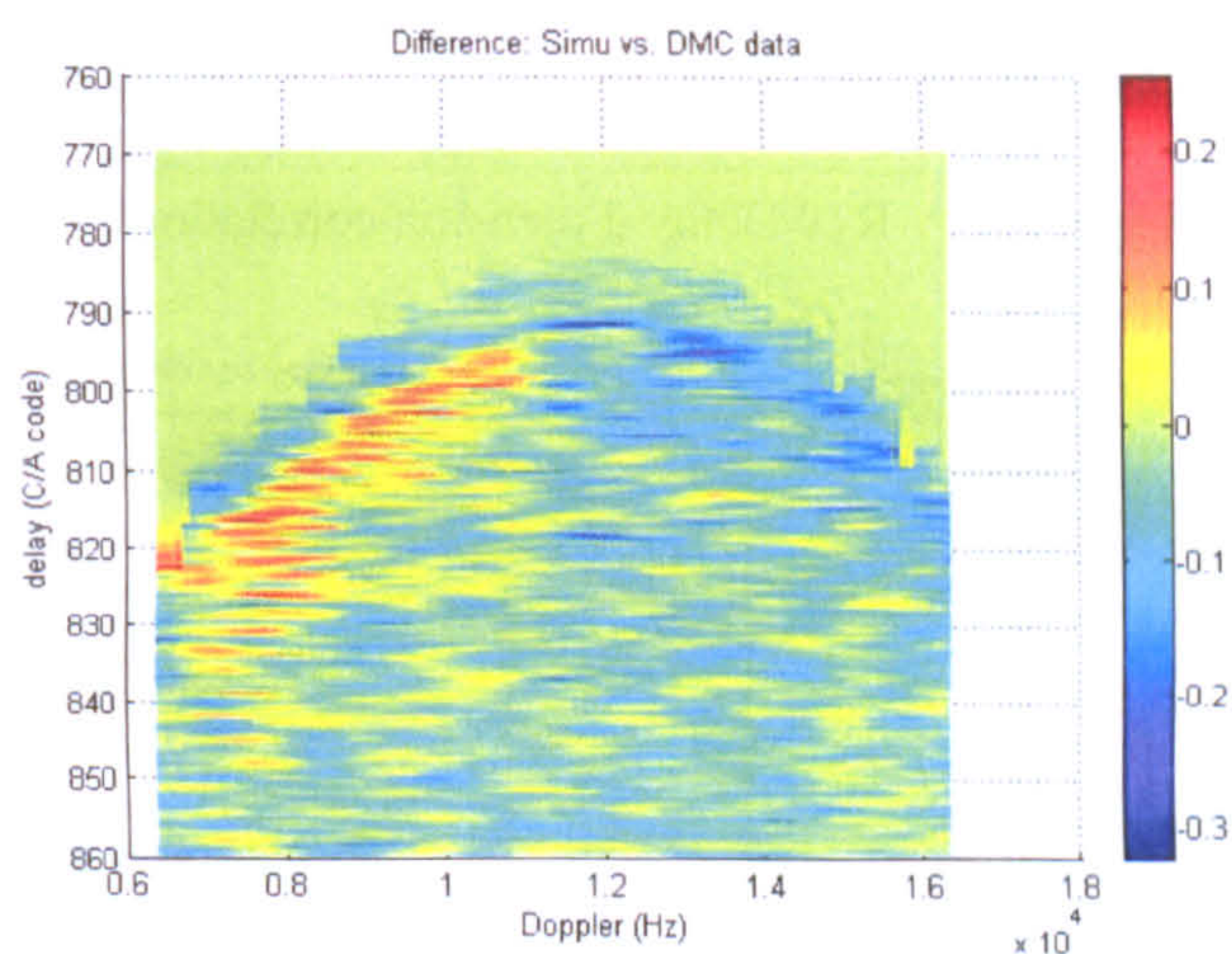


Figure I-63 : Difference between UK-DMC R12 DDM and the simulation

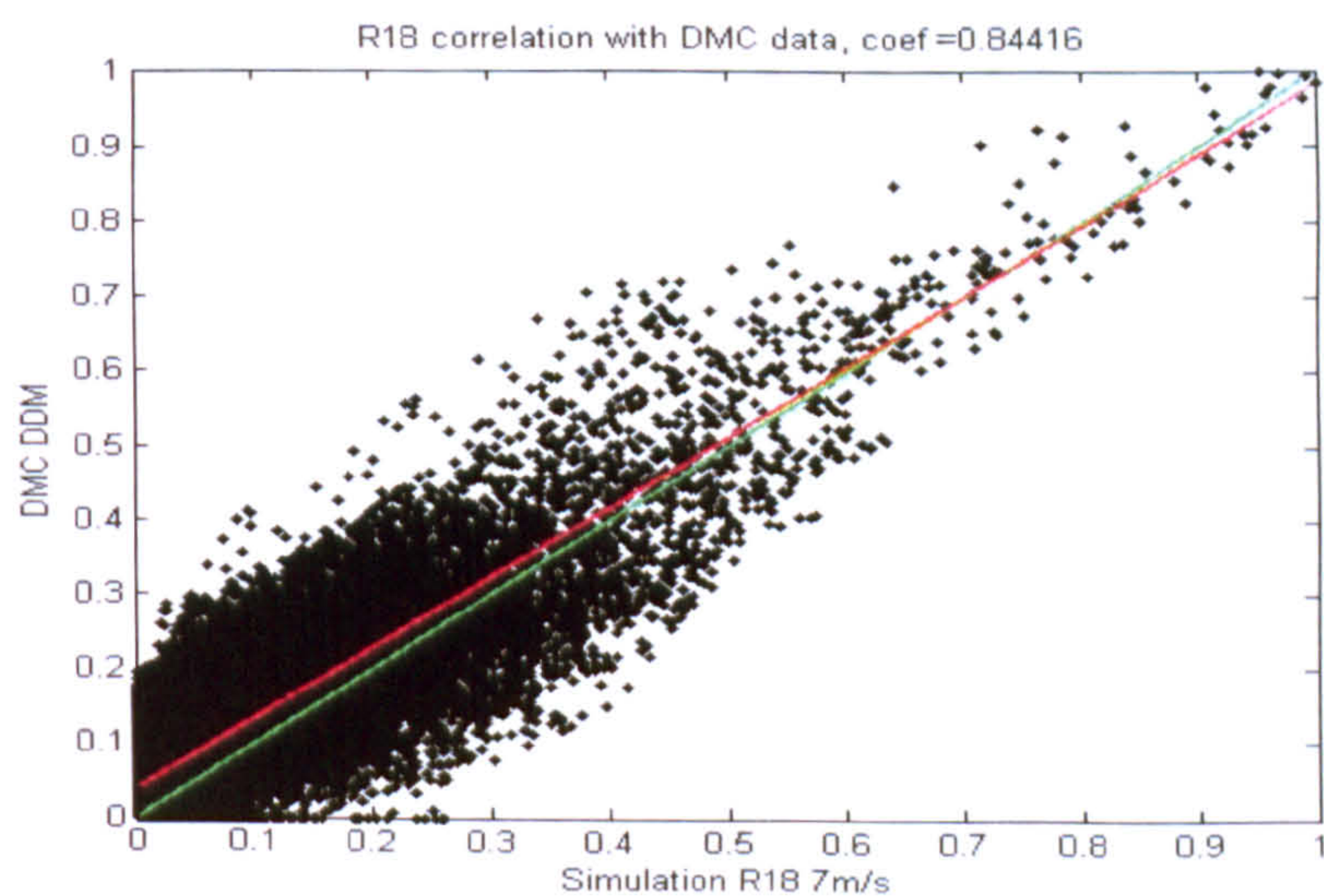


Figure I-64 : The point-to-point correlation of UK-DMC R18 DDM and the Simulation.

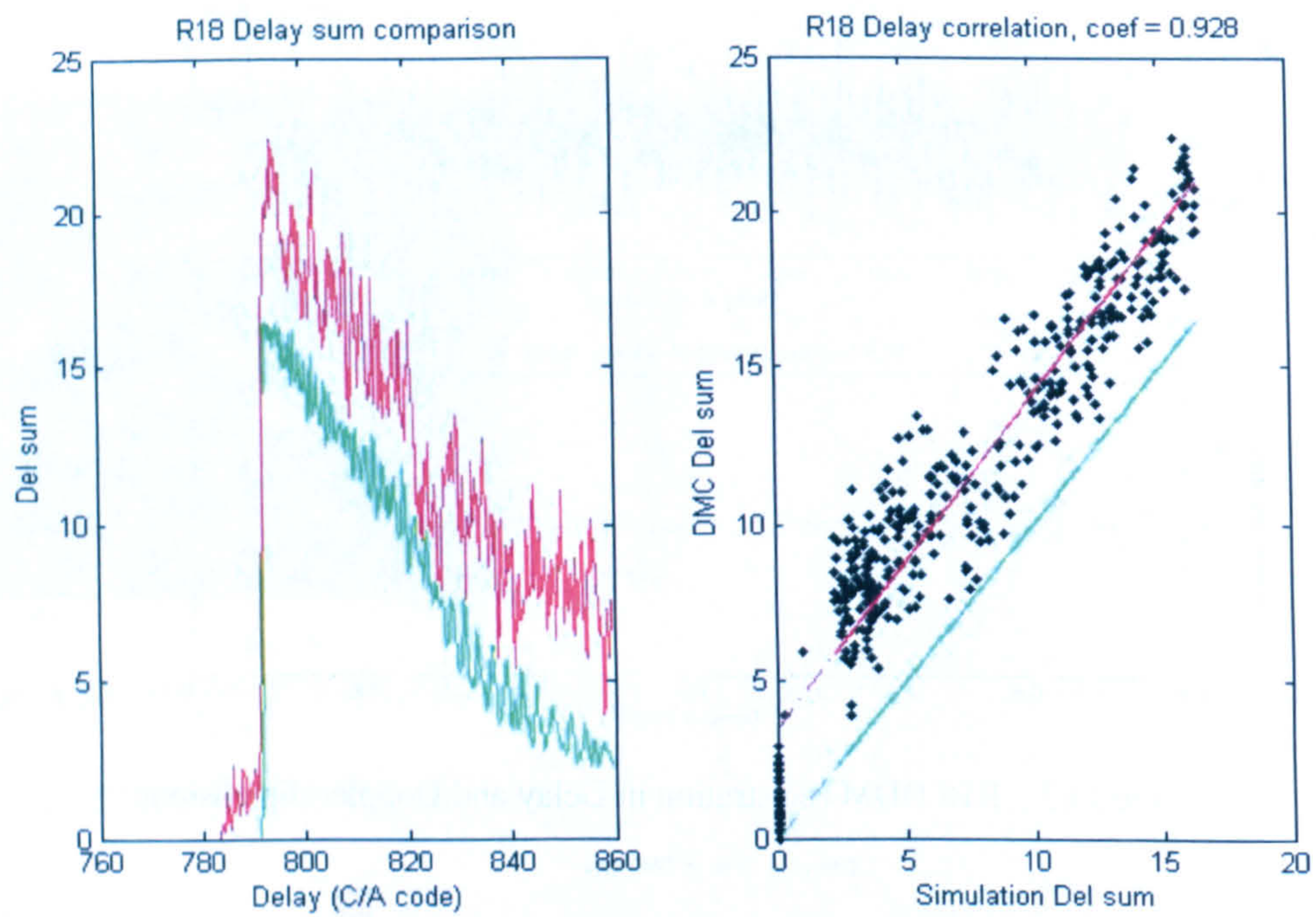


Figure I-65 : R18 Delay dimension correlation

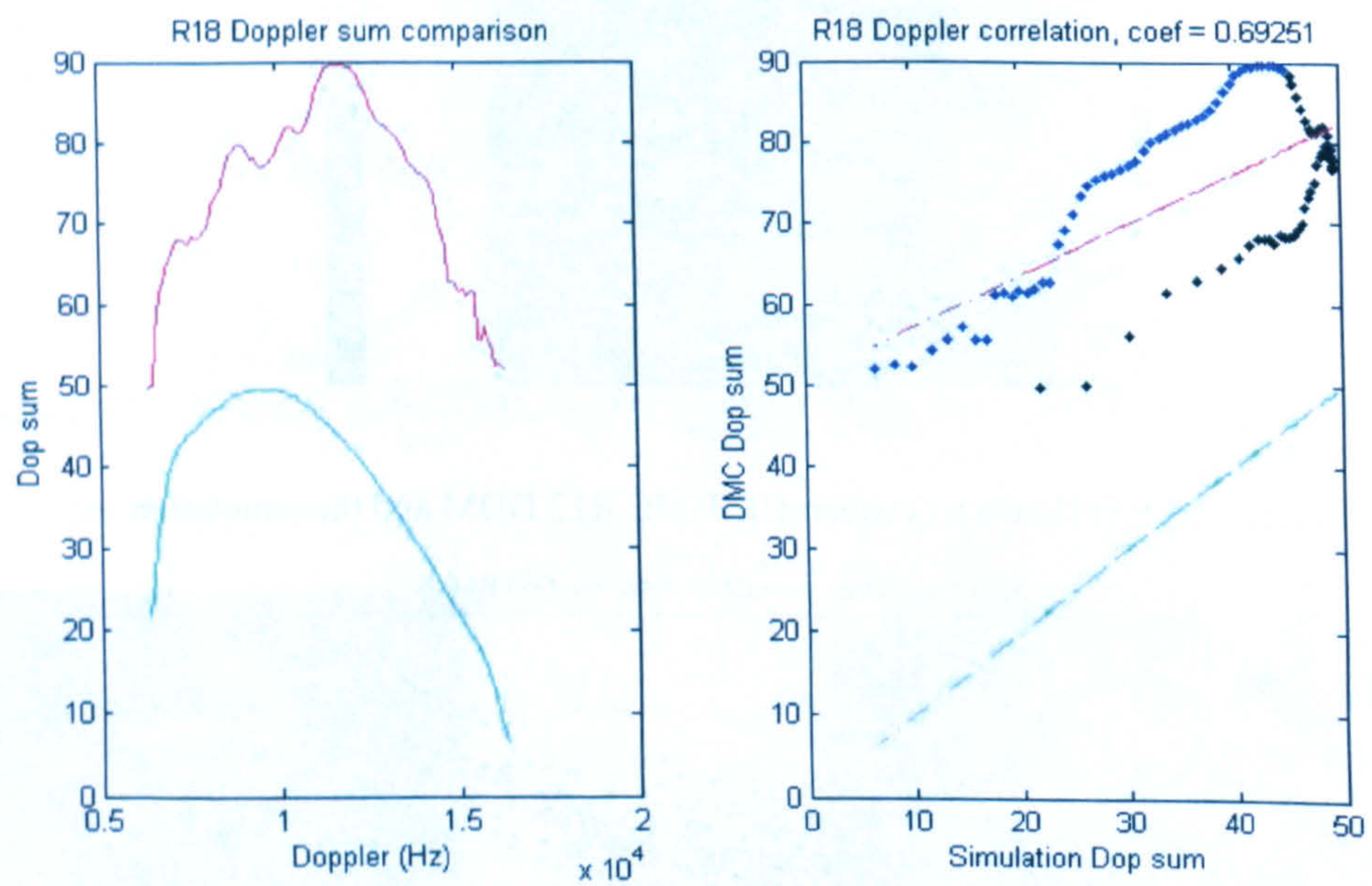


Figure I-66 : R18 Doppler dimension correlation

Appendix II

Sensitivity Analysis of Elfouhaily Modelled Slope PDF

This section is the extended discussion of section 4.4, providing some extra simulated results for analysing the sensitivity of Elfouhaily modelled slope PDF. Wind speed, wind direction and observing incident angle are three input factors to determine the shape of a Gaussian slope PDF. Wind speed has the major effect on the slope PDF among these three parameters, when wind direction and incident angle only have minor influence.

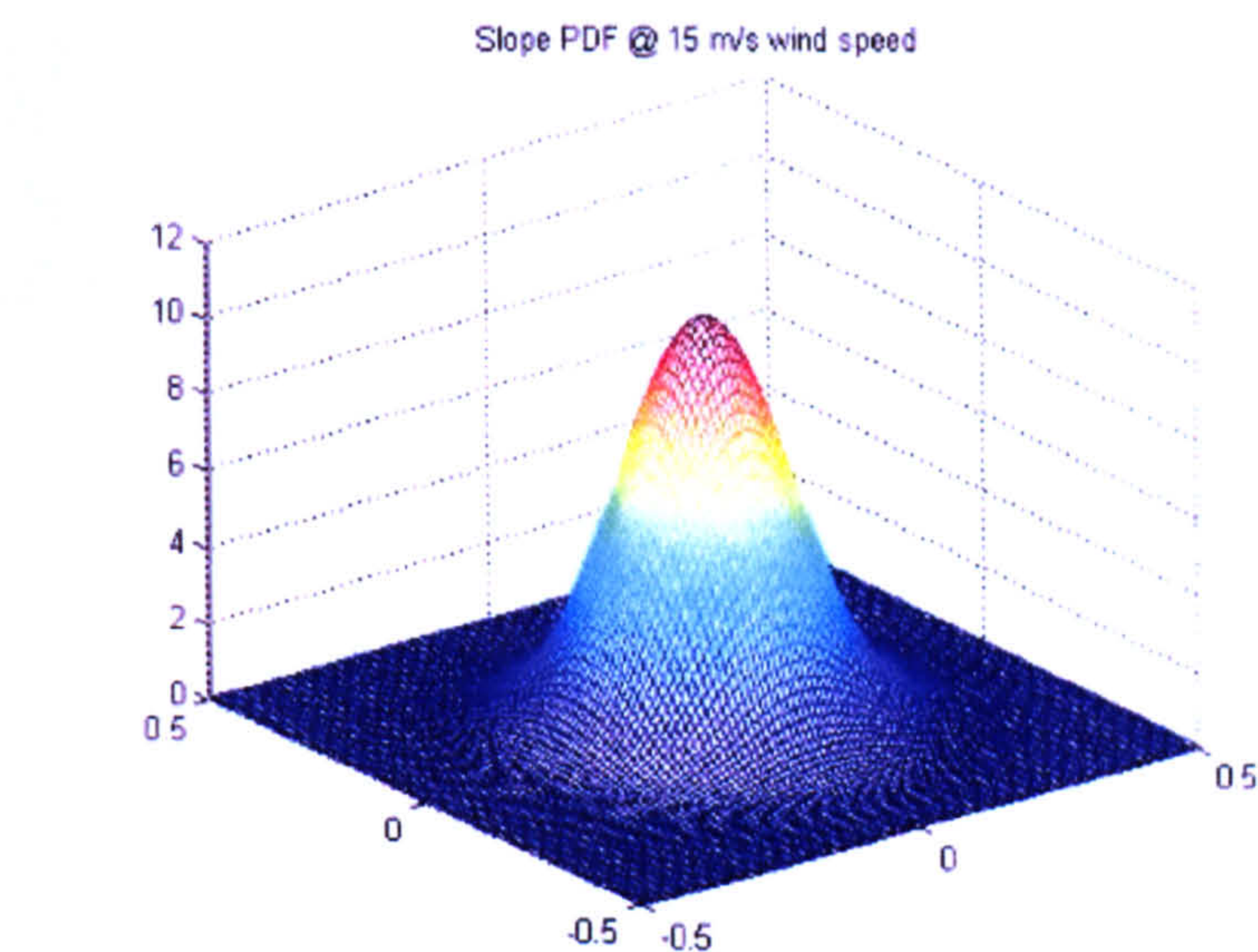


Figure II-1: A typical simulated Elfouhaily wave slope PDF.
(wind speed 15 m/s, wind direction 0°, incident angle 0°)

Wind speed effect

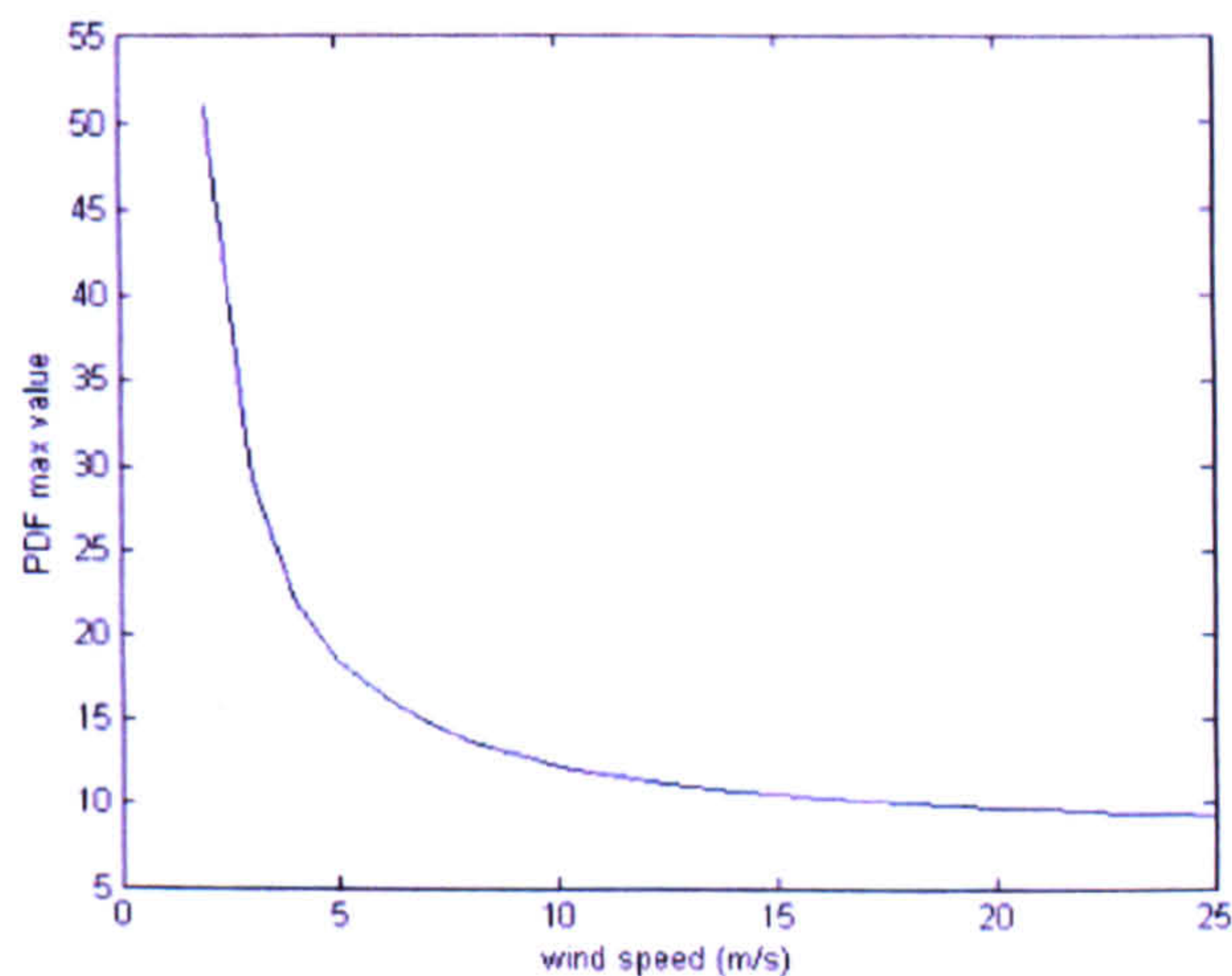


Figure II-2 : Slope PDF peak value changes with wind speed.

Wind direction effect

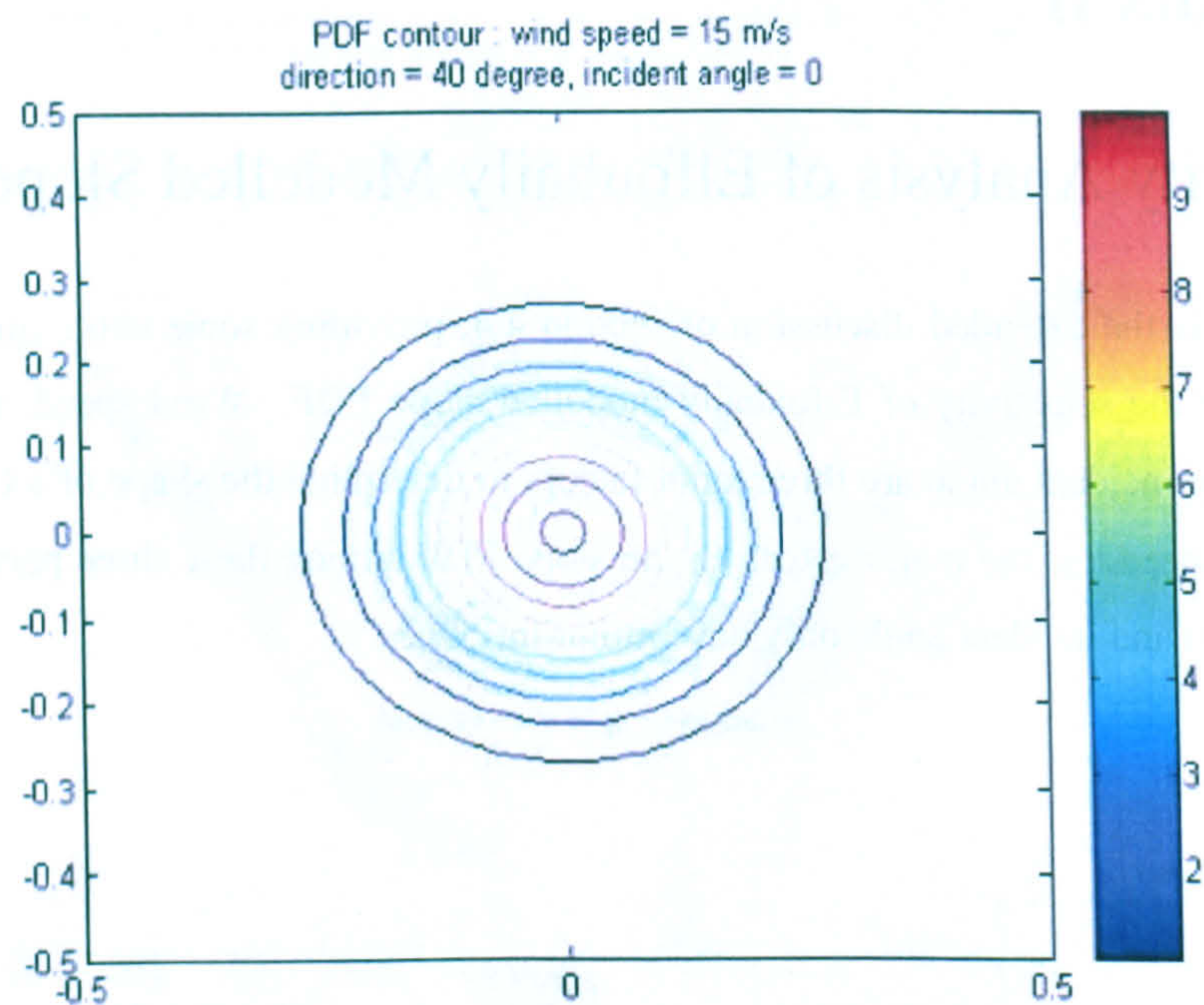


Figure II-3 : A typical Elfouhaily slope PDF contour with a 40° wind direction.
The pattern is not tilted with the wind direction angle.

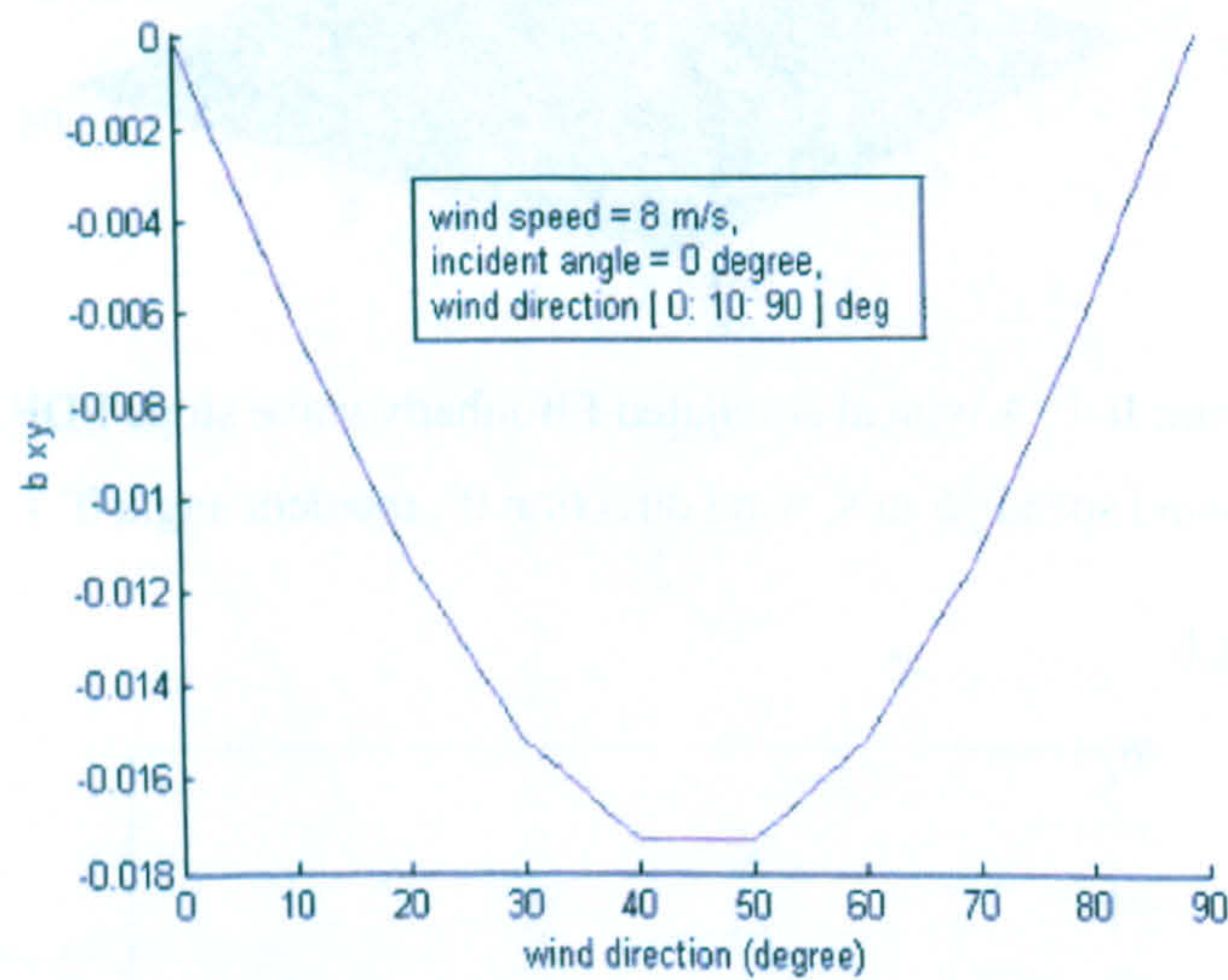


Figure II-4 : Slope PDF b_{xy} changes with wind direction.
(wind speed 8 m/s, incident angle 0° - to achieve the maximum difference)

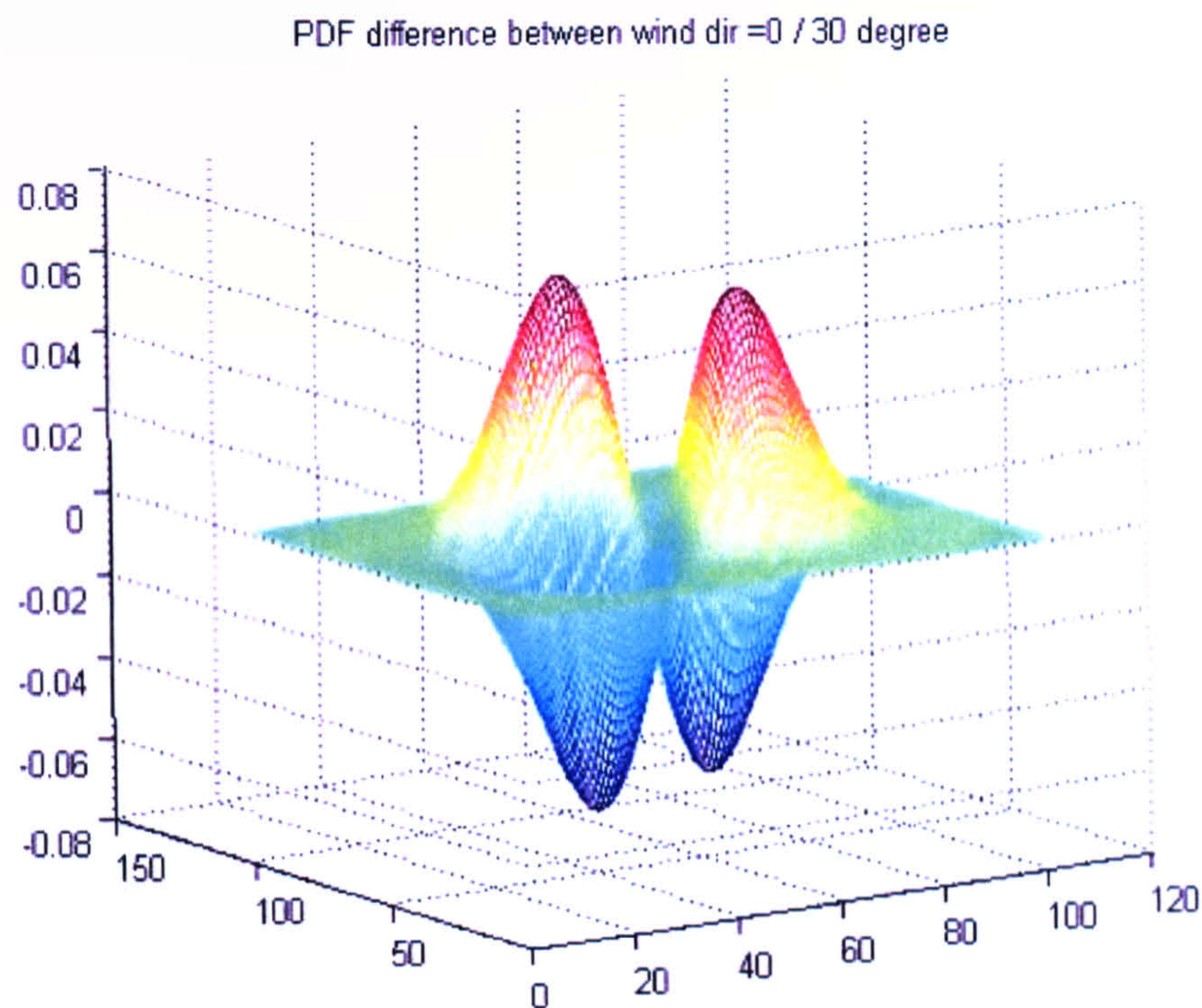


Figure II-5 : Slope PDF difference between 0° and 30° wind direction input.
(wind speed 15 m/s , observing incident angle 30°)

Compared to the scale of the slope PDF in Figure II-1, the difference between two PDFs under different wind direction is very small. Therefore we consider it negligible in our Elfouhaily slope PDF analysis.

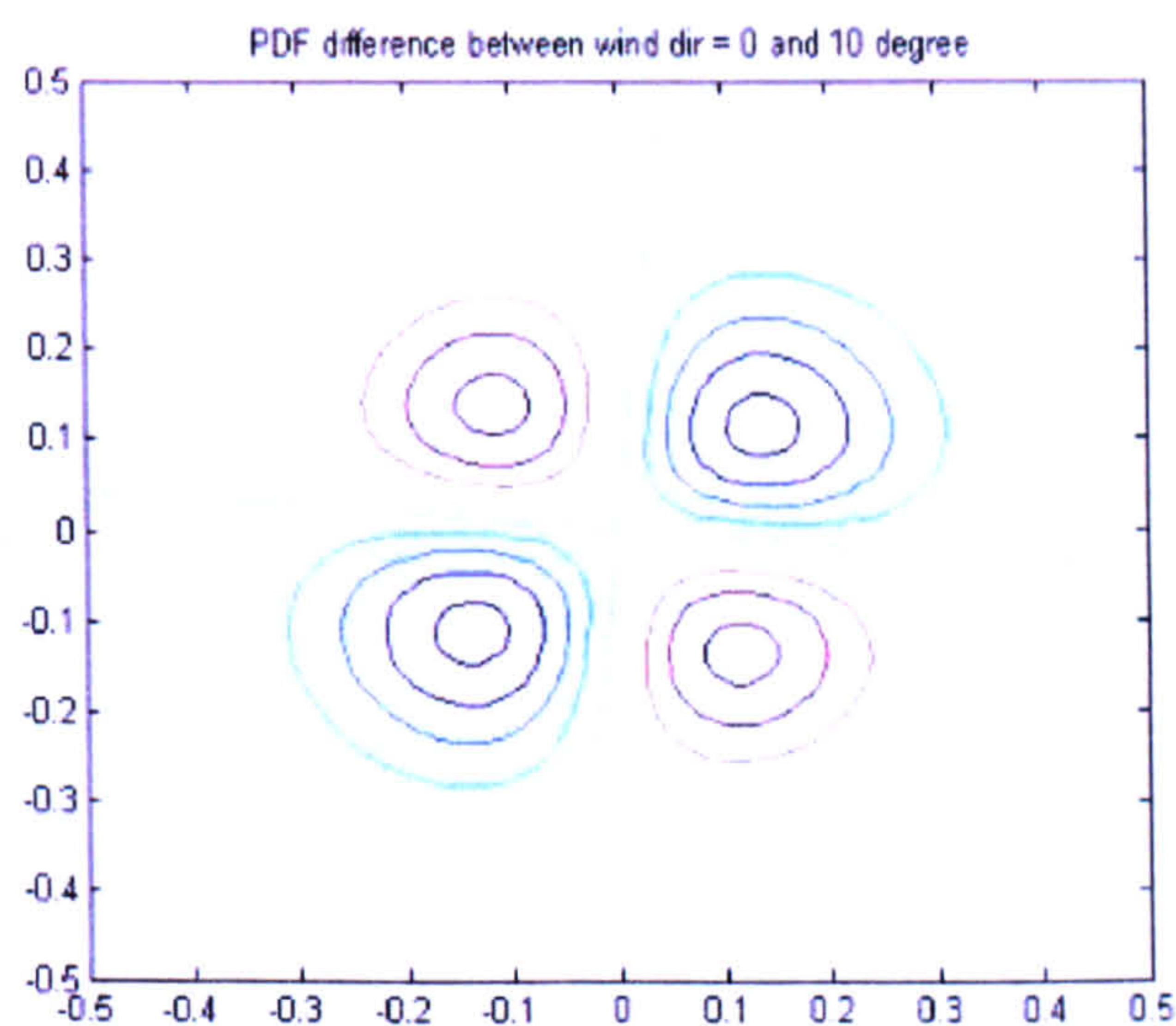


Figure II-6 : Contour of PDF difference map between 0° and 10° wind direction input.

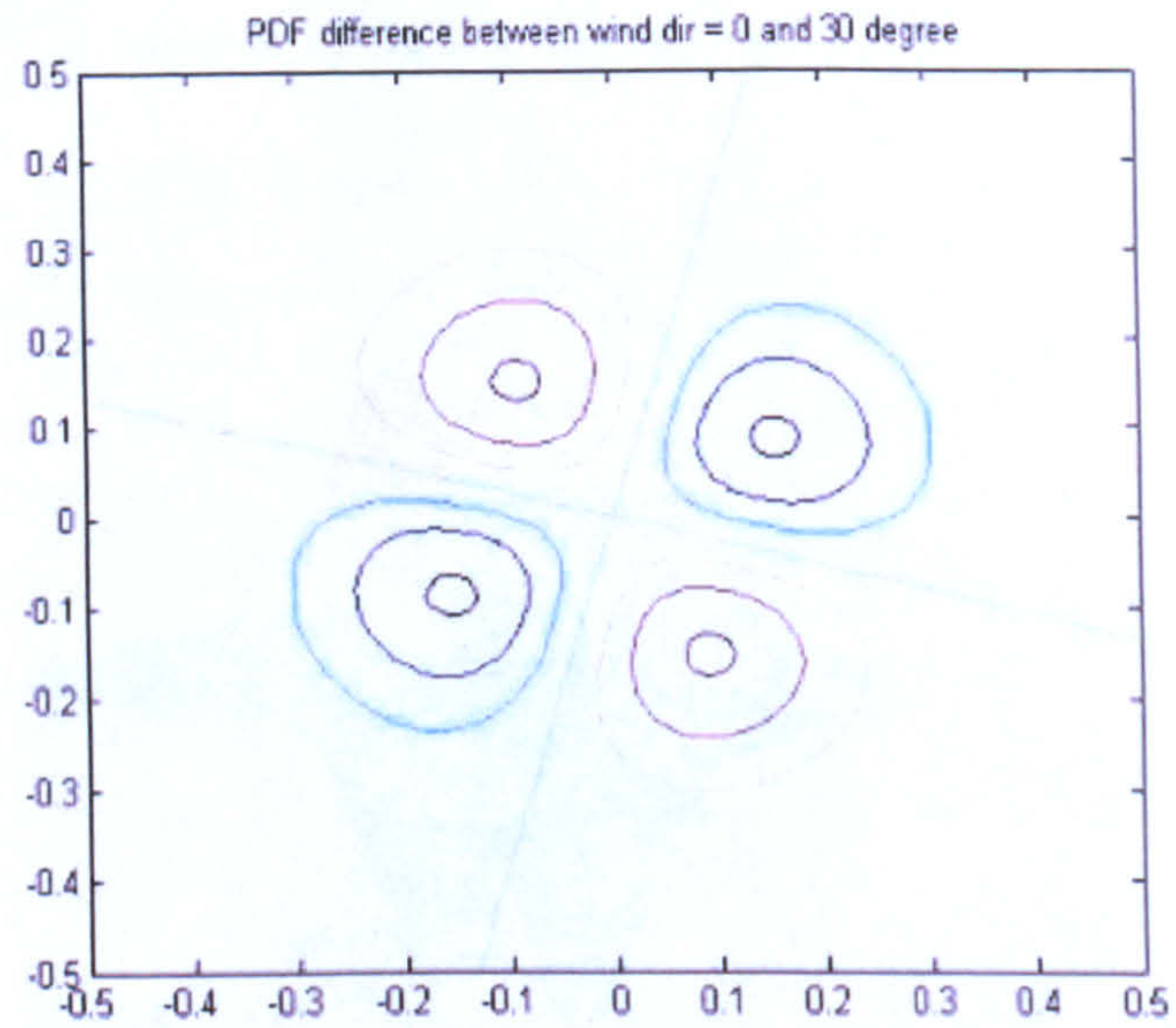


Figure II-7 : Contour of PDF difference map between 0° and 30° wind direction input.

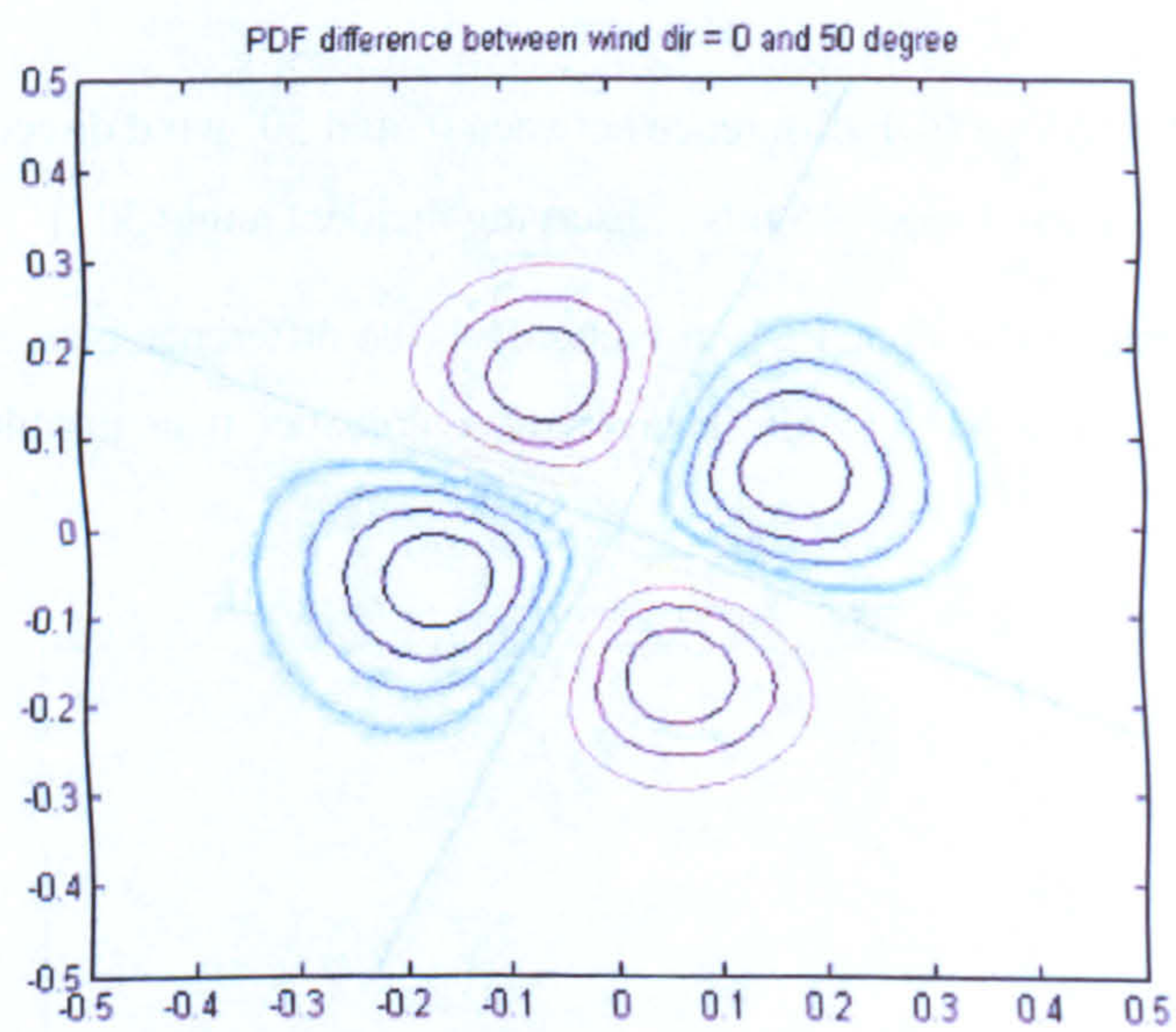


Figure II-8 : Contour of PDF difference map between 0° and 50° wind direction input.

Observing incident angle effect

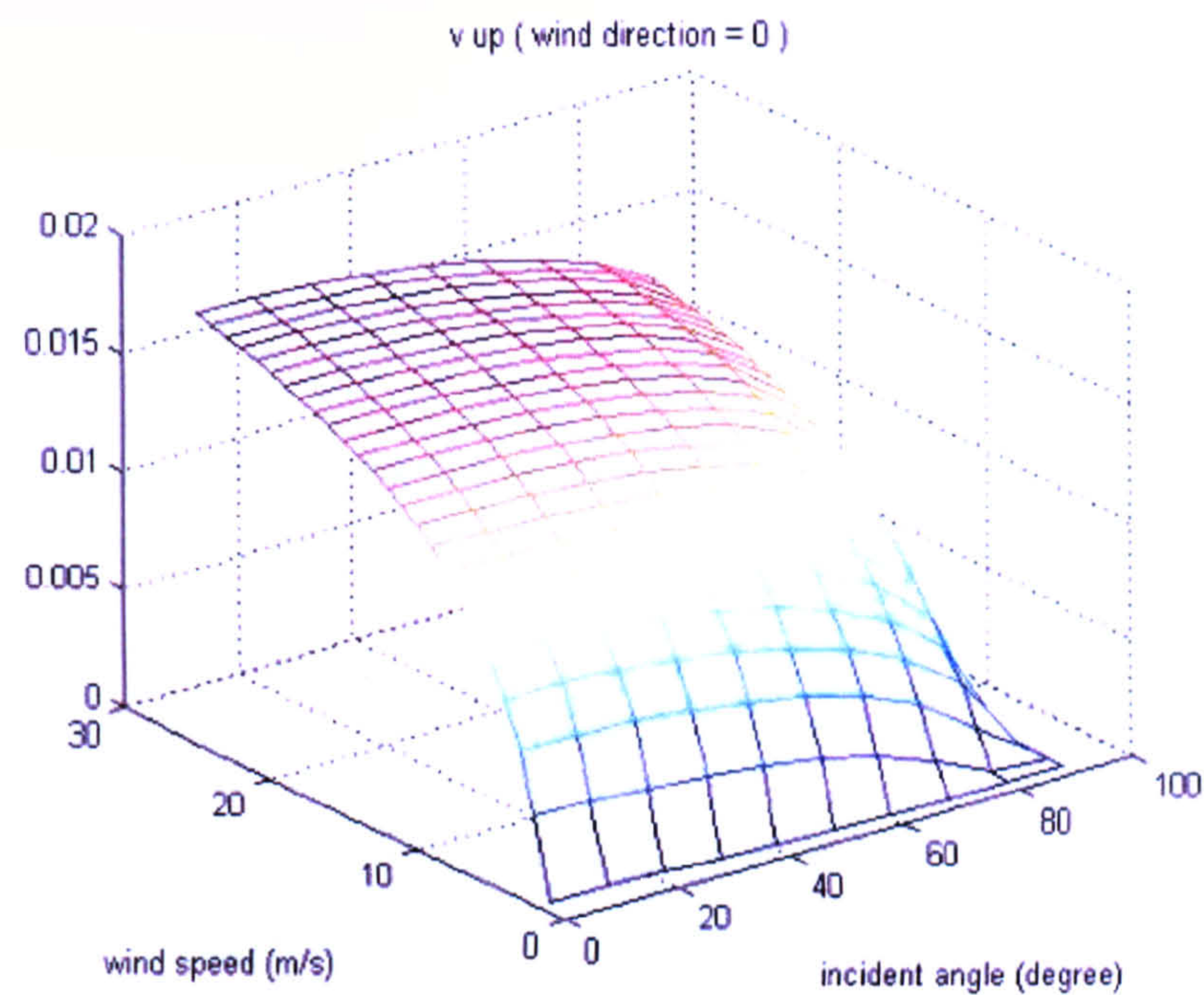


Figure II-9 : Slope PDF σ_x changes with wind speed and observing incident angle.

Appendix III

The Differential Method Inversion of R12 and R13

The following is the results of R12 and R13 inversion experiment via the Differential Method (section 6.3). Synthetic DDMs with different noise levels and the real UK-DMC data have been applied in this inversion study and the more thorough output are presented in this section. Without mentioning, the ForWaRD algorithm (section 5.3.2) is used to deconvolve DDMs which are blurred with GPS Ambiguity Function and noise.

1. R12 Case

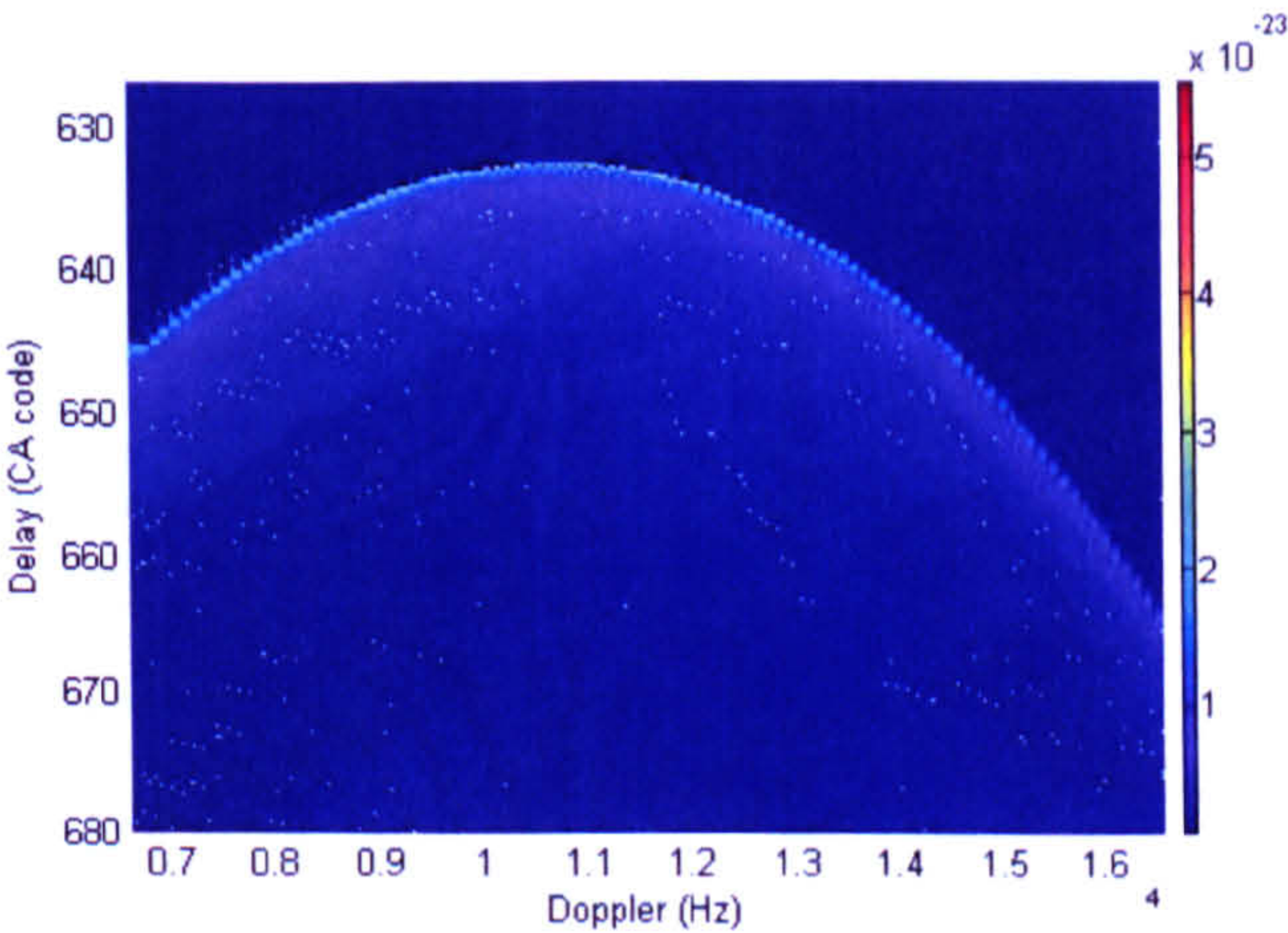


Figure III-1: Simulated ideal DDM (without GPS AF and noise-free).

BSNR = 200 dB

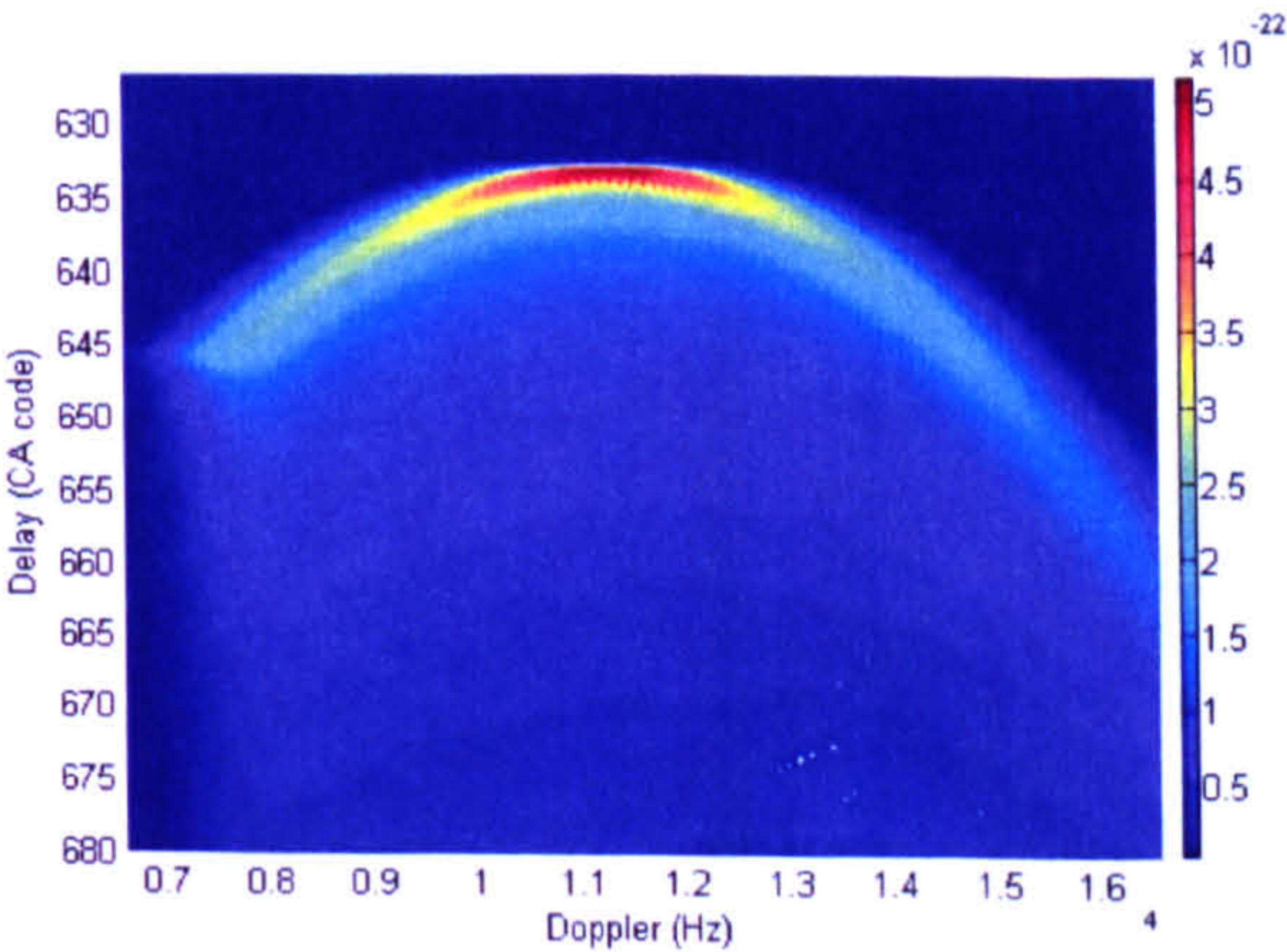


Figure III-2: AF blurred DDM with noise.

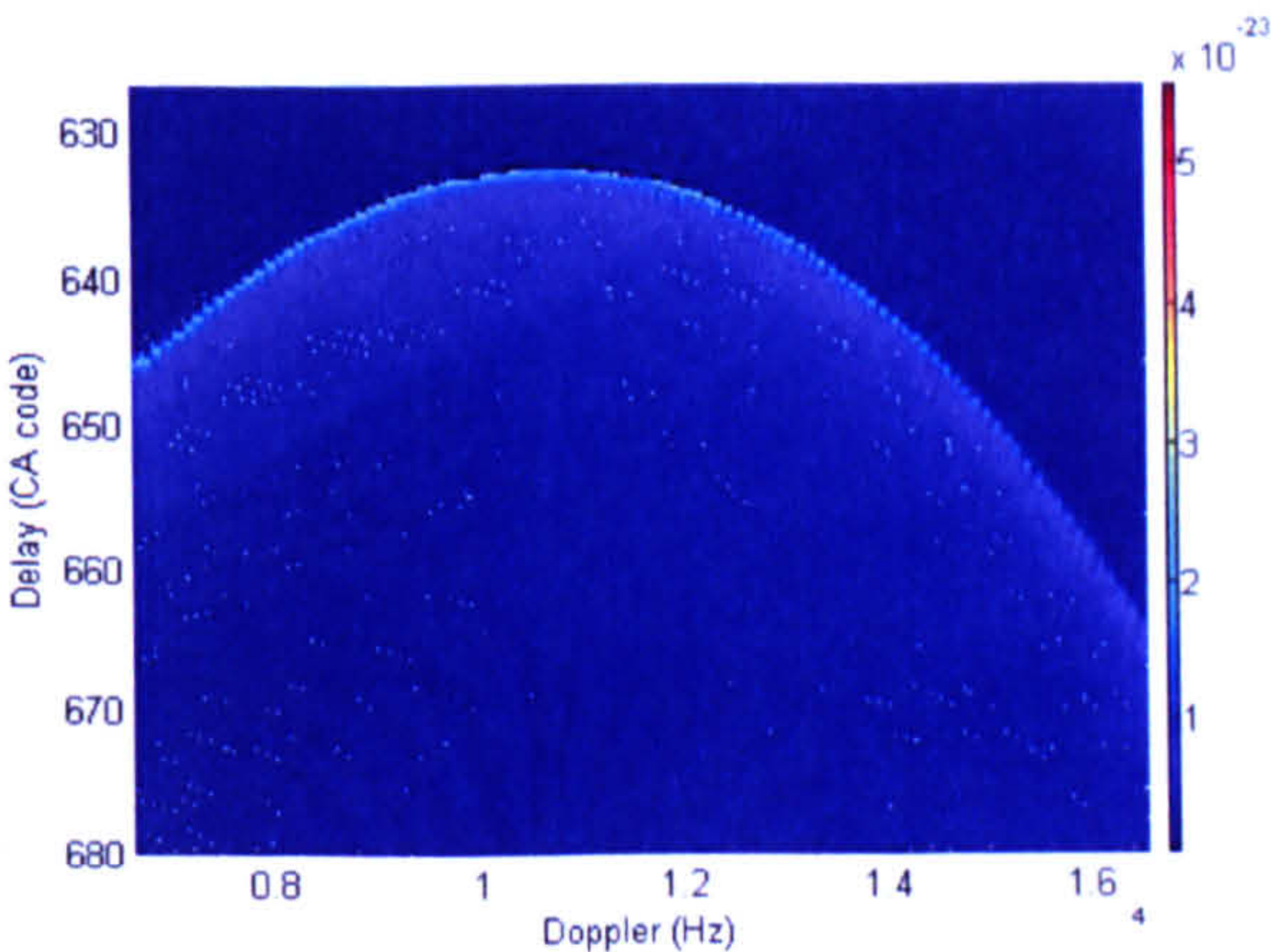


Figure III-3: Deconvolved DDM (SNR 98.95 dB).

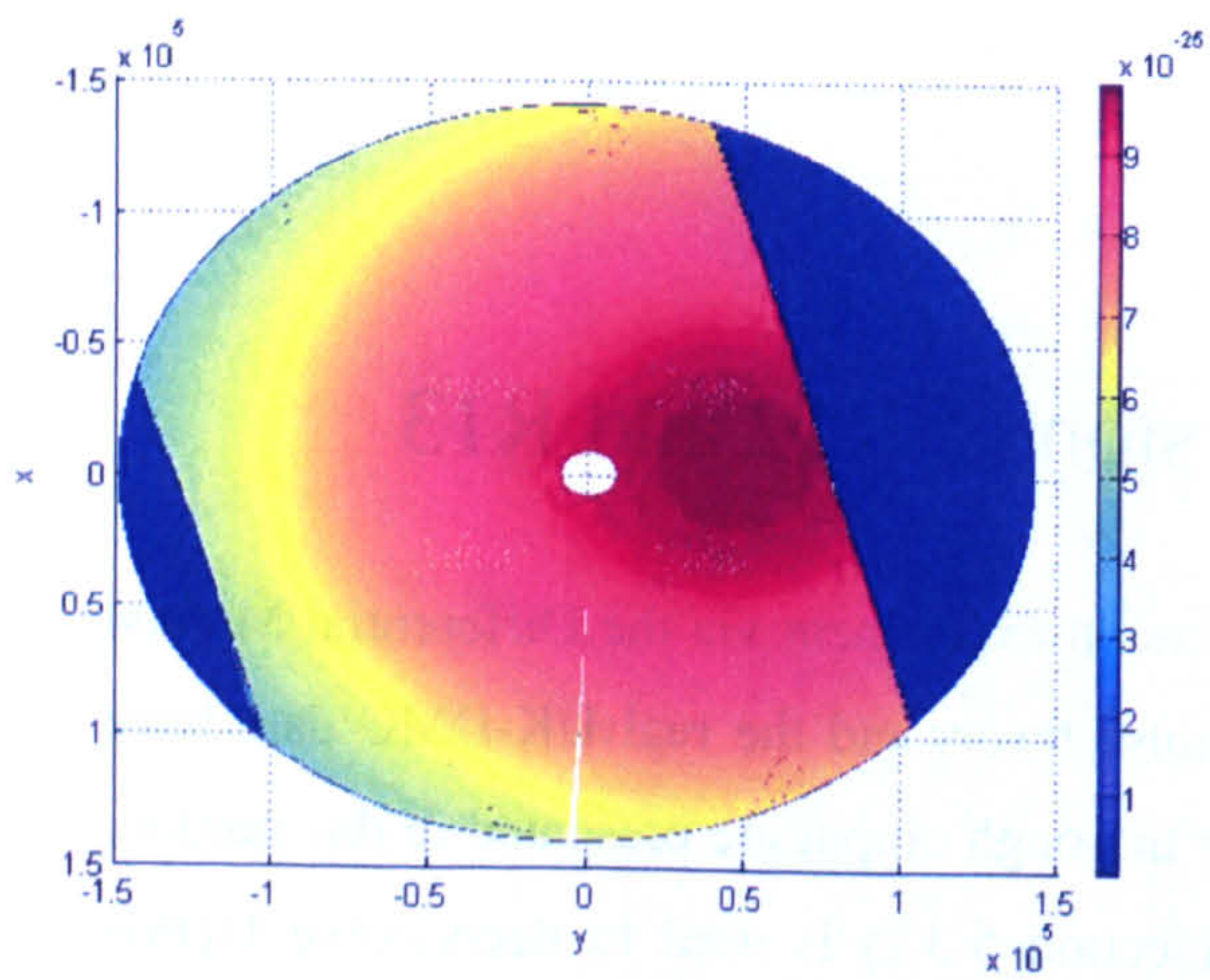


Figure III-3: Inversed spatial energy map.

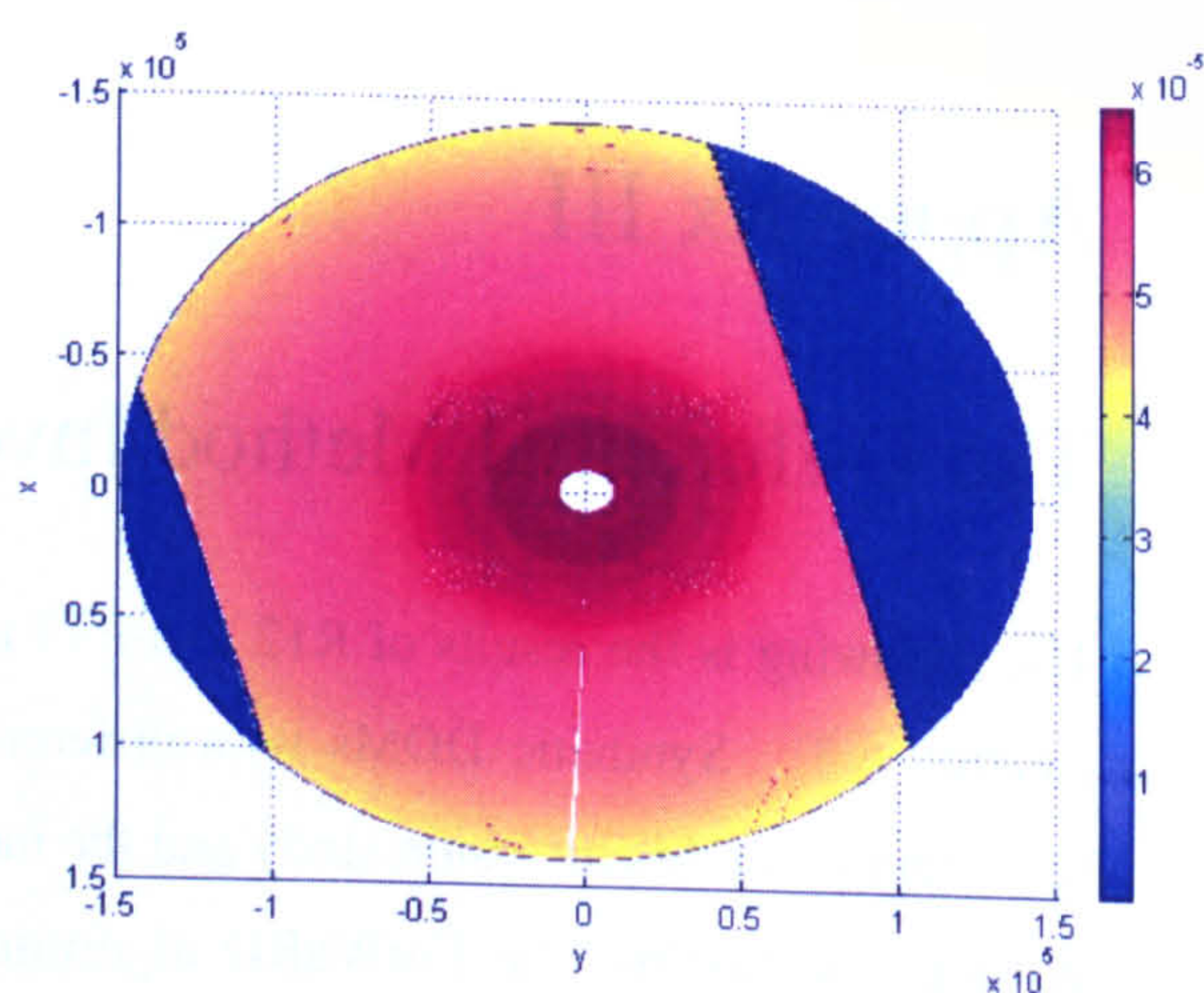


Figure III-4: Inversed slope probability map.

BSNR = 150 dB

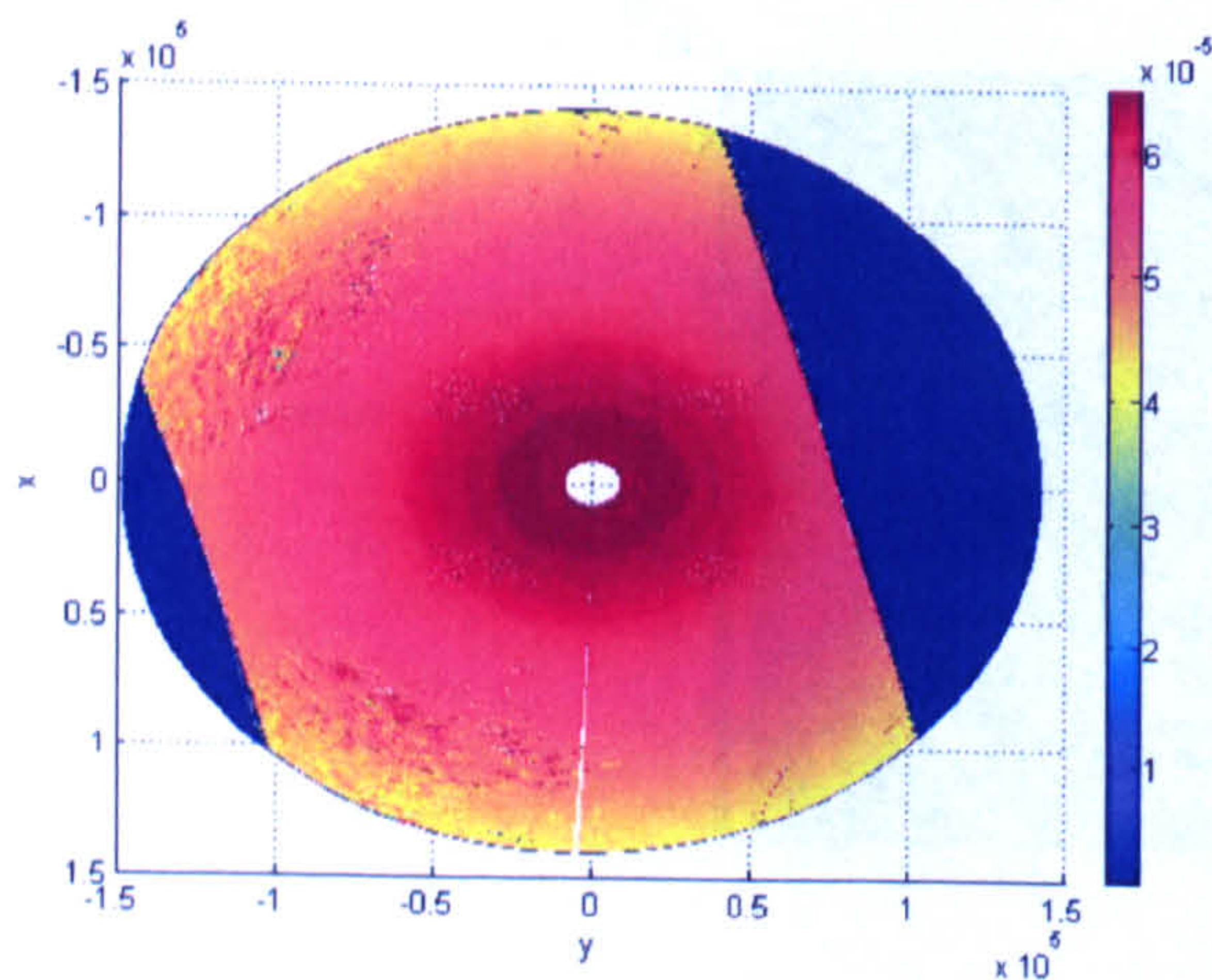


Figure III-5: Inversed slope probability map.

BSNR = 120 dB

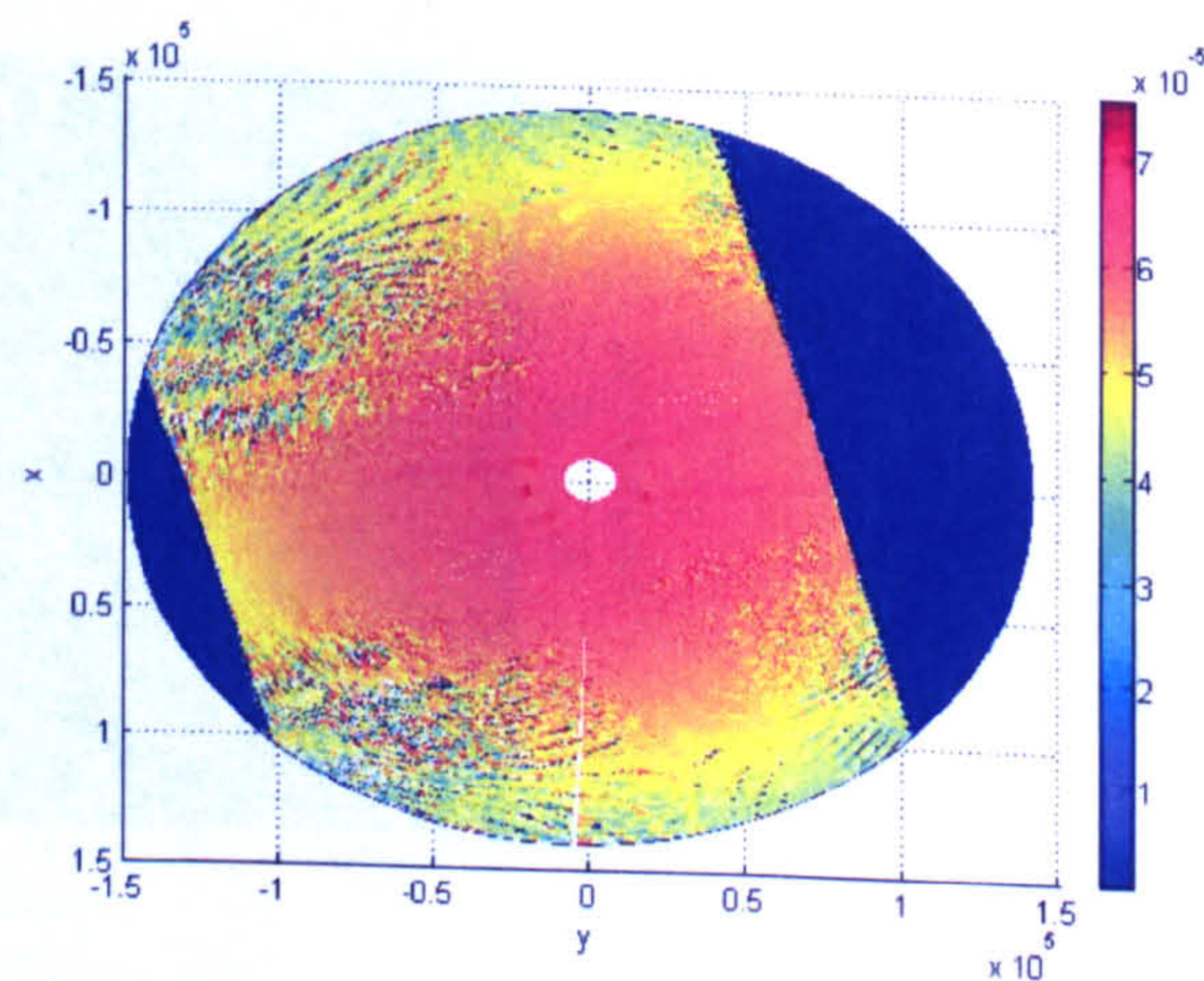


Figure III-6: Inversed slope probability map.

BSNR = 100 dB

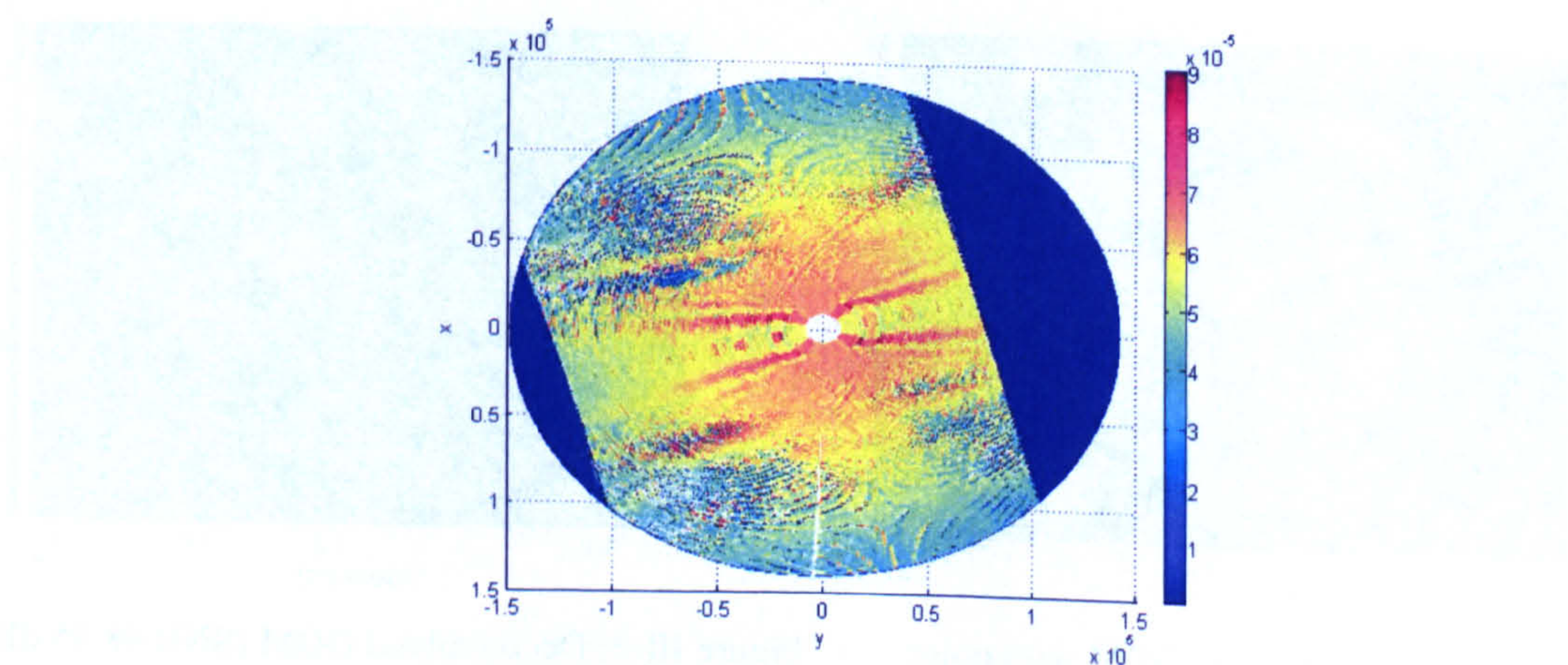


Figure III-7: Inversed slope probability map.

UK-DMC R12 DDM Inversion

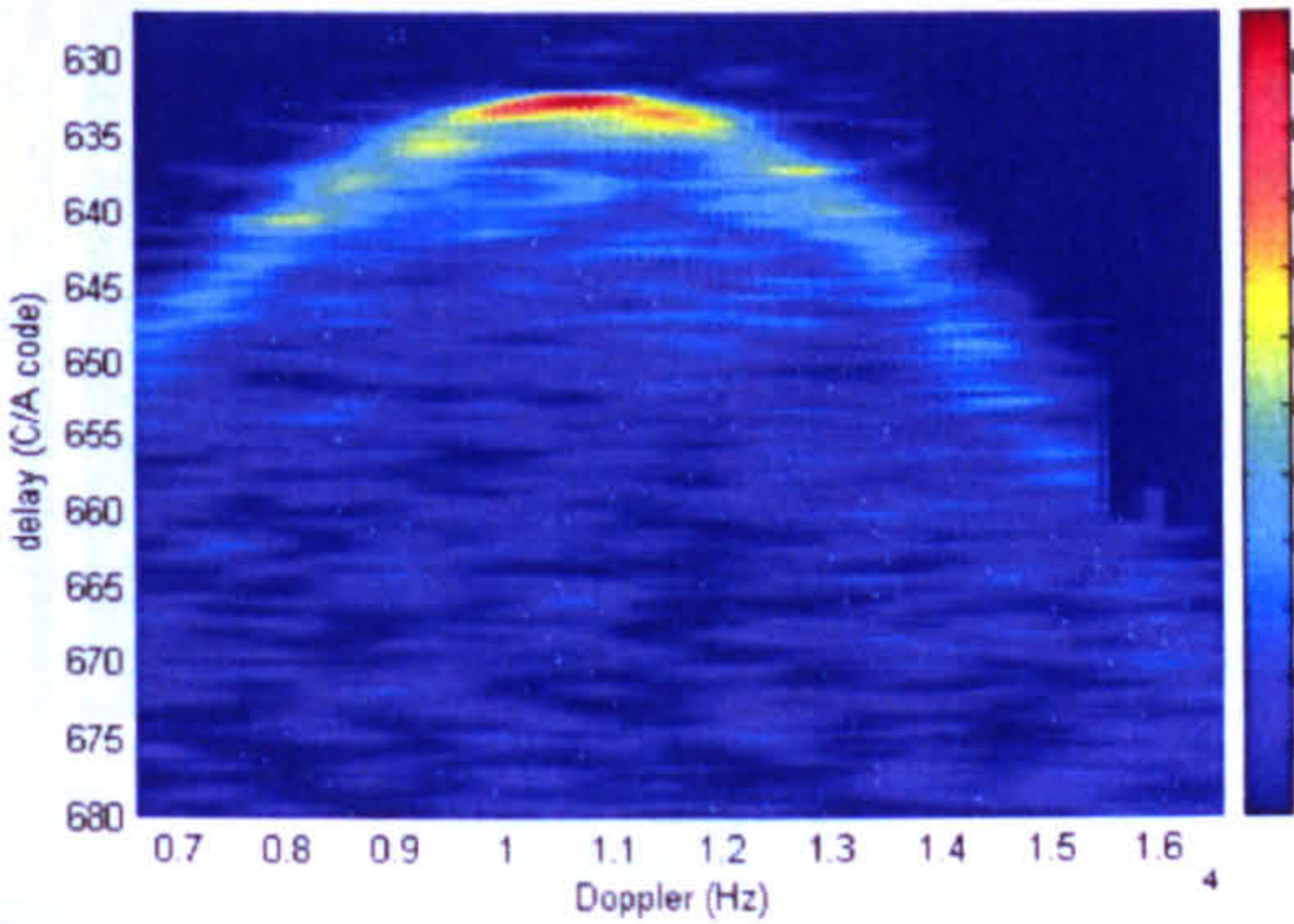


Figure III-8: UK-DMC R12 DDM.

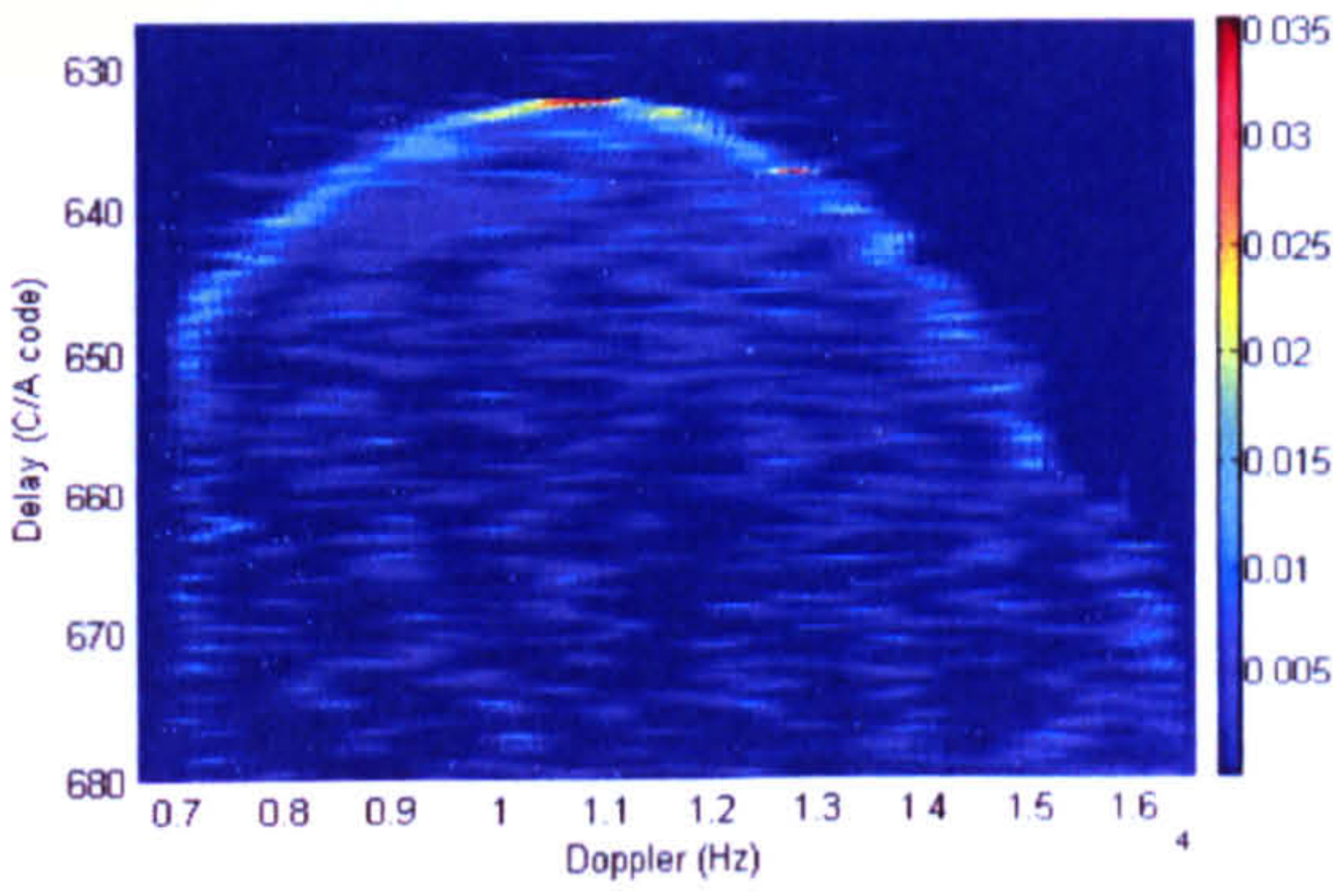


Figure III-9: Deconvolved R12 DDM.

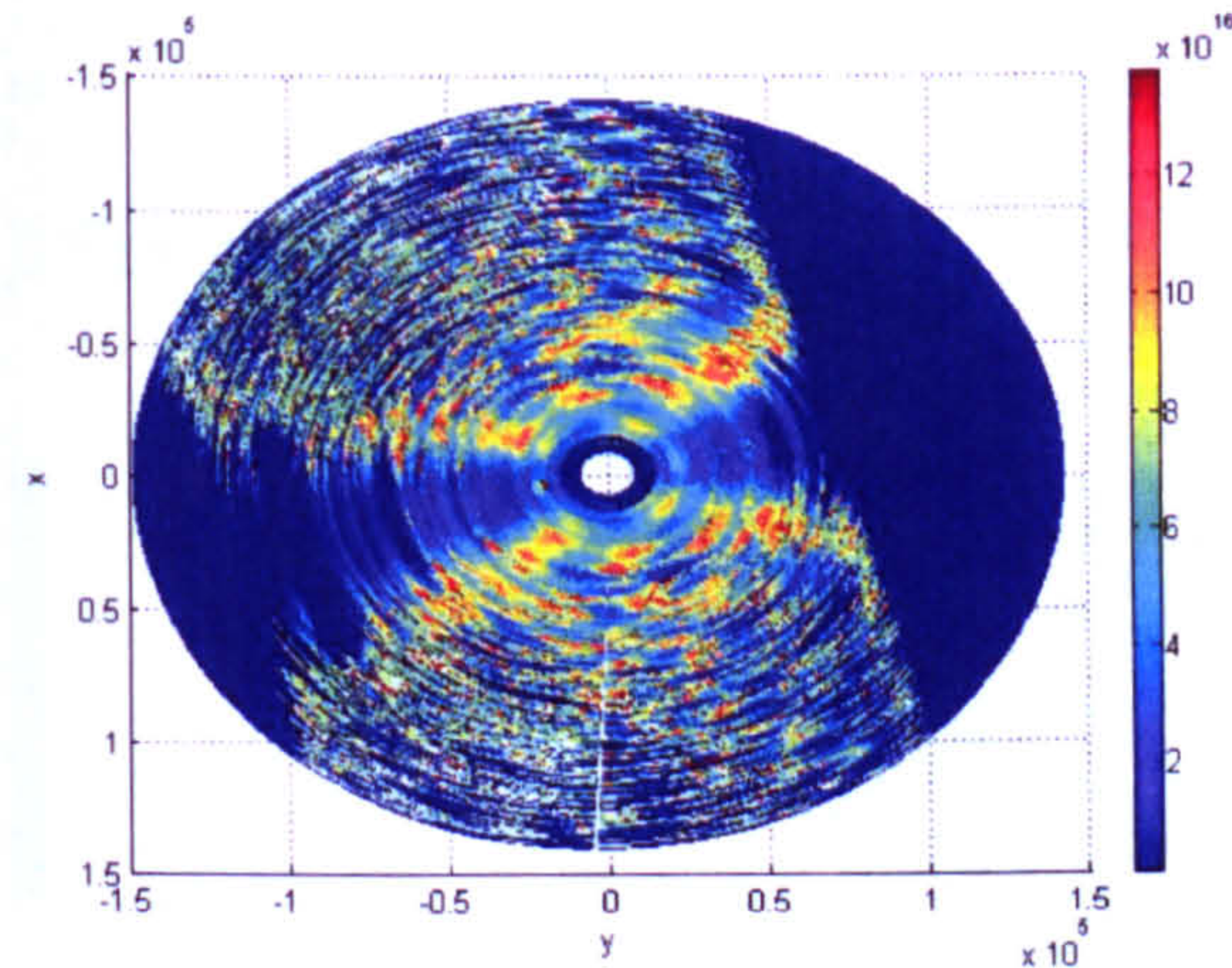


Figure III-10: Inversed slope probability map.

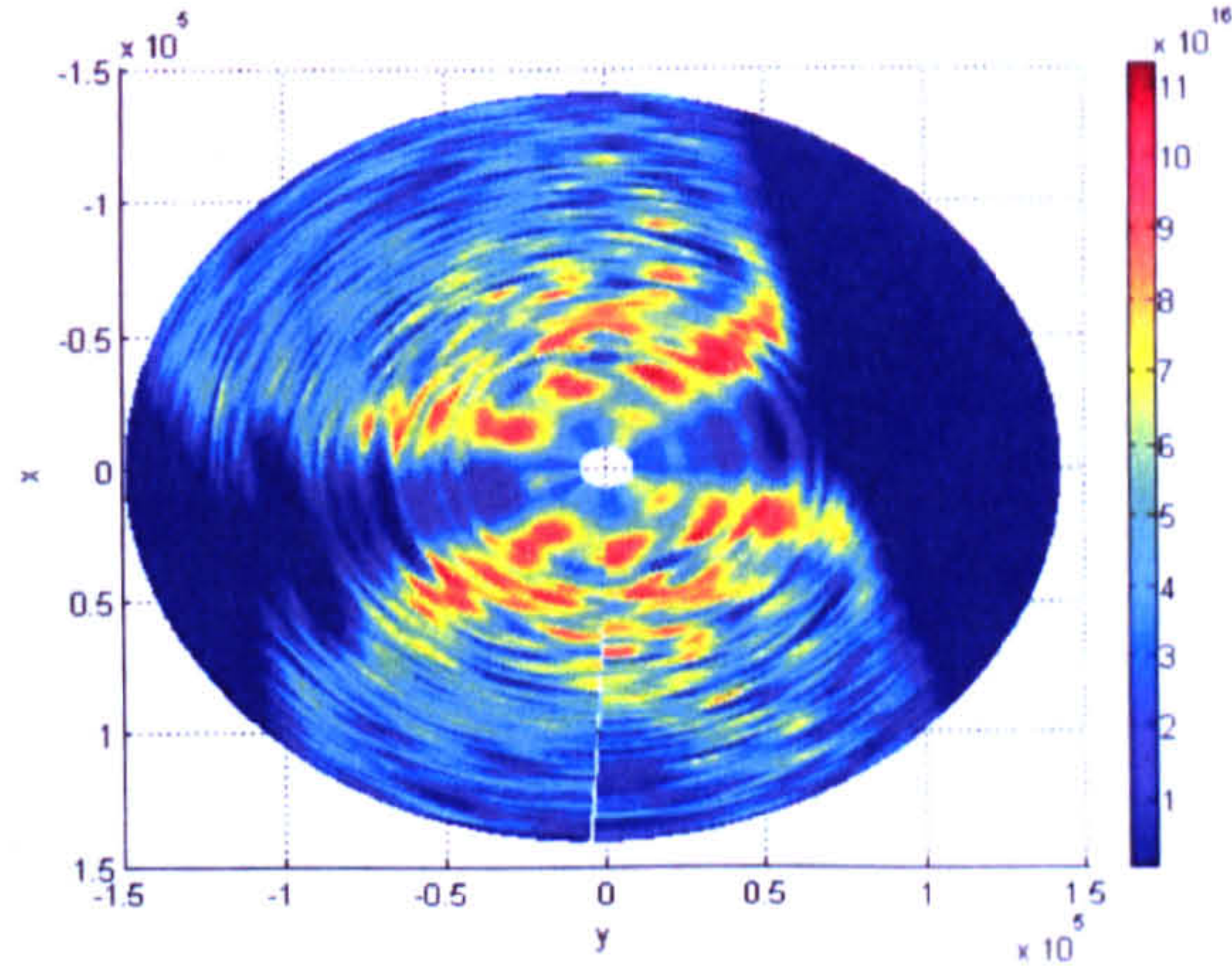


Figure III-11: Filtered slope probability map.

2. R13 Case

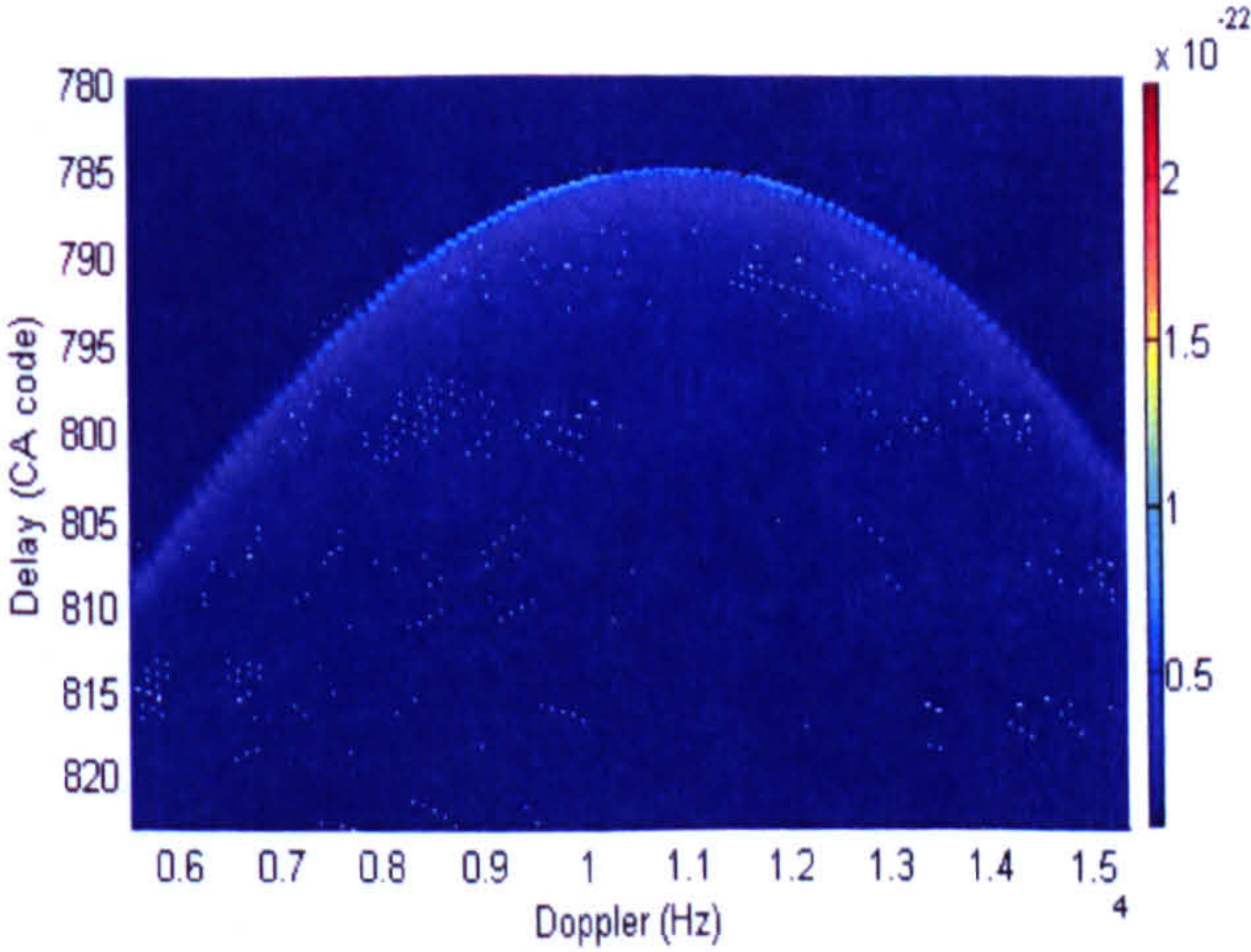


Figure III-12: Simulated ideal DDM (without GPS AF and noise-free).

BSNR = 200 dB

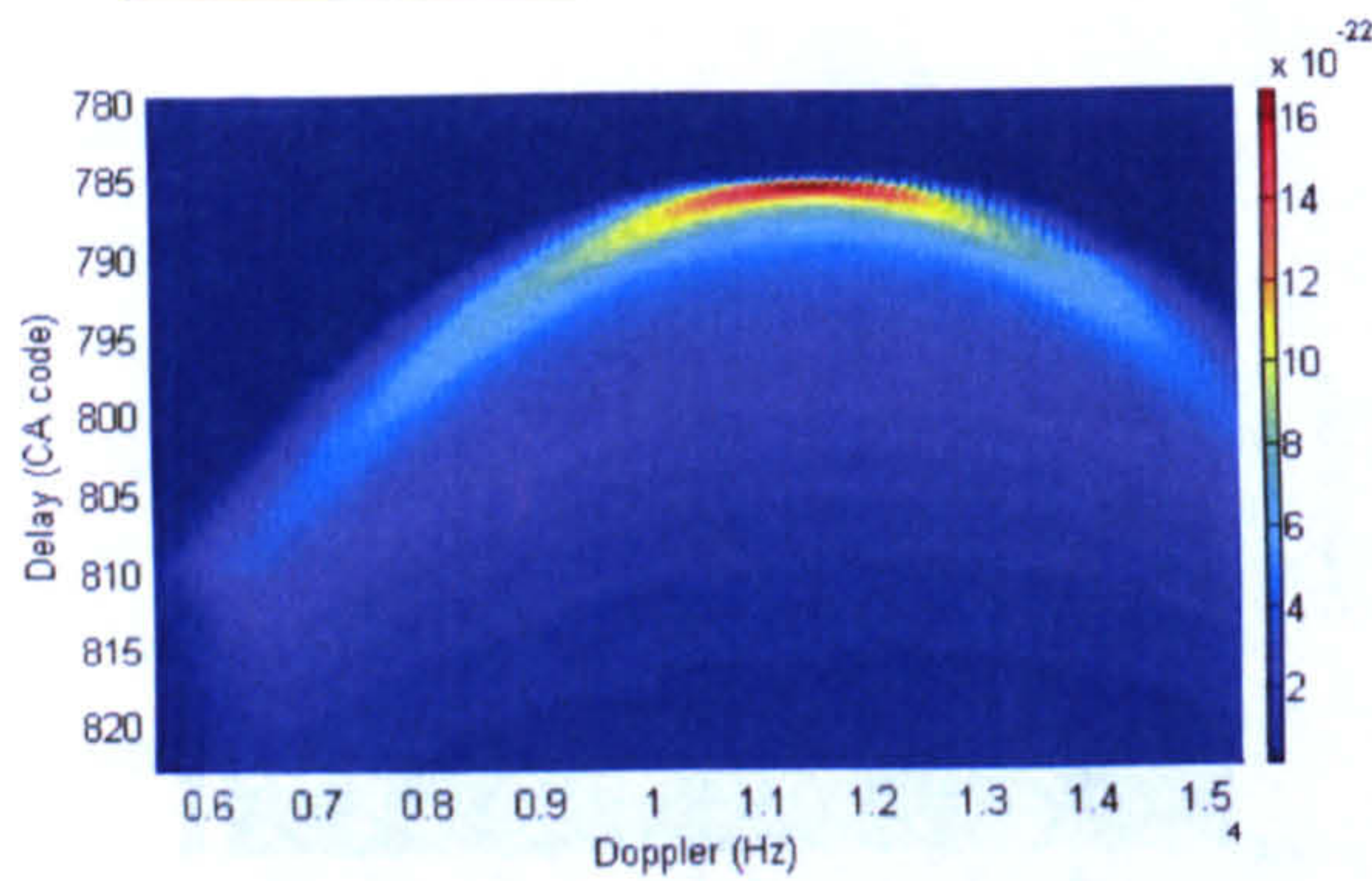


Figure III-13: AF blurred DDM with noise.

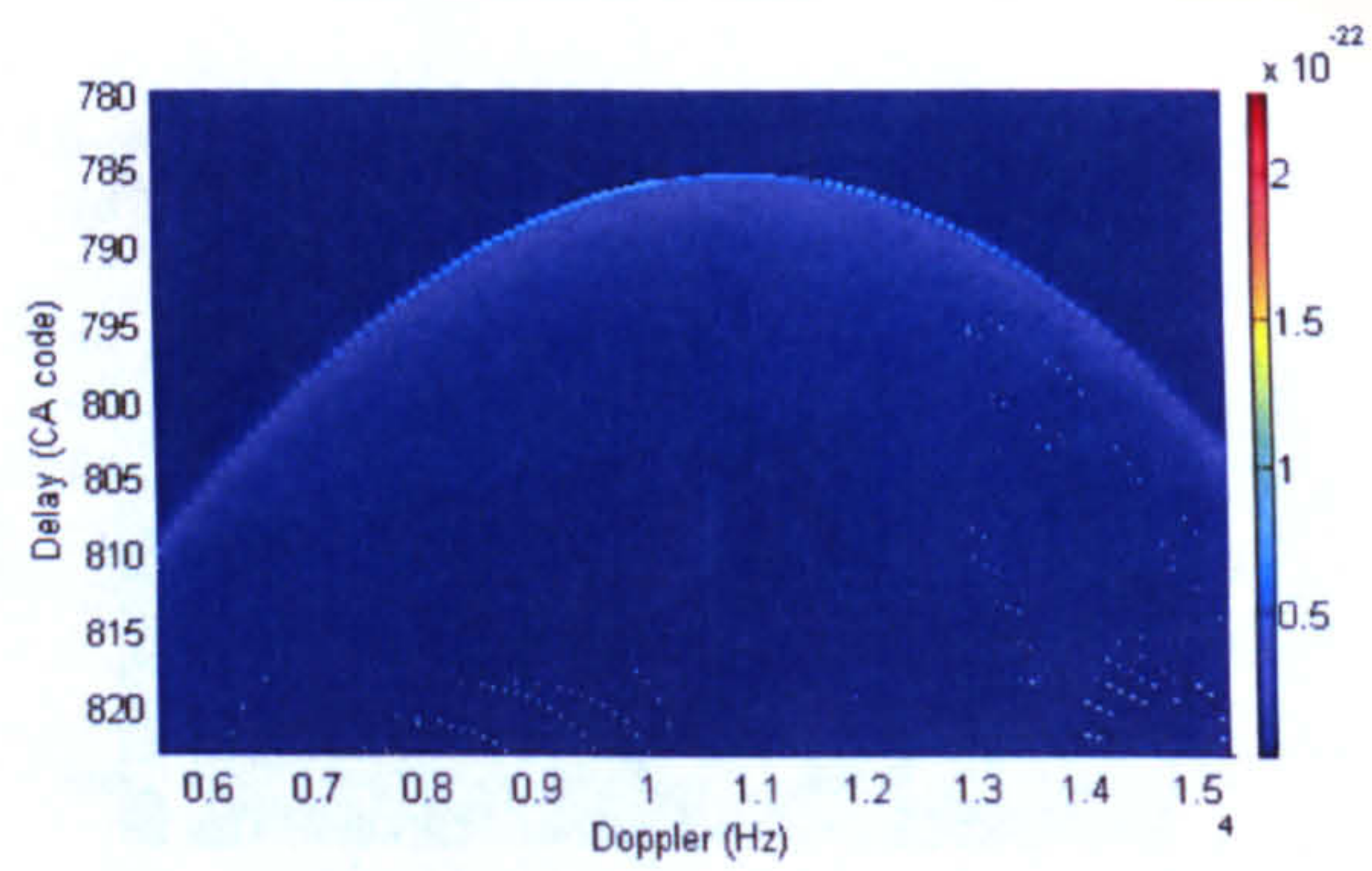


Figure III-14: Deconvolved DDM (SNR 99.11 dB).

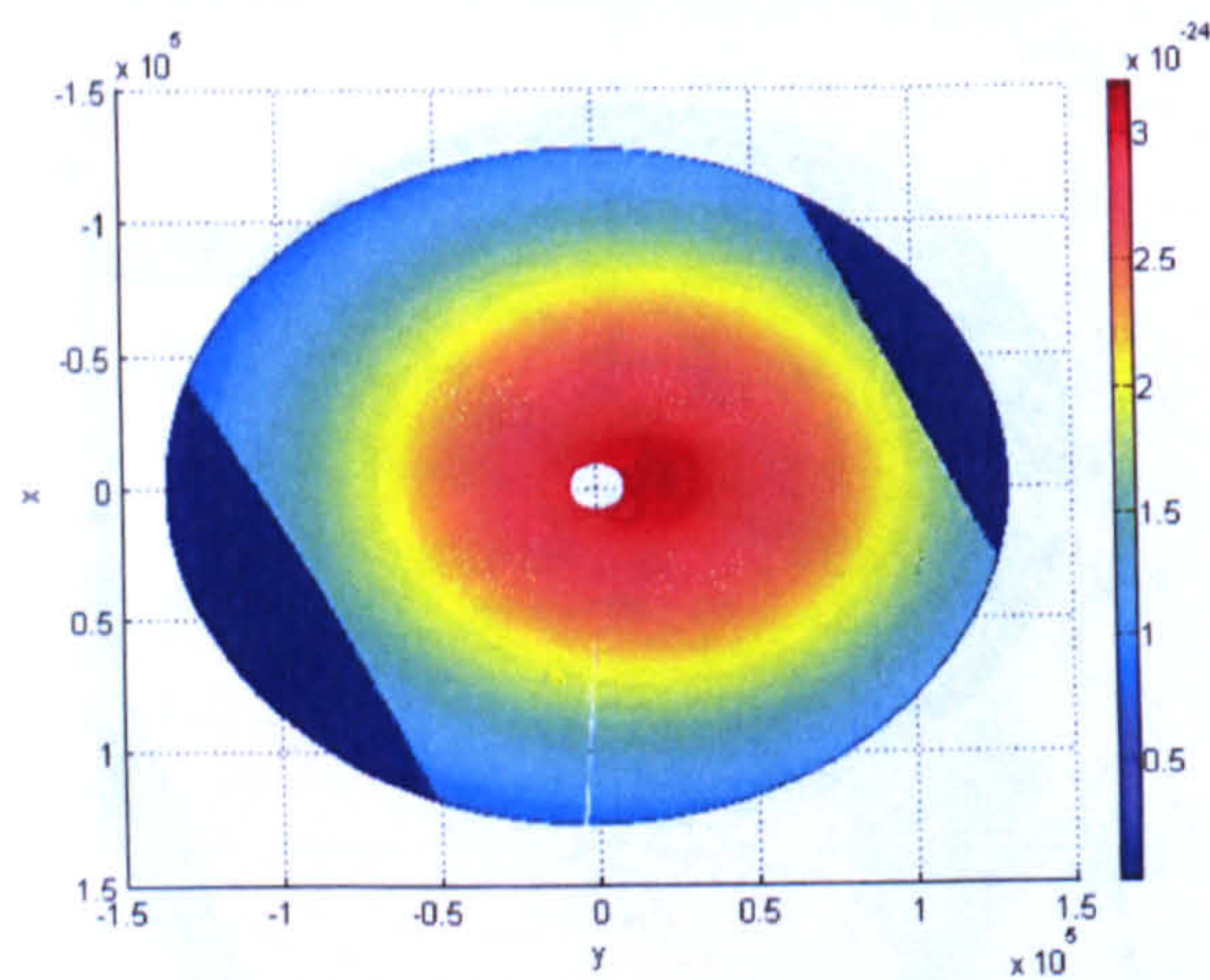


Figure III-15: Inversed spatial energy map.

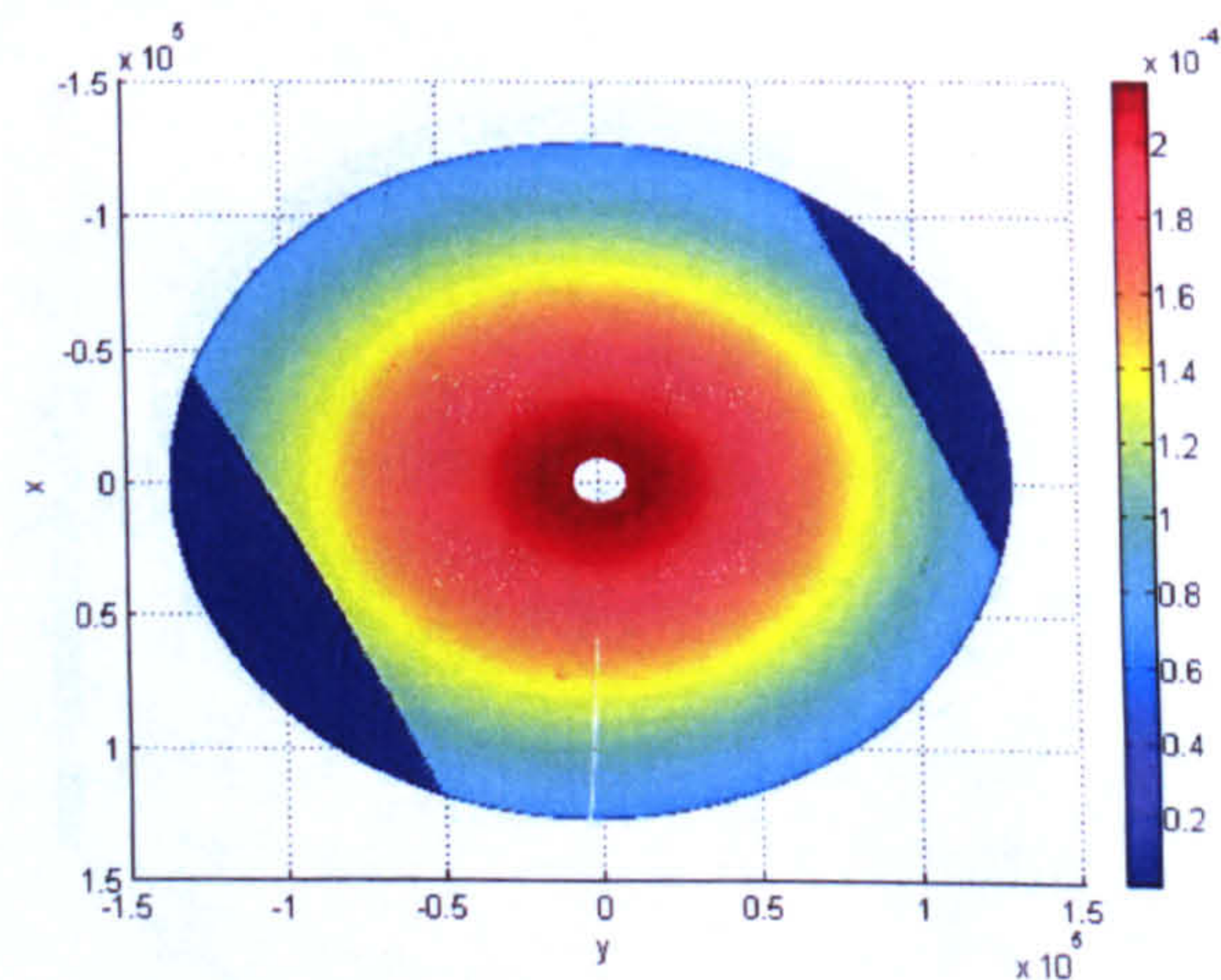


Figure III-16: Inversed slope probability map.

BSNR = 150 dB

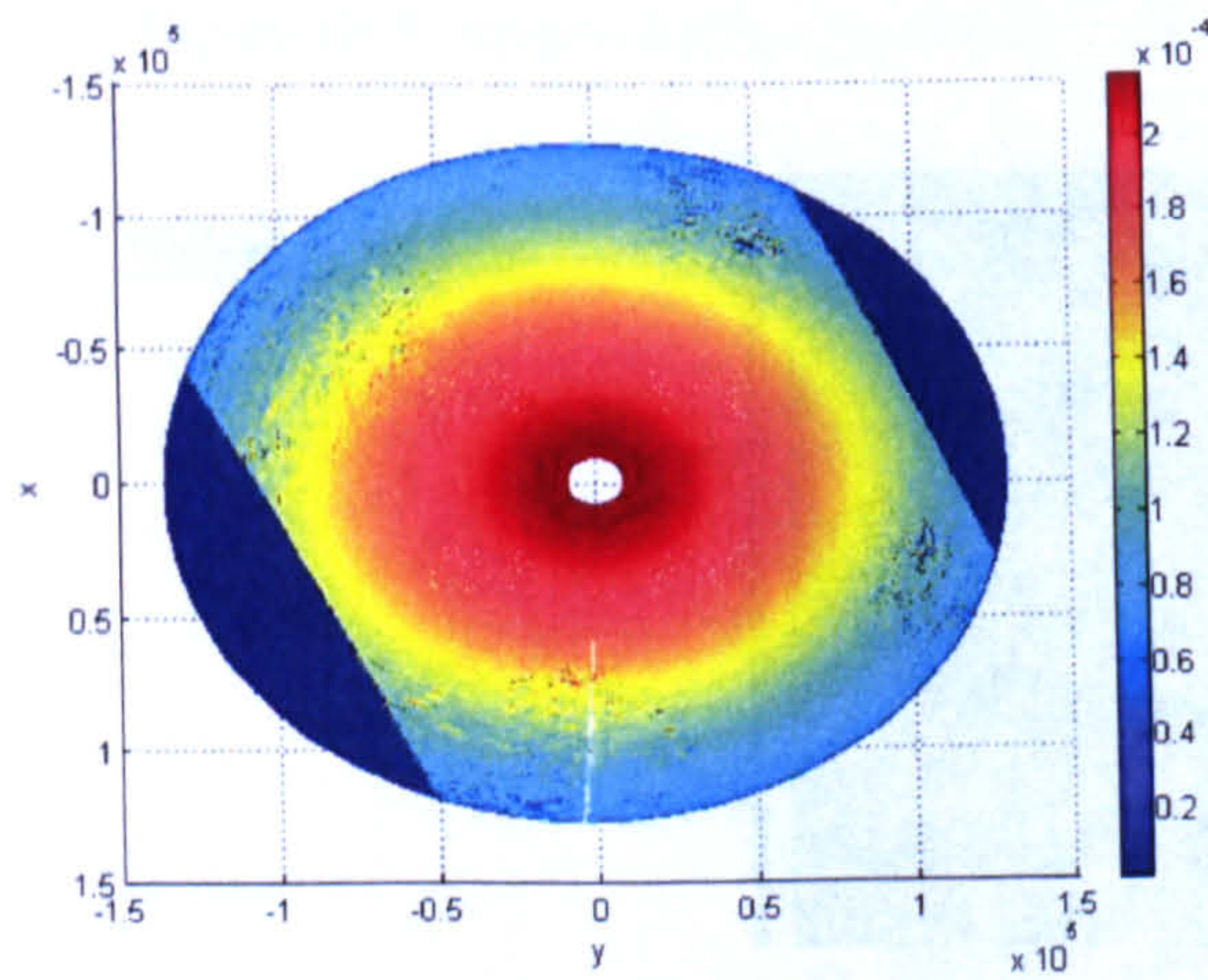


Figure III-17: Inversed slope probability map.

BSNR = 120 dB

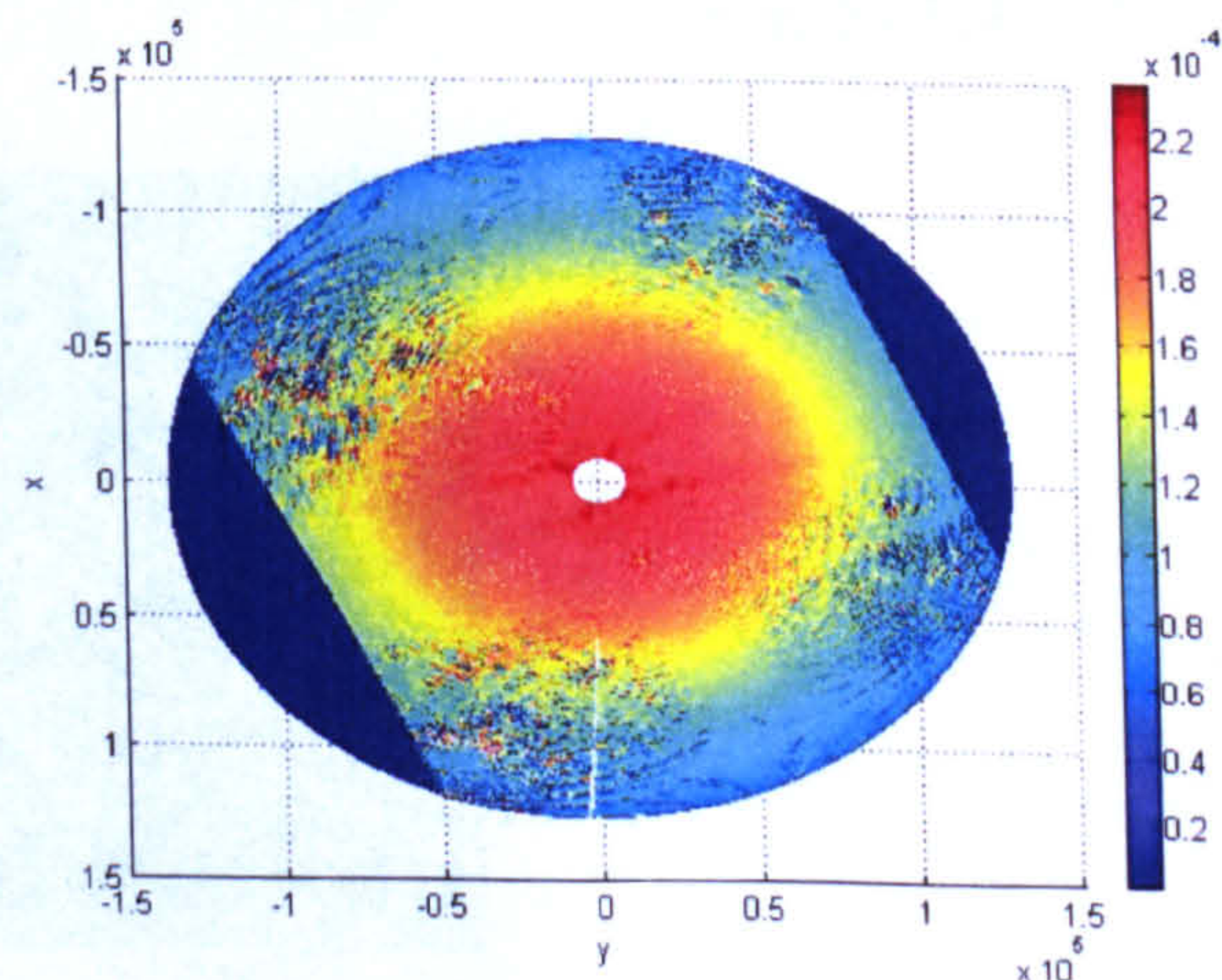


Figure III-18: Inversed slope probability map.

BSNR = 100 dB

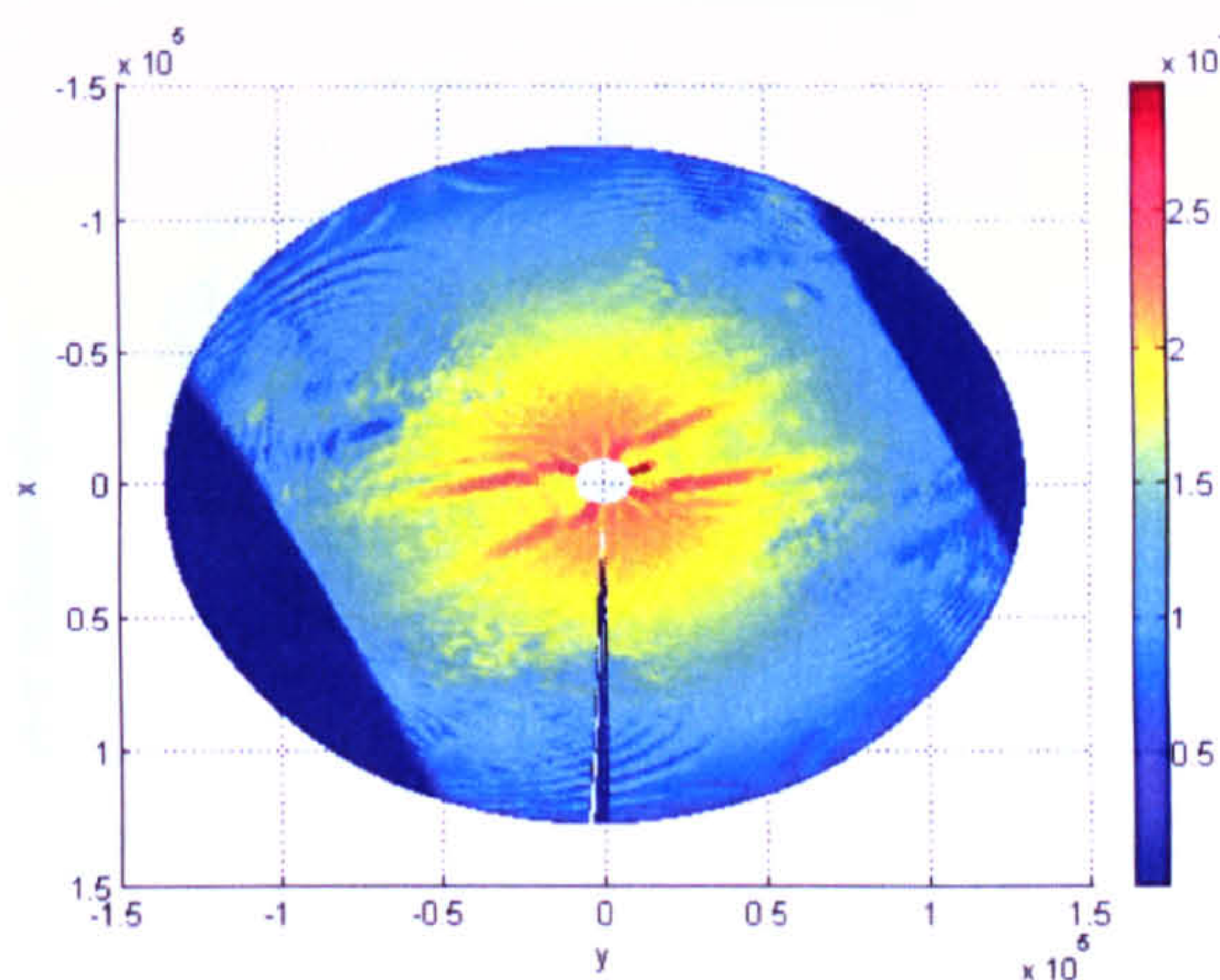


Figure III-19: Filtered slope probability map.

BSNR = 80 dB

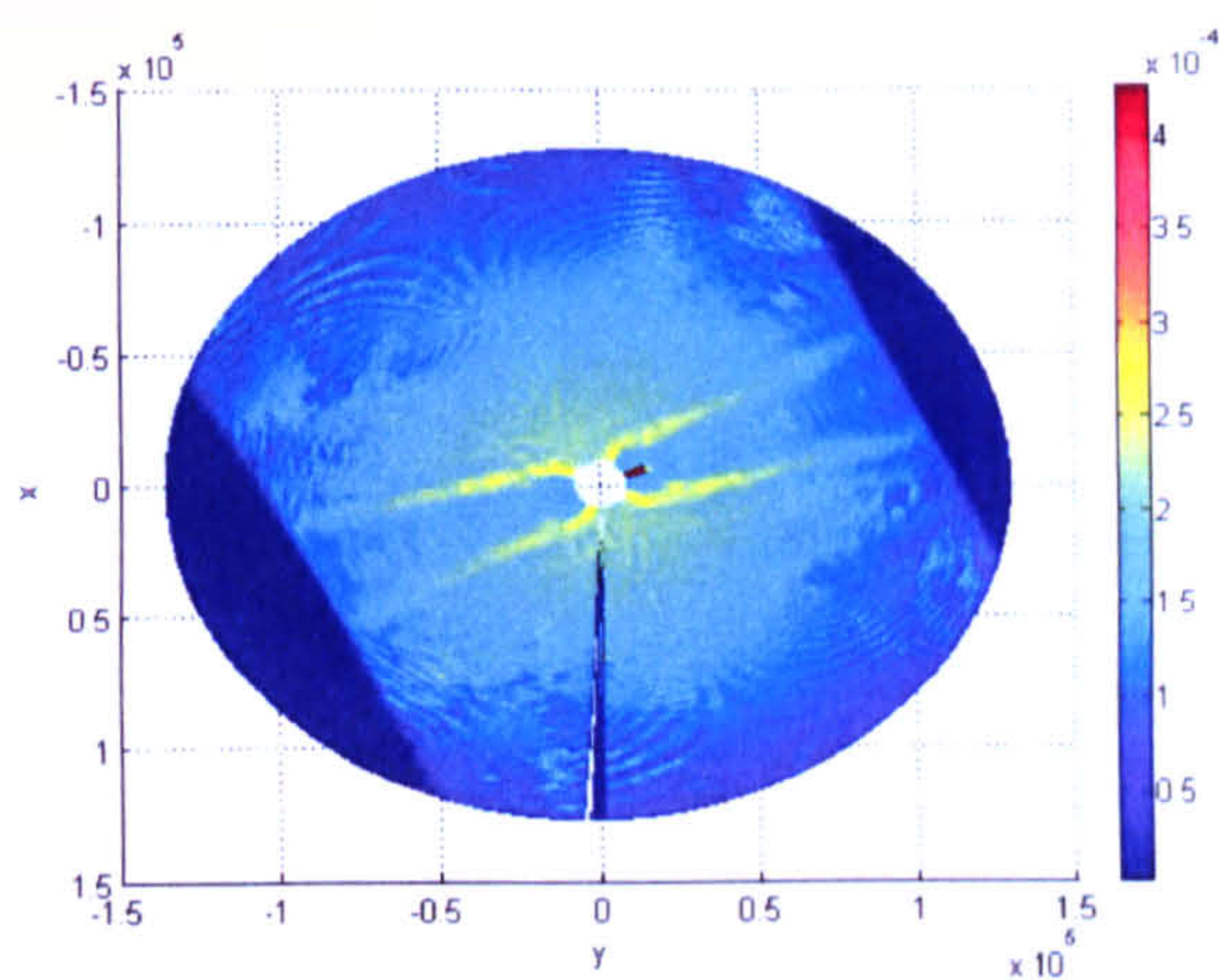


Figure III-20: Filtered slope probability map.

BSNR = 60 dB

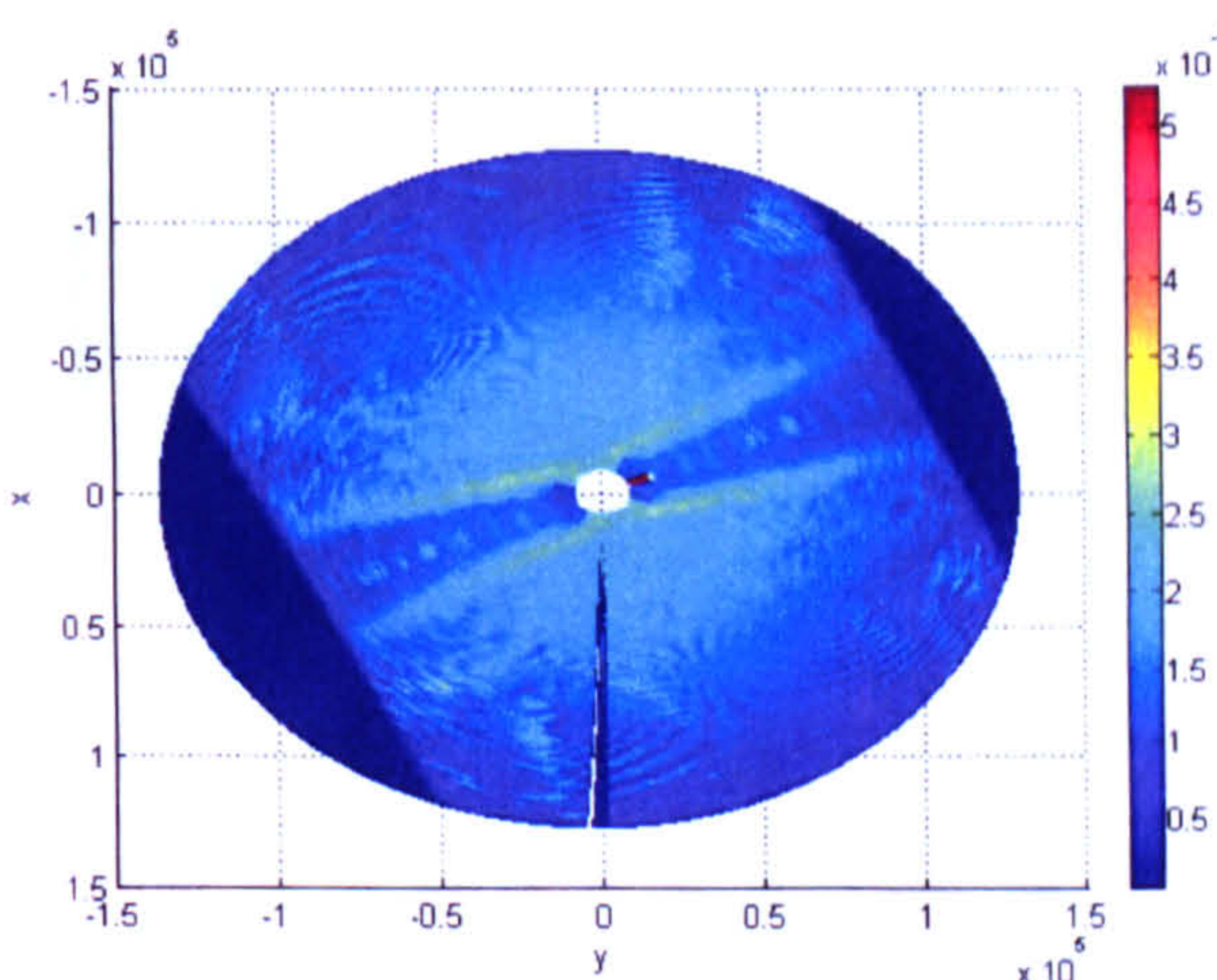


Figure III-21: Filtered slope probability map.

UK-DMC R13 DDM Inversion

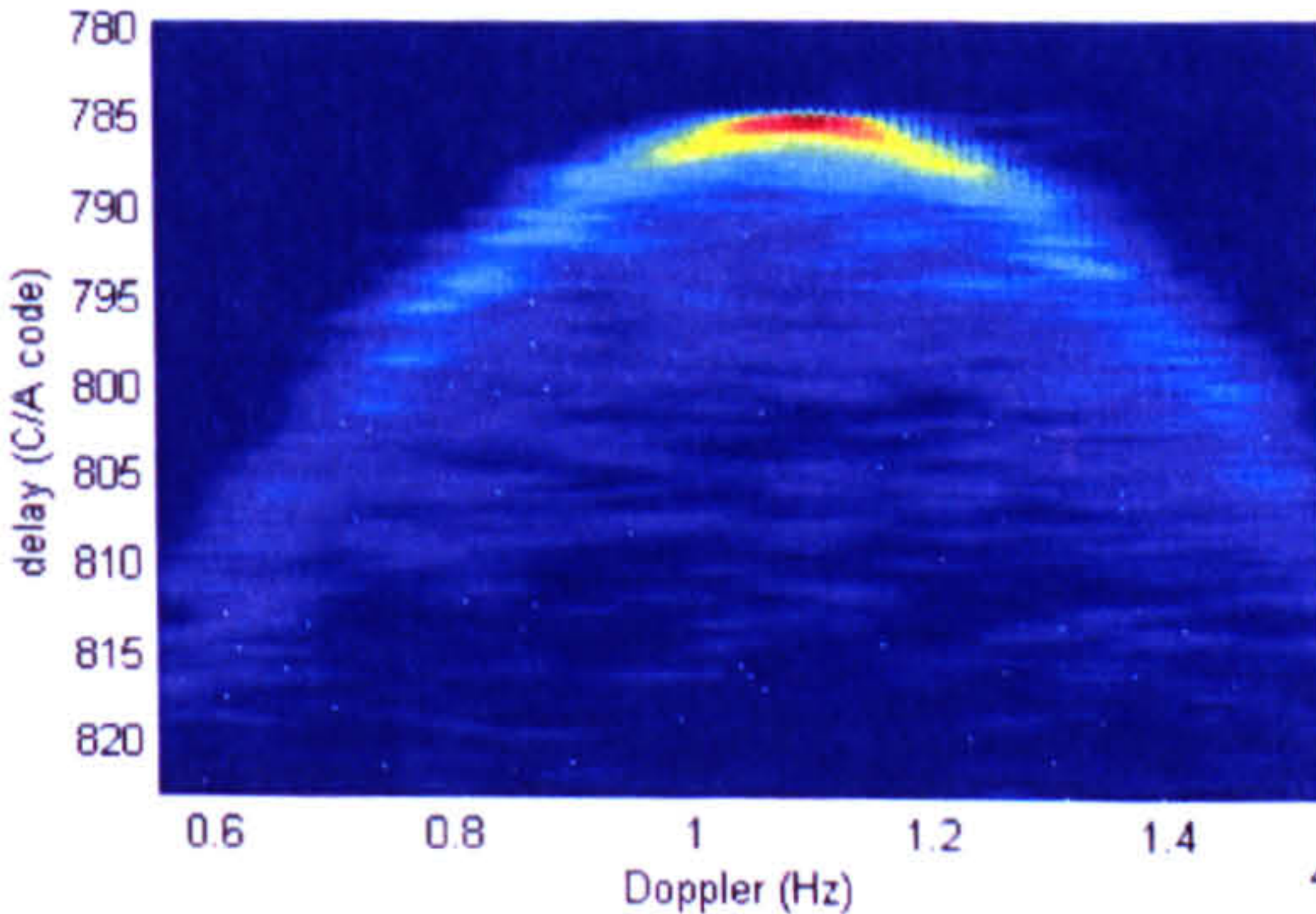


Figure III-22: UK-DMC R13 DDM.

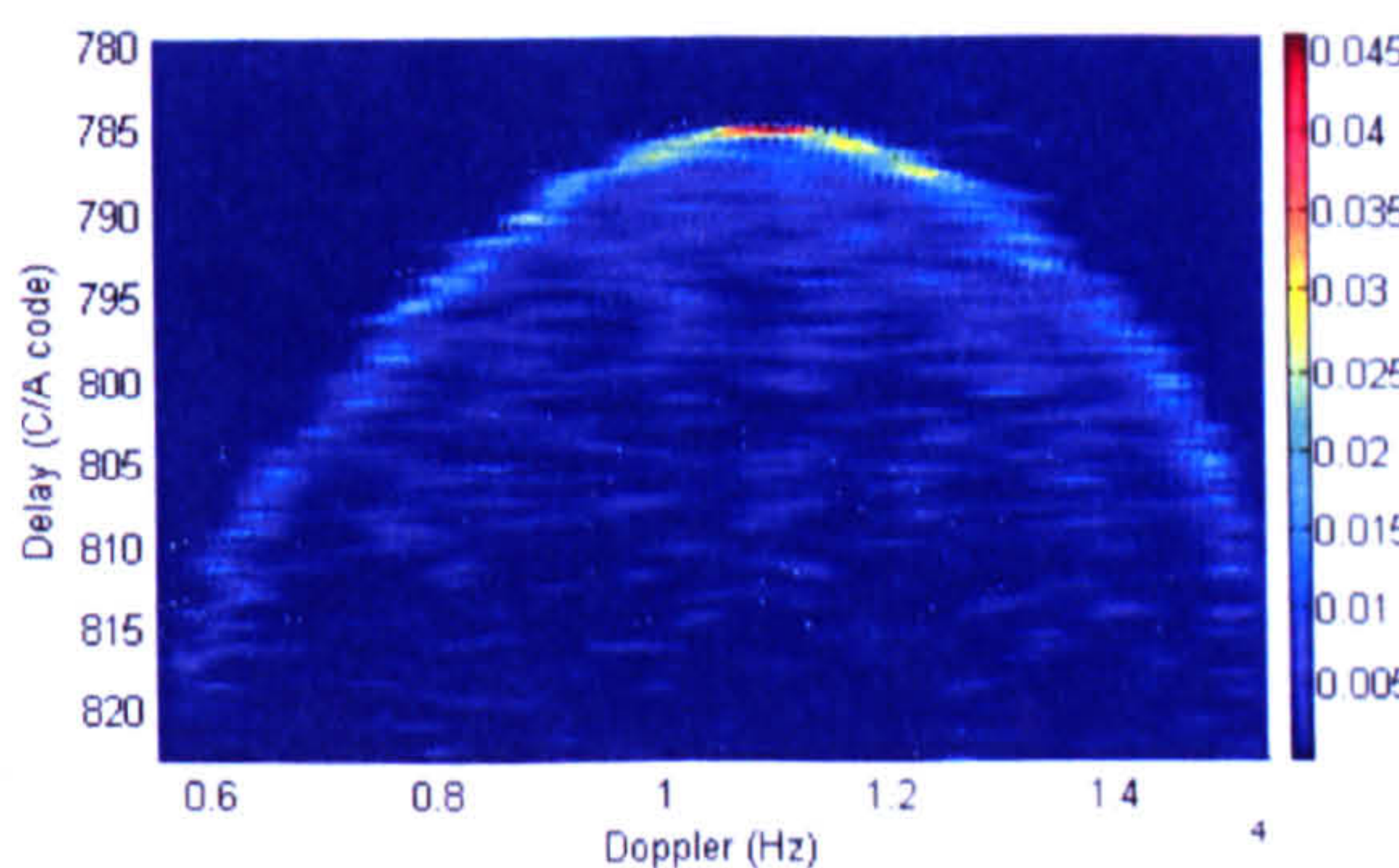


Figure III-23: Deconvolved R13 DDM.

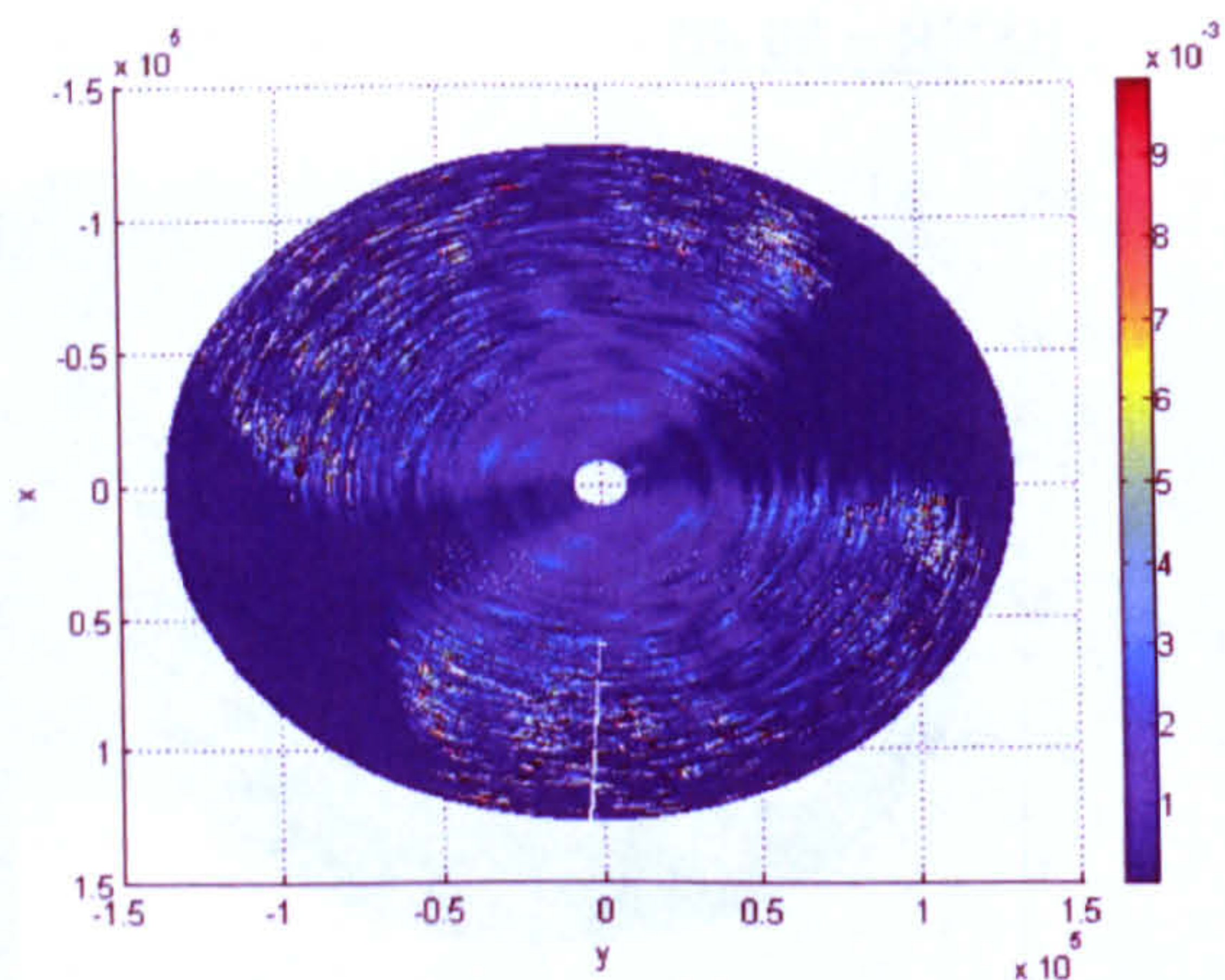


Figure III-24: Inversed spatial energy map.

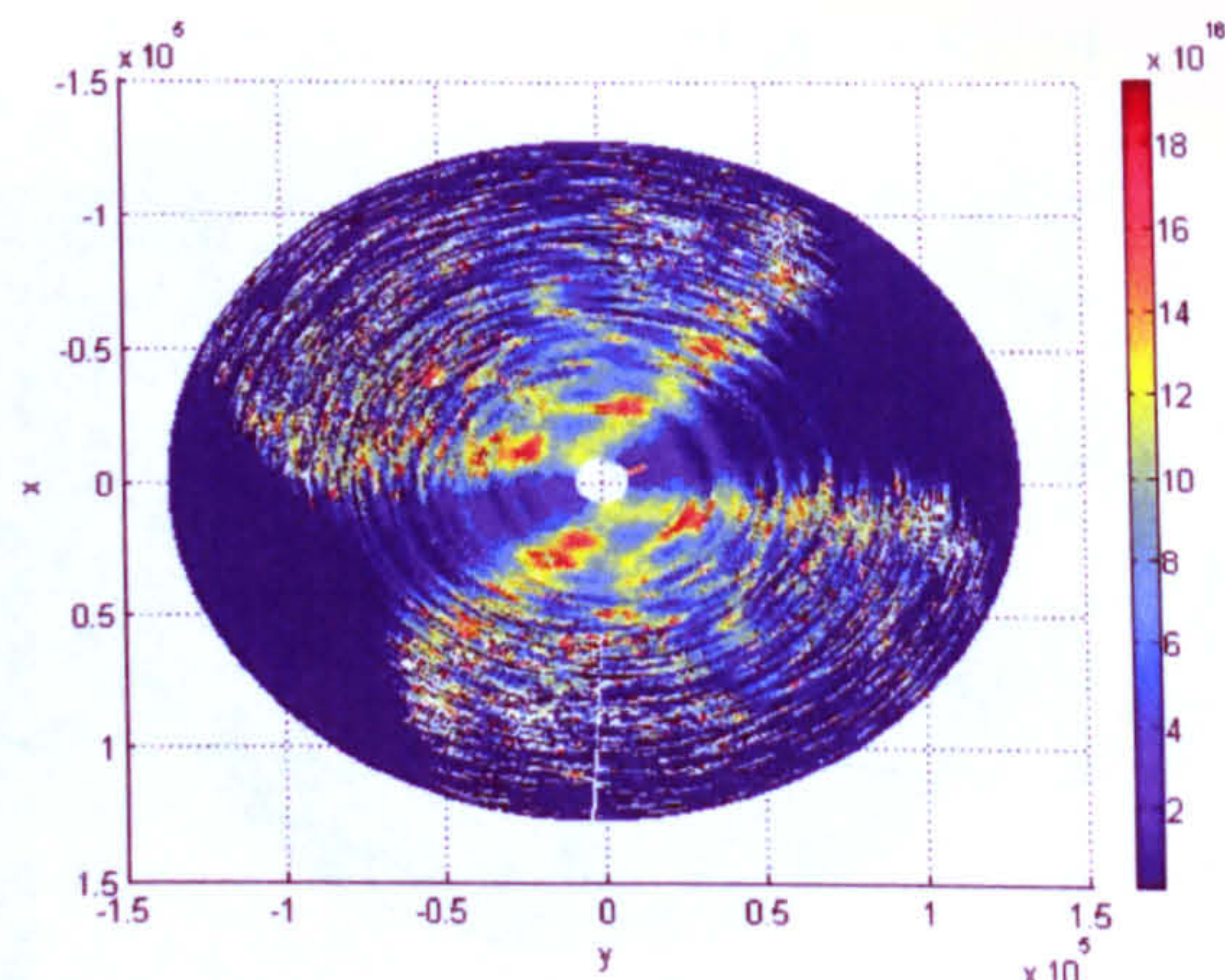


Figure III-25: Inversed slope probability map.

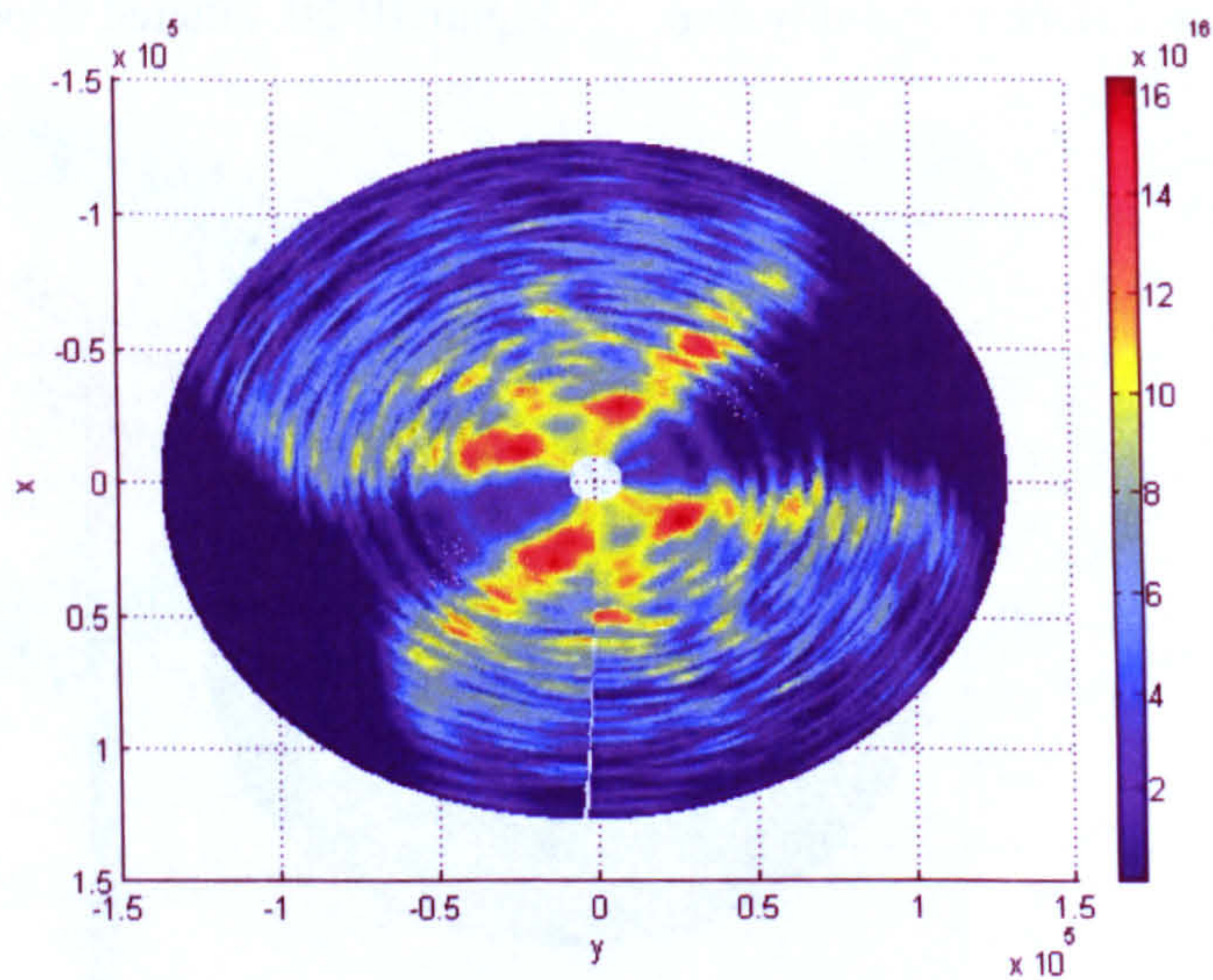


Figure III-26: Filtered slope probability map.